Microstructural Characterisation of Continuously Cooled Steels and Steel Welds

by

Fabio Di Martino

Institute of Polymer Technology and Materials Engineering

Loughborough University

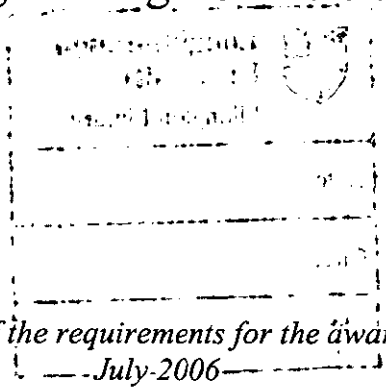

Submitted in partial fulfilment of the requirements for the award of Doctor of Philosophy,
July-2006

Acknowledgements

I would like to sincerely thank my supervisor, Professor Rachel Thomson, for her guidance and support throughout the course of my PhD studies.

I am grateful to both Corus and Loughborough University for the funds provided towards the realisation of this work.

I would like to particularly thank Dr. Graham Thewlis from Corus for his enthusiastic support, and the important contribution made towards this work and Dr Sally Parker from Corus, for her valuable help and suggestions.

I am very grateful to Mr. John Bates, who on several occasions devoted his time to my research work, allowing me to become experienced in the use of scanning electron microscopy.

Many thanks to Mr. David Hall for his cooperation during the use of dilatometry, without which this work would not have been possible; to Dr. David Ross for his unconditional help for several different issues; to Dr. Geoff West for his constant encouragement and help.

I would also like to deeply thank my beloved ones, especially my sister Irene, my mother Antonia and my father Pino, for their great support and for always encouraging me with true passion which was essential in completing this research. I could not have done this without your help!

Last, but not least, I would like to express my gratefulness towards Hula for her unpredictable and unique friendship, for her love and support; towards Daniela for her words, her dishes and for all the time she dedicated to me; towards Mastro Rotafixa for his essential, bare steel; towards all my friends, the amazing people that made my experience here an unforgettable part of my path.

Finally a special moral gratitude to Che, a symbol. Axé.

Abstract

Fe-Mn-Si-C steels are currently the most widely used type of steel for structural, building and automotive applications. Additionally, these steels also find important applications within welded structures, due to their low cost and versatility with regard to chemical composition and heat treatments because of the possibility to tailor their final mechanical properties. The production of a specific component made out of such steels generally involves continuous cooling heat treatments. Therefore, the way in which an optimum balance is achieved between the heat treatment parameters, the alloy composition and the desired microstructure for a specific application, is a vital step in the investigation of Fe-Mn-Si-C steels.

The effects of varying austenitising temperature and cooling rate on the microstructure evolution of Mn-Si low carbon steels have been investigated in this research. This study has focussed on four alloys having similar carbon and silicon contents, but varying manganese contents. Accurate heat treatments were carried out using dilatometry. The application of several different cooling rates (ranging from 2 to 400°C sec^{-1}) and two austenitising temperatures (1100 and 1300°C) produced a wide spectrum of microstructures, originating from both diffusional and displacive reactions. A detailed characterisation of all of the phases present was performed using optical microscopy, scanning electron microscopy (SEM), transmission electron microscopy (TEM), electron back scattered diffraction (EBSD) and micro-hardness measurements. The use of high-resolution/high-magnification techniques for phase identification in continuous cooling heat treatments and steel welds provided an atlas of microstructures, which could be related to existing microstructural classification schemes which are based on optical microscopy investigations.

The identification and complete characterisation of a ferrite-carbide aggregate (FCA) which did not meet any existing classification criterion was achieved. The characteristics of the FCA phase, including its morphology, crystallography, temperature range of formation, influence on other phase transformations and resulting mechanical properties, have been determined.

All of the microstructures produced have been carefully quantified', resulting in the production of CCT diagrams. These diagrams clearly show the effects of austenite grain size, chemical composition and cooling rate on the final microstructures.

The outcome of the research should prove very useful in the development of accurate computer models for microstructural evolution. The results obtained provide a firm foundation for the detailed analysis and prediction of complex microstructures formed under continuous cooling conditions and are applicable to both steels and steel welds.

List of Symbols and Abbreviations

α	ferrite
ΔG	Gibbs free energy
ΔG_m	maximum value of the change in chemical potentials between the two phases.
Δl	variation in length
Δx	variation in carbon composition
γ	austenite
ζ_β	volume fraction of the phase β
B	Bainite
B_0	upper temperature limit for bainite formation
BCC	Body Centred Cubic lattice
B_S	Bainite transformation start temperature
CC	Continuous Cooling (heat treatment)
CCT	Continuous Cooling Transformation (diagram)
EBSD	Electron Back Scattered Diffraction
EBW	Electron Beam Weld
FCA	Ferrite-Carbide Aggregate
FCC	Face Centred Cubic lattice
Fe_3C	cementite
G	constant growth rate
HAZ	Heat Affected Zone
HV	hardness number
I	nucleation rate per unit volume
IPF	Inverse Pole Figure
IPS	Invariant Plane Strain
IT	Isothermal (transformations or heat treatments)
I_v	nucleation rate
LB	Lower Bainite
M	Martensite
MP	Microphase
M_S	Martensite transformation start temperature
NP-LE	Non-Partition Local Equilibrium
p	Péclet number
P	Pearlite
PF	Primary Ferrite

r_c	critical radius of the plate tip, at which growth stops
SEM	Scanning Electron Microscope
SE	Secondary Electrons
t	transformation time
T	Temperature
T_0	locus of points at which ferrite and austenite have the same free energy
T_C	period of time required by a sub-unit to reach its limiting size
T_S	transformation start temperature
TEM	Transmission Electron Microscope
UB	Upper Bainite
V	total volume of the sample
V_c	interface controlled growth velocity of a flat interface
V_β	Volume of the β phase
WF	Widmanstätten Ferrite

Contents

		Page
Acknowledgments		i
List of Symbols and Abbreviations		ii
Abstract		iv
Contents		v
1.	**Introduction**	**1**
2.	**Literature Review**	**6**
	2.1 Phases in Steels	
	2.1.1 $\gamma \rightarrow \alpha$ Transition	9
	2.1.2 Eutectoid Reaction	11
	2.1.3 Ferrite-Carbide Aggregate (FCA)	13
	2.3.1.1 Relevance of FCA in Classification Schemes	15
	2.1.4 Martensite	16
	2.1.5 Bainite	21
	2.1.6 Acicular ferrite	22
	2.2 Bainite Reaction	**24**
	2.2.1 What is Bainite?	25
	2.2.2 Overview of Transformation Mechanism	26
	2.2.3 Morphologies of Bainite	31
	2.2.3.1 Upper Bainite	31
	2.2.3.2 Lower Bainite	33
	2.2.4 Considerations on Surface Relief Effect	34
	2.2.5 Thermodynamics	35
	2.2.6 Kinetics	39
	2.2.6.1 Nucleation of Bainite	40
	2.2.6.2 Growth of Bainite	41
	2.2.6.3 Overall Transformation Kinetics	42
	2.2.7 Carbide Precipitation	43
	2.2.8 Role of Carbon and Other Alloying Elements	45
	2.2.9 Other Theories on Bainite	49
	2.2.10 Unresolved Issues	52

2.4 Continuous Cooling Transformations and Models 53
2.4.1 Thermodynamics and Kinetics Aspects of Transformations in Steel 53
2.4.2 Continuous Cooling Transformations Diagrams 57
2.4.3 Models 60
2.4.4 Weld Microstructures 65

3. Experimental Methods 68
3.1 Introduction 69
3.2 Materials 69
3.3 Sample Preparation 70
3.4 Dilatometry 72
3.5 Optical Microscopy 74
3.6 Micro-Hardness 74
3.7 Scanning Electron Microscopy (SEM) 75
3.8 Electron Back Scattered Diffraction (EBSD) 78
3.8.1 Data Interpretation 81
3.9 Energy Dispersive X-ray Analysis (EDX) 83
3.10 Thermodynamic Calculations 83
3.11 Phase Quantification 84
3.12 Summary 85

4. Heat Treatments 86
4.1 Introduction 87
4.2 TTT Diagram and Austenitisation 87
4.2.1 Austenite Grain Size Effect 88
4.3 Isothermal Heat Treatments 90
4.3.1 Microstructures of Isothermally Treated Samples 91
4.3.2 Discussion of Isothermal Heat Treatments 1300/IT740/10 and 1300/IT740/30 97
4.3.3 Discussion of Isothermal Heat Treatments 1300/IT650/5 and 1300/IT650/30 98
4.3.4 Discussion of Isothermal Heat Treatments 1300/IT530/30 and 1300/IT530/30 104
4.4 Continuous Cooling Heat Treatments 108
4.4.1 Alloy Y7N1, Austenitisation at 1100°C 110

4.4.1.1 Cooling Rate 2°C s^{-1} 111
4.4.1.2 Cooling Rate 5°C s^{-1} 112
4.4.1.3 Cooling Rate 10°C s^{-1} 113
4.4.1.4 Cooling Rate 25°C s^{-1} 115
4.4.1.5 Cooling Rate 50°C s^{-1} 116
4.4.1.6 Cooling Rate 60°C s^{-1} 117
4.4.1.7 Cooling Rate 75°C s^{-1} 119
4.4.1.8 Cooling Rate 100°C s^{-1} 120
4.4.1.9 Cooling Rate 150°C s^{-1} 121
4.4.1.10 Cooling Rate 200°C s^{-1} 122
4.4.1.11 Cooling Rate 400°C s^{-1} 122
4.4.2 Alloy Y7N1, Austenitisation at 1300°C 123
4.4.2.1 Cooling Rate 10°C s^{-1} 124
4.4.2.2 Cooling Rate 50°C s^{-1} 125
4.4.3 Considerations on High Cooling Rate Dilation Curves 127
4.5 Summary 129

5. Microstructural Characterisation: Phases in Steels 130
5.1 Introduction 131
5.2 Analysis of Single Phase Microstructures 132
5.3 Phase Identification 137
5.3.1 SEM Analysis (InLens Imaging) 137
5.3.2 Ferrite 139
5.3.3 Pearlite 142
5.3.4 Ferrite Carbide Aggregate (FCA) 144
5.3.5 Widmanstätten Ferrite 146
5.3.6 Bainite 149
5.3.6.1 Upper Bainite 149
5.3.6.2 Lower Bainite 152
5.3.7 Martensite 155
5.3.8 Tempered Martensite 158
5.3.9 Microphase 160
5.3.10 Features 163
5.3.11 Atlas of Microstructures 166
5.4 Phase Identification for Continuous Cooling Heat Treatments 172
5.4.1 Intermediate Cooling Rate 172
5.4.2 **Austenitisation at 1300°C, cooling at 10°C s-1 173**

5.4.3 Austenitisation at 1100°C, cooling at 10°C s-1 174
5.4.4 Austenitisation at 1300°C, cooling at 50°C s-1 176
5.4.5 Austenitisation at 1100°C, cooling at 50°C s-1 178
5.5 Slow Cooling Experiments 180
5.6 Fast Cooling Experiments 183
5.7 Summary 185

6. FCA Characterisation 186
6.1 Introduction 187
6.2 The Importance of Phase Identification in the Field of Modelling 187
6.3 Observation of Ferrite-Carbide Aggregate (FCA) 188
6.4 Micro Hardness 193
6.5 SEM (InLens) Investigation of FCA 197
6.5.1 Etching Effect 200
6.5.2 Carbide Morphology 201
6.6 Hold-Quench Experiments 203
6.7 TEM Analysis 217
6.7.1 Carbide Morphologies Observed in Thin Foils 217
6.7.2 Matrix Analysis 221
6.7.3 Carbide Morphologies Observed on Replica's 223
6.7.4 Electron Diffraction Patterns 225
6.8 EBSD Analysis 229
6.9 Transformation Sequence 248
6.9.1 Cooling rate of 10°C s-1 248
6.9.2 Cooling rate 50°C s-1 262
6.10 Summary 267

7. Compositional Effects 268
7.1 Introduction 269
7.2 Heat Treatments, dilatometry and optical analysis for alloy HOM146 269
7.2.1 Austenitisation at 1100°C; Cooling Rate of 2°C s^{-1} 260
7.2.2 Austenitisation at 1100°C; Cooling Rate of 5°C s^{-1} 270
7.2.3 Austenitisation at 1100°C; Cooling Rate of 10°C s^{-1} 271
7.2.4 Austenitisation at 1100°C; Cooling Rate of 25°C s^{-1} 271
7.2.5 Austenitisation at 1100°C; Cooling Rate of 50°C s^{-1} 272

7.2.6 Austenitisation at 1100°C; Cooling Rate of 75°C s^{-1} 273
7.2.7 Austenitisation at 1100°C; Cooling Rate of 100°C s^{-1} 274
7.2.8 Austenitisation at 1100°C; Cooling Rate of 150°C s^{-1} 274
7.2.9 Austenitisation at 1100°C; Cooling Rate of 200°C s^{-1} 275
7.3 Heat Treatments, dilatometry and optical analysis for alloy HOM148 276
7.3.1 Austenitisation at 1100°C; Cooling Rate of 2°C s^{-1} 277
7.3.2 Austenitisation at 1100°C; Cooling Rate of 5°C s^{-1} 277
7.3.3 Austenitisation at 1100°C; Cooling Rate of 10°C s^{-1} 278
7.3.4 Austenitisation at 1100°C; Cooling Rate of 25°C s^{-1} 278
7.3.5 Austenitisation at 1100°C; Cooling Rate of 50°C s^{-1} 279
7.3.6 Austenitisation at 1100°C; Cooling Rate of 75°C s^{-1} 280
7.3.7 Austenitisation at 1100°C; Cooling Rate of 100°C s^{-1} 280
7.3.8 Austenitisation at 1100°C; Cooling Rate of 150°C s^{-1} 281
7.3.9 Austenitisation at 1100°C; Cooling Rate of 200°C s^{-1} 281
7.4 High-magnification analysis of alloy HOM146 282
7.5 High-magnification analysis of alloy HOM148 288
7.6 Morphology of Precipitates 303
7.7 The Effects of Manganese 304
7.8 Alloy HOM133 Analysis 310
7.9 Summary 315

8. Thermodynamics of the FCA Formation and Kinetics of the Continuous Cooling Transformations 316
8.1 Introduction 317
8.2 Thermodynamic Considerations of FCA, Bainite and Martensite 317
8.2.1 Variation of the M_S Temperature 317
8.2.2 Variation of the T_S Temperature 318
8.3 Role of Carbon in the FCA Formation 323
8.4 Isopleth: Section of a Phase Diagram 326
8.5 Size Effect on Pearlite and FCA 329
8.6 Transformation Sequence 332
8.7 Phase Quantification 334
8.8 Discrepancies between Predictions and Measurements 347
8.9 CCT Diagrams 350
8.10 Summary 360

9. Conclusions and Further Work 361

9.1 Conclusions 362

9.1.1 Microstructural Evolution during Continuous Cooling 362

9.1.2 Characterisation of FCA and Solution to Classification Scheme Problems 364

9.1.3 Transformation Sequence Assessment 366

9.1.4 Compositional Effects 367

9.1.5 Thermodynamics and Kinetics Considerations 368

9.2 Further Work 369

10. Reference List 371

1. Introduction

1. Introduction

Fe-Mn-Si-C steels are currently the most widely used type of steel for structural, building and automotive applications. Additionally, these steels also find important applications within welded structures, due to their low cost and versatility with regard to chemical composition and heat treatments because of the possibility to tailor their final mechanical properties. The production of a specific component made out of such steels generally involves continuous cooling heat treatments. Therefore, the way in which an optimum balance is achieved between the heat treatment parameters, the alloy composition and the desired microstructure for a specific application, is a vital step in the investigation of Fe-Mn-Si-C steels.

The effects of continuous cooling heat treatments on the final microstructure are extremely important if a tight control of the heat treatments has to be achieved in order to minimise processing costs and optimise the material properties. The use of continuous cooling heat treatments often produces complex microstructures and involves simultaneous phase transformations, therefore the main market-driven requirements are the understanding of the mechanisms governing the simultaneous transformations, the identification of each phase forming during cooling and, finally, the development of predictive models. Such models have the potential to minimise production costs through an effective and reliable prediction of the final properties of a component as a function of composition and heat treatment parameters. Furthermore, a study of continuous cooling processes in steels is believed to be of great relevance because the kinetics of simultaneous phase transformations is the subject of ongoing investigations, in an attempt to identify all of the necessary thermodynamic and kinetic parameters.

The starting point for the understanding of simultaneous transformations and the development of predictive models is the complete characterisation of the phases formed during cooling. This is a fundamental step in order to define the microstructural evolution and the subsequent study of the transformation kinetics. The fact that the transformation conditions under continuous cooling are different from the isothermal case makes the application of the characterisation of phases formed isothermally inadequate in some cases. For this reason, knowledge of phases formed under isothermal conditions cannot directly be extended and applied to the continuous cooling situation. The assessment of the nature of a phase is usually aided by classification schemes which have been developed with the aim of

characterising complex microstructures resulting from equally complex heat treatments. However, these classification schemes generally refer to optical microscope analysis. This approach can be very effective for most of the phases formed during cooling, however, it is not sufficient when very fine phases or features (such as microphases) have to be identified. In this context, the use of techniques capable of high resolution and high magnification offers the advantage of a detailed morphological observation for each phase at very high magnifications, which reveals microstructural features which are otherwise impossible to observe. On the other hand, the fact that the existing classification schemes are based on specific characteristics of phases analysed optically, requires a link to be made between the morphology of such phases with those observed via scanning electron microscopy (SEM) and transmission electron microscopy (TEM). An extensive classification of phases performed by means of high magnification techniques is also required due to the lack of information currently available, which can then be linked to the existing classification schemes based on optical observation.

The approach used for the development of existing models for microstructural evolution is usually based on the knowledge of isothermal transformation kinetics. This has been extended to the case of continuous cooling heat treatments, assuming a successive series of isothermal steps. As a result, the main parameters applied to isothermal transformations are still regarded as valid in order to predict the phases formed during continuous cooling. However, there is an intrinsic limitation in this approach, which is represented by the fact that some phases can only form under continuous cooling conditions and their thermodynamics and kinetics are not well known, and neither is their influence on the overall microstructural evolution.

The main aim of this research was to gain a fundamental understanding of each of the phases formed during continuous cooling and the factors determining their formation. In particular, the analysis of low carbon Mn-Si steels heat treated under continuous cooling conditions concentrates on the full characterisation of phases, which do not fit into any existing classification, eventually present in the final microstructures. This issue is particularly important in the category of phases that are generally referred to as ferrite-carbide aggregate. This represents a phase which is not predicted by existing models and it has an impact on the final properties of the alloy. Furthermore, the necessity of assessing the nature of each phase forming during cooling and understanding under which conditions the phase forms is important because it influences all the of the other phases forming during cooling, and the final mechanical properties of an alloy.

A literature review, focussed on the most relevant aspects of Fe-C-Mn-Si steels, phase classification, welds and models was undertaken during this work and is presented in chapter 2.

From an experimental point of view, this research study initially focussed on the microstructural characterisation of a number of low carbon steels, containing different amounts of silicon and manganese, which were heat treated under several different conditions, as discussed in chapter 4. Attention was focussed on two heat treatment parameters: austenitising temperature variation and cooling rate variation. In this way, a wide range of microstructures was obtained and a detailed study of the microstructural evolution was carried out.

This was followed by a systematic characterisation of phases formed during continuous cooling heat treatment, by exploiting the potential of investigation techniques with very high resolution. This part of the research, discussed in chapter 5, contributed to improvement of the accuracy of existing classification schemes, and it allowed for a complete characterisation of a microphase, otherwise impossible through the conventional schemes based on optical microscopy.

The complete characterisation of the FCA phase involved the use of dilatometry in conjunction with microhardness testing, SEM, TEM and EBSD, as discussed in chapter 6. Each of the experimental techniques provided results which were then linked in order to determine conclusively the morphology of this phase, its nature, crystallographic characteristics, orientation characteristics and finally the position of the phase formation within a suitable transformation sequence.

The effects of varying composition and, in particular manganese content, on the transformations and final microstructures are described in chapter 7. This aspect of the investigation provided a better understanding of the formation of FCA, and the effects of each phase transformation on the other phases.

Finally, the principles underlying in the FCA formation are discussed in chapter 8, linking all of the experimental evidence which was presented in the previous chapters with thermodynamic predictions. Furthermore, a detailed phase quantification analysis is presented. This has been related to the transformation sequence and resulted in the production of CCT diagrams for the alloys studied, also including all the phase fields identified. The importance of the CCT diagrams is significant in order

to understand the final microstructures in relation to the heat treatments, in addition to the kinetics of the phase transformations taking place during cooling.

The conclusions drawn from this research are presented in chapter 9, together with a discussion of the possible areas for its future development.

2. Literature Review

2.1 Phases in Steel

The starting point of any analysis regarding steel, which is the most widely used metallic material for its versatility in properties as well as production processes, is the iron-carbon equilibrium phase diagram. The main features of the phase diagram are fundamental for the comprehension of the behaviour of any steel, even the most complex. Although it is constructed from knowledge of thermodynamic equilibrium conditions, it represents an essential foundation for transformations taking place under non-equilibrium conditions that lead to the formation of metastable phases[1, 2]. A typical phase diagram for a plain carbon steel is shown below:

Figure 2.1[1, 2]*: The iron-carbon (iron-cementite) phase diagram*

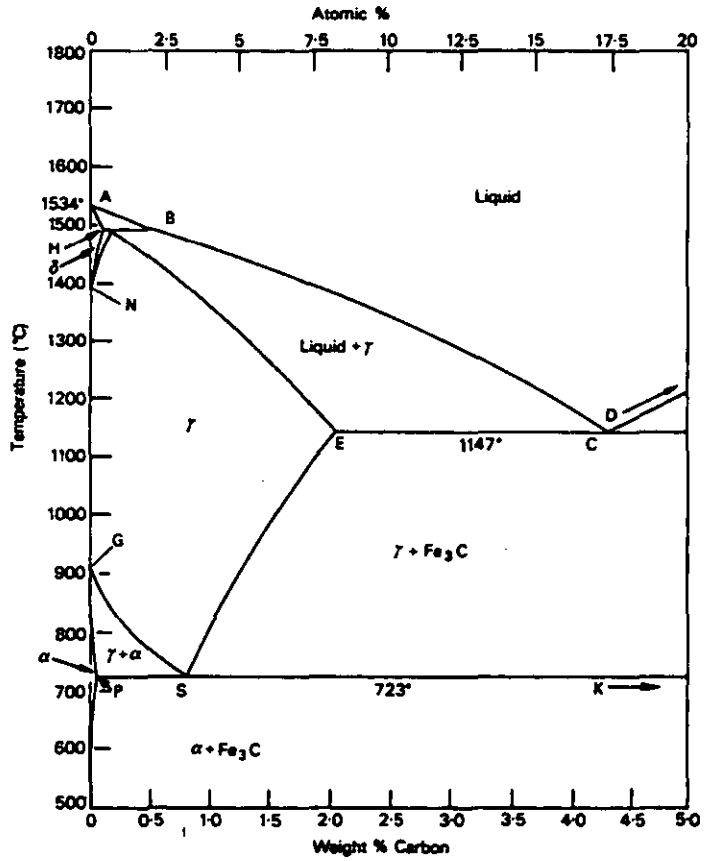

The diagram shown in figure 2.1 represents the metastable equilibrium between iron and iron carbide, cementite. This stoichiometric compound, Fe_3C, forms when the carbon solubility in iron is exceeded. The carbon content of cementite is 6.67

wt.%, which corresponds to 25 at.% C. It is very hard and brittle and influences the properties of the steel, depending on its amount, size and shape.

As iron undergoes allotropic transformations, different phase fields relating to different crystal structures can be identified in the phase diagram. The high temperature body centred cubic (bcc) phase which forms just after solidification is called δ-ferrite. Further cooling leads to the formation of a face centred cubic (fcc) crystal of iron which is called austenite or γ. At lower temperatures, the lattice structure transforms again into body centred cubic, and is named α-ferrite, or simply ferrite, as it is of much greater practical importance than δ-ferrite.

The fcc structure and the larger lattice parameter of γ compared to the bcc structure of ferrite, allows a much easier accommodation of interstitial carbon atoms in solid solution. For this reason, the maximum solubility of carbon in austenite is 2.11 wt.% C (point E in the diagram) whilst a maximum level of 0.02 wt.% C (point P) is possible in α-ferrite. The major characteristics of the binary phase diagram derive directly from this solubility difference for carbon.

Critical points (i.e. important transformation temperatures) can be identified in the diagram. The first of these is the eutectoid temperature, 723°C, at which the eutectoid reaction takes place. At this temperature, indicated as the A_1 temperature in the diagram, austenite transforms to a eutectoid mixture of ferrite and iron carbide. The carbon content at the eutectoid in the binary system is 0.77 wt.% C (point S). Secondly, the A_3 temperature is the one at which ferrite first appears upon cooling. It can be seen that the A_3 point varies depending on the carbon content in a binary system (from point G to point S in the diagram), and, more generally, on the alloy composition in a multicomponent system. The A_3 temperature for pure iron occurs at 910°C (point G) whereas it coincides with the A_1 (point S) temperature for eutectoid steels[2]. Finally, the A_4 and A_2 points represent respectively the temperature at which γ transforms to δ-ferrite, 1390°C for pure iron (point N), and the Curie temperature at which iron changes its magnetic behaviour from ferromagnetic to paramagnetic, which is 769°C for pure iron. It should be emphasised that the transformation temperatures are sensitive to the conditions imposed, i.e. cooling, heating or equilibrium. Therefore, depending on the heating cycle adopted to detect the critical points, different values can be found. The major factors influencing these changes are the heating or cooling rates, and the alloy composition.

2.1.1 $\gamma \rightarrow \alpha$ Transition

Steels can be classified as hypoeutectoid, eutectoid and hypereutectoid according to their carbon content[2, 3]. In hypoeutectoid steels, the primary (or proeutectoid) microconstituent formed, in the two phase field $\alpha + \gamma$ at temperatures higher than the eutectoid, is primary ferrite. On the other hand, in eutectoid steels, the structure is constituted of pearlite as discussed in section 2.1.2. Finally, cooling a hypereutectoid alloy through the two phase field, $Fe_3C + \gamma$, will produce cementite as the primary microconstituent. Generally speaking, further slow cooling through the eutectoid temperature produces a mixture of pearlite in a ferritic matrix in hypoeutectoid steels and a mixture of pearlite in a cementite matrix in hypereutectoid steels. The intrinsic brittleness of the iron carbide matrix may require further heat treatment in the case of a hypereutectoid steel in order to improve the mechanical properties.

The alloys used in this research are typically low carbon, therefore, the main microconstituent on which attention will be focused is primary ferrite. Two different forms of ferrite forming via a diffusional mechanism exist: allotriomorphic ferrite and idiomorphic ferrite[2]. The first category, which forms at the highest temperatures (800-850°C), includes all forms of ferrite which are crystalline in internal structure but not in outward form. It implies that the limiting surfaces of the crystal are not regular and that they do not display the symmetry of its internal structure. Thus allotriomorphic ferrite, which nucleates at prior austenite grain boundaries, tends to grow along the γ grain boundaries at a faster rate than in the direction normal to the boundary plane, so that its shape is strongly influenced by the presence of the boundary and hence does not necessarily reflect its internal symmetry. There is a well defined orientation relationship between a grain of allotriomorphic ferrite and the γ grain on which nucleation occurs. This is a typical Kurdjumov-Sachs[1, 2] relationship of the following type:

$$\{1\ 1\ 1\}_\gamma \ // \ \{1\ 1\ 0\}_\alpha$$
$$\{1\ -1\ 0\}_\gamma \ // \ \{1\ -1\ 1\}_\alpha$$

This type of orientation relationship is maintained until the temperature permits the mobility of curved or random γ-α boundaries to dominate with respect to a coherent interface. At lower temperatures the latter dominates and the growth characteristics

change leading to different morphology, typical of Widmanstätten ferrite as it will be discussed later.

Idiomorphic ferrite nucleates intragranularly, for instance on the surface of inclusions, which represent high free energy points for nucleation. The crystals of idiomorphic ferrite are usually equiaxed and can possess irregular curved boundaries or have a defined crystallographic orientation relationship[2]. Typical microstructures of allotriomorphic and idiomorphic ferrite are shown in figure2.2a-b respectively.

Figure 2.2[2]: *a) Allotriomorphic ferrite, 0.34C steel* *b) Idiomorphic ferrite, 0.34C steel*

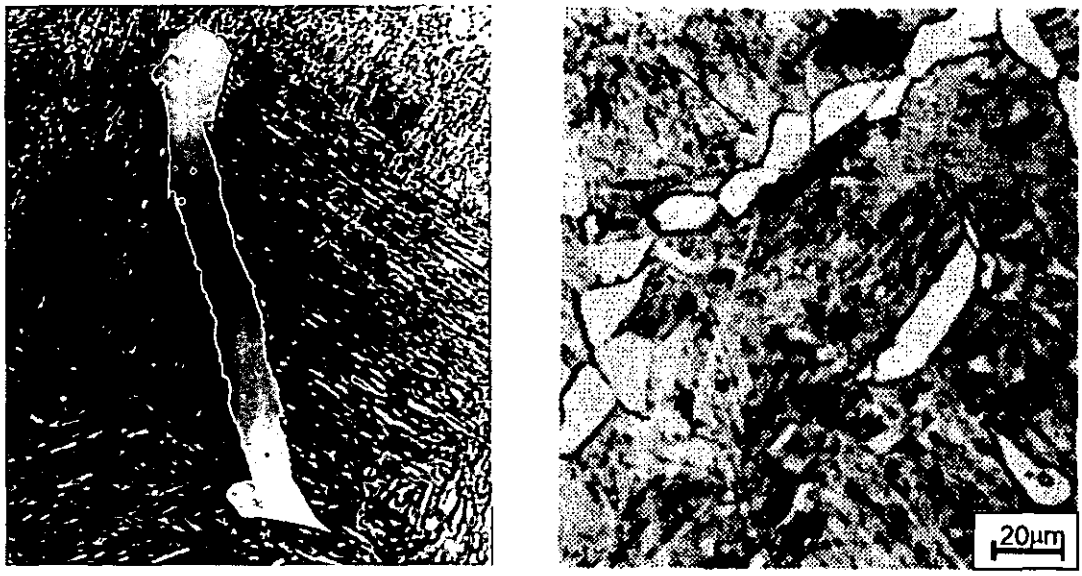

In addition to the two categories discussed above, there are two other types of ferrite which nucleate at lower temperatures and higher degrees of undercooling and grow generating a sideplate or lath morphology. Widmanstätten ferrite (WF) nucleates either at austenite grain boundaries (GB) or on pre-existing allotriomorphs. Their growth follows well defined matrix planes. Ferrite plates can also nucleate entirely intragranularly, having the same characteristics of Widmanstätten ferrite growth kinetics.

Figure 2.3[2, 4]*: a) WF nucleated on allotriomorphic ferrite b) Intragranularly nucleated WF*

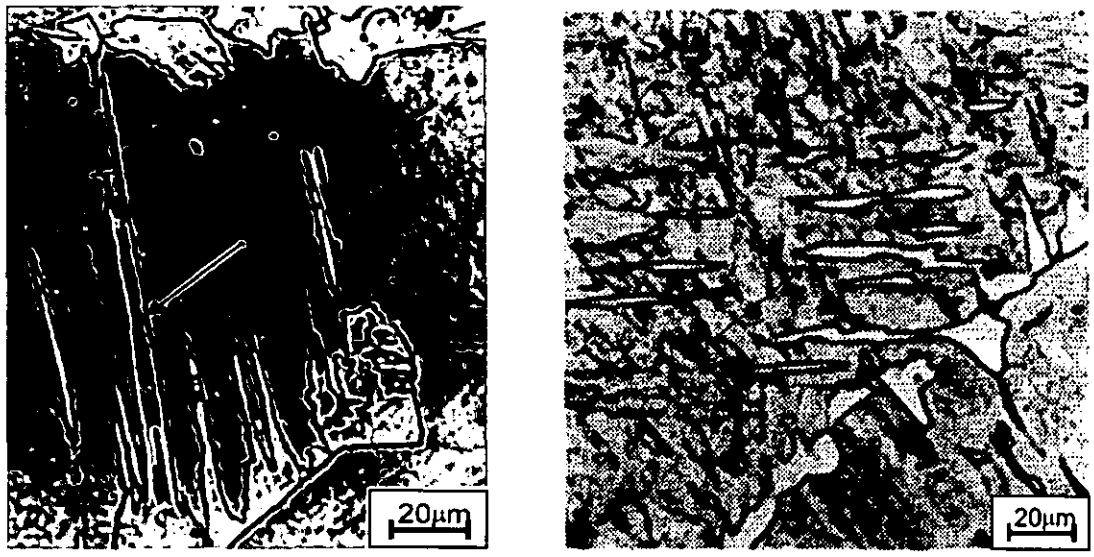

Primary Widmanstätten ferrite grows directly from the austenite grain boundaries, whilst secondary Widmanstätten ferrite grows from protuberances on primary ferrite grain boundaries. The laths grow into the austenite grains maintaining the Kurdjumov-Sachs relationship. Primary Widmanstätten ferrite is favoured by large austenite grain boundaries which prevent impingement of primary ferrite and allow room for growth of the ferrite laths. The most important parameter affecting the growth of Widmanstätten ferrite is the temperature, determined either by the cooling rate or the isothermal transformation temperature, depending on the type of heat treatment. The presence of a coherent or semicoherent interface with matrix, in addition to a surface relief effect that accompanies the growth of the ferrite laths suggests that the characteristics of the formation of Widmanstätten ferrite can be associated with a displacive type of transformation which has common characteristics with bainite. Indeed, often the distinction between the two phases (especially upper bainite) can be very difficult.

2.1.2 Eutectoid Reaction and Pearlite

A eutectoid reaction can be defined as an invariant solid-solid reaction through which one solid transforms to a mixture of two solid products at constant composition. In the case of a plain carbon steel having a composition of 0.77 wt.% C, on cooling under equilibrium conditions (i.e. very small rate of change of temperature) through the eutectoid temperature, the fully austenitic structure

transforms at a constant composition into a mixture of α-ferrite and cementite which differ in carbon content:

$$\gamma_{(0.77\ wt.\%C)} \rightarrow \alpha_{(0.0218\ wt.\%C)} + Fe_3C_{(6.67\ wt.\%C)}$$

Hence, carbon diffusion under equilibrium conditions takes place redistributing itself between the two phases with the restriction of the maximum solubility in ferrite. As lattice reconstruction is kinetically favoured by short diffusion distances, the growth of the two phases occurs simultaneously and the resulting structure is lamellar. This mixture of α and Fe_3C developed in the iron carbon system is called pearlite. In the case of hypoeutectoid steels, primary ferrite forms first, enriching the surrounding austenite with carbon. The carbon content eventually reaches the eutectoid composition, causing the remaining austenite (whose amount is determined by the lever rule) to transform into pearlite. If the steel is hypereutectoid the precipitation of cementite as primary constituent depletes the carbon content of the untransformed austenite. Analogously to the case of hypoeutectoid steels, eventually the austenite carbon content reaches the eutectoid composition leading to the formation of pearlite via eutectoid decomposition of the remaining austenite. Figure 2.4 shows a typical pearlitic structure of a eutectoid steel which transformed via eutectoid reaction into a ferritic/pearlitic structure.

Figure 2.4[5]: *Pearlite lamellae*

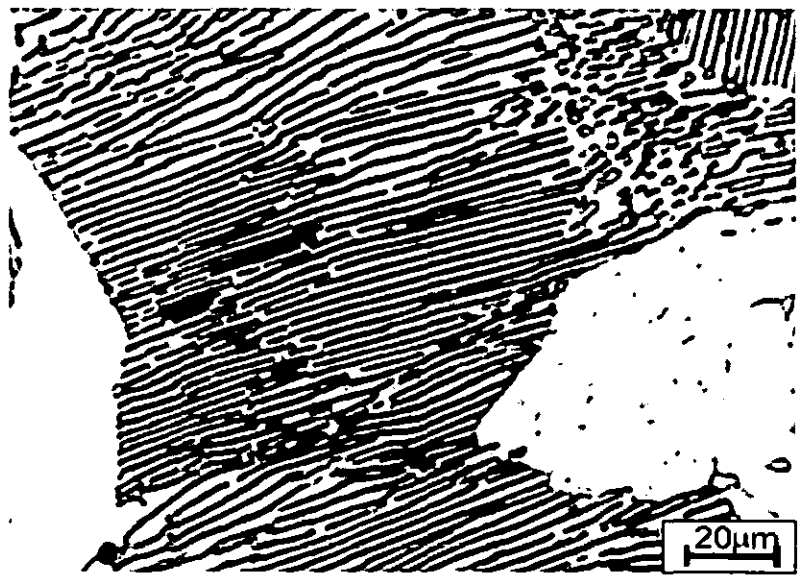

The lamellae spacing in pearlite is an important parameter in determining the mechanical properties of the steel produced. It is very sensitive to transformation temperature as expected. The diffusion distances increase as the transformation temperature approaches the equilibrium eutectoid temperature. Therefore, by increasing the degree of undercooling, the lamellar spacing decreases and the diffusion of carbon takes place over shorter distances.

2.1.3 Ferrite-Carbide Aggregate (FCA)

A significant part of the present research has been dedicated to the identification and classification of a phase which did not appear to fit any classification scheme. This phase is extensively discussed in chapter 6. An example of this phase is shown in figure 2.5.

Figure 2.5[6]*: Ferrite carbide aggregate, a phase which has not been in a universally recognised way by previous researchers*

Many previous works that have been studied, did classify the dark etching FCA phase in different ways. It is therefore important to resolve the unanswered questions about the FCA phase to improve classification schemes and to understand its formation mechanism. Furthermore, the analyses have generally been limited to optical microscopy, whereas SEM imaging under InLens detection conditions appears to not have been applied to this problem. In a previous work, the FCA are defined as martensite/austenite regions (M/A) or pearlitic regions between *granular bainite* grains[7-10]. Granular bainite is a term frequently used to describe the bainite that occurs during continuous cooling transformation. This terminology is used widely

in industry, where most steels undergo non-isothermal heat treatments. The microstructure forms gradually during cooling, resulting in rather coarse sheaves of bainite. The optical microstructure then gives the appearance of blocks of bainite and austenite, so that it is appropriate to use the adjective "granular". A characteristic (although not unique) feature of granular bainite is the lack of carbides in the microstructure. Instead, the carbon that is partitioned from the bainitic ferrite stabilises the residual austenite, so that the final microstructure contains both retained austenite and some high carbon martensite in addition to the bainitic ferrite.

The study of austenite decomposition carried out by Garlipp utilising the Jominy test, defines the FCA, present in microstructures formed at cooling rates of 10 and 50°C s^{-1}, as "probable bainite"[6].

In an investigation on steels with very similar composition to that of alloy Y7N1 carried out by Ming-Chun Zhao[11, 12], FCA in the sample cooled at 50°C s^{-1} were considered as cementite and "island constituents" e.g. 'M/A' which is considered as coexisting austenite and martensite. These type of structures known as M/A are associated with the retained austenite which enriches in carbon as the bainitic plates grow and is partially retained to room temperature while a certain amount transforms to martensite upon further continuous cooling. In the same study, in the samples cooled at 1°C s^{-1} the resulting mixed microstructure, constituted of acicular ferrite, ferrite and pearlite, and the FCA present at the boundaries was classified as pearlite.

The work of Wu on HSLA steels[13] show a phase which is similar to the FCA however has also been classified as pearlite in some cases or a mixture of bainite and acicular ferrite[14]. A number of authors have dealt with microstructures formed on continuous cooling. The work of Lemaire, Copreaux and Roch[15] is the one that is most closely related to the present work. The authors identify fibrous cementite precipitation in low carbon manganese (1.9 wt.%) steels. The alloy tested received continuous cooling heat treatments under unspecified conditions. In their study some calculations based on interphase precipitation have tried to relate the precipitation of carbides in the FCA with a possible transformation theory. The hypothesis of interphase precipitation has been considered, although this type of precipitation theory has been developed for micro-alloyed steels (e.g. with Vanadium additions). The approach has been to link the diffusion length of carbon to the ledge motion which would take place if interphase precipitation would be the mechanism involved in the formation of FCA. The critical austenite carbon content to allow precipitation should be the same as the one in the carbide. The results showed that there is a certain agreement between the spacing between two arrays of carbides and the

diffusion length of carbon. However, the model on which the calculations are based would not take into account the fact that the temperature is varying and therefore the local conditions vary at the same time. Furthermore, the interphase type of precipitation would relatively explain the morphology of the FCA at low cooling rates, but it wouldn't at higher cooling rates, where the carbides appear more disordered and in many cases interconnected.

2.1.3.1 Relevance of FCA in Classification Schemes

The development of predictive models able to indicate with confidence the microstructure formed in alloys which are continuously cooled and in heat affected zones (HAZ) in the welding field, is today a challenging field of research and one of the present work's aims is to contribute to the enhancement of such models. The complexity of the microstructure formed, especially in HAZ, represents the main obstacle, both for the understanding of the kinetics governing the simultaneous transformations taking place during cooling, as well as the accurate identification of each microstructural constituent which affects the final properties of the alloy. The characterisation of any complex microstructure goes beyond the mere phase identification exercise, and indeed the aid of classification schemes is usually needed. The main schemes regarding HAZ microstructures are the International Institute of Welding (IIW) microstructure classification scheme for weld metals and the classification schemes developed by G. Thewlis for HAZ microstructures and continuously cooled steels microstructures. The mechanisms of formation of the principal structures and the characteristic ferrite morphologies produced in the reconstructive and displacive transformation regimes of ferrous materials are usually described in classification schemes and each phase is referred to with an appropriate and unique terminology (usually using acronyms). The identification of a phase can be usually achieved by means of flow charts with guidelines for identifying the principal structures.The classification schemes are extremely useful tools which, if properly used, can lead to a rapid and conclusive identification of a phase by means of light microscopy. The present work provides an indication of those aspects of the classification schemes which need to be implemented. It should be noted that not only does the classification of a phase its identification, but also the knowledge of the nature of the phase and therefore its influence on the properties of the whole microstructure in question.

An example of the use of classification schemes is the identification of ferrite-carbide aggregates and the meaning of its classification. The pearlite classification includes a ferrite-carbide aggregate phase which is supposed to form as the temperature is lowered, as a result of thinning, distortion and bending of the lamellae. This definition does not explain clearly the relationship between the pearlite and the ferrite carbide aggregates, nor does it provide information about the actual appearance of the phase and the transformation mechanism. The phase is currently thought of being part of the category of pearlite. However, in order to conclusively classify it, further experimental evidence is needed, so as to establish any potential similarities and/or differences with other phases, such as pearlite and lower bainite. Furthermore, although not possible to be resolved by means of light microscopy, ferrite carbide aggregates formed under continuous cooling conditions in low carbon, low alloy steels have been previously identified as pearlite or lower bainite. This highlights the level of uncertainty still present in some areas.

In light of the considerations just made, it appears that two main problems should be addressed in the context of classification schemes: one is related to the unequivocal link between a unique and accurate classification of a specific phase, and the knowledge of the nature of this phase, together with its effects; the other one is the need to identify criteria to allow for the phase classification of regions not easily resolved optically, such as micro-phases.

2.1.4 Martensite

This chapter has so far considered the products of transformations close to equilibrium conditions. The rearrangement of atoms possible in such transformations, however, is controlled by the imposed cooling rate and the actual temperature at which the transformation can take place. High cooling rates (e.g. line AB in the TTT diagram in figure 2.6) can lead to the formation of metastable phases, that from a thermodynamic point of view do not represent the most stable and therefore the lowest free energy structures, are able to form from a kinetic point of view. From the TTT diagram for a eutectoid steel, shown in figure 2.5, it can be seen that low temperature reactions may lead to the formation of different phases with different transformations mechanisms (M_S dotted line in the TTT diagram).

***Figure 2.6[2]**: TTT diagram for a eutectoid steel*

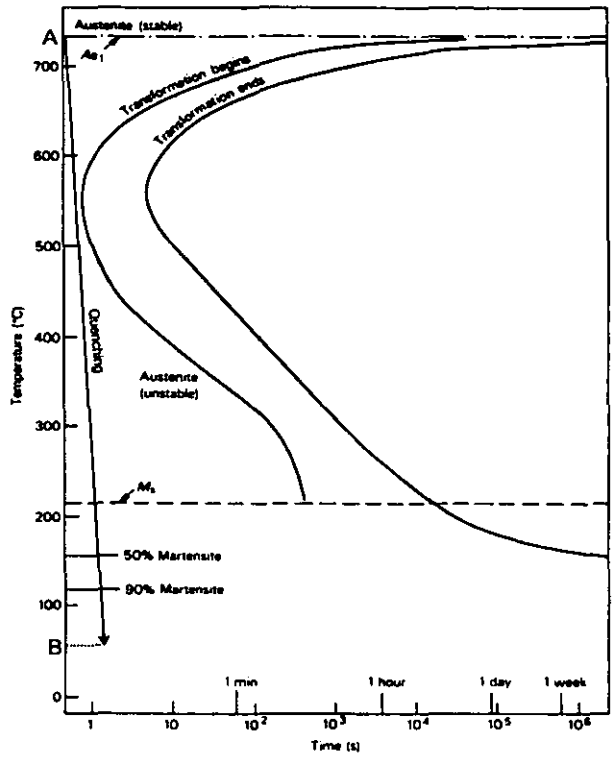

When diffusion of carbon atoms (and therefore by implication the diffusion of substitutional atoms) is prevented by very high cooling rates and low transformation temperatures, a supersaturated solid solution of carbon in iron, called martensite, forms. Martensite is a phase that results from a diffusionless solid state transformation mechanism. As it is not diffusion, but shear that determines the reaction characteristics, the martensite reaction is an athermal transformation. Generally speaking, athermal transformations are independent of time, proceed without thermal activation and are a function of the transformation temperature.

The lattice change occurs via a shear mechanism which transforms the fcc crystal in a body centred tetragonal (bct) crystal whose lattice parameters 'a' and 'c' vary as a function of the carbon content of the austenitic parent phase. When the carbon content of the supersaturated solution of carbon in iron tends to zero, a bcc crystal structure is formed, as the lattice distortions caused by the presence of excess carbon are reduced, and eventually eliminated. A schematic of the tetragonal unit cell identified in the austenite lattice can be seen in figure2.7:

Figure 2.7*[2]*: Lattice correspondence for martensite formation from austenite

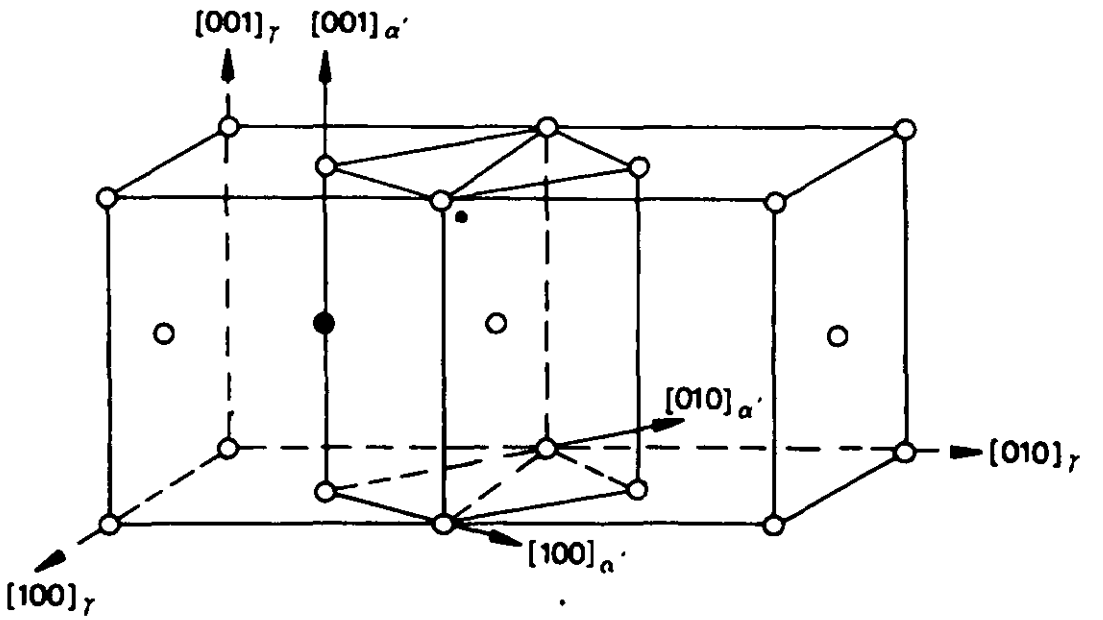

The shear process occurs via a lattice invariant deformation, which can be of two types: twinning or slip. A twin in a crystalline solid occurs between two adjacent regions of the same crystal lattice, where one of the regions is related to the other by a simple shear[16]. On the other hand, a shear mechanism caused by slip takes place when the passage of many slip dislocations on parallel slip planes causes a microscopic deformation. The two mechanism are shown in figure 2.8.

Figure 2.8*[2]*: Lattice invariant deformations, slip and twinning

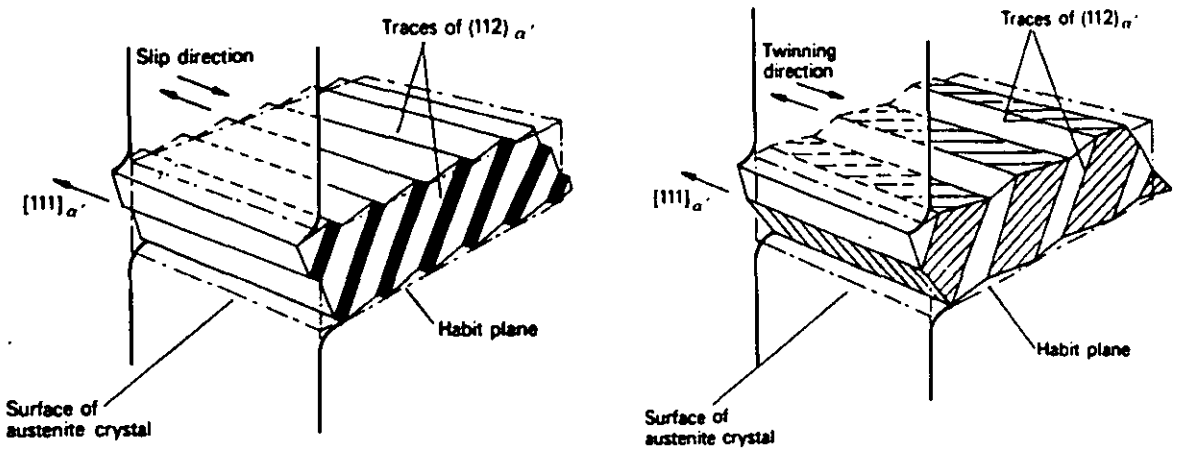

The driving force for martensite formations, which is an athermal transformation characterised by a shear mechanism, derives from the free energy difference

between austenite and martensite, the strain energy and the interfacial energy between the γ matrix and martensite. The conditions at the interface are described as paraequilibrium, for which the phase fractions and compositions are uniquely fixed representing the minimum free energy state in the absence of substitutional element partitioning i.e. equal composition of the parent and product phase[16, 17]. However, although martensite formation is classically considered to be diffusionless as implied by paraequilibrium, there is evidence of carbon diffusion between martensitic ferrite and retained austenite as demonstrated by recent researches[18].

The nucleation rate of martensite is relatively low whilst the growth rate is extremely high, as occurs in athermal transformations. As no long range diffusion can take place during a martensitic transformation, the reaction product must have the same composition as the parent phase. A transformation start temperature (M_S) and a transformation finish temperature (M_f) can be identified for martensite, which vary depending on the alloying composition. A valid empirical relationship for predicting the influence of alloying elements on M_S found by Andrews[2], is the following:

$$M_S\ (°C) = 539 - 423\ (\%C) - 30.4\ (\%Mn) - 17.7\ (\%Ni) - 12.1\ (\%Cr) - 7.5\ (\%Mo)$$

As the carbon content of the steel increases, eventually the interstitial carbon atoms cannot be accommodated in a bct structure and the γ lattice is stabilised down to very low temperatures.

Typical microstructures of martensite observed optically at different magnifications are shown as follows.

Figure 2.9[4]: *Martensitic microstructures; as quenched (right); particular of martensite plates (left)*

The origin of the microstructure of martensite is the cause of a very high strength which is however impaired by a very high brittleness deriving from the elevated

internal stresses due to the heavily dislocated plates or laths. Therefore, in order to optimise the mechanical properties of martensite, keeping the advantage offered by the very high strength, heat treatments are usually performed. Tempering processes are usually performed on as-quenched martensite by re-heating it. Tempering causes diffusion which is the main factor influencing the various tempering stages. Four distinct stages, which overlap in some cases, can be identified during tempering[2, 16]:

- *stage 1*: up to 250°C precipitation of ε-carbide followed by partial loss of tetragonality of the lattice;
- *stage 2*: between 200 and 300°C the decomposition of austenite takes place;
- *stage 3*: between 200 and 350°C ε-carbide evolves to the more stable cementite whilst martensite loses its tetragonality;
- *stage 4*: above 350°C cementite coarsens and spheroidises whilst recrystallisation of ferrite takes place, drastically reducing the dislocation density.

Tempering greatly improves the toughness of the steel due to the characteristics of the final microstructure i.e. spheroidised cementite and recrystallised ferrite. However, as the tempering is conducted until the fourth stage, the strength and hardness of the steel decrease considerably.

Carbide precipitation can be influenced by the application of externally applied stresses during the tempering process. As the magnitude of the applied stress is increased, the number of crystallographic orientation variants decreases, becoming unique when the steel is subjected to large stresses (between 500 and 950 MPa)[19].

It should be noted that the formation of ε-carbide, is possible during so-called auto-tempering. This phenomenon is very similar to the first stage tempering, but it occurs upon cooling from M_S to room temperature. Naturally, the extent of auto-tempering is more appreciable in steels with high M_S, such as the commercial Fe-C-Mn low alloy YZN1 steel.

ε-carbides usually form from the parent martensite phase upon low temperature tempering. These carbides possess hexagonal symmetry and their stoichiometry is variable in the range 25 – 33.3%. The origin is related to martensite supersaturation which leads to internal stresses that, in turn, lead to lattice relaxation via carbide precipitation[16, 19]. The orientation relationship found between the carbides and the martensitic matrix is the one found by Jack[20]:

$$(0\ 1\ 1)_{\alpha}\ //\ (0\ 0\ 1)_{\varepsilon}$$
$$(1\ 1\ -1)_{\alpha}\ //\ (-1\ 2\ 0)_{\varepsilon}$$
$$(1\ -1\ 1\ )_{\alpha}\ //\ (3\ -1\ 0)_{\varepsilon}$$

Precipitation of ε-carbide has been also reported in austenite prior to tempering. This phenomenon has been hardly reported in literature due to the very low diffusivity of carbon in austenite at the low transformation temperatures of ε-carbide precipitation. The structure presents ε-carbides as tiny particles "decorating the planar arrays of closely space dislocations (tempering at 300°C)". An explanation for such an unusual phenomenon is based on austenite enrichment by interstitials during isothermal holding[21].

A study performed on low alloy steels[21] showed that the precipitated phase appears as thin ribbons which are often paired, in addition to a dependence of ε-carbide precipitation on defects such as microtwins present in the martensitic structure. Past studies have shown that the hexagonal lattice symmetry of the ε-carbides can evolve to the more ordered orthorhombic structure, referred to as η-carbide or ε'-carbide as a derivative of the ε-carbide structure[19].

2.1.5 Bainite

The presence of a wide temperature range between the reconstructive bay and the martensite start temperature in the TTT diagram shown in figure2.5 indicates the possibility of formation of other types of microstructures[1]. In this region, the microstructure that forms is characterised by the plate morphology of the ferrite and the presence of cementite that precipitates as particles. This phase is generally called bainite, after Bain who first identified its presence. In the case of athermal transformations, at cooling rates slower than that needed for the formation of martensite, but higher than the ones that allows pearlite formation, bainite forms. In the case of isothermal transformations, the formation of bainite usually occurs in the temperature range of 250-550°C. However, this is strictly linked to the alloy composition and the transformation conditions. The nature of bainite changes as the transformation temperature changes. Two main morphologies can be identified. Upper bainite occurs at higher transformation temperatures and is characterised by the presence of carbides only between the ferrite plates. Lower bainite forms at lower temperatures and is characterised by the precipitation of cementite particles

additionally within the ferrite plates as the diffusion distances possible are shorter. The nature of bainite will be discussed in details in the following chapter as it forms a major focus of this research programme.

2.1.6 Acicular Ferrite

Some of the most exciting recent developments in wrought and welded steel technology has involved "acicular ferrite"[2]. Generally speaking this is a chaotic structure constituted of intragranularly nucleated ferrite plates. Heterogeneous nucleation occurs on non-metallic inclusions from which growth of different plates occurs along various directions from the nucleation points. The chaotic structure, compared to the other structures characterised by ferrite plates such as Widmanstätten ferrite and bainite, offers a higher resistance to cleavage cracking. Acicular ferrite is thought of as a desirable microstructure which leads metallurgists to voluntarily add non-metallic inclusions (usually titanium nitride cores surrounded by glassy phase containing manganese, silicon and aluminium oxides) in order to control intragranular nucleation, making it energetically favoured with respect to the competitive mechanism of grain boundary nucleation. The main factors controlling acicular ferrite formation are[14]:

- the retarding of the nucleation and growth of ferrite at the austenite grain boundaries
- the encouragement of a high nucleation rate on inclusions and dislocation substructures in the intragranular regions

In respect of the first factor, fully acicular structures can be achieved by inhibition of grain boundary nucleation as demonstrated for microalloyed forging steels[22]. Furthermore, it has been observed that boron variations have a profound effect on the intragranular nucleation of ferritic plates, at a given austenite grain size[14].

The second factor needs some clarification. Generally speaking, the dislocation substructure caused by different thermal contractions of the inclusion in steels (continuously cooled), may provide additional sites for intragranular nucleation of ferrite through a reduction in the total strain energy. In this sense, the most effective inclusions are $MnOSiO_2$, Al_2O_3 and MnS[14].

The appearance of acicular ferrite in three dimensions is lenticular, which becomes plate like when observed in two dimensions[1, 2] with an aspect ratio approximately of 0.1, although this argument is quite controversial.

The comparison between a low alloy steel containing low titanium and high titanium is shown in figure 2.9a-b. The structure for the low Ti addition is mainly constituted by bainitic ferrite which is a structure which possess a higher degree of order, whereas the structure for the high Ti addition is mainly acicular ferrite. In figure2.10c-d are shown a typical non-metallic inclusion and acicular ferrite plates intragranularly nucleated at inclusions.

Figure 2.10[23]*: a) Bainitic structure*

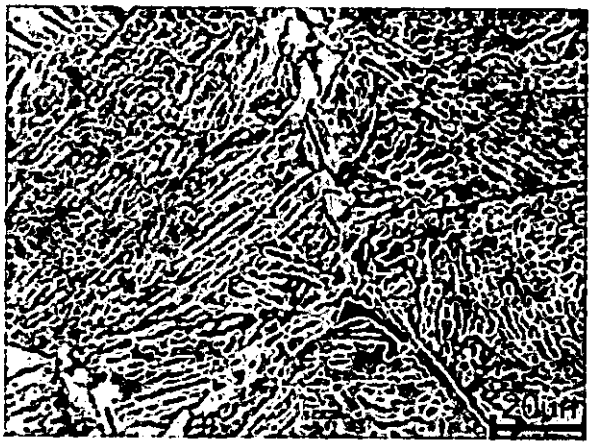

b) Acicular ferrite structure

Figure 2.10[1]*: c) Non-metallic inclusion*

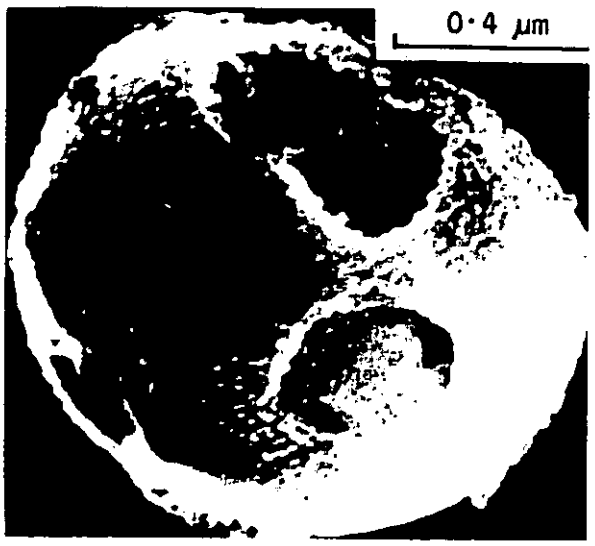

d) Acicular ferrite plates

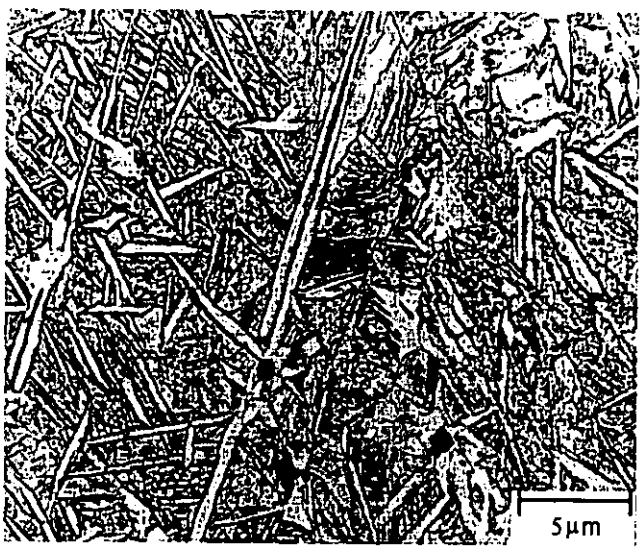

One of the most accredited theories on the nature of acicular ferrite is that this phase is intragranularly nucleated bainitic ferrite[19]. This hypothesis has been

investigated in an interesting way by Bhadeshia[14, 24] In order to prove this, the mechanism of transition from upper to lower bainite has been researched in the case of acicular ferrite in welds with high carbon content. Metallography confirmed the presence of cementite particles within the acicular ferrite plates which in turn is characteristic of a transition from "upper acicular ferrite" to "lower acicular ferrite" comparable to the bainitic transition.

2.2 The Bainite Reaction

The transition from reconstructive transformations to displacive transformations is not sudden. In fact, a gradual change in temperature from the diffusional transformation range causes gradual change in transformation conditions. The thermodynamic properties, e.g. chemical potential of a particular phase, specific volume, composition, and the kinetic parameters, e.g. activation energy for a transformation, diffusivity of a species, driving force for a transformation, gradually change. These strongly influence which product phase is favoured to form at a certain temperature, as well as the transformation mechanism. Between the two extreme transformation products formed via a diffusion based mechanism, i.e. ferrite/pearlite, and via a purely displacive mechanism, i.e. martensite, exists a wide temperature range between approximately 250 and 550°C within which the formation of a new microstructural constituent is observed. Its morphology is a result of neither a purely reconstructive nor a purely displacive mechanism and its peculiar morphology consists of fine aggregates of ferrite plates and cementite particles[2]. The formation of bainite is also possible via athermal treatments, by applying cooling rates high enough to prevent pearlite or ferrite formation and lower than that required for martensite formation. Depending on the transformation temperature, two different morphologies of bainite are possible. Upper bainite, which is characterised by the eventual presence of carbides *between* the ferrite plates, forms in the temperature range 400 - 550°C. Lower bainite, which is characterised by the presence of carbides between and *within* the ferrite plates, forms in the temperature range 250 - 400°C. Both phases have the common characteristic of ferritic plates or laths, aggregated to form so-called sheaves of bainite.

2.2.1 What is Bainite?

The research of several workers has led to the possibility of defining bainite in three different ways, depending on the point of view under which the bainite reaction is analysed[25]. A description of bainite referring to the microstructural characteristics of the reaction product can be summarised as follows:

- *bainite is the product of a competitive mechanism of eutectoid decomposition;*

This definition implies that the formation of bainite that usually takes place in the temperature interval between 250°C and 550°C, occurs via a non-lamellar non-cooperative mechanism. This leads to the formation of two reaction products i.e. ferrite plates or laths and cementite particles, whose growth kinetics are different.

Another definition of bainite from consideration of the overall reaction kinetics affirms that[25]:

- *bainite possesses its own C shaped curve on a TTT-diagram lying below the pearlite C curve in appropriately alloyed steels;*

This definition needs some qualifications because in Fe-C and some Fe-C-X diagrams, where X stands for a substitutional alloying element, the bainite curve extensively overlaps with the pearlite curve. On the TTT diagram, a bainite start temperature, B_S, can be identified (although there is some controversy about the identification of a unique transformation start temperature[26]. As the isothermal transformation temperature approaches the B_S temperature the bainite reaction becomes increasingly incomplete, the proportion of bainite being relative to the amount of ferrite phase allowed by the lever rule. As expected, the bainite reaction totally ceases as the B_S temperature is reached and does not take place at all at higher temperatures.

The third definition of bainite relates to the typical surface relief effect observed after the transformation on a polished surface:

- *the growth process of bainitic ferrite plates occurs by means of either a martensitic mechanism at growth velocities in excess of that allowed by carbon diffusion controlled processes or by a martensitic transformation of the iron lattice paced by interstitial diffusion of carbon atoms;*

The latter definition has been supported by evidence of a displacive transformation mechanism similar to the martensitic one, characterised by an invariant plane strain surface relief effect (IPS SRE)[1, 26-29], the characteristics of which will be discussed in more detail in the following section. It has however been argued that the bainitic transformation presents well defined characteristics of shear in the lattice change from the FCC to the BCC structure, but that these cannot always be regarded as IPS and therefore related to martensitic type of transformations[25, 30-33].

It should be highlighted that whilst the first definition of bainite, based on microstructural features requires the presence of two microstructural constituents i.e. ferrite and cementite, the other two definitions include the possibility of a bainite structure entirely constituted of ferrite.

The three descriptions of bainite given above are directly related to views of the bainite reaction that in many instances are not in agreement in some case are in direct opposition. This derives from the fact that to date no clear and definitive evidence appears to have been presented that could entirely confirm one theory with respect to the others, although extensive research has been performed in the bainite field (this is also supported by the fact that many prediction models based on assumptions not entirely verified and approximation factors, truly predict the bainite transformation characteristics only under certain circumstances). This has given rise to an interesting controversy regarding the way the bainite reaction can be explained and therefore modelled for practical applications, leaving a wide range of interpretation possibilities still open. In the present research programme, the most widely accepted theory explaining bainite formation and its main characteristics will be presented, Different point of view will be treated as well in order to provide a more complete overview of the issues regarding the bainite reaction.

2.2.2 Overview of Transformation Mechanism

Bainite nucleation occurs similarly to martensite, but it is accompanied by interstitial carbon partitioning[1, 34, 35] After a stable nucleus forms, the growth of a bainitic plate occurs via a martensitic mechanism, followed by rejection of carbon. For this reason, the bainite reaction is defined to take place under partial supersaturation conditions. The diffusionless growth is possible thanks to a decrease in the surface to volume ratio. The relatively high temperatures involved in the upper bainite transformation, however, provide enough energy to carbon in order to overcome the activation energy for interstitial diffusion. Therefore, the excess carbon

is rejected into the residual austenite, soon after the FCC → BCC phase change has taken place. The carbon then precipitates from the enriched austenite, leading to the presence of cementite between the bainitic plates, typical of the upper bainitic morphology. On the other hand, as the transformation temperature lowers, the carbon mobility gradually decreases, up to a temperature at which the structural transition from upper to lower bainite takes place. The carbon which no longer has the opportunity to partition into the surrounding austenite, precipitates within the plates, from the supersaturated ferrite, giving the typical lower bainitic appearance[1, 34, 35]. The two processes, which are a function of the transformation temperature, are schematically shown in figure 2.11 below.

Figure 2.11: *Schematic illustration of Upper and Lower Bainite Formation*

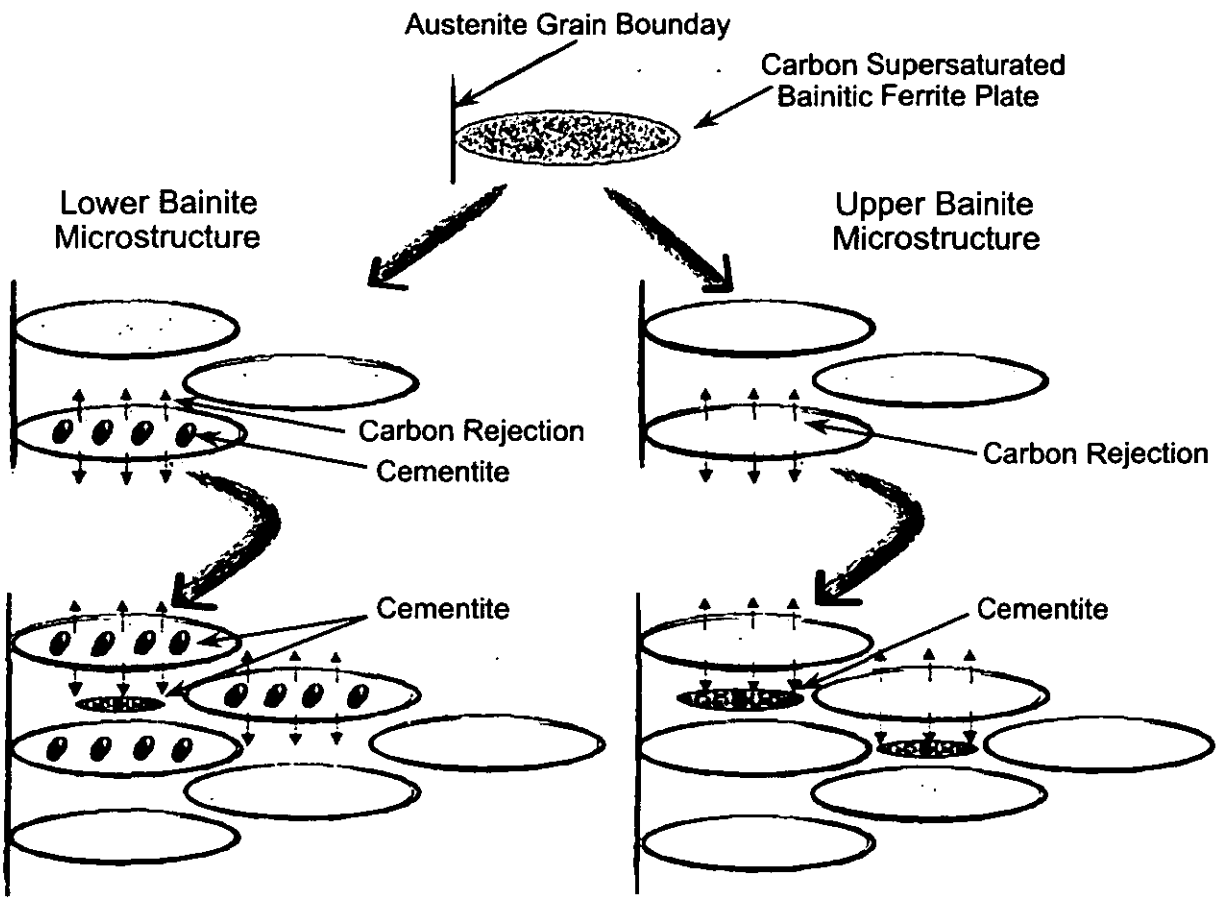

The qualitative representation in figure 2.10 demonstrates that the bainite reaction involves four different processes:

- Diffusionless bainitic ferrite formation from austenite
- Carbon rejection from the bainitic ferrite plates to surrounding austenite
- Carbide precipitation from enriched austenite

- Carbide precipitation from partially supersaturated ferrite

This leads to the necessity of dealing with simultaneous transformations when modelling the bainite reaction which has made this task a difficult one, as will be discussed later in section 2.3.

Another factor to consider is the characteristic invariant plain strain deformation associated with the transformation of bainite. An invariant plane strain (IPS) is the result of the combined effects of lattice deformation and lattice-invariant deformation . It is characterised by the fact that a single plane, the habit plane, is neither rotated nor distorted as a consequence of the transformation taking place. In the case of bainitic transformations it is characterised by the tilting of a free surface about the intersection lines with a plate of bainitic ferrite[1]. An IPS implies that the tilting of a free surface has to be homogeneous on a macroscopic scale, implying that a net atomic displacement has taken place. However, in order to set the significance of a net atomic displacement in the context of a displacive transformation the maximum tolerable extent of diffusion that can take place has to be assessed. Indeed, the occurrence of diffusion with some appropriate restriction does not directly mean that a reconstructive transformation is taking place. In general terms, when a shape change (homogeneous deformation), caused by a net atomic displacement, takes place, a lattice correspondence can be identified. This means that a series of corresponding vectors exists between the two unit cells of the parent and product phase structures. It should be noted that a lattice correspondence does not necessarily imply an atomic correspondence in the lattices. For this reason, the diffusion of interstitial atoms, either short or long range, does not affect the lattice correspondence. On the other hand, the diffusion of the solvent i.e. iron atoms, and of the substitutional atoms has to occur over distances that allow the preservation of a lattice correspondence, otherwise the transformation can be classified as reconstructive. This is possible by means of the displacement of solvent and substitutional solute atoms among the sites specified by the lattice correspondence i.e. without creating or destroying any specified site. Experimental evidence, together with crystallographic theories, has led to the conclusion that a convincing transformation mechanism of bainite formation in accordance with the conditions explained above is a martensitic type change[1, 2] i.e. IPS with large shear component. Such a coordinated movement of atoms cannot take place across grain boundaries and that is why bainite plate growth is confined within the prior austenite grain boundary where nucleation has taken place. This is quite different from the

characteristics of reconstructive transformations, such as allotriomorphic ferrite formation, which usually imply the formation of a new grain boundary structure[34].

A schematic of an IPS of a lattice invariant deformation, characteristic of martensitic transformations is shown in figure 2.12:

Fig2.12[1]*: Schematic illustration of the phenomenological theory of martensite crystallography*

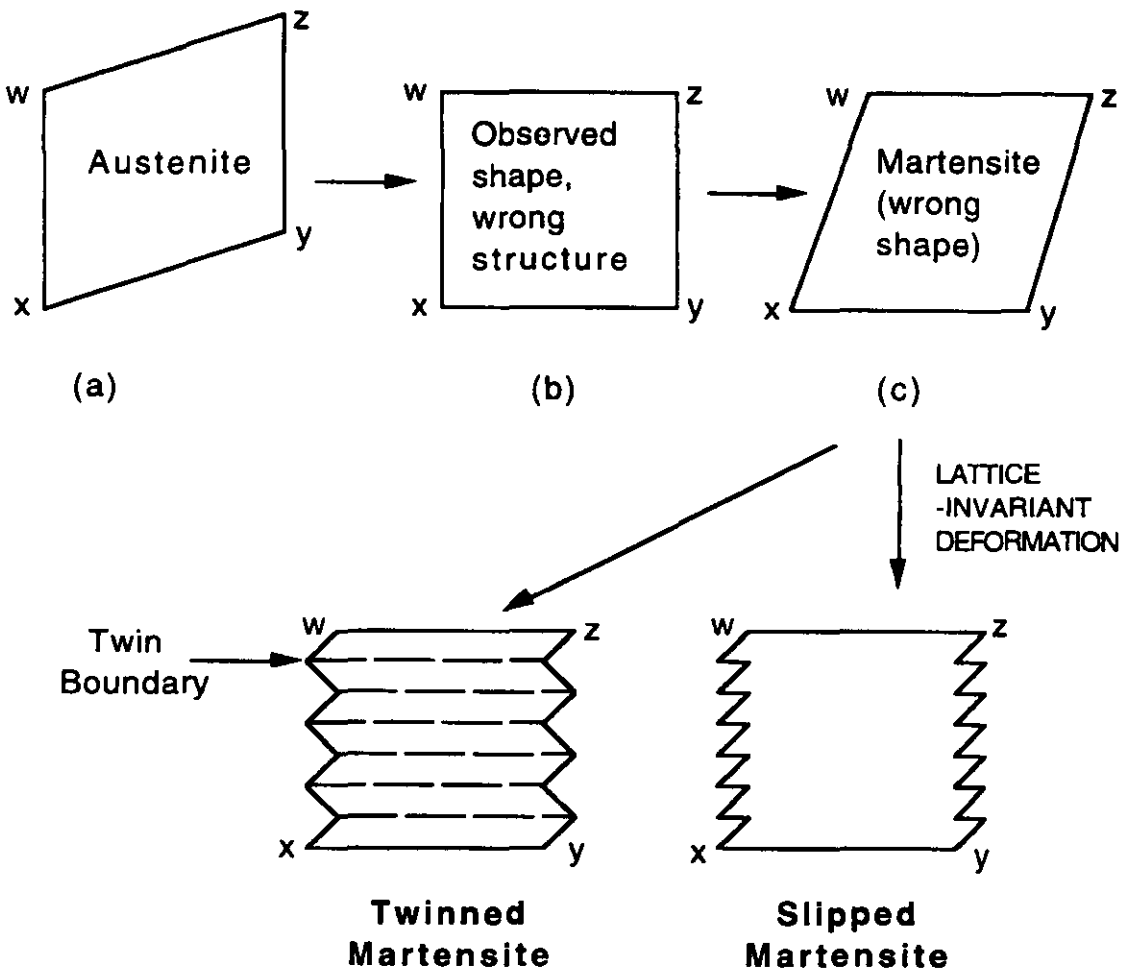

The result of an IPS on a free surface of bainitic ferrite analysed by means of high resolution atomic-force microscope can be seen in figure2.13.

Figure 2.13[1]*: Displacement caused by the shape change associated with a sub-unit formation (atomic mass force spectroscopy measurement)*

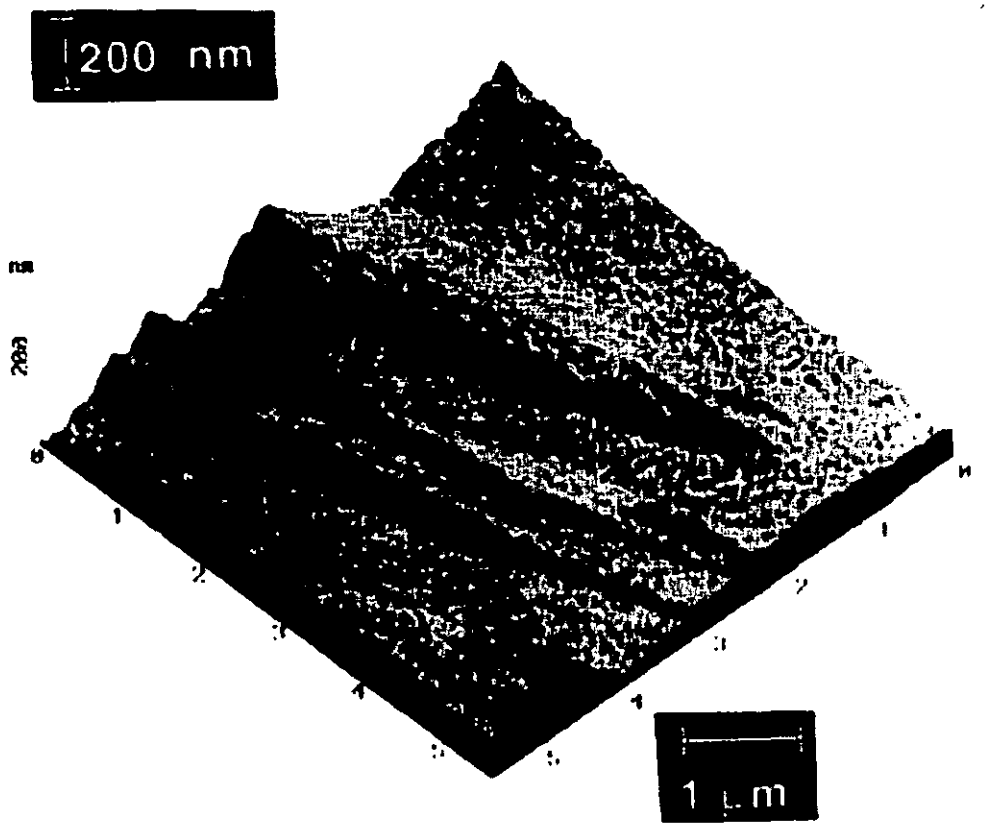

The shape deformation associated with the transformation causes induced plastic accommodation in the austenite surrounding the ferrite plate. As a consequence, the coherency of the transformation interface is lost and this in turn causes the transformation to stop prematurely. For the transformation to proceed, the nucleation of a new bainitic ferrite plate is necessary. This results in the typical sheaf microstructure of bainite[34].

As mentioned earlier, the partitioning of substitutional elements does not occur even at the finest measurable scale using atom probe field ion microscopy. This supports the point of view that the bainite reaction is essentially a displacive transformation[34].

Another important characteristic associated with the bainite reaction is the observation of the incomplete reaction phenomenon which takes place in alloys containing elements that prevent any carbide precipitation in the case of upper bainite e.g. high silicon alloys. In these steels, the transformation stops when it becomes thermodynamically impossible[34]. This interesting phenomenon will be explained in more detail in the following sections.

The morphology of the plates is the result of a strain energy minimisation process due to the shape change. The formation of ferrite via a reconstructive mechanism at

very low growth rates is possible by continued annealing of the bainitic ferrite-residual austenite mixture for long periods.

These are the main characteristics linked to the bainite reaction. A more detailed analysis is presented in the following sections.

2.2.3 Morphologies of Bainite

Depending on the transformation temperature, it is possible to make a distinction between two different morphologies of bainite because of their associated features. At higher transformation temperatures, the bainite reaction product is called *upper bainite*[1, 2] whilst at lower transformation temperatures, the reaction product is called *lower bainite*[1, 2].

2.2.3.1 Upper Bainite

Generally speaking, the dimensions of the plates within a single sheaf of upper bainite are of the order of 0.2 μm thick and 10 μm in length.

The upper bainite (figure 2.14) is usually obtained in the temperature range 400-550 °C. The high temperatures involved allow excess carbon diffusion in the growth stage of each plate, towards the surrounding austenite. This avoids the precipitation of carbides within a single lath, leading to the presence of precipitates only between the plates. Nucleation of ferrite plates begins at kinetically favoured sites, which, in the absence of inclusions, are represented by the austenite grain boundaries. The plates grow in parallel arrays which form sheaves. Each individual ferrite plate constituting a sheaf is usually called sub-unit, having a well defined crystallographic habit[1, 2].

The growth of each plate is characterised by an IPS which causes the surrounding austenite to plastically deform. In fact, at the high transformation temperatures, the austenite is not capable of maintaining the shape change accompanying the transformation. The strain produced is relaxed by the plastic deformation which causes a local increase in dislocation density at the transformation interface. This is responsible for the premature halt of the sub-unit growth although from a thermodynamic point of view, a lower free energy level could be achieved if the ferrite plates could grow further, the kinetic barrier makes the growth of a single

sub-unit restricted to a size which is much smaller than the size of an austenite grain. [1, 2]. Naturally, the resistance to growth is greater as the strength of the austenite increases.

The displacive origin of the bainitic transformation, suggested by the shape change associated with the sub-unit growth, is responsible for an orientation relationship between parent phase and product. The Kurdjumov-Sachs type orientation relationships based on experimental data support the hypothesis that a pair of the most densely packed planes of the two lattices is approximately parallel, as is a corresponding pair of close-packed directions within those planes. A difficulty in identifying an orientation relationship is represented by the fact that the habit planes determined experimentally by means of optical facilities, are the results of an average of the habit planes of each sub-unit constituting a sheaf of bainite. The scattering resulting by this factor in addition to the variation in habit plane due to temperature, chemical composition and transformation time makes the identification of a better defined orientation relationship between austenite and bainite still difficult to obtain.

The upper bainite formation presents two distinct stages, the diffusionless formation of a ferrite plate and the sudden rejection of carbon into the surrounding austenite. Since this gets enriched in carbon, eventually, cementite precipitation either in the form of discontinuous particles or continuous film depending on the carbon concentration[1, 2]. High silicon, or aluminium alloys preserve the austenite at room temperature by avoiding carbides precipitation.

Figure 2.14[36]***:*** *Upper bainite microstructure. Bainitic plates surrounded by martensite*

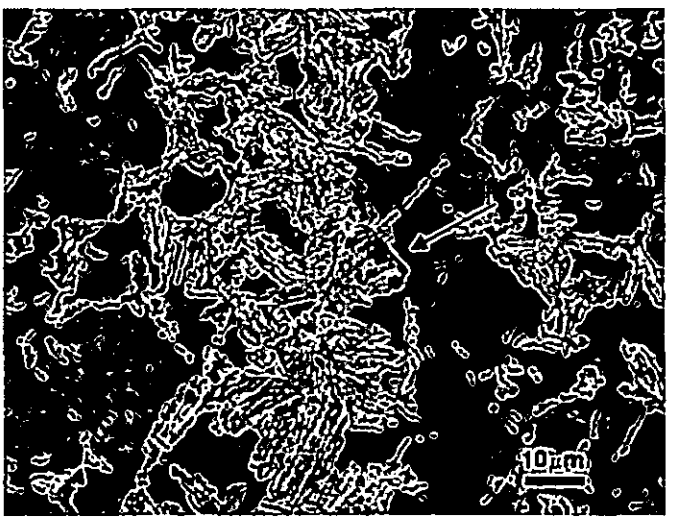

2.2.3.2 Lower Bainite

If the bainite reaction takes place at temperatures in the range 250-400 °C the transformation product assumes the characteristics of lower bainite. The main morphological characteristic distinguishing lower bainite from upper bainite is the presence of cementite particles inside the plates.

This morphological feature (figure 2.15) is a direct consequence of the transformation kinetics. The lower reaction temperature results in a reduced energy of the carbon atoms, compared to the case of upper bainite, which prevents sufficient amount of carbon from diffusing/partitioning into the austenitic phase. Therefore, some of the carbon precipitates directly from the growing bainitic ferrite which is supersaturated, because the carbon solubility in ferrite of 0.02 wt.%. This type of precipitate has to be distinguished by those precipitating from the carbon-enriched austenite. The main consequences of the lower diffusivity of carbon at lower reaction temperatures are the extremely fine dimensions of the carbides and their distribution. Usually, the thickness of a cementite particle in lower bainite is of the order of few nanometres while the length is about 500 nm. In terms of mechanical properties, fewer and finer cementite particles between the plates increase toughness by a crack deflection mechanism in the case of crack propagation along the sub-units boundaries. It is well known that the coarser cementite particles present in upper bainite often offer a high activation energy site for crack nucleation, as their surface is larger. Overall, the lower bainite tends to be tougher and stronger than upper bainite due to the carbide characteristics and the sub-units and sheaves dimensions.

Figure 2.15[36]***:*** *Lower bainite microstructure. Bainitic laths surrounded by martensite*

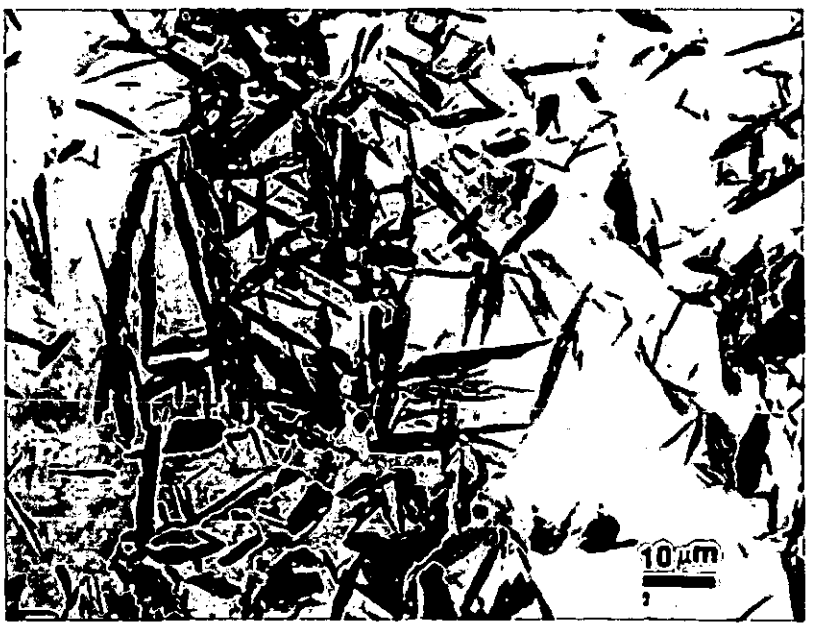

2.2.4 Considerations on the Surface Relief Effect

A peculiar characteristic associated with the bainite reaction is the phenomenon of the shape change, which is very important for the determination of the bainitic transformation mechanism. Indeed, the understanding of the shape change characteristics can provide useful information regarding the displacive or reconstructive nature of the transformations, as well as information about the strain energy associated with the transformation.

In the case of bainite the totals absence of diffusion of any type of atoms is excluded, although it presents the martensitic characteristic of displacive transformation. Partition of interstitial atoms is in fact permitted, without affecting the IPS shape change. The diffusion of substitutional atoms as well as the iron atoms is supposed to occur just over few interatomic distances. The experimental observation supports the idea of minimal substitutional atom diffusion and the presence of a semi-coherent and glissile interface between the bainitic plates and the surrounding austenite therefore leading to the conclusion that a displacive transformation mechanism[1] applicable to the bainite reaction.

At this point, it should be noted that there exists quite a considerable criticism of the theory reported above with respect to the significance of the surface relief effect.

The work of Aaronson[32] has led to the conclusion that a sessile interfacial structure on the broad faces of bainitic ferrite plates is present. This observation was derived through both modelling and TEM for the observation of the dislocation structure on the broad face of a ferrite lath. It was observed that the sessile structure consisted of misfit dislocations whose Burger's vector was never pure screw. It has been argued that the sessile interface is the result of a transformation of the former glissile interfacial structure forming during bainite growth, when the samples are quenched. However, although a sessile interface possesses a lower energy structure, it seems highly unlikely that this can provide a sufficient driving force for such a large scale change in interface dislocation structure[32].

As a consequence of these conclusions obtained by Aaronson, the ferrite formation could not take place by means of a martensitic type of transformation whose necessary condition is the presence of a glissile dislocation structure that can allow an IPS surface relief. On the basis of considerations made by Christian and Cahn[32], the presence of a sessile interface does not prevent the bainitic ferrite to preserve a lattice correspondence with the parent phase. This is supported by the fact that the surface relief encountered in bainite is considered as being tent shaped

and not IPS, therefore being incompatible with a martensitic type of transformation and implying at the same time a ledgewise diffusional growth mechanism.

Another view of the surface relief effect supporting a ledgewise growth mechanism for bainite is discussed in the work carried out by H. S. Fang[31]. The observation of the microstructure of bainite laths and plates by means of TEM and STM techniques suggests that ultra fine structures can be identified in bainite, so called sub-sub-units whose width is of the order of 30 nm, which was defined in Fang's work as the minimal structural constituent of bainite. The implications of this observation for the surface relief characteristics are the fact that the latter is actually constituted of smaller surface relief corresponding to the ultra fine structures and the fact that the nature of the relief is a tent shape suggesting that growth mechanism of bainite is based on sympathetic nucleation and edgewise growth[31]. This is supported by the evidence of carbide nucleation in the austenite region close to the α/γ reaction front, and their direction of growth toward the austenite region.

2.2.5 Thermodynamics

Figure 2.16[1]***:*** *Origin of the T_0 construction on the Fe-C phase diagram; the T_0 line is the locus of points corresponding to equal free energies between austenite and ferrite.*

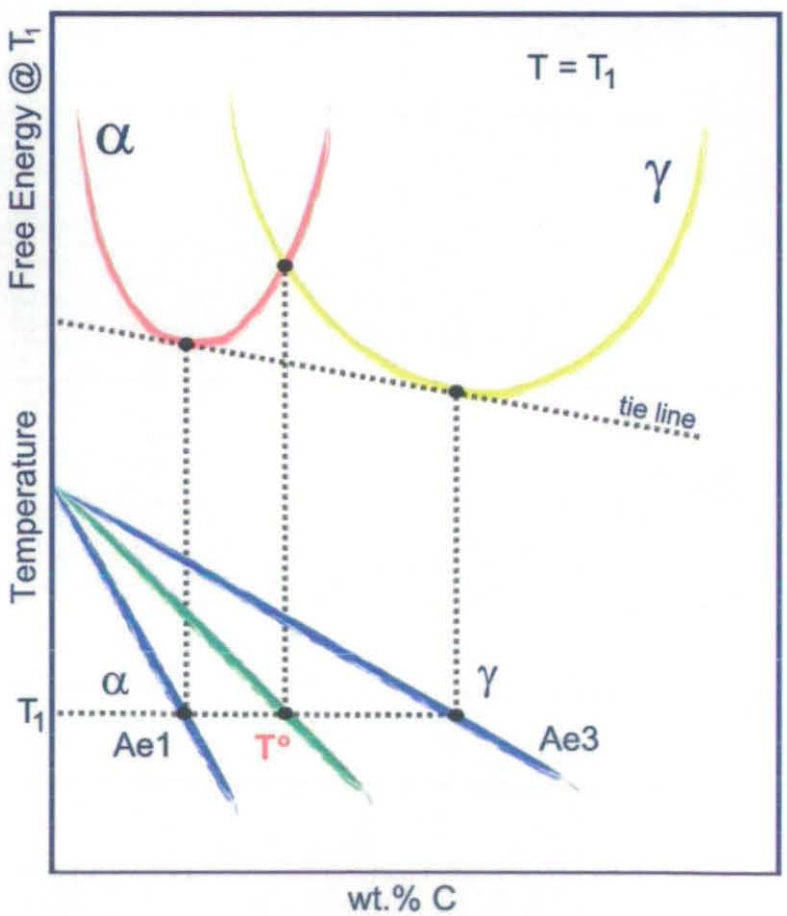

Figure 2.16 illustrates a section of the Fe-C diagram in which it can be seen that the lines A_{e1} and A_{e3} in the T vs. wt.% C region of the diagram, represent the locus of points relative to the carbon concentration of austenite and ferrite when the two phases are in thermodynamic equilibrium as a function of temperature. These equilibrium concentrations can be found at a particular temperature, e.g. T_1 in the diagram, by considering the free energy curves of the two phases at that particular temperature as a function of carbon concentration. The tie line to the two curves (i.e. the common tangent to the free energy curves of two phases) unequivocally identifies the equilibrium carbon concentrations at the chosen temperature as shown in the diagram. The T_0 line represents the locus of the points at which austenite and ferrite possess the same free energy at the same carbon content as a function of temperature.

Experimentally it has been observed that the transformation to bainite stops at an austenite carbon concentration corresponding to the T_0 curve in some alloys containing manganese and high silicon, which prevents carbide precipitation through a ferrite stabilising effect, therefore making it possible to measure the actual austenite carbon content at the transformation interface. The analogy with martensitic transformation thermodynamics suggests that the growth stage is diffusionless, with carbon being trapped at the transformation interface and soon afterwards rejected into the surrounding austenite. The displacive nature of the transformation implies that the driving force for the transformation is provided by the difference in free energy between the parent and product phase at the transformation temperature, which in turn means that the driving force is totally consumed when the two phases have the same free energy. Furthermore, diffusionless growth implies that the transformation can take place at temperatures below T_0, at which the free energy of bainitic ferrite is lower than that of austenite, allowing a larger driving force to be available. According to this view, as the interface of a bainite plate advances, carbon is rejected into the surrounding matrix which becomes enriched. The austenite carbon concentration therefore increases toward the T_0 value. As this value is reached, the growth of other ferrite plates becomes thermodynamically impossible, according to the incomplete reaction phenomenon. This is shown schematically below in figure 2.17.

Figure 2.17 [2]*: Illustration of the incomplete reaction phenomenon; the transformation stops at the T_0 line. By lowering the temperature the To line allows more product to form*

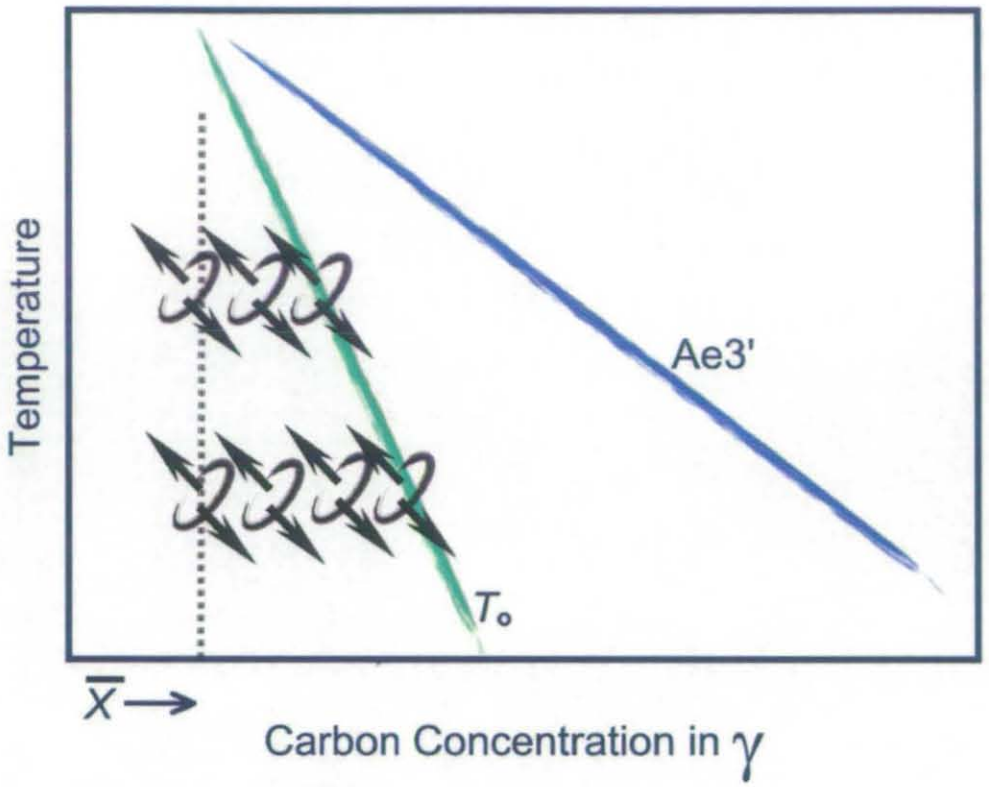

A bainitic ferrite plate growing at a certain temperature rejects the excess carbon into the surrounding austenite. Therefore, the next plate has to grow into a matrix enriched in carbon. This process means that the thermodynamic conditions at the transformation interface of newly nucleated plates change gradually, until eventually the austenitic matrix composition reaches the T_0 boundary. For the transformation to proceed it is then required that the temperature decreases, so that a larger carbon content is allowed in the austenitic phase at T_0.

The view of a displacive, diffusionless transformation similar to the martensitic transformation is based on evidence obtained by means of X-ray techniques, TEM, quantitative metallography and dilatometry. These experimental techniques have provided data for the austenite carbon concentrations well below the ones predicted by equilibrium or paraequilibrium theories (i.e. diffusion based processes where carbon partitioning is the controlling factor i.e. relative to carbon concentration at A_{e3} line) and in quite good agreement with that given by the T_0 curve[2]. This is represented in figure 2.18.

Figure 2.18[19]*: Experimental data showing compatibility with incomplete reaction theory in austenite to ferrite transformations*

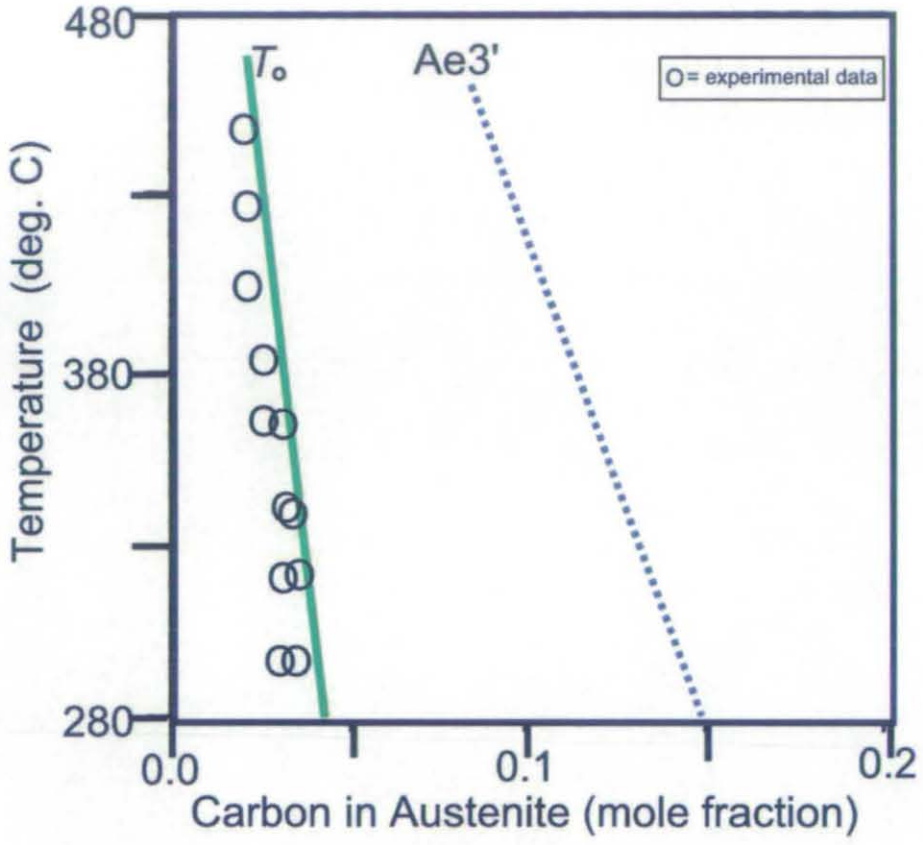

From a mechanical properties point of view, the incomplete phenomenon reaction, which is microstructurally reflected in the presence of stabilised austenite within the ferrite plates, leads to an overall improvement. In this context, the carbon content of the austenite, after the bainite reaction has reached completion, is an important parameter because it determines further reconstructive transformations e.g. the formation of pearlite. These can take place over a very long period of time in some cases due to the fact that the system wants to reach a lower free energy level.

It should be born in mind that many workers have argued that the observed values of carbon concentration connected to the growth velocity data are in agreement with a diffusion-based mechanism as it will be explained in section 2.5. The mechanism of growth is intrinsically linked to the thermodynamic description given above and depends on the behaviour of the solute atoms during transformation[1]. It has been experimentally proved that no detectable substitutional solute element partitioning occurs. However, substitutional atoms can play an

important role in influencing the kinetics of carbon diffusion at the transformation front via a solute drag effect. From the observation of the kinetics of Fe-C-Ni alloys it has been postulated that a strong interaction of the substitutional elements at the transformation front is present. A possible mechanism is solute drag effect[37]. Furthermore, the observation has been made that the volume fraction of bainite formed under isothermal conditions in alloys with increasing Cr content strongly depends on the alloying elements composition[37]. This suggests that a strong interaction with the advancing interface takes place and as a consequence, the incomplete transformation phenomenon cannot be explained by means of the T_0 equilibrium described above, invoked for displacive transformations.

In order to assess the thermodynamics of the bainite transformation it is critical to take into account the invariant plane strain shape change due to the displacive transformation, because it affects the estimation of the driving force for bainite reaction. In this context, the surface relief effect is responsible for most of the stored energy of bainite that comes from distortions in the lattice caused by the shape change[1, 2] The studies of Bhadeshia based on the early research of Christian on strain energy relationships[1]have led to the evaluation of the stored energy in bainite due to shear and uniaxial dilatational strains. This is estimated as 400 J mol^{-1} for an isolated bainite plate elastically accommodated in the surrounding austenite. Under these conditions, direct comparison with the energy stored in martensite, which is 600 J mol^{-1}, can be done. The lower strain energy in bainite is due to the fact that the aspect ratio of the plates is usually lower than those found in bainite. It has been argued that the value of 400 J mol^{-1} is not a constant and can vary depending on the transformation variables e.g. the temperature. Furthermore, because in practice the strain energy is plastically accommodated by the surrounding austenite, the above value should theoretically constitute an upper limit[1].

2.2.6 Kinetics

Both individual platelets and the sheaves of bainite grow at rates much faster than that permitted solely by the diffusion of carbon[1, 2]. The subsequent conclusion is that ferrite growth occurs under carbon supersaturation conditions. The product phase therefore inherits the composition of the parent phase, although the interstitial solute atoms, i.e. carbon in this case, are soon rejected into the surrounding matrix as the transformation interface advances. The hypothesis of partial supersaturation of carbon has not yet been fully proved experimentally.

Partition of carbon does take place in the nucleation stage of bainite, which is supposed to occur via a displacive mechanism similar to that of martensite, with the main difference being that the kinetically favourable sites are represented by the austenite grain boundaries. Another current idea[25] supports the view that nucleation of bainite does not have to be distinguished from nucleation of Widmanstätten ferrite, with which it shares the same mechanism of formation. This will be discussed further in section 2.2.9.

2.2.6.1 Nucleation of Bainite

From general thermodynamic nucleation theory, the favourable nucleation event of an embryo is determined by a reduction in free energy generally caused by a reduction in surface energy of the newly formed phase. In the case of metastable transformations, a critical size of fluctuation exists i.e. critical size of an embryo, beyond which growth becomes thermodynamically and kinetically favoured.

Naturally, the free energy change associated with the formation of a nucleus of radius r and the change in surface energy determine the energy barrier that has to be overcome in order to achieve stable nucleation. From heterophase nucleation theory, the activation energy for nucleation is associated with a critical radius size determined by the balance between interfacial energy and change in chemical and strain energy i.e. corresponding to a value of $\Delta G = 0$.

Considering the case of bainitic ferrite nucleation it is found that nucleation takes place by dissociation of dislocations. Therefore, in contrast to heterophase nucleation theory, a proportionality of the following type has been found from experimental results

$$G_N \propto \beta T$$

where the term G_N refers to the minimum activation energy for a nucleation event, T is the transformation temperature at which displacive transformation takes place and β is a negative constant[1, 2]. From the experimental evidence it can be assumed that nucleation is strictly connected to the thermally activated migration of glissile partial dislocations which gives rise to dissociation. This is also supported by the fact that it is possible to observe two different sets of transformation units whose sizes are either very small (i.e. corresponding to very fine embryo platelets) or very large (i.e.

corresponding to rapid growth). The presence of an intermediate size would be expected in the case of heterophase nucleation where the growth velocities are much smaller than in the case of a displacive mechanism. A suitable relationship for nucleation rate according to this theory is the following:

$$I_V = C_3 \exp \{ (-C_4/RT) - (C_4 \Delta G_m / C_2 RT) \}$$

where:

- I_v is the nucleation rate
- C_3, C_4 are constants obtained by fitting to experimental data
- C_2 is a constant obtained by the slope of the G_N function
- ΔG_m is the maximum value of the change in chemical potentials between the two phases.

2.2.6.2 Growth of Bainite

Generally speaking, the rate of a growth process is determined mainly by two factors: the solute diffusion at the transformation front and the interface mobility. The extent at which the two distinct processes dissipate the available free energy determines the nature of the growth process. In fact, in the case that the majority of the change in free energy is due to solute diffusion, e.g. interstitial carbon diffusion, the growth process is said to be diffusion-controlled. Under the opposite conditions, an interface-controlled process is said to take place, with the interface mobility being the predominant factor. The latter is the case of displacive transformations like martensite growth when the diffusion of the solute atoms at the interface becomes a negligible factor to consider. However, in practice for most of the growth processes there is a balance between the two factors such that the growth velocities due to interface mobility have to match the values determined by solute partitioning.

Although a displacive character of the bainitic transformation and a glissile structure of the interface (i.e. high interface mobility even at low temperatures) have been identified, the growth velocity of bainite sub-units compared to typical velocities of martensite growth is much smaller[1, 2]. It has been argued that this could be an indication of the diffusive nature of the bainite transformation. On the other hand, this could be due to the plastic work performed as bainite grows. The measured lengthening rate of a sub-unit measured by means of hot stage photo-emission

electron microscopy has been estimated as 75 $\mu m\ s^{-1}$, which is much larger than the growth rate predicted for instance by paraequilibrium i.e. 0.083 $\mu m\ s^{-1}$[11].

The general equation developed by Trivedi, utilised in order to determine the lengthening rate, V_l of a bainite plate is the following:

$$f_1 = (\pi p)^{0.5} \exp\{p\}\mathrm{erfc}\{p^{0.5}\}\ [1 + V_l f_1 S_1\{p\}/V_C + r_C f_1 S_2\{p\}/r]$$

where:

- p is the Péclet number[1]
- V_c is the interface controlled growth velocity of a flat interface
- r_c is the critical radius of the plate tip, at which growth stops
- S_2 is a function of the Péclet number
- S_1 is a term deriving by the non-diffusional characteristics of growth

The Péclet number is given by:

$$P = V_l r / 2\ D'$$

where:

- r is the tip radius of the plate considering a geometry of parabolic cylinder
- D' is the weighted average diffusion coefficient of carbon in austenite

The above equation has also been modified to predict the lengthening rate of a bainitic plate when its geometry is needle-like.

The general equation utilised in order to determine the lengthening rate of a bainite sheaf, V_S, is the following[1]:

$$V_S = V_l [t_C / (t_C + \Delta t)]$$

where:

- T_C is the period of time required by a sub-unit to reach its limiting size
- Δt is the time elapsed before the next sub-unit is stimulated

2.2.6.3 Overall Transformation Kinetics

Typically, phase volume fraction evolution is described by the Johnson-Mehl-Avrami theory[1]. This theory, which strictly applies to isothermal transformations, has also been modified in order to deal with events such as simultaneous transformations occurring during continuous cooling processes as will be discussed in section 2.3. It is important to point out that the Johnson-Mehl-Avrami theory takes into account the impingement between particles through the extended volume concept.

The classical Johnson-Mehl-Avrami equation for the determination of the volume fraction in the case of single phase precipitation is the following:

$$\zeta_\beta = V_\beta/V = 1 - \exp(-1/3\pi G^3 I t^4)$$

where:

- ζ_β is the volume fraction of the phase β
- V_β is the volume of the β phase
- V is the total volume of the sample
- G is a constant growth rate
- I is the nucleation rate per unit volume
- t is the transformation time at the transformation temperature.

This equation has been derived under the assumptions of random nucleation and constant growth rate. In practice, however, reasonable trends can be obtained using such a relationship. For instance, in agreement with real cases, the equation predicts that the maximum volume fraction of bainite decreases as the transformation temperature reaches the B_s temperature, consistent with the incomplete reaction phenomenon[19].

2.2.7 Carbide Precipitation

In the case of upper bainite, a typical Pitsch orientation relationship type has been found between the carbides precipitating from the austenitic matrix and the matrix itself. The orientation relationship is the following[1]:

$$[0\ 0\ 1]_{Fe_3C} \ //\ [-2\ 2\ 5]_\gamma$$

$$[1\ 0\ 0]_{Fe_3C}\ //\ [5\ -5\ 4]_{\gamma}$$
$$[0\ 1\ 0]_{Fe_3C}\ //\ [-1\ -1\ 0]_{\gamma}$$

Depending on the amount of carbon present in the alloy, the precipitate can be either in the form of particles or a continuous film between the ferrite plates. The first case occurs when the carbon concentration is low whilst the latter takes place at high carbon concentrations. Generally speaking, the carbon is soon rejected from the growing ferrite plates formed by displacive mechanism into the surrounding austenite, which becomes enriched. As new bainitic plates grow and release excess carbon, the austenite becomes stabilised on cooling to room temperature. However, at a transformation temperature which is high enough to allow carbon diffusion away from the ferrite plates, part of the carbon precipitates from the austenite forming the thermodynamically stable cementite phase. Precipitation of carbides from the austenite phase can be avoided in the presence of ferrite stabilisers such as silicon and aluminium. In this case the microstructure of upper bainite will consist purely of bainitic ferrite plates and stabilised austenite.

A characteristic feature of the precipitates inside the plates, in the lower bainite scenario, is their particular "tempering" orientation relationship similar to that found in the case of tempered martensite. The Bagaryatski orientation relationship describing the "tempering" orientation is the following[1]:

$$[0\ 0\ 1]_{Fe_3C}\ //\ [-1\ 0\ 1]_{\gamma}$$
$$[1\ 0\ 0]_{Fe_3C}\ //\ [1\ 1\ 1]_{\gamma}$$
$$[0\ 1\ 0]_{Fe_3C}\ //\ [-1\ 2\ -1]_{\gamma}$$

Usually, in the case of bainitic ferrite, the cementite particles are found to precipitate following just one of the three orientation relationships listed above. They tend to arrange themselves in order to form parallel arrays at angles of about 60° with the ferrite plates[38]. The most accredited explanation of this difference between cementite in martensite and cementite in lower bainite is that the nucleation sites for cementite in bainite are at the austenite-ferrite interface. Therefore, the orientation adopted is such that the minimum mismatch with both phases can be achieved. However, this point of view could support both a displacive theoretical approach (i.e. displacive step followed by carbon diffusion) and a fully diffusional theoretical approach. Indeed, it could be argued that the precipitation at γ/α interface is in perfect accordance with a diffusion based transformation that would not necessarily

need to relate to a displacive step as it will be shown in sections 2.2.9. It has also been proposed that carbide precipitation is influenced by the stress associated with the displacive growth of lower bainite. The effect would be less pronounced in the case of martensite tempering because the driving force for carbide precipitation is larger[1, 16].

In lower bainite, iron carbides do not always constitute the carbides present inside the plates. Indeed, depending on the reaction temperature and composition other transition carbides can precipitate. This is commonly encountered in high silicon alloys in which the ferrite stabilising effect of silicon leads to the precipitation of epsilon carbides in preference to cementite. The appearance of ε-carbides in some lower bainites but cementite in others can be understood in terms of a theory of martensite tempering due to Kalish and Cohen[1, 38].

Precipitation of carbides from enriched austenite in upper bainite does not directly influence the formation of bainite, except for the fact that precipitation from γ causes a carbon depletion which allows further transformation to take place[38].

Whilst Aaronson et. al supported the view that nucleation of carbides is of the interphase type i.e. carbides nucleate at the transformation interface, therefore nucleation occurs in both austenite and ferrite, Bhadeshia[38] has developed a theory based on the hypothesis that nucleation takes place after the passage of the transformation interface[1, 38]. The evidence supporting this view is that in high silicon alloys precipitation in lower bainite has been found to be consistent with it as showed by crystallographic considerations on the carbides and matrix phase.

2.2.8 Role of Carbon and Other Alloying Elements

It is widely recognised that within the temperature regime of bainitic reaction, the thermal energy available is not sufficiently high to confer to substitutional atoms present in the lattice the required kinetic energy to overcome the activation energy for diffusion. High-resolution experiments performed in order to study the local composition before and after transformation has taken place have confirmed that no long-range redistribution of substitutionals is present. The lack of diffusion of the solute atoms (i.e. iron atoms), and substitutional elements is in agreement with a displacive mechanism for the bainite transformation. However, this does not totally exclude the possibility of a diffusion based mechanism, which justifies the absence of long-range redistribution of large atoms by means of the energetic argument, still admitting carbon diffusion as the rate determining step of the reaction.

The conditions at the interface determine the nature of the transformation at the reaction front. The possible models describing a scenario in which no change in composition and ratio of iron to substitutional atoms is observed are negligible partitioning local equilibrium (NP-LE), the paraequilibrium mode, the partial carbon supersaturation and finally the martensitic mode. The possible composition variations present at the transformation front for a variety of possible growth mechanisms are illustrated in figure2.19:

Figure 2.19: *Possible composition profiles at transformation front*[1]

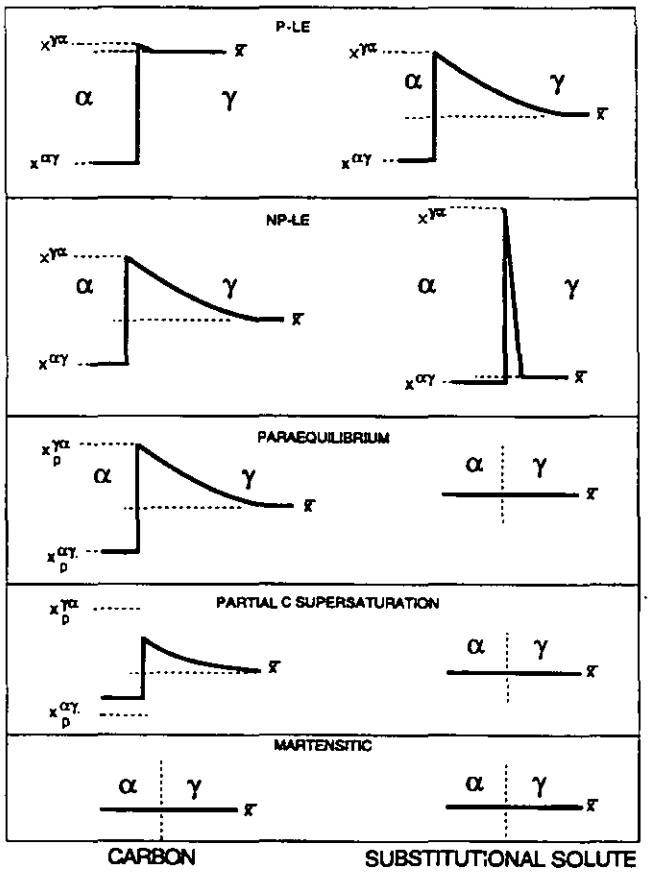

The martensitic mode can be excluded as a valid real description of the interface conditions due to the fact that at the transformation temperatures typical of the bainite formation, carbon diffusion takes place, either during the growth process, determining the advancing interface growth velocity, or soon afterward ferrite plates form by a displacive mechanism. This is excluded in a purely martensitic type of transformation. The NP-LE mode implies that the product phase, ferrite, and the parent phase, austenite, possess nearly the same substitutional element composition. However, in order to compensate for the small diffusivity of the alloying element, a large gradient is present at the interface. This type of condition is usually

applicable when large under-coolings are used and a diffusion based growth mechanism takes place.

When the iron to substitutional atoms ratio is constant across the interface and therefore no net redistribution of the solvent and substitutional atoms occurs, paraequilibrium conditions are obtained. Diffusion of carbon still takes place and slow diffusion of iron and substitutional atoms takes place at the incoherent interface, therefore reconstructive transformation can be described by paraequilibrium conditions as well as displacive transformations. It should be highlighted that all the boundary conditions between the two extremes of partitioning local equilibrium and paraequilibrium imply some perturbation of the solute content at the transformation interface[1]. Therefore, the fact that experimental analysis to date has failed to identify any substitutional element variation at the interface suggests that a displacive mechanism is likely to take place. Such a scenario could be described by paraequilibrium conditions, however, experimental data obtained under appropriate conditions (e.g. avoiding carbide precipitation at the interface) have demonstrated that the carbon concentration at he interface is much lower than the equilibrium one. Therefore, the partial carbon supersaturation model that would explain both the fact of a smaller amount of carbon partitioning than the equilibrium one, and a displacive transformation mechanism is one of the most accredited and one on which very effective prediction models are based.

The school of thought supporting a diffusion controlled mechanism[32, 33, 37] have often invoked the solute drag effect at the interface in order to explain the lower carbon composition values experimentally observed after transformation.

The role of carbon, its distribution and its diffusion characteristics strongly influence the kinetics of carbide precipitation in both upper and lower bainite. This is strongly interrelated to the alloy composition and the transformation temperature. Two distinct types of carbides can be identified depending on whether they form within the bainite plates or from the carbon enriched austenite. The former precipitates in lower bainite and their precipitation kinetics are very fast as they form at the reaction front of the bainite plates as it advances. The latter precipitates from the surrounding matrix and the precipitation usually presents a lag behind the bainite formation. The extent of the delay of precipitation depends strongly on the alloying addition and reaction temperature, as well as the holding time at the reaction temperature under isothermal conditions. The rate of precipitation observed for carbides formed from carbon enriched austenite is usually much lower than the precipitation rate of carbides forming within the bainitic ferrite as the reaction proceeds. This is a result of the different diffusivity of carbon in the two different

phases and the extent of supersaturation which is clearly much larger in the α phase. Furthermore, alloying elements such as silicon have an effect on the kinetics of carbide precipitation from austenite. Such elements which act as ferrite stabilisers due to their very low solubility in cementite, and significantly reduce the available driving force for precipitation, making it kinetically unfavourable. This is reflected in some extreme cases by the complete absence of carbides in suitably alloyed bainitic steels. The same type of influence on the precipitation rate of carbides from the austenite matrix are promoted by chromium, copper and are also observed in some low-alloy low-carbon steels.

The effects of these alloying elements on the kinetics of carbide precipitation occurring during the bainite reaction has not been yet fully understood and utilised for prediction purposes. However, by relating the available data to the theory of bainite transformation and with thermodynamic and kinetic predictions, information on the nature of the precipitation characteristics of these carbides can be established. The low transformation temperatures involved in lower bainite formation imply that a different mechanism of precipitation has to be invoked than a diffusion based mechanism which would require long range diffusion of large atoms (i.e. iron and substitutional elements). The work of Andrews, Hume-Rothery followed by the more recent of Yakel has led to the development of kinetic models which do not fully explain the mechanism of formation of cementite. However, consistent with the view of a displacive bainitic transformation, these models support the absence of substitutional atoms diffusion and a displacive type of mechanism occurring under paraequilibrium conditions with carbon diffusion possible at very low temperature. In fact, the activation energy for diffusion of substitutional elements such as molybdenum (which acts as a strong carbide former), is too high at low temperatures and the diffusion distances involved would allow carbides with very limited sizes (as has been demonstrated by the work of Stark and Smith[1]). The presence of such carbides should be identifiable in bainite plates if the transformation mechanism was not be displacive, considering that the rate of growth of a bainitic plate (supposing its occurrence via a reconstructive mechanism) should be consistent with the diffusion rate at the reaction front of substitutional element. To date the presence of such carbides has not been observed.

The effects of alloying elements on the bainite start temperature, B_s, derive directly from the influences of the alloying elements on the $\gamma \rightarrow \alpha$ transformation. It should be noted that the B_S temperature is different from the theoretical upper temperature limit for bainite formation (B_0 temperature), which is defined by the

intersection between the thermodynamic equilibrium curve of the austenite → ferrite transformation by coherent growth and the thermodynamic equilibrium curve of the austenite → cementite transformation. The B_S (practical upper temperature limit) is approximately 50°C lower than the B_0 point, as shown in figure 2.20 below:

Figure2.20[26]*: Schematic of the location of B_S and B_0 temperatures for plain carbon steels*

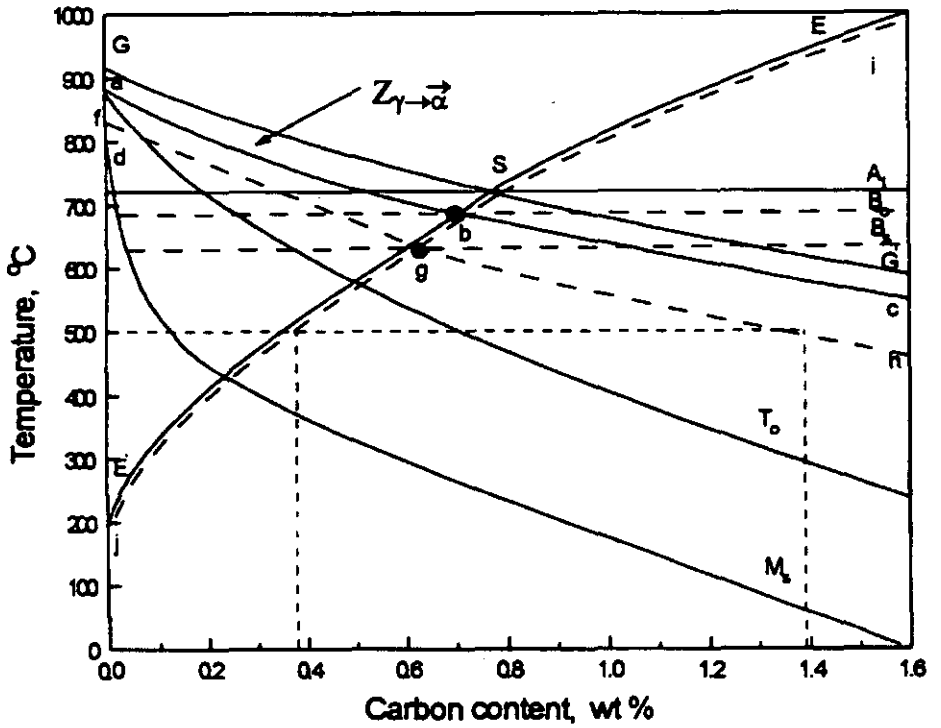

A formula for the prediction of the B_s temperature for a wide range of commercial steels, which resume the effect of the major alloying elements expressed in wt.%, is the following:

$$B_S\ (°C) = 630 - 45Mn - 40\ V - 35\ Si - 30\ Cr - 25\ Mo - 20\ Ni - 15\ W$$

which can be applied when prior full austenitisation has been achieved[26].

2.2.9 Other Theories on Bainite

A different point of view on the nature of bainite formation and the characteristics of bainite growth has been provided by Enomoto[39]. He put forward the view that from the growth kinetics data, incomplete reaction phenomenon and the rearrangement of carbides observed within the bainite plates, it can be deduced that carbon partition

occurs during transformation rather than redistribution after transformation has taken place. Diffusion of alloying elements (substitutional atoms) within and near the boundaries probably has a large influence on transformation behaviour. In this context, the phenomenon of solute drag can be invoked as responsible for the absence of relevant substitutional element diffusion at the transformation interface. However, such hypothesis has still to be effectively proven by experimental data.

The research carried out by Quidort and Brechet[37] has led to the support of a diffusion based mechanism for nucleation and growth of bainitic ferrite. In particular, they proposed that the nucleation step can be described by classical nucleation theories. Paraequilibrium conditions at the transformation front determine the carbon concentration in the parent and product phase, which in turn controls the growth rate of the ferrite plates. Although a quantitative description of the role of carbides is still lacking, carbides represent extra sink for carbon, therefore providing additional flux which accelerates the transformation. The action of solute drag exerted by the substitutional elements on the growth kinetics has to be taken into account, as their influence on growth velocities under paraequilibrium conditions predicted by thermodynamic theory is much lower than the experimentally observed one. The work of Quidort and Brechet has led to the development of a model which predict the nucleation and growth rate with the advantage of presenting a minimal number of adjustable parameters, i.e. temperature and carbon contents, valid for isothermal and continuous cooling conditions. It should be pointed out that the degree of accuracy decreases at higher cooling rates. In this case the model overestimates the fraction of bainite formed. The main reason for this has been proposed to be the possible formation of carbides at the interface due to the transition from upper bainite. These can act as sink for carbon, altering the predicted kinetics. Another theoretical approach supporting a diffusion based mechanism for the bainitic transformation and an edgewise type of growth has been provided by Hillert[40]. The study of the growth velocities for the bainite reaction support an edgewise type of growth mechanism typical of Widmanstätten ferrite formation processes. This hypothesis is supported by the fact that strong evidence of growth occurring under the circumstance of carbon supersaturation of ferrite is absent. Indeed, the characteristic high growth velocities typical of martensitic (displacive transformations) are not encountered during the bainite growth process. This is an indication of the fact that the interfacial characteristics of a martensitic process, which influences the growth mechanism, are not of the same type as the interface properties of the bainitic laths interface (i.e. α / γ interface). The instance that martensitic interfacial characteristics are encountered under some conditions does not necessarily imply high growth velocities and carbon

supersaturation during the bainite reaction. The crystallographic features of the α / γ interface thus become of minor relevance for the determination of the diffusional or displacive character of the bainitic transformation, in particular when an edgewise type of growth mechanism is considered to take place.

A possible way to determine the nature of the bainitic reaction carried out by some researchers[28, 29] is the observation of the interfacial characteristics of bainite and martensite in order to identify similarities and differences that can bring under a common denominator the two transformations or otherwise highlight different reaction paths. The work of Purdy[30] has concentrated on the role of defect signatures which can be usefully interpreted as fingerprints of a particular type of reaction mechanism e.g. diffusion based or displacive. Three different categories of defects can be present in the microstructure of a phase, which are:

- interfacial defects: defects which come from interfacial mismatch between two phases e.g. austenite and bainite;
- trailing defects: which are defects left behind the transformation interface; in the case of martensitic transformations trailing defects are usually found as twins;
- inherited defects: which are defects induced in the parent phase that can be found in the product phase after transformation has occurred.

Significant difference has been found between interfacial defects present in bainite and in martensite. The first type is characterised by optimal interfacial matching that determines the habit plane interface structures, whilst in contrast, the martensite/austenite interface, capable of moving in an athermal fashion is glissile. Although there has not been a wide range of experimental data on trailing defects, the presence of twins characteristically found in the martensitic phase, have not yet been revealed in any bainitic structure. Finally, inherited defects have not received great attention, although they could represent an effective means of characterising the transformation mechanism. For instance, in a displacive transformation, defects may be subjected to the same type of deformation as the matrix, therefore revealing its nature, or in the case of a diffusion based mechanism could change their structure via a reconstructive mechanism. The evidence obtained by Purdy support the idea that the structure of the planar bainitic interface is generated by energy minimisation which allows the interface to adapt a glissile motion. Therefore the transformation mechanism is believed to be fundamentally different than that of martensite i.e. a displacive mechanism.

An interesting view of the bainitic reaction reconciling the two opposite views can be found in the work of Muddle[27]. The fact that the bainitic transformation is diffusion based, as it unquestionably involves carbon diffusion, does not necessarily imply a diffusion controlled mechanism of transformation, which is accredited to be of a displacive nature with IPS characteristics. Generally speaking, the author supports the fact that the two different views can converge by invoking a nucleation-limited growth model.

2.2.10 Unresolved Issues

The very complex, fascinating and controversial field of research of the bainite reaction still presents a number of unresolved issues, about which there are in some cases opposite interpretations and in others simply a lack of knowledge due to inadequate attention.

The main key issues which need further investigation are[34]:

- The possibility that interstitial diffusion during the growth stage of bainitic plates is a determining factor and that the mechanism of formation is not displacive;
- The need for a better theory describing auto-catalytic nucleation in order to define more reliable fitting constants used in the modelling field
- The quantitative modelling of the carbide precipitation which is surprisingly a very neglected area, especially in view of the fact that in most steels containing bainite, the presence of carbides is a unavoidable
- The factors affecting the austenite to bainite transformation when the parent phase is plastically deformed. This is a critical factor in production processes involving thermomechanical treatments.

It is worth note that regarding the last issue, it has been found that the bainite microstructure can be mechanically stabilised through plastic deformation which causes retardation of the transformation. This is a type of mechanism which has not yet been encountered in any reconstructive transformation and that is possible only in displacive transformations. Naturally, this evidence supports the view of a displacive nature of the bainite reaction[34].

2.4 Continuous Cooling Transformations & Models

In the industrial context, isothermal heat treatments are not the most practical to carry out. These, in fact, involve the rapid cooling of the alloy from a temperature in the austenite phase field, and then isothermal holding at the elevated temperature chosen for the heat treatment. Instead, most of the heat treatments performed on steels, involve the continuous cooling of the alloy from the austenitising temperature to room temperature at a certain cooling rate. The heat treatments can be very complex, depending on the type of microstructure which has to be achieved, involving various steps at different cooling rates joined with isothermal stages. However, the continuous cooling option is the most viable and advantageous from a cost point of view than the isothermal processing route.

2.4.1 Thermodynamics and Kinetics Aspects of Transformations in Steel

In order to understand the phase transformations taking place during continuous cooling, it is useful to introduce some considerations regarding thermodynamics and kinetics aspects of transformations. The phase transformations taking place in steels, in the solid state belong to the category of heterogeneous transformations. Heterogeneous transformations include all transformations in which *at an intermediate stage the assembly can be divided into microscopically distinct regions of which some have transformed and others have not*[41]. This implies that transformations start at determined sites in the parent phase through a process widely known as nucleation.

Heterogeneous transformations are divided into two main groups: nucleation and growth reactions and martensitic reactions. Generally speaking, the first type of transformations are characterised by being dependent on both time and temperature. At a given temperature the amount of transformation increases with time (the relationship being dependent on several parameters) until the system reaches a minimum of free energy. Naturally, in some cases the rate of transformation is so slow that it cannot be detected in practice. Within the transformation temperature range, the amount of transformation does not depend on the temperature, as the system will always try to reach completion (i.e. the minimum free energy

configuration of the assembly). However, the transformation rate will drastically vary with temperature. The velocity of reaction increases with decreasing temperature until the free energy of formation of a stable nucleus decreases to a larger extent compared to the thermal energy available for the reaction. As the temperature is lowered further, eventually the thermal energy decreases more rapidly than the free energy and, as a consequence, the reaction rate start to decrease again. Therefore, the reaction rate reaches a maximum at a temperature below the equilibrium transformation temperature, and decreases again as the temperature is lowered further. Another characteristic of nucleation and growth transformations is the irreversibility. Indeed, as these transformations are diffusion based and the atoms can move freely without respecting any relationship with the parent phase lattice, a correlation between original lattice and product position cannot be identified, nor recovered by reversing the transformation. Furthermore, composition, atomic volume and shape of the product phase are not related to those of the parent phase. Unless the transformation produces Widmanstätten structures, usually there isn't an orientation relationship between the lattices of the parent and product phases. Finally, nucleation and growth reactions taking place in the solid state are favoured by plastic deformations. Nucleation becomes usually easier in deformed regions as the driving force is increased[41].

Martensitic transformations, on the other hand, have different and in some cases opposite characteristics compared to nucleation and growth reactions. Being athermal, the transformation extent is independent of time. Once the transformation has overcome the incubation time, the growth of the phase proceeds extremely rapid. The amount of transformation is dependent on temperature. When cooling, the transformation start temperature is fixed, providing that parameters such as chemical composition do not change during cooling. The transformation proceeds if the temperature is lowered below the martensite start temperature until the martensite finish temperature is eventually reached. Martensitic transformations are reversible in the sense that the atomic configuration of the parent phase can be obtained by heating (reversing the transformation). Therefore, a definite orientation relationship between parent and product phase can always be identified in martensitic reactions. Compared to nucleation and growth reaction, the influence of deformation and applied stresses is more important in martensitic reactions. Without entering into details, usually the applied stresses increase the amount of transformation and in some cases render the transformation possible even at temperatures higher than the M_S temperature. Another important characteristic of martensitic transformation is that the chemical compositions of the parent and product phases are the same[41].

In the present research, the attention focussed on reaction involving precipitation has been significant. These are discontinuous reactions which are diffusion and interface controlled. Long range transport of mass is involved and the growth is thermally activated. They can be either eutectoid or discontinuous precipitation reactions.

In both transformations the transformed regions are duplex and usually consist of one or more colonies of parallel crystals (e.g. lamellar) of the product phases The transformed regions usually originate at grain boundaries growing hemispherically into the untransformed region of the grain. Usually, the duplex regions originating from a single nucleus are referred to as cells. The crystals belonging to a cell possess the same orientation. Furthermore, even in the instance that one of the two product phases is the same as the parent one, the boundary between the transformed region and the untransformed one is incoherent. Two type of reactions which are important in practice are the formation of a duplex region from a third phase (e.g. eutectoidal reactions) and the precipitation reaction from a supersaturated phase (e.g. precipitation from supersaturated α). In the first case the duplex region has an incoherent boundary with the parent phase. In the second case, although one of the two product phases is the same as the parent matrix, both orientation and chemical composition will be different.

In both processes, theoretically three different possibilities have been proposed, regarding diffusion: volume diffusion through the matrix, diffusion through the incoherent boundary (short circuit diffusion) and diffusion and diffusion through the product phase. However, practical evidence on favour of any one of these arguments has not bee found. This is due to the fact that the growth process involves too many unspecified variables which make the modelling of it based on physical laws, an extremely difficult task[41].

In the case of matrix diffusion for a lamellar type of the duplex region, a concentration gradient will be present as the parent phase in the near vicinity of the alpha phase will be enriched in solute (carbon in the case of pearlite in steel). In this context the hypothesis is that solute diffusion occurs normally to the lamellae and parallel to the cell boundary. The compositions within the product lamellae during growth will be uniform, and it is usually considered to be the equilibrium composition at the reaction temperature.

The case that the main diffusion paths are in the product rather than in the parent phase has been investigated as well. The diffusion rate pf carbon in ferrite is circa hundred times larger than the one in austenite. However, in this case it seem certain that diffusion occurs along short diffusion circuits such as cell boundaries, in order to allow high growth rates. The incoherent boundary is particularly effective

since it sweeps through the matrix as the product grows and it is favourably orientated for achieving segregation in the required direction. This type of boundary diffusion becomes dominant compared to lattice diffusion as the temperature is lowered as it requires lower activation energy. Furthermore, in the case of discontinuous precipitation, the amount of segregation required for growth is quite small compared to the eutectoidal reaction.

Figure 2.21[41]: ***Comparison between solute segregation in continuous and discontinuous precipitation;*** *less solute segregation is required for discontinuous precipitation*

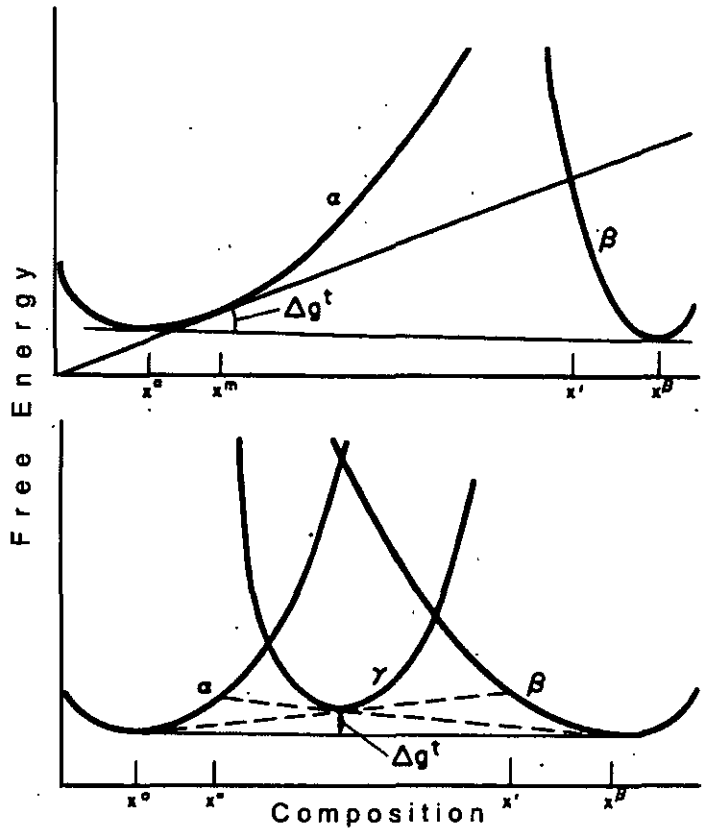

In the case of discontinuous precipitation, every time the formation of β phase(second phase), with a composition richer than x' in figure 2.21 above, happens, there is a corresponding lowering in free energy. This is true even when the amount of β phase is so small that the composition of the α phase is almost identical to the initial matrix composition x^m. On the other hand, for the eutectoidal reaction to be possible, the composition of the α phase must be lower than x'' whilst the composition of the β phase has to be higher than x', so that the net free energy can be reduced. Therefore, the eutectoidal reaction compared to the discontinuous precipitation needs a large fraction of the equilibrium segregation to be accomplished as the cells grow[41].

2.4.2 Continuous Cooling Transformation Diagrams

The description of austenite decomposition at a constant temperature is performed using time-temperature-transformation (TTT) diagrams. These have to be modified in order to be provide a valid representation for transformations occurring under gradual change of temperature, i.e. continuous cooling.

A plot representing the transformation taking place under continuous cooling conditions is called a continuous cooling transformation (CCT) diagram. The first two factors to consider when modifying a TTT diagram are the delay of start and finish transformation times and the decrease in start temperature. This causes the isothermal curves to be shifted to longer times and lower temperatures as shown in figure2.19a. In order to construct a CCT diagram the cooling curves have first to be superimposed on the isothermal curves. The transformation start time is found at the intersection of the cooling curve with the isothermal curve relative to the beginning of the reaction, whilst the finish time can be identified at the point of crossing between the cooing curve and the completion transformation curve. The microstructural products of the transformation are usually indicated in the diagram. An example for a eutectoid steel subjected to fast and slow cooling which led respectively to fine and coarse pearlite formation is shown in figure2.22b.

Figure 2.22[34, 42]*: a) shifting of the isothermal curves b) rapid and slow cooling curves*

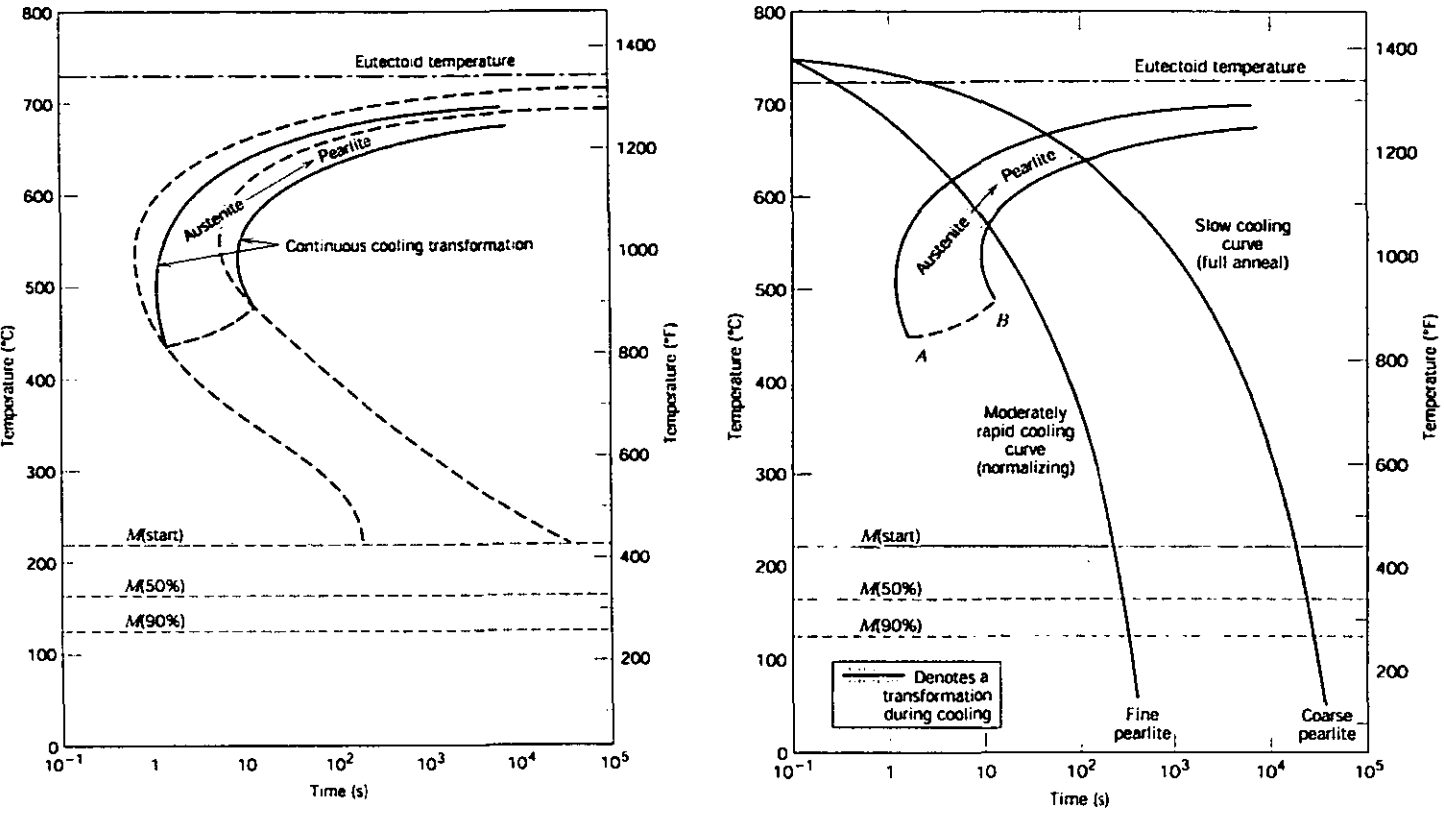

Each CCT diagram requires a specification of the alloy's chemical composition, the austenitisation conditions, the austenite grain size and the cooling conditions[34, 43, 44]. In fact, not only the cooling rate, but all of these factors can profoundly influence the final microstructure of a steel. For instance, the prior austenite grain size greatly influences the transformation kinetics by promoting the nucleation of reconstructive phases which are preferentially favoured at γ grain boundaries.

Furthermore, a CCT diagram is usually partitioned in phase domains. For these reasons, the CCT diagrams lack the generality of the TTT diagrams and are suitable for particular processes under specific conditions.

Normally, as shown in figure2.19b, bainite will not form when a eutectoid alloy is cooled to room temperature, because all the austenite transforms to pearlite before the bainite transformation becomes possible. Hence, for any cooling curve passing through the dashed line AB in figure2.19b, the transformation ceases at the point of intersection, whilst any untransformed austenite at that point, will transform to martensite upon cooling to room temperature i.e. it will start when it crosses the M_S temperature. An important characteristic regarding the martensitic transformation in the context of continuous cooling transformations is the theoretical existence for any alloy of a critical quenching rate, which represents the minimum quenching rate

required in order to achieve a fully martensitic microstructure. As expected, in a CCT diagram the critical quenching rate will be tangent to the pearlitic nose as shown in figure2.23a[27]. An example of a CCT diagram showing the main phase fields formed under continuous cooling conditions for steel type 4340[43] is shown in figure2.23b.

Figure 2.23[43]*: a) critical quenching rate* *b) phase fields in a typical CCT diagram*

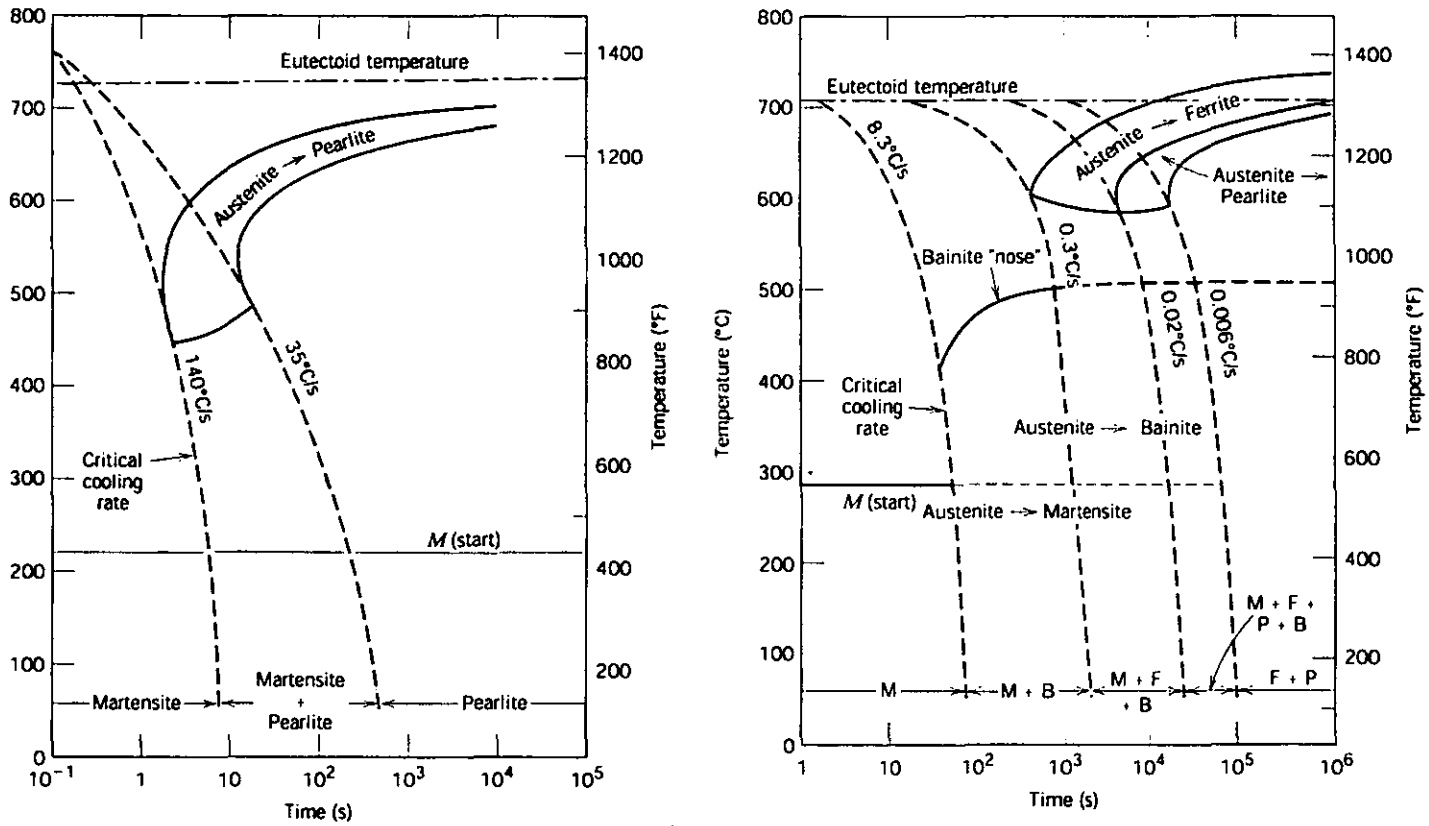

Mixed microstructure fields are obtained when a boundary between two phases domains is intersected by a cooling curve. In addition to the domain boundaries volume fraction contours can be found in a CCT diagram. These indicate the progress of a phase transformation in terms of volume fraction of austenite that has transformed into one or more phases. An example is shown in figure 2.24.

Figure 2.24[1]*: constant volume fraction curves in a CCT diagram*

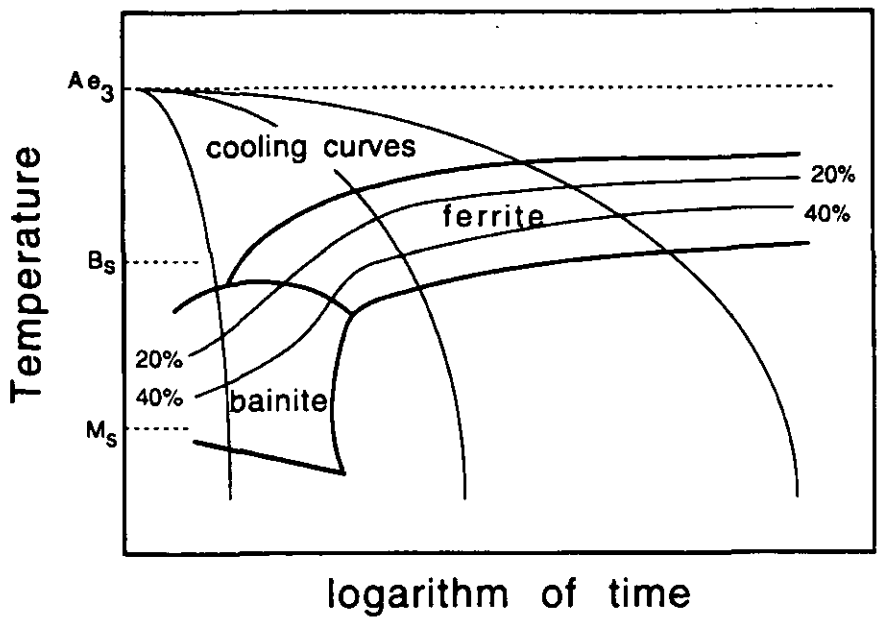

2.4.2 Models

Models exist for the prediction of microstructures as a function of composition and thermomechanical processing route. The advantage offered by the development of accurate models is the very small number of experimental trials needed to validate the model compared to the much more expensive experimental design approach.

Models, however, have usually dealt either with continuous cooling or isothermal processes without considering complex discontinuous cooling paths which make the prediction of even single phase reactions difficult. Furthermore, in the case of multiple reaction processes, the mutual interactions between the transformations (occurring sequentially or simultaneously) which are mainly of a compositional nature (in the case of alloy rejection) and a geometric nature (impingement and variation of favourable nucleation site number) make the prediction a very challenging task.

The general pattern followed in order to build a model is schematically summarised in figure 2.25:

Figure 2.25[2]*: schematic diagram illustrating the stages in the development of a physical model*

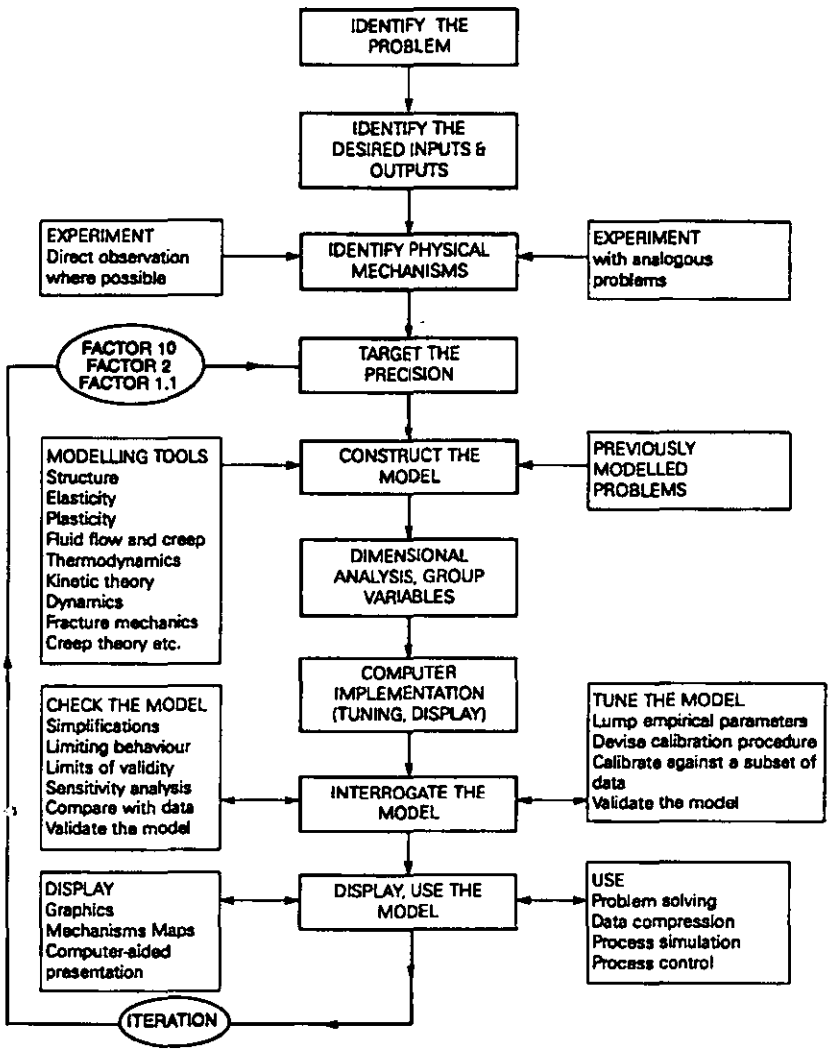

It is a fundamental principle that when identifying the most likely physical mechanisms involved in the transformation which should be modelled, the most advanced theory available should be used, highlighting the areas of which that show a lack of knowledge and/or need approximations to be made. In order to best assess the theoretical assumptions for the real mechanisms involved, as well as to determine any necessary approximations, data can be further investigated. However, it is necessary to make a balance between the precision of data and the capability of the theoretical prediction, to move forward with the development of models[2].

The bainitic microstructure is of considerable importance in the design of high strength steels in which it is necessary to control microstructure development. For this reason, the development of predictive models, applicable to the formation of

bainite under continuous cooling conditions has been addressed by many researchers.

As an example, the recent results in the modelling field obtained by Azuma, Fujita, Takahashi and Iung[35] will be discussed, who developed a new model to predict the bainite formation considering four different aspects, with the advantage of treating the bainite reaction not as a single reaction phenomenon, but rather that it consists of bainitic ferrite and cementite formation:

- bainite formation in the austenitic matrix under isothermal conditions;
- carbon evacuation from bainitic ferrite to austenite;
- cementite precipitation in bainitic ferrite (LB case);
- cementite precipitation in austenite (UB case).

The steels utilised in the study are Fe-C-Si-Mn alloys which make this model relevant for the present research project. The model is based on the assumption that bainite formation occurs under diffusionless conditions, followed by sudden rejection of carbon into the surrounding austenitic matrix, therefore, it follows the point of view on the bainite reaction proposed by Bhadeshia[1].

The nucleation of sub-units is associated with carbon diffusion and dealt with as an auto-catalytic process. Therefore, the nucleation rate is $I_{\alpha\beta}$ is given by:

$$I_{\alpha\beta} = (1+\beta V_{\alpha\beta})I_0$$

where $V_{\alpha\beta}$ is the bainitic ferrite volume fraction and β is auto-catalysis constant and I_0 is the initial nucleation rate, which depends on the initial nucleation site density, the activation energy for carbon diffusion in austenite and the driving force for bainite formation[1, 35].

The width of the sub-units is considered as a function of temperature, austenite strength and the driving force under para-equilibrium conditions.

The rate controlling process of the carbon rejection is the diffusion of carbon into austenite. Cementite precipitation in the bainitic plates is considered to take place under paraequilibrium conditions and it is treated by classical nucleation theory. The carbon concentration profile at the α_B / γ interface is given by[35]:

$$X^{\gamma}_C = X^{o\gamma}_C + (X^{\gamma\alpha}_C - X^{o\gamma}_C)\mathrm{erfz}[Z/2(D^{\gamma}_C t_d)^{0.5}]$$

where X^{γ}_C is the C concentration normal to the α / γ interface in austenite, $X^{o\gamma}_C$ is the C concentration at the interface under paraequilibrium and $X^{\gamma\alpha}_C$ is the concentration in the austenitic phase. D^{γ}_C is the carbon diffusion coefficient in austenite and t_D is the time required to decarburise a bainitic ferrite grain. Diffusion of any substitutional elements, iron included, does not occurs at the low temperatures involved in lower bainite formation, where cementite precipitation takes place within the bainite plates. The nucleation rate for cementite precipitation in a bainitic plate, $I_{\theta\alpha B}$, is given by:

$$I_{\theta\alpha B} = N_{0\theta\alpha B} RT/h \exp(-Q_C^{\alpha}/RT)\exp(-\Delta G^{\alpha\rightarrow\theta^*}/RT)$$

where Q_C^{α} is an activation energy term for carbon diffusion in ferrite, $\Delta G^{\alpha\rightarrow\theta^*}$ is chemical driving force for nucleation of cementite under paraequilibrium conditions.

Cementite precipitation in austenite is treated in the same way as that occurring within bainitic plates, adapting the parameters to the different matrix structure. Again, cementite precipitation is considered to take place under para-equilibrium conditions.

The model constructed under these hypotheses and considering the above parameters showed good agreement between the predicted values and the experimental ones of phase volume fractions (bainitic ferrite, austenite, and cementite) in both upper and lower bainite conditions, as a function of isothermal process conditions[35].

The attention on modelling the precipitation of carbides during the bainite reaction, which is an aspect which has been usually neglected in most of the past works, has been discussed by Bhadeshia[34]. The basic theory through which carbide precipitation is treated is by modifying the Johnson-Mehl-Avrami theory. Such models have been initially developed in order to predict simultaneous precipitation occurring in power plant bainitic/martensitic steels.

Another model has been developed by Reti[45], which takes into account the austenite grain growth and relates this to the prediction of the progress of ferrite, pearlite, upper and lower bainite simultaneously for low alloy hypoeutectoid steels. The model is based on coupled differential equations[45].

Models based on different theories explaining the bainite transformation such as diffusional growth invoking the solute drag effect, as discussed in section 2.2.9, have also been developed. An example is that developed by Quidort and Brechet which is based on carbon diffusion limited growth with paraequilibrium at the interface[46].

In addition to models which primarily focus on the formation of bainite, others have been developed in order to predict austenite decomposition for steels subjected to continuous cooling heat treatments which have a microstructure which is a mixture of many transformation products, each of them forming via a particular transformation mechanism defining the product reaction. In this scenario it is very important to consider the interactions and the overlapping of the various reactions occurring during the heat treatment process, which can often result in simultaneous transformations. The interactions between the phase reactions can be of a "physical" nature when hard impingement takes place or diffusional when the various thermal or diffusion fields overlap. Typically, phase volume fraction evolution is described by the Johnson-Mehl-Avrami theory. Bhadeshia and Jones have modified it in order to deal with events such as simultaneous transformations occurring during continuous cooling processes which lead to the formation of ferrite, Widmanstatten ferrite and pearlite. The detailed principles on which the development of the model is based are presented in the paper by Bhadeshia and Jones[47]. The steel analysed in the study is 0.18C-1.15Mn-0.18Si with austenite grain sizes of 30, 55 and 100 μm. Slow cooling rates have been applied ranging from 11 to 101 °C/min (equivalent to 1.6°C/sec). The model permits the evaluation of the volume fractions of pearlite, primary ferrite and Widmanstatten ferrite, which are plotted as a function of temperature at the various cooling rates. These, in turn can be related to the mechanical properties of the steels, e.g. using methods for determining the strength of mixed microstructure. It has been observed that Widmanstatten ferrite formation is favoured by large austenite grain size. In fact Widmanstatten ferrite usually develops as secondary ferrite from a primary ferrite layer. On the other hand, an increasing cooling rate favours the formation of Widmanstatten ferrite. Furthermore, this phase clearly increases in amount with γ grain size as well as with increasing cooling rate, the γ grain size effect being the more pronounced. Finally, increasing the C content at higher cooling rates, reduces the Widmanstatten ferrite volume fraction because of the suppression of the temperature at which the phase nucleates and also because of the growth rate suppression[47]

2.4.3 Weld Microstructures

The fabrication of engineering structures often involves the welding of steel parts. The understanding of the microstructure transformations occurring when two parts are joined by means of welding is therefore of paramount importance. The metallurgy of a weld can be divided into two main categories: the metallurgy of the fusion zone, which represents the microstructure of the portion of the two metal which is bonded together; the heat affected zone (HAZ) which is constituted by those regions in the near vicinity of the weld where the heat input during the welding changes the microstructure without involving melting of any phase[2].

Generally speaking, the microstructures obtained in the fusion zone include allotriomorphic ferrite nucleated at austenite grain boundaries, Widmanstätten ferrite and acicular ferrite nucleated mostly at oxides deriving from the welding process, and can be very complex. Depending on the design of the weld process the presence of martensitic regions, as well as bainite, degenerate pearlite and retained austenite are also possible. Usually, these phases constitute very small regions which are often classified under the common name of 'microphases'. The presence of bainite is usually avoided, in favour of acicular ferrite whose nucleation is often voluntarily promoted by the addition of nucleating agents such as non-metallic inclusions. This has the aim of increasing the mechanical properties of the joint due to the anisotropic characteristics of the ferrite plates, as discussed in section 2.1.5. It is important to highlight the peculiar growth of the δ-ferrite grains from the liquid metal at the weld joint, which then transform to austenite. This is anisotropic presenting elongated austenite grains along the direction of the heat flow.

This section focuses on the microstructure which develops in the HAZ. The microstructure and therefore the mechanical properties of the HAZ are mainly determined by the heat flow generated from the welding. The heat diffuses from the fusion zone through the metal, which therefore experiences a heating and cooling cycle. Naturally, as the distance from the fusion boundary, i.e. the region where the joining takes place and where usually melting of the metal occurs, increases, the thermal cycle gradually varies. In fact, the peak temperature at a distance x from the fusion boundary as well as the heating rate decrease as the distance x from the fusion boundary increases[2]. On the other hand, the cooling rate is less sensitive to the distance variation and it is usually defined with reference to the time $\Delta t_{8\text{-}5}$ required to the metal to cool over the range 800-500°C, range within which austenite decomposes by solid state transformation.

The temperature gradient across the HAZ leads to a well defined microstructural sequence which can be resumed as follows[2]:

- the adjacent regions to the fusion zone are subjected to very high heating rates which cause full transformation to austenite above the A_{e3} temperature which is usually higher than the corresponding equilibrium temperature due to the heating rate. The annealing which results from heating above the A_{e3} temperature leads to the formation of a coarse grained austenite zone
- as the distance from the fusion boundary increases and the peak temperature decreases, the grain structure becomes finer giving rise to a region of fine grained austenite, the dimension of the grains being usually in the range 20-40μm
- eventually, at a certain distance the microstructure transforms to austenite only partially during heating. The portion of the microstructure which does not transform to austenite becomes tempered
- finally, as the temperature decreases below the A_{e1} point the heat flow causes tempering of the microstructure

The microstructure sequence for a 0.1wt.% C steel in relation to the Fe-C equilibrium diagram is shown in figure2.26 below:

***Figure 2.26[2]**: microstructure sequence found in a HAZ depending on the distance from the fusion zone*

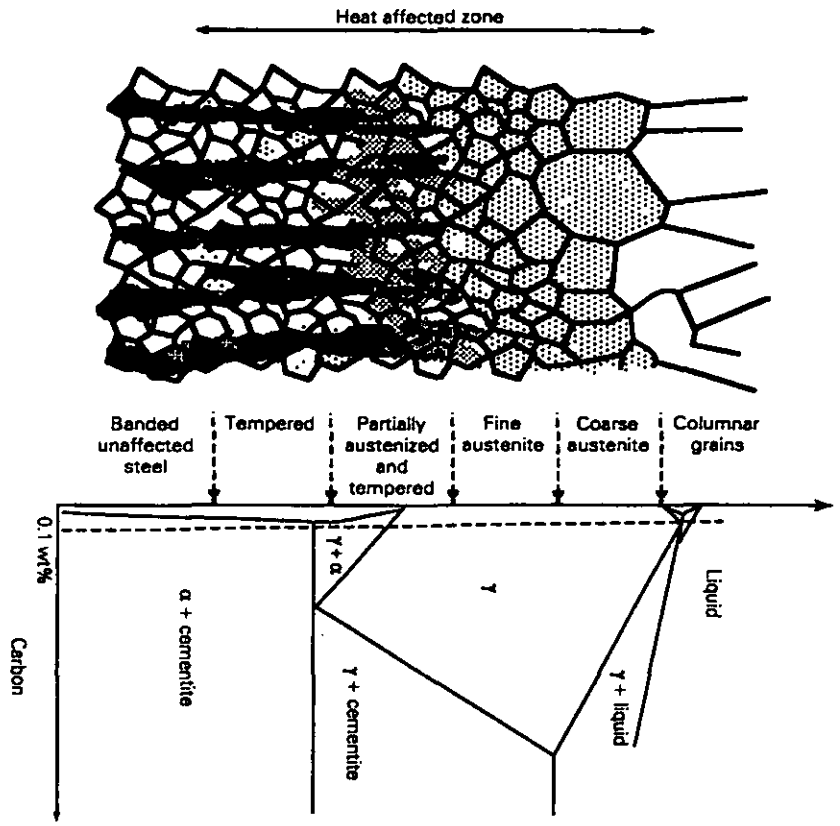

The influences on the mechanical properties deriving from the decomposition of austenite in the coarse grained structure are usually beneficial thanks to the fact that the coarse structure causes an increase in hardenability making it easier to avoid intermediate transformation products which could be detrimental. The fine grained zone usually transforms into ferrite phases with lower hardness values and increased toughness.

The hardenability of the austenite grains in the partially transformed zone have a higher carbon concentration due to the lower peak temperature as can be seen from the equilibrium diagram. This causes a significant increase in hardenability. This usually has a detrimental effect on the final properties. Indeed, depending on the magnitude of the cooling rate, the austenite regions can be either be retained at room temperature or transform to martensite, which then constitute hard and brittle zones which can affect the toughness of such regions. When the cooling rate is not high enough to induce martensite formation, the austenite transforms to a mixture of cementite and ferrite whose characteristic depends on the cooling rate. The brittleness of the cementite can locally impair the toughness of the steel[2].

This research project will have implications for the welding field as it represents one of the most important industrial contexts where the characterisation of microstructures formed under continuous cooling conditions and the possibility of modelling such microstructures is a critical aspect for process optimisation.

3. Experimental Methods

3.1 Introduction

This chapter describes the materials investigated, in addition to the experimental techniques utilised for this research. The investigation has been concerned with the complete characterisation and classification of the phases produced during isothermal and continuous cooling transformations applied to a conventional structural Fe-Si-Mn-C steel. The main attention has been focussed on the factors influencing the simultaneous transformations which can occur under continuous cooling conditions.

Dilatometric tests have been performed under both isothermal and continuous cooling conditions. A variety of different heat treatment conditions were chosen, resulting in a range of phases present and different microstructural conditions. In addition, quantitative information was recorded concerning the phase transformation kinetics. The analysis of the specimens after the heat treatments was performed primarily by means of optical microscopy and scanning electron microscopy (SEM), together with, energy dispersive X-ray (EDX) analysis and electron back scatter diffraction (EBSD) techniques. Micro-hardness testing has been performed on all the continuously cooled specimens in order to gather information for phase characterisation. Thermodynamic and kinetic calculations for the prediction of the time-temperature-transformation diagram of the alloy treated, in addition to determination of M_S and M_f temperatures, have also been carried out.

3.2 Materials

A number of different materials were provided by Corus for this work. Four conventional structural hypoeutectoid Fe-Si-Mn-C low alloy steels (Y7N1, HOM146, HOM148, Z9PIB) were used, in addition to a similar steel (alloy HOM133) which had been electron beam welded (EBW). All the samples provided were previously homogenised. Their compositions are given in table 3.1. A few other alloys were used in the research programme to provide 'example' microstructures of each of the different phases. These were as follows:

- 1.1 wt.% C annealed plain carbon steel
- 0.5 wt.% C annealed plain carbon steel
- 0.1 wt.%C annealed plain carbon steel
- 0.11 wt.% C, 9 wt.% Cr, 1 wt.% Mo martensitic steel, as quenched
- 0.11 wt.% C, 9 wt.% Cr, 1 wt.% Mo martensitic steel, tempered
- 1.15 wt.% C, 2.20 wt.% Cr, 1 wt.% Mo bainitic steel, austempered at 560 °C for 10 minutes

Table 3.1: *Chemical compositions of materials investigated in this research*

Composition (wt.%)	YZN1	HOM133	HOM146	HOM148	Z9P1B
Fe	Balance	Balance	Balance	Balance	Balance
C	0.13	0.13	0.17	0.17	0.16
Si	0.28	0.31	0.29	0.31	0.26
Mn	0.86	1.02	0.52	1.56	0.51
N	-	0.0044	-	-	0.0084
Al	-	-	-	-	0.033
Cr	-	-	-	-	0.01
Ti	<0.005	<0.005	<0.005	<0.005	<0.005
Cu	-	-	-	-	0.01
S	-	<0.002	-	-	0.004
P	-	<0.005	-	-	0.012
Mo	-	-	-	-	0.5
Ni	-	-	-	-	0.01
B	-	-	-	-	<0.0005
Nb	<0.005	<0.005	<0.005	<0.005	-
V	-	<0.005	-	-	-

3.3 Sample Preparation

The materials that underwent dilatometric analysis were machined to solid cylindrical bars, of 3 mm in diameter and 10 mm in length (a schematic diagram of the sample is shown in figure 3.1a).

Figure 3.1a: *Schematic illustration of a cylindrical sample the diameter is 3 mm and the length (z axis) is 10 mm.*

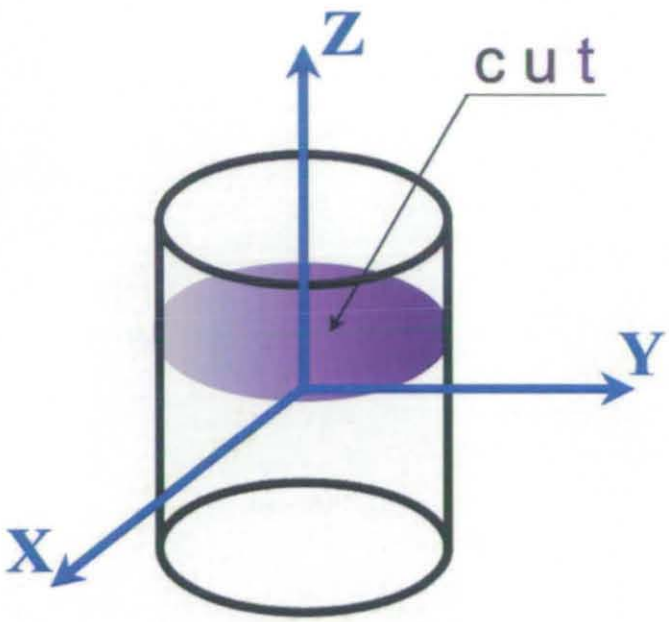

After dilatometry was performed, the samples were first cut into smaller cylindrical sections as shown and then metallographically prepared in order to examine the samples optically and by means of scanning electron microscopy. The sections were obtained using a Struers Accutom-5 circular saw, equipped with an Al_2O_3 blade suitable for cutting metals with a hardness >500 HV. The cuts were performed along the plane XY in figure 3.1. The dimensions of the discs were 3 mm in diameter and 2 mm in thickness. The small sample sizes allowed the remainder of the dilatometry sample to be used for further analysis, for example thermal etching or transmission electron microscopy (TEM).

After being mounted in conducting Bakelite, all specimens for optical and scanning electron microscopy were subjected to metallographic preparation. Grinding was carried out on the sample by hand, using water-cooled silicon carbide paper. The grit paper grade sequence was 240, 400, 800 and 1200 grit. Pre-polishing was then performed on a silk napped cloth with 6 μm diamond particles and subsequent final polishing was carried out on a short nap synthetic cloth with 1 μm diamond particles. Some samples were additionally polished using 0.02 μm colloidal silica paste in order to produce a deformation free surface suitable for EBSD analysis.

The electron beam welded sample i.e. HOM133, was provided in the form of a rectangular plate-shape of dimensions 40 mm x 20 mm x 10 mm. A schematic illustration is shown in figure 3.1b:

Figure 3.1b: *Schematic illustration of the rectangular EBW sample*

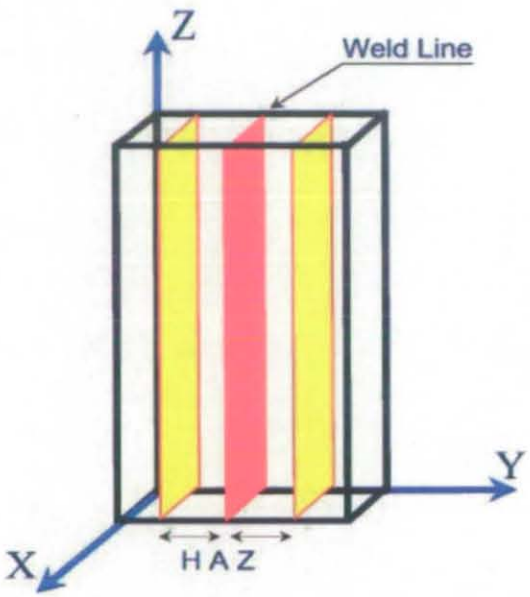

The sample HOM133 was not mounted in conducting Bakelite prior to analysis. The weld was produced along the Z direction so that the heat affected zone (HAZ) developed along the Y direction in both directions away from the weld line.

3.4 Dilatometry

The study of the factors influencing the microstructure of a steel during heat treatment are critically important for the assessment of the properties of the final product. In this sense, dilatometry is one of the most powerful investigation techniques for the study of solid-solid phase transformations in steels. The main principle underlying the dilatometry analysis is the monitoring of the transformation evolution in terms of dimensional changes caused by the formation of one or more phases when a thermal cycle is applied. The user can apply any thermal cycle, including continuous heating, continuous cooling and isothermal treatments. The machine is able to record the dimensional changes due to the variation in the specific volume of a sample during phase transformation. The results are presented in the form of a dilation curve whose shape depends strictly on the heat treatment parameters, in addition to the alloy composition. The dilation curve produces

information which is of immense practical value especially in the field of heat treatment and welding, concerning the transformation kinetics as well as the determination of start and finish transformation temperatures.

A Bähr Dilatometer Type 805 has been used in this work. A set of heat treatments have been performed on the alloys investigated. These included continuous cooling experiments at cooling rates ranging from 2 to 400°C/sec, isothermal heat treatments, interrupted continuous cooling heat treatments (which involved a continuous cooling step followed by a quenching step), hold-quench heat treatments (which involved a continuous cooling step, followed by an isothermal stage and a quenching step to room temperature) and ageing heat treatments.

The main source of error in dilatometry is the possibility of thermal gradients during the cooling of the sample. The position of the thermocouple and the sample dimensions and shape are critical factors. The most suitable specimen shape is a hollow cylinder which lowers the possible thermal gradients along the sample radius. With decreasing cooling rates, the accuracy improves. The most reliable test for the transformation start temperatures are obtained by using taper-ended specimens having the thermocouple attached to their coolest tip. In the present study, the use of solid cylindrical samples was mainly determined by the necessity of microstructure observation using TEM. These errors were minimised because the Bähr 805 machine is equipped with two gas valves which can allow extremely high cooling rates to be achieved even in solid samples, whose dimensions are not relatively small. In this case, the 3 mm diameter samples were small enough to ensure that an even cooling rate was reached throughout their length and width. Therefore, the reliability of the data obtained is believed to be kept within minimal error. Figure 3.2 shows a schematic illustration of the dilatometry cell.

Figure 3.2: *Schematic illustration of the dilatometry cell*

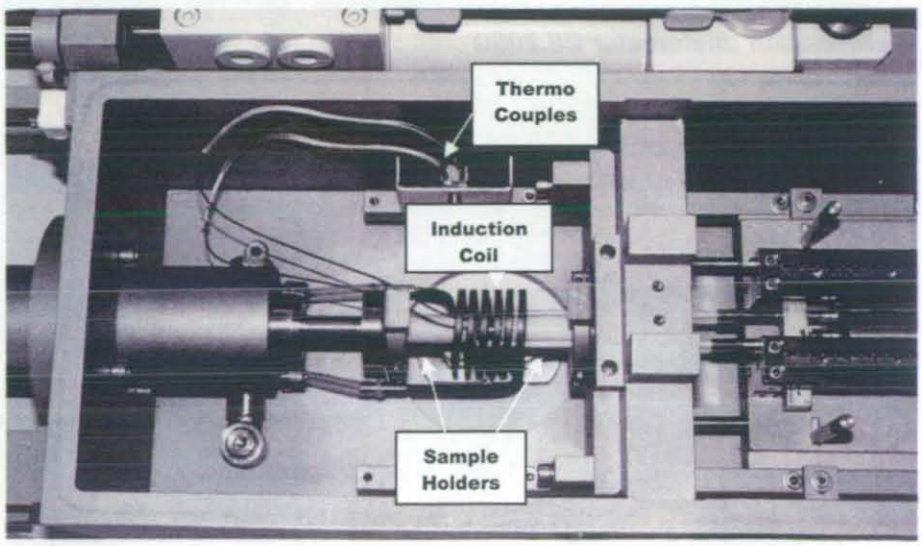

Kinetic information about phase transformations can be effectively derived from a dilation curve. Most of the models developed in the past have considered the volume change to product phase amount at a certain stage of the process using a linear relationship. This is true only for single phase transformations. Furthermore, most of the models cannot provide any information about the chemical composition of the phases from a dilation curve.

3.5 Optical Microscopy

After metallographic preparation and etching in 2% nital (nitric acid in methanol), the samples were examined in a Reichert MEF-3 optical microscope.

The main aim of using optical microscopy was to get an indication of the morphology and extent of all phases present in the specimens. It also provided a very useful means for phase quantification of the continuously cooled samples after dilatometry was performed. Optical micrographs at 500X and 1000X magnification were taken and montages were produced. Finally, by using grids placed manually over the images, the phase percentage of each reaction product could be determined and compared.

3.6 Micro-Hardness

Measurements of micro-hardness were carried out using a Reichert Micro-Hardness tester. A load of 20 g was applied for 6 seconds on each of the tested specimens. The micro-hardness numbers were then calculated from the following equation:

$$HV = 1854.4\frac{P}{d^2} \text{ [kg/mm}^2\text{]}$$

where *HV* is the micro-hardness number, *P* is the load in grams, and *d* is the diagonal of the indentation in micrometers (i.e. the ocular reading multiplied by 0.157 μm).

3.7 Scanning Electron Microscopy (SEM)

Scanning electron microscopy (SEM) is a technique that enables the resolution of features otherwise not observable by means of optical microscopy, based on high magnification (x100 to x1000000) of the surface of bulk samples. In this research work, a LEO 1530VP field emission gun scanning electron microscope (FEGSEM) was used. It is a fully computerised instrument easily controlled by the use of a keyboard and a mouse. The machine is equipped with a thermally assisted field emission source which has a very fine tungsten tip with a radius of few microns. The electrons are extracted by the application of strong field with a voltage of approximately 5kV (1-20kV range). The different signals that can be detected by a SEM are schematically shown in figure 3.3:

Figure 3.3: *Schematic illustration of the signals emitted from the specimen*

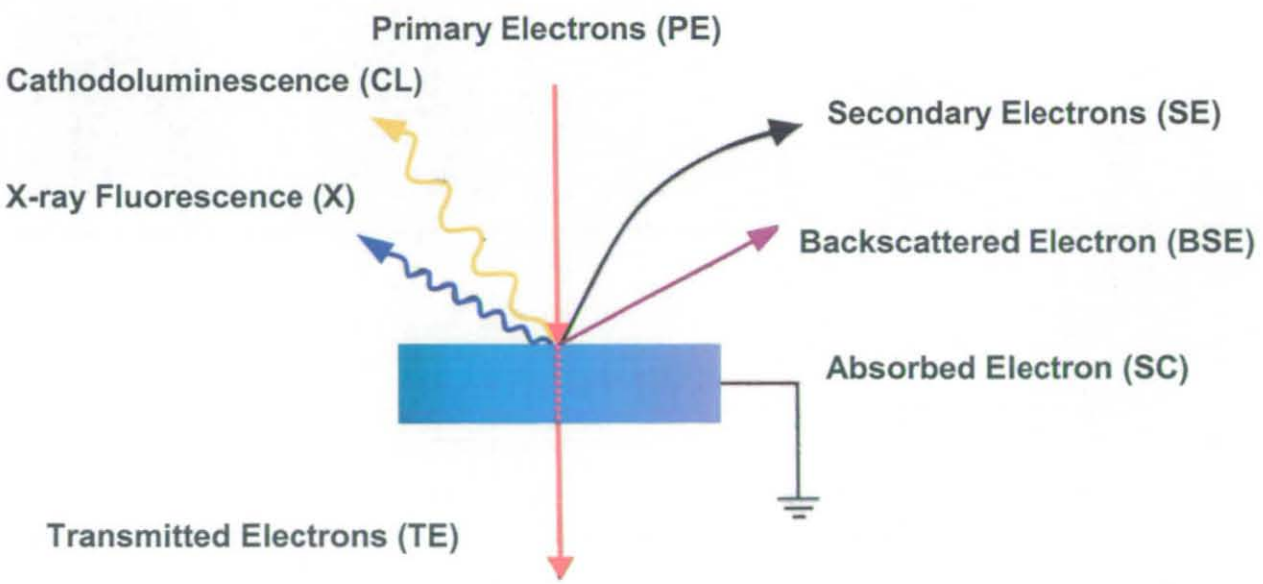

The primary electron of high energy irradiated on the specimen can generate several types of electrons with different energies, depending on their nature, which are related to a specific type of detection and data analysis. These are summarised as follows:

- secondary electrons (SE) of low energy
- backscattered electrons (BS) of higher energy
- transmitted electrons (TE) of higher energy
- absorbed electrons (SC)

In addition to the signals deriving from electron emission, two more signals can be detected:

- X-ray fluorescence (X) of short wavelength
- cathodoluminescence (CL) of longer wavelength

Figure 3.3 illustrates that the type of information obtained depends on the specific electron-specimen interactions and on the extent and depth of the interaction volume. After interacting with the irradiated electrons, the electrons within the specimen may be ejected, and depending on the energy possessed by the ejected electron it can be classified as a secondary or backscattered electron. Secondary electrons possess very low energy and can only be detected near the surface and are therefore very sensitive to topography. Electrons can also be backscattered from the nucleus of atoms hit by irradiated electrons. In this case, the backscattered electrons possess a much higher energy than the secondary electrons because they come from the inner shells and not from the valence shells. The strength of the signal of the backscattered electrons depends on the mean atomic number of the atoms hit by the beam. The higher the atomic number, the stronger the signal emitted and the brighter the appearance of the respective particles.

The secondary electron imaging mode provides good resolution (within the nanometre range) and a good depth of field for surface imaging. The backscattered electron imaging mode instead yields a compositional observation of the surface, with a resolution within the several 10's of nanometre range to 100 nm. An additional facility on the FEGSEM used in this work was an InLens detection mode.

The InLens detection mode, which has been extensively used in this research, offers the advantage of providing a very good observation of the surface features. The images are derived from true secondary electrons which eliminated any possible

topographic effect which can result from the use of the secondary electron imaging mode. In fact, three types of secondary electrons exist (figure 3.4):

- SE type 1 which generate a signal with high spatial resolution
- SE type 2 which degrade the spatial resolution
- SE type 3 which degrade the image contrast by adding a false information from the chamber wall

Figure 3.4: *Schematic diagram showing the signals present in secondary electron imaging*

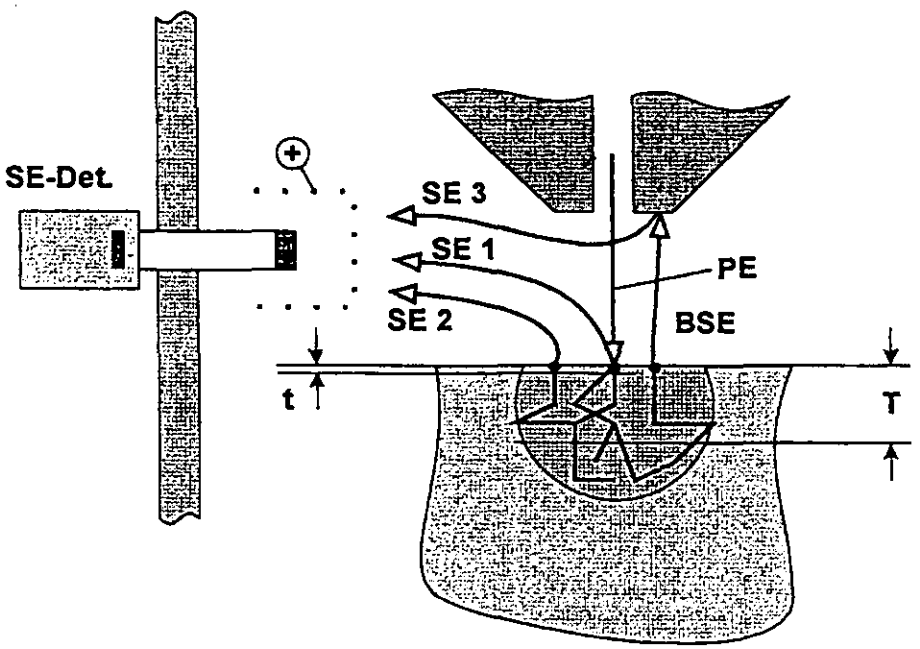

When the In-Lens detection mode is utilised, the SE collection takes place through a retarding field (called a booster voltage) onto a coaxial detector placed above the final detection lens. The advantages offered by this technique are:

- rotationally symmetric collecting field, uniform illumination
- no distortion of the primary beam
- short working distances are possible
- high collection efficiency through a large collection angle
- diffuse illumination with edge enhancement
-

The above advantages led to the choice of the InLens detection mode for imaging purposes in this work.

3.8 Electron Back Scattered Diffraction (EBSD)

Electron Back Scattered Diffraction (EBSD) is a technique which allows crystallographic information to be obtained from samples using an SEM. In EBSD, a stationary electron beam strikes a tilted sample. As a consequence electrons are back scattered and the diffracted electrons form a pattern on a fluorescent screen. This pattern is characteristic of the crystal structure and orientation of the sample region from which it was generated. The diffraction pattern can be used to determine the crystal orientation, grain boundary misorientations, phase discrimination, and to provide information about local crystalline characteristics (e.g. texture). The possibility of scanning the beam throughout a selected region of a sample allows the production of a map which reveals the constituent grain morphology, orientations and boundaries. Therefore, a complete and quantitative representation of the sample microstructure can be established with EBSD.

The main components of an EBSD system integrated on an SEM are:

- A sample tilted at 70° from the horizontal.
- A phosphor screen which is fluoresced by collecting electrons from the sample to form the diffraction pattern.
- A sensitive charge coupled device (CCD) video camera for viewing the diffraction pattern on the phosphor screen.
- A vacuum interface for mounting the phosphor and camera in an SEM port.
- A computer to control EBSD experiments, analyse the diffraction pattern and process and display the results.

A schematic diagram is shown in figure 3.5:

Figure 3.5: Schematic diagram showing an EBSD system setup

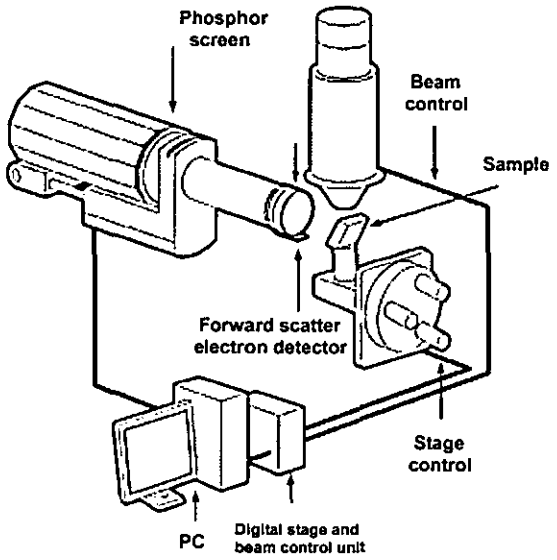

The mechanism by which the diffraction patterns are formed is complex. The atoms in the material inelastically scatter a fraction of the electrons with a small loss of energy to form a source of electrons close to the surface of the sample. Some of these electrons are incident on atomic planes at angles which satisfy the Bragg equation:

$$n\lambda = 2d\sin\theta$$

where n is an integer, λ is the wavelength of the electrons, d is the spacing of the diffracting plane, and θ is the angle of incidence of the electrons on the diffracting plane. These electrons are diffracted to form a set of paired large angle cones corresponding to each diffracting plane. The regions which diffract electron with enhanced intensity between the two cones are used to form an image on the fluorescent screen in which the typical Kikuchi bands of the electron backscatter diffraction pattern (insert picture) can be individuated. The centre lines of the Kikuchi bands correspond to the projection of the diffracting planes on the phosphor screen. Each Kikuchi band can be indexed by the Miller indices of the diffracting crystal plane which formed it. The intersections of the Kikuchi bands correspond to the intersection of zone axes in the crystal with the phosphor screen. These points can be labelled by the crystal direction corresponding to the zone axis. A schematic diagram is shown in figure 3.6.

Figure 3.6: *Schematic diagram showing the collections of backscattered electrons for the production of Kikuchi patterns*

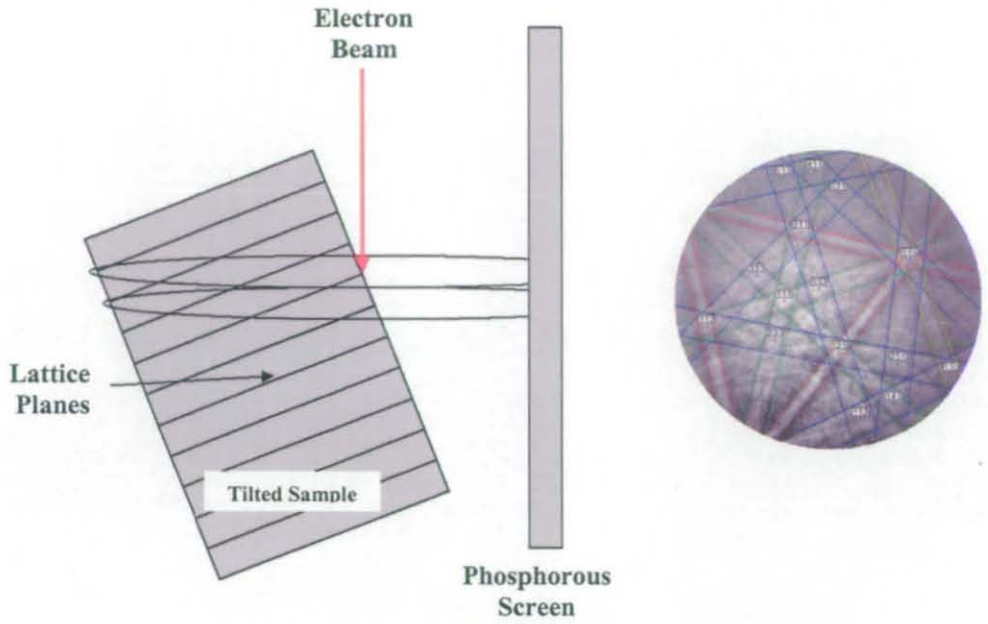

The width w of the Kikuchi bands close to the pattern centre is given by:

$$w \approx 2l\theta \approx nl\lambda/d$$

where l is the distance from the sample to the screen Hence, planes with wide d-spacings give thinner Kikuchi bands than narrow planes. Because the diffraction pattern is bound to the crystal structure of the sample, as the crystal orientation changes the resultant diffraction pattern also changes. The positions of the Kikuchi bands can therefore be used to calculate the orientation of the diffracting crystal.

In crystal orientation mapping, the electron beam is scanned over the sample on a grid of points and at each point a diffraction pattern obtained and the crystal orientation measured. The resulting data can be displayed as a crystal orientation map and processed to provide a wide variety of information about the sample microstructure (insert picture of typical orientation map). The orientation maps are based on the sample normal, rolling and transverse directions. At each point in the map, the crystallographic direction corresponding to the particular sample direction is calculated and a colour allocated according to its position in the so called inverse pole figure.

In crystal orientation mapping a grain is defined by the collection of neighbouring pixels in the map which have a misorientation less than a certain threshold angle. The distribution of grain sizes can be measured from the data collected for the map.

In addition, the distribution of grain boundary misorientation angles and the distribution and position of special grain boundaries can be shown. The individual crystal orientation measurements collected by crystal orientation mapping can be used to show the crystallographic textures developed in the sample. The various textures in the sample can be separated automatically, their volume fractions calculated, and the regions of the sample from which they originate shown.
The quality of the diffraction pattern is influenced by a number of factors including local crystalline perfection, sample preparation, surface contamination and the phase and orientation being analysed. Image quality maps provide the advantage of showing the quality of each single point of the map itself, but in addition to that, they will often reveal features invisible in the electron image such as grains, grain boundaries and surface damage such as scratches.

EBSD can be used to discriminate crystallographically dissimilar phases by comparing the interplanar angles measured from the diffraction pattern, with calculated angles. This is achieved by selecting the best fit from a set of candidate phases belonging to a database. A typical example is the differentiation between alpha ferrite (BCC crystal) and austenite (FCC crystal) in steels.

3.8.1 Data Interpretation

The maps obtained after performing a particular EBSD scan can be related to a statistical distribution of data and vice versa. This can be done for example by retaining a unique colour coding in both the map and the statistical representation such as in the case of the pole figure (figure 3.7). The "standard" maps comprise three main types: microtexture, diffraction patterns diffuseness and misorientation.

A microtexture map is usually displayed in terms of Euler angles that describe the orientation of a crystal. A colour is associated to each of the angles or crystal axes and a map is created by following this scheme. An example is shown in figure 3.7a. By relating the colour key to the colour of the grains the crystallographic orientation of the sample can be understood.

The diffraction pattern diffuseness or quality is the map which most resembles a secondary electron image. An example is given in figure 3.7b. The quality of the patterns obtained during scanning a particular area is indicated by using a greyscale. As the greyscale increases the pattern quality decreases. The quality of a pattern is strictly related to the lattice strain (and therefore a cause of poor pattern quality can be poor surface preparation).

The role of a misorientation map is to delineate grain boundaries and sub-boundaries. The most common misorientation maps show high and low angle boundaries, characterised by different colours. The threshold can be set by the user although it is widely accepted that a low angle boundary is defined so below a threshold limit of 2°. An example of a misorientation map is shown in figure 3.7c.

Figure 3.6: *a) Euler angle map for an aluminium alloy sheet; b) pattern quality map of the same region in the aluminium alloy sheet; c) grain boundary map of the same region*[48]

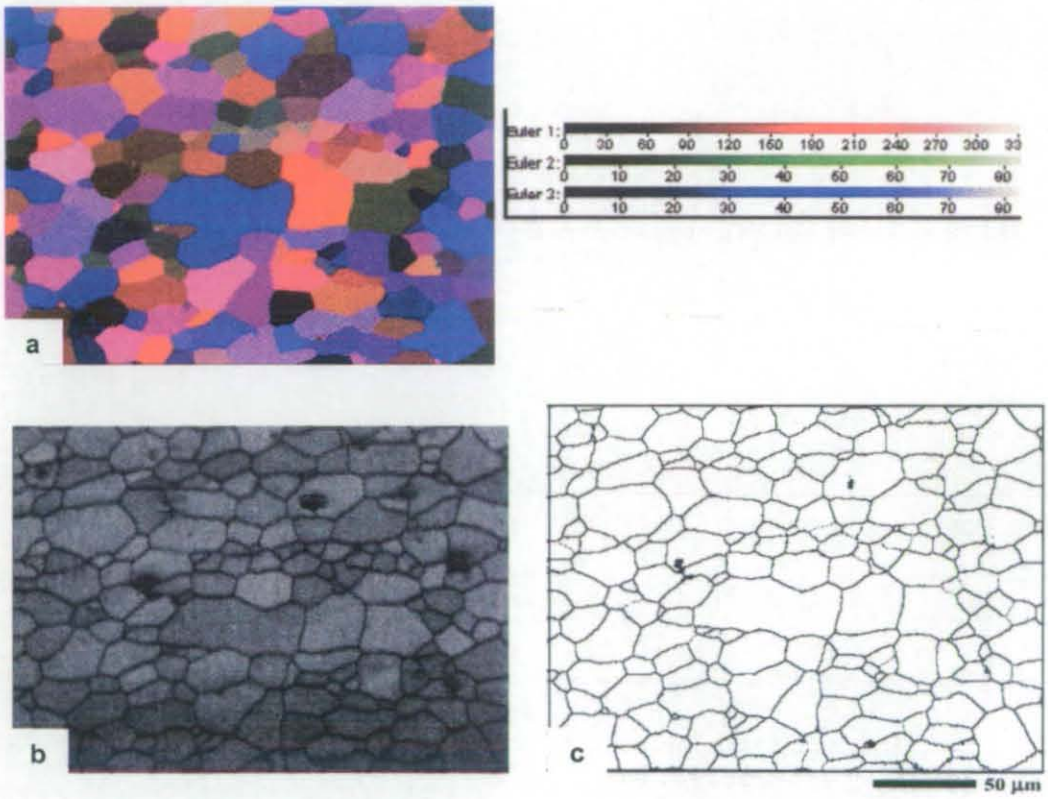

3.9 Energy Dispersive X-ray (EDX) Analysis

SEM also allows for the selection of particles and/or phases which are then analysed by means of energy dispersive X-ray (EDX) analysis. This is used to investigate and identify phases, by defining their chemical composition. The elements present within the analysed specimen are identified according to the energy possessed by the X-rays that are emitted by each element. Furthermore, a quantification of each of the elements present is possible since the number of X-rays emitted is approximately proportional to the concentration of that element in the specimen.

In the present work, an EDAX Pegasus combined EDX and EBSD (electron back scatter diffraction) system was used attached to the LEO 1530VP FEGSEM.

It should be noted that the beam interacts with the specimen over a volume approximately 1 μm in extent and therefore it is hard to obtain EDX data from small particles without interference from the matrix.

3.10 Thermodynamic Calculations

Thermodynamic and kinetic calculations were performed by means of MUGC46[4] which is a computer code developed by H.K.D.H. Bhadeshia, Phase Transformations Group, Department of Materials Science and Metallurgy, University of Cambridge and available on the Materials Algorithms Project website. The software provides a powerful means for modelling the thermodynamic and kinetics of solid-solid phase transformations in steels using a FORTRAN code. Although in the present research it has been utilised for TTT diagram prediction, the software is capable of predicting an enormous amount of phase diagrams, kinetic and thermodynamic information for a wide range of ferrous alloys.

The MTDATA software developed by the National Physical Laboratory allows thermodynamic predictions based on Gibbs free energy minimisation. It provides a facility for retrieving thermodynamic data from databases, compiling data sets for the elements of interest, and assessing these data. It is possible to calculate binary and

ternary equilibrium phase diagram, as well as equilibria in higher order multicomponent, multiphase systems. These are further discussed in chapter 8.

3.11 Phase Quantification

Phase quantification of the various microstructures of the alloy YZN1, HOM146 and HOM148 produced under continuous cooling conditions has been carried out. The phase quantification was carried out on a portion of the microstructure optically observed at a magnification of X500. This has been possible by producing montages of the optical micrographs. Each montage contained six optical micrographs. Grids containing 726 square boxes have been utilised to analyse the relative phase percentages by point counting each phase as shown in figure 3.7.

Figure 3.7: *example of a montage and a grid utilised for phase quantification performed by point counting*

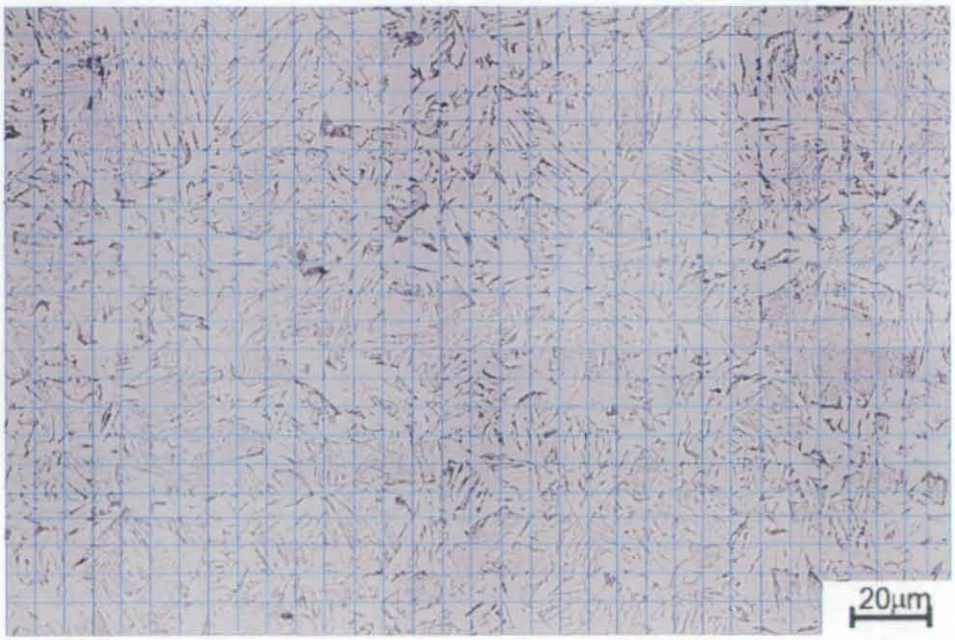

The mixed microphase within the Widmanstätten ferrite has been counted separately, although the data has been associated to Widmanstätten ferrite when the transformation sequence had to be determined as well as the transformation start and finish temperatures for each of the phases formed. The nature of these small microphase regions was not always unequivocally possible to determine as

martensitic, pearlitic or M/A, for instance. Furthermore, as the resulting microstructure was very fine, the distinction between Widmanstätten ferrite, having very fine mixed microphase, and upper bainite was not always straightforward. Therefore, in this case the relative phase percentages of WF and bainite are prone to a certain degree of error. This is discussed further in chapter 8.

3.12 Summary

This chapter describes the principles behind the experimental techniques, justifying their choice made in order to gather the data required to understand the aspects characterising the phase transformations investigated. These techniques include:

- Dilatometry
- Scanning Electron Microscopy (SEM) (InLens detection)
- Transmission Electron Microscopy (TEM)
- Electron Back Scattered Diffraction (EBSD) Analysis
- Energy Dispersive (X-ray) Analysis
- Optical Microscopy
- Micro-Hardness
- Thermodynamic and Kinetics Predictions
- Phase quantification

All the materials used in this research have been listed with the relative chemical composition. These steels can be defined as low alloy Fe-Mn-Si-C low carbon low alloy steels.

4. HEAT TREATMENTS

Microstructures Formed under Isothermal and Continuous Cooling Conditions

4.1 Introduction

The study of modern structural low alloy Fe-Mn-Si-C steels which are continuously cooled, requires an optimum balance between the heat treatment parameters, the alloy composition and the desired microstructure, which should be fit for the purpose required. The effects of continuous cooling heat treatments, which represent the most widely industrially used production option, on the final microstructures are described in this chapter.

The investigation begins with the observation of the microstructure as a function of the heat treatment parameters. The aim of the present chapter is to show the path that has been undertaken in order to determine the identification of each transformation product, which is essential in order to relate the microstructures to the kinetic information that can be obtained from the dilatometry curves. The use of continuous cooling conditions often produces complex microstructures and involves simultaneous phase transformations, therefore, as a starting point, isothermal heat treatments at three different temperatures have been performed and relatively simple microstructures investigated. In the continuous cooling heat treatments two variables have primarily been considered: the effect of the austenitising temperatures and the effect of cooling rate. Two austenitising temperatures have been chosen, 1100°C and 1300°C, which result in different prior austenite grain sizes. A range of cooling rates between 2 and 200°C s^{-1} have been used, in order to cover reconstructive transformations, displacive transformations and the intermediate transformation regime in which both types may occur. The primary aim is to characterise all of the resulting microstructures and relate the observations to the heat treatment conditions used.

4.2 TTT Diagram and Austenitisation

The calculated time-transformation-temperature diagram in figure 1 shows the predicted transformation curves for the steel Y7N1. It can be seen that the reconstructive (diffusional) curve is far over to the left and therefore such transformations are likely to be very fast. The estimated start temperature range for Widmanstätten ferrite (WF) is 720 – 660°C. The bainite start (B_S) temperature is

approximately 594°C whilst the martensite start (M_S) temperature is approximately 475°C. Naturally, the accuracy of a calculated TTT diagram depends on the accuracy of the model used.

Figure 4.1: *Predicted time-transformation-temperature diagram for steel Y7N1*

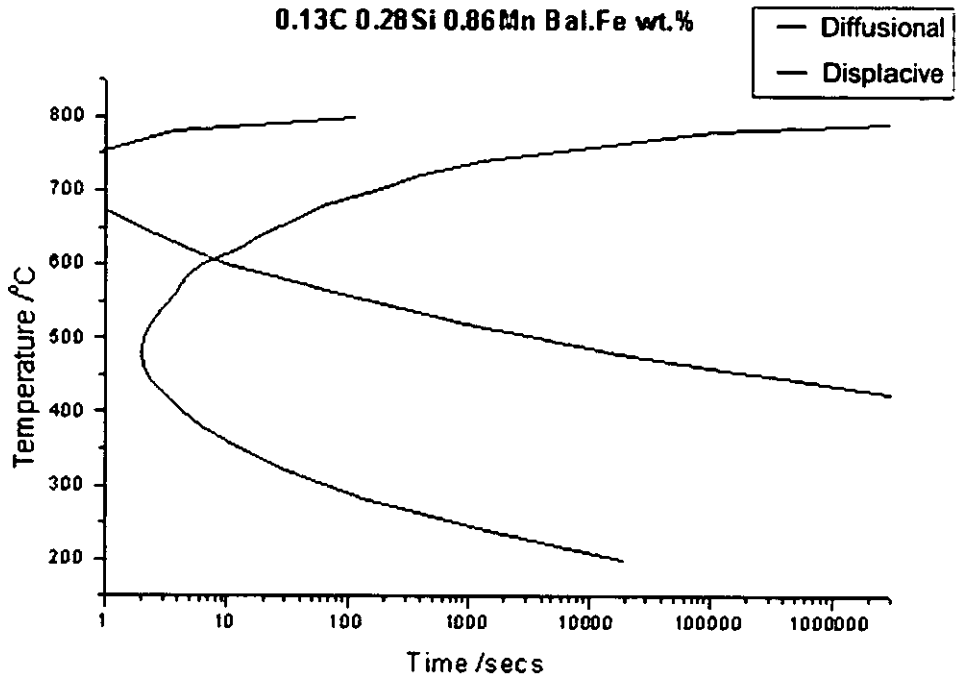

4.2.1 Austenite Grain Size Effect

Two different austenitising temperatures, 1300 and 1100°C, were used for this research to allow the determination of the effect of grain size on microstructural evolution. The austenite grain sizes, which were measured at Corus by means of thermal etching for two representative cooling rates of 10 and 50°C s^{-1}, are:

- 105 μm at 1300°C and 10°C s^{-1}
- 97 μm at 1300°C and 50°C s^{-1}
- 31 μm at 1100°C and 10°C s^{-1}
- 26 μm at 1100°C and 50°C s^{-1}

The austenite grain size increases with the austenitising temperature as a consequence of the higher thermal energy available for grain growth. On the other

hand, lower cooling rates allow more time for growth and the result is a slightly lower measured grain size when the cooling rate increased from 10 to 50°C s^{-1}. The measurements clearly show the consequences of increasing the austenitising temperature: the grain size after austenitising at 1300°C is approximately three times larger than that at 1100°C. This has a significant effect on the kinetics of the phase transformations taking place during cooling.

It is opportune at this point to summarise the effect of grain size on phase transformation[1,2]:

- a smaller grain size offers more nucleation sites at the grain boundaries for both displacive and reconstructive transformations. However, it has been observed that reconstructive transformations are more sensitive to the austenite grain size;
- for reconstructive transformations, an increase in austenite grain size has the effect of reducing the overall reaction rate. This is mainly due to the presence of less kinetically favoured sites for nucleation;
- an increase in polygonal ferrite caused by a decrease in γ grain size, leads to a finer microstructure of the second phase (e.g. bainite), due to an increase in C content of γ, a decrease in the number of nucleation sites and an decrease in the space of growth allowed for the second phase
- as austenite grain size reduces bainite nucleation rate increases;
- bainite growth rate increases as austenite grain size decreases if the sheaf volume remains lower than the maximum sheaf volume allowed by the austenite grain size
- bainite growth rate decreases under the circumstances that a decrease in austenite grain size leads to a reduction in total volume transformed per nucleus. This occurs when rapid growth can take place from a limited number of nucleation sites

4.3 Isothermal Heat Treatments

In addition to the experiments performed under continuous cooling conditions, a set of isothermal experiments, monitored by means of dilatometry, was performed on alloy Y7N1 and alloy Z9P1B. Three transformation temperatures for isothermal holding were chosen principally by consideration of the TTT diagram of alloy Y7N1, to ensure that each temperature results in a defined microstructural scenario. In order to favour diffusion based transformations, the first heat treatment was performed at 740°C, in the reconstructive nose. Secondly, in order to study the transition between reconstructive and displacive transformations, the temperature of 650°C was chosen in the Widmanstätten ferrite regime. Finally, the lowest temperature was selected as 530°C in the bainitic range to provide a full range of microstructures. Samples of alloy Y7N1 were also held for two different times at 740 and 650°C in order to study the microstructure evolution. At 530°C, sample Y7N1 and sample Z9P1B were held for 30 seconds in order to provide microstructure comparison as a function of composition. The isothermal heat treatment conditions are summarised in table 4.1.

Table 4.1: *List of isothermal heat treatments and their nomenclature*

Alloy	T_γ (°C)	Holding T (°C)	Holding Time (s)	Nomenclature
Y7N1	1300	740	10	1300/IT740/10
Y7N1	1300	740	30	1300/IT740/30
Y7N1	1300	650	5	1300/IT650/5
Y7N1	1300	650	30	1300/IT650/30
Y7N1	1300	530	30	1300/IT530/30
Z9PIB	1300	530	30	1300/IT530/30 (Z9P1B)

Isothermally treated samples were initially analysed in order to provide a baseline for the identification of the phases formed during the continuous cooling heat treatment. Furthermore, by relating the predicted TTT diagram to the optical microstructures of the isothermally treated samples and referring to a classification scheme, it was possible to determine much more easily the nature of each phase.

The appearance of each phase observed using optical microscopy, was then directly compared with the morphology of the phases in the continuously cooled samples.

Each sample tested in the dilatometer was first austenitised at a temperature, T_γ, of 1300°C for two seconds. This time was considered to be sufficient to achieve full austenitisation. The samples were then quenched to the transformation temperature by imposing a cooling rate of approximately 250°C s^{-1}. After the isothermal transformation each sample was quenched to room temperature. Therefore it was expected that all the untransformed austenite, which did not possess a sufficient carbon content to stabilise it to room temperature, would have transformed to martensite. The full complete phase characterisation performed by low and high magnification techniques of the continuously cooled samples will be treated in detail in subsequent chapters, the characterisation of the isothermally treated samples is discussed in full in this chapter.

4.3.1 Microstructures of Isothermally Treated Samples

The microstructure of the samples of Y7N1 steel isothermally heat treated at 740°C held respectively for 10 and 30 seconds are shown in figure 4.2a and b:

Figure 4.2a-b: *Microstructures of samples Y7N1 1300/IT740/10 and 1300/IT740/30 observed optically. a) Y7N1 held at 740°C for 10 s, microstructure comprised of PF, WF and M; b) Y7N1 held at 740°C for 30 s, microstructure comprised of larger PF regions and M*

a)

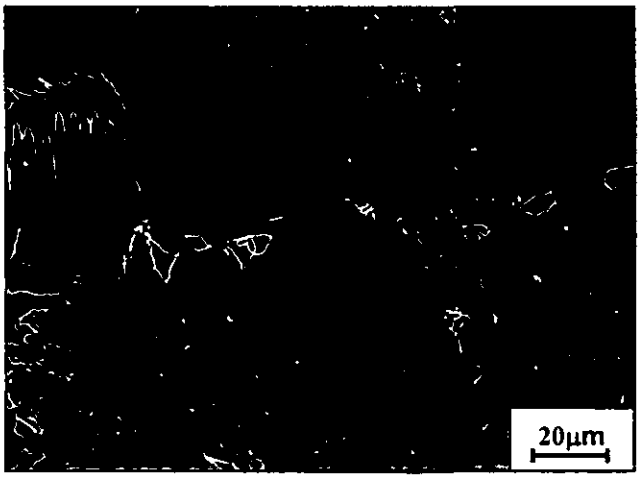

b)

At the highest temperature of 740°C, the main microstructural constituents are allotriomorphic ferrite nucleated on prior austenite grain boundaries and grown during isothermal holding, and martensite formed during quenching to room temperature. The amount of Widmanstätten ferrite plates is very limited at high temperature. However, it is interesting to note the presence of ferrite sideplates growing into the surrounding austenite which were "frozen" upon quenching, revealed by optical observation of the samples held at 740°C for 10 seconds.

The intermediate temperature, i.e. 650°C, has been chosen in the bay region between the reconstructive and displacive transformations. The microstructure of the samples of Y7N1 steel isothermally heat treated at 650°C held respectively for 5 and 30 seconds are shown in figure 4.3a and b:

Figure 4.3a-b: *Microstructures of samples Y7N1 1300/IT650/5 and 1300/IT650/30 observed optically. a) Y7N1 held at 650°C for 5 s, microstructure comprised of PF, WF and M; b) Y7N1 held at 650°C for 30 s, microstructure comprised of WF regions and M. Most of the austenite transformed into WF*

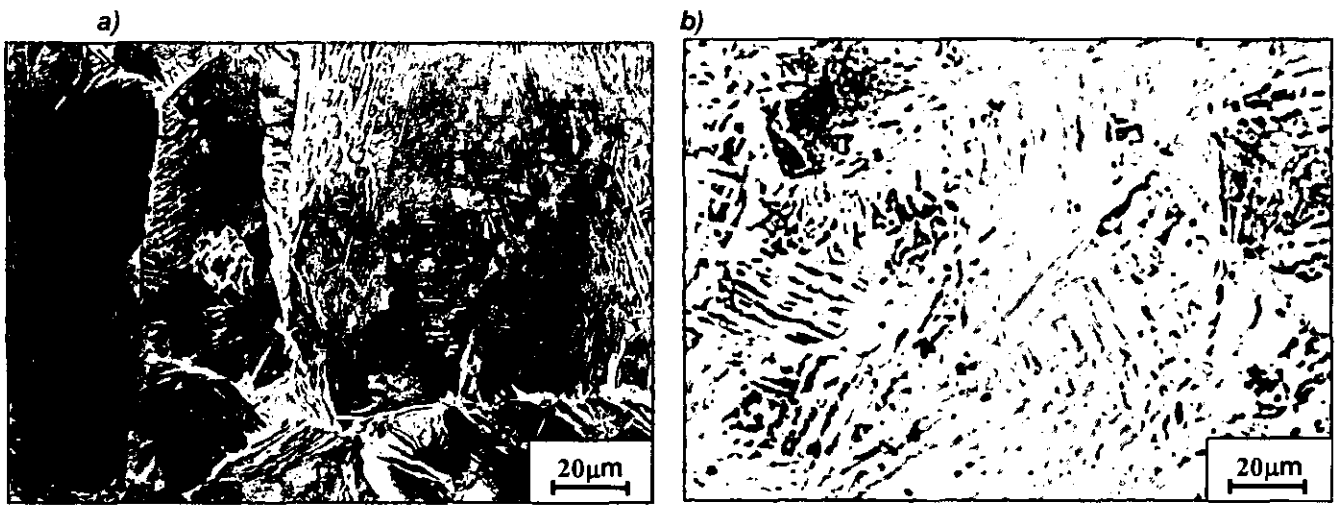

At the intermediate temperature of 650°C, the isothermal holding visibly led to the formation of Widmanstätten ferrite and a certain amount of upper bainite which often appears to have a coarse microstructure. The ferrite plates growing into the austenite can be easily seen in the micrograph for the holding time of 5 seconds. The dominant microstructure at these early stages of transformation is however martensite formed upon quenching to room temperature. Figure 4.3b clearly shows that the microstructure is dominated by Widmanstätten ferrite after 30 seconds whose growth rate is sufficient to reach more than 80% volume fraction, with a relatively small amount of pearlite and ferrite, in addition to martensite formed after quenching and retained austenite.

The microstructure of the sample Y7N1 isothermally treated at 530°C for 30 seconds is shown in figure 4.4.

Figure 4.4: *Optical micrograph showing sample Y7N1 held at 530°C for 30 s, microstructure comprised of WF, B and M*

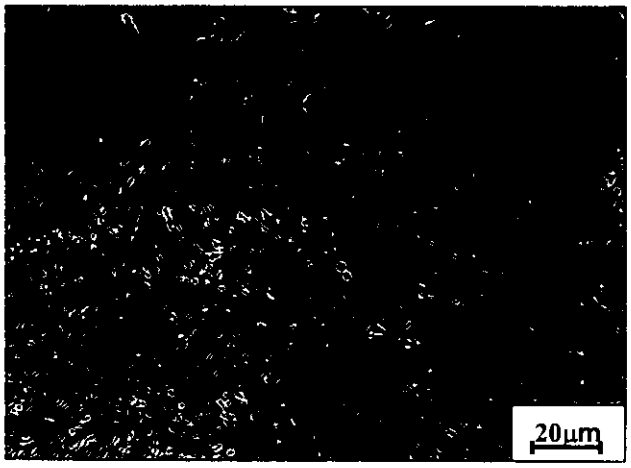

The lowest temperature, i.e. 530°C, was selected according to the predicted TTT diagram in the bainitic region. The transformation temperature was intermediate between the bainite start temperature and the M_S temperature so that a predominantly bainitic microstructure could be obtained.

The microstructure of alloy Y7N1 shown in figure 4.4 is predominantly bainitic with the rate of bainite reaction very fast compared, for instance, to that of allotriomorphic ferrite. Small Widmanstätten ferrite regions having a fine structure had the chance to form at the lowest temperature chosen for isothermal holding.

The effects of a variation in composition on the bainite reaction were investigated by analysing the behaviour of alloy Z9P1B whose composition can be found in table 3.1 in the experimental section, and compare it with the behaviour of alloy Y7N1. The microstructure of the sample Z9P1B steel isothermally heat treated at 530°C held for 30 seconds are shown in figure 4.5.

Figure 4.5: *Optical micrograph showing sample Z9P1B held at 530°C for 30 s, fully bainitic*

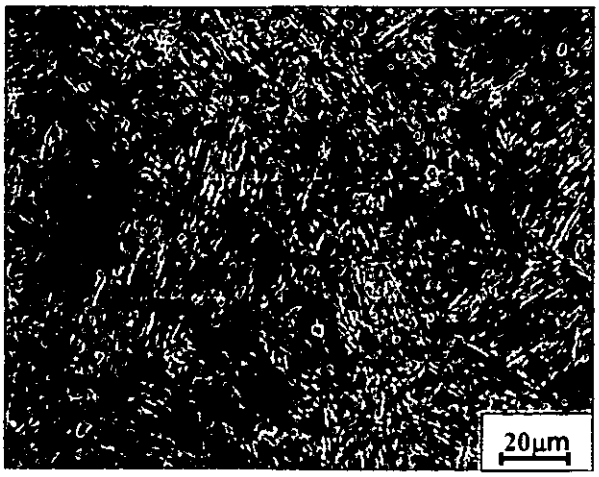

It was observed that the microstructure of Z9P1B was dominated by bainitic ferrite, both upper and lower, and was significantly finer than the corresponding sample of alloy Y7N1. The lower manganese content and the molybdenum addition are the main elements responsible for the different microstructure.

4.3.2 Discussion of Isothermal Heat Treatments 1300/IT740/10 and 1300/IT740/30

The microstructure observed can be directly related to the transformation mechanism dominating at the transformation temperature and to the information provided by the dilatometry experiments. At the highest isothermal heat treatment temperature, i.e. 740°C, the dominant transformation mechanism is expected to be reconstructive from the predicted TTT diagram, and the microstructure produced if the transformation were allowed to go to completion should be mainly primary ferrite formed at austenite grain boundaries and/or pearlite. The amount of idiomorphic ferrite is strictly connected to the amount of dispersed particles inside the austenite grains. There are only a few inclusions in these samples, and therefore the amount of idiomorphic ferrite is expected to be low, with allotriomorphic ferrite being the dominant ferrite morphology. Martensite and stabilised austenite may also be present, depending on the amount of carbon rejected into the surrounding austenite, precipitated in the form of carbides or forming the pearlite lamellae, with their relative amounts being related to the holding time. The TTT diagram indicates a very fast reconstructive reaction start between 700°C and 750°C. From the dilatometry plots for samples isothermally treated for ten and thirty seconds, in figure 4.6a-b and figure 4.7a-b, (i.e. temperature as a function of time and change in length as a function of time) it can be seen that the phase change $\gamma \rightarrow \alpha$ starts relatively quickly and evolves very slowly as indicated by the gradual variation in the slope of the curve. This is more evident in the plot for the transformation interrupted at thirty seconds (figure 4.7).

Figure 4.6a: *T versus t curve of sample Y7N1 austenitised at 1300°C, held at 740°C for 10 s*

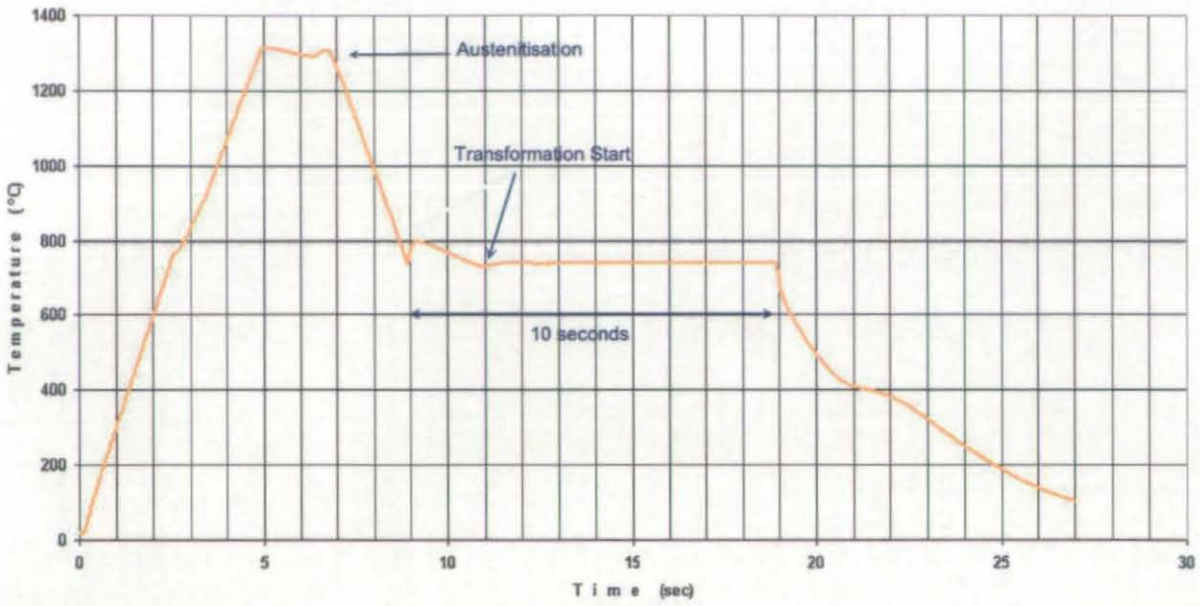

Figure 4.6b: *Dilation curve of sample Y7N1 austenitised at 1300°C, held at 740°C for 10 s*

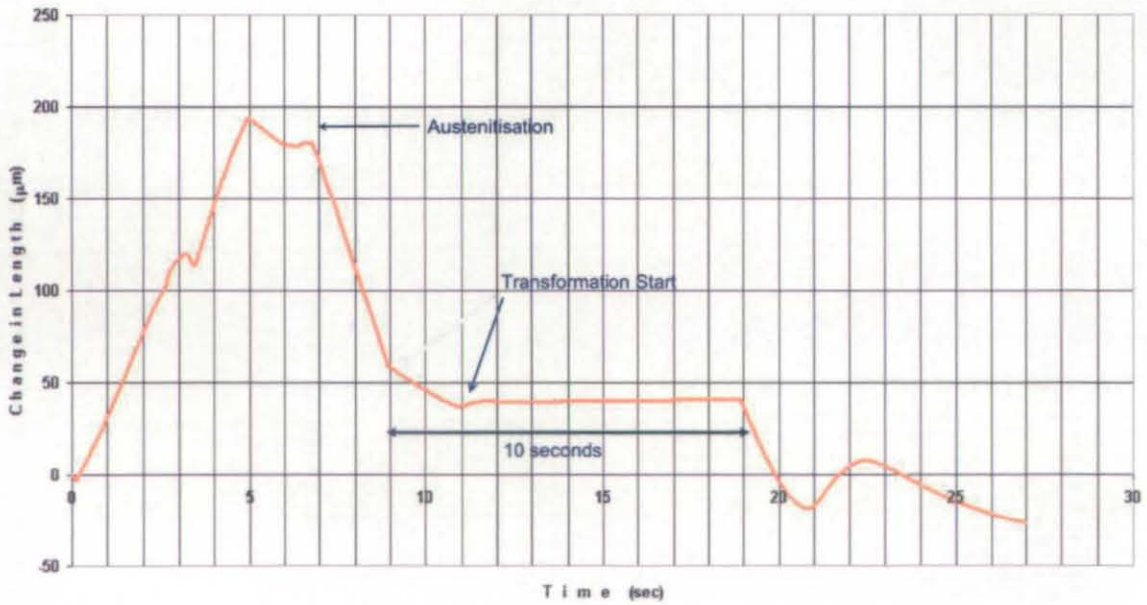

Figure 4.7a: *T versus. t curve of sample Y7N1 austenitised at 1300°C, held at 740°C for 30 s*

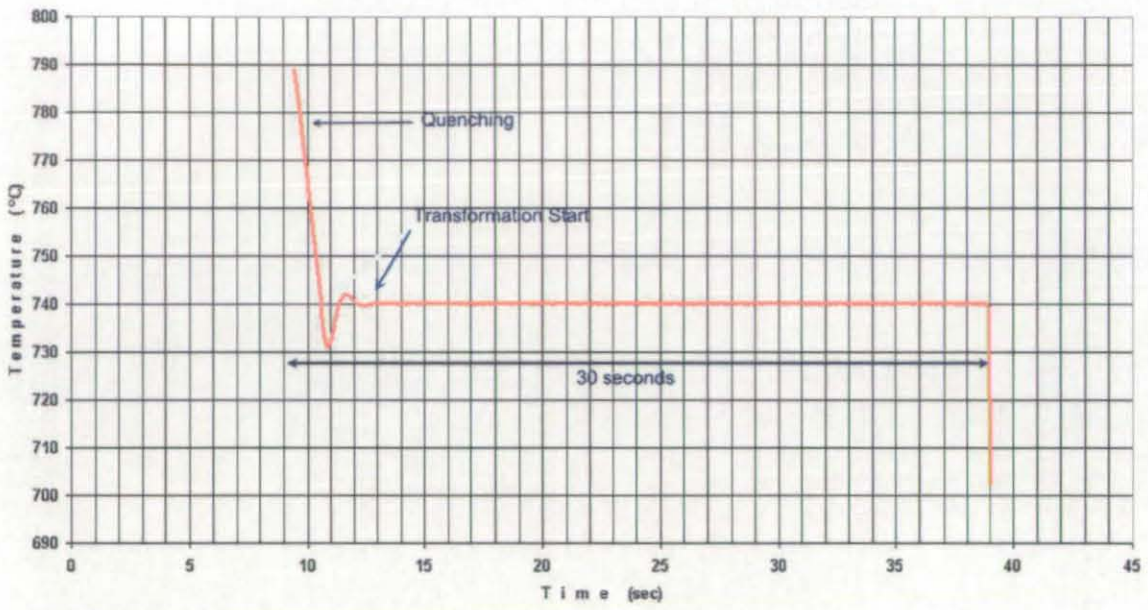

Figure 4.7b: *Dilation curve of sample Y7N1 austenitised at 1300°C, held at 740°C for 30 s*

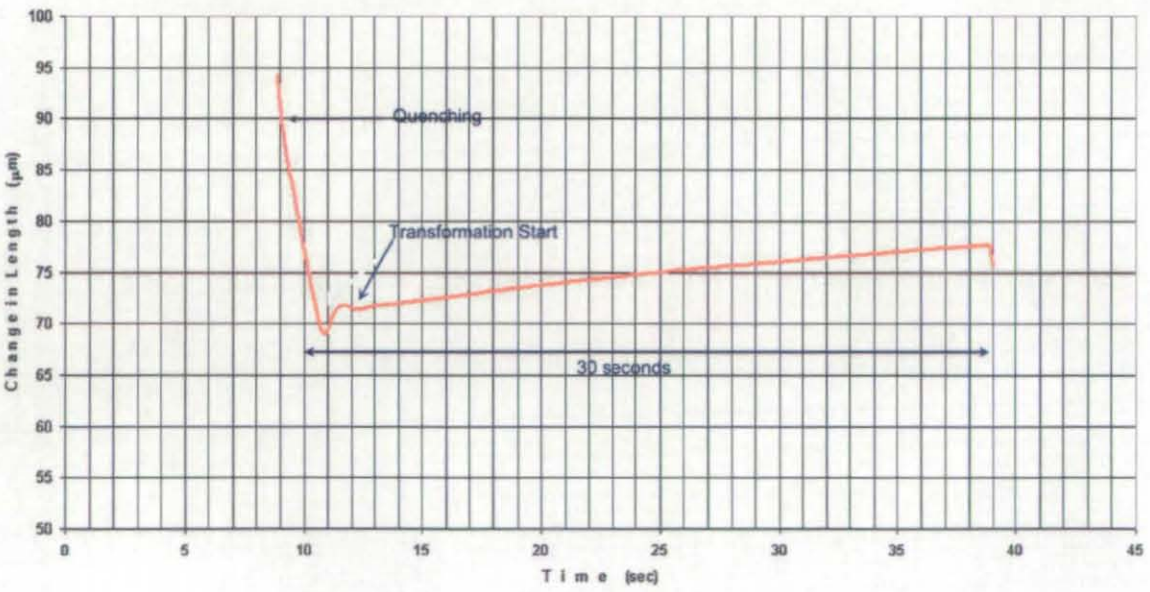

The optical micrographs (figures 4.2a-b) show that after thirty seconds the amount of ferrite significantly increases compared to after isothermal treatment for ten seconds, as implied by the slow growth velocities appropriate to diffusional processes. The dilatometry plot shown in figure 4.7b reflects the slow primary ferrite growth occurring over the thirty seconds of isothermal holding. The change in length

curve continuously increases (at constant gradient) indicating that the volume fraction of ferrite increases proportionally with the holding time. As a consequence of the slow growth rate of primary ferrite, the largest proportion of both samples, held for ten and thirty seconds, primarily comprises martensite formed upon quenching to room temperature. The main microstructural features of the isothermally treated samples at 740°C held for 10 and 30 seconds, have been observed by means of SEM using the InLens detection mode, as shown in figure 4.8.

Figure 4.8: *Microstructural features of sample Y7N1 held at 740°C for 10 (a and c) and 30 seconds (b and d)*

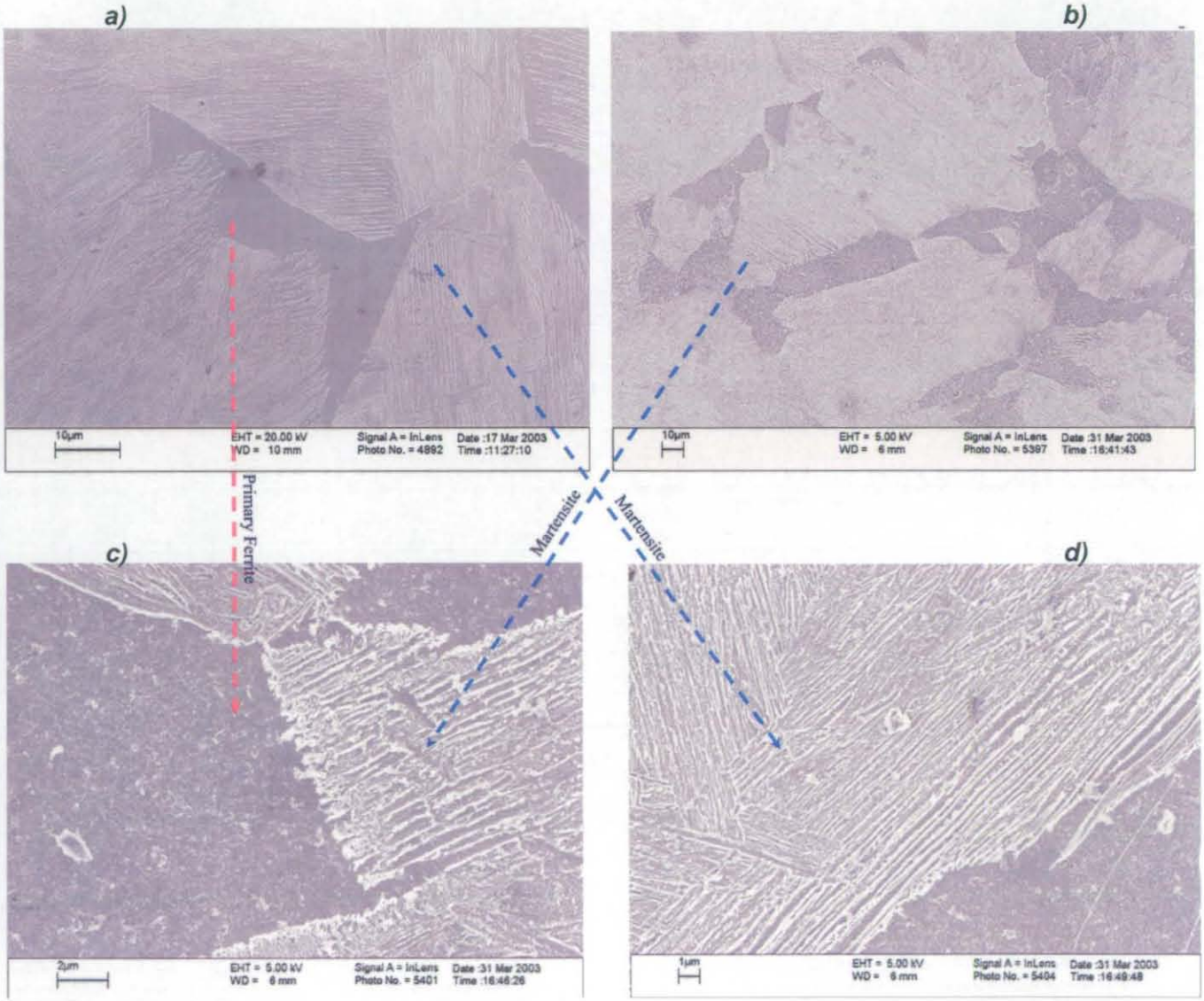

4.3.3 Discussion of Isothermal Heat Treatments 1300/IT650/5 and 1300/IT650/30

The presence of manganese in alloy Y7N1 should limit the formation of polygonal ferrite, by prolonging the incubation time. This is a consequence of the γ stabilising effect of Mn. It should also favour the growth of side plates of Widmanstätten ferrite which can be seen in figure 4.3a. In addition, it causes an increase in the $\gamma \rightarrow \alpha$ transformation temperature.

The purely diffusional transformation of both allotriomorphic ferrite and pearlite is reflected in their slow growth processes. However, the higher driving force associated with the Widmanstätten ferrite formation and the displacive component of Widmanstätten ferrite growth explains the microstructural evolution observed from 5 seconds to 30 seconds after isothermal holding at 650°C.

The final microstructure depends on the competition between the different types of transformation mechanism. It is very interesting to observe the microstructure produced at the transition temperature between the reconstructive and displacive curves. In fact, the distinction between Widmanstätten ferrite and bainite (upper morphology) at this temperature is difficult to discern using optical microscopy, and there is still some debate on the nature of the two transformation mechanisms and their differences. One useful characteristic to enable differentiation of the two phases optically is the high aspect ratio of Widmanstätten ferrite plates, which result in parallel arrays. Both bainite and Widmanstätten ferrite tend to grow directly from prior austenite grain boundaries. From the optical micrographs, Widmanstätten ferrite appears to be dominant following these heat treatments.

After 5 seconds at 650°C the Widmanstätten ferrite transformation starts and the plates have the opportunity to grow into the surrounding austenite as shown in figure 4.3. However, the dilatometry plot, shown in figure 4.9b below, suggests that the transformation is interrupted at its early stages and the larger proportion of austenite transforms to martensite upon quenching. The microstructure comprises of ferrite plates and martensite, both easily visible in figure 4.10.

Figure 4.9a: *T versus. t curve of sample Y7N1 austenitised at 1300°C, held at 650°C for 5 s*

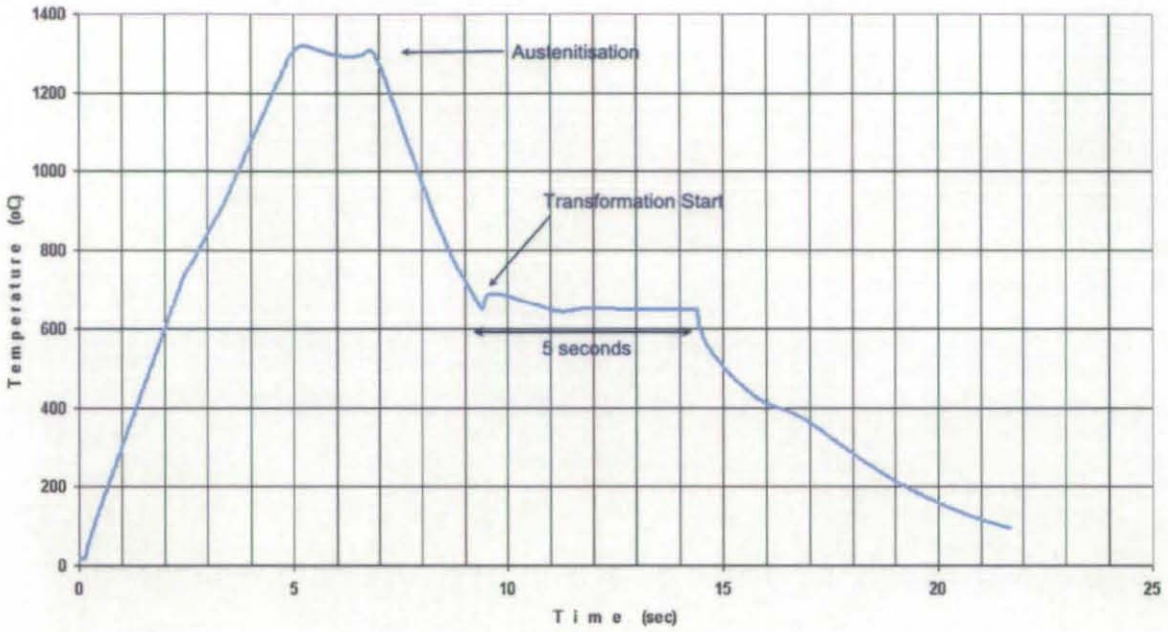

Figure 4.9b: *Dilation curve of sample Y7N1 austenitised at 1300°C, held at 650°C for 5 s*

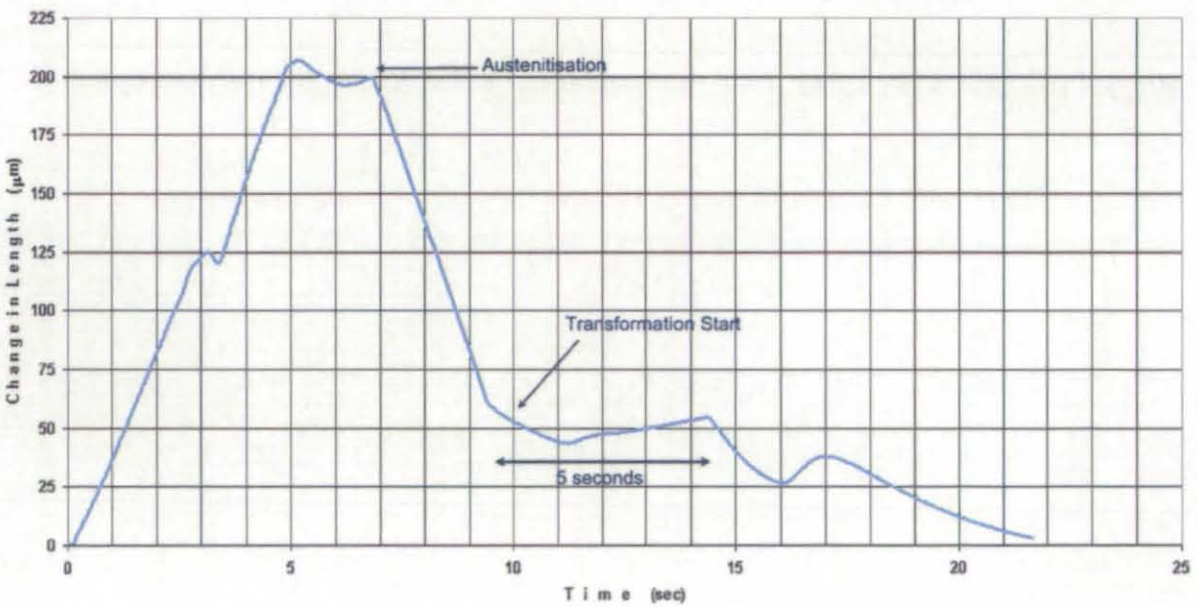

The main microstructural features of the samples held at 650°C for 5 s have been analysed by means of SEM and are presented in figure 4.10.

Figure 4.10: *Microstructural features of sample Y7N1 held at 650 °C for 5 seconds*

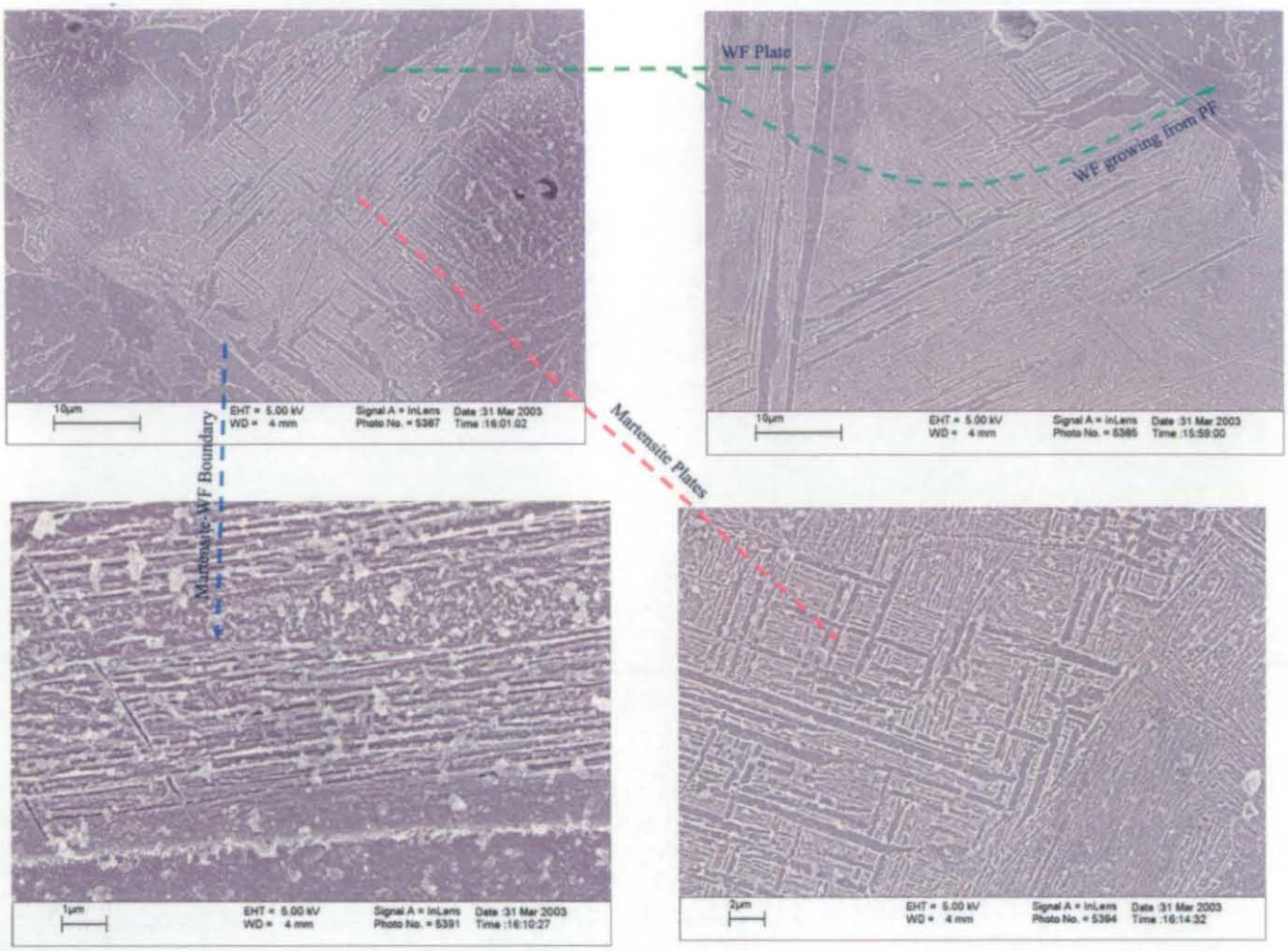

On the other hand, holding for 30 seconds at the same transformation temperature was sufficient for the transformation to reach completion. From the dilatometry plots shown in figure 4.11b it can be seen that there is no further change in length (i.e. $\Delta L \cong$ constant) after approximately 28 seconds at 650°C.

Figure 4.11a: *T versus. t curve of sample Y7N1 aust. at 1300°C, held at 650°C for 30 s*

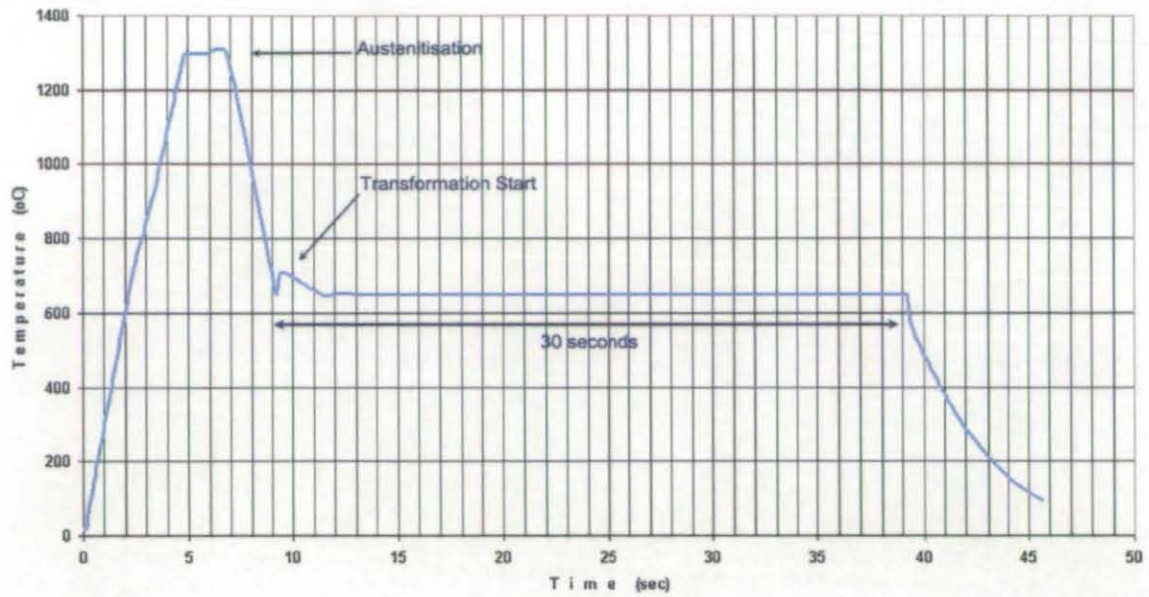

Figure 4.11b: *Dilation curve of sample Y7N1 austenitised at 1300°C, held at 650°C for 30 s*

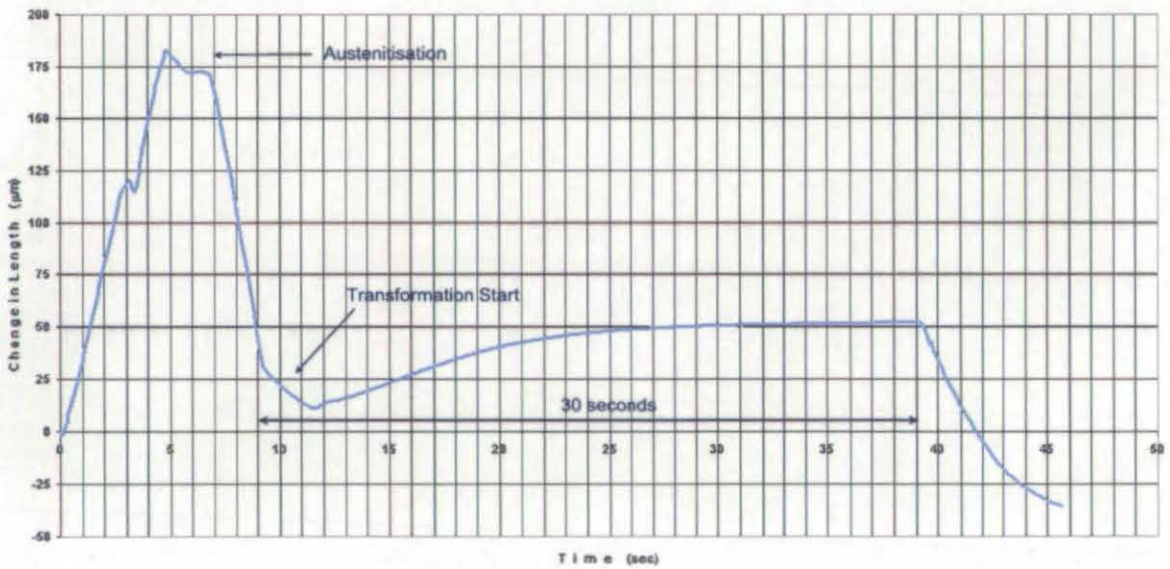

The results of the observation of the sample isothermally transformed at 650°C for 30 s, performed by means of SEM, are presented in figure 4.12.

Figure 4.12: *Microstructural features of sample Y7N1 held at 650°C for 30 seconds*

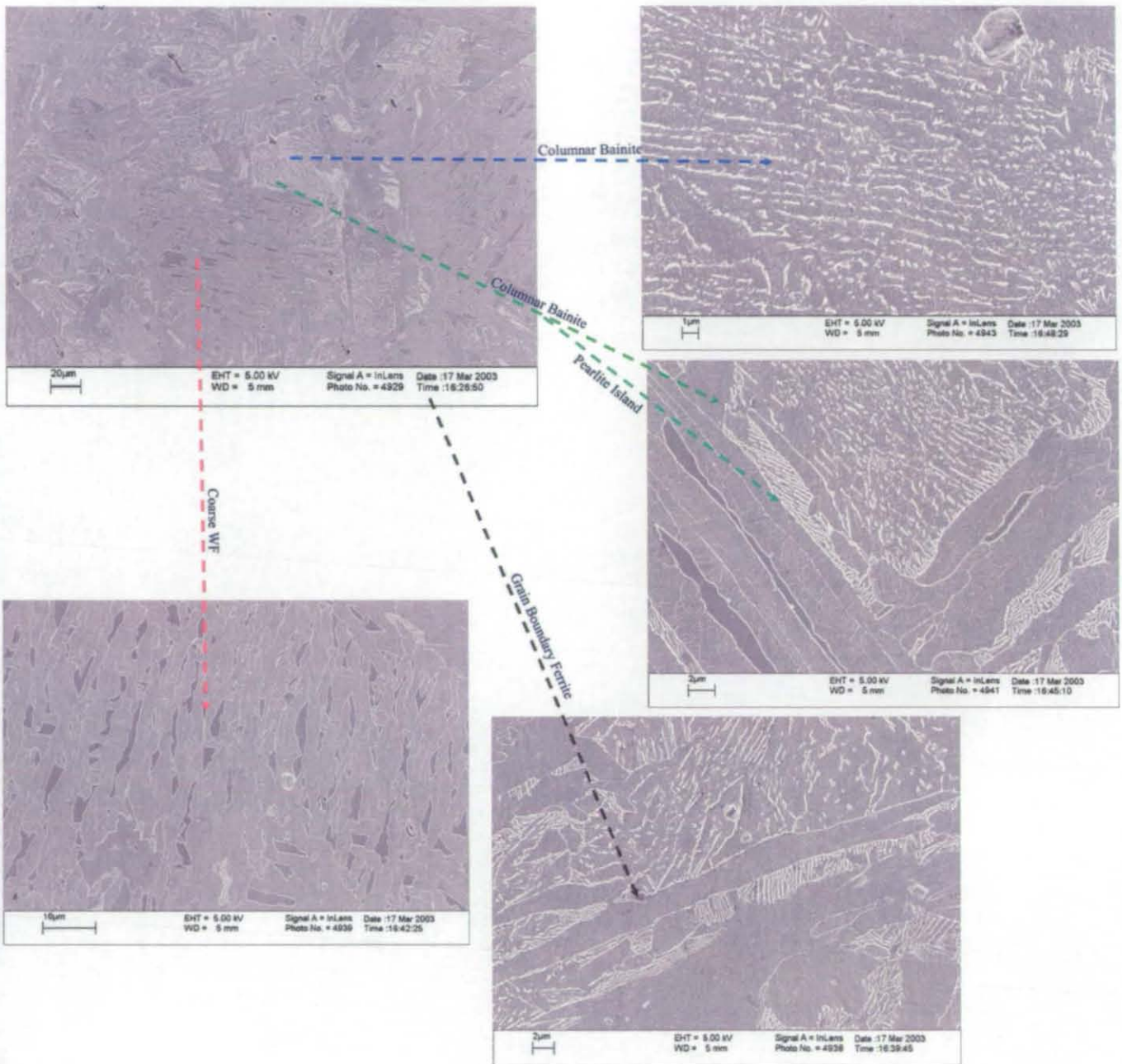

The structure of Widmanstätten ferrite appears to be very coarse, with a high aspect ratio. In some instances, the plates grow from grain boundary ferrite.

It is also interesting to note the development of the pearlitic phase which was found in very small regions or "islands" between ferrite plates. It is probable that the low carbon content of the alloy can locally increase, favouring pearlite formation. The

fact that manganese addition considerably lowers the growth rate of pearlite further justifies the limited presence of pearlite, as well as its relatively coarse structure.

One of the most interesting features revealed by SEM is the presence of what has been classified as columnar bainite in the literature[1]. This phase is characterised by a morphology comprising a non-lamellar aggregate of cementite and ferrite, the overall shape of which is like an irregular and slightly elongated colony as shown in figure 4.12. The carbide morphology is mainly needle-like. However, at the ferrite austenite interface, the cementite particles become coarser, forming a different microstructure layer which is more akin to the lamellar morphology of pearlite. It is interesting to observe that columnar bainite has usually been encountered only in hypereutectoid steels or in low carbon content steels transformed at high pressures. It should be noted that the eutectoid composition is shifted to lower carbon concentrations by hydrostatic pressure. There is no IPS surface relief accompanying the growth of columnar bainite, and therefore it may be more similar to pearlite than bainite[1]. The growth mechanism of columnar bainite is still not very clear and its presence in alloy Y7N1 under the described isothermal conditions is peculiar and could be associated with the formation of a ferrite carbide aggregate, which will be discussed in chapter 6.

Secondary constituents such as martensite and retained austenite are mostly found in the microphase regions between Widmanstätten and/or bainitic plates. The microphase islands found in between Widmanstätten ferrite are very coarse. Considering that the transformation has reached completion, it is probable that the amount of retained austenite is larger than the amount of the martensitic phase. The main reasons determining the retention of austenite to room temperature are the constraint exerted by the surrounding ferritic phase (i.e. Widmanstätten ferrite or bainitic ferrite) which prevents the volume expansion associated with the $\gamma \rightarrow \alpha'$ transformation, the possible austenite stabilisation due to local carbon enrichment, although this effect should be quite limited in view of the low carbon content of alloy Y7N1, and finally the possibility that the incomplete phenomenon reaction takes place in the upper bainitic regions. The latter hypothesis, however, is open to debate. Indeed, the incomplete reaction phenomenon has been observed and investigated in alloys with high silicon contents, which prevent carbide precipitation, which in turn allows partition (or rejection, depending on the view of the bainite transformation) of carbon into the surrounding austenite. It should be noted however, that this aspect of the transformation could be more relevant at the lowest isothermal transformation

temperature (i.e. 530°C), as at 650°C the dominant microstructure constituent is Widmanstätten ferrite.

4.3.4 Discussion of Isothermal Heat Treatments 1300/IT530/30 and 1300/IT530/30(Z9P1B)

The dominant mechanism of transformation at 530°C was, as expected, found to be displacive. Considering that the M_S temperature for alloy Y7N1 was estimated as approximately 475°C, it is assumed that the formation of any martensite in this sample is subsequent to the isothermal holding.

From the dilatometry plot, figure 4.13b, it is clear that the transformation reaction rate is very high after quenching from the austenitising temperature and the transformation reaches completion after approximately six seconds as indicated by the fact that no change in length was recorded after this period of time. The nucleation time appears to be very low and the growth rate very high as indicated by the change in length versus time plot at thirty seconds shown in figure 4.13b. These characteristics are typical of a displacive transformation, whose growth takes place extremely quickly after the nucleation stage has occurred.

Figure 4.13a: *T versus t curve of sample Y7N1 aust. at 1300°C, held at 530°C for 30 s*

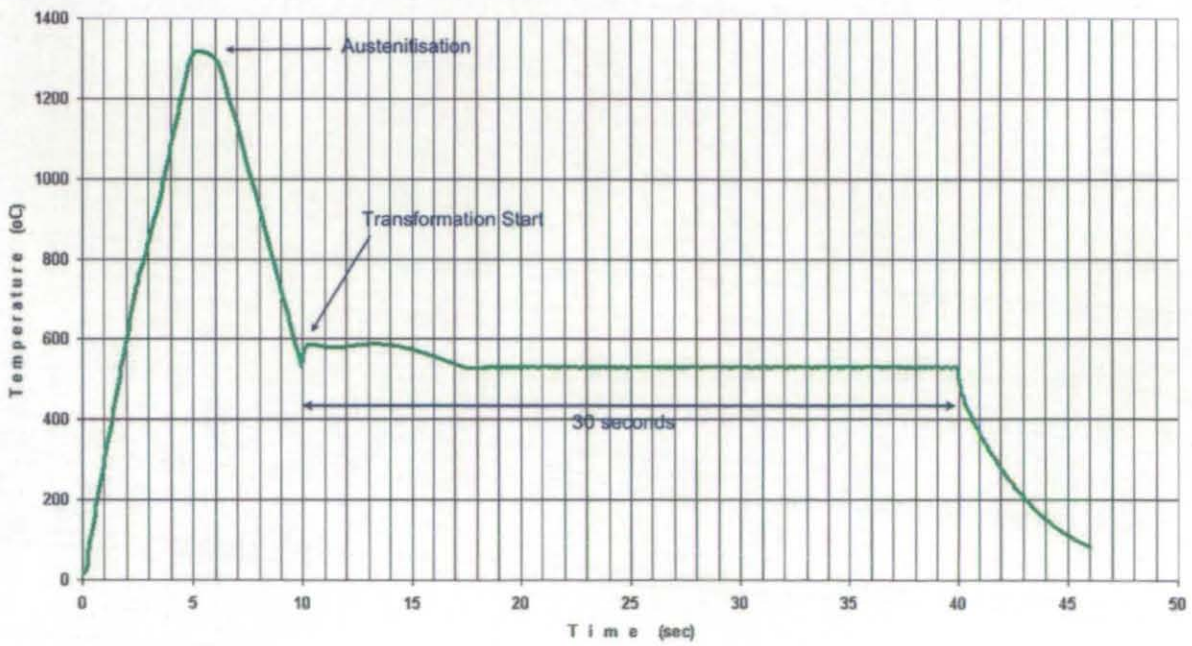

Figure 4.13b: *Dilation curve of sample Y7N1 austenitised at 1300°C, held at 530°C for 30 s*

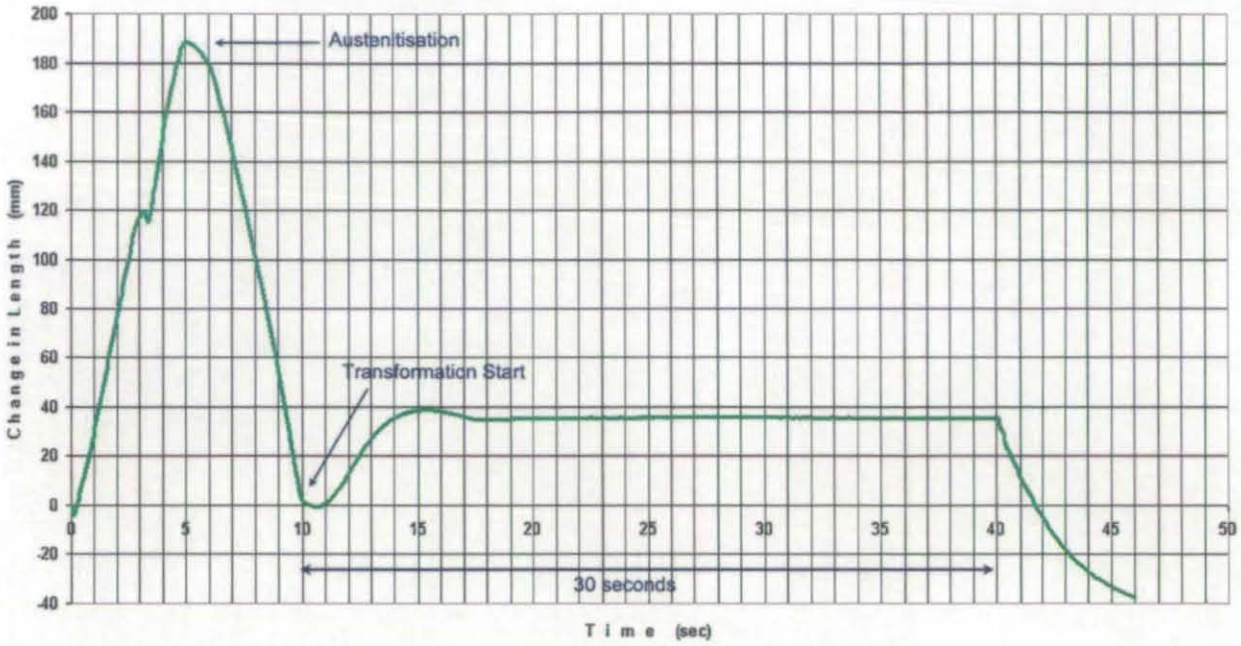

From the optical micrographs presented in figure 4.4, the phase which is bainitic ferrite (bright regions) is dominant, and occupies approximately 70% of the microstructure. Naturally, the structure is much finer than the one formed at 650°C. In this case, in fact, it becomes more difficult to distinguish between upper bainite and Widmanstätten ferrite. It is interesting to observe the various structures of the microphase which become finer and finer due to the transition from Widmanstätten ferrite to upper bainite. The different morphologies in some cases appear to result from phase orientation in a particular grain observed. The microstructure observed by means of SEM is shown in figure 4.14.

The isothermal treatment at the lowest temperature chosen led to the formation of dark etching areas viewed optically. This phase will be discussed in more detail in the following sections concerned with the continuous cooling experiments. The sample treated at 530°C is the only one with this type of structure, which is similar to that found in the continuously cooled samples. The useful information provided by the isothermal heat treatment is the fact that this dark etching phase could be a product of transformation at the holding temperature of 530°C.

The dilatometry plot in figure 4.15b shows that no change in length ΔL takes place approximately between 19 and 40 seconds holding time in the dilatometry plot. The fact that there is a low carbon content in the alloy makes it unlikely that such large areas could be stabilised austenite. These considerations lead to the

conclusion that this phase is not constituted of stabilised austenite or martensite formed during cooling. The latter possibility, however, needs further investigation in the context of auto-tempering taking place during continuous cooling transformation in order to be completely ruled out.

It is possible that stabilised γ is present within the bainite plates, and is visible at high magnification. It should also be noted that the bainite plates are very long (10-15 μm).

Figure 4.14: *Microstructural features of sample Y7N1 held 530°C for 30 seconds*

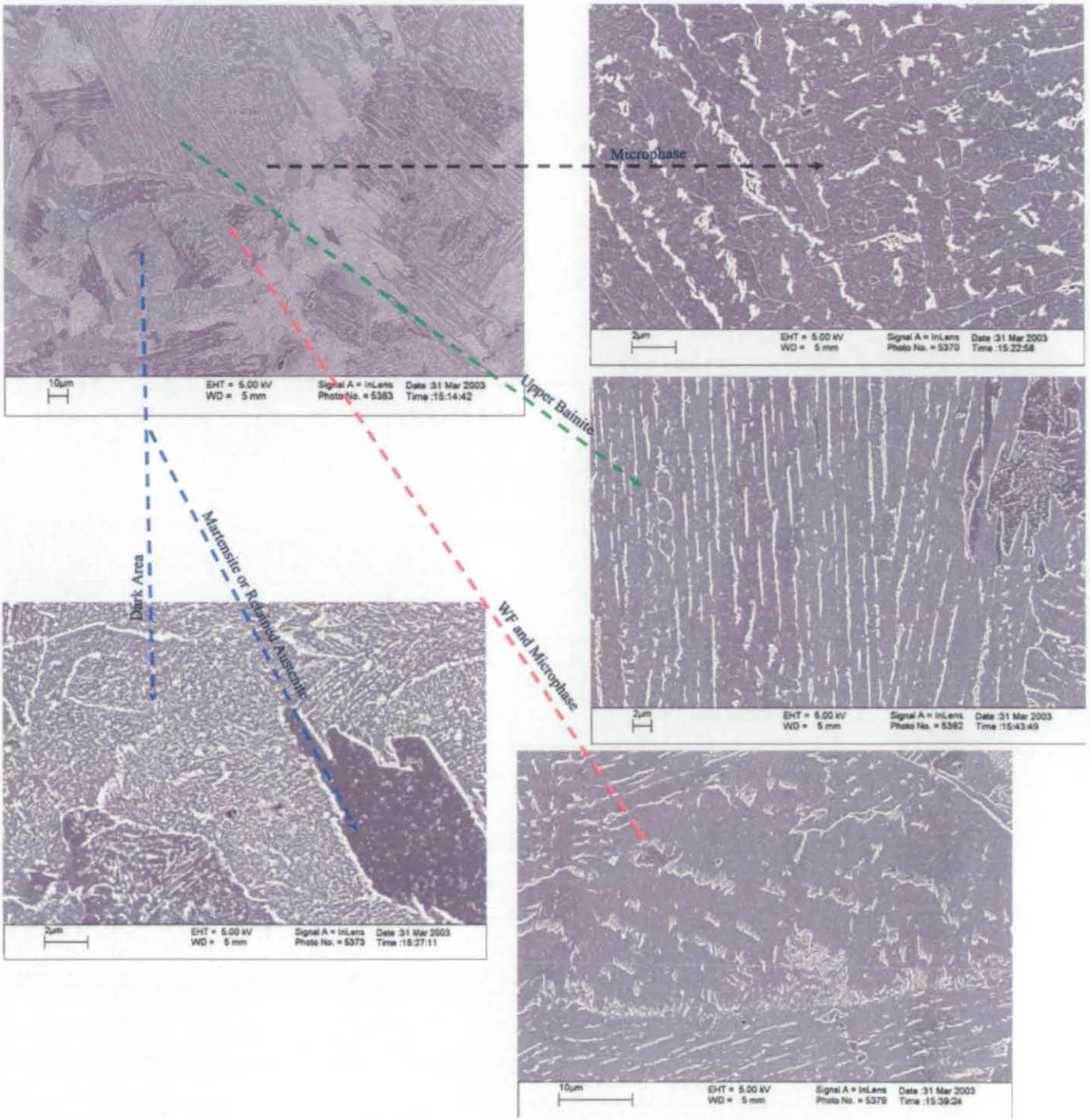

The dilatometry plots for sample Z9P1B held at 530 °C for 30 seconds are shown in figure 4.15a-b.

Figure 4.15a: *Dilation curve of sample Z9P1B austenitised at 1300°C, held at 530°C for 30 s*

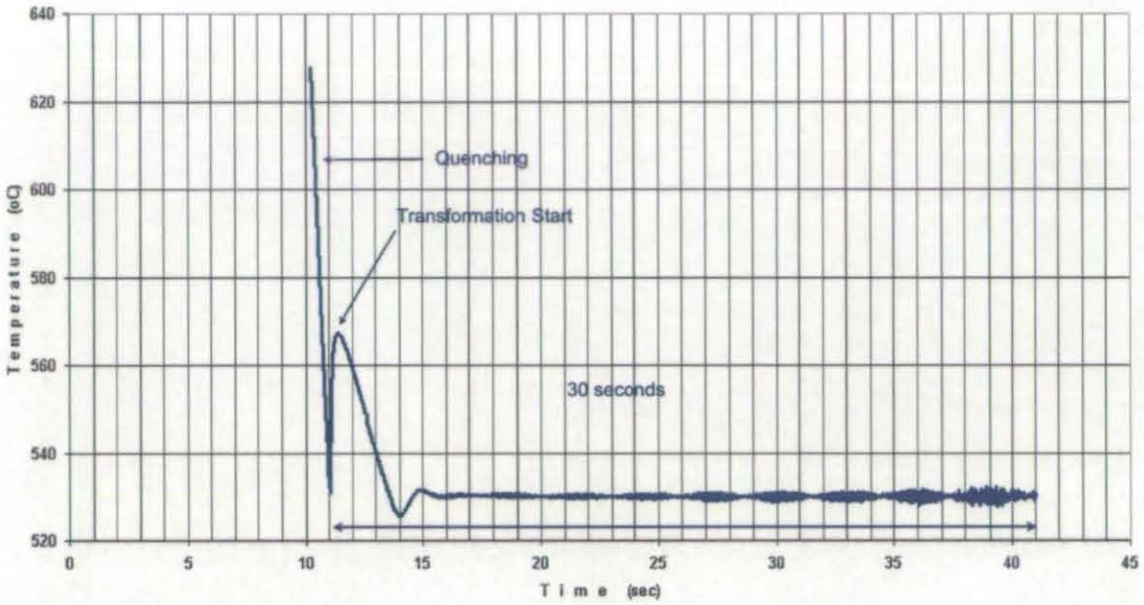

Figure 4.15b: *Dilation curve of sample Z9P1B austenitised at 1300°C, held at 530°C for 30 s*

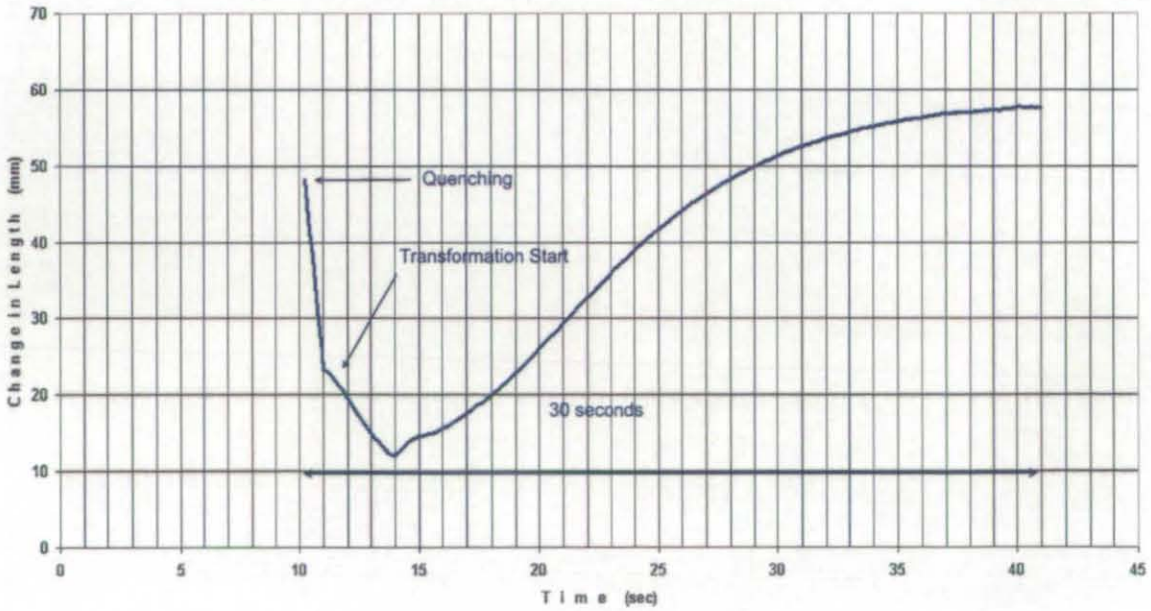

The kinetics of transformation in sample Z9P1B are very different from alloy Y7N1. In fact, the curve shows that the transformation is much slower and nearly reaches completion after 30 seconds at the transformation temperature. The effects

of molybdenum addition are very visible both from the dilatometry curve and the optical micrographs. Molybdenum is a strong carbide former as it is usually found not in solid solution, but in the form of thermodynamically stable carbides. Although belonging to the ferrite former category, its strength in this sense is not significantly high. It retards the ferrite-pearlite formation, depresses the bainite start temperature (it has the strongest effect after carbon) and encourages the bainite reaction. In fact, fully bainitic structures have been obtained by adding 0.002 wt.% B (which markedly retards the ferrite formation) to a 0.5 wt.% Mo steel.

The microstructure obtained from isothermal heat treatments at the three different temperatures, offer a view of the microstructural evolution and behaviour of sample Y7N1 as a function of temperature. It can be seen how a decrease in transformation temperature under isothermal conditions, causes a change in the microstructure, as well as in the rate of reactions, from the reconstructive to the displacive regime.

4.4 Continuous Cooling Heat Treatments

By varying austenitisation and cooling conditions a wide range of complex microstructures can be obtained. In order to study the effects of such factors on the final microstructures several heat treatments have been performed on alloy Y7N1. The austenitisation step has been typically carried out at two austenitising temperatures of 1100°C and 1300°C, and the cooling stage has been performed at cooling rates varying from 2 to 400°C s^{-1} in order to study the transition from microstructures in which the dominant constituents formed via a reconstructive mechanism, to those where phases formed via a displacive mechanism dominate. This offers the possibility of investigating the mutual interactions between the different phase transformations taking place during cooling.

A dilation curve obtained from a cooling experiment indicates recorded changes in volume of the sample, which are directly related to the beginning and subsequent development of a phase transformation. A typical dilation curve for a continuous cooling heat treatment is shown in figure 4.16:

Figure 4.16: *Example of a typical dilation curve obtained by continuously cooling alloy Y7N1, the three main curves of interest for the analysis of phase transitions are indicated*

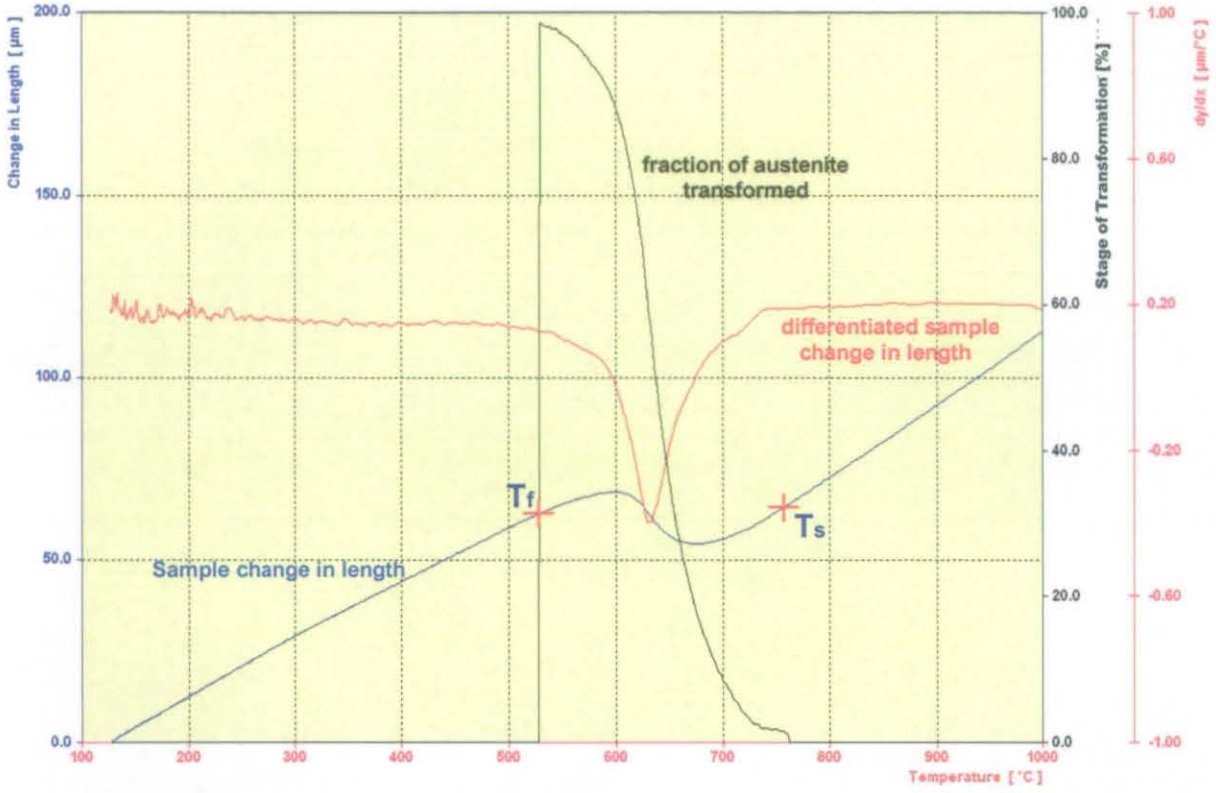

The transformation start temperature, T_S, represents the beginning of the overall transformation taking place during cooling (and *not* the individual transformation start temperatures). The transformation finish temperature can be also identified. It should be highlighted that the determination of start and finish transformation temperatures (the latter being of less relevance) are prone to a degree of error due to the fact that the method adopted for their determination was manual with deviation from a straight line indicating the start of transformation. The sharpness of the curve can be indirectly related to the nucleation and growth characteristics of a transformation that is taking place. Indeed, if over a particular transformation temperature range the dominant transformation process is diffusional (e.g. reconstructive transformations), the observed change in slope of the dilatometry curve is less pronounced and it occurs over a broader temperature range. This can be attributed to the fact that a reconstructive transformation involves longer growth times and smaller growth rates than a displacive or diffusionless transformation. This in turn is reflected in the volume changes detected during the cooling step. Naturally, a wide range of transformations with different nucleation and growth mechanisms can take place during cooling from the austenite phase field to room temperature, depending on

thermodynamic and kinetic conditions, and the microstructures produced can be very complex. Useful information that can be derived from a dilatometry curve is which transformation mechanism is dominant. Therefore it is possible to determine a transformation mechanism for particular heat treatment parameters and the type of alloy. Additionally, the rate of transformation and the percentage transformed can be obtained by differentiation of the dilatometry curve.

Microstructural analysis is an essential step in enhancing the information available from the dilatometry curve. Furthermore, once each phase has been identified, phase quantification is needed in order to assess the transformation kinetics (e.g. transformation start temperatures) from the dilatometry curves. Generally speaking, this can be done by directly relating the phase percentage to a particular portion of the curve for that transformation, once a suitable transformation sequence in accordance with experimental evidence and theoretical knowledge has been determined.

At the initial stages of the research, a simple and realistic transformation sequence that has been considered to take place under continuous cooling conditions is the following:

$$PF / P \rightarrow WF \rightarrow BF \rightarrow M$$

where:

- PF is primary ferrite nucleated at prior γ boundaries
- P is pearlite
- WF is Widmanstätten ferrite
- BF is bainitic ferrite
- M is martensite

This transformation sequence is therefore based on the assumption that higher temperature (reconstructive) transformations precede lower temperature (displacive) transformations. However, a small fraction of austenite, present in microphase regions, can eventually transform into martensite. In addition to untransformed austenite and martensite, the microphase regions include M/A (regions containing martensite and austenite), pearlitic islands and precipitates of various nature. Stabilised austenite can remain in the microstructure after the heat treatment, due to carbon stabilisation or due to the incomplete reaction phenomenon. The above transformation sequence, however, does not take into account the composition

variations caused by the simultaneous transformations taking place, which can greatly influence the kinetics of each possible phase transformation. Therefore, the enrichment in carbon of surrounding austenite at the advancing interface of ferrite could eventually lead to the formation of pearlitic areas for instance, favoured by a larger carbon composition, at a lower temperature than that predicted by the TTT diagram for a fixed composition. This is discussed further in subsequent chapters.

4.4.1 Alloy Y7N1, Austenitisation at 1100°C

4.4.1.1 Cooling Rate 2°C s^{-1}

Figure 4.17: *Dilation curve and optical microstructure of sample Y7N1 1100/2*

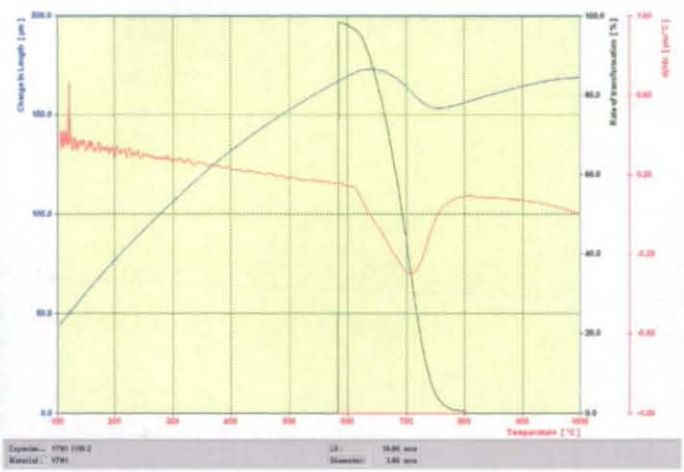

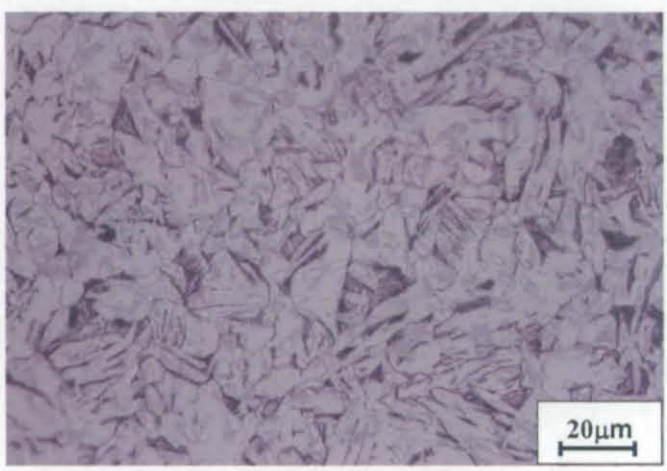

This cooling rate is the slowest that has been imposed on alloy Y7N1 in order to investigate the effect on microstructure. The transformation start temperature was estimated to be approximately 810°C, and the transformation finish temperature as approximately 576°C. Therefore, the cooling curve lies in the reconstructive regime for alloy Y7N1. From the dilation curve in figure 4.17 it can be observed that a peculiar characteristic of the curve is that the gradient of the curve is quite low between 620°C and 740°C (i.e. the slope of the dilation curve is low and the curve itself is not sharp). The rate of transformation curve shows that most of the transformations are occurring over a wide range of temperature and at high temperatures. Therefore, the dilation curve suggests that the transformations are taking place in a reconstructive temperature regime and the growth rate is slow and presumably diffusion controlled.

Consistent with the dilatometry curve characteristics, the expected microstructure of the sample austenitised at 1100°C and cooled at 2°C shown in figure 4.17b consisted of primary ferrite, nucleating at prior austenite grain boundaries, and pearlite. The pearlite lamellae are not resolvable at the magnification of X500 but from classification schemes, it is known that it there is a dark response on etching. The pearlite regions are very small, usually having a dimension of less than 6 μm on average. Pearlite formation becomes possible in small pools of carbon enriched austenite, which as the temperature decreases and the carbon content increases are able to transform via the eutectoid reaction. As the carbon content of the alloy is quite low, the amount of pearlite is much lower than primary ferrite. The transformation rate as expected is very low. The peak rate occurs at 690°C approximately and the largest fraction of austenite transforms over a wide range of temperature i.e. 120°C. The microstructure of the alloy cooled at 2°C s^{-1} should result in low strength, low hardness and high ductility and toughness. The microstructure obtained is quite easy to analyse and classify, with the phases formed being only ferrite and pearlite. It should be noted that the rate of transformation should be a level profile. The increase in slope has been attributed to an experimental error.

4.4.1.2 Cooling Rate 5°C s^{-1}

Figure 4.18: *Dilation curve and optical microstructure of sample Y7N1 1100/5*

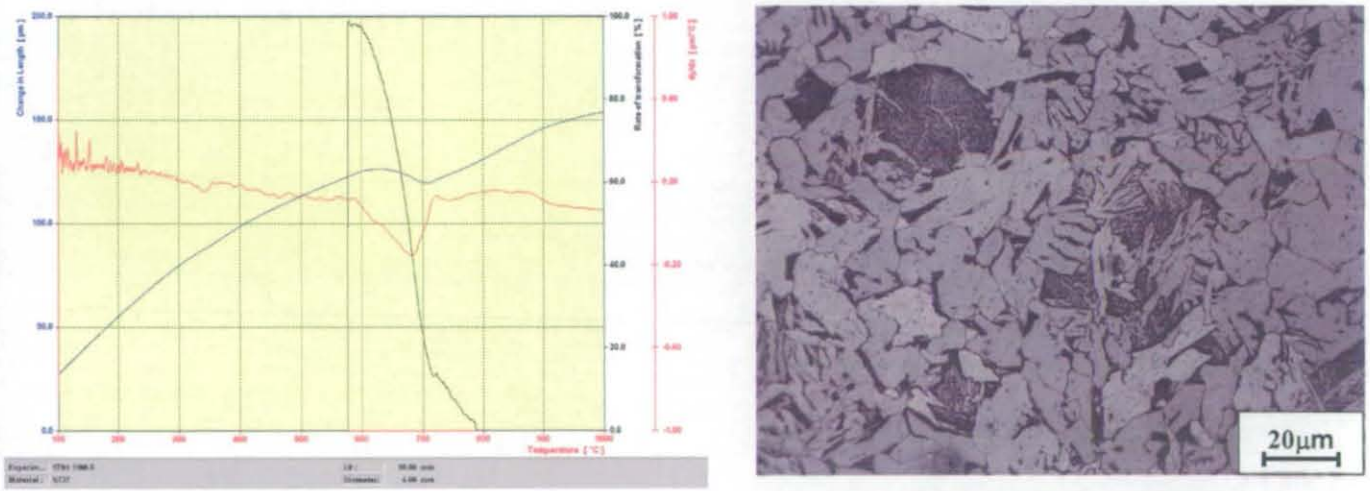

At 5°C s^{-1} the microstructure is less coarse compared to the one obtained at 2°C s^{-1}. However, an interesting feature is the presence of a phase which gives a dark etching response and has a "spongy" appearance. The etching response is lighter than that obtained for the pearlite. The features within the grains of this phase are not resolvable under the light microscope. The dimensions of the grains are much larger

than the pearlite regions found between the primary ferrite grains in the 2°C s^{-1} sample. The nature of this phase is therefore uncertain and a conclusive identification cannot be obtained by optical microscopy. The rest of the microstructure comprised primary ferrite and small pearlitic regions. A small fraction of the microstructure consisted of coarse Widmanstätten ferrite with aligned microphase. The transformation start temperature has been estimated to be ~792°C. and the transformation finish temperature ~567°C. From the dilation curve in figure 4.18 it can be observed that, analogously to the previous case, the slope of the change in length *versus.* temperature curve is low between 720°C and 590°C. The rate of transformation curve shows that the peak rate is at ~685°C and the majority of the transformation takes place over a wide range of temperature, i.e. ~100°C. The microstructure produced by cooling at 5°C s^{-1} is more complex than at 2°C s^{-1} although the phase identification is still relatively straightforward. The main difference lies in the presence of the coarse dark etching phase. The appearance is similar to that of pearlite, but it could be confused with lower bainite as well. The low cooling rate, however, suggests that phases such as bainite are not likely to form. The properties of the alloy are expected to be similar to those obtained at 2°C s^{-1} although strength and hardness should increase at the expenses of ductility and toughness. The impact on the mechanical properties of the dark etching phase is unclear and cannot be assessed without full characterisation of the phase.

4.4.1.3 Cooling Rate 10°C s^{-1}

Figure 4.19: *Dilation curve and optical microstructure of sample Y7N1 1100/10*

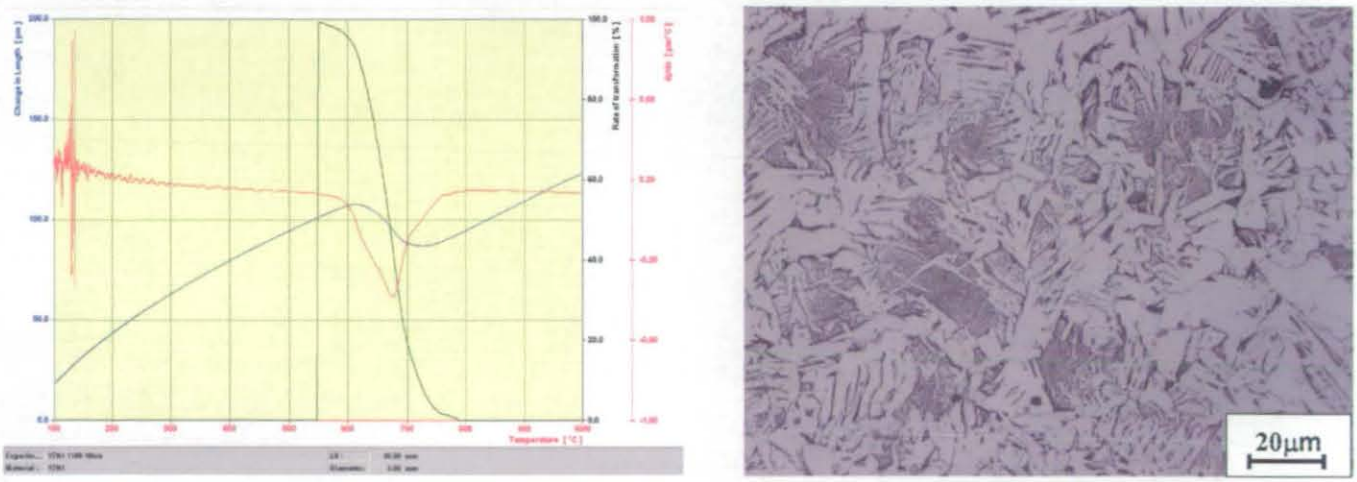

The diagram in figure 4.19 illustrates the dilation curve obtained for sample Y7N1 austenitised at 1100°C and cooled to room temperature at 10°C s^{-1}. Together with

the cooling rate of 50°C s^{-1}, this cooling rate produced one of the most interesting samples in terms of microstructure and it has been the focus of extensive investigation which will be discussed in full subsequently. The phase transformations started at a temperature of ~779°C and finished at ~551°C. The resulting microstructure is much finer than in the previous two cases and the observation of the microstructure shows that there is a radical change in the transformation pattern, as there is extensive formation of Widmanstätten ferrite, and therefore, a displacive component involved in the formation of this phase is reflected in the dilatometry data. The microstructure of the sample austenitised at 1100°C and cooled at 10°C s^{-1} is more complex compared to ones produced at lower cooling rates as the microstructural constituents are primary ferrite nucleating at prior austenite grain boundaries, pearlite islands, Widmanstätten ferrite observed with aligned microphase as well as end on, and finally the dark etching phase. By observing the dilatometry curve it can be seen that the competition between displacive and diffusion based transformation has led to another scenario as the cooling rate was increased. It can be assumed that a large proportion of the product phases is the result of reconstructive transformation which leads to the formation of pearlite islands, the dark etching phase previously mentioned, in addition to primary ferrite. In addition, the formation of Widmanstätten ferrite has been favoured by a higher cooling rate, a lower time allowed for diffusion and the lower transformation start temperature which is a direct consequence of the imposed cooling rate for a given austenite grain size and the alloy composition. The main features of the dilatometry curve are the narrowing of the temperature range within which the largest fraction of austenite transformed, which in this case is approximately 90°C. The transformation rate increased considerably and is reflected in the sharpness of the curve in the temperature range between 650°C and 700°C, within which the majority of the microstructure transformed. The peak rate was recorded at ~675°C.

The dark etching phase becomes smaller in dimensions and more irregular in shape than in the sample cooled at 5°C s^{-1}. The dimensions of the dark etching regions are much larger (between 10 and 25 μm) compared to those of pearlite (smaller than 5 μm) as well as those of the microphase regions (smaller than 4 μm). This difference in dimensions, observed in the sample cooled at 5°C s^{-1}, becomes a systematic factor aiding the distinction between pearlite and the dark etching phase. Another interesting feature is represented by the microphase itself. These portions of the microstructure originated from austenite trapped between the growing Widmanstätten ferrite plates. The role of the local composition, especially

represented by local carbon enrichment caused by the diffusion of carbon away from the advancing interface of the sideplates, is crucial in determining the nature of the microphase regions. Optical observation does not allow a precise identification of such regions. Furthermore, it is not straightforward to identify the temperature at which they formed, nor whether they formed contemporarily or subsequently to the formation of the ferrite plates. All of these factors determine the nature of the microphase regions and in order to be validated they need investigation using high magnification techniques, such as SEM. The mechanical properties should follow the trend expressed in the previous sample where the increase in cooling rate is likely to cause an increase in hardness and strength of the alloy, at the expense of ductility and toughness. The quantitative hardness analysis will be discussed in full in chapter 6.

4.4.1.4 Cooling Rate 25°C s^{-1}

Figure 4.20: *Dilation curve and optical microstructure of sample Y7N1 1100/25*

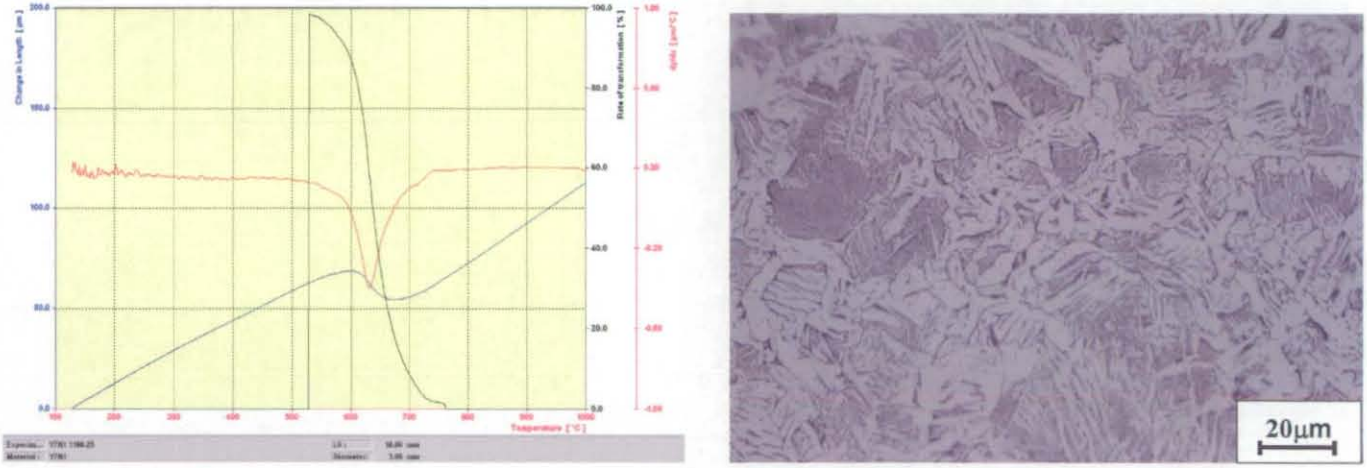

At 25°C s^{-1} the microstructure is finer compared to that obtained at 10°C s^{-1}. The dimensions of the dark etching regions vary from coarse grains (20μm across) developing near primary ferrite regions, to smaller regions (less than 10μm across) developed between Widmanstätten ferrite plates. The microstructure is primarily composed of Widmanstätten ferrite, which is visibly finer compared to that formed at 10°C s^{-1}. The distinction between Widmanstätten ferrite and upper bainite, as the former becomes increasingly fine, is quite difficult using only optical microscopy. However, the aspect ratio between microphase and ferrite sideplates, which is a factor helping the distinction between the two phases, suggests that at 25°C s^{-1} the

formation of upper bainite is negligible. The presence of primary ferrite is still considerable. This is due to the fact that alloy Y7N1 tends to nucleate primary ferrite at austenite boundaries even at very high cooling rate, as indicated by the predicted TTT diagram. Nucleation of Widmanstätten ferrite takes place at prior austenite grain boundaries (referred to as primary WF) as well as on polygonal ferrite (secondary WF). The transformation start temperature is ~753°C whilst the transformation finish temperature has been estimated as ~549°C. From the dilation curve in figure 4.20 it can be observed that the slope of the change in length versus. temperature curve is grater between 600°C and 670°C. The rate of transformation curve shows that the peak rate is approximately at 630°C and the majority of the transformation takes place over a narrower range of temperature i.e. 80°C. The phase identification presents the same problems discussed for the sample cooled at 10°C s^{-1}. Furthermore, the microstructure is even finer and the microphase identification becomes harder.

4.4.1.5 Cooling Rate 50°C s^{-1}

Figure 4.21: *Dilation curve and optical microstructure of sample Y7N1 1100/50*

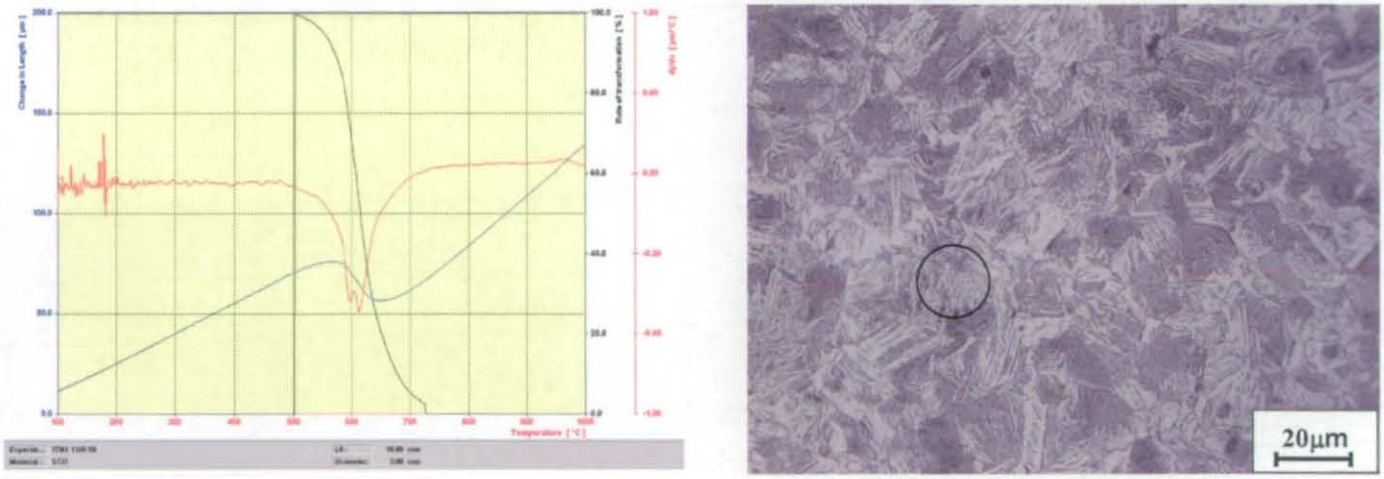

In addition to the sample cooled at 10°C s^{-1}, the one cooled at 50°C s^{-1} has been the centre of extensive investigation. This cooling rate produced phases formed via purely reconstructive reactions, as well as, phases formed via a displacive stage during their formation. Furthermore, at this cooling rate the dark etching phase is still present, together with upper bainite. From the dilatometry data, the transformation start temperature was estimated to be ~720°C, and the transformation finish temperature has been estimated as being ~511°C. From the dilation curve in figure

4.21 it can be seen that a peculiar characteristic of the curve is that the slope is high between 560°C and 640°C. This indicates that at least one of the transformations taking place presumably had a strong displacive component. Indeed, the presence of upper bainite can be observed in the optical image shown in figure 4.21 (an upper bainitic area is indicated by a black circle). The transformations reach completion in a temperature interval of about 70°C.

The optical analysis of sample austenitised at 1100°C and cooled at 50°C showed that the microstructure consists of regions of primary ferrite nucleated at prior austenite grain boundaries, primary and secondary Widmanstätten ferrite with associated microphase, upper bainite and the dark etching phase. The Widmanstätten ferrite becomes very fine at this cooling rate and it can be confused with the coarse upper bainite present in the microstructure, which makes it difficult to accurately determine the volume fraction of each constituent. The dark etching phase is still present in significant amounts in the microstructure, with the dimensions of the irregular grains being typically less than 20 μm. The distribution of the dark etching phase appears even throughout the sample. This is due to the fact that the dimensions are on average smaller compared to the samples cooled at lower cooling rates and the volume fraction of the phase does not appear to have diminished considerably. The etching response appears darker compared to the lower cooling rates discussed above which could correspond to a change in the morphology of the phase.

4.4.1.6 Cooling Rate 60°C s^{-1}

Figure 4.22: *Dilation curve and optical microstructure of sample Y7N1 1100/60*

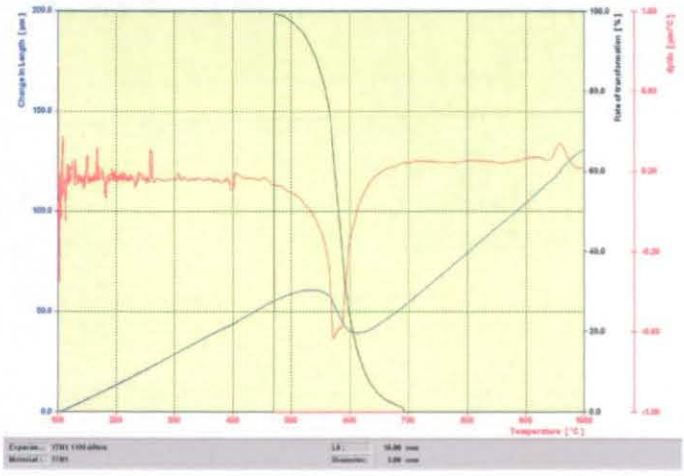

Cooling rates between 50 and 75°C s^{-1} are important because there is the transition from the dominant reconstructive character of the reactions taking place during cooling and the displacive ones. This transition is expected to be reflected in the microstructures of the samples. The Widmanstätten ferrite, being the major constituent at 50°C s^{-1}, is replaced by upper bainite when the cooling rate in increased to 60°C s^{-1}. Lower bainite starts to form and becomes dominant at cooling rates higher than 75°C s^{-1}. Furthermore there is a gradual decrease in the area fraction of the dark etching phase with increasing cooling rate.

The microstructure of the sample austenitised at 1100°C and cooled at 60°C shown in figure 4.22 consists of very fine primary ferrite layers nucleating at prior austenite grain boundaries, fine Widmanstätten ferrite (secondary WF being dominant), upper bainite which appears finer than that observed for the 50°C s^{-1} cooling rate and which constitutes small regions of whose volume fraction is still very low, and finally, the dark etching phase whose dimensions and distribution appears very similar to the sample cooled at 50°C s^{-1}. The microphase regions between the ferrite sideplates appear as very fine layers when they are not observed end on. The nature of these microphases at this cooling rates should be mainly M/A, because the formation of pearlite is unlikely. However, their exact classification requires high magnification techniques. At 60°C s^{-1} the transformation start temperature was estimated to be ~715°C and the transformation finish temperature ~493°C. From the dilation curve in figure 4.21 it can be observed that the peak transformation rate is at 580°C and that nearly 80% of the total austenite transformed in the temperature range 550 - 615°C. The rate of transformation curve shows that most of the transformations are occurring over a narrow range of temperature. As the cooling rate increases, the transformation temperature range is expected to become increasingly narrow. This increase in rate of transformation over a narrow temperature range is consistent with the dominant transformation mechanism being displacive as the cooling rate increases. At a cooling rate of 60°C s^{-1}, the formation of martensite was not observed in the micrographs, or indicated in the dilatometry curve.

4.4.1.7 Cooling Rate 75°C s^{-1}

Figure 4.23: *Dilation curve and optical microstructure of sample Y7N1 1100/75*

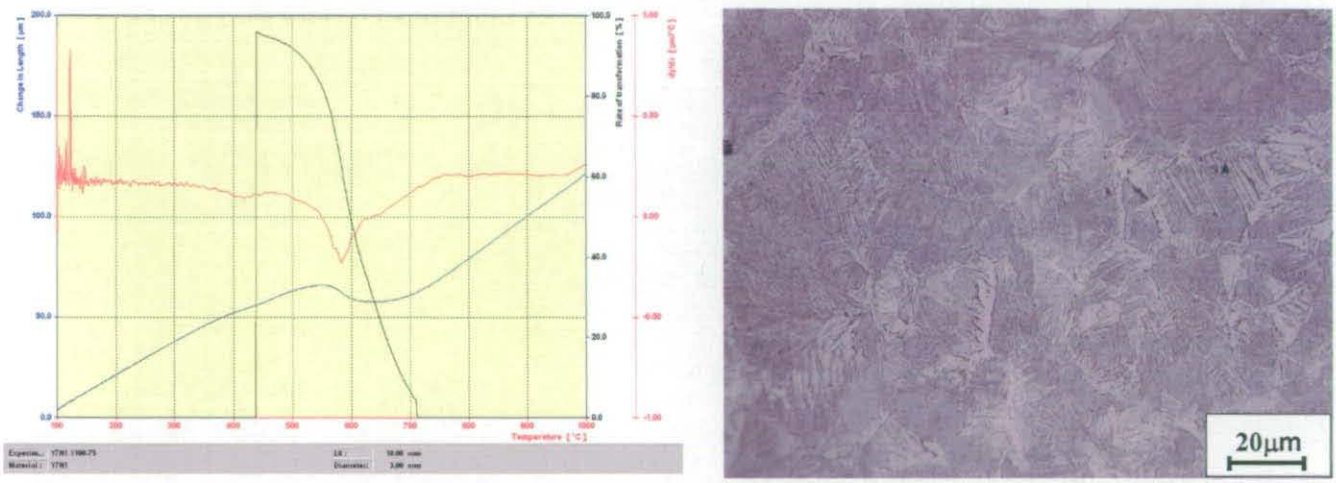

At the cooling rate of 75°C s^{-1} the displacive transformations dominate. The constituents of this sample are primary ferrite, Widmanstätten ferrite, upper and lower bainite, a very small fraction of dark etching phase, and very limited regions of martensite.

The nucleation of primary ferrite still takes place at prior austenite grain boundaries, but the growth ceases quickly, resulting in a thickness of these ferrite regions of only a few microns. The transformation then proceeds through the formation of small Widmanstätten ferrite regions, whilst a large proportion of the austenite transforms to upper bainite and lower bainite. From the dilatometry curve it can be seen that there is a second change in slope at 400°C which, in terms of volume fraction of austenite transformed, is negligible. This change in slope could be related to formation of martensite. The transformation start temperature was approximately 700°C and the transformation finish temperature was ~463°C. The peak transformation rate is at 570°C and the majority of transformation occurs in the temperature range 540 - 610°C. The change in length versus temperature curve shows an interesting characteristic which was found in the samples cooled at rates greater than 75°C s^{-1}. The slope of the curve changes very gradually over a large temperature range beginning at the start transformation temperature. After the temperature has decreased by ~70°C, the curve becomes very sharp. In the first part of the curve, only a small fraction of the total volume of austenite transformed. The

transformation appears to be relatively slow. This could be linked to the nucleation and growth of primary ferrite, occurring over a wide temperature range, before the displacive transformations start and causes the curve to change its slope in a sharp manner over a narrow temperature range. This behaviour will be treated in more detail in section 4.4.3. At this cooling rate, the formation of martensite has been observed optically, although the martensite regions are quite small and their volume fraction is insignificant. The microstructure appears finer, as expected. The regions of lower bainite increased considerably compared to the sample cooled at 60°C s^{-1}. The fraction of the dark etching phase appears very low and in this sample it is hard to differentiate between regions of lower bainite and small regions of the dark etching phase.

4.4.1.8 Cooling Rate 100°C s^{-1}

Figure 4.24: *Dilation curve and optical microstructure of sample Y7N1 1100/100*

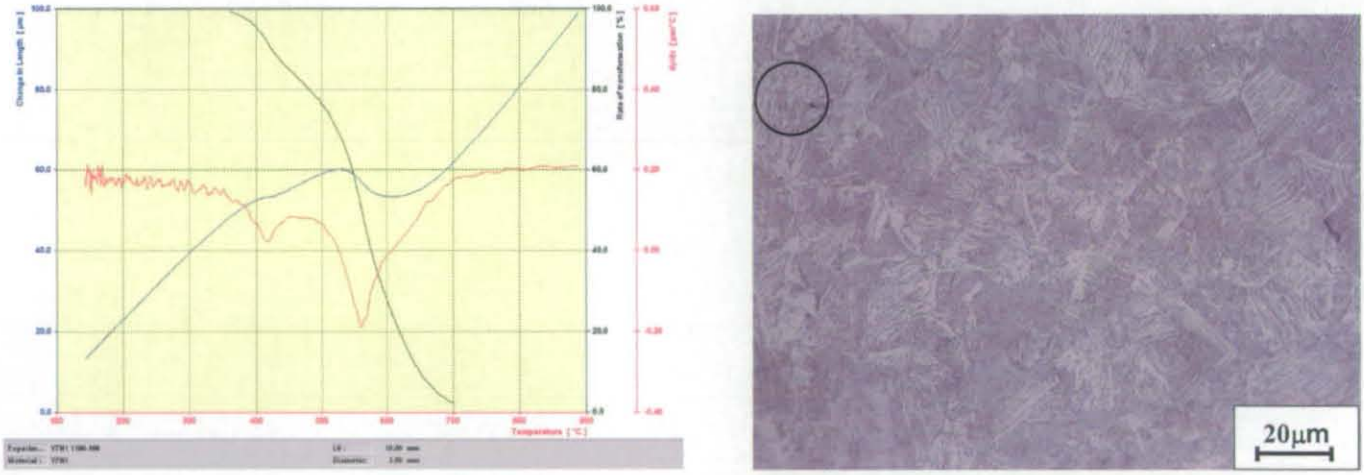

At a cooling rate of 100°C s^{-1}, the amount of both primary ferrite and Widmanstätten ferrite becomes extremely small and the bainite and martensite reactions are the dominant processes. Although the optical image shown in figure 4.24 does not show very clearly the fine microstructural features, at high magnification (X1000) it can be that the dominant bainitic morphology is the lower. A lower bainite area is indicated in figure 4.24 by a black circle. The upper bainitic ferrite plates are very fine. From the dilatometry curve it is clear that there is now an additional change in slope at approximately 400°C, which is reflected in the microstructure. There are therefore two distinct peaks in the differentiated change in length curve. The transformation start temperature was ~670°C. The transformation

finish temperature was estimated as ~388°C. The peak transformation rate is at 560°C although there is a second peak related to the martensitic formation at 420°C. The same sort of dark etching phase as observed at lower cooling rates was not apparent in this microstructure.

4.4.1.9 Cooling Rate 150°C s^{-1}

Figure 4.25: *Dilation curve and optical microstructure of sample Y7N1 1100/150*

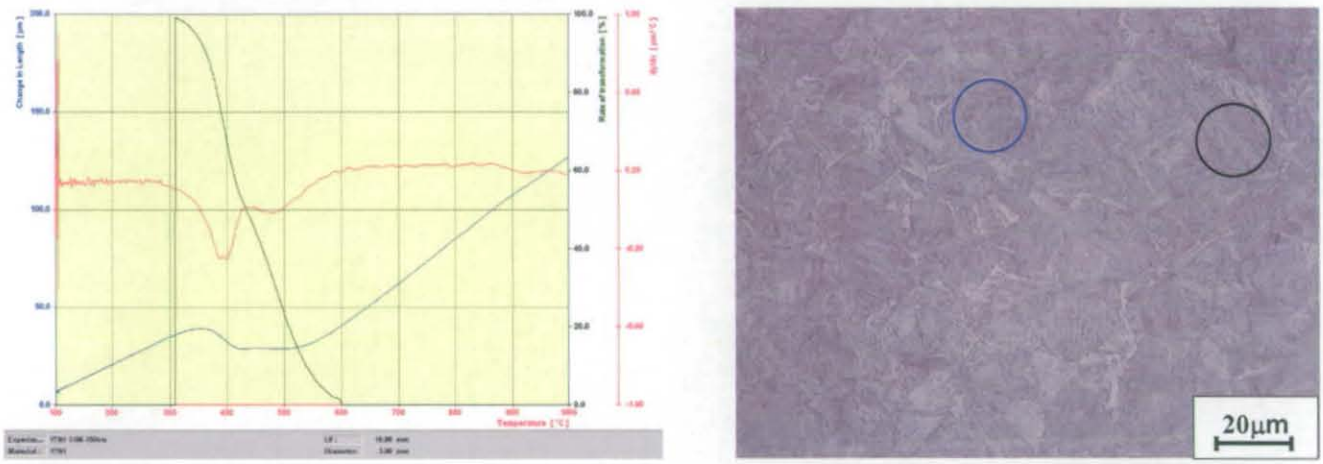

At a cooling rate of 150°C s^{-1} the microstructure is mainly comprised of martensite and lower bainite, with some small regions of upper bainite remaining. A martensitic region is indicated in figure 4.25 by a blue circle, whilst a lower bainite region is indicated by a black circle. The transformation start temperature was ~612°C and the transformation finish temperature was estimated as ~326°C. The peak transformation rate is at 500°C. Both the optical micrograph and the dilatometry plot in figure 4.25, indicate that martensite dominates the microstructure. However, it should be noted that the peaks representing the bainite and the α' transformations are no longer distinct.

4.4.1.10 Cooling Rate 200°C s^{-1}

Figure 4.26: *Dilation curve and optical microstructure of sample Y7N1 1100/200*

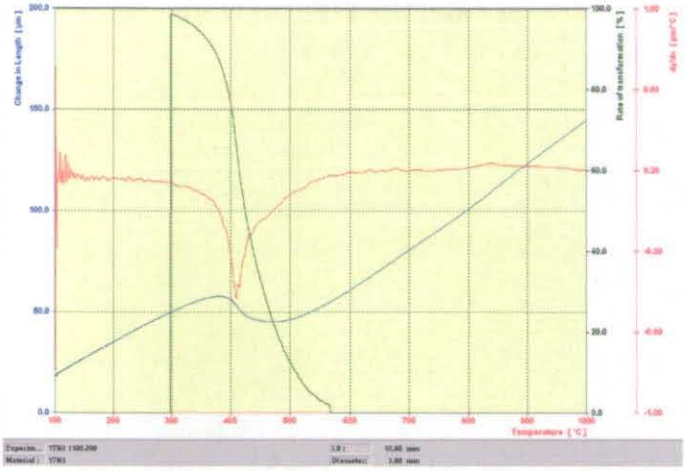

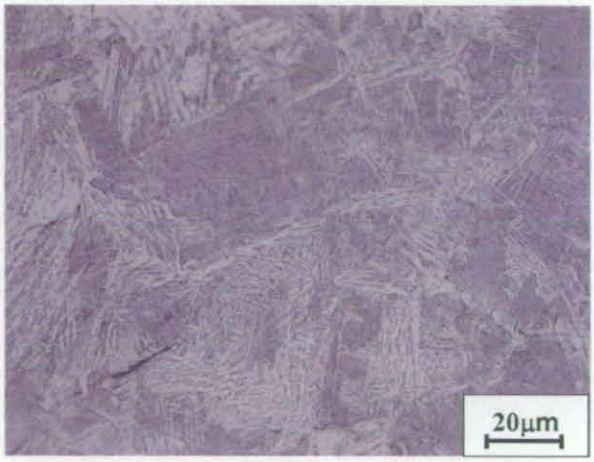

At a cooling rate of 200°C s^{-1} the microstructure is almost completely martensitic, with minor amounts of lower bainite. The transformation start temperature was ~557°C and the transformation finish temperature was estimated as ~300°C. The peak transformation rate is at 410°C. At this cooling rate, the transformation takes place over a narrow temperature range of approximately 50°C. The low carbon content of the alloy Y7N1 suggests that the presence of retained austenite should not be significant.

4.4.1.11 Cooling Rate 400°C s^{-1}

Figure 4.27: *Dilation curve and optical microstructure of sample Y7N1 1100/400*

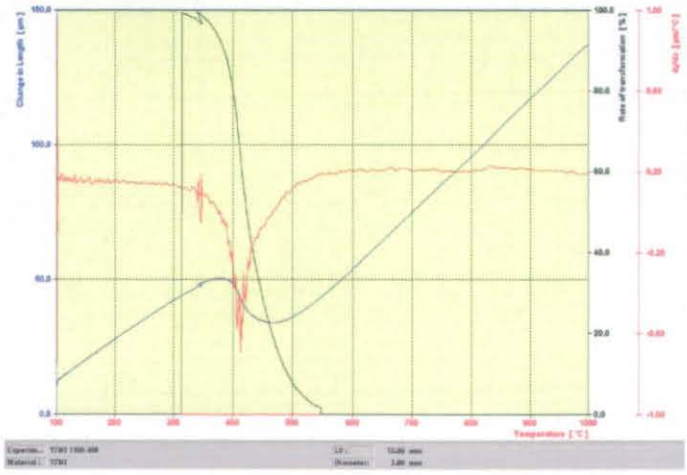

At a cooling rate of 400°C s^{-1}, the dilation curve and the optical images of the microstructure (figure 4.27) are very similar to those at a cooling rate of 200°C s^{-1}, although the microstructure can now be considered to be fully martensitic. The transformations start at ~516°C and finish at ~290°C. The peak rate of transformation is at 410°C approximately. The transformation reaches completion in a temperature interval approximately of 50°C.

4.4.2 Alloy Y7N1, Austenitisation at 1300°C

In general, the microstructures obtained after austenitisation at 1300°C are coarser (up to 25°C s^{-1}) compared to those after austenitisation at 1100°C. This is due to the lower number of nucleation sites available for nucleation of primary ferrite on prior austenite grain boundaries. On the other hand, as observed for alloy Y7N1 austenitised at 1100°C, increasing the cooling rate (e.g. from 10 to 50°C s^{-1}) favours the formation of phases which form via a mechanism with strong displacive component i.e. Widmanstätten ferrite and upper bainite, at the expenses of primary ferrite. Pearlite is again present in small pearlitic islands which usually develop between ferritic grains or in microphase regions present between the Widmanstätten ferrite plates. Another consequence of the increase in austenite grain size is the variation of transformation start temperatures, which generally decrease. As the available energy for nucleation is lower due to the presence of fewer grain boundaries, which can act as high energy nucleation sites, the transformation start temperature decreased compared to the samples austenitised at 1100°C.

When the cooling rate is high enough to produce phases via a displacive mechanism (e.g. 50°C s^{-1} and above), the larger grain size has an influence on the hardenability of the alloy. The two most important variables which influence hardenability are grain size and composition. The hardenability increases with increasing austenite grain size, because the grain boundary area is decreasing. This means that the sites for the nucleation of ferrite and pearlite are being reduced in number, with the result that these transformations are slowed down, and the hardenability is therefore increased.

These considerations are reflected in the dilation curves and the corresponding microstructures. As the trend is similar for all the heat treatments compared to the ones treated for the austenitisation at 1100°C, in this section only two representative cooling rates will be discussed in full.

4.4.2.1 Cooling Rate 10°C s^{-1}

Figure 4.28: *Dilation curve and optical microstructure of sample Y7N1 1300/10*

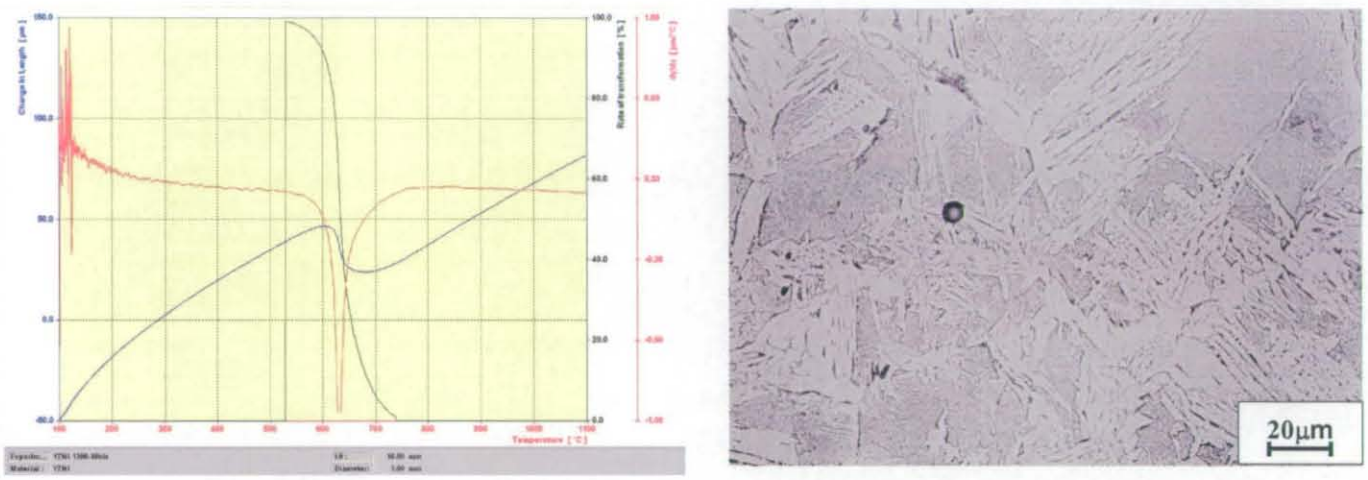

At a cooling rate of 10°C s^{-1} the transformation start temperature has been estimated as being approximately 756°C whilst the transformation reaches completion at approximately 516°C. The transformation rate reaches its peak at approximately 630°C and most of the transformations take place in a temperature interval of 75°C. The microstructure (figure 4.28) is comprises of primary ferrite, Widmanstätten ferrite and the associated microphase regions, pearlite islands and the dark etching phase previously discussed. The dominant microstructural constituent in this case is Widmanstätten ferrite. This is due to the fact that the higher austenitising temperature favours the formation of phases with a displacive component. Therefore, the overall transformation starts at lower temperatures whilst the formation of Widmanstätten ferrite, upper and lower bainite takes place at lower cooling rates. On the other hand, the regions of ferrite are coarser and the grains of dark etching phase are in some case much larger compared to those formed after austenitising at 1100°C. In fact, the grain dimensions of the dark etching phase observed to be up to 40 μm.

4.4.2.2 Cooling Rate 50°C s^{-1}

Figure 4.29: *Dilation curve and optical microstructure of sample Y7N1 1300/50*

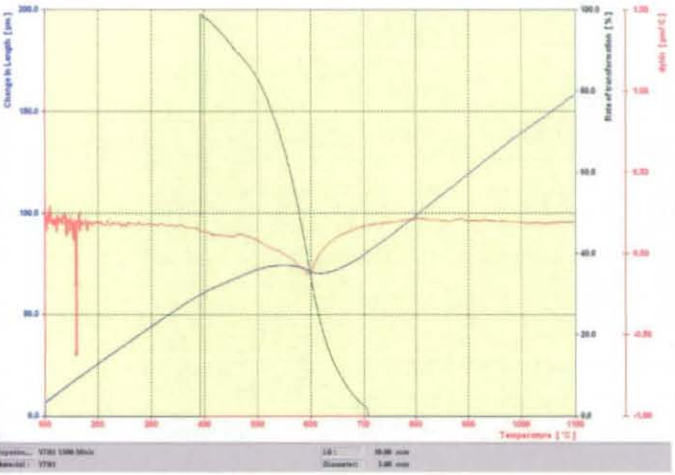

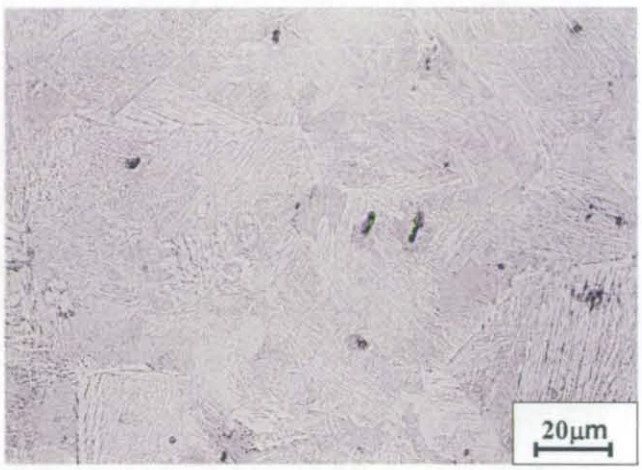

When the cooling rate was increased to 50°C s^{-1} the transformation start temperature was ~408°C, whilst the transformation reaches completion at ~516°C. The peak in transformation rate was at ~600°C. Figure 4.29 shows that the microstructure is comprised mainly of upper bainite, with some primary ferrite, Widmanstätten ferrite and the associated microphase regions, pearlite islands and the dark etching phase being present. The dominant microstructural constituent is upper bainite, although it is difficult to distinguish from the fine Widmanstätten ferrite which also forms at this heat treatment conditions. A comparison of the microstructures produced at 50°C s^{-1} by austenitising at 1100°C and 1300°C enables the effect of austenite grain size to be seen clearly. The formation of upper bainite is much easier in when the austenitising temperature is higher. Additionally, the finer microstructure causes the dimensions of the dark etching phase to be small (less than 10µm).

At cooling rates greater than 150°C s^{-1} the microstructure can be considered to be fully martensitic after austenitising at 1300°C.

For completeness and for comparison purposes, the transformation start and finish temperatures for the heat treatments having the austenitising steps performed at 1100 and 1300°C are listed in table 4.2.

Table 4.2: *Transformation start and finish temperature for alloy Y7N1 austenitised at 1100°C*

Cooling Rate (°C s^{-1})	Alloy Y7N1 austenitised at 1100°C		Alloy Y7N1 austenitised at 1300°C	
	T_s (°C)	T_f (°C)	T_s (°C)	T_f (°C)
2	810	566	761	530
5	792	557	757	512
10	779	551	756	516
25	753	549	735	502
50	720	511	694	408
60	715	493	679	383
75	700	463	655	355
100	671	398	604	321
150	612	326	536	286
200	557	300	487	269
400	516	290	443	232

4.4.3 Considerations on High Cooling Rate Dilation Curves

In order to gain a better understanding of the data obtained from the dilatometry measurements performed at high cooling rates (from 75°C s^{-1} to 400°C s^{-1}), the behaviour of alloy Y7N1, austenitised at 1100°C and cooled at 150°C s^{-1}, will be hereafter discussed and compared with that of alloy Y7N1, austenitised at 1300° and cooled at 150°C s^{-1}. The predicted TTT diagram shown in figure 4.1 indicates that even at very high cooling rate the nucleation of primary ferrite at prior austenite grain boundaries may occur, although at very high cooling rates the presence of ferrite is

observed to be negligible. Nonetheless, the formation of very fine regions of ferrite can be recorded by the dilatometry, prior to the onset of the dominant displacive transformations (i.e. bainitic ferrite and martensite). As previously discussed, the austenite grain size does have an important effect on the final microstructure. A small austenite grain size obtained by austenitising at 1100°C is able to promote the formation of primary ferrite at higher temperatures than those related to the larger austenite grain size, obtained by austenitising at 1300°C. On the other hand, the formation of a phase with a strong displacive component, such as bainite, is not favoured by small austenite grain sizes, therefore the hardenability is reduced when the alloy is austenitised at lower temperatures (i.e. 1100°C).

Figures 4.30 and 4.31 show the dilation curves of alloy Y7N1, cooled at 150°C s^{-1} and austenitised at 1100°C and 1300°C, respectively. Both samples exhibit similar microstructures, primarily consisting of bainitic ferrite and martensite; however, the corresponding dilatation curves appear significantly different.

Figure 4.30: *Dilation curve of alloy Y7N1 austenitised at 1100°C and cooled at 150°C s^{-1}*

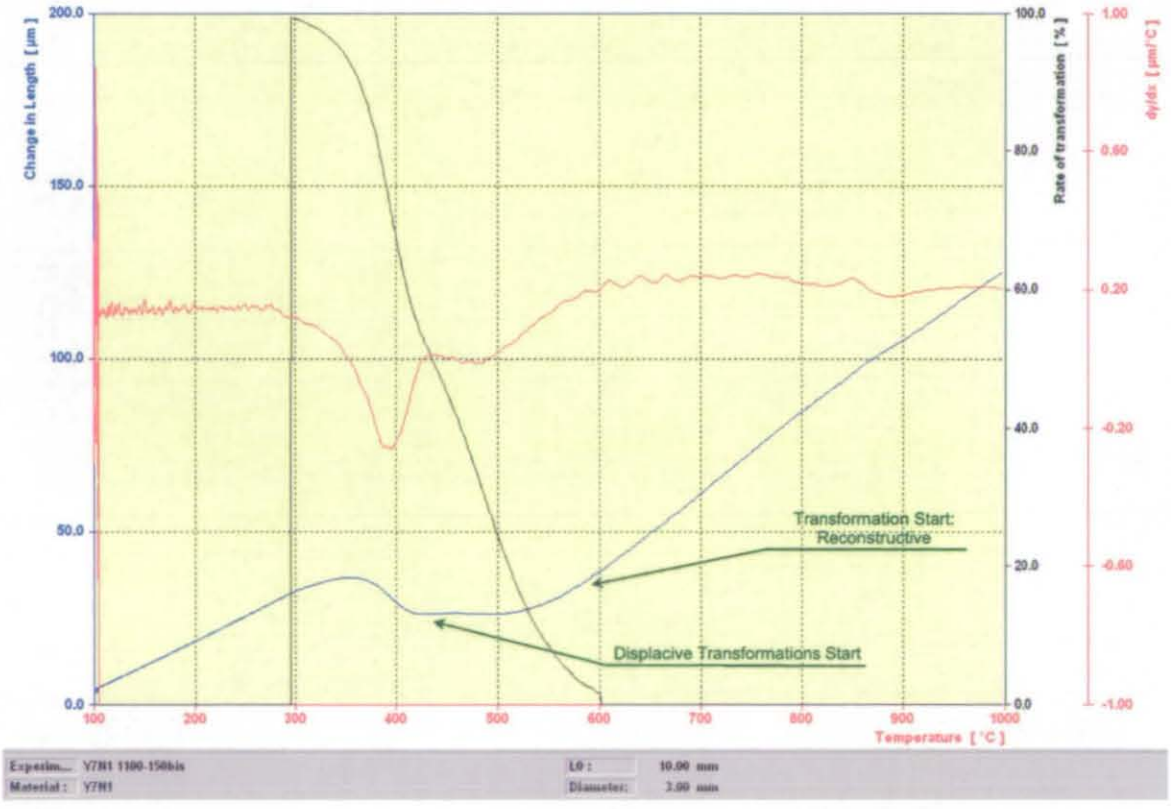

Figure 4.31: *Dilation curve of alloy Y7N1 austenitised at 1300°C and cooled at 150°C s^{-1}*

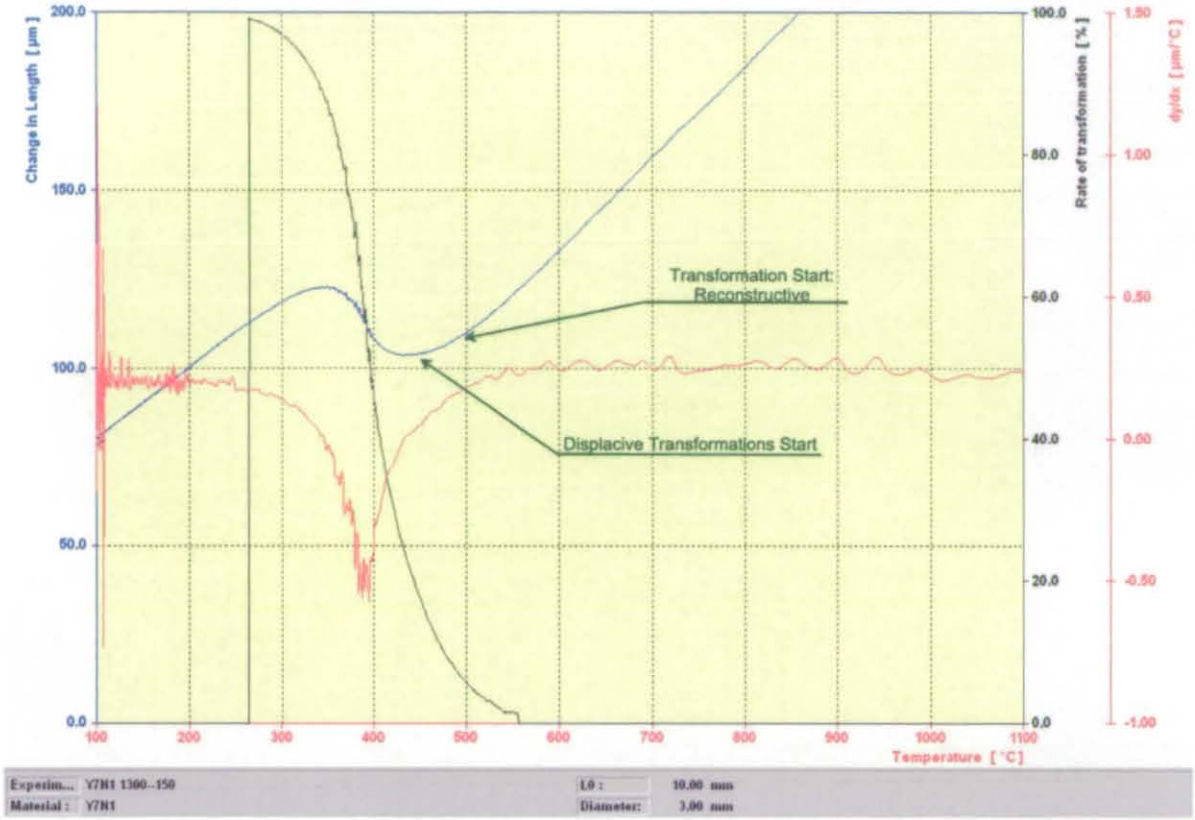

The curve obtained after austenitising at 1100°C (figure 4.31) presents a region between 610°C and 440°C where the change in slope occurs gradually, with a portion over which the slope actually appears to remain constant. This trend would suggest that the transformation rate is low, as well as the overall austenite percentage transformed. The curve obtained after austenitising at 1300°C (figure 4.31), on the other hand, displays a different trend. Indeed, in this case a marked change in the slope of the curve is observed at the transformation start temperature, i.e. 536°C. Furthermore, no 'plateau-type' regions are present.

Such differences between the two dilation curves are thought to stem from the effects of the austenite grain size.

In the sample austenitised at 1100°C, the primary ferrite formation starts to occur at a higher temperature, but the reconstructive transformation becomes soon suppressed due to the high cooling rate. The displacive transformations are hindered by a small grain size, hence there is a certain time lag (or delay) between the end of the reconstructive transformations and the onset of the displacive ones (i.e. bainite

and martensite formation). The dilation curve therefore shows the two opposite effects of the austenite grain size on reconstructive and displacive transformations.

The opposite behaviour is observed when the austenitising temperature is raised up to 1300°C, in that the transformation start temperature of ferrite is suppressed to a lower temperature (i.e. 536°C), with its nucleation becoming increasingly less favoured as the temperature decreases. The displacive transformations, on the other hand, are enhanced and become the dominant reaction mechanism at higher temperatures than in the sample austenitised at 1100°C (i.e. ~460°C). As a consequence of this, there is no time lag between the end of the reconstructive transformations, which result in the formation of few extremely fine layers of primary ferrite, and the onset of the displacive ones. This also explains the shape of the dilatation curve usually obtained from samples which have been cooled at low cooling rates, at which the formation of lower bainite and martensite is not expected to occur.

4.5 Summary

The transformation kinetics under both isothermal and continuous cooling conditions at two different grain sizes have been investigated. The influence of such variation on the transformation kinetics of alloy Y7N1 showed that in general the transformation start temperatures are lower when the austenitising temperature is lower. The influence of such variation on each transformation product will be covered in the following chapters. The dilatometry analysis provided information about the overall transformation taking place at a particular cooling rate, indicating the dominant character of the phase reactions, i.e. whether reconstructive or displacive. The microstructural analysis showed the microstructural evolution in relationship to the cooling rates. At low cooling rates between 2 and 50°C s^{-1} the dominant phases are primary ferrite, pearlite, Widmanstätten ferrite and a dark etching phase whose nature will be defined in the following chapters. Increasing the cooling rate from 50 to 200°C s^{-1} causes the gradual increase of bainite and martensite, and the latter becomes the only phase present at the highest cooling rates.

5. Microstructural Characterisation:

Phases in Steels

5. Microstructural Characterisation:

Phases in Steels

5.1 Introduction

The first step in the understanding of simultaneous transformation kinetics and the development of predictive models for complex microstructures is the complete characterisation of the phases formed under continuous cooling heat treatment. This allows an assessment of microstructural evolution and the influence of heat treatment conditions on the phase transformations taking place. The determination of the nature of a phase by linking its characteristics to classification schemes based solely on optical observation is well established. For these reasons, the aims of this chapter are twofold:

- to provide a systematic characterisation of phases formed during continuous cooling heat treatment by exploiting the potential of investigation techniques with higher resolution than optical microscopy;
- to study the influence of heat treatment conditions and compositional effects on the phase transformations taking place under continuous cooling conditions.

The techniques capable of high resolution and high magnification utilised offer the advantage of a detailed morphological observation for each phase at very high magnifications, which can reveal microstructural features which are otherwise impossible to observe utilising optical microscopy. On the other hand, the fact that the existing classification schemes are based on specific characteristics of phases analysed optically, makes it necessary to link the morphology of each phase positively identified with light microscopy (low magnification) with those observed with SEM and TEM (low and high magnification). The identification of the nature of each microphase region cannot be achieved, unless high magnification techniques are used. Another factor justifying an extensive classification of phases performed by high magnification techniques is the lack of such a scheme which can be linked to the classification based on optical observation.

A range of microstructures was obtained by continuously cooling a Fe-C-Mn-Si alloy under different conditions as described in chapter 4. The microstructural analyses were systematically carried out using optical microscopy, scanning electron microscopy (SEM) and transmission electron microscopy (TEM). Furthermore, a set of known single phase microstructures, comprising solely of pearlite, ferrite, bainite and martensite, originating from samples of known composition, under isothermal conditions, were analysed in order to provide a reference point and guidelines for phase identification.

5.2 Analysis of Single Phase Microstructures

Continuously cooled steels generally have complex microstructures and therefore initially a set of known samples was analysed with SEM in order to provide a baseline of microstructures to assist with phase identification of more complex structures. All the samples where etched using a solution of 2% Nital.

The first set of microstructures includes three annealed plain carbon steel samples:

- 1.1 wt.% C annealed plain carbon steel
- 0.5 wt.% C annealed plain carbon steel
- 0.1 wt.% C annealed plain carbon steel

The steels were cooled slowly from an austenitising heat treatment, hence, the microstructures are a result of reconstructive transformations, as discussed in chapter 2.1.

The amount of cementite increases with increasing carbon concentration with the 1.1 wt.% C steel having some primary cementite and a pearlitic matrix; the 0.5 and 0.1 wt.% C steels both containing primary ferrite and pearlite, the 0.1 wt.% C having more ferrite than the 0.5 wt.% C steel. The samples were observed using SEM, and it was observed that the lamellae characterizing the pearlitic were clearly visible at low magnification and their morphology could be accurately observed at high magnification. This was also true for the primary cementite and the primary ferrite. Figures 5.1a-d show the appearance of primary ferrite and pearlite observed by means of SEM.

Figure 5.1: a) *1.1wt.% Hypereutectoid* ***b)*** *Pearlite. Lamellae of Fe_3C and α*

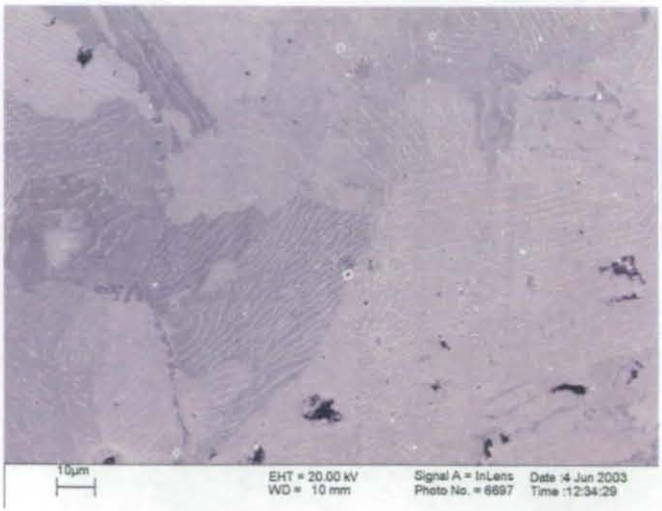

Figure 5.2: a) *0.5wt.% C. Ferritic-Pearlitic matrix.* ***b)*** *Pearlitic structure. Lamellae of Fe_3C*

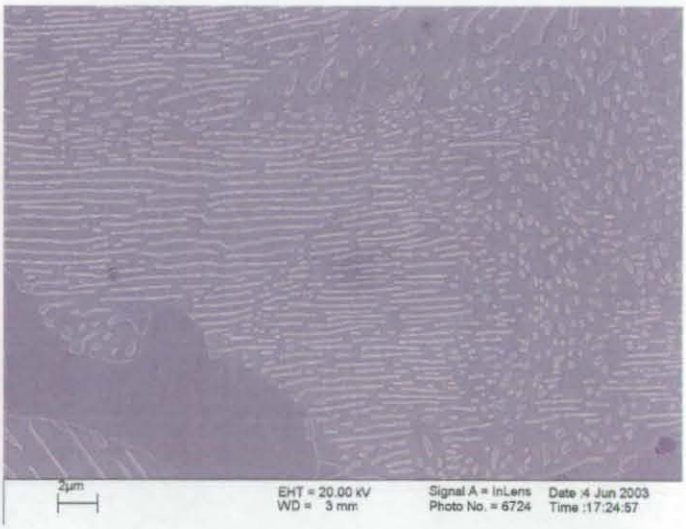

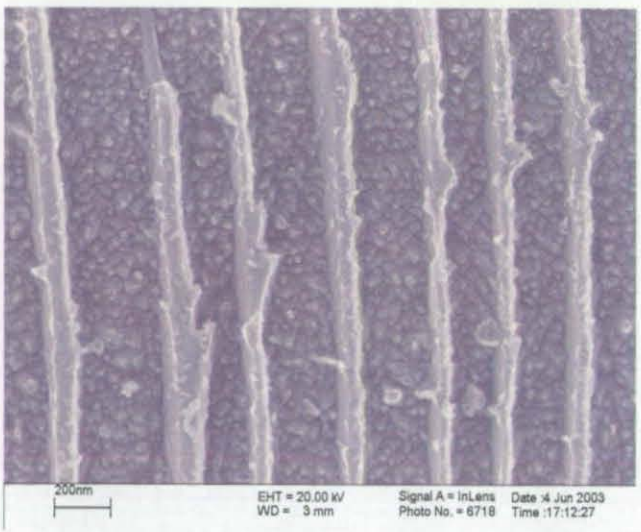

Figure 5.3: a) *0.1wt.% C. Ferritic matrix* ***b)*** *Radial section of a pearlitic lamellae*

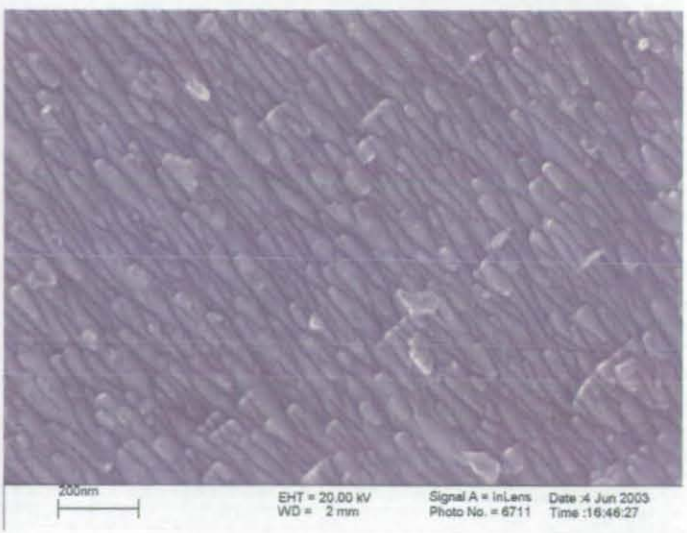

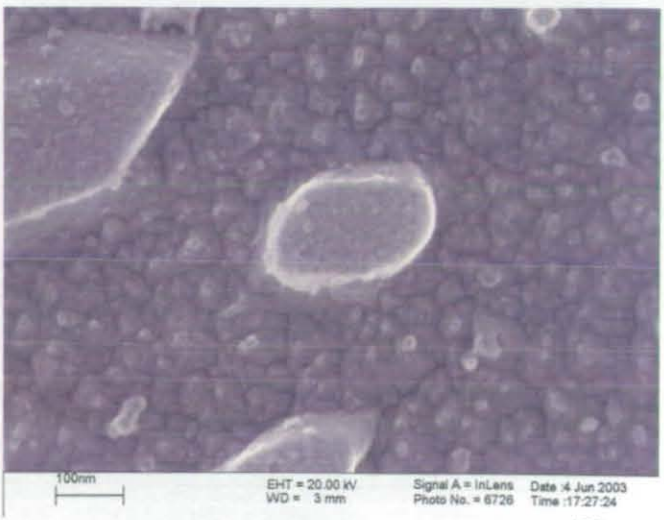

The second set of 'standard' microstructures comprised two plain carbon steels with a martensitic microstructure:

- 0.4 wt% C, as quenched
- 0.4 wt.% C, tempered

Optical microscopy and the heat treatment conditions indicated that the microstructure was fully martensitic (in both samples). The as quenched sample shows the martensitic, however it should be noted that the surface showed considerable relief when compared to Ferritic samples. This is consistent with the mechanism of the martensite transformation. The tempered sample additionally contained precipitates as expected, which originated during the tempering process. The small rounded particles form through the precipitation of carbides (cementite if the tempering process goes to completion), whose carbon comes from the supersaturated martensitic matrix. Figures 5.4a-b show the appearance of the martensitic matrix in the as-quenched state at different magnifications. Figures 5.6a-f show the appearance of the matrix and the precipitates of the tempered sample at various magnifications. Figure 5.6f shows one of these precipitates at very high magnification.

Figure 5.4a-b: *appearance of the surface of a martensitic region (as quenched sample) observed by means of SEM*

a)

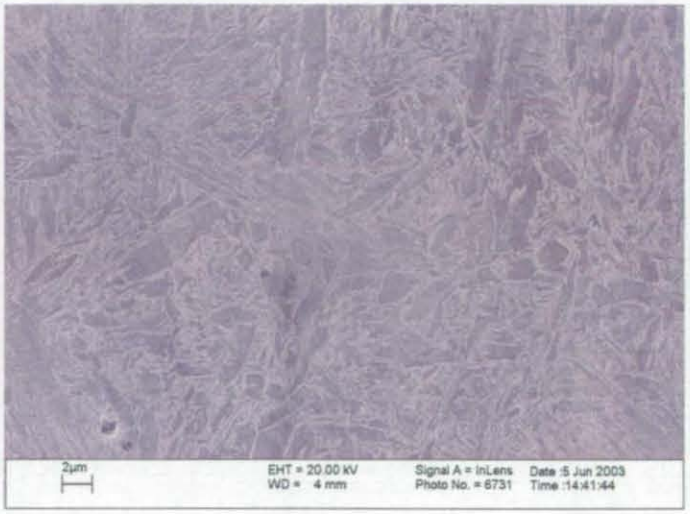

b)

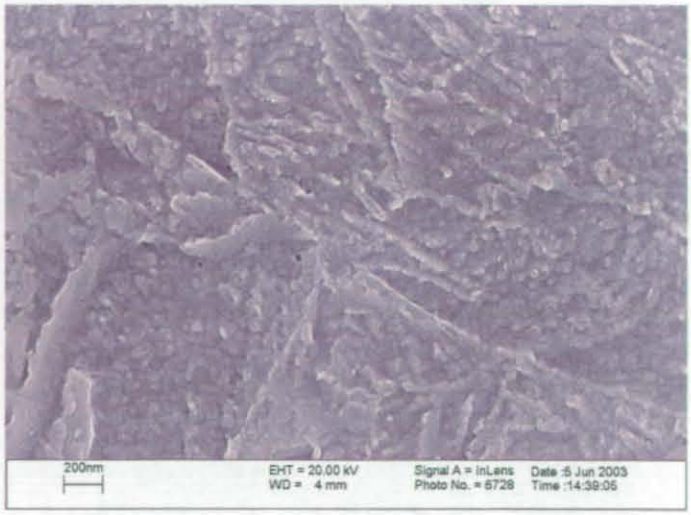

Figure 5.5a-f: *tempered martensite observed by means of SEM*

a)

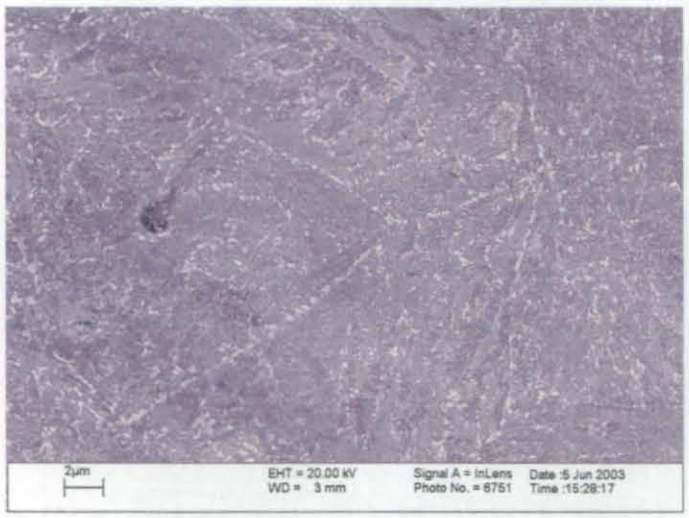

b)

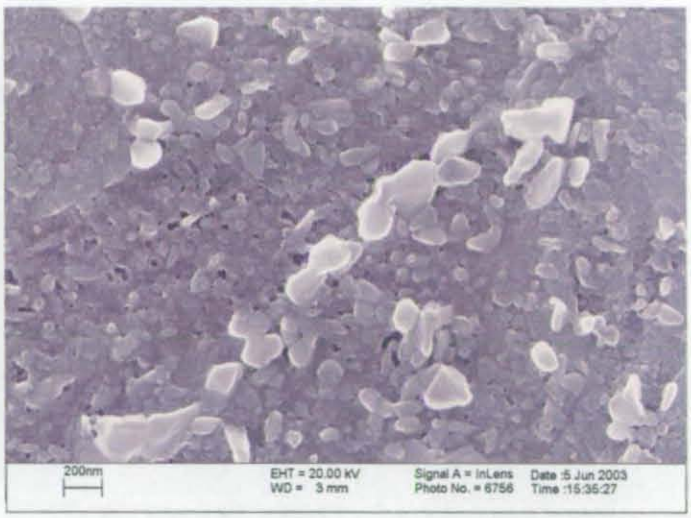

c)

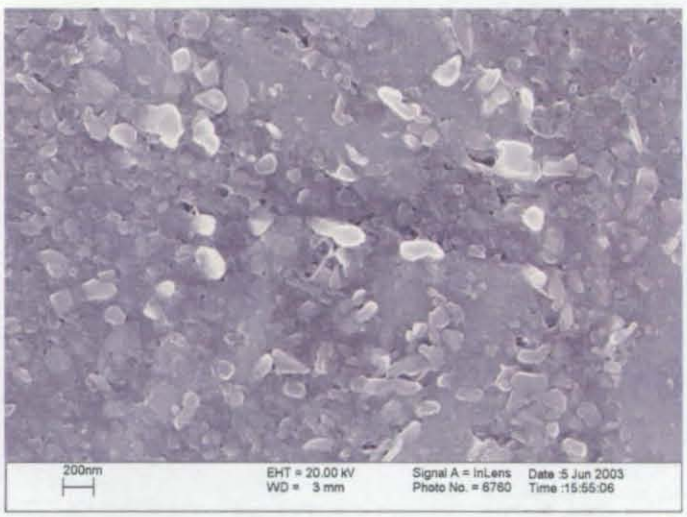

d)

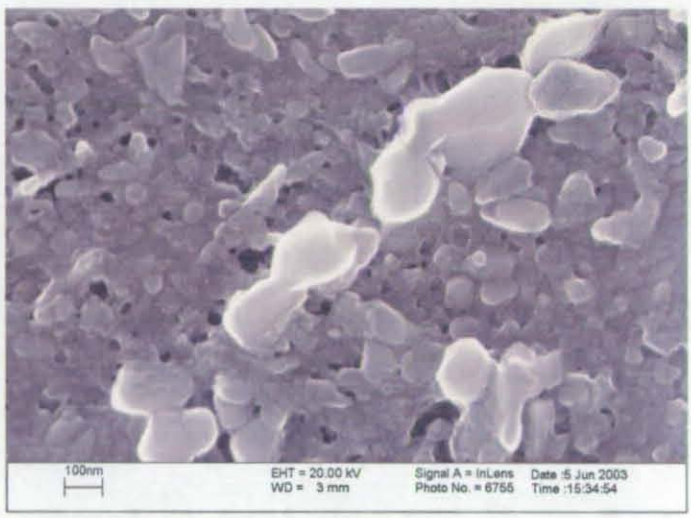

e)

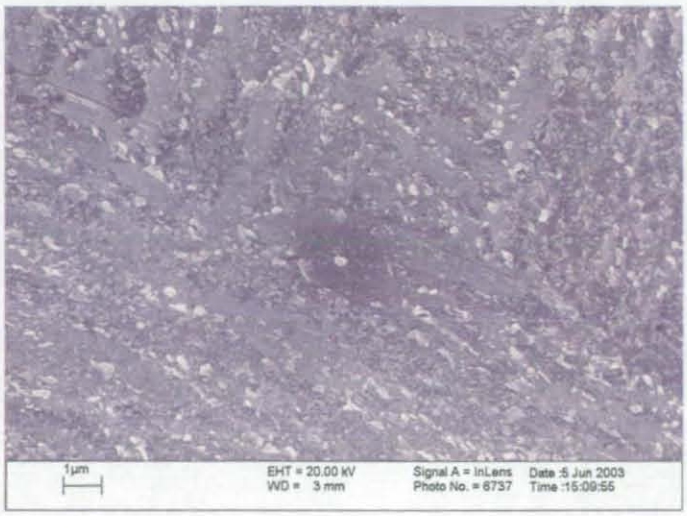

f)

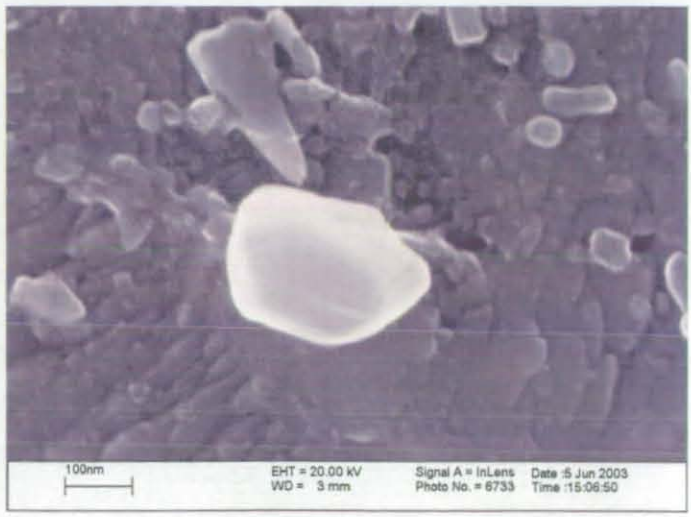

Finally, a 2.20 wt.% Cr, 1.0 wt.% Mo bainitic sample austempered at 560°C for 10 minutes to create a primarily bainitic microstructure has been analysed:

Figure 5.6a-h: *Bainitic Sample, including small auto-tempered martensite regions*

a)

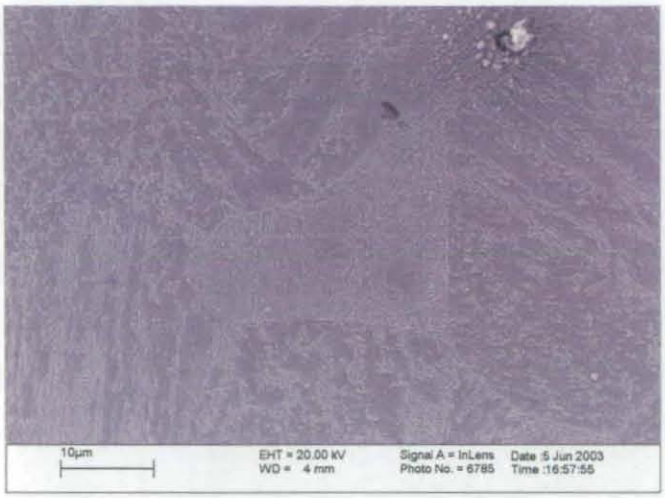

b)

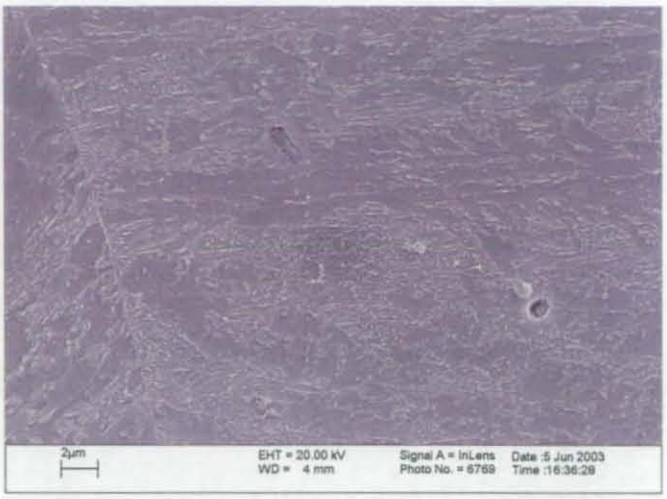

c)

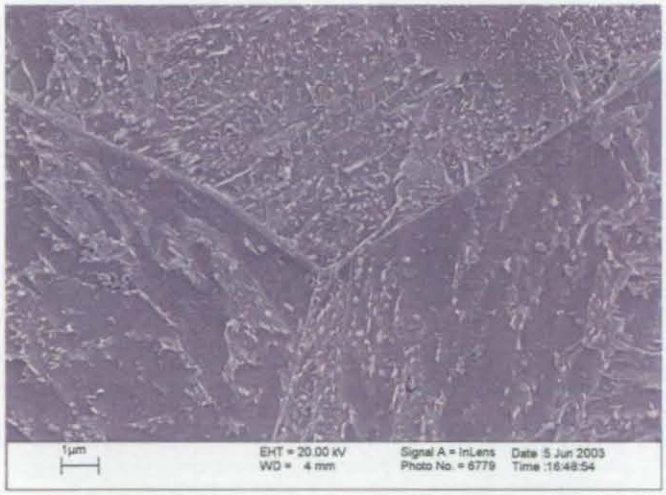

d)

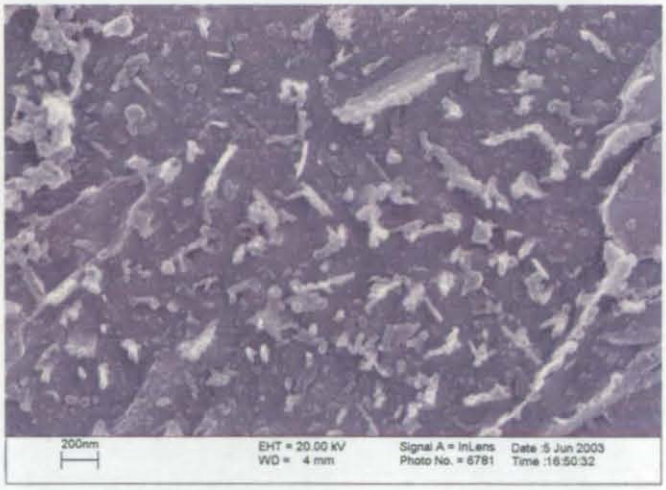

e)

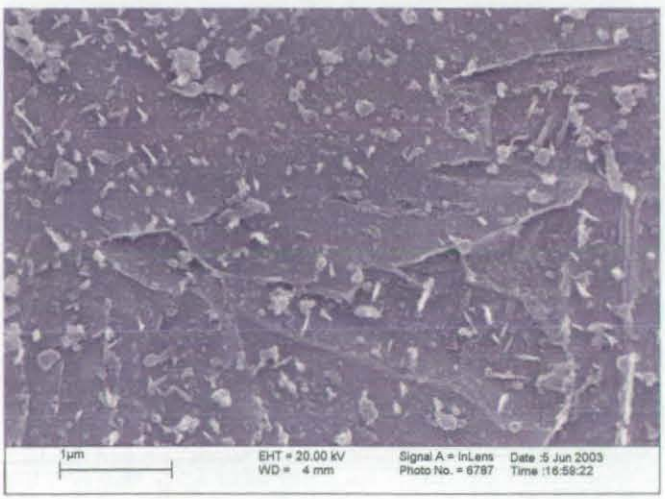

f)

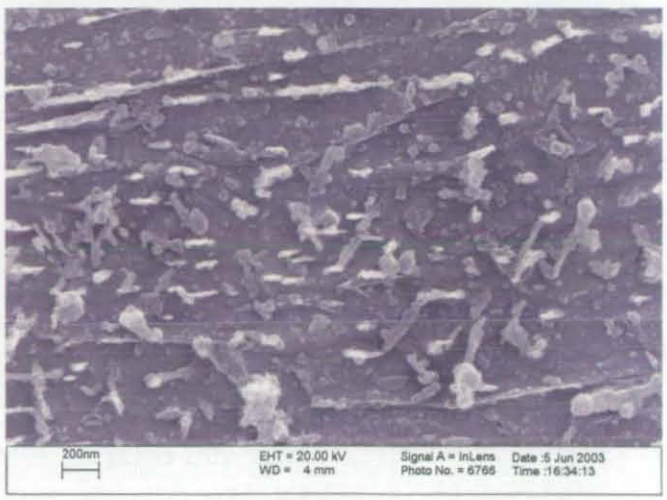

g)

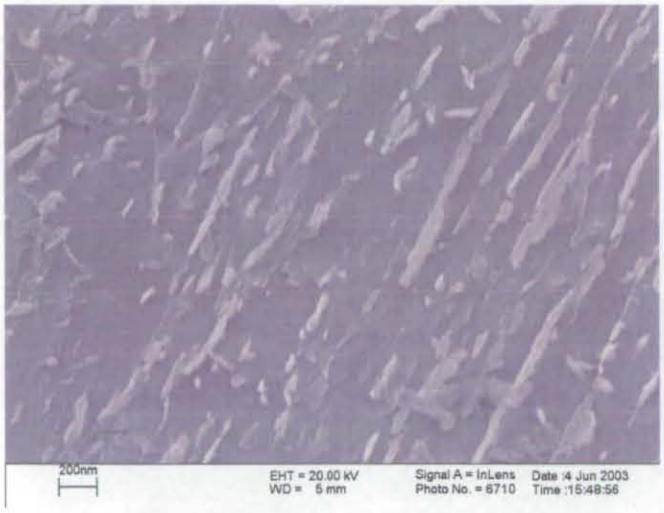

h)

The predominant structure (more than 90%) is the one represented in figure 5.6b. This structure, having a large number of precipitates represents lower bainite. The appearance of the surface recalls that of martensite, indicating the displacive component involved in the bainitic transformation (which is much larger in the case of the lower morphology), with the addition of the precipitates, which help the distinction between lower bainite and as-quenched martensite. The sample contained limited regions of martensite. Figure 5.6h shows a particular of a martensitic region of the matrix where auto-tempering took place as indicated by the orientation of the carbides which are aligned along three directions.

5.3 Phase Identification

5.3.1 SEM Analysis (InLens Imaging)

The continuous cooling heat treatments performed on alloy Y7N1 under different conditions produced a wide range of microstructures. The identification of each phase involved the use of optical, scanning and transmission electron microscopy at low and high magnifications. The use of optical microscopy is probably the quickest way to identify and quantify the phases present in a microstructure. However, figure 5.7 shows a good example of the limitations inherent in optical microscopy. The microstructure shown in figure 5.7 has been obtained by cooling alloy Y7N1 at

10°C s^{-1} after austenitising at 1100°C. The regions of microphase represent a considerable portion of the microstructure and therefore, their influence on the overall transformation should not be neglected.

Figure 5.7: *Advantages offered by SEM (InLens detection); the optical analysis allows very large areas to be observed but detailed characterisation of certain phases (e.g. microphase) is not possible. The SEM (InLens) allows morphological analysis of each microstructural constituent to extremely fine scales*

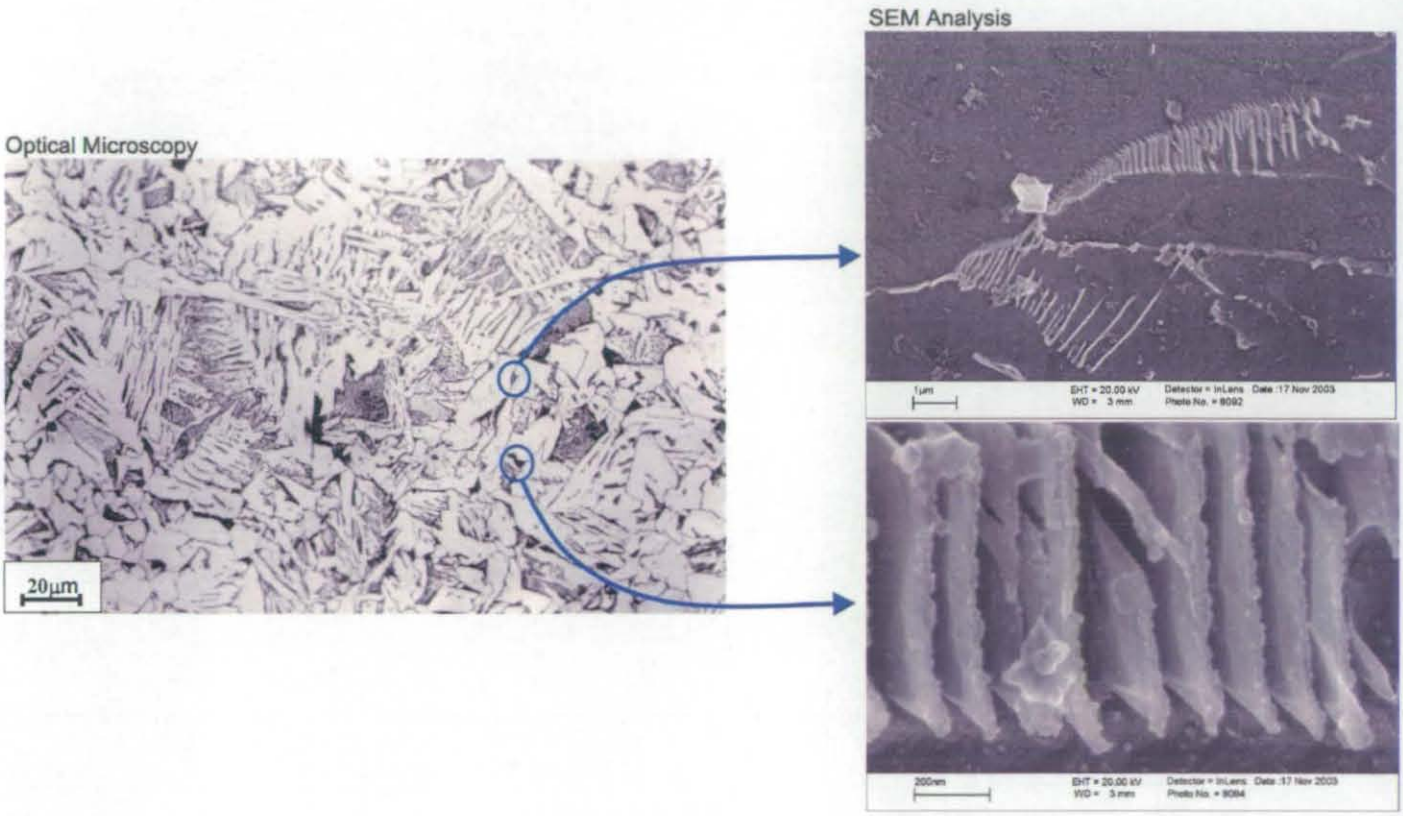

The following sections 5.3.2 to 5.3.9 illustatrate systematically the morphology of each phase present in the steels analysed, observed by means of SEM.

5.3.2 Ferrite

Figure 5.9: *Optical micrograph showing primary ferrite regions obtained by continuously cooling alloy Y7N1*

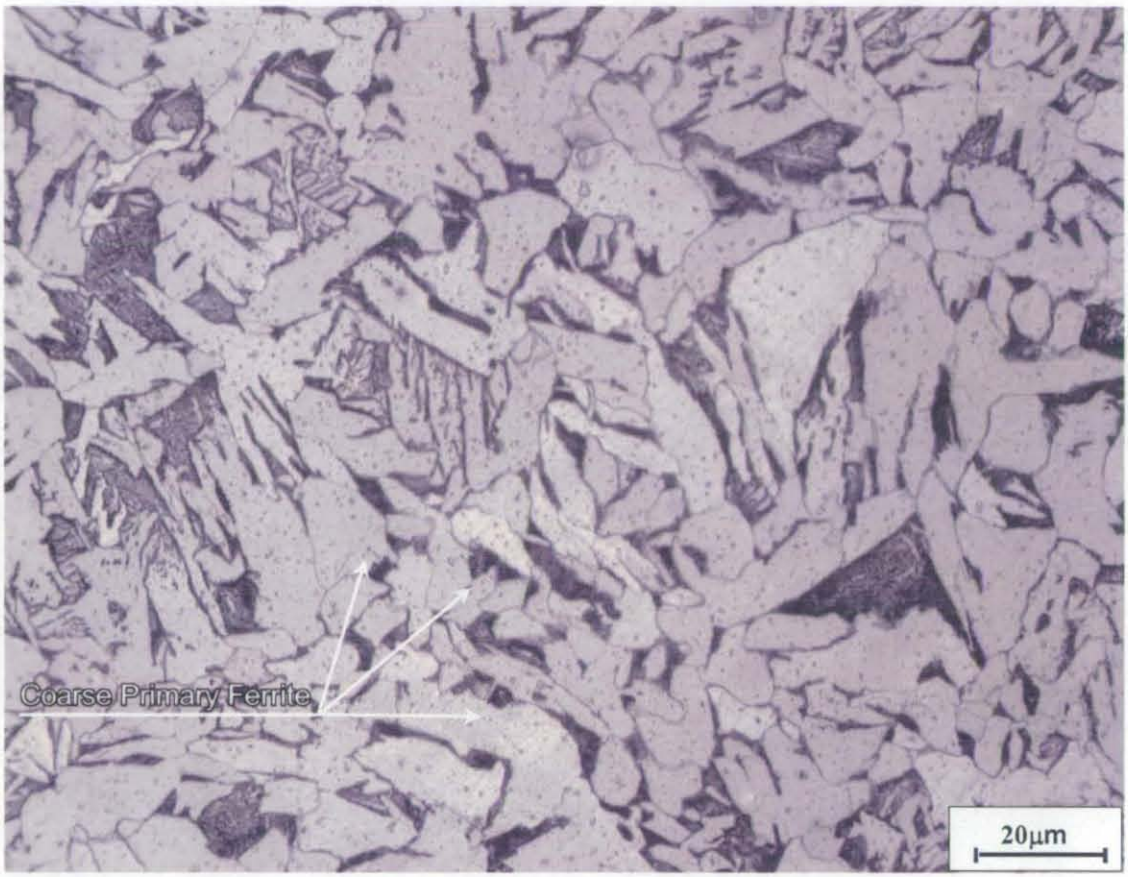

In hypoeutectoid steels the first phase forming during cooling below the Ae_3 temperature is primary ferrite. The mechanism of formation is reconstructive. This implies nucleation of ferrite grains on prior austenite grain boundaries and the growth of a new network of grains through the rearrangement of all atoms (interstitial and substitutional) occurring via a diffusional mechanism. At high temperatures the rate limiting step for grain growth is the diffusion of substitutional atoms (PLE conditions). This type of ferrite is usually referred to as allotriomorphic ferrite.

At lower transformation temperatures the intragranular nucleation of ferrite grains (for example on inclusions) becomes kinetically favoured and the resulting phase is referred to as idiomorphic ferrite. It should be noted that at lower transformation temperatures and at high undercooling, the rate controlling step becomes the diffusion of carbon. Under an optical microscope, primary ferrite has a bright response to etching and has a blocky appearance, as shown in figure 5.9. Analogously, the scanning electron microscopy at low magnifications provides a

vision of the ferrite phase which does not show any lath structures and has a smooth surface. A very interesting aspect of ferrite, when observed at very high magnifications, is the appearance of the surface: a granular morphology is observed comprised of a large number of "hills" presumably pointing toward the direction of growth. The TEM analysis, on the other hand, shows a ferritic matrix without the presence of laths or boundaries within the same ferrite grain. The presence of band contours is usually associated with primary ferrite grains. Naturally, the different growth conditions are reflected in different growth morphologies. Usually, the ferrite allotriomorphs nucleating at prior austenite grain boundaries develop in the form of polygons. This morphology is dominant at low cooling rates, as shown in figure 5.9. In a low carbon low alloy steel, at low cooling rates (e.g. 2°C s^{-1}) the austenite has the chance to fully transform into a mixture of allotriomorphs with polygonal shapes and small pearlitic regions. As the cooling rate increases, the ferrite grains also assume the morphology of 'veins' along prior austenite grain boundaries. The dimensions of the primary ferrite grains depend on the austenite grain size and the cooling rate. As the austenite grain size increases, the ferrite grains become coarser. As the cooling rate increases, the resulting microstructure is finer. Figures 5.10a and b show the appearance of primary ferrite at low magnification, produced in a sample cooled at 2°C s^{-1}. If the contrast is unaltered, the ferritic regions, which have bright appearance when observed optically, appear as the darkest regions in the SEM. Furthermore, the InLens detection enhances the brightness of regions with a second (or more) phase that provides some relief (such as pearlite, boundaries or precipitates).

Figure 5.10a-d: *SEM images showing primary ferrite regions (dark contrast)*

a) ***b)***

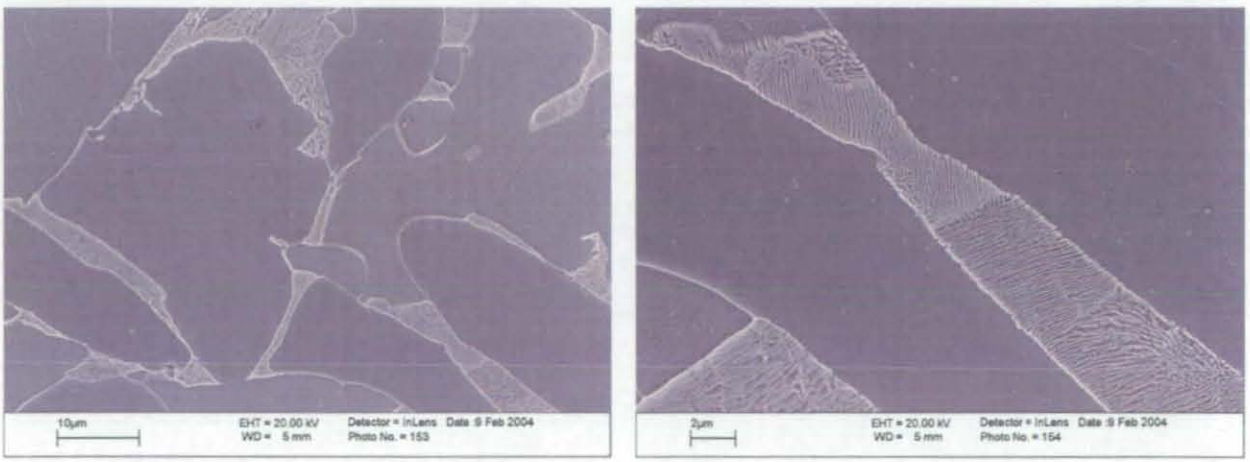

c)

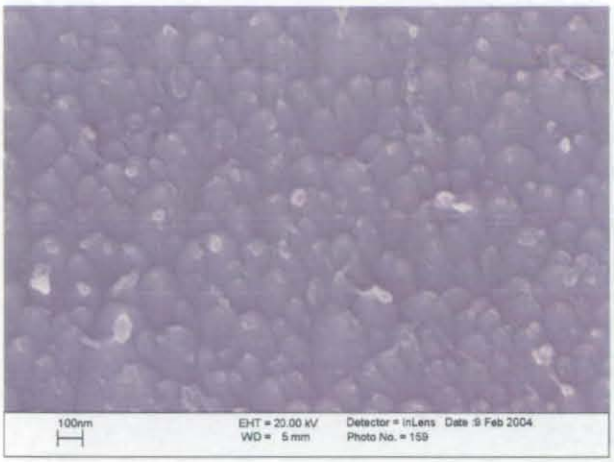

d)

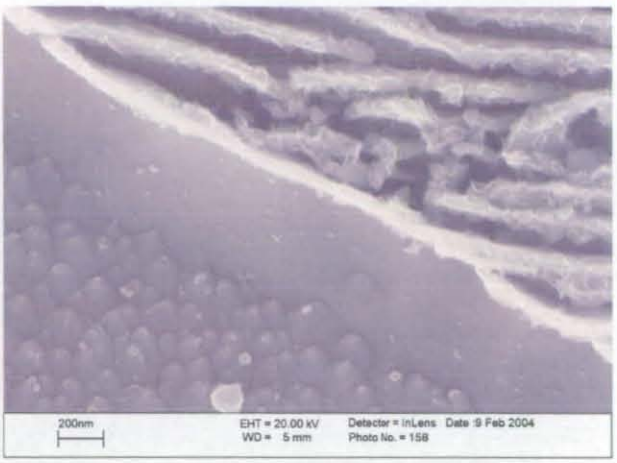

The surface of the ferrite allotriomorphs is smooth and does not show the presence of any lath structure or sub-boundary structure within each large grain formed at high temperature. It is interesting to observe the structure at high magnification which can be seen in image 5.10c. The fact that all the "granules" point toward the same directions may indicate a relation with the growth direction of a ferrite grain. The boundary structure between a ferrite grain and a pearlite region at high magnification is shown in figure 5.10d.

5.3.3 Pearlite

Figure 5.11: *Optical micrograph showing fine pearlite obtained by continuously cooling at 2°C s^{-1} alloy Y7N1*

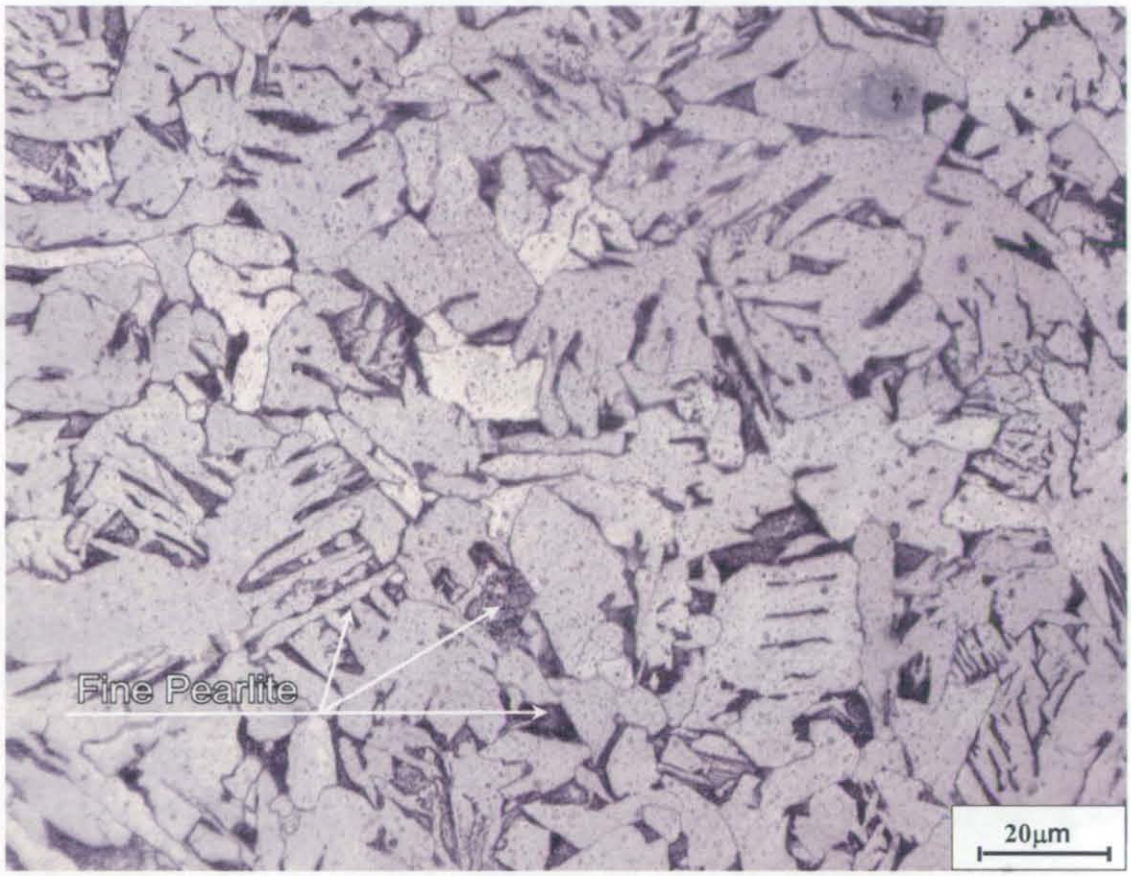

Pearlite forms via a eutectoid reaction, which can be defined as an invariant solid-solid reaction through which one solid transforms to a mixture of two solid products at constant composition. In the case of a low carbon steel the eutectoid composition is approximately 0.77 wt.% C. In the case of hypoeutectoid steels, when cooling at low cooling rates (e.g. 5°C s^{-1}) primary ferrite forms first, enriching the surrounding austenite with carbon. The carbon content eventually reaches the eutectoid composition, causing the remaining austenite (whose amount is determined by the lever rule) to transform into pearlite. The lamellae spacing in pearlite is very sensitive to transformation temperature. The diffusion distances increase as the transformation temperature approaches the equilibrium eutectoid temperature. Therefore, by increasing the degree of undercooling, the size of the spacing decreases as the amount of free energy available for the transformation decreases.

Usually pearlite nucleates on prior austenite grain boundaries or on inclusions or other heterogeneities. When forming at high transformation temperatures pearlite nodules are quite easily identifiable from the presence of the alternate lamellae of ferrite and cementite which are usually visible and coarse. However, identification can become difficult as the transformation takes place at lower temperatures. In fact, the pearlite structure becomes increasingly finer and eventually irresolvable with an light microscope. In these cases, the phase appears as a dark etching phase. In low carbon low alloy steels, at low cooling rates (although greater than $1°C\ s^{-1}$), the pearlite regions are observed between ferrite grains and have a fine structure which is sometime not resolvable with the optical microscope. Identification of very fine pearlite, which often forms under continuous cooling conditions, requires experience, as it can be confused with martensite or bainite. The observation of the phase at high magnifications by means of SEM and TEM, clearly show the lamellar nature of the phase and the absence of features typical of displacive transformations, such as a sheaf structure. An extremely fine lamellar structure can be observed in pearlite "pools" between ferrite grains and in microphase regions (figures 5.12a-d). In figures 5.12a and c two other characteristics can be observed: the distortion of the lamellae and, more interestingly, a variation in growth direction within the same pearlite grain.

Figure 512a-d: *SEM images showing pearlitic regions (bright contrast)*

a) ***b)***

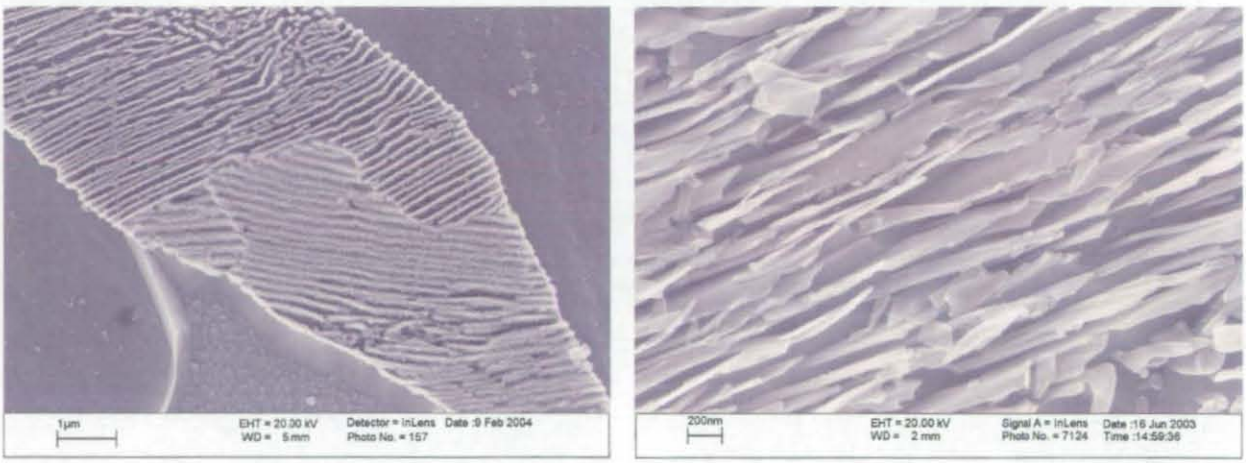

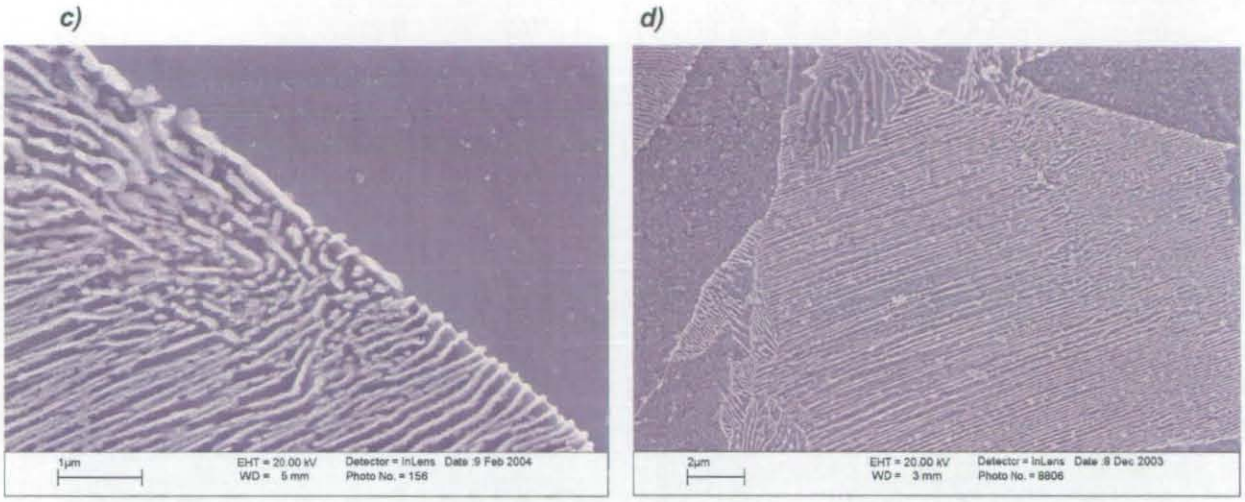

5.3.4 Ferrite Carbide Aggregate (FCA)

Figure 5.13: *Optical micrograph showing FCA regions obtained by continuously cooling at 10°C s^{-1} alloy Y7N1*

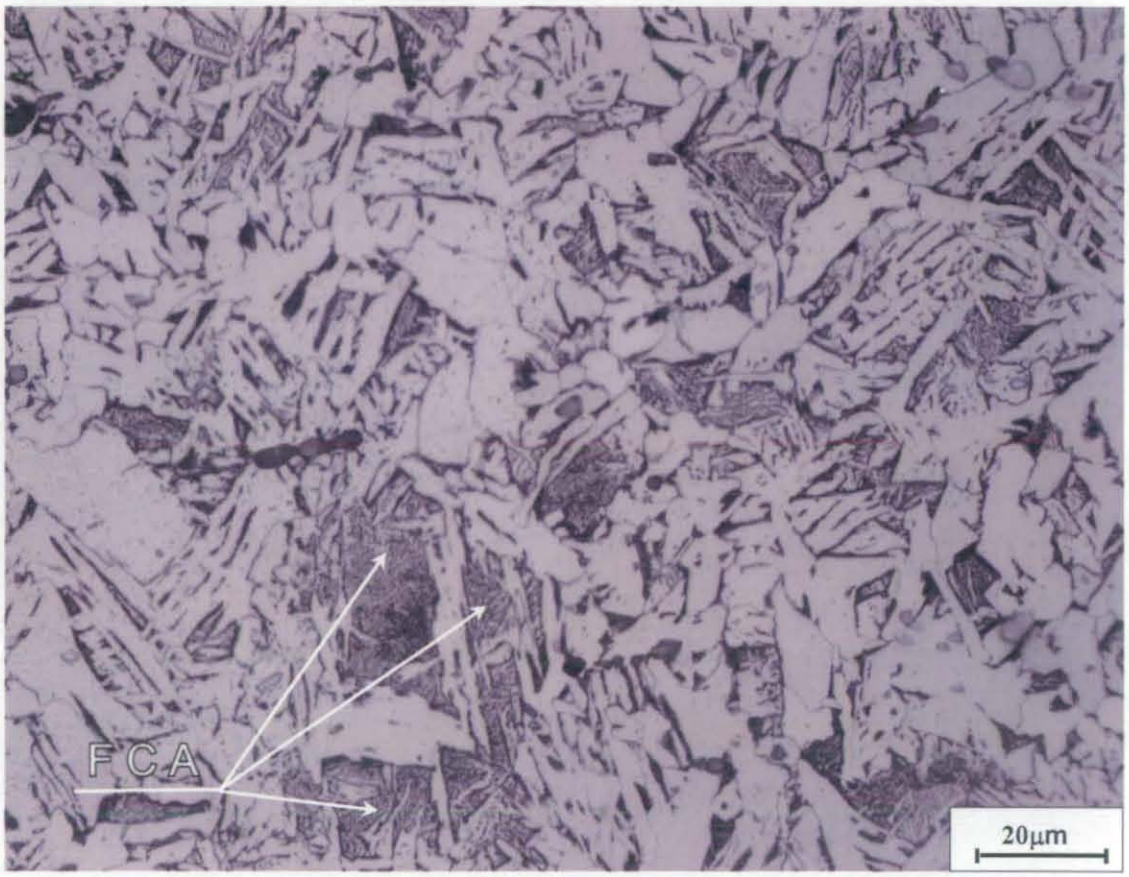

This constituent has been the focus of the present research. It has not received significant attention in the past and, as a consequence, its identification and classification is not straightforward. FCA consists of a ferritic matrix with fine

interspersed carbides which usually precipitate in arrays. The presence and morphology of carbides, however, are not resolvable under a light microscope. In fact, the phase appears as dark etching regions usually adjacent to primary ferrite grains or Widmanstätten ferrite plates. It has a spongy appearance which is somewhat similar to irresolvable pearlite, although this phase forms at higher cooling rates and at lower temperatures compared to pearlite. The assessment of the nature of the FCA phase and the stages at which it forms in a transformation sequence suitable for continuous cooling heat treatments of low carbon low alloy steels will be discussed in detail in the following chapter.

The high magnification analysis allows the determination of the main microstructural characteristics of this phase, which are otherwise impossible by using optical microscopy. At low cooling rates (e.g. 10°C s^{-1}) the carbides are coarser (50-100 nm) and arrays can be clearly distinguished. On the other hand, an increasing cooling rate (e.g. 50°C s^{-1}) leads to a reduction in size of the precipitates, which become closer and in some instance interconnected with a "tadpole" like shape. The precipitation occurs usually in the form of particles or very small fibres.

Figure 5.14a-f: *SEM images showing FCA regions*

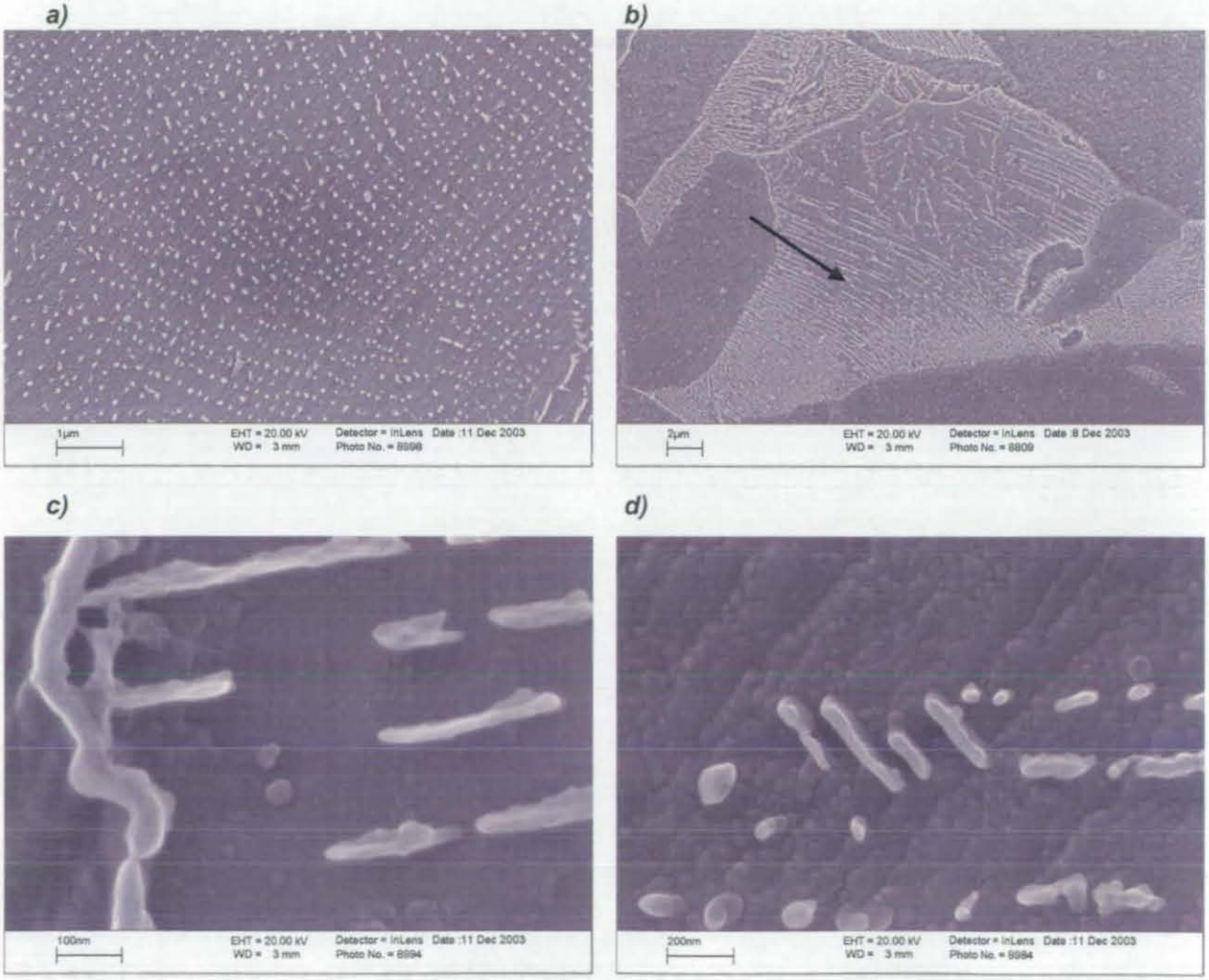

e) f)

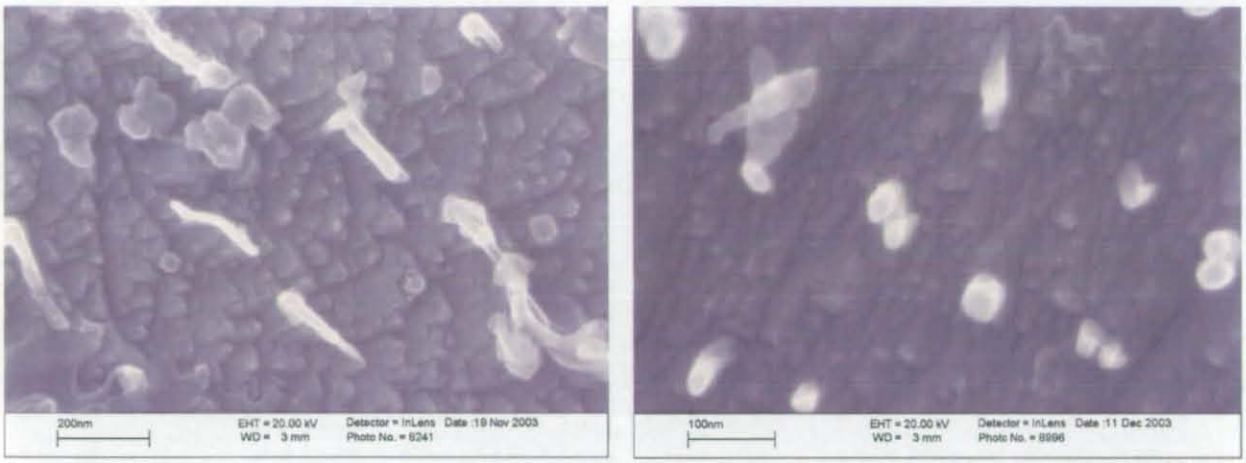

Figure 5.14a shows the morphology of FCA obtained by cooling at 10°C s^{-1}. At low cooling rates the structure of the particles is ordered and they are distributed in arrays with a periodic spacing. The appearance of the particles can be spherical or elongated on the form of small fibres (this will also depend on the section observed). Figure 5.14b shows the lamellae breakdown (indicated by a black arrow) observed in a sample cooled at 5°C s^{-1}. The breakdown of pearlite lamellae and the subsequent formation of the FCA typical morphology, both take place in the same grain and indicate the possible importance of the role of local carbon composition on the mechanism of formation. Figures 5.14c-f show high magnification details of the precipitates, matrix and boundaries.

5.3.5 Widmanstätten Ferrite

The SEM observation of primary Widmanstätten ferrite shows that it grows directly from the austenite grain boundaries, consistent with theory, whilst secondary Widmanstätten ferrite grows from protuberances on primary ferrite grain boundaries. Primary Widmanstätten ferrite is favoured by large austenite grain boundaries which prevent impingement of primary ferrite and allow room for growth of the ferrite plates. The most important parameter affecting the growth of Widmanstätten ferrite is the temperature, determined either by the cooling rate or the isothermal transformation temperature, depending on the type of heat treatment.

Figure 5.15: *Optical micrograph showing Widmanstätten ferrite regions obtained by continuously cooling at 50 °C s^{-1} alloy Y7N1 and interrupting the cooling at 580 °C*

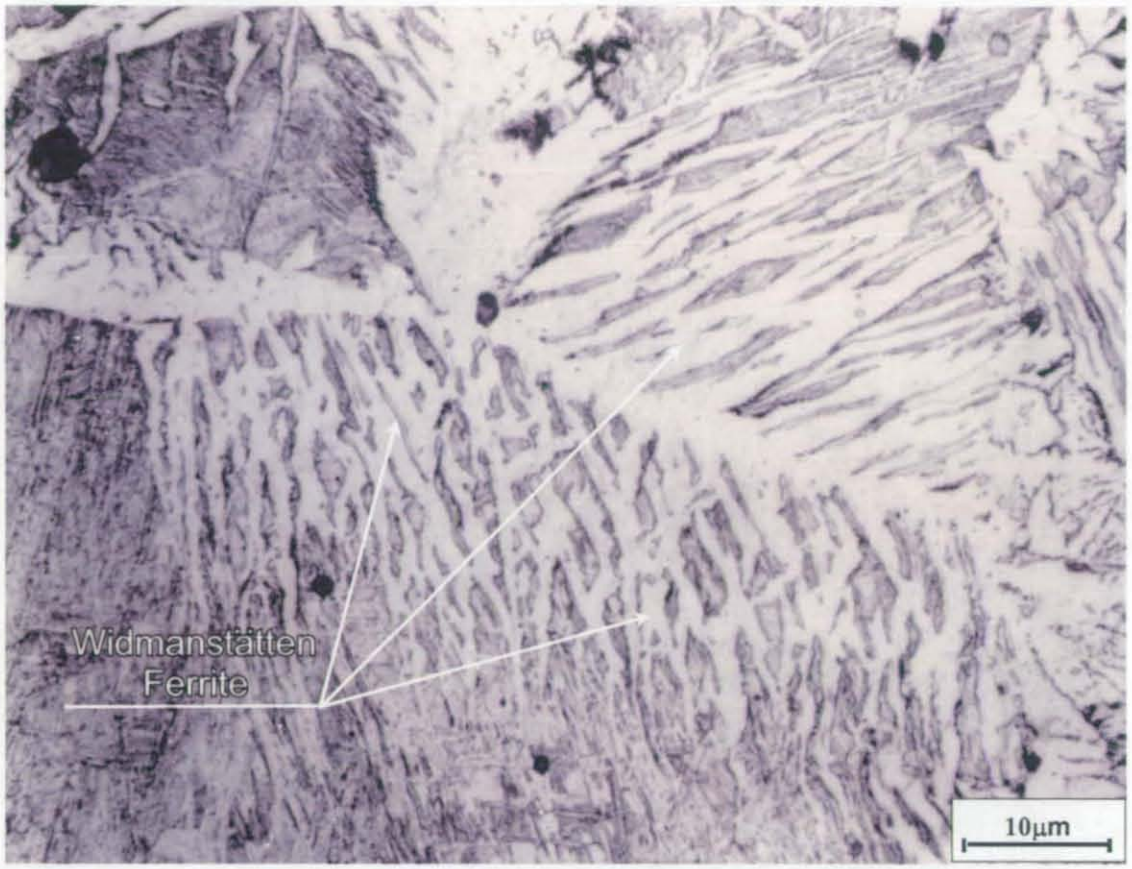

The presence of a coherent or semicoherent interface with the matrix, in addition to a surface relief effect that accompanies the growth of the ferrite laths suggests that the characteristics of the formation of Widmanstätten ferrite can be associated with a displacive type of transformation with some similarities to bainite.

The aspect ratio of the plates is usually high (10:1) resulting in parallel arrays. The growth mechanism is thought to occur under paraequilibrium conditions (i.e. diffusion of interstitial atoms). The distinction from upper bainite can be very difficult. However, Widmanstätten ferrite forms at higher temperatures compared to bainite, shows a coarser structure and the size of the microphase regions between the ferrite plates are relatively large (the size being between a third or a fourth compared to the adjacent plates). The nature of microphase between the plates can be austenitic, martensitic, pearlitic or a mixture of these phases.

Furthermore, Widmanstätten ferrite plates tend to grow with a common crystallographic orientation. The plates are characterised by the absence of subunits and the adjacent plates are usually separated by low angle boundaries. In the image at high magnification, the boundaries can be easily observed and their aspect recalls that of fine austenite layers which link the microphase regions, as shown in figure

5.16 using high resolution SEM analysis. The nature of each microphase can be easily assessed, the presence of laths, the appearance of boundaries and the appearance of the ferrite matrix in the plates can be analysed and the nature of the phase can be effectively identified. As a result the distinction from bainite becomes much easier. For commodity, the nature of the microphase has been specified in each figure caption.

Fig 5.16a-f: *SEM images showing Widmanstätten ferrite regions comprised of ferrite plates (dark contrast) and microphase regions (bright contrast)*

a) *retained austenite*

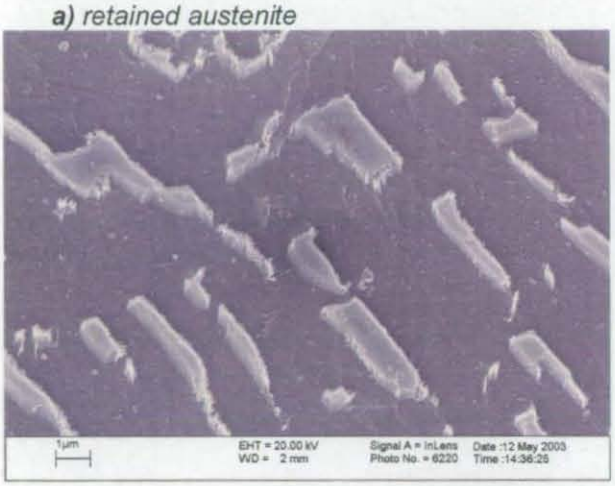

b) *retained austenite*

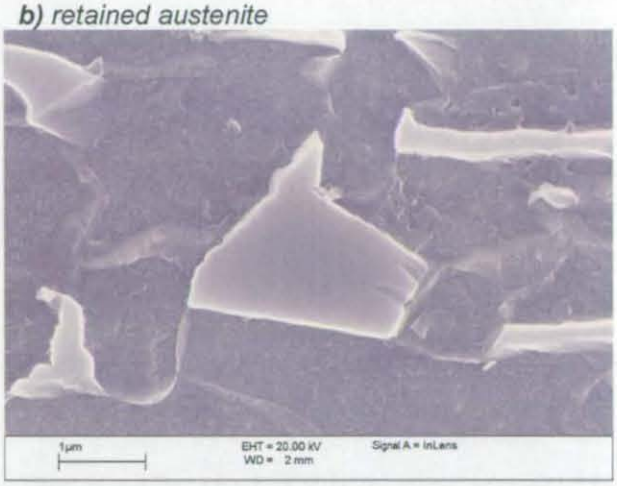

c) *retained austenite*

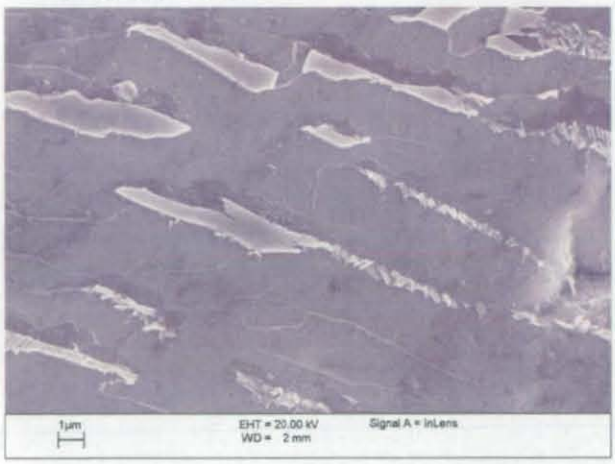

d) *retained austenite*

e) *pearlite (end on)*

f) *retained austenite and pearlite*

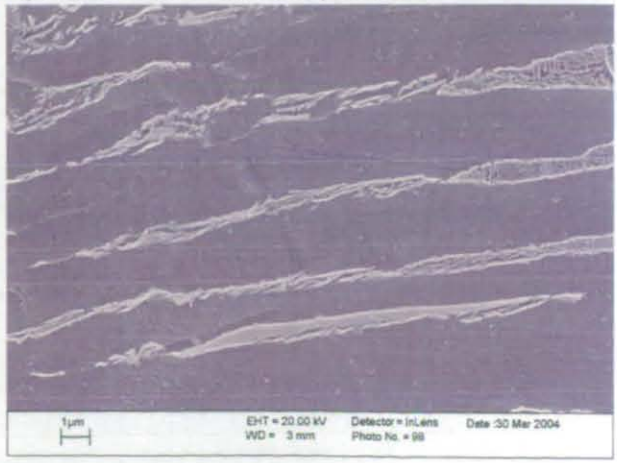

The microstructures shown in figures 5.16a-f comprise Widmanstätten ferrite plates and the microphase separating them. The dimensions, shape and nature of the microphase changes depending on the heat treatment conditions and the local composition. The microphase in image 5.16e is observed end on, and the boundaries separating single sideplates can also be observed. Finally, image 5.16f shows an instance in which the effects of variation of local composition along a distance of a couple of microns can be different to such an extent that will result in different transformations in each microphase region.

5.3.6 Bainite

The nature of bainite changes as the transformation temperature reduces. Two main morphologies can be identified. Upper bainite occurs at higher transformation temperatures and is characterised by the presence of carbides only between the ferrite plates. Lower bainite forms at lower temperatures and is characterised by the precipitation of cementite particles additionally within the ferrite plates as the resulting diffusion distances are shorter. Although there is still controversy about the exact mechanism of bainite growth, the most widely recognized mechanism involves a diffusionless stage causing the $\gamma \rightarrow \alpha$ transition at temperatures lower than that at which the two phases have the same free energies. The ferrite formed would then be supersaturated in carbon, which would rapidly partition into austenitic layers between the bainitic plates or precipitate in the form of cementite, between or within the laths, depending on whether the upper or lower morphology is formed.

From a microstructural point of view, bainite can grow directly from prior austenite grain boundaries or intragranularly, when nucleation takes place on an inclusion. A characteristic feature which can help the phase identification is the sympathetic nucleation of bainitic plates.

5.3.6.1 Upper Bainite

The identification of an upper bainitic microstructure is not always straightforward because it has similarities with Widmanstätten ferrite. Especially at high temperatures (550-650°C depending on the alloy composition), or at intermediate cooling rates (e.g. 50°C s^{-1} for a low carbon low alloy steel) where the two phases coexist and the

bainitic laths are coarser, the distinction between the two becomes quite difficult. In, fact, when Widmanstätten ferrite microphase becomes very fine and, on the other hand, when precipitates between the bainitic laths are coarse, under a light microscope the two phases can appear very similar.

Figure 5.17: *Optical micrograph showing upper bainite regions obtained by continuously cooling at 60 °C s^{-1} alloy Y7N1*

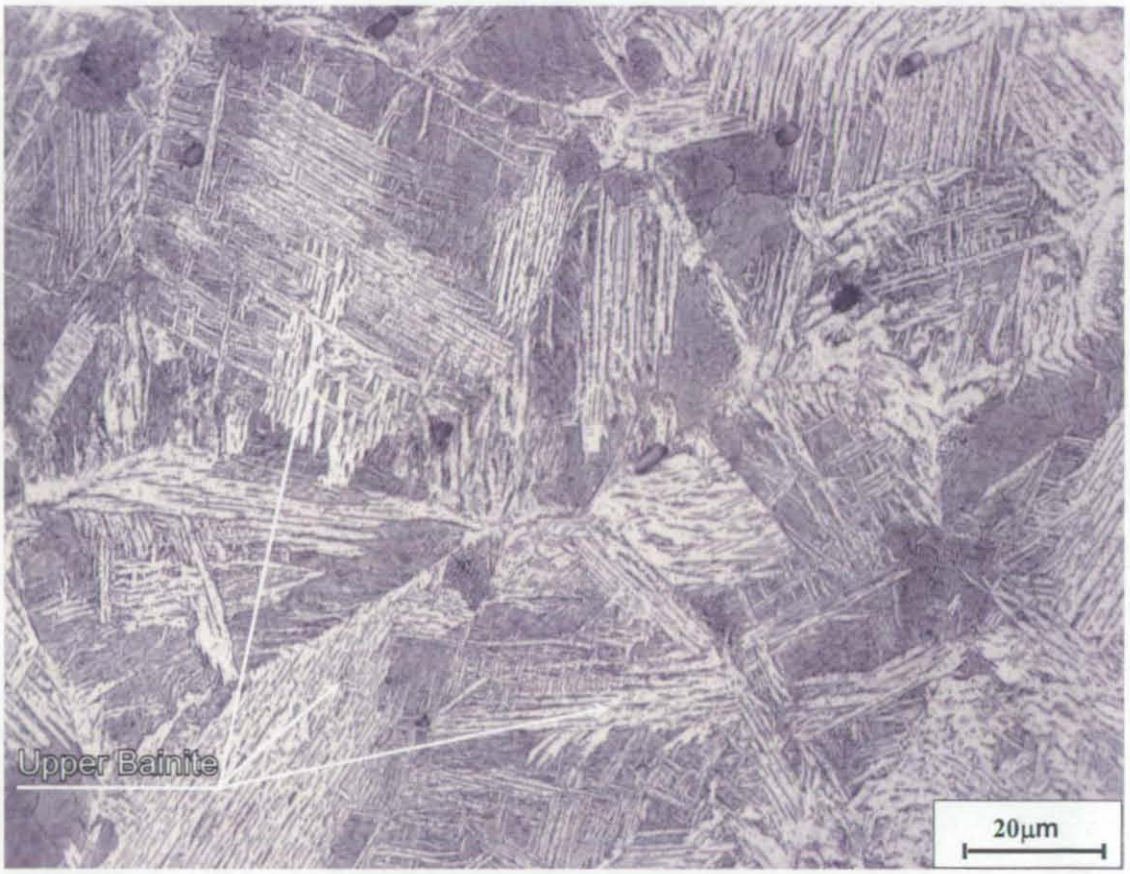

Using SEM InLens detection, the identification of upper bainite becomes much easier. The austenitic layer between the laths can be observed, in addition to the precipitates eventually present between the laths. Furthermore, the possibility of observing the nature of the regions between the laths aids identification: in fact, in the case of bainite the layers are only austenitic whilst in WF, the nature can be different, ranging from pearlite, M/A, austenite or martensite depending on the heat treatment conditions and the local composition profile.

Figure 5.18a-d: *SEM images showing upper bainite regions*

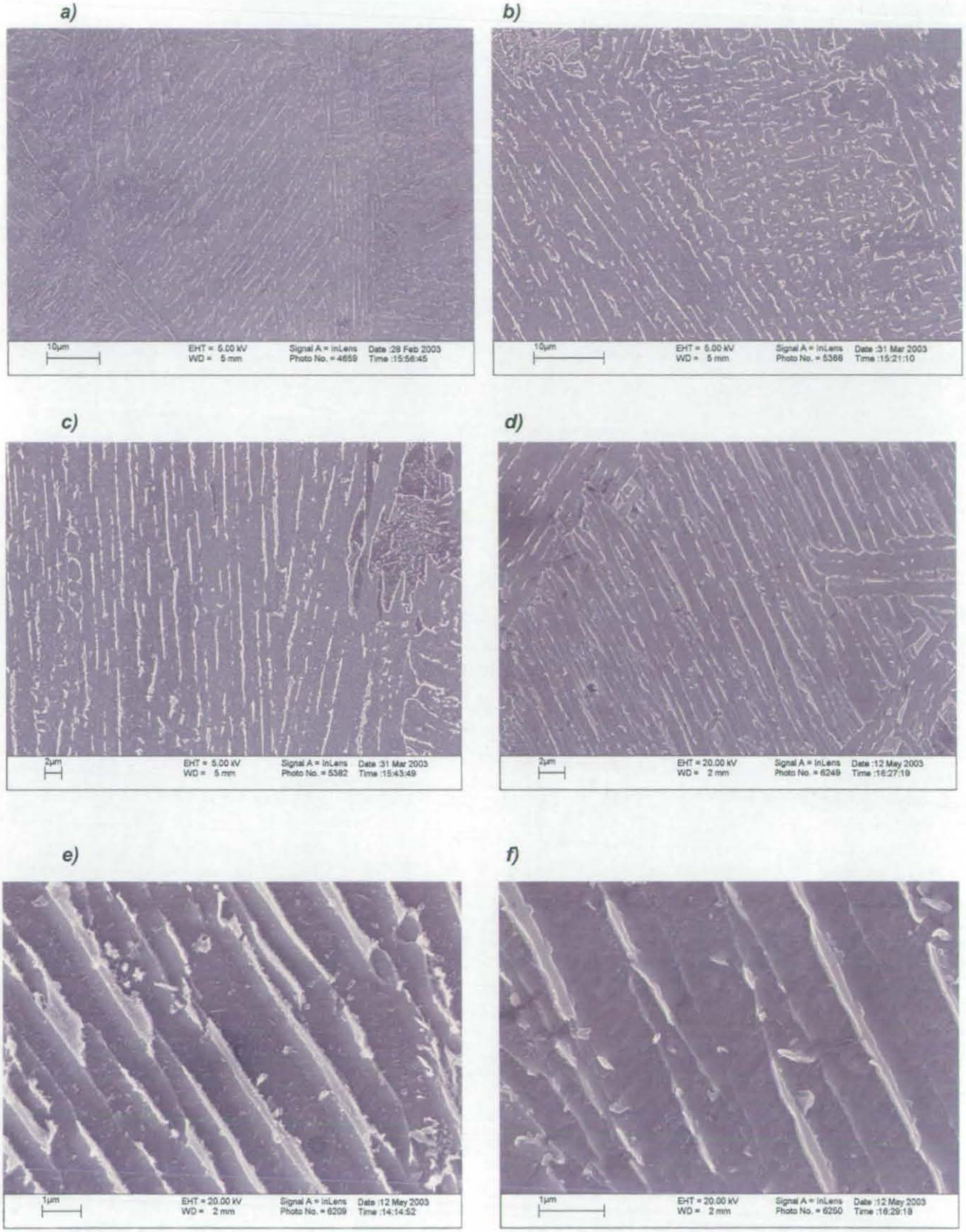

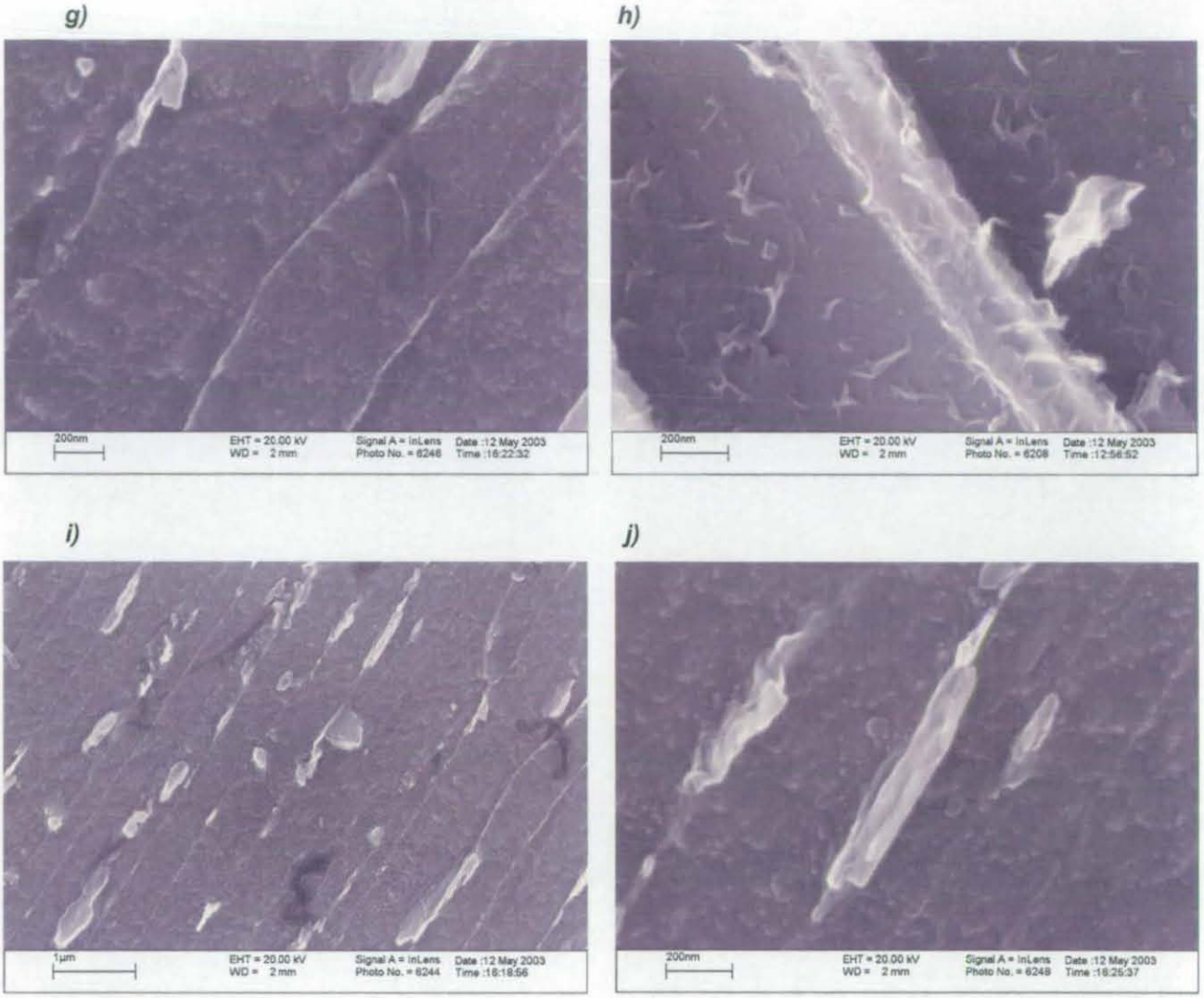

The images in figures 5.18a-d show at low magnification the structure of upper bainite obtained by cooling alloy Y7N1 at 50°C s^{-1}. The morphology of laths, austenite layers and cementite precipitates at high magnification can be observed in figures 5.18f-j.

5.3.6.2 Lower Bainite

The presence of carbides within the bainitic laths, which are one of the morphological features determining the difference with upper bainite are not always easy to resolve under a light microscope due to the size/resolution limit. Furthermore, the cross section of upper bainite sheaves can be confused with lower bainite.

Figure 5.19a-b: *Optical micrographs showing lower bainite regions obtained by continuously cooling at 75°C s^{-1} (a) and isothermally holding at 530°C for 30 s (b) alloy Y7N1*

a)

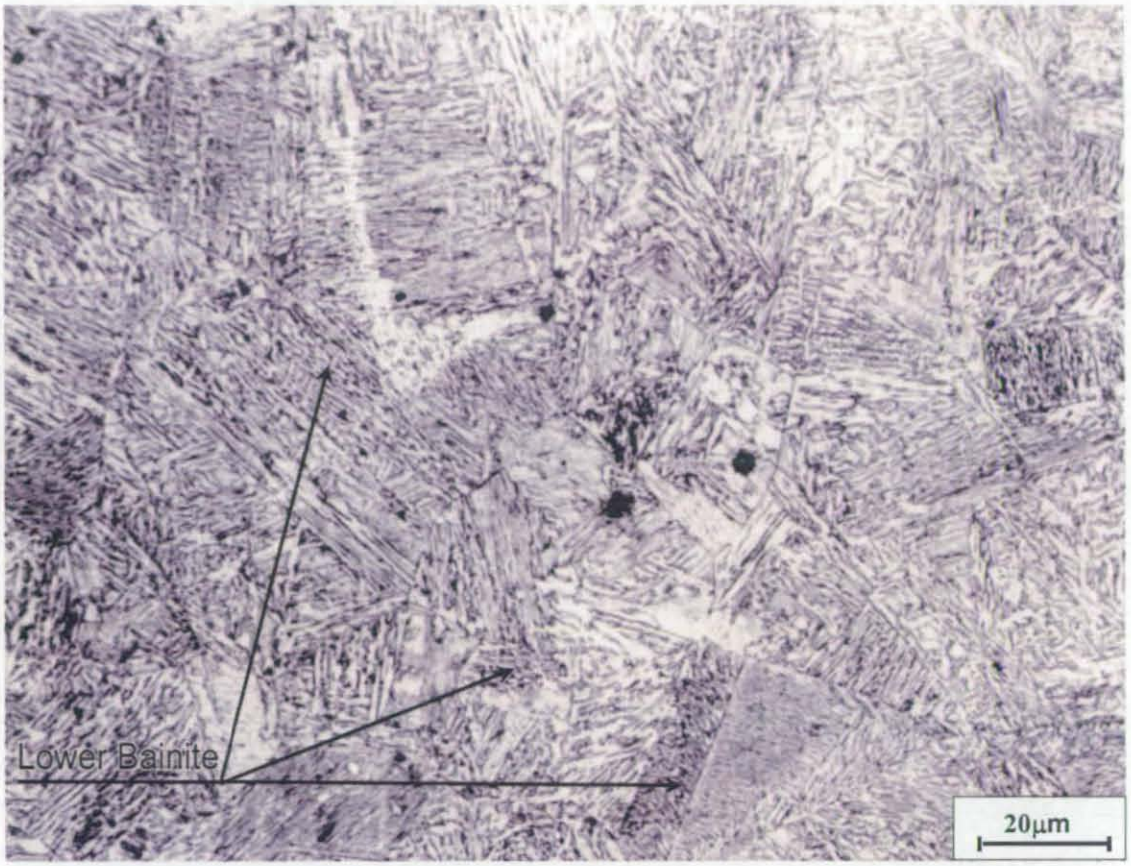

b)

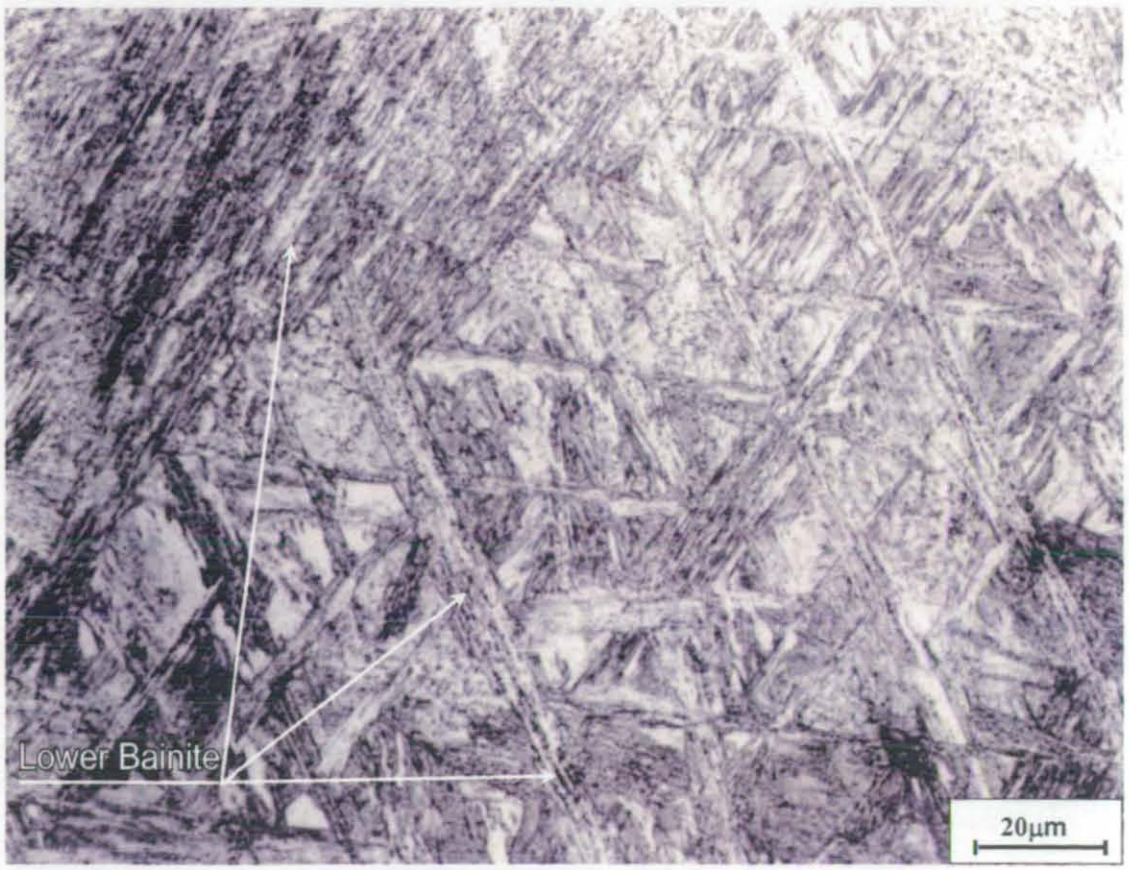

The appearance of the ferrite laths in lower bainite closest to the observations of martensite laths. The precipitates between and within the laths can be easily identified, leading to a confident identification of this phase. Furthermore, the appearance of the lower bainitic ferrite laths can be compared with those of upper bainite which appear very different, possibly supporting the idea of a larger shear component in the lower morphology transformation mechanism

.

Figure 5.20e-f: *SEM images showing lower bainite regions*

a)

b)

c)

d)

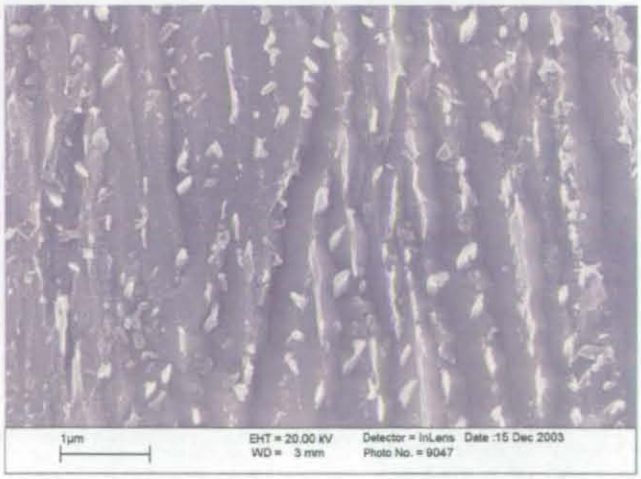

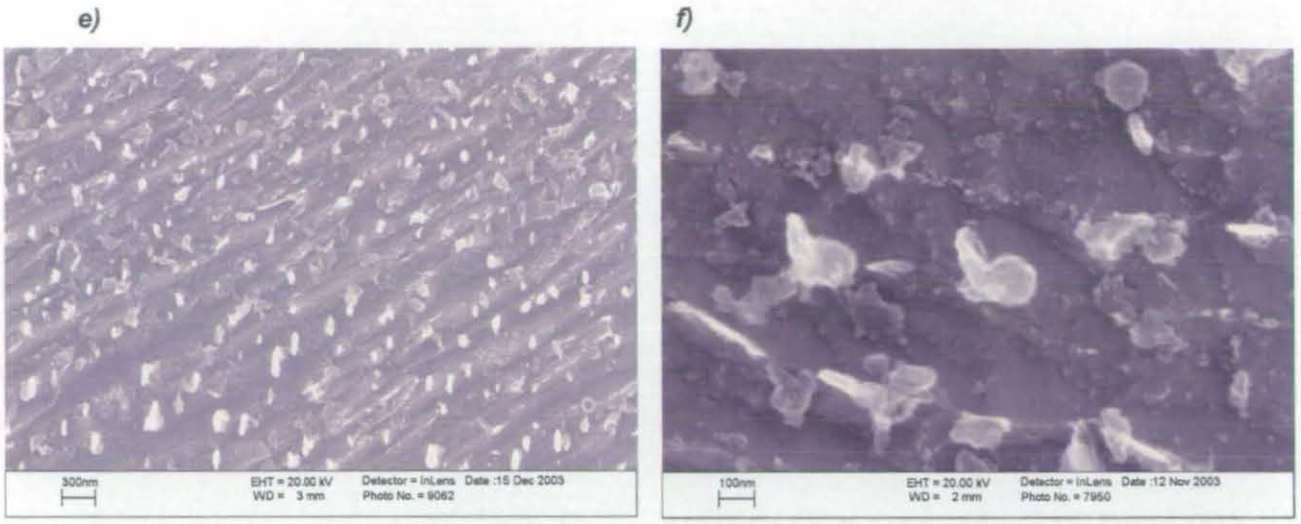

The images shown above highlight the differences with the upper bainite morphology. The appearance of the laths recalls that of martensite and not that of Widmanstatten ferrite. The precipitates are within and between the laths. High magnification images of such precipitates are shown in figures 5.20c-f.

5.3.7 Martensite

Figure 5.21: *Optical micrograph showing martensite regions ontained by continuously cooling at 10 °C s^{-1} alloy Y7N1 and interrupting the cooling stage at 624 °C*

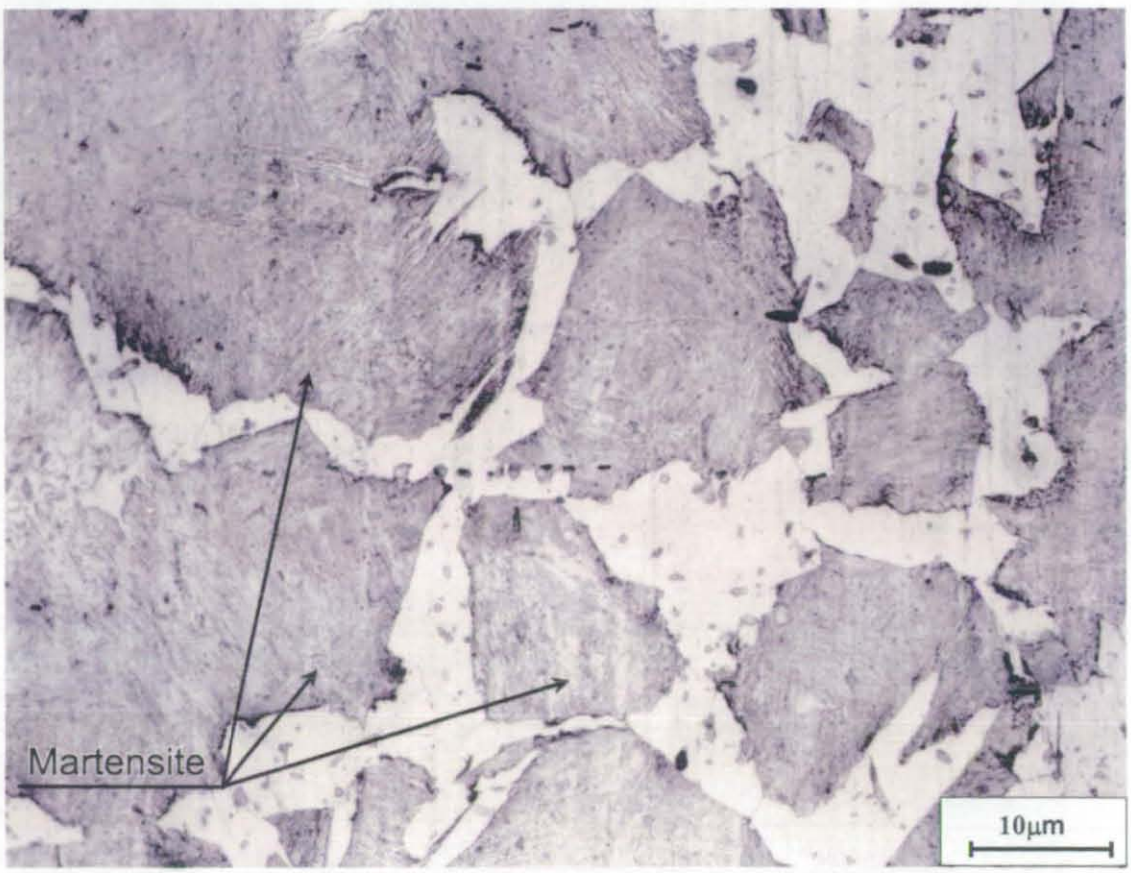

When diffusion of carbon atoms (and therefore by implication the diffusion of substitutional atoms) is prevented by very high cooling rates and low transformation temperatures, a supersaturated solid solution of carbon in iron, called martensite, forms. Martensite is a phase that results from a diffusionless solid state transformation mechanism. The lattice change occurs via a shear mechanism which transforms the fcc crystal in a body centred tetragonal (bct) crystal whose lattice parameters 'a' and 'c' vary as a function of the carbon content of the austenitic parent phase. In low carbon steels the most common morphology of martensite observed consists of laths grouped in sheaves. A substructure consisting of cells of high density of dislocations is present in each lath. As the carbon content increases, the presence of twinned martensite can be observed. Compared to pearlite it has a slow etching response.

Scanning electron microscopy at high magnification clearly shows the nature of martensitic phase and its characteristic the features. In the low carbon alloy studied, the laths of martensite can be individually observed. The appearance of the structure of the martensitic laths which formed via a purely displacive mechanism is very different from the one observed in primary ferrite.

Figure 5.21a-f: *SEM images showing martensite regions*

a) ***b)***

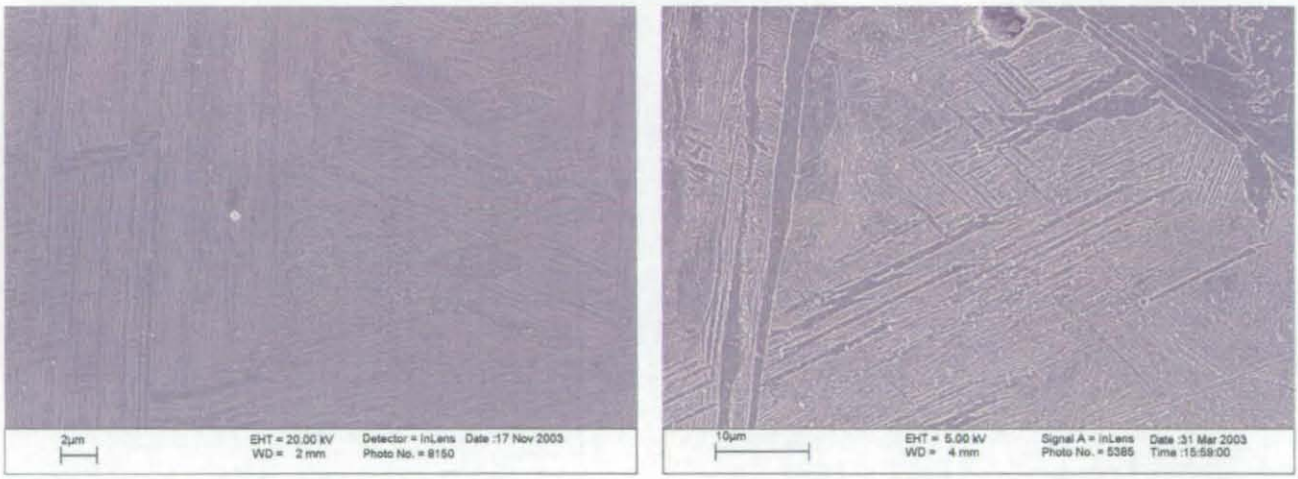

c)

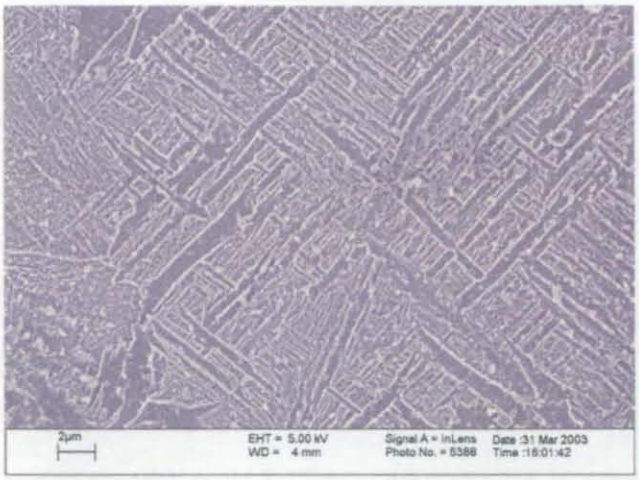

d)

e)

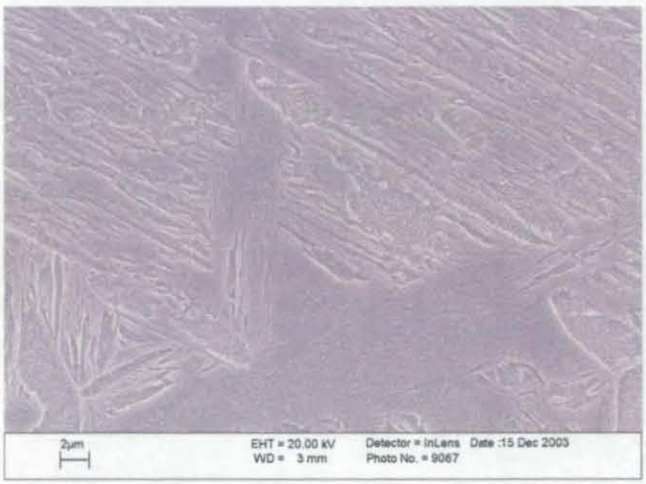

f)

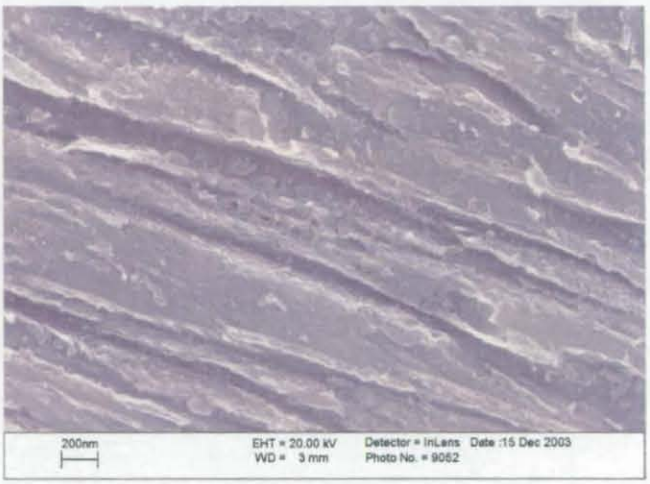

The structure of martensite is shown at different magnifications in figures 5.21a-f above. At high magnifications (figure 5.21f), the effect of shear on the morphology is evident. This can be compared with the appearance of a ferritic matrix formed reconstructively.

5.3.8 Tempered Martensite

Figure 5.22: *Optical micrograph showing tempered martensite location in martensite regions ontained by continuously cooling at 10 °C s^{-1} alloy Y7N1 and interrupting the cooling stage at 624 °C; the tempered martensite is not resolvable*

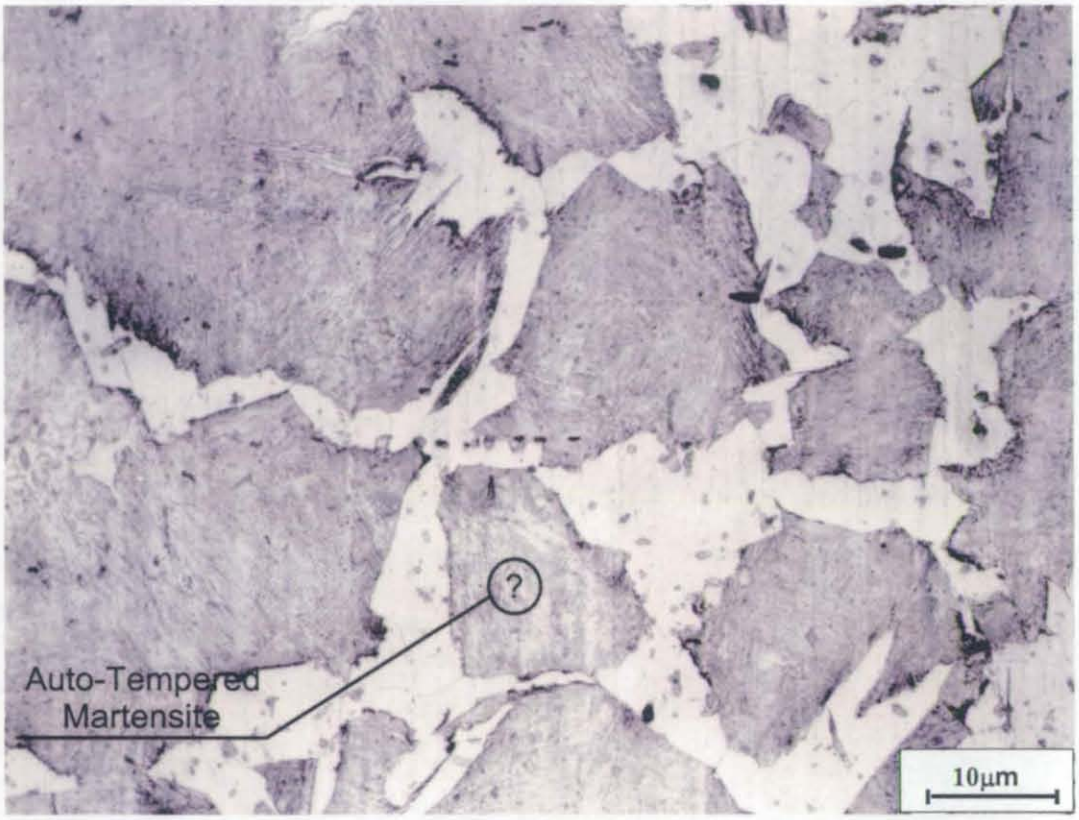

Figure 5.23: *Optical micrograph showing tempered martensite regions ontained by tempering a martensitic steel*

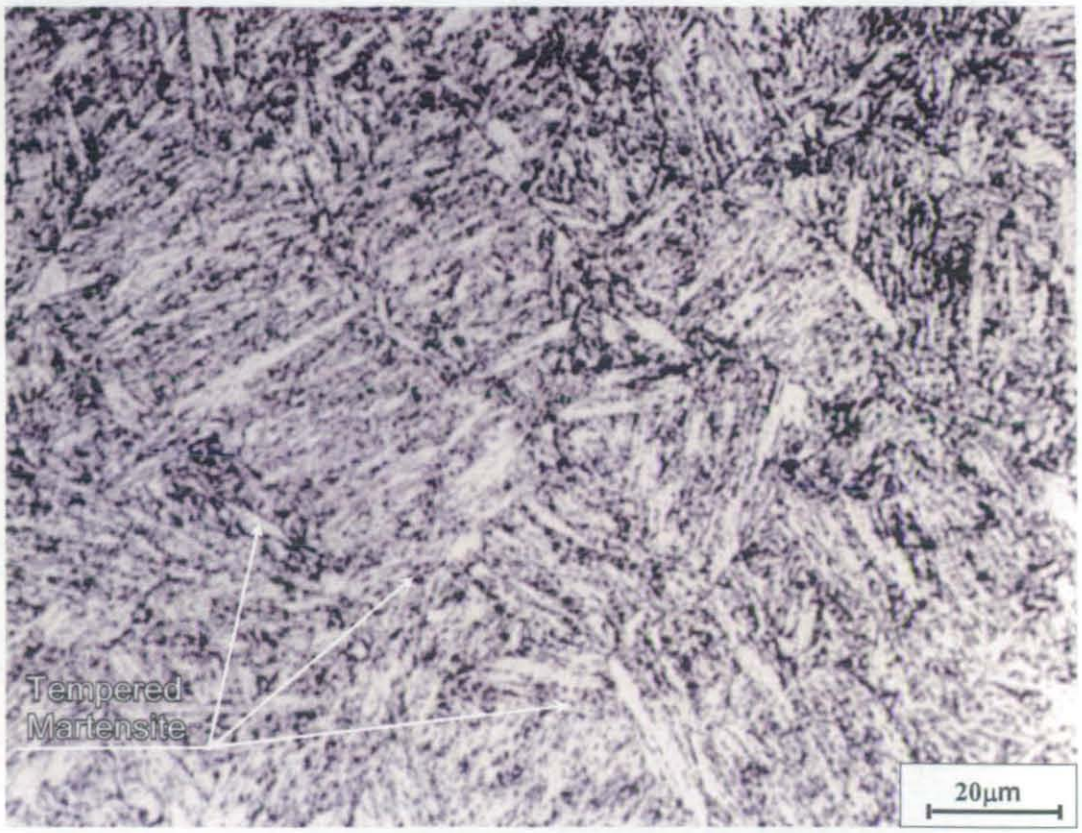

Tempering processes are usually performed on as-quenched martensite by re-heating it. Tempering causes diffusion, which is the main factor influencing the various tempering stages. Four distinct stages, which overlap in some cases, can be identified during tempering[2,16]:

- *stage 1*: up to 250°C precipitation of ε-carbide followed by partial loss of tetragonality of the lattice;
- *stage 2*: between 200 and 300°C the decomposition of austenite takes place;
- *stage 3*: between 200 and 350°C ε-carbide evolves to the more stable cementite whilst martensite loses its tetragonality;
- *stage 4*: above 350°C cementite coarsens and spheroidises whilst recrystallisation of ferrite takes place, drastically reducing the dislocation density.

It should be noted that the formation of ε-carbide, is possible during so-called auto-tempering. This phenomenon is very similar to the first stage tempering, but it occurs upon cooling from M_S to room temperature. Naturally, the extent of auto-tempering is more appreciable in steels with a high M_S, such as the commercial Fe-C-Mn low alloy Y7N1 steel. In this research the microstructure of auto-tempered martensite has been investigated up to very high magnifications. The structure of the carbides observed by means of SEM can be directly compared with the TEM images. The presence of regions of autotempered martensite and their extent, cannot be observed with a light microscope. The high magnification analysis of the microstructure of low carbon low alloy steel showed that the autotempering effect takes placed to a considerable extent even at cooling rates higher than 150°C s^{-1}. Small regions of autotempered martensite are shown in figures 5.24a-b (indicated by a black arrow).

Figure 5.24a-b: *SEM images showimng tempered martensite regions in alloy Y7N1*

a) ***b)***

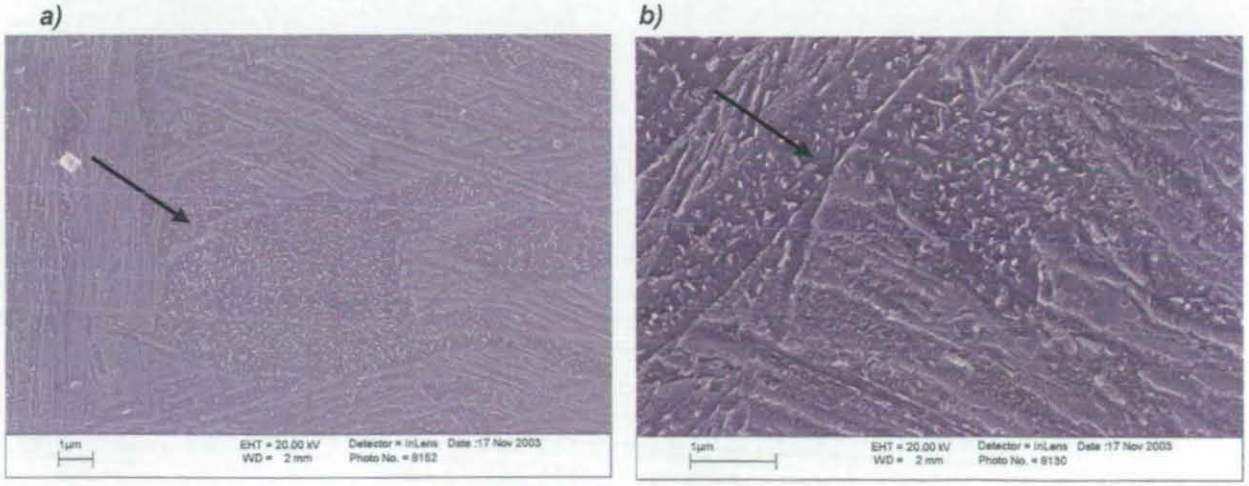

Under continuous cooling conditions, the amount of microphase between Widmanstätten ferrite plates, or developing between ferrite plates is usually significant at cooling rates comprised between 5 and 50°C s^{-1}. As the amount of carbon enriching the austenite in the microphase regions is fundamental in determining the mechanism of transformation in the microphase regions, it is important to understand their nature. This provides different types of information: about the amount of available carbon in the austenite in relation to the amount of microphase; about the effect of cooling rates and carbon content on the microphase regions itself; about the overall role of these pools of carbon enriched austenite on the simultaneous transformations taking place under continuous cooling conditions. At low cooling rates usually the microphase regions comprise of pearlite with extremely fine lamellae. As the cooling rate increases, two factors influence the nature of the microphase: the amount of carbon and the temperature of transformation which determines which mechanism (reconstructive or displacive) is more favoured. If the carbon content is high the microphase regions will be mainly composed of retained austenite. Otherwise, martensite will be present. It is common however to find a mixture of the two phases. In interrupted continuous cooling experiments (section 6.10) and hold-quench experiments (section 6.6) the effect of cooling rate and isothermal holding time on the nature of microphase has been observed. Generally speaking, interrupting the cooling stage at high temperatures and, therefore, influencing the local carbon concentration, causes the microphase to remain austenitic or to transform into martensite. The interruption at low temperatures usually allows the formation of pearlite or FCA. Finally, isothermally holding favours the transformation of all microphase regions into pearlite.

Figure 5.25a-p: *SEM images showing microphase regions, developed in alloy Y7N1 under continuous cooling conditions, of different natures*

a) *pearlite*

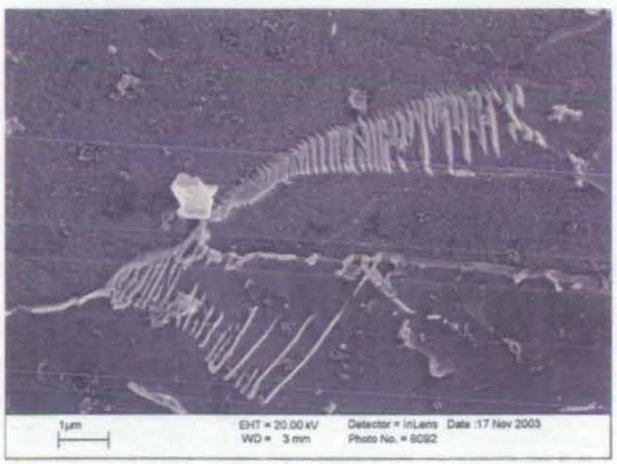

b) *pearlite lamellae*

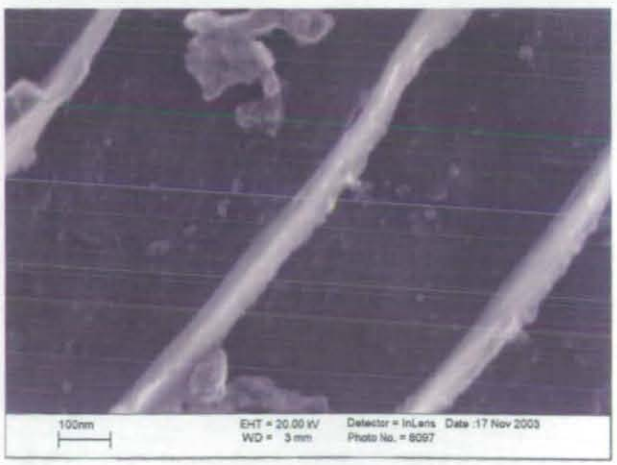

c) pearlite

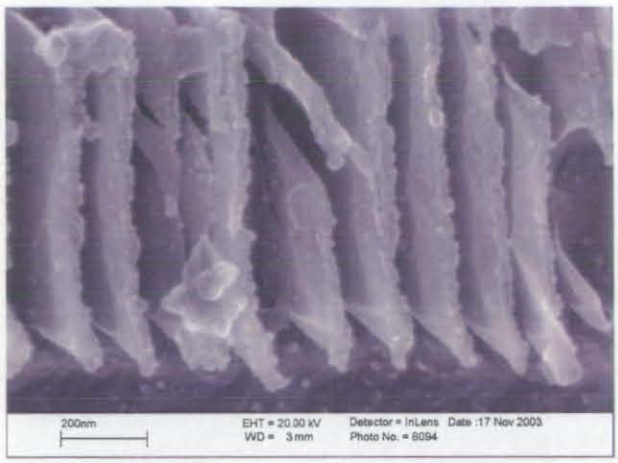

d) austenite and FCA

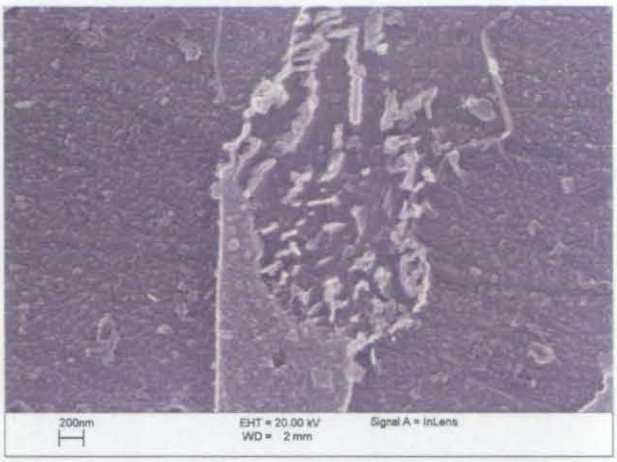

e) austenite

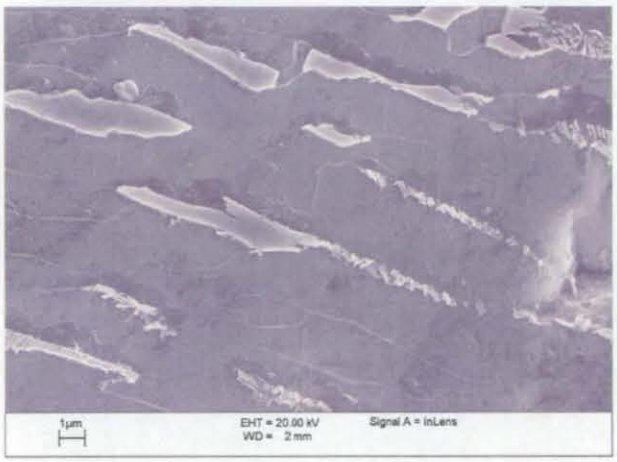

f) austenite

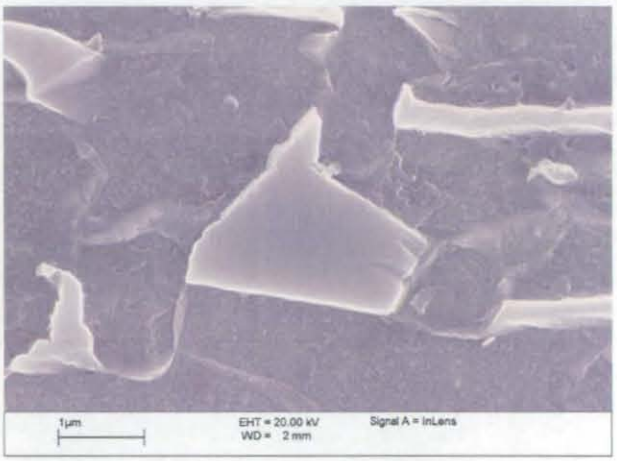

g) austenite and pearlite

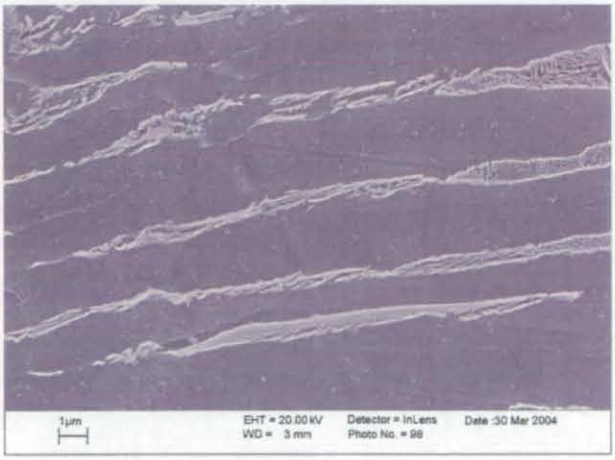

h) austenite and pearlite

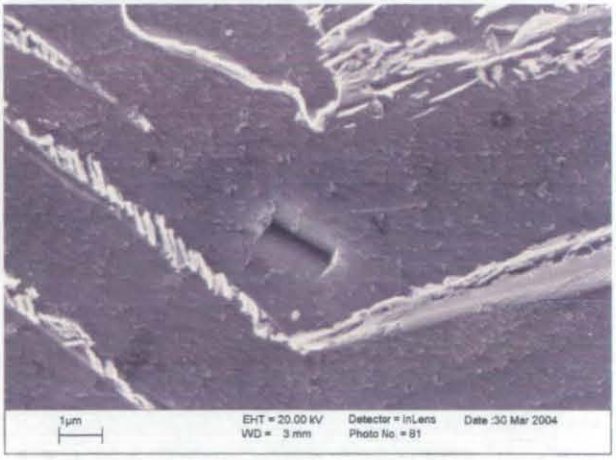

i) martensite and austenite (M/A)

j) austenite and martensite

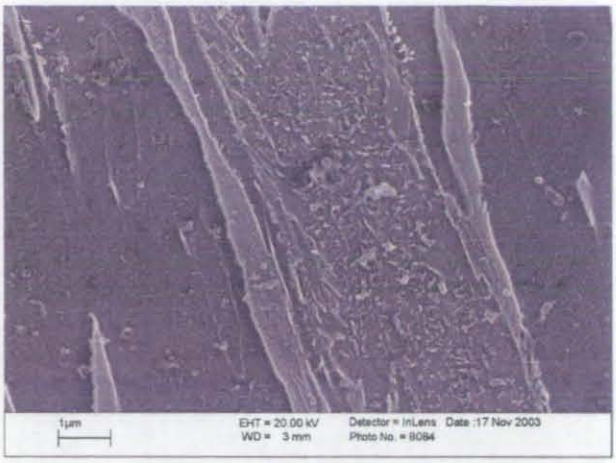

k) pearlite

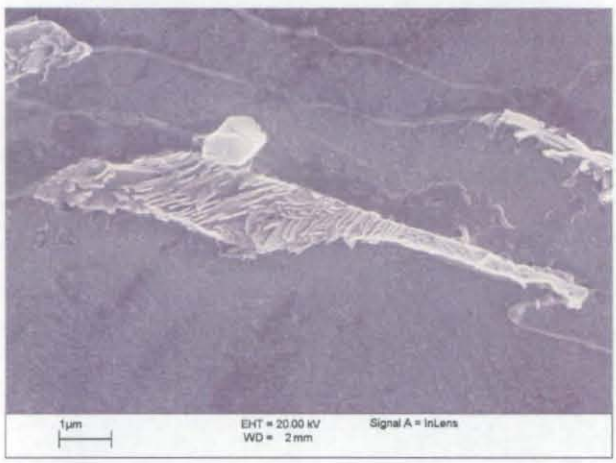

l) pearlite

m) pearlite

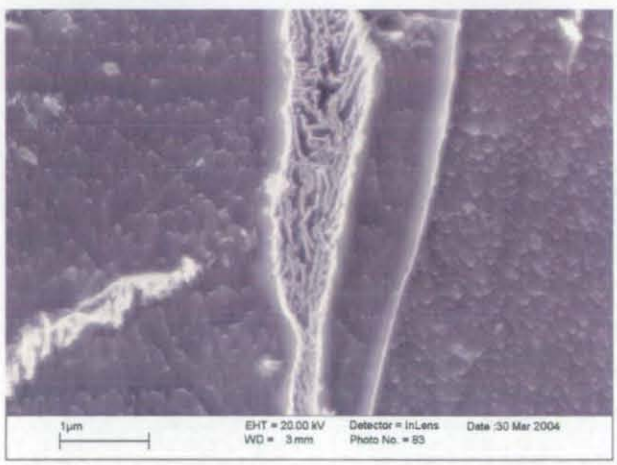

n) coexisting pearlite and austenite

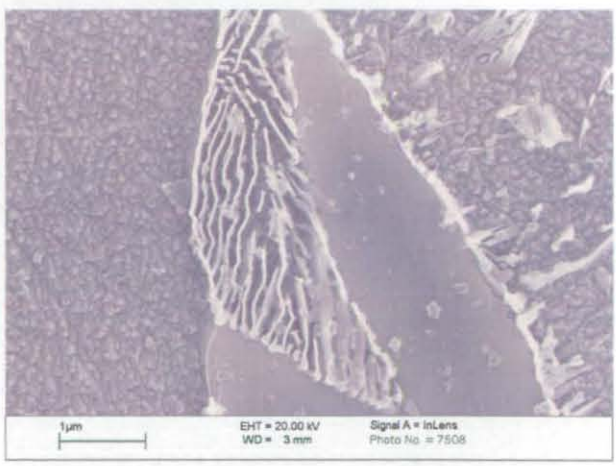

o) austenite and pearlite

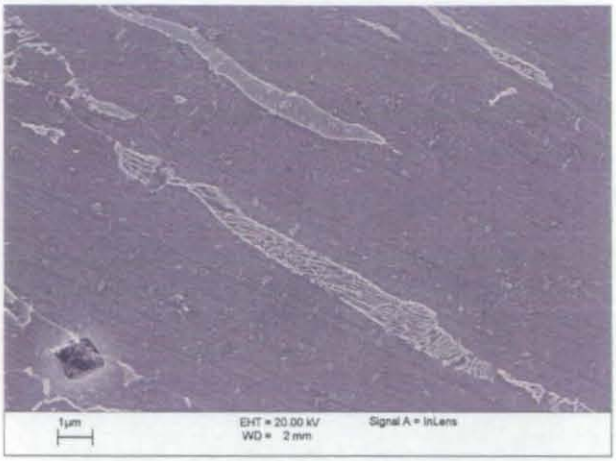

A series of microphases including untransformed austenite, pearlite, martensite, autotempered martensite, pearlite coexisting with martensite, M/A, are visible above. The nature of each microphase region is specified in each figure caption. Figures 5.25a-o clearly illustrate the different possible nature of what is commonly called microphase. In figure 5.25n an interesting microphase region comprising pearlite and austenite is shown.

Even though microphase regions are quite small and their effect on mechanical properties is often neglected or incorporated in a more macroscopic view, they demonstrate the important effects of local conditions on the transformations taking place during cooling. They show the complexity of simultaneous transformations.

5.3.10 Features

One fascinating advantage offered by SEM InLens imaging is the possibility of resolving very interesting and peculiar features formed under continuous cooling conditions. This is the case of geometrically regular colonies of precipitates in ferritic regions, the structure of laths observed at very high magnification, boundaries with a peculiar ledge structure, sites where nucleation of phases (e.g. pearlite lamellae) take place. All these features are restricted to very small regions of a microstructure and their effect on the properties of the alloy could be neglected. However, they possess nonetheless an importance from a theoretical point of view. In fact, they belong to areas of research which still don't have clear explanations. Figures 5.26a-g show precipitates found in FCA regions of alloy Y7N1respectively observed by means of SEM and TEM (the TEM results will be discussed in section 6.8). Diffraction patterns have been obtained in some case although indexing has not

been achieved, apart in one case where the pattern was indexed as χ carbide. This data could not be fully explained. The difficulty in analysing these types of precipitates is the fact that they grow in small colonies and their fraction is extremely small. Images 5.26h-l show the morphology of FCA boundaries whilst images m-n show the morphology of a martensite lath formed upon quenching alloy Y7N1. Figures 5.26h-j show the morphology of an FCA boundary where the nucleation of the precipitates has taken place in a lamellar fashion. Figure 5.26k-l show the morphology of a martensite lath boundary nucleated on primary ferrite. Figure 5.26m shows a very peculiar boundary which present ledges. Figure 5.26n shows a type of precipitate formed at low cooling rate (5°C s^{-1}).

Figure 5.26a-n: *SEM images showing specific microstructural features whose identification was not possible by referring to known classification schemes*

a)

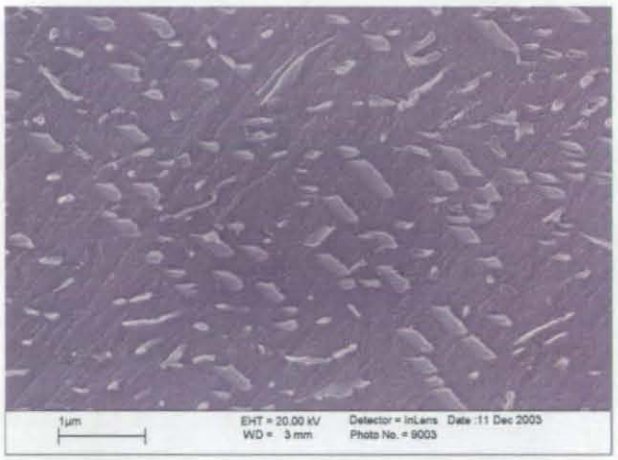

b)

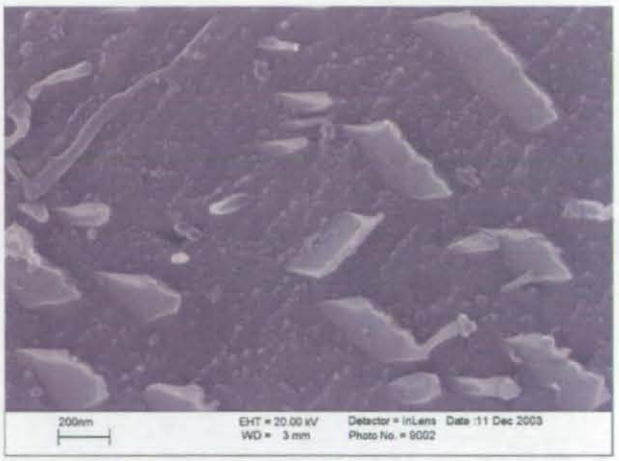

c)

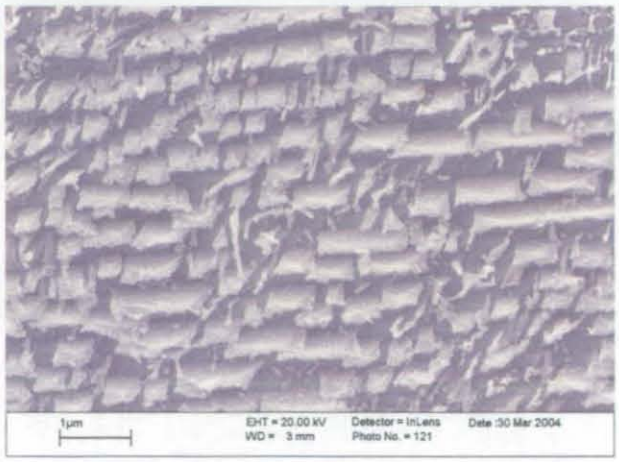

d)

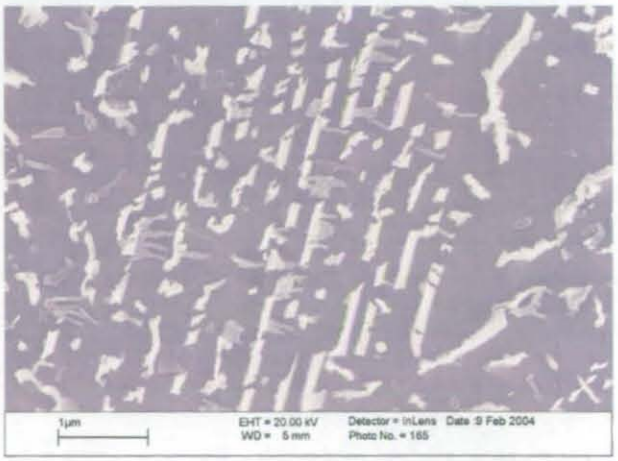

e)


200nm
EHT = 20.00 kV
WD = 3 mm
Detector = InLens
Photo No. = 96
Date :30 Mar 2004

f)

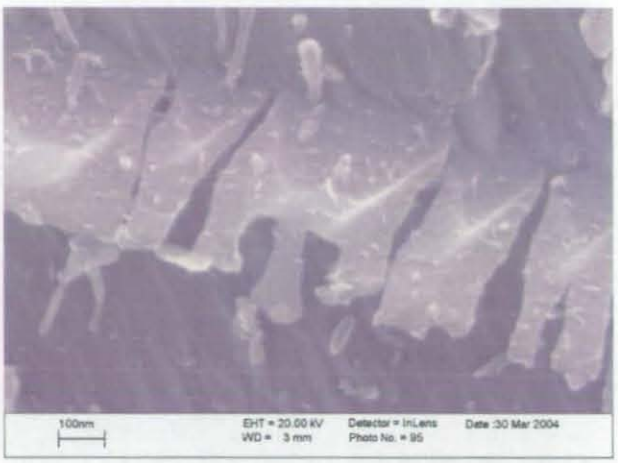
100nm
EHT = 20.00 kV
WD = 3 mm
Detector = InLens
Photo No. = 95
Date :30 Mar 2004

g)

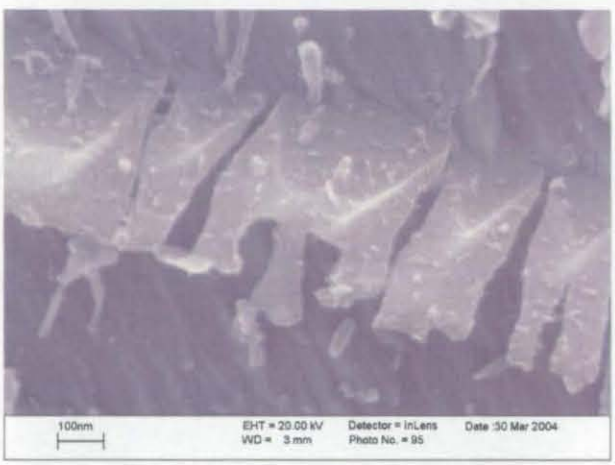
100nm
EHT = 20.00 kV
WD = 3 mm
Detector = InLens
Photo No. = 95
Date :30 Mar 2004

h)

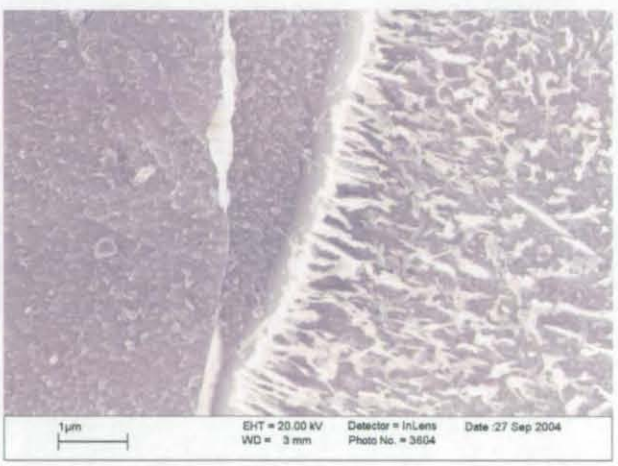
1µm
EHT = 20.00 kV
WD = 3 mm
Detector = InLens
Photo No. = 3604
Date :27 Sep 2004

i)

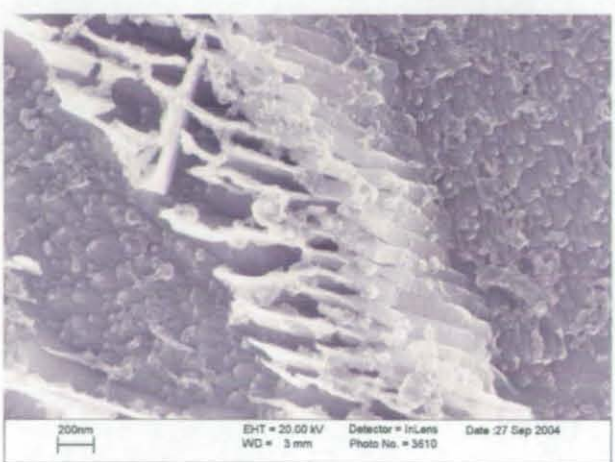
200nm
EHT = 20.00 kV
WD = 3 mm
Detector = InLens
Photo No. = 3610
Date :27 Sep 2004

j)


100nm
EHT = 20.00 kV
WD = 3 mm
Detector = InLens
Photo No. = 3602
Date :27 Sep 2004

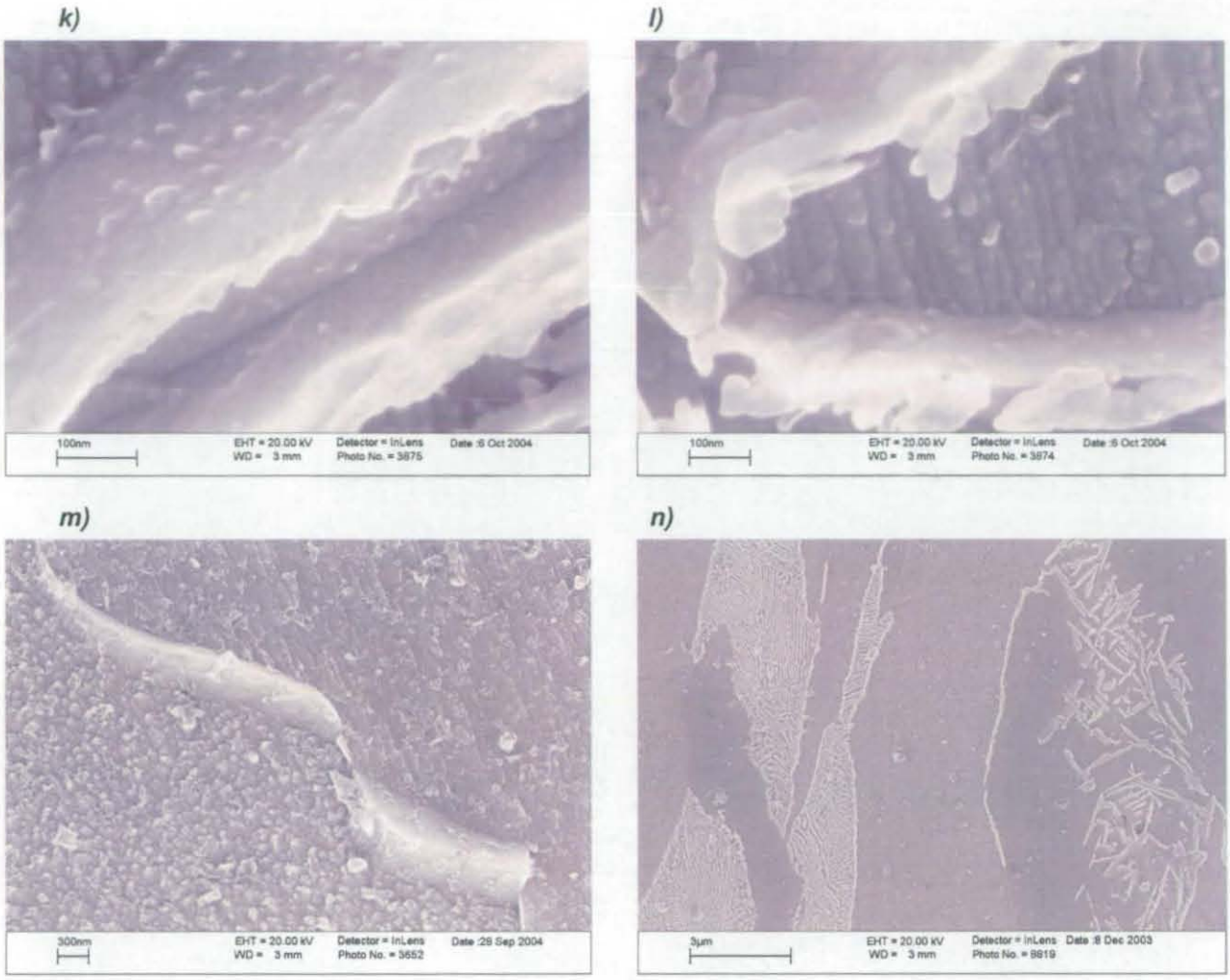

5.3.11 Atlas of microstructures

The microstructures presented in figures 5.8a-i illustrate the morphology of each phases observed by means of optical microscopy, compared with the morphology observed by means of SEM at three different magnifications, and also with TEM.

Figure 5.8a-i: *This set of images represent a concise microstructure atlas which can be utilised in order to classify continuously cooled microstructures. Each set of images contain an optical micrograph showing the morphology of a phase at low magnifcation, an SEM imgae of the same phase at a magnification comparable to the magnification of the optical micrograph, two more SEM images of the same phase at high and very high magnifcation and, finally, a TEM image whose magnification is comparable to that of the SEM image. a) Primary Ferrite; b) Pearlite; c) FCA (ferrite-carbide aggregate); d) Widmanstätten Ferrite; e) Upper Bainite; f) Lower Bainite; g) Martensite; h) Tempered Martensite; i) Microphase regions.*

a) Primary Ferrite

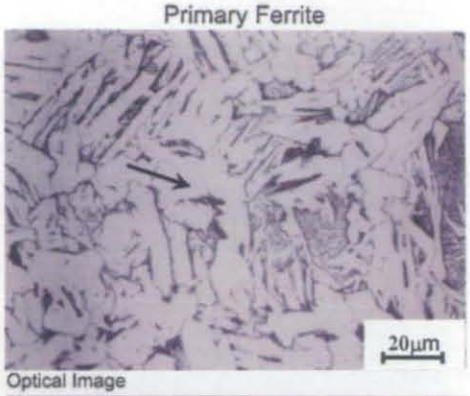

Optical Image

SEM Image Low Mag

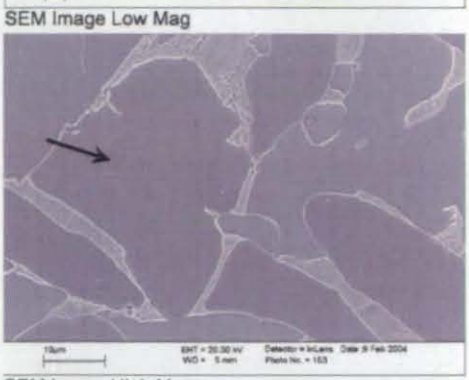

SEM Image High Mag

SEM Image High Mag

TEM Image

b) Pearlite

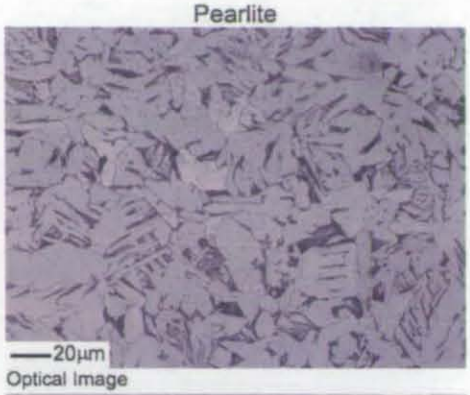

Optical Image

SEM Image Low Mag

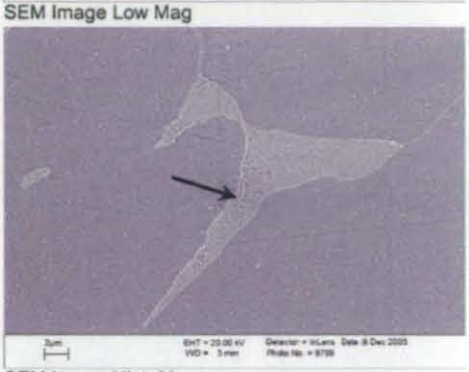

SEM Image High Mag

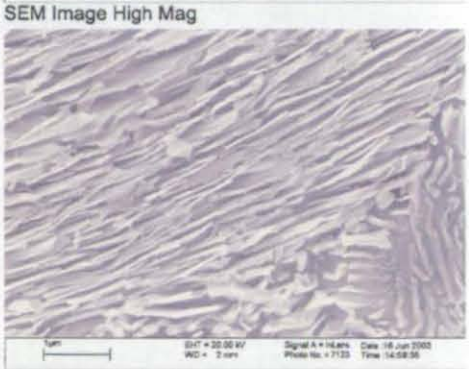

SEM Image High Mag

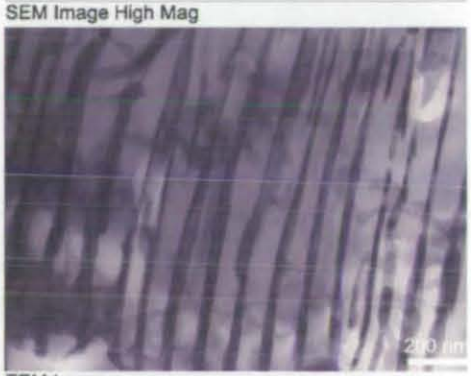

TEM Image

c) Ferrite Carbide Aggregate

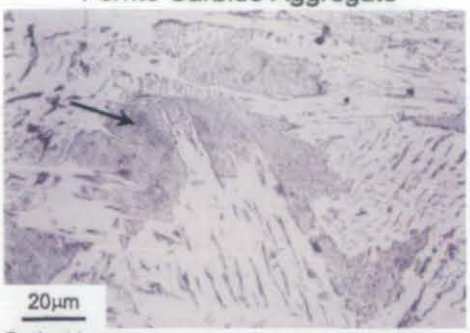

Optical Image

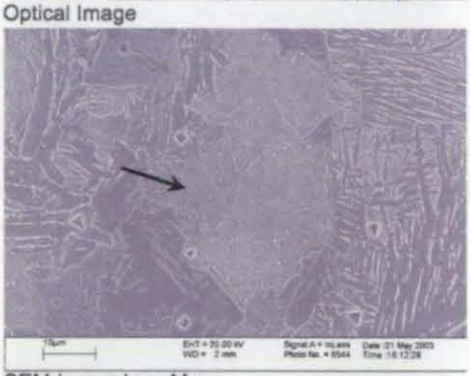

SEM Image Low Mag

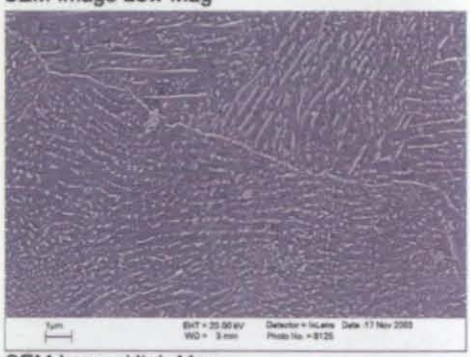

SEM Image High Mag

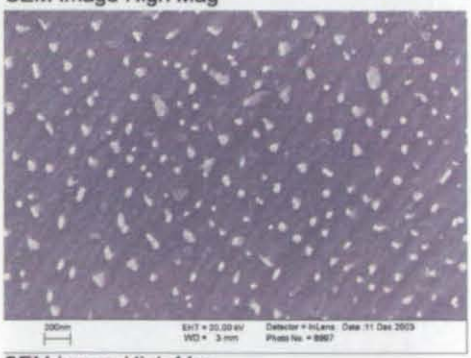

SEM Image High Mag

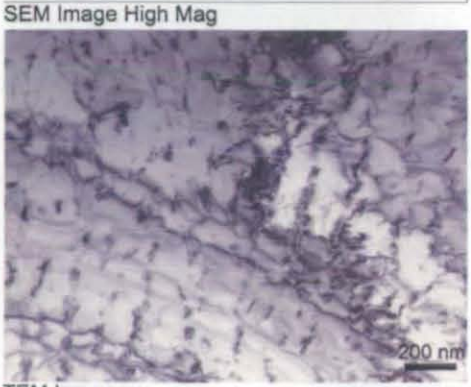

TEM Image

d) Widmanstatten Ferrite

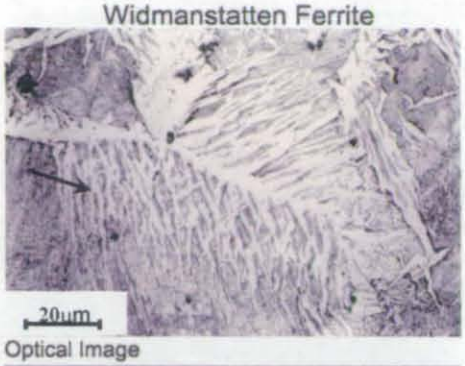

Optical Image

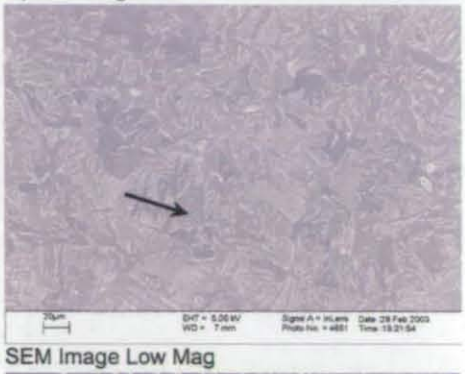

SEM Image Low Mag

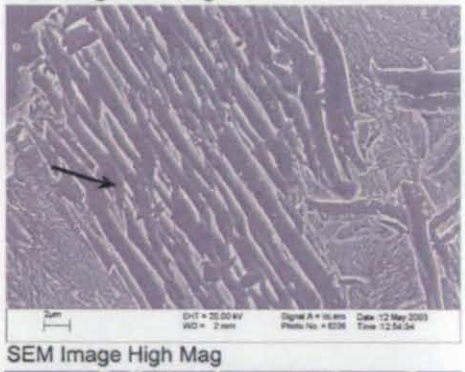

SEM Image High Mag

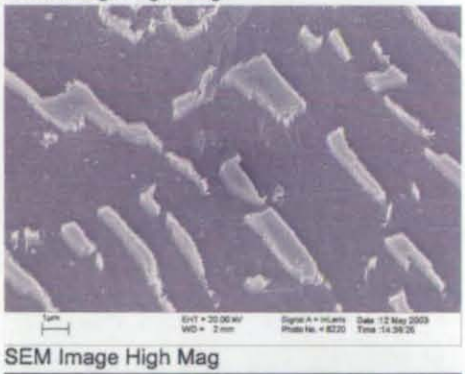

SEM Image High Mag

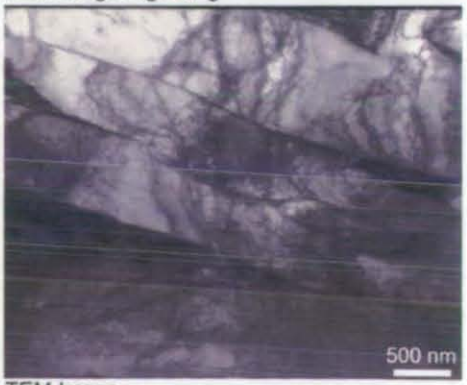

TEM Image

e) Upper Bainite

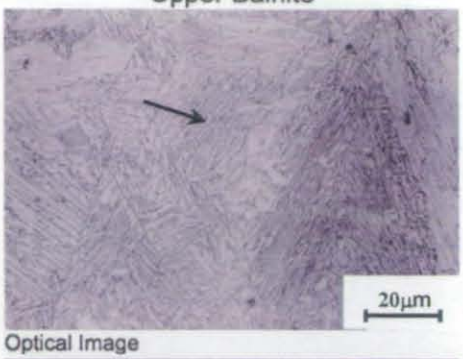

Optical Image

SEM Image Low Mag

SEM Image High Mag

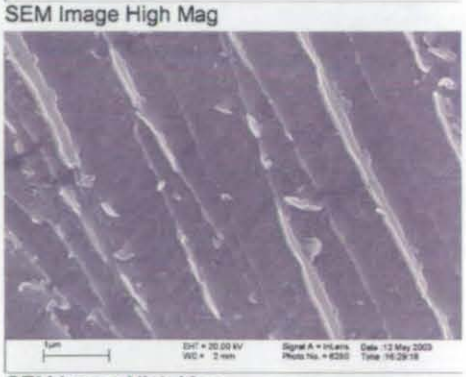

SEM Image High Mag

TEM Image

f) Lower Bainite

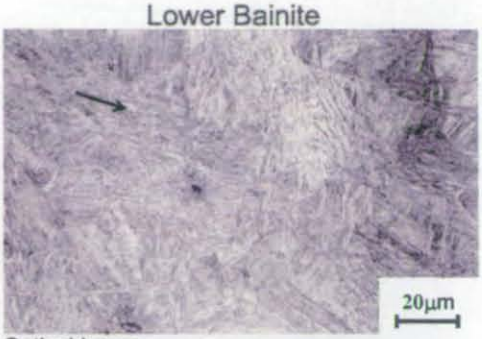

Optical Image

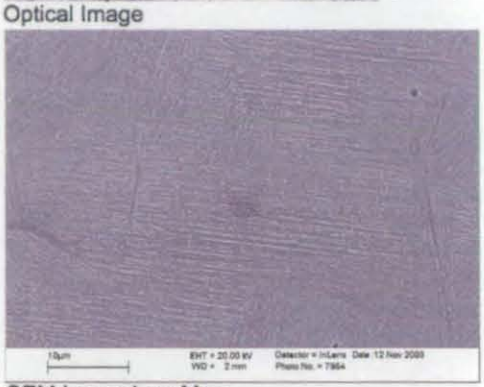

SEM Image Low Mag

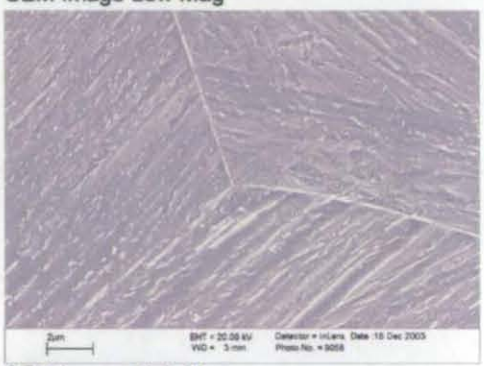

SEM Image High Mag

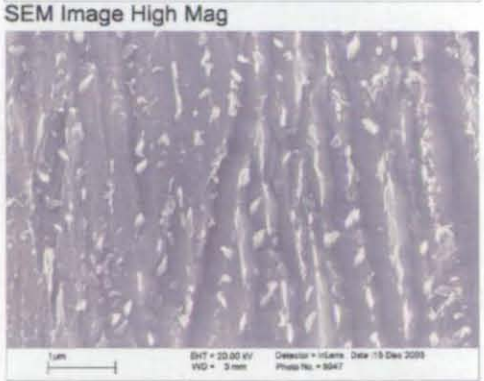

SEM Image High Mag

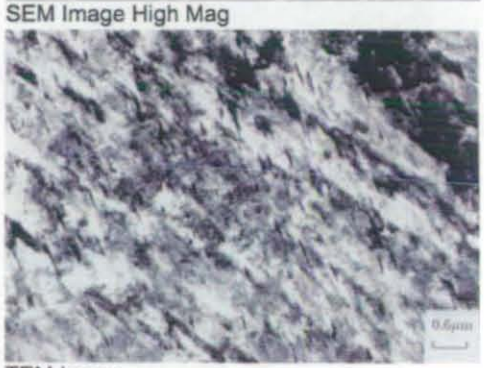

TEM Image

g) Martensite

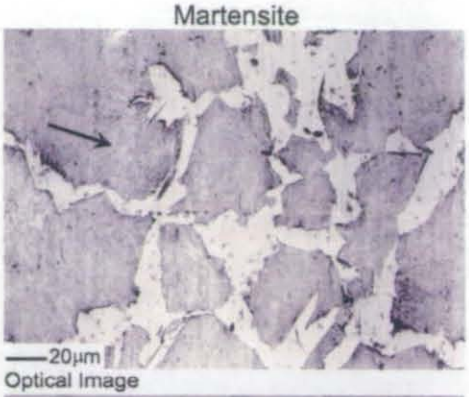

Optical Image

SEM Image Low Mag

SEM Image High Mag

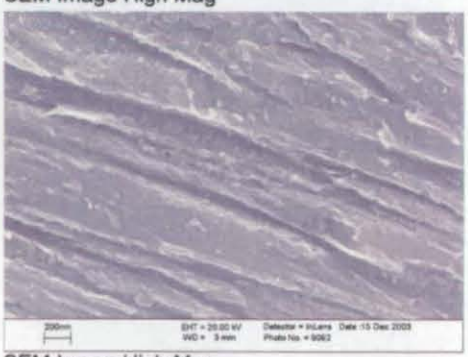

SEM Image High Mag

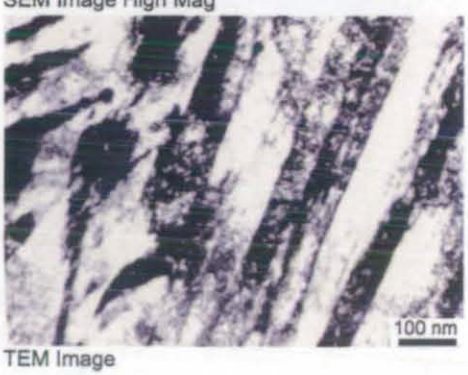

TEM Image

h) Tempered Martensite

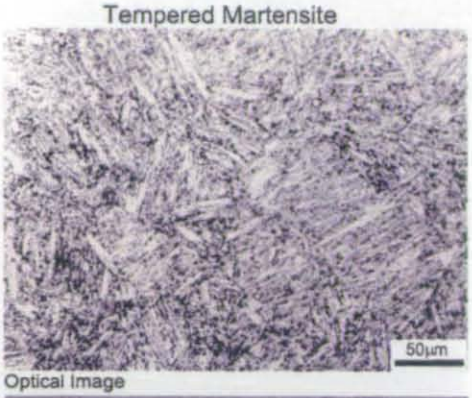

Optical Image

SEM Image Low Mag

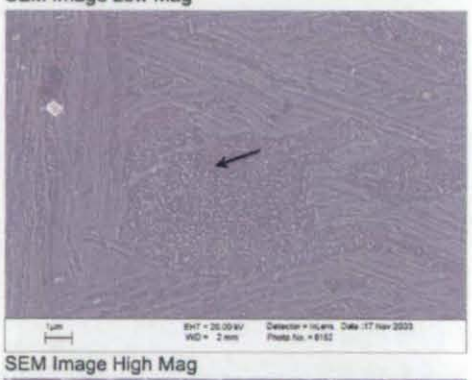

SEM Image High Mag

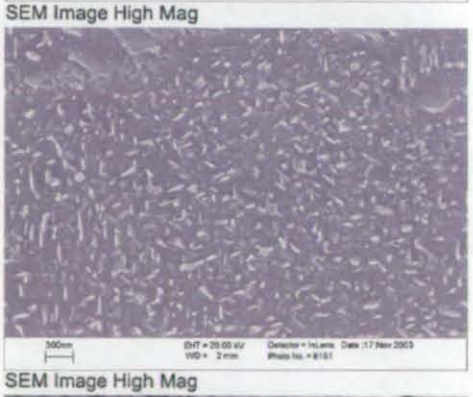

SEM Image High Mag

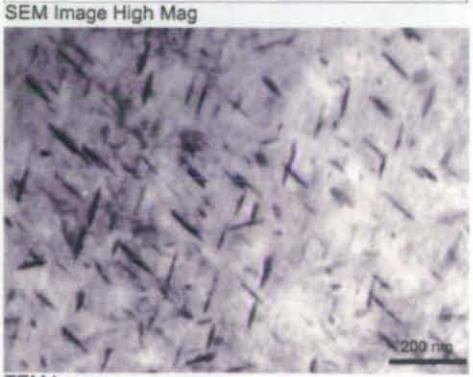

TEM Image

Microphase Nature

i)

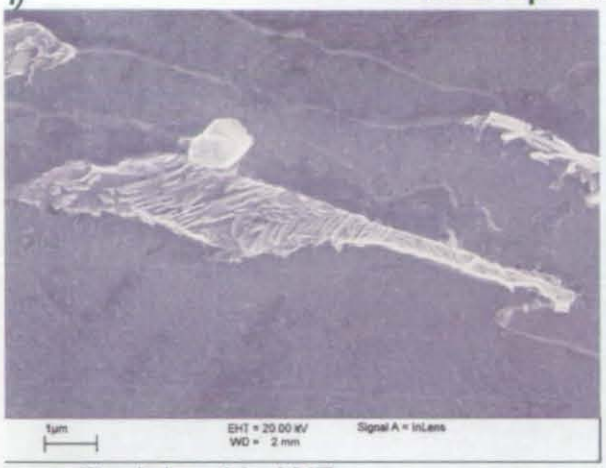

pearlite island in WF

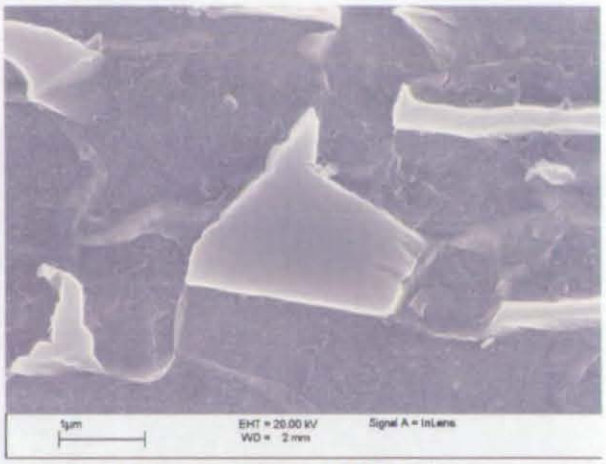

retained austenite in WF

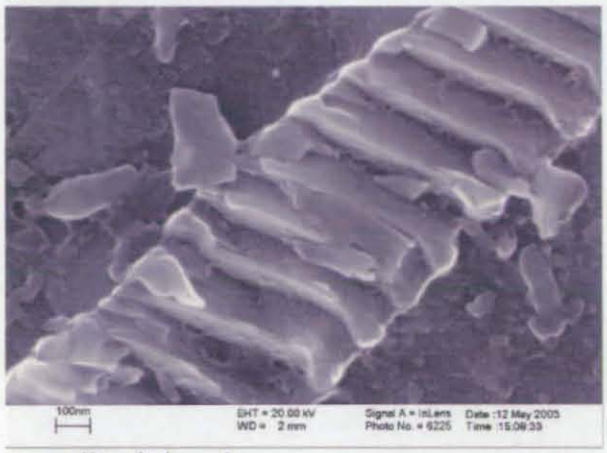

pearlite island

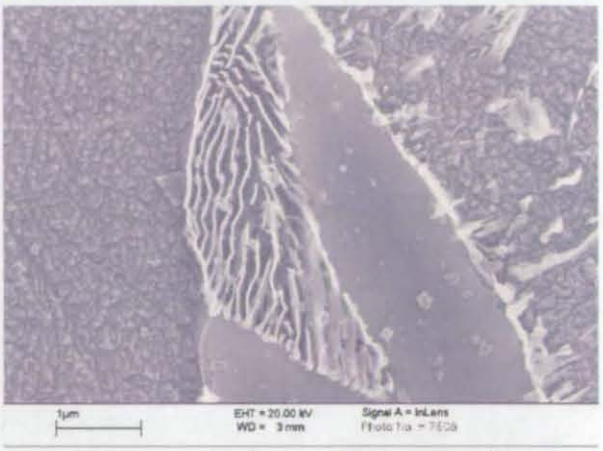

pearlite coexisting with austenite (in WF)

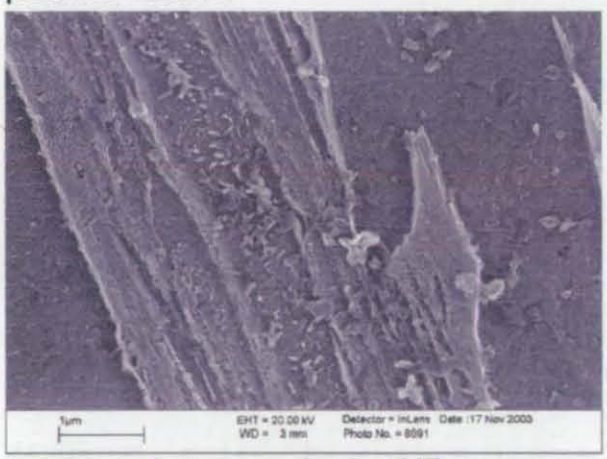

tempered martensite in WF

martensite in WF

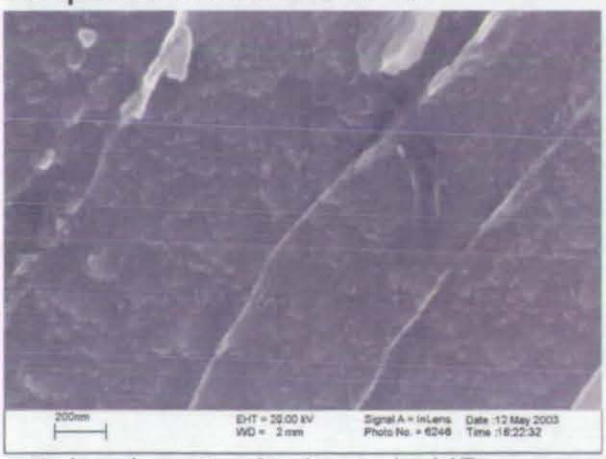

retained austenite layer in UB

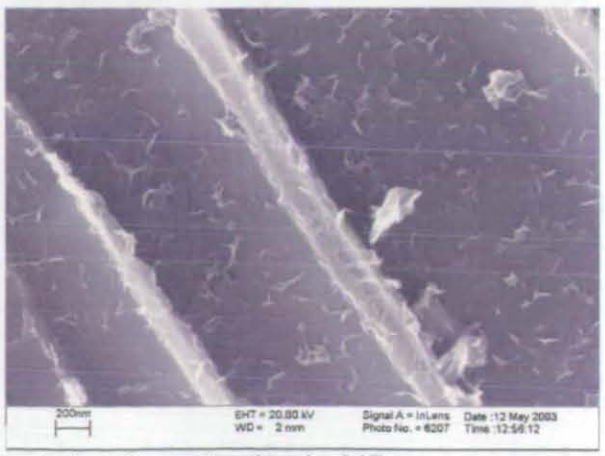

retained austenite in UB

5.4 Phase Identification for Continuous Cooling Heat Treatments

5.4.1 Intermediate Cooling Rate

Once the possibilities offered by high magnification techniques for aiding phase identification have been presented, they can be put into practice in order to identify the phases formed under continuous cooling conditions for alloy Y7N1. The first set of heat treatment performed on sample Y7N1 under continuous cooling conditions are the following:

***Table 5.1**: Intermediate continuous cooling heat treatments*

Aust Temp (°C)	Cooling Rate (°C s^{-1})	Transformation Temperatures (°C)		Classification
		Start	Finish	
1300	10	756	516	Y7N1 1300/10
	50	694	408	Y7N1 1300/50
1100	10	779	551	Y7N1 1100/10
	50	720	511	Y7N1 1100/50

The analysis of the microstructures started from the four samples austenitised at 1300°C and 1100°C and cooled to room temperature at 10 and 50°C s^{-1}. The samples were firstly optically observed at various magnifications i.e. X200, X500 and X1000. As the microstructure of the samples cooled at 25°C s^{-1} lead to morphologies present both in the samples cooled at 10 and 50°C s^{-1}, they will not be treated in detail.

The interpretation of the nature of the phases, the transformation sequence and the kinetic processes determining the behaviour of simultaneous transformations is a challenging task. The approach undertaken in order to simplify as much as possible the investigation has focussed first on the phase identification, which has been achieved by linking the optical observation to the high magnification SEM analysis. The microstructures produced at intermediate cooling rates (i.e. from 10 to 50°C s^{-1}) are the most complex ones within the range of cooling rates investigated.

5.4.2 Austenitisation at 1300°C, cooling at 10°C s^{-1}

As discussed in chapter 4 the microstructure obtained after austenitising at 1300°C and cooling at 10°C s^{-1} is constituted of primary ferrite, Widmanstätten ferrite with associated microphase, pearlitic pools usually found between primary ferrite regions and the dark etching phase named FCA. Picture 5.1 shows a correlation of the morphology of each microstructural constituent observed by means of SEM, to the correspondent region on the large section of the sample observed optically.

Figure 5.27: *Microstructural constituents of sample Y7N1 1300/10 observed optically and by means of SEM*

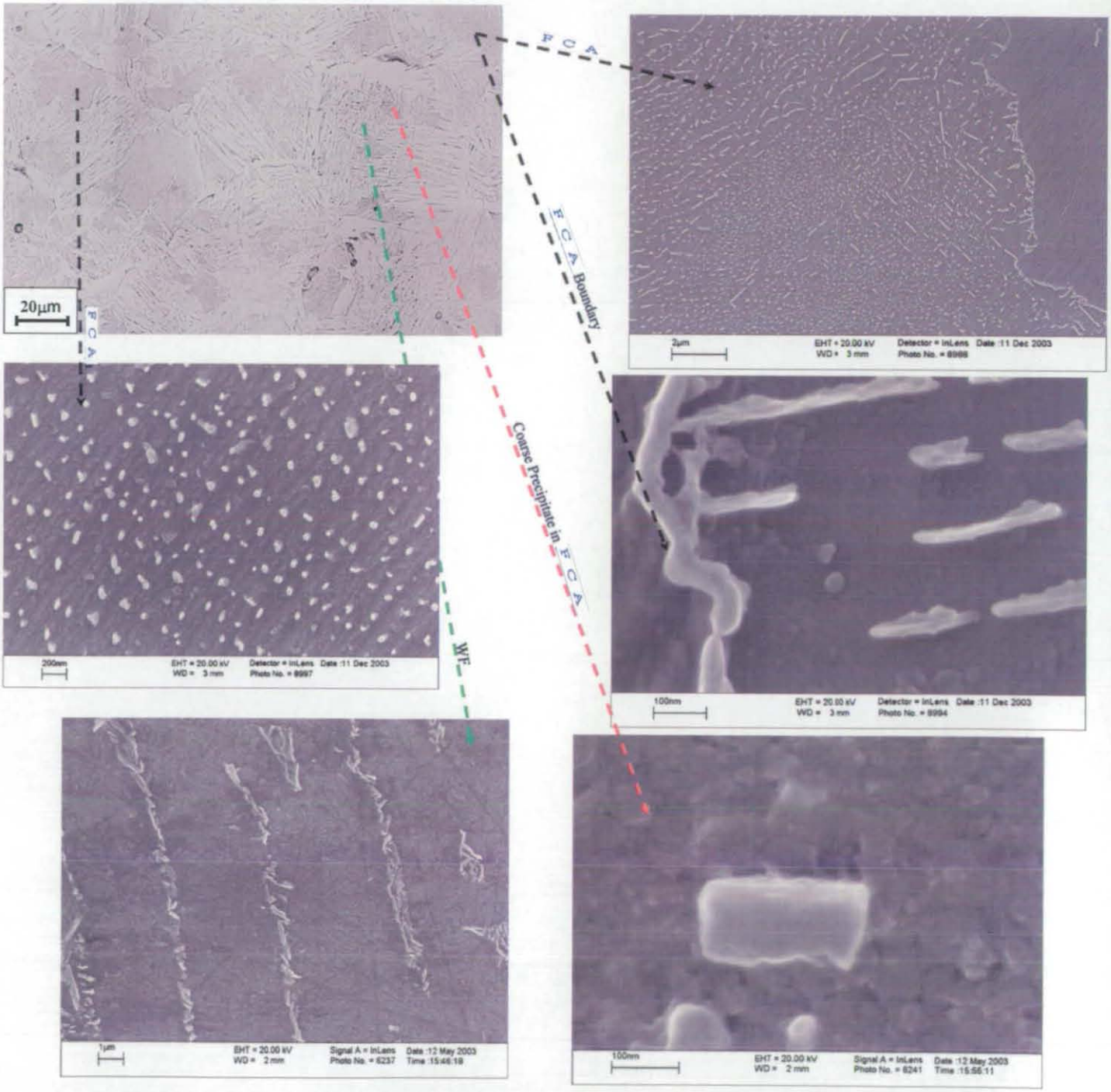

The primary ferrite regions nucleating on prior austenite boundaries have dimensions varying from 4 to 20 μm. The secondary Widmanstätten ferrite plates nucleating on primary ferrite have dimensions varying between 2 and 6 μm. The nature of the Widmanstätten ferrite microphase regions is, in the vast majority of cases, pearlitic. In some case, the nature of the microphase cannot be ascribed to a pearlitic classification, however, there is always an extent of precipitation in the microphase regions which, although it is not lamellar, suggests that the transformation takes place reconstructively at high temperature. The fact that there is no presence of retained austenite, martensite or M/A regions is allowed by the relatively low cooling rate. The thickness of the microphase regions is about 1-2 μm on average. The morphology of the FCA phase present in this sample, observed at high magnification, shows a discrete distribution of small particles, ranging between 40 and 100 μm, distributed in close arrays. The morphology of the boundaries between an FCA region and a ferritic region (being either primary or Widmanstätten ferrite) is irregular and shows a precipitation mode of the first particles which recalls the lamellar morphology.

5.4.3 Austenitisation at 1100°C, cooling at 10°C s^{-1}

Figure 5.29 shows the morphology of each phase present in this sample, which are the same phases observed in the previous one, although dimensions and volume fractions vary due to the lower austenitising temperature.

The dimensions of the primary ferrite allotriomorphs are smaller and range from 5 to 15 μm. On the other hand, the secondary Widmanstätten ferrite plates have slightly larger dimensions varying between 3 and 8 μm. The heat treatment conditions cause the microphase associated to the Widmanstätten ferrite to transform nearly entirely to pearlite. In some cases certain type of ferrite carbide aggregate of unspecified nature form, although it is presumable that the precipitation takes place under reconstructive conditions.

The morphology of the FCA phase is similar to the previous case although what appear to be precipitates are less ordered within the same grain.

Figure 5.29: *Microstructural constituents of sample Y7N1 1100/10 observed optically and by means of SEM*

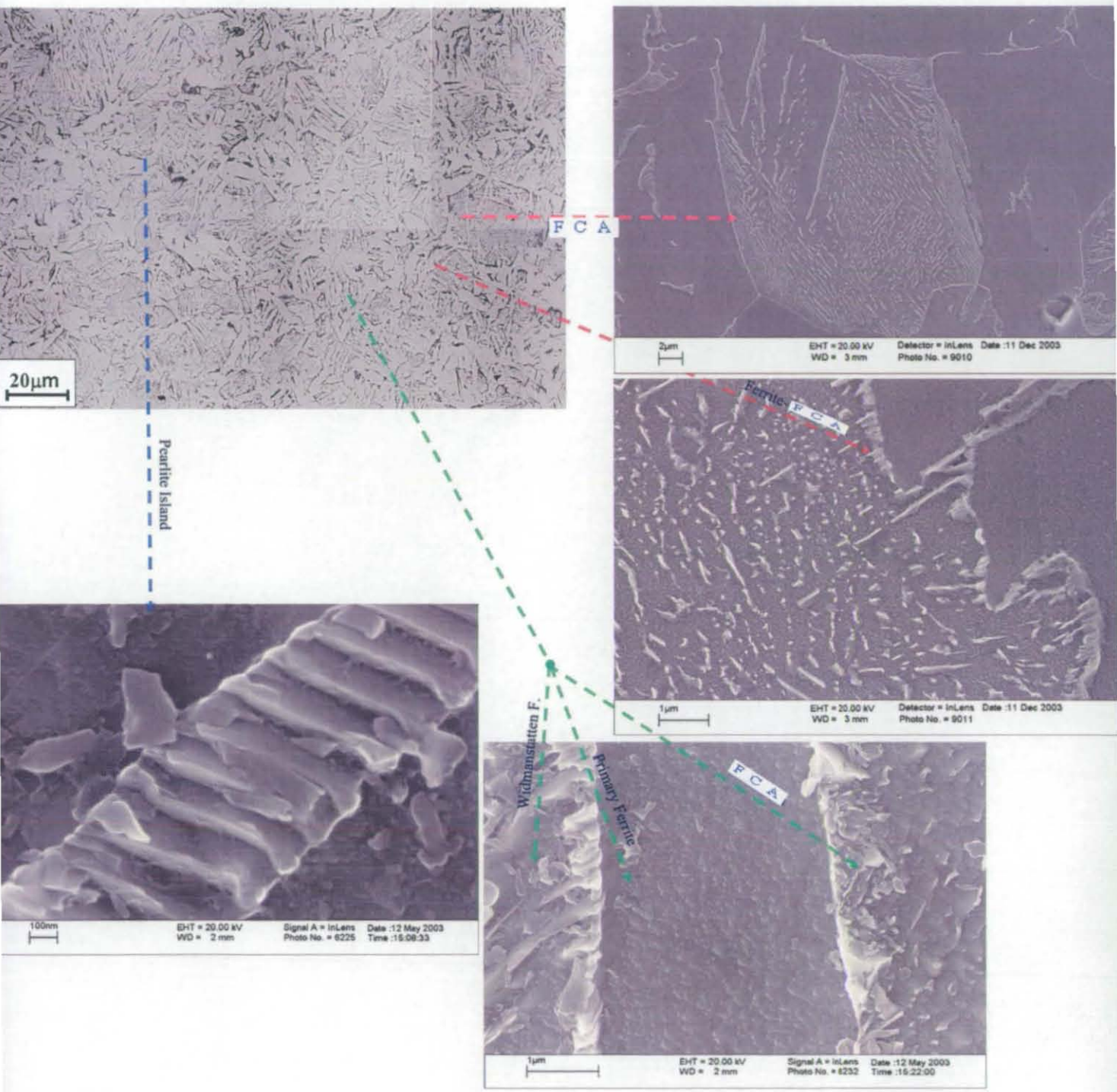

5.4.4 Austenitisation at 1300°C, cooling at 50°C s^{-1}

Increasing the cooling rate up to 50°C s^{-1} still produces a complex microstructure although at this cooling rate the transformation take place at lower temperatures, the microstructure becomes finer and the formation of bainite becomes possible, therefore implying that the b transformation conditions are less close to those for purely reconstructive transformations, compared to lower cooling rates. This is reflected in the microstructure. This has been observed optically and particular microstructural features observed at high magnification by means of SEM are shown in figure 5.30.

Figure 5.30: *Microstructural constituents of sample Y7N1 1300/50 observed optically and by means of SEM*

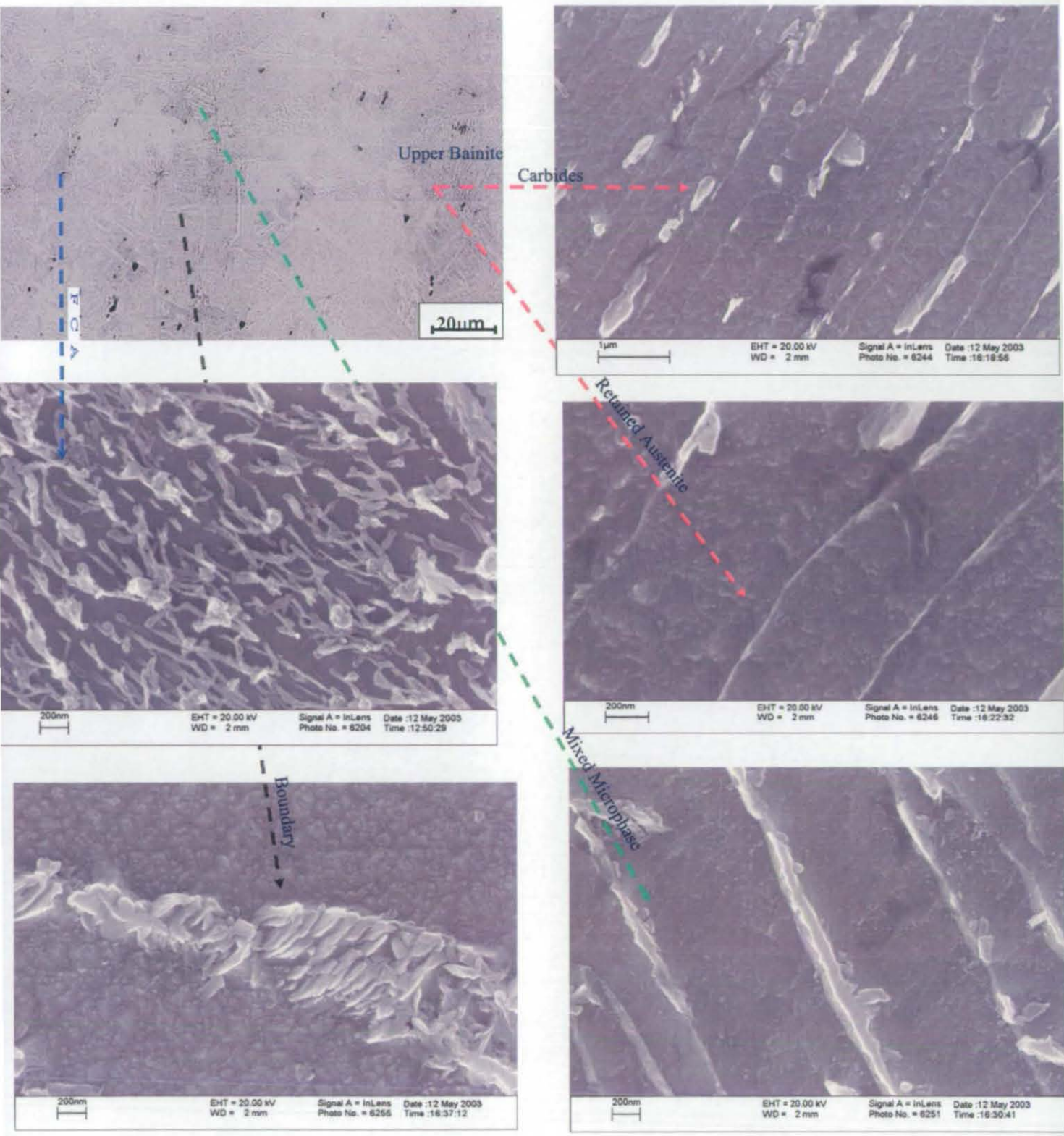

The high magnification analysis allows the observation of the upper bainite laths and the measurement of their dimensions. Typical values of bainite plate thickness vary between 0.1μm and 0.4 μm as stated in the literature. These values fit with the dimension of the phase between the retained austenite layers shown above in figure 5.30. This suggests that the SEM pictures for upper bainite truly represent bainite plates as well as retained austenite and carbides within the plates. The dimensions of the Widmanstätten ferrite plates range from 1 to 4 μm. At this cooling rate, the microphase between the Widmanstätten ferrite sideplates have different natures, depending on the local composition and the temperature at which they try to transform. A small part can undergo reconstructive transformation and transform to pearlite or some kind of ferrite carbide aggregate. In most cases, however, the microphase transforms into M/A, or retained austenite. The dimensions of the primary ferrite layers which form first, nucleating at prior austenite grain boundaries, do not grow larger than 4 μm. The analysis of the FCA phase shows that the small particles can become interconnected and, when distributed in arrays, the distance between each array appears to be smaller.

5.4.5 Austenitisation at 1100°C, cooling at 50°C s^{-1}

As previously shown in table 4.2, the T_S is significantly higher than in the case of sample Y7N1 austenitised at 1300°C where the austenite grain size of 105 μm was on average 74 μm larger. The lower austenitising temperature adopted influenced greatly the austenite grain size, therefore determining different thermodynamic and kinetic conditions.

The microstructure of the sample observed optically and particular microstructural features observed at high magnification by means of SEM are schematically shown in figure 5.31:

Figure 5.31: *Microstructural constituents of sample Y7N1 1300/10 observed optically and by means of SEM*

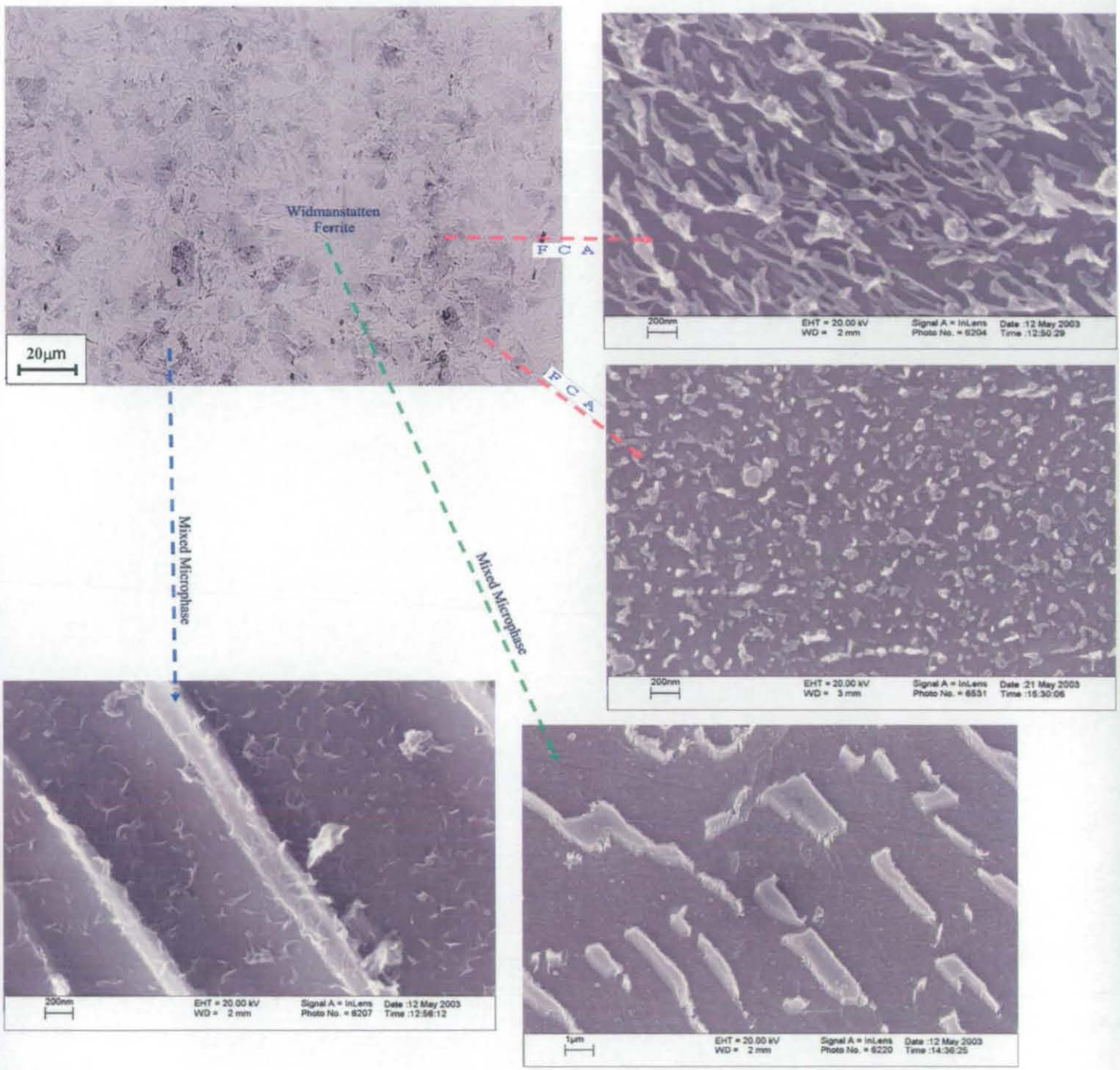

Due to the lower austenitising temperature, the Widmanstätten ferrite still dominates as it appears qualitatively from the optical analysis. The plates are finer than the ones formed at 10°C s^{-1} and do not overcome 4 μm, although the vast majority have smaller dimensions. The distinction between upper bainite forming at 50°C s^{-1} and fine Widmanstätten ferrite is not always straightforward, especially if performed optically. The SEM in this case shows clearly the regions which can be

classified as Widmanstätten ferrite, as the microphase regions can easily be distinguished from the austenite layers or the precipitates between bainitic paths, from shape, morphology and dimensions. None of the microphase regions observed had undergone reconstructive transformations. They appear to be constituted mainly of untransformed austenite and M/A.

As in the previous sample, it can be seen that the dark etching phase, FCA, presents more than one structure. On of the two structures appears to be more ordered and constituted of precipitates within which a certain degree of alignment can be identified (figure 5.31 second SEM image, clockwise). A possibility could be that these are two different sections of the same phase. Another possibility could be represented by the fact that the nature of the two different morphologies could be different. Finally the different microstructures could be a result of different local carbon composition as well as a certain different degree of etching.

5.5 Slow Cooling Experiments

Slow cooling experiments were performed imposing a cooling rate of 2 and 5°C s^{-1} on alloy Y7N1 in order to analyse the consequences on the microstructure and in particular on the FCA formation, which is the only phase that could not be positively identified after optical and SEM analysis.

Table 5.2: *List of slow cooling heat treatments*

Aust Temp (°C)	Cooling Rate (°C s^{-1})	Transformation Temperatures (°C)		Classification
		Start	Finish	
1300	2	761	530	Y7N1 1300/2
	5	757	512	Y7N1 1300/5
1100	2	810	566	Y7N1 1100/2
	5	792	557	Y7N1 1100/5

The microstructures observed optically showed that the transformation mechanism at such cooling rate is reconstructive and the microstructure is constituted of large primary ferrite grains and small pearlitic regions, usually formed between ferritic grains. The SEM analysis of the samples provided evidence of the gradual transition in morphology from pearlite to the typical FCA structure at 5°C s^{-1}. Considering the low cooling rate and the consequent large time allowed for carbon diffusion, the regions which are not ferritic present a fully lamellar structure at 2°C s^{-1}. However, at

5°C s^{-1} some small regions are present where the morphology is not lamellar. Lamellae break-down can be observed, as previously observed in samples cooled up to 50°C s^{-1}. The main feature of sample Y7N1 austenitised at 1100°C and 1300°C and cooled at 2 and 5°C s^{-1} are presented in figure 5.32 and 5.33.

Figure 5.32: *Microstructural features of sample Y7N1 1300/2 and 1300/5*

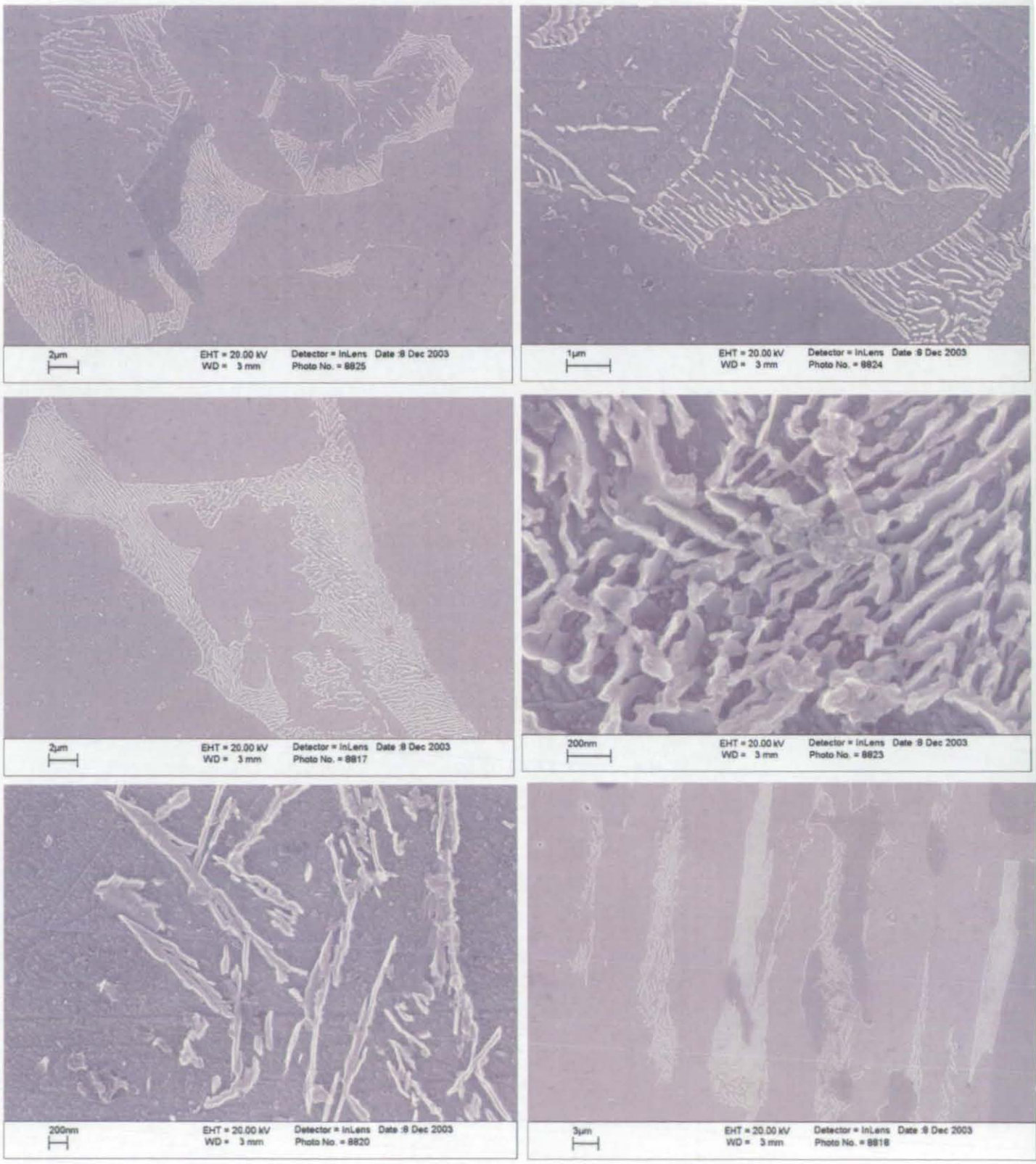

Figure 5.33: *Microstructural features of sample Y7N1 1100/2 and 1100/5*

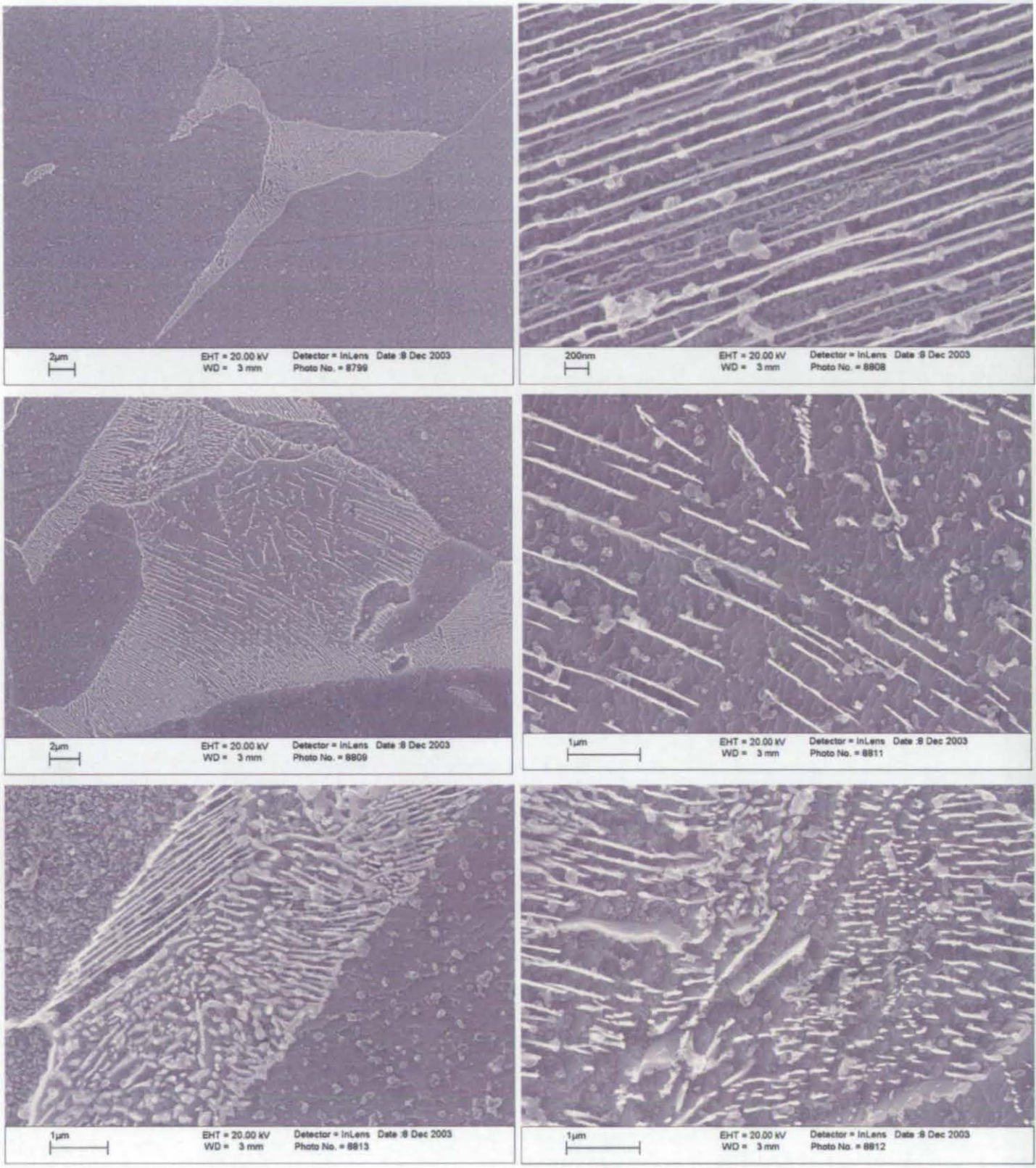

5.6 Fast Cooling Experiments

A set of fast cooling experiments has been performed on alloy Y7N1 in order to study the effect of increasing cooling rate on the microstructure and on the eventual formation of dark etching areas. It is interesting in this scenario to understand which is the maximum cooling rate at which the formation of the dark etching phase is still possible, for a given composition and austenitising temperature.

The list of heat treatments performed at high cooling rates is presented as follows:

Table 5.3: *List of fast cooling heat treatments*

Aust Temp (°C)	Cooling Rate ($°C\ s^{-1}$)	Transformation Temperatures (°C)		Classification
		Start	Finish	
1300	75	655	355	Y7N1 1300/75
	100	604	321	Y7N1 1300/100
1100	75	700	463	Y7N1 1100/75
	100	671	398	Y7N1 1100/100

The main microstructural features have been analysed by means of SEM. A common feature is the presence of phases formed via displacive mechanism such as martensite and bainite. A characteristic of such phase is the appearance of the ferritic matrix which is often very disordered and providing a surface relief appearance. The presence of FCA was not observed. Below are shown examples of the microstructures examined followed by the dilatometry curve for each cooling condition which are mainly constituted of lower bainite and martensite.

Figure 5.34: *Microstructural features of sample Y7N1, fast cooling experiments*

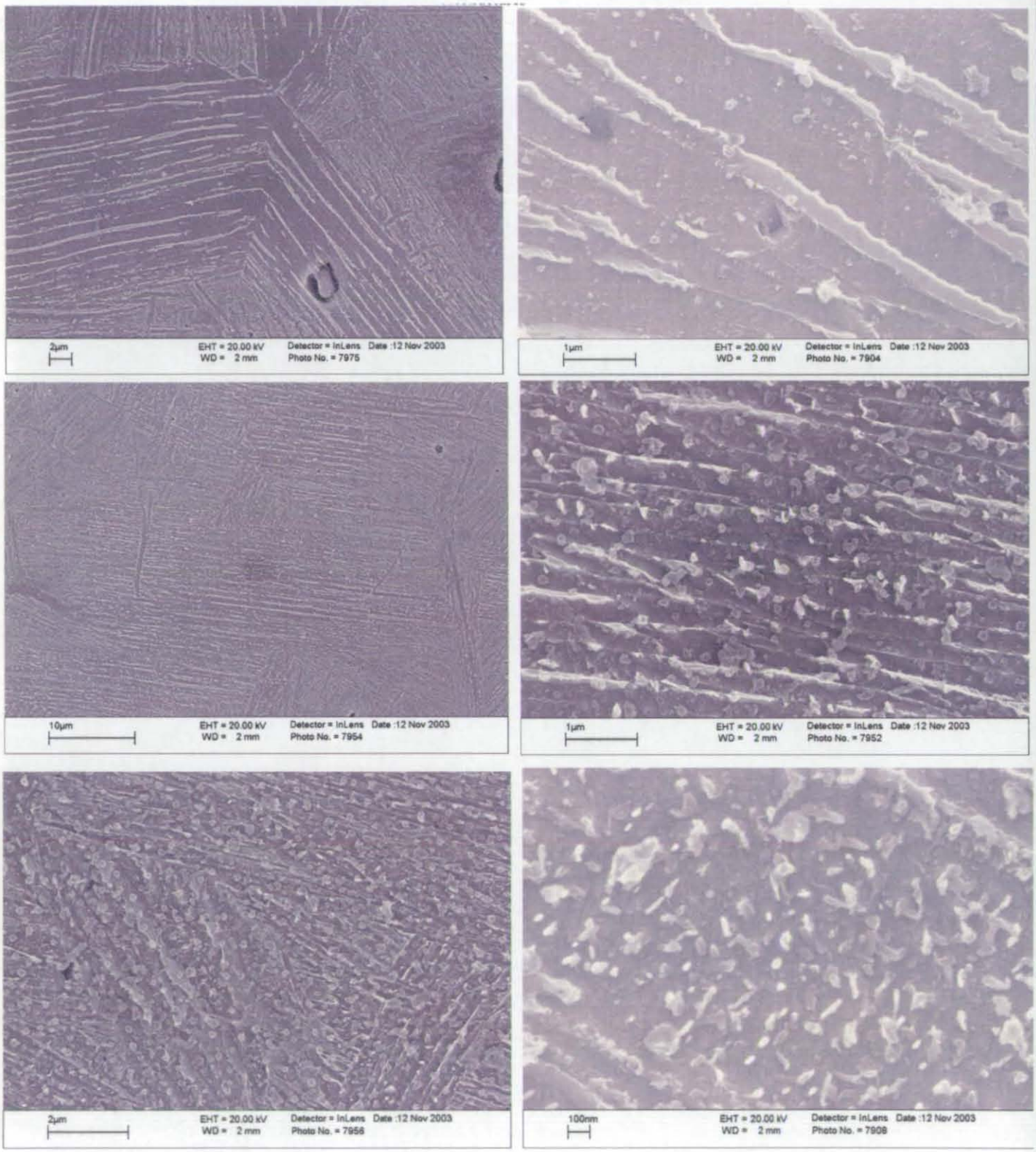

5.7 Summary

The microstructural features of each phase present in the microstructures obtained by heat treating alloy Y7N1 have been analysed by means of low and high resolution techniques. The use of SEM has allowed the analysis of each phase and its identification, when possible, with the advantage of analysing each detail of each phase which could help its identification. The high magnification images obtained by means of SEM have been directly compared with the corresponding images obtained by means of TEM. The analysis described in this chapter shows the potential of the use of the InLens detection mode in the SEM. A confident identification of the known phases which, depending on the heat treatment conditons and the alloy treated, can often be optically irresolvable, has been achieved. All of the phases which have formed in these steels used as a result of the heat treatment applied have been positively identified, with the exception fo a phase comprising ferrite and presipitates. This is discussed in the following chapter. In addition, particular attention has been paid to the phases which comprise "microphase" regions, often described rather loosely in the literature.

6. FCA Characterisation

6.1 Introduction

This chapter focuses on the phase identified as a ferrite-carbide aggregate (FCA) in the samples discussed in chapter 4 and 5, therefore linking the microstructural observation to the phase identification. The results presented in this chapter will ultimately be linked to the theoretical aspects of the phase transformations discussed in chapter 8. FCA has been previously classified as pearlite or lower bainite, because of its similarities with both phases, and its relatively fine microstructure. The uncertainty in identifying such phase derives as well from the fact that it does not fit unequivocally existing phase classification schemes. The fraction of this phase was significant in the alloys treated in the range 5-70°C s^{-1} in particular. It is therefore necessary to assess its nature and to understand under which conditions this phase forms, in addition to its impact on the final properties of the alloy.

6.2 The Importance of Phase Identification in the Field of Modelling

Technological development has allowed an impressive improvement in materials modelling activities. Their goal is to be able to predict the properties of an alloy in terms of the microstructure which, in turn, depends on heat treatment and alloy composition. The understanding of the nature of each phase forming during heat treatments and their mechanism of formation are therefore of primary importance during the development of models. "Classifying and quantifying the microstructures of steels has long been a contentious issue."[14]. This is, in particular, the case with 'microphase' and extremely fine phases such as ferrite-carbide aggregates, which are included in a broad category that does not specify clearly the aspects characterising each particular constituent included in this category. It should be noted that in order to improve models, the classification of a phase and its identity, together with knowledge of the nature of the phase and therefore its influence on the properties of the whole microstructure are essential.

The importance of understanding the nature of each phase is therefore many-fold. It improves the accuracy of classification schemes and aids in understanding the

overall kinetics of a reaction in heat treatments where simultaneous transformations can influence each other, and therefore it also aids the understanding of mechanisms governing the kinetics of other phases formation. Furthermore, it contributes to the improvement of the accuracy of predictive models, especially in the field of welding and continuous cooling heat treatments where the kinetics are complex and, in some case, still unclear. Finally, it helps in the understanding of the impact of each phase on the final properties of a microstructure.

In alloy Y7N1, HOM146, HOM148 and HOM133, a phase, initially named ferrite-carbide aggregate (FCA), has been observed. The phase, which has a dark etching response, has been presented briefly in chapters 4 and 5 and the previous work carried out on this phase has been discussed in section 2.1.3. The path undertaken to identify and characterise FCA by using several different analysis approaches and techniques is presented and discussed in the following sections. The research has moved along two parallel directions: the identification and classification of the phase and the understanding of the transformation kinetics. The phase classification involved the optical observation, high magnification-high resolution analysis (SEM analysis, TEM analysis and EBSD) and microhardness. The study of the transformation kinetics (which will be discussed in more detail in chapter 8) involved the use of dilatometry and high magnification-high resolution techniques (SEM, TEM and EBSD).

6.3 Observation of Ferrite-Carbide Aggregate (FCA)

The microstructures observed in Y7N1 are the result of heat treatments performed under continuous cooling conditions, covering a wide range of cooling rates, from 2 to 400°C s^{-1}, as discussed in chapter 4. Two different austenitising temperatures were investigated: 1100°C and 1300°C. As the conclusions are in most cases the same, the 1300°C austenitisation effects will be mentioned only when necessary, otherwise similar conclusions drawn from 1100°C austenitisation can be assumed. At cooling rates between 5°C s^{-1} and 75°C s^{-1} the presence of a phase which gives a dark etching response and possesses a "spongy" appearance, has been observed. From an optical analysis of the microstructures (figure 6.1), the

phase appears in grains with varying shape and dimension depending on the cooling rate and the austenitising temperature (i.e. the austenite grain size).

Figure 6.1: *Example of FCA optically observed*

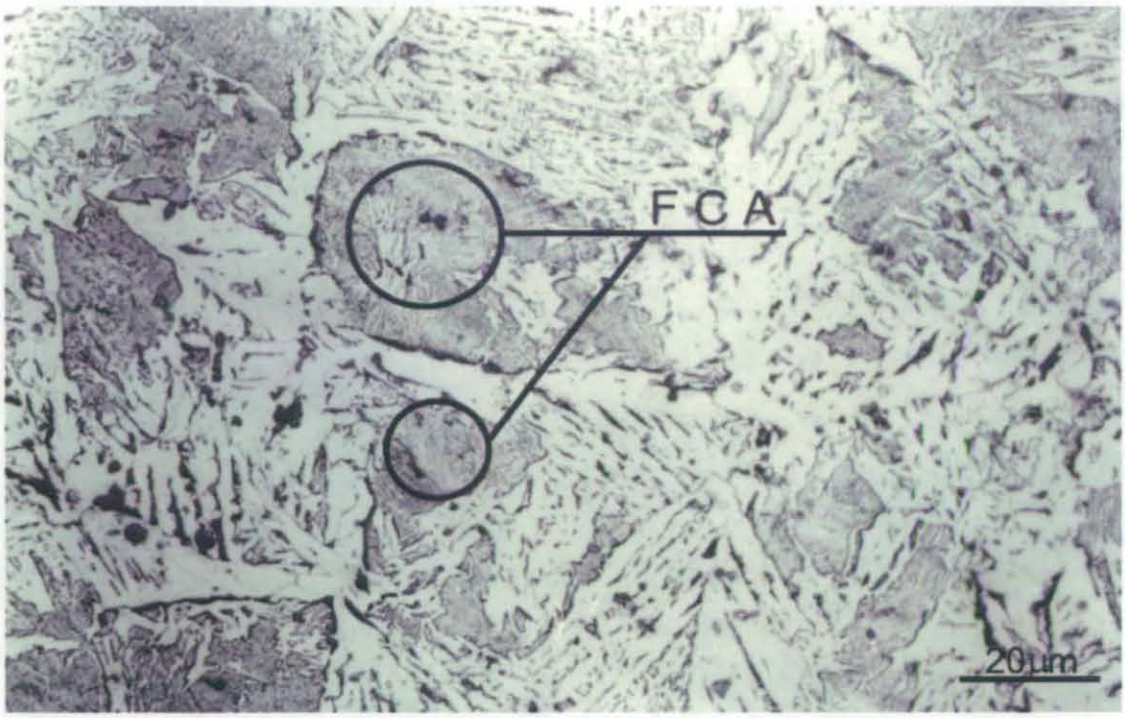

This suggests that the kinetics of the transformations occurring during cooling and the heat treatment parameters have an influence on the development of such phase. The characteristics of the phase observed using light microscopy do not meet specifically and unequivocally any phase in the classification schemes. The closest phase to which it could be related is a ferrite-carbide aggregate, although this definition does not clarify how the constituents of the phase form and how the exact morphology of the phase looks like. It then appears necessary to understand when such phase forms, how the phase forms, what the phase is and how the phase formation is influenced by the heat treatment parameters. In order to do this the research has initially focussed on the analysis of the effects on the microstructures of two cooling rates (10°C s^{-1} and 50°C s^{-1}) and two austenitising temperatures (1100°C and 1300°C), although the complete characterisation involved the analysis of several other heat treatment conditions.

The optical observation suggests that increasing the cooling rate causes the average dimensions of the FCA grains to decrease. On the other hand, increasing austenitising temperatures led to larger dimensions of the grains for a given cooling rate. The optical representation of these variations is shown in figure 6.2.

***Figure 6.2**: microstructures observed optically microstructures of alloy Y7N1 heat treated under four different conditions, showing the presence of FCA regions*

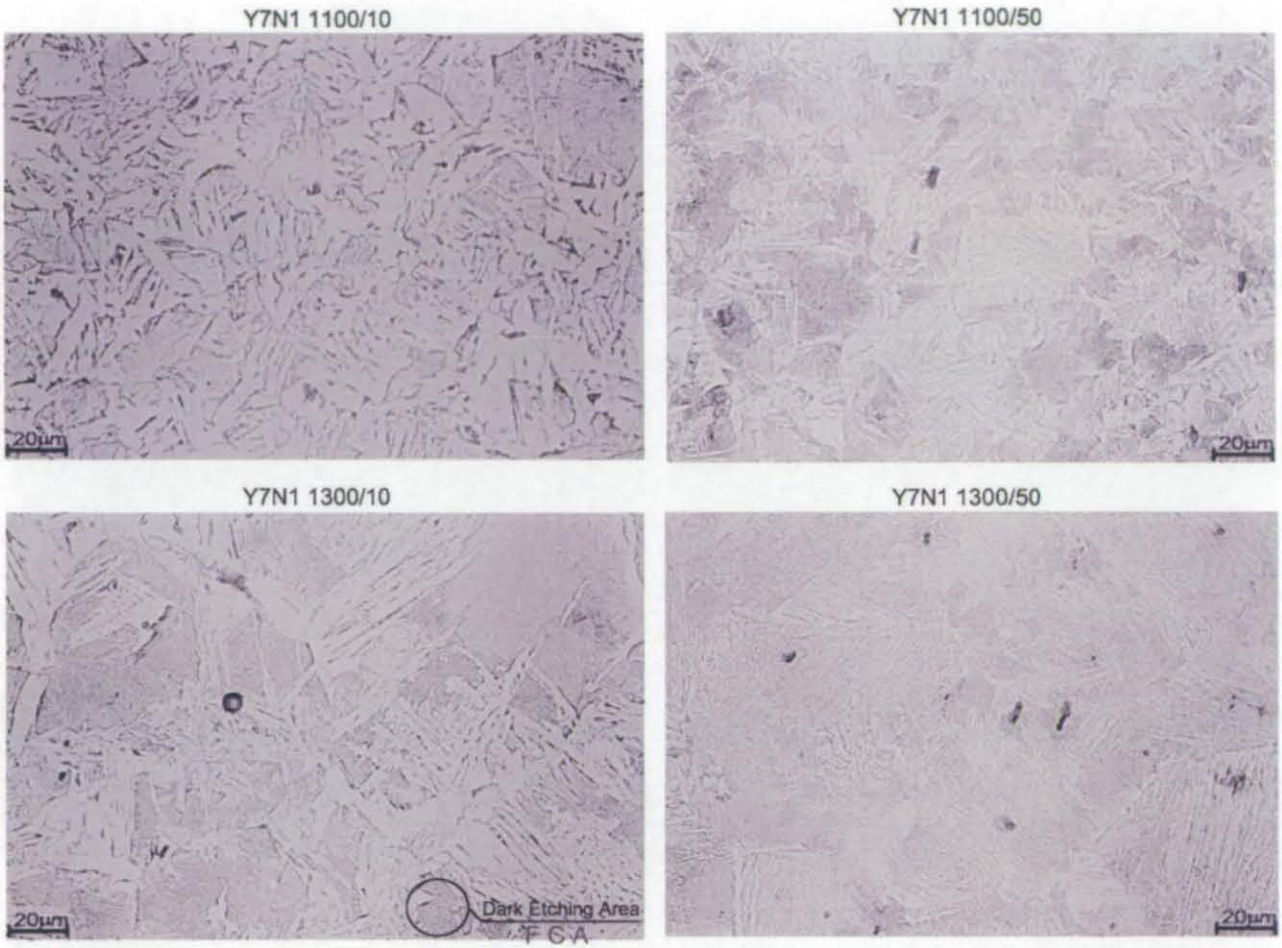

Furthermore, the FCA phase appeared to develop in most cases in grains adjacent to Widmanstätten ferrite. Although the use of other investigation techniques is required in order to confidently assess a possible transformation sequence, the optical analysis has provided some information in such in this respect in that the FCA phase appears to form after both primary ferrite and Widmanstatten ferrite and therefore, at the final stages of cooling.

Figure 6.3: *Temperature-Time profile for WF and FCA formation providing an indication of a possible transformation sequence*

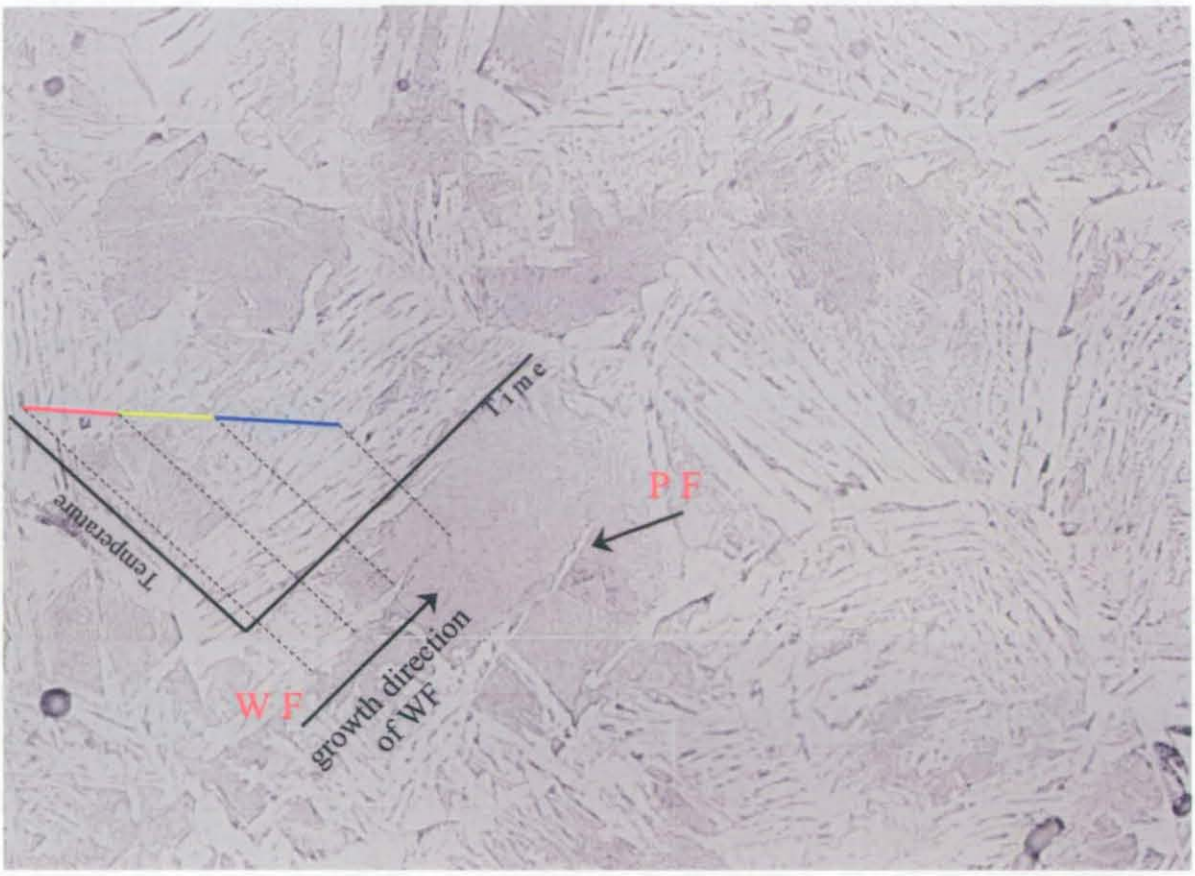

The qualitative schematic shown above describes how the Widmanstätten ferrite grows into austenite at higher temperatures. The austenite then transforms to the dark etching FCA region at lower temperature. Considering the opposite boundary of the FCA grain, which is constituted of primary ferrite nucleating at prior austenite grain boundaries, it can be seen as well that the process which produces the FCA takes place at lower temperatures. Therefore, it seems that the Widmanstätten ferrite growth precedes the formation of the FCA. In this context, the work of T. Reti[45] has brought evidence that between 600 and 500°C in continuous cooling processes, austenite decomposition starts first with Widmanstätten ferrite and upper bainite formation followed by the transformation of the remaining austenite into degenerate pearlite, although the chromium-rich alloy studied has a very different composition compared to alloy Y7N1. Another possibility on which the attention will be focussed, is the possibility that the formation of the FCA is due to auto-tempering of martensite. Auto-tempering relates to the formation of carbides within martensite during quenching due to the unavoidable carbon diffusion. It especially occurs in alloys with

high M_S. During the first stage of tempering (which could be compared to a certain degree of auto-tempering) preferential precipitation of ε-carbides has been observed in low alloy steels. The phase appears as thin ribbons which are often paired or as tiny particles "decorating the planar arrays of closely space dislocations"[28].

The occurrence of auto-tempering would explain the formation of very small carbides due to both the low carbon content and the small time allowed for diffusion. The resulting martensitic phase should be softer than the as-quenched structure. Considering that the M_S temperature has been calculated as 475°C, this implies that at a cooling rate of 10°C s^{-1} 37.5sec are available for diffusion of carbon and carbide formation via auto-tempering, whilst at a cooling rate of 50°C s^{-1} 7.5sec are available for carbon diffusion.

Another aspect which can be explored by means of optical observation is the comparison between the dimensions of pearlite regions and FCA regions which formed in alloy Y7N1 at different cooling rates. This would result helpful when differentiating the two phases. In alloy Y7N1, under continuous cooling conditions, pearlite forms only at low cooling rates (i.e. up to 5°C s^{-1}). The amount of carbon available is considerably low (0.13 wt.% C) and the fraction of pearlite is much lower compared to primary ferrite. The dimensions of the pearlite regions are therefore small, ranging from 1 to 5 μm width. On the other hand, the regions of FCA, which develop as the cooling rate is increased (i.e. from 5°C s^{-1} upward), have dimensions ranging from 5 to 40 μm depending on the austenitising and cooling conditions. The composition of alloy Y7N1 and the heat treatments applied, cause both pearlite and FCA to be irresolvable optically, although pearlite regions formed at low cooling rates give a darker etching response (close to black) compared to the FCA formed at higher cooling rates. However, the indications of the dimensions of the grain lie on a path which supports the idea that the two phases are different rather than being two variations of the same phase. In fact, the low carbon content of the alloy goes against the evidence of a countertendency on the grain dimensions. If pearlite and FCA would be the same phase, with the FCA having a finer morphology due to the higher cooling rate, it is unlikely that both dimensions of the grain and volume fraction would increase as the cooling rate increases. A comparison between the dimensions and characteristics of pearlite and FCA are shown in figure 6.4.

Figure 6.4: *Comparison between P and FCA dimensions (sample Y7N1 austenitised at 1300°C and cooled at 5°C s^{-1})*

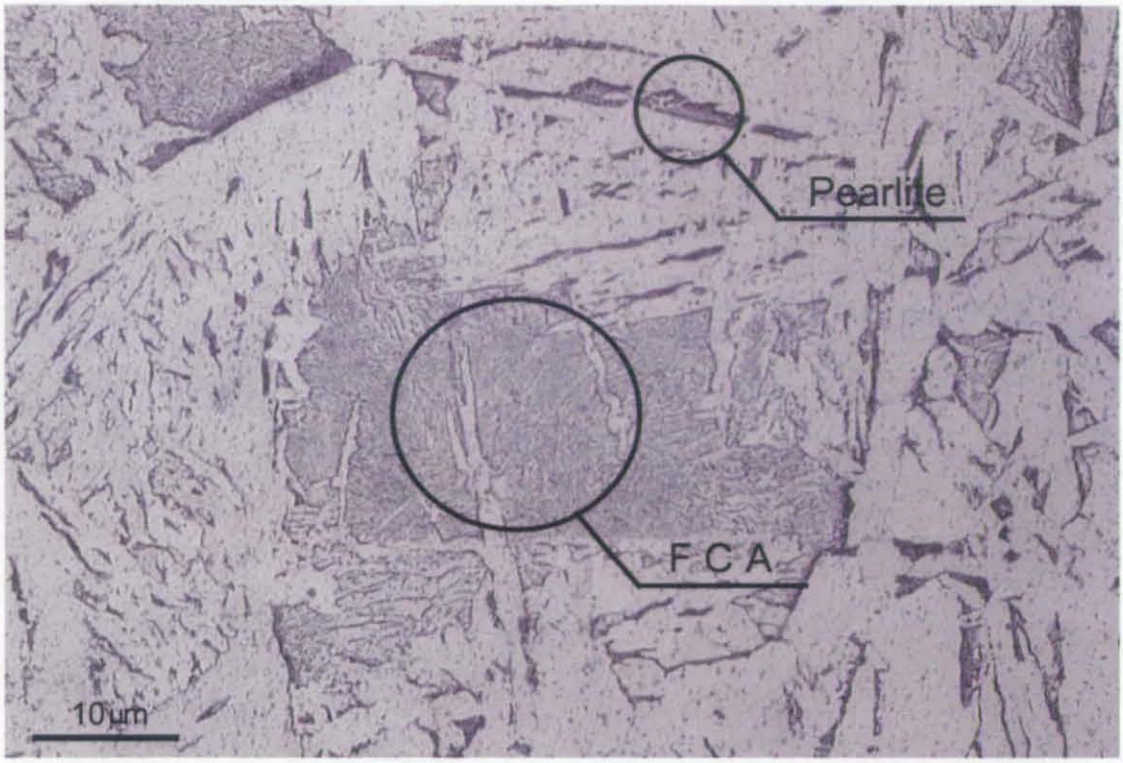

6.4 Microhardness

In order to obtain more information about the possible nature of the FCA, microhardness measurements were performed on each of the continuously cooled sample.

Figures 6.5a-d show the microhardness results for samples Y7N1 1100/10, 1100/50, 1300/10 and 1300/50 respectively.

Figure 6.5a: *Microhardness data for Y7N1 aust. at 1100°C, cooled at 10°C s^{-1}*

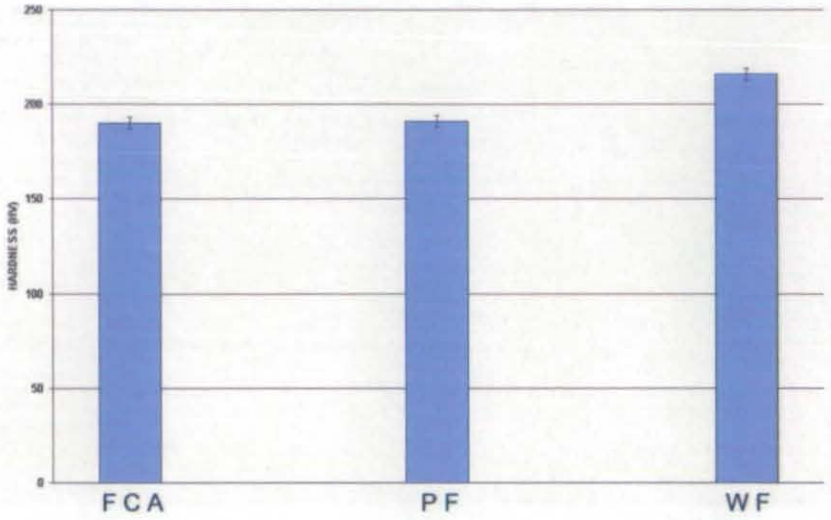

Figure 6.5b: *Microhardness data for Y7N1 aust. at 1100°C, cooled at 50°C s^{-1}*

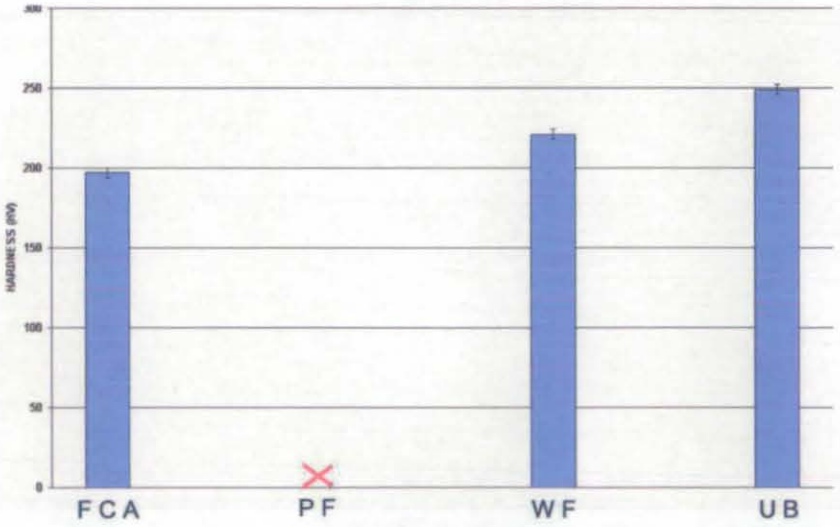

Figure 6.5c: *Microhardness data for Y7N1 aust. at 1300°C, cooled at 10°C s^{-1}*

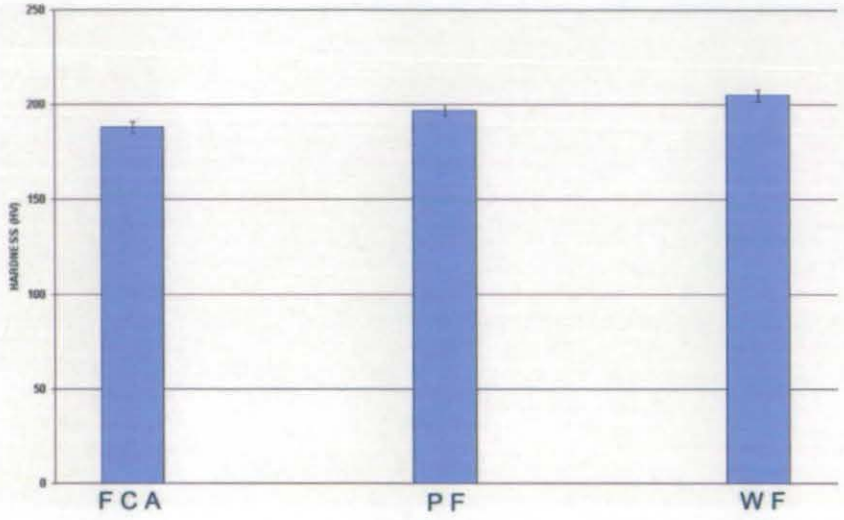

Figure 6.5d: *Microhardness data for Y7N1 aust. at 1300°C, cooled at 50°C s^{-11}*

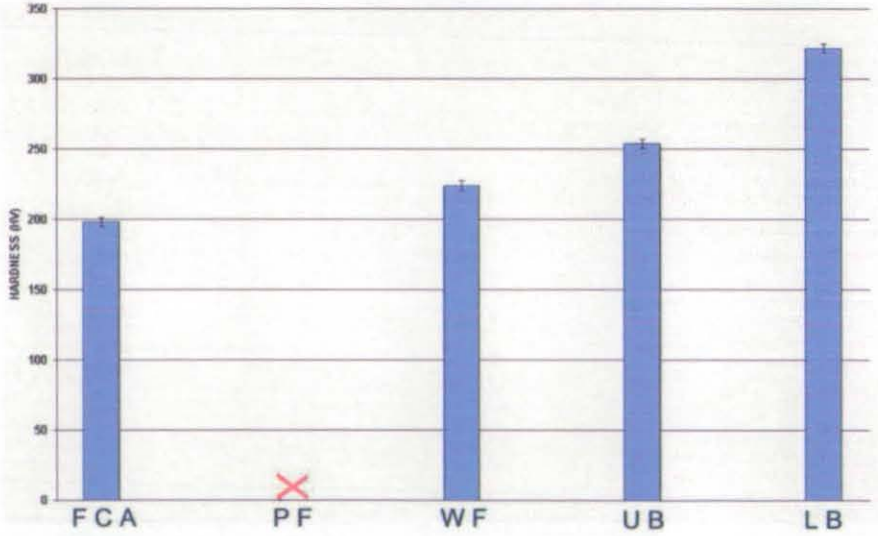

By comparing these results the influence of cooling rate and austenite grain size on the hardness of each phase can be appreciated. The microhardness data showed that, as expected, reconstructively formed phases such as ferrite (~190 HV) are softer than Widmanstätten ferrite (~220 HV) and bainite (~250HV). Furthermore, an increase in cooling rate causes a general increase in average hardness of each phase. Surprisingly, the hardness of the FCA was always been found to be between the hardness of primary ferrite and the hardness of Widmanstätten ferrite. Therefore the FCA is much closer in hardness to ferrite than to bainite or martensite. The hardness is indeed of the same order of primary ferrite and this would make presume the formation of a soft FCA matrix via a reconstructive mechanism. It is interesting to compare the above results with the microhardness data relative to pearlite formed at very low cooling rates (image 6.6):

Figure 6.6: *Microhardness data for alloy Y7N1 cooled at 2°C s^{-1}*

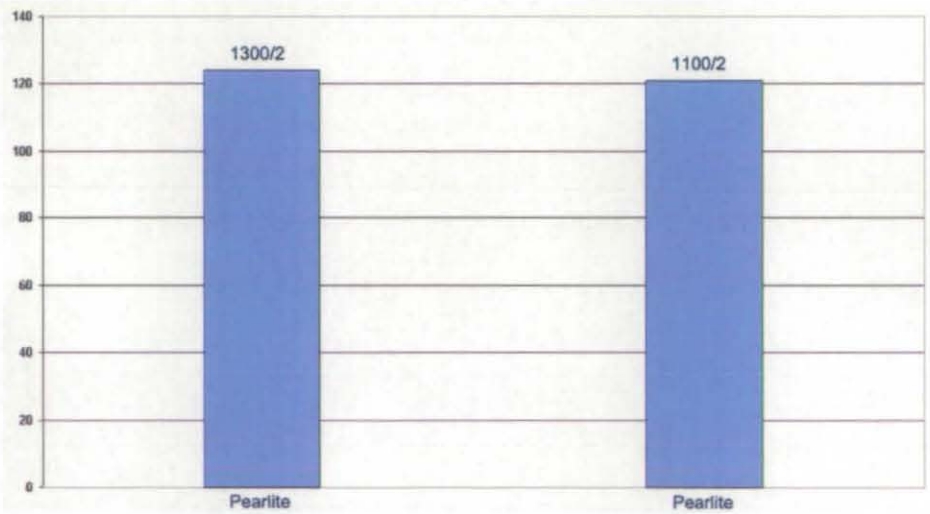

On the other hand, increasing the cooling rates causes the disappearance of the FCA phase from the microstructures and the formation of bainite and martensite, whose hardness is considerably higher than that of FCA. (images 6.7a-d).

Figure 6.7a: *Microhardness data for Y7N1 aust. at 1100°C, cooled at 75°C s^{-1}*

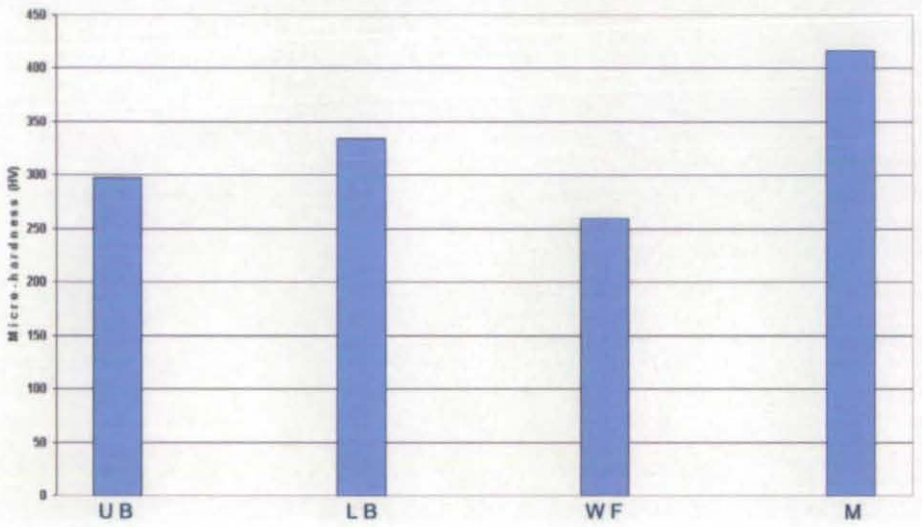

Figure 6.7b: *Microhardness data for Y7N1 aust. at 1100°C, cooled at 100°C s^{-1}*

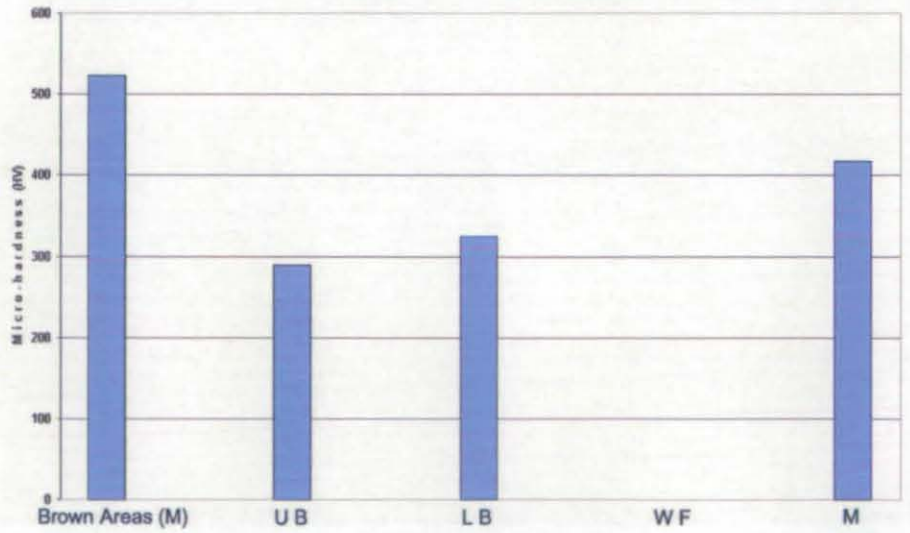

Figure 6.7c: *Microhardness data for Y7N1 aust. at 1300°C, cooled at 75°C s^{-1}*

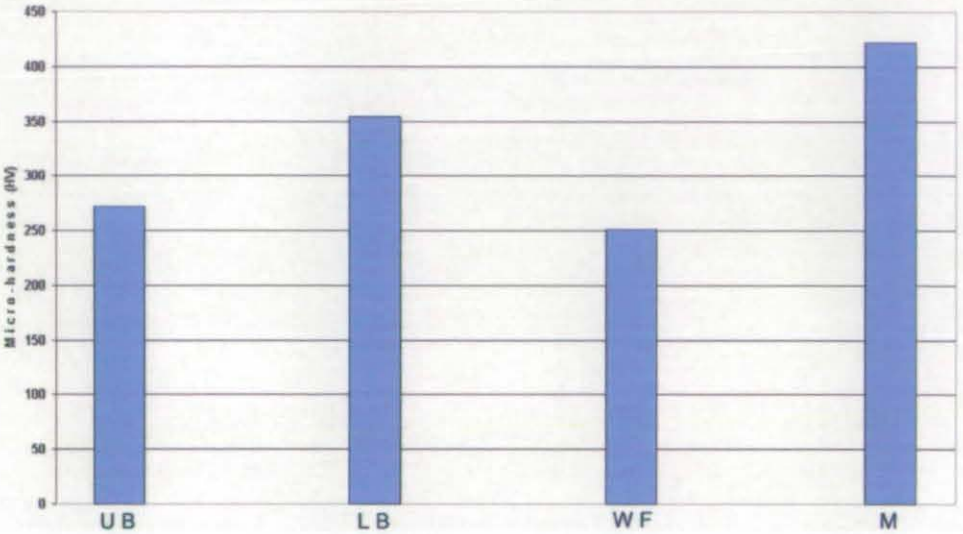

Figure 6.7d: *Microhardness data for Y7N1 aust. at 1300°C, cooled at 100°C s^{-1}*

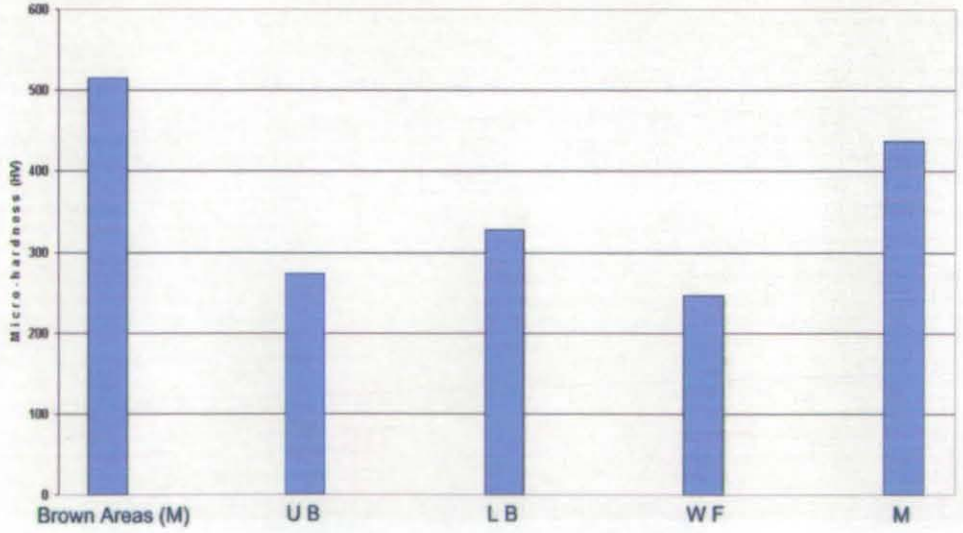

The "brown areas" labelled in figure 6.7d refers to martensite regions close to the edge of the samples tested which appeared to be brown coloured as a consequence of an etching effect.

6.5 SEM (InLens) Investigation of FCA

High magnification SEM analysis was used in order to resolve microstructural features which could not be discerned using optical microscopy, and in particular the morphology of the FCA.

Figure 6.8 shows a direct comparison between the optical analysis of sample Y7N1 austenitised at 1300°C and cooled at 10°C s^{-1} and the SEM analysis. The main microstructural components, which are sometimes irresolvable optically, have been observed at high magnification using SEM. This allows confident phase identification or, as in the case of FCA, is a necessary investigation step for the determination of the nature of a phase.

Figure 6.8: *Comparison between optical analysis and SEM (InLens) analysis for alloy Y7N1*

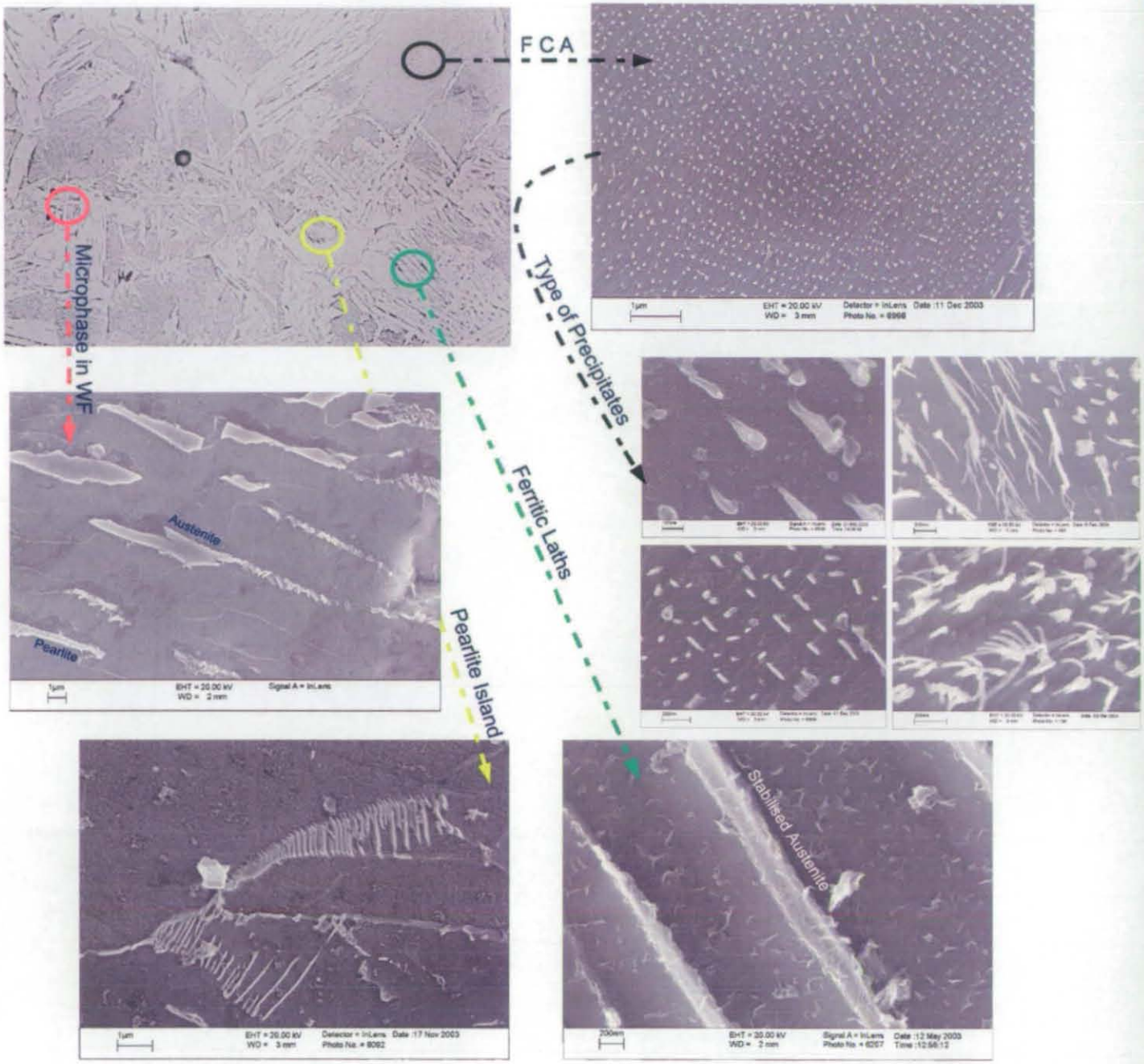

A few examples of the morphology of FCA phase at high magnification are shown in figure 6.9a-l. The attention has been focussed on the matrix and the morphology and distribution of the second phase.

Fig. 6.9a-l: *examples of FCA morphology; matrix and second phase*

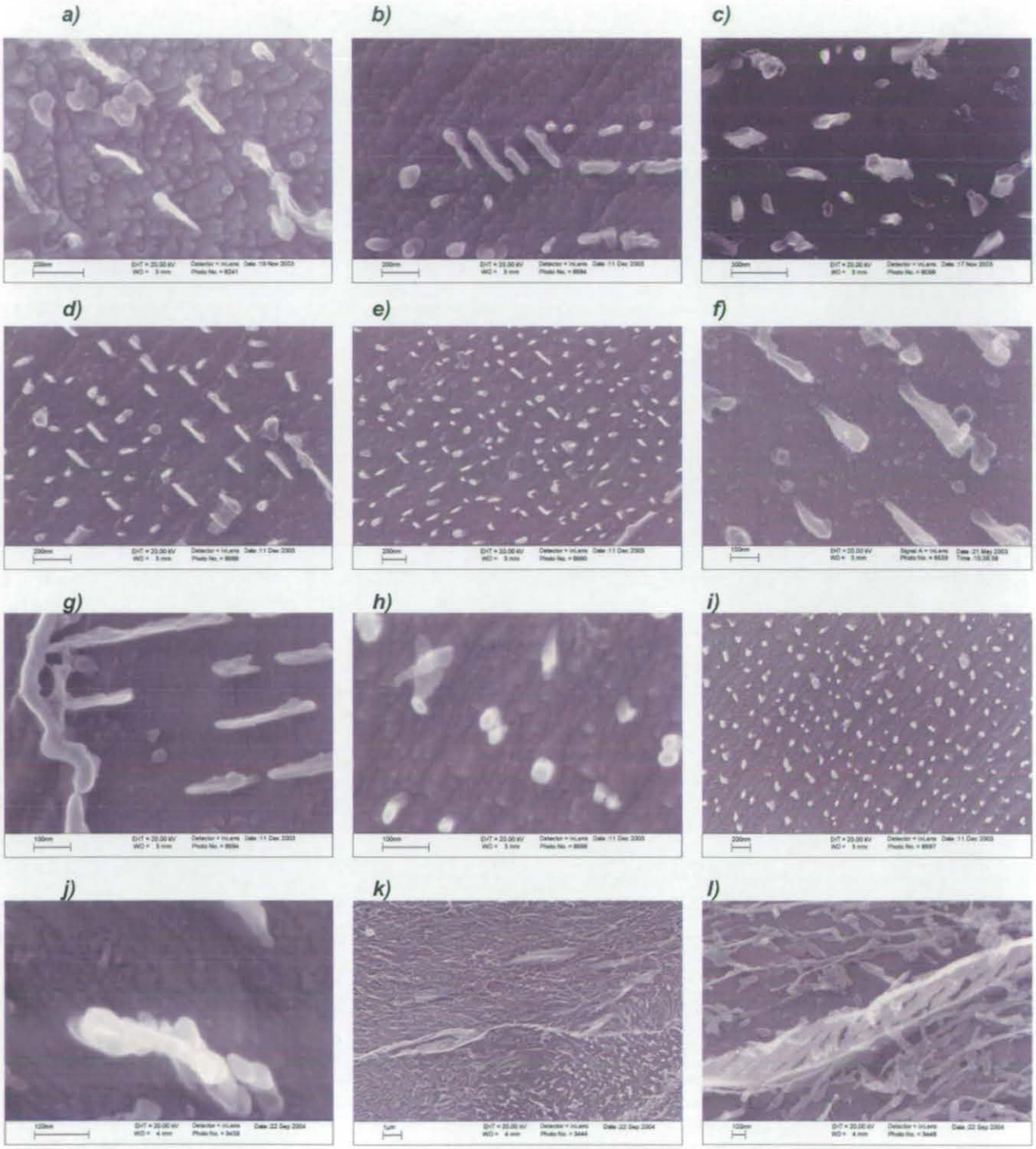

The peculiar features observed highlight several differences with the appearance of lower bainite and pearlite. At first, the FCA phase appears as being constituted of two constituents. A matrix which is presumably ferritic, and a second phase in the form of small precipitates. Different morphologies of them, which cannot be distinguished by optical means, have been observed. They present different shape, dimension, alignment, orientation and spacing between them. Most likely, depending on the local concentration profile, the cooling rate, the alloy composition and the orientation of the two-dimensional section of the grain which is observed, the appearance of the FCA varies. Nonetheless common characteristics, which link all the different morphologies under a common categorization, can be identified. The growth of the precipitates which begins at grain boundary sites is usually lamellar. Small lamellae, whose dimensions range between 100 nm and 0.5 μm, soon break down and are substituted along their growth direction by small precipitates. The precipitates can be either discrete or partially interconnected, although usually a certain spacing, periodically repeated between them, is observed. When the particles are discrete the shape is usually regular and varying from a fibrous aspect to a nearly spherical one. On the other hand, when the precipitates appear very close and sometime interconnected, their shape is quite irregular and in many cases it reminds the shape of "tadpoles".

In both cases a common orientation between the precipitates is present and it follows the growth direction of the lamellae nucleating at the boundaries, when these are clearly visible. The particles dimensions usually range between 20 and 100 nm although in some cases are larger then 200 nm especially in the FCA where the precipitates appear to be interconnected.

The matrix appearance is similar in all aspects to primary ferrite. In comparison with the appearance of bainitic ferrite and martensite observed using SEM InLens detection, the FCA matrix and, more in general, the ferritic phases forming via a mechanism that does not have a shear component, appear to be much smoother and do not present any type of laths or indication of surface relief.

6.5.1 Etching Effect

In order to ascertain that the appearance of the dark etching FCA was not a result of an etching effect, SEM imaging has been performed on sample YZN1 austenitised at 1100°C and cooled at 10°C s^{-1} and subsequently etched for three different times of 5, 10 and 15 seconds. The etching solution used was a 2% Nital

solution (nitric acid in methanol). The images of the microstructure appearance at the three different etching stages are shown in figure 6.10a, b, c and d below. After having analysed the microstructures it can be concluded that it does not seem to have any appreciable etching effect that could determine the morphology of the FCA in such a systematic fashion.

Figure 6.10a: *5 seconds etching*

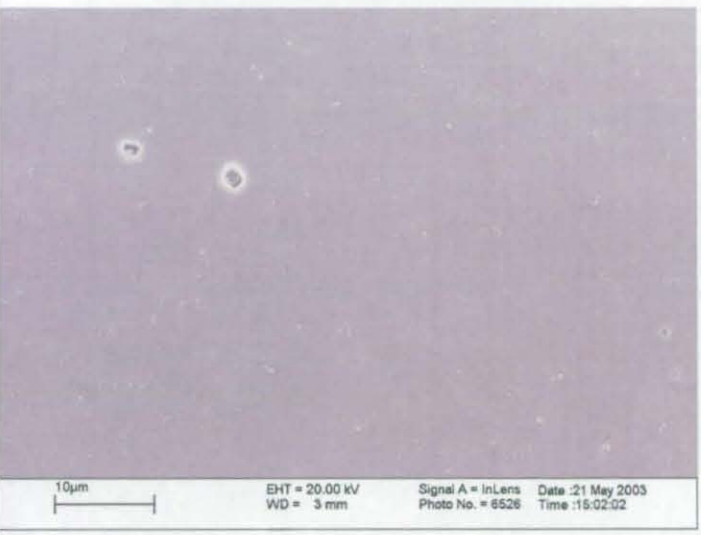

Figure6.10b: *10 seconds etching*

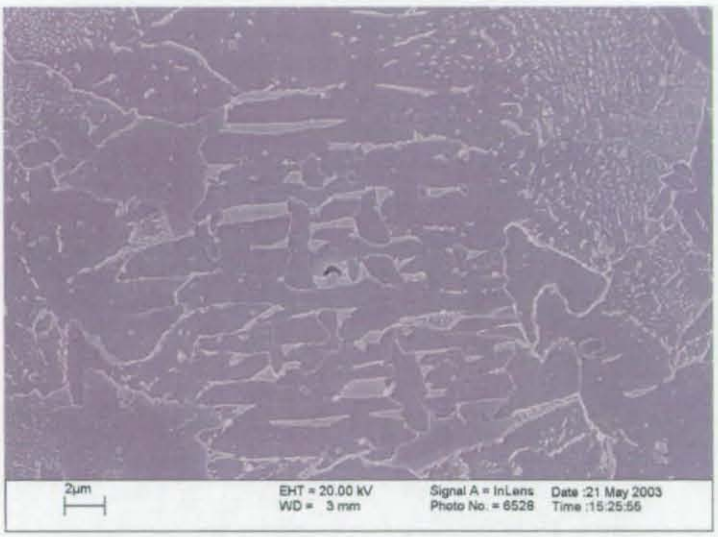

Figure 6.10c: *10 seconds etching*

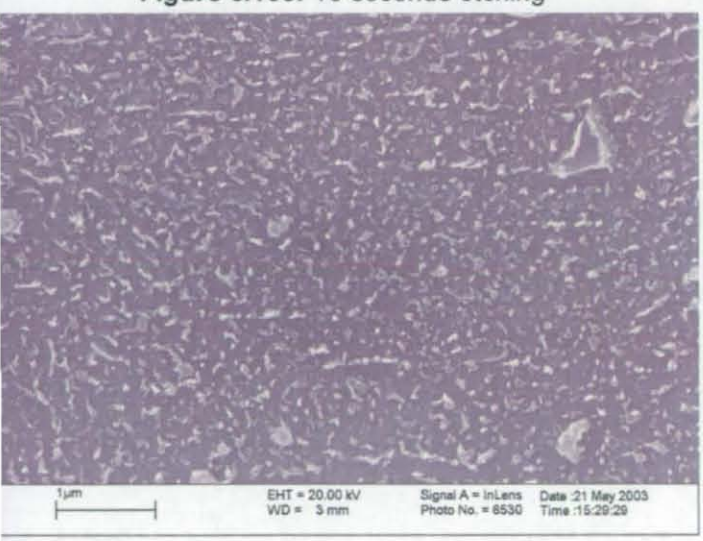

Figure 6.10d*: 15 seconds etching*

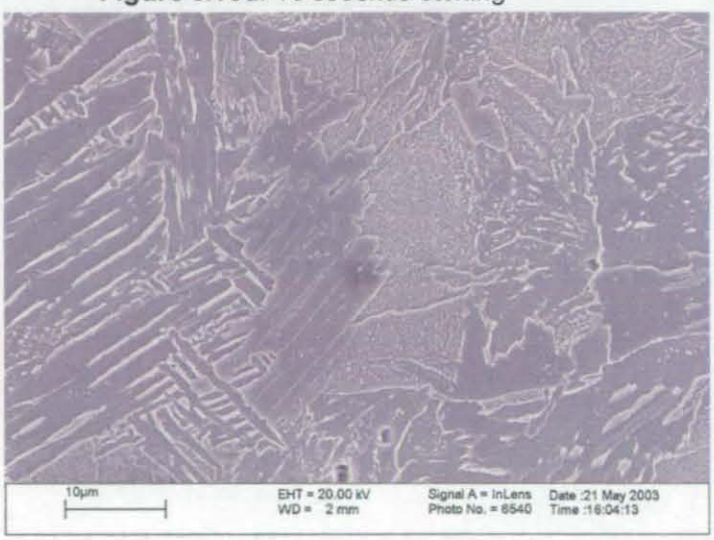

6.5.2 Carbides Morphology

Austenitisation at 1300°C and cooling at 10°C s^{-1}

Depending on the heat treatment conditions, the grain size of the FCA and the morphology of the second phase vary. At low cooling rates and high austenitising temperatures (i.e. Y7N1 1300/10) the size of the FCA grains ranges from 10 to 60 μm. The morphologies of the precipitates observed can be particle distributed in arrays, small regular fibres with a certain degree of alignment, irregularly shaped particles, fibres and small lamellae. The different types of precipitates found in Y7N1 1300/10 are shown in figure 6.11a.

Figure 6.11a: *The morphology of precipitates formed after austenitisation at 1300°C and cooling at 10°C s^{-1}*

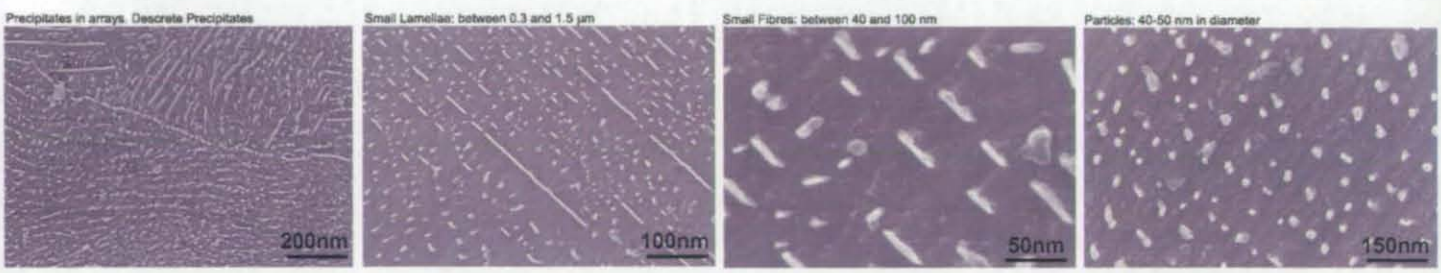

The average particle size is 50 nm, whilst small fibres measure on average 80 nm. Small lamellae range between 0.3 and 1μm. The particles, fibres and lamellae are usually distributed in arrays. The spacing between two precipitate arrays ranges between 100 and 400 nm approximately.

Austenitisation at 1100°C and cooling at 10°C s^{-1}

At low cooling rates and low austenitising temperatures the FCA grain size varies between 5 and 40 μm, being on average smaller than in the case of higher austenitising temperatures. The predominant morphologies of the second phase in the FCA grains are small particles and small fibres. Occasionally, the presence of small lamellae has been observed. The different carbide morphologies of Y7N1 1100/10 are shown in figure 6.11b.

Figure 6.11b: *The morphology of precipitates formed after austenitisation at 1100°C and cooling at 10°C s^{-1}*

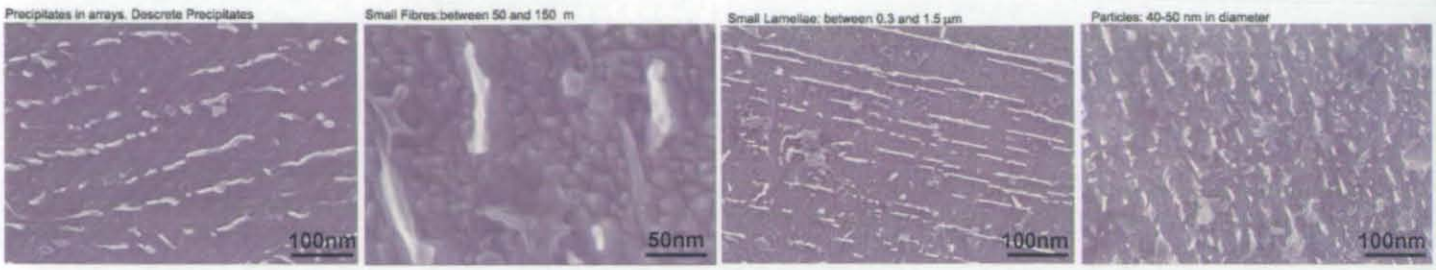

The average particle size is 50 nm. A small fibre morphology is more common then particles. The average size of small fibres is 150 nm. Small lamellae range between 0.3 and 3 µm, and were often observed in the form of precipitate arrays whose spacing ranged between 100 and 400 nm approximately.

Austenitisation at 1100°C and cooling at 50°C s^{-1}

When the cooling rate is increased another type of morphology is observed in addition to particles and small fibres: a tadpole-shaped precipitate is observed. Furthermore, the precipitates appear to be partially interconnected. Small lamellae formation does not take place. When precipitation occurs in arrays, the spacing between the arrays is smaller than at lower cooling rates and it usually ranges between 50 and 300 nm. At low austenitising temperatures and high cooling rates (e.g. Y7N1 1100/50) the grain size of FCA ranges between 5 and 30 µm. The carbide morphologies of Y7N1 1100/50 are shown in figure 6.11c.

Figure 6.11c: *The morphology of precipitates formed after austenitisation at 1100°C and cooling at 50°C s^{-1}*

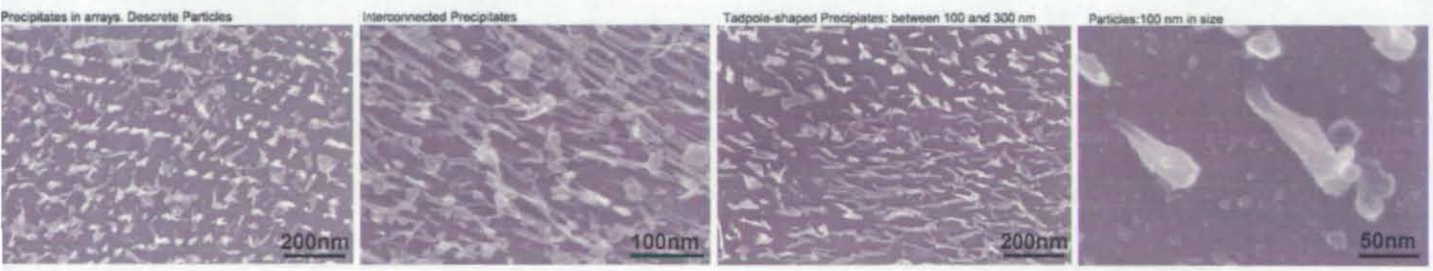

The average particle size is 50 nm. Whilst in the case of tadpole-shaped precipitates, the average size is 200 nm. The presence of particles is very limited.

Austenitisation at 1300°C and cooling at 50°C s^{-1}

At high cooling rates and high austenitising temperatures (e.g. Y7N1 1300/50) the same considerations applied to Y7N1 1100/50 are valid, although the FCA grain size can reach 40 μm. The carbide morphologies of Y7N1 1300/50 are shown in figure 6.11d.

Figure 6.11d: *The morphology of precipitates formed after austenitisation at 1300°C and cooling at 50°C s^{-1}*

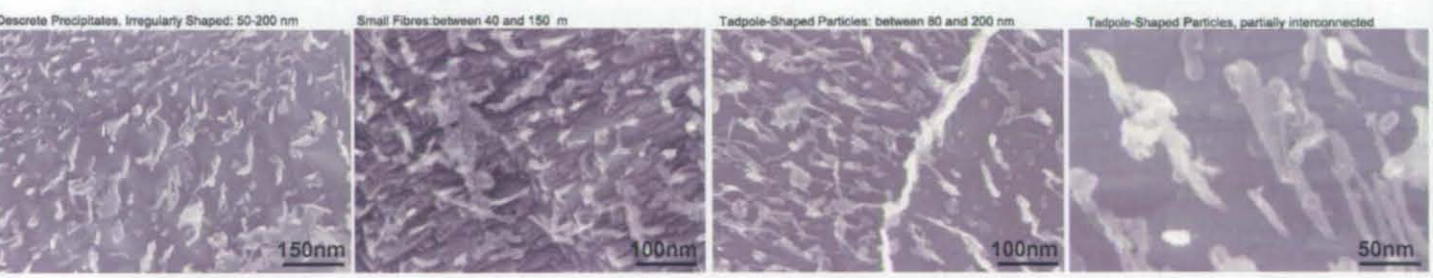

6.6 Hold-Quench Experiments

In order to explore the possibility of auto-tempering of martensite as being responsible for the formation of the FCA phase a series of hold-quench experiments were monitored using of dilatometry. The same austenitising and cooling conditions adopted to heat treat the first set of four Y7N1 samples (i.e. 1300/50. 1300/10, 1100/50 and 1100/10) were chosen, but instead of cooling from the austenite phase field to room temperature, the cooling was interrupted at T_f. In order to observe any microstructural change in the microstructure due to possible auto-tempering, the samples were then held at T_f for a determined period of time, followed by quenching to room temperature.

The hold-quench heat treatments performed on sample Y7N1 are listed in the following table:

Table 6.1: *Hold-quench heat treatments*

Aust Temp (°C)	Cooling Rate (°C s^{-1})	Transformation Finish Temp (°C)	Hold time at Tf (s)	Final Cooling	Classification
1300	10	537	116	Quench	1300/10/116s at Tf/q
1300	50	345	16	Quench	1300/50/16s at Tf/q
1100	10	564	118	Quench	1100/10/118s at Tf/q
1100	50	492	18	Quench	1100/50/18s at Tf/q
1300	10	537	0	Quench	1300/10/iTf/q
1100	10	564	0	Quench	1100/10/iTf/q

The microstructures of the six samples were observed both optically and by means of SEM. Microhardness and phase quantification have been performed on all the samples. The results provided the same information for all the samples, and therefore in order to present the main findings the case of sample Y7N1 austenitised at 1300°C and cooled at 10°C s^{-1} is discussed at this point.

The microstructural features observed by means of SEM and linked to the microstructure observed optically for sample Y7N1 1300/10/116s at T_f/q and sample Y7N1 1300/10/iT_f/q and sample Y7N1 1100/10/iT_f/q are shown in figures 6.12a-c.

Figure 6.12a: *Microstructural features of sample Y7N1 1300/10/116s at T_f/q*

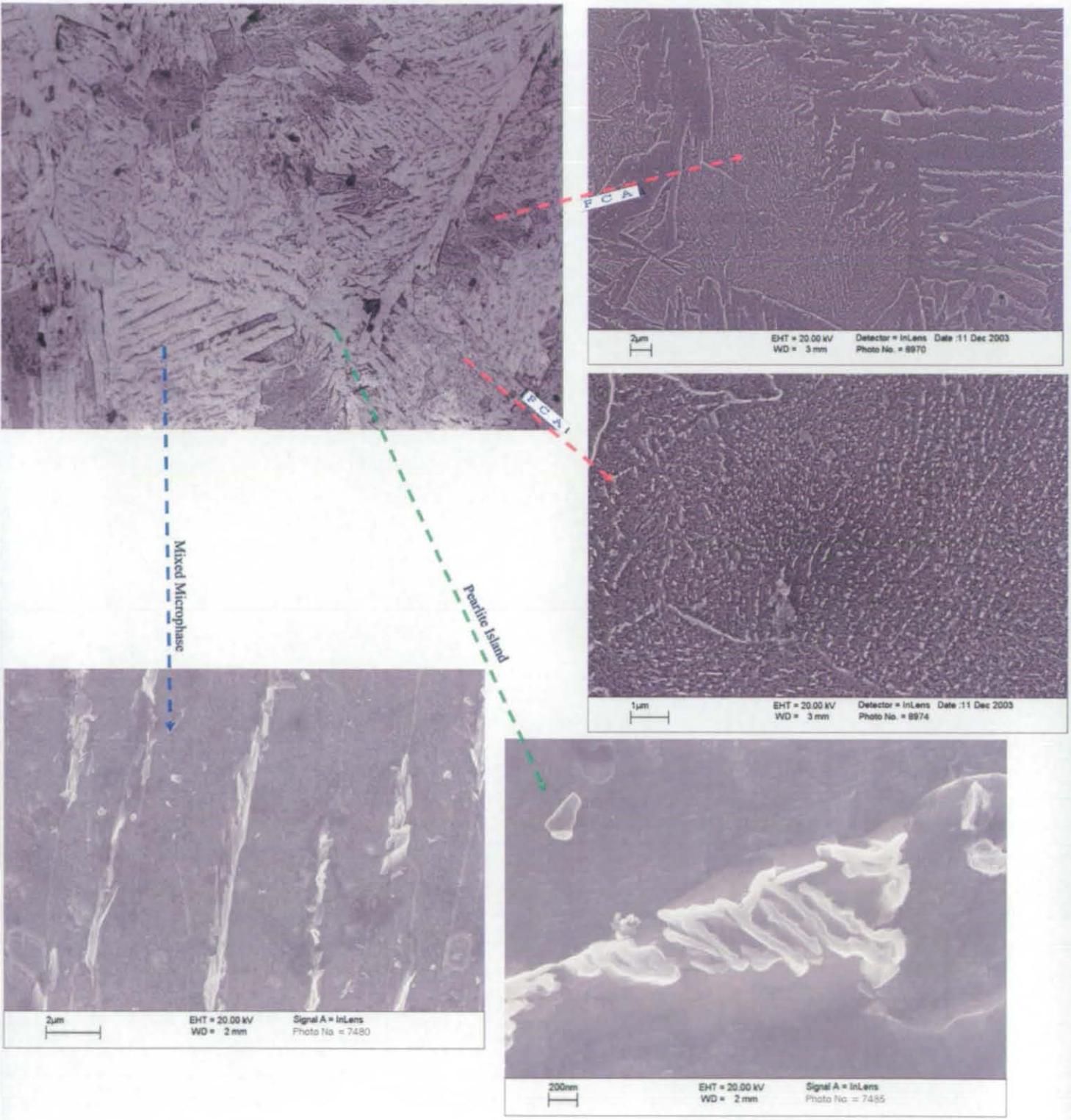

Figure 6.12b: *Microstructural features of sample Y7N1 1300/10/iT$_f$/q*

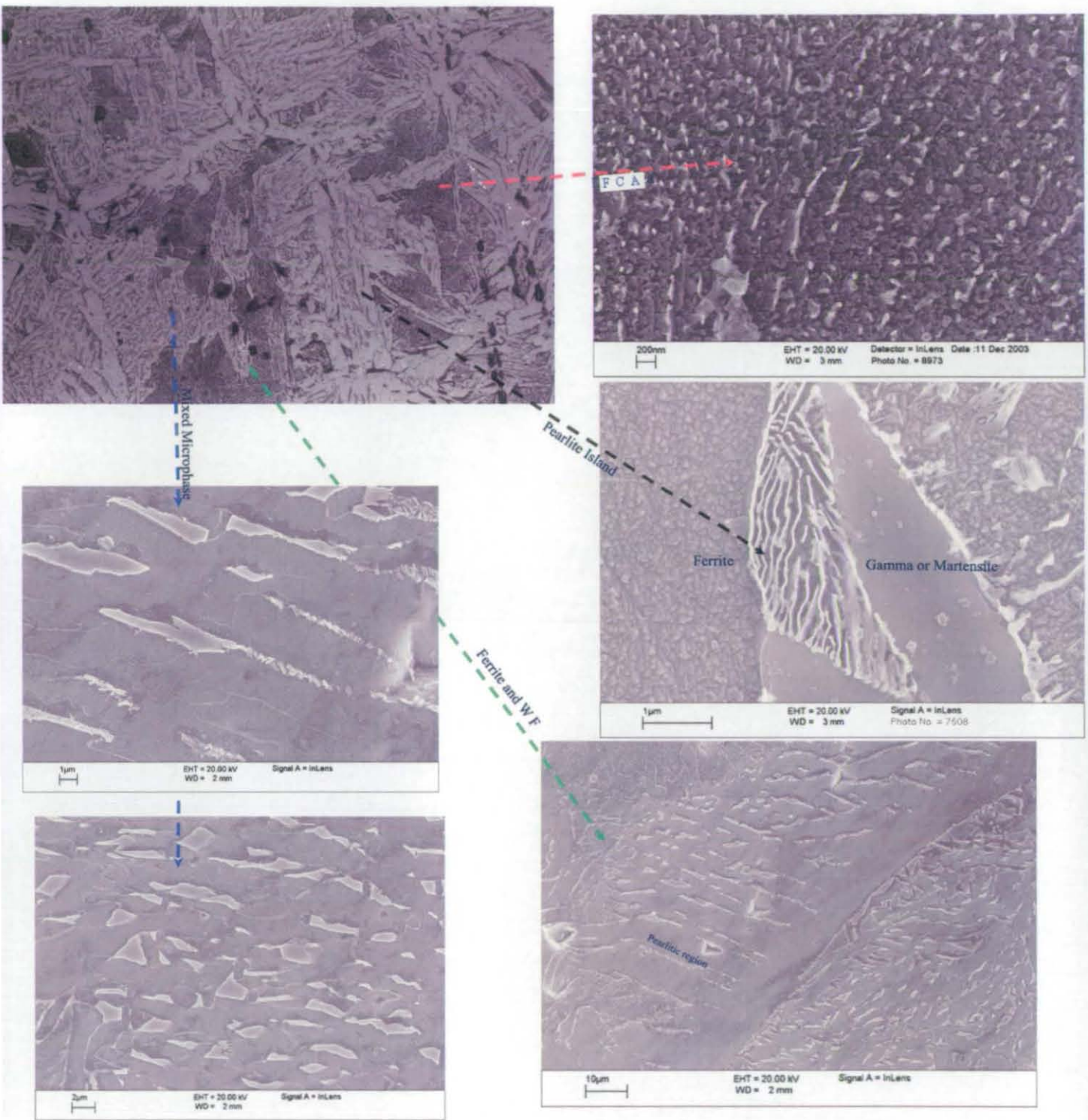

Figure 6.12c: *Microstructural features of sample Y7N1 1100/10/iT$_f$/q*

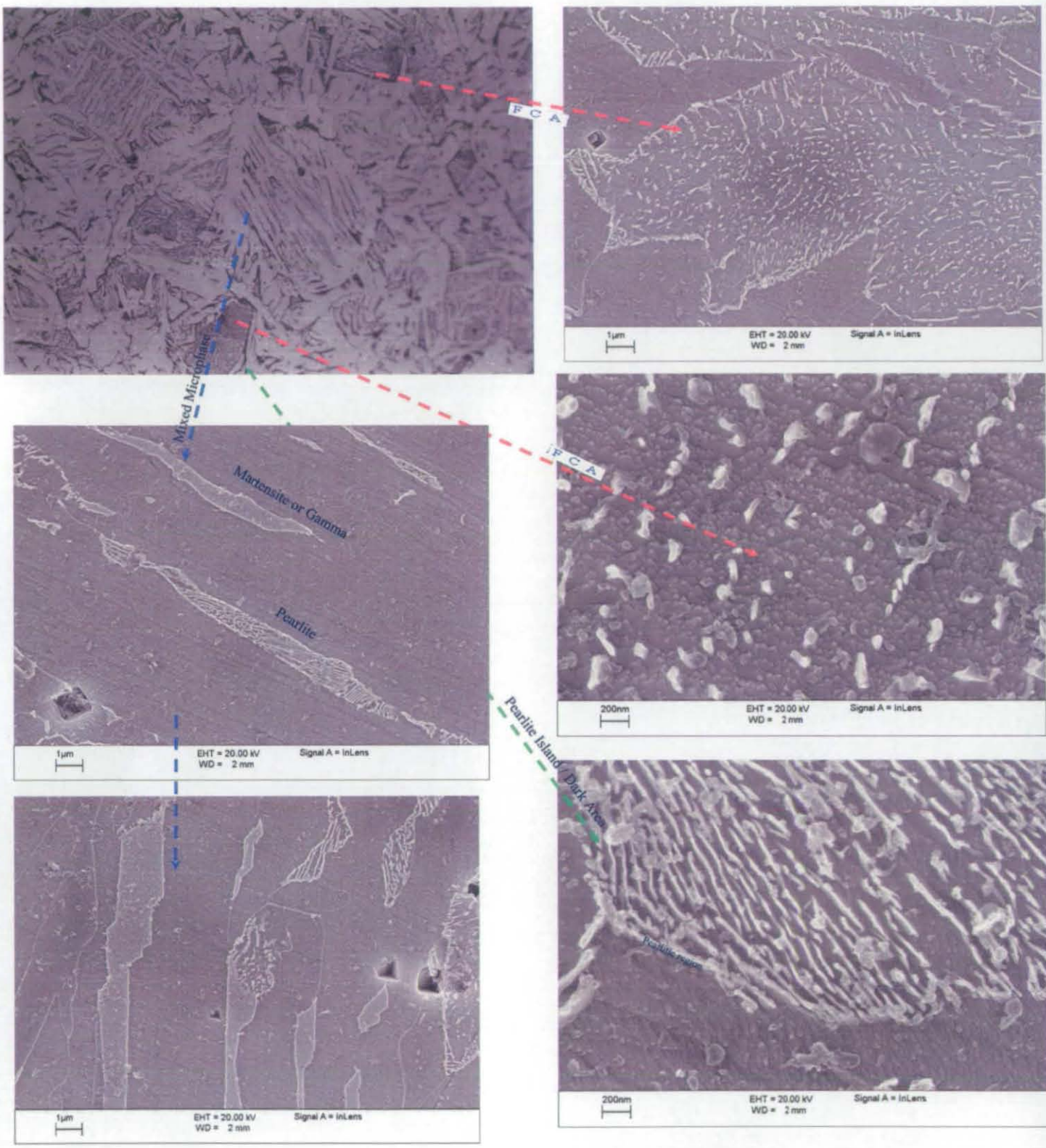

In some case it was observed a certain coarsening of the precipitates in the FCA regions (average size of 80nm). This aspect could be due to the fact that holding at T_f allows more time for diffusion of carbon at a temperature at which the activation energy for diffusion is very easily overcome. However, this aspect should be further investigated. The main information gathered from the microstructural observation of the hold-quench samples is the fact that no appreciable change in microstructure has been observed compared to the continuously cooeld samples. This suggests that the nature of the FCA phase is not martensitic and that auto-tempering did not take place during cooling to room temperature.

It is interesting to note that depending on the dimension and local carbon concentration certain microphase regions had the chance to transform to pearlite whilst others remained untransformed. Furthermore, from the SEM images, the lamellar structure of the FCA near the boundaries is visible.

The microhardness data obtained for all the six samples also followed the same trend as the continuously cooled samples and are presented below in figures 6.13a and b for sample Y7N1 1300/10/iT_f/q and sample 1300/50/16s at T_f/q :

Figure 6.13a: *Microhardness plot for heat treatment Y7N1 1300/10/iT_f/q*

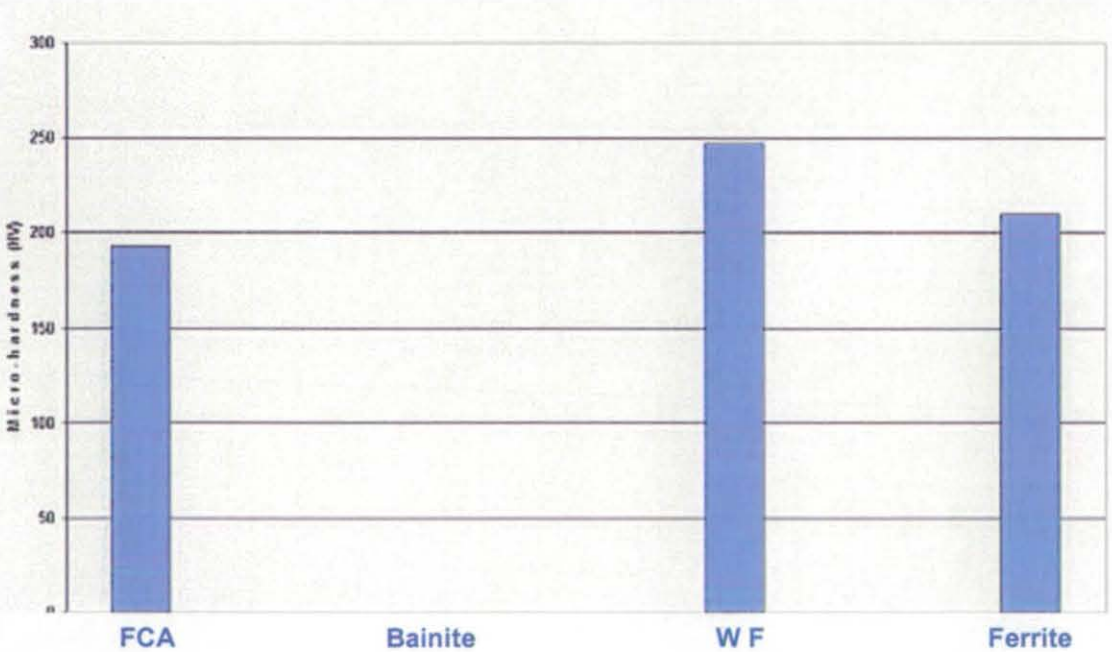

The presence of bainite in the samples cooled at 10°C s^{-1} was negligible.

Figure 6.13b: *Microhardness plot for heat treatment Y7N1 1300/50/16s at T/q*

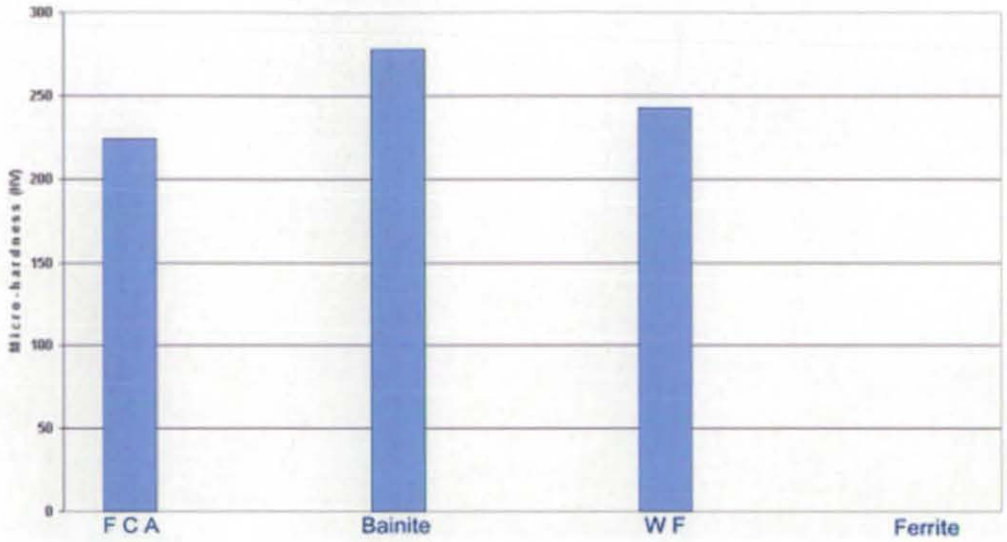

The dimensions of the primary ferrite regions in the samples cooled at 50°C s^{-1} were too small to provide reliable microhardness measurements in the samples cooled at 50°C s^{-1}.

In order to be definitively certain about the microhardness data for the FCA in respect of the indents relative to the microstructural regions the indentations were observed by means of SEM as shown below.

Figure 6.14: *Microhardness indentations on sample Y7N1; hold-quench experiments*

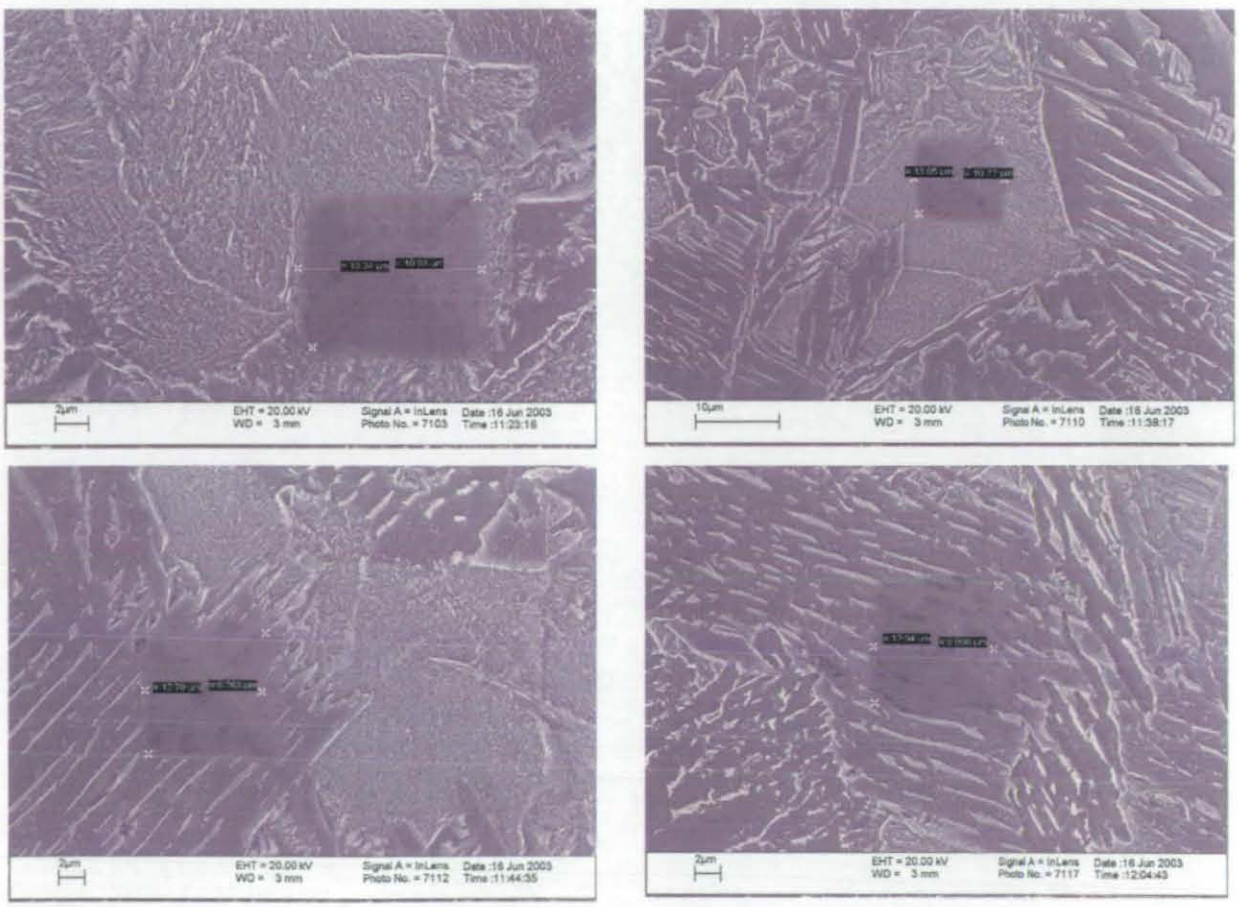

In order to investigate the stability of the precipitates and the effects of isothermal holding on the FCA morphology, ageing experiments have also been performed. The isothermal holding has been carried out at two different temperatures, for three different lengths of time. The set of ageing heat treatments is listed in table 6.2.

Table 6.2: *List of ageing experiments performed on alloy Y7N1*

Aust. Temp (°C)	Cooling Rate (°C s^{-1})	Isothermal Holding Temperature (°C)	Isothermal Holding Time (hrs)	Classification
1300	10	200	3	1300/10/3hrs at 200°C
1300	10	200	6	1300/10/6hrs at 200°C
1300	10	200	9	1300/10/9hrs at 200°C
1300	10	400	3	1300/10/3hrs at 400°C
1300	10	400	6	1300/10/6hrs at 400°C
1300	10	400	9	1300/10/9hrs at 400°C

As it will be treated in section 6.8, gathering diffraction patterns from both the matrix of the FCA and the precipitates was not an easy task due to the fine dimensions of the second phase and the magnetic nature of the sample which made the rotation of the sample and therefore the achievement of good patterns for both matrix and precipitates, impossible. The nature of the precipitates was not certainly known, and it was plausible to think that their nature was a non-stable iron-manganese-silicon carbide. Therefore, after an ageing treatment, the precipitates could have evolved toward a more stable and easily identifiable carbide (e.g. cementite). In addition, the morphological analysis provided valuable micrographs of the FCA microstructure.

The various ageing heat treatments were all found to provide similar microstructural features and will not be treated separately. The morphology of the FCA observed after ageing at 3, 6 and 9 hrs is extremely similar to the morphology observed in the continuously cooled samples. In some grains however, the dimensions of the precipitates are coarser, which could be attributed to the effects of ageing time and temperature. The dominant morphologies of the precipitates are irregularly shaped particles and 'tadpole' shaped interconnected particles. In addition, coarse elongated precipitates, which present a very peculiar lamellar structure (figure 6.15d), can be seen in few FCA grains. These constituents could however be sections of pearlite islands. The FCA phase seems to be very stable as significant changes in the morphology have not been observed. It was also very interesting to note that all the microphase regions observed in the aged samples, which were

cooled at 10°C s^{-1}, were pearlitic after ageing rather than retained austenite and, hence, had the time to fully transform.

The following set of images show the dilation curves for each of the ageing experiments and the morphologies of the FCA phase observed by means of SEM.

Figure 6.14: *Dilation curves for the ageing experiment 1300/10/3hrs at 200°C*

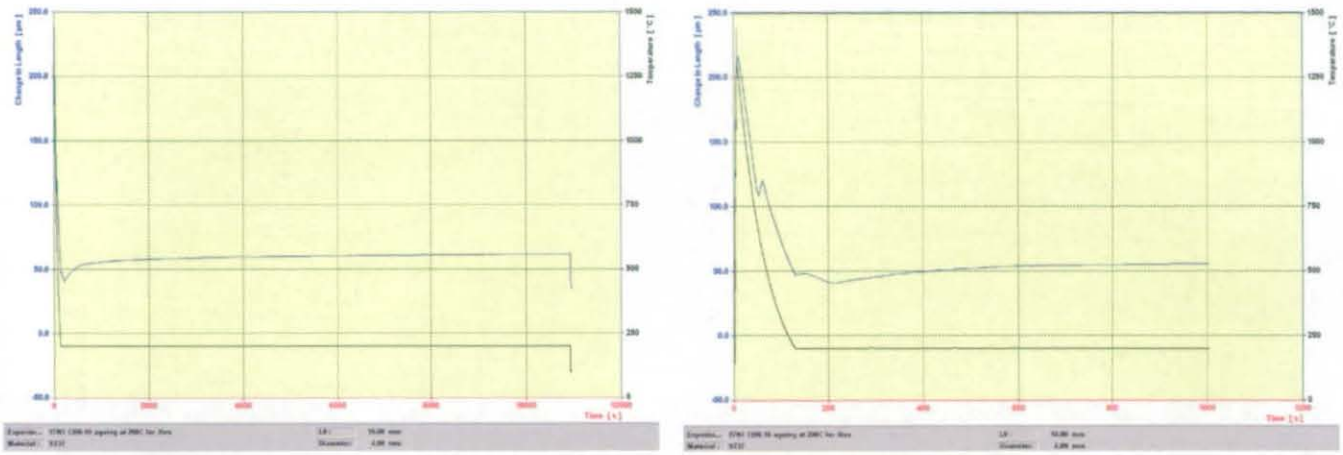

The two dilation curves in figure 6.14 represent the same ageing heat treatment. The plot on the right shows the initial stages of ageing, whilst the plot on the left shows the entire heat treatment. During the ageing heat treatment, the recorded change in length is minimal and is not due to major transformations taking place. The same considerations apply to all the ageing heat treatments.

Figures 6.15a-f show the morphology of the FCA phase observed by means of SEM. At low magnification, the structure looks the same as that observed prior to the ageing heat treatments (cf. figure 6.8 and 6.9). At higher magnification it can be seen that the shape of the precipitates is usually irregular and they coarser than the non aged samples.

Figure 6.15a-f: *FCA morphologies of sample 1300/10/3hrs at 200°C observed by SEM*

a)

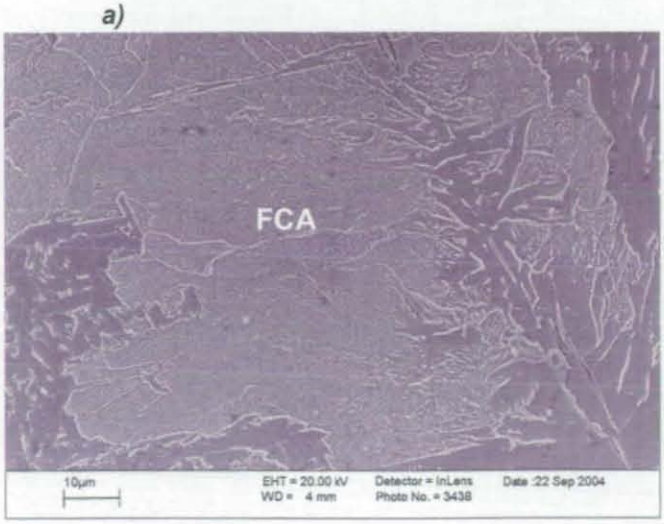

b)

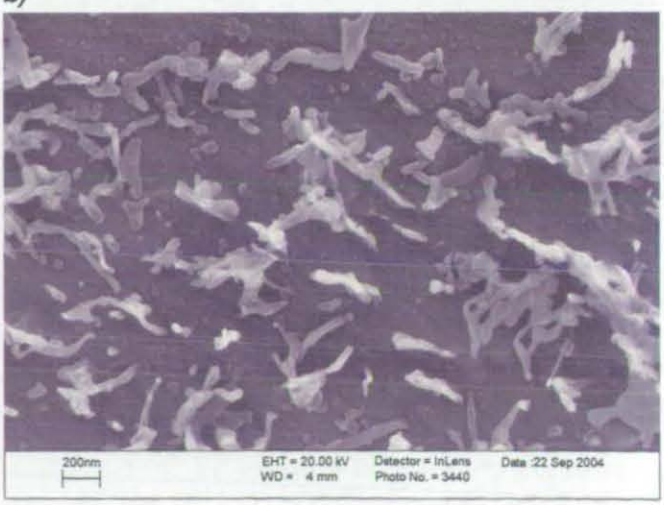

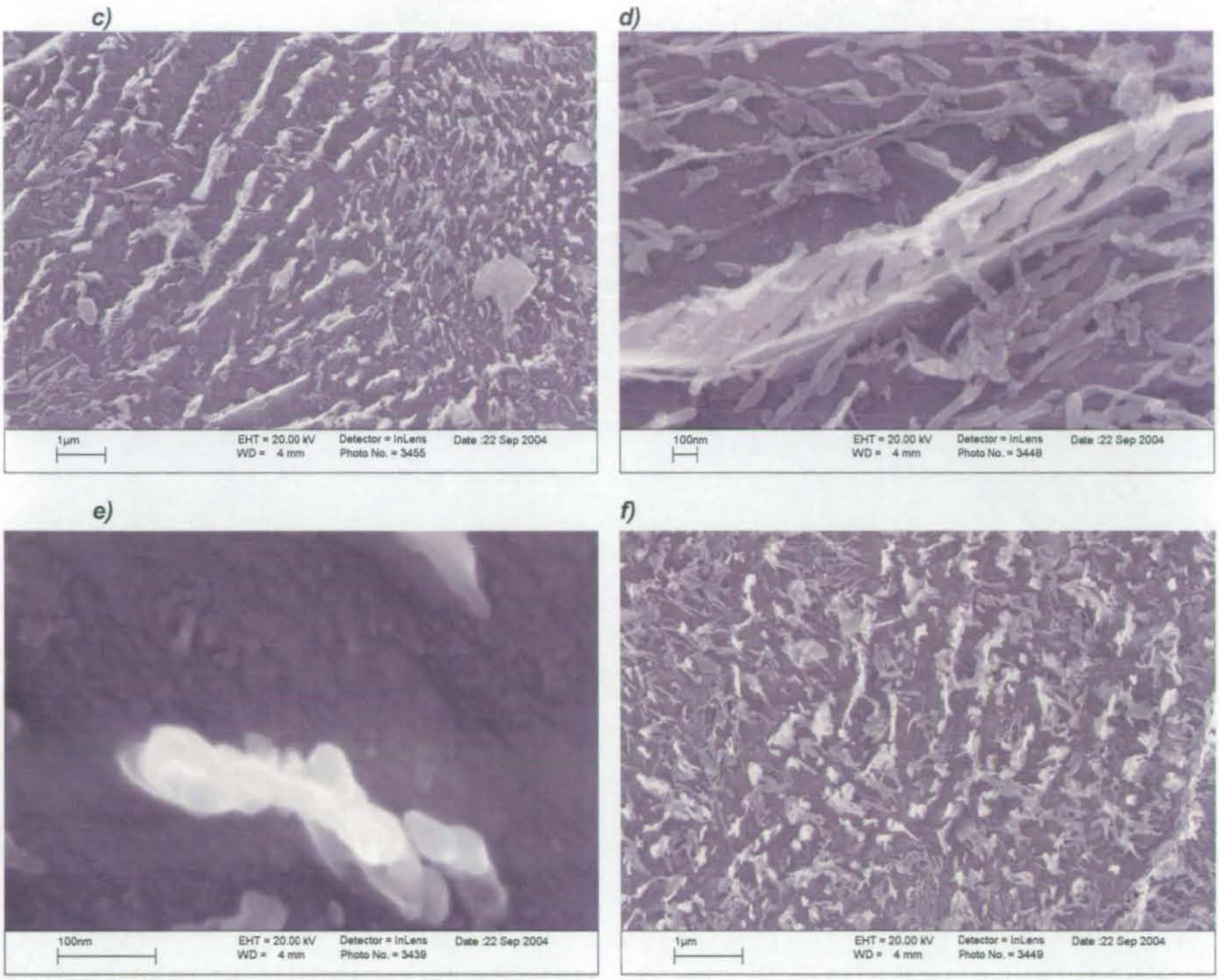

Figure 6.16: *Dilation curves for the ageing experiment 1300/10/6hrs at 200°C*

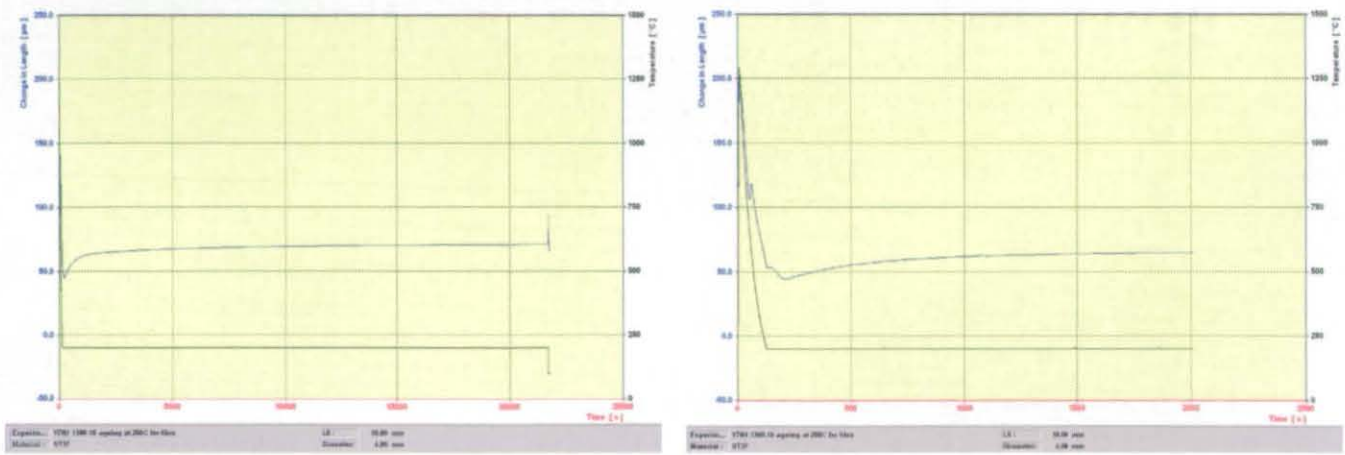

Figure 6.17a-d: *FCA morphologies of sample 1300/10/6hrs at 200°C observed by means of SEM*

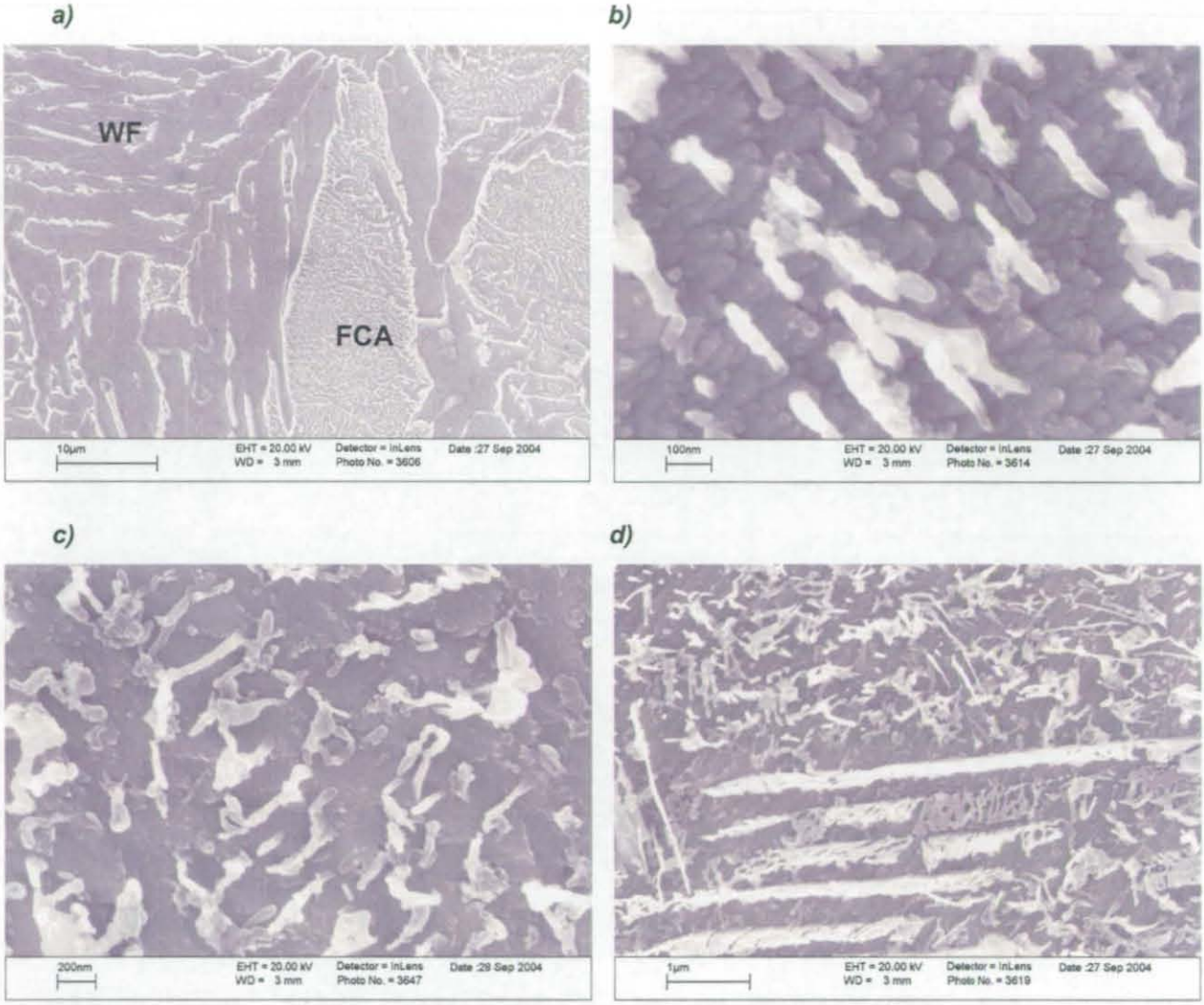

Figure 6.18: *Dilation curves for the ageing experiment 1300/10/9hrs at 200°C*

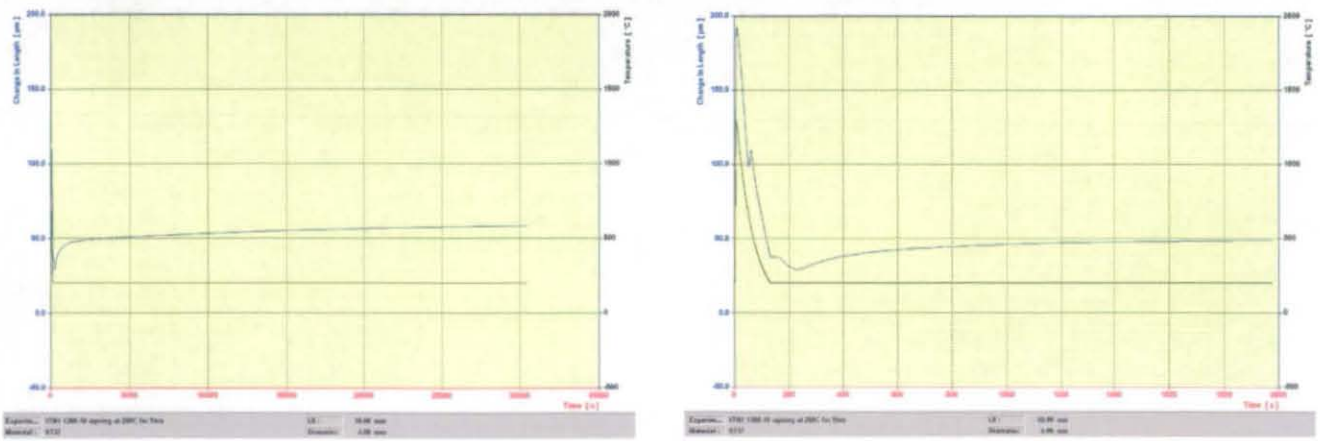

Figure 6.19a-d: *FCA morphologies of sample 1300/10/9hrs at 200°C observed by means of SEM*

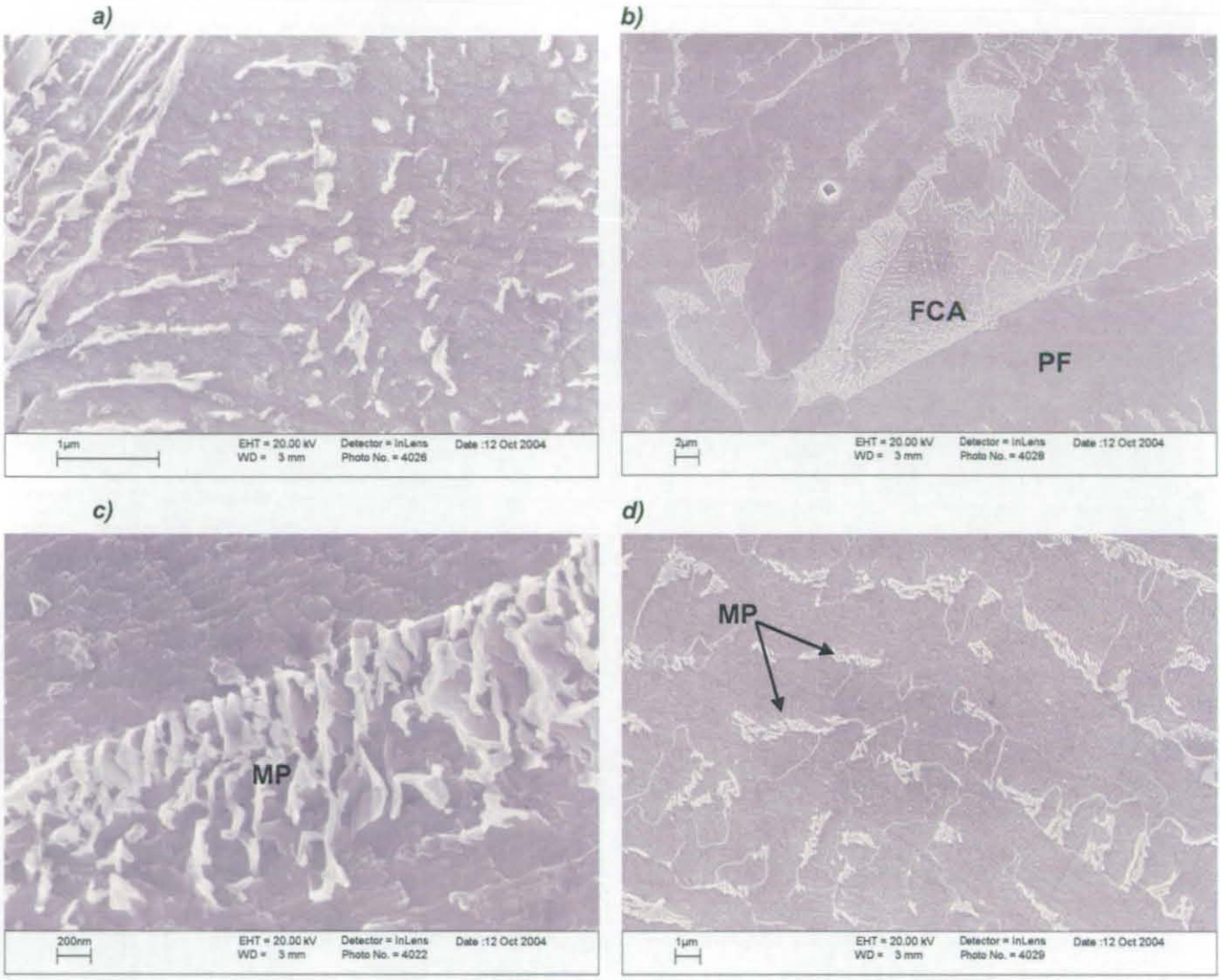

Increasing the ageing temperature to 400°C did not produce any considerable effect, as shown in figures 6.20, 6.21 and 6.23.

Figure 6.20a-b: *FCA morphologies of sample 1300/10/3hrs at 400°C observed by means of SEM*

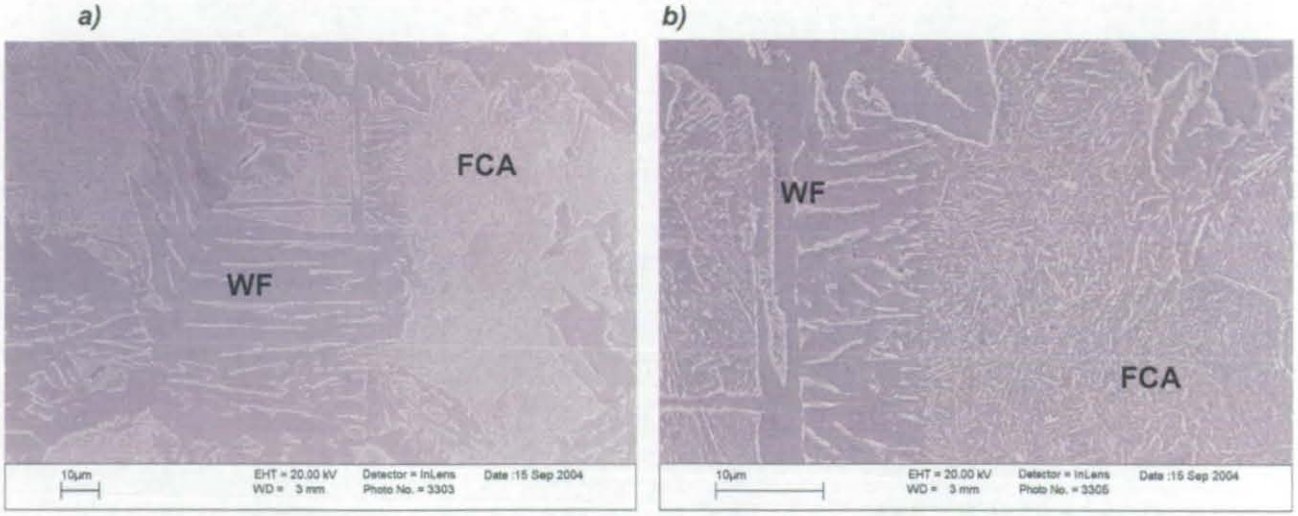

Figure 6.21a-b: *FCA morphologies of sample 1300/10/6hrs at 400°C observed by means of SEM*

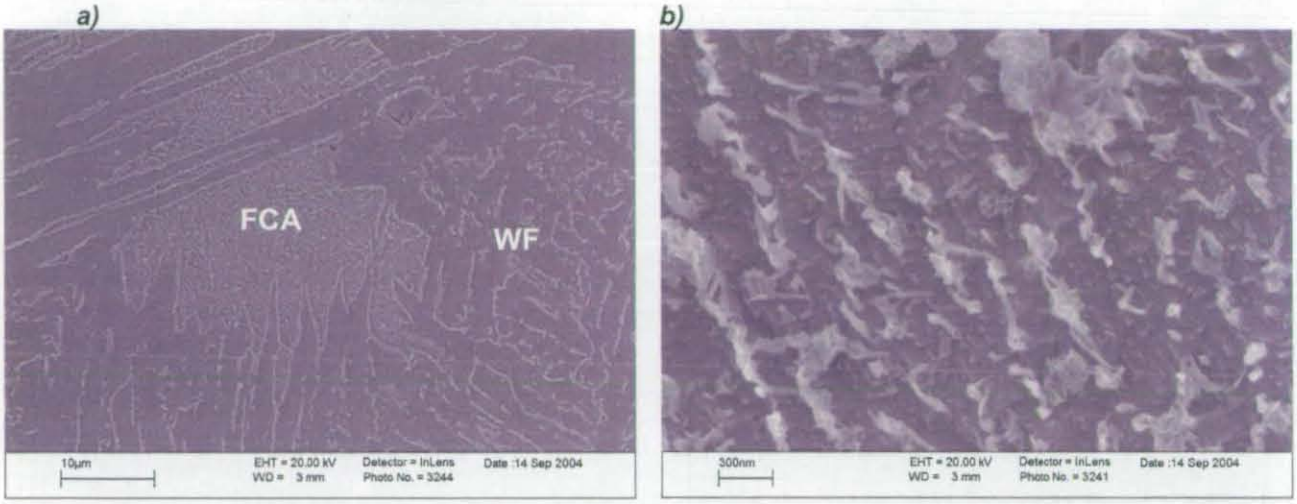

Figure 6.22a-f: *FCA morphologies of sample 1300/10/9hrs at 400°C observed by means of SEM*

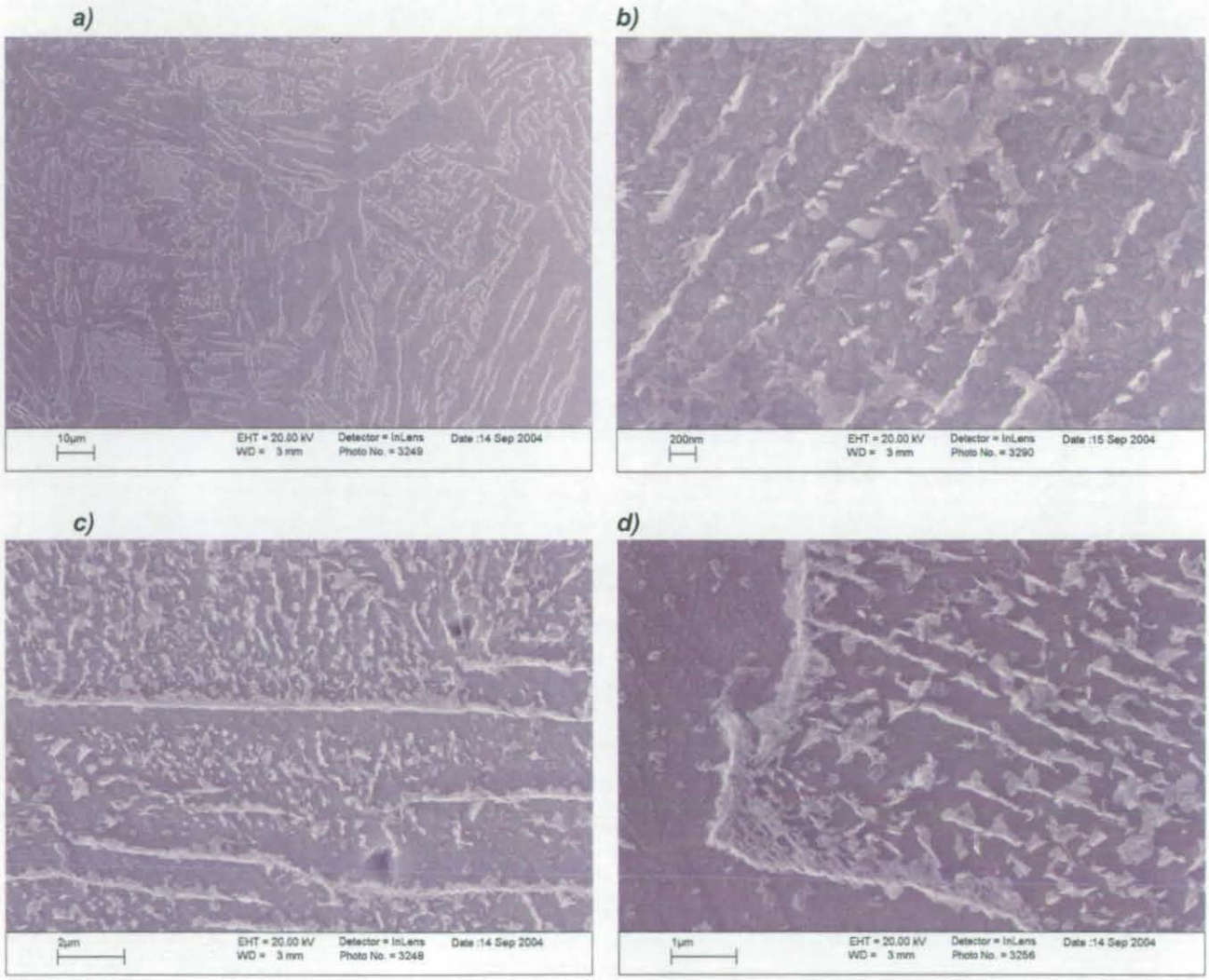

e)

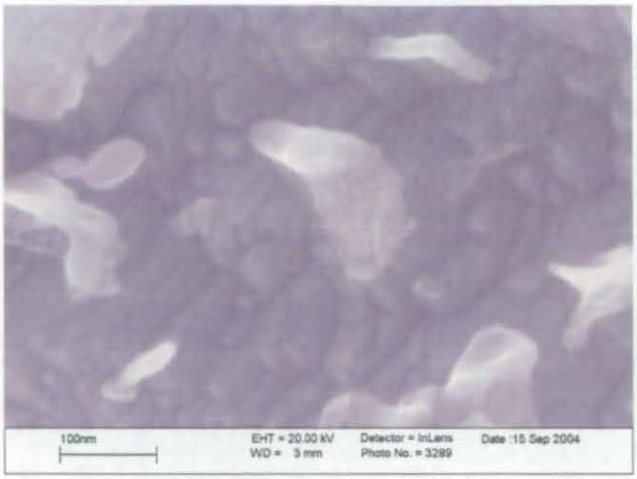

f)

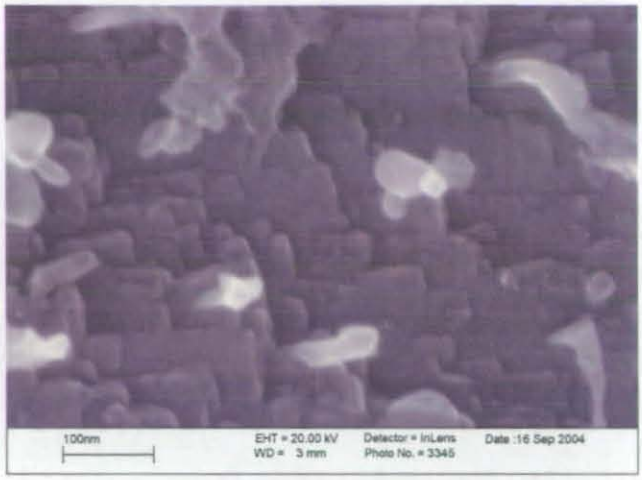

6.7 TEM Analysis

In order to obtain crystallographic information and accurate morphological characteristics of the FCA, transmission electron microscopy (TEM) has been performed on alloys Y7N1 and alloys HOM146 and HOM148. The results provided by TEM can be directly compared with the information obtained with SEM analysis and represent a means of validation of the latter.

6.7.1 Carbide Morphologies Observed in Thin Foils

The microstructural features observed in Y7N1 and shown in figures 6.23a-o are typical of the FCA observed by means of SEM. It can be seen that the small precipitates develop from the boundary of a grain and that a particular direction of growth can be identified. Furthermore, in order to differentiate the morphology of the FCA phase from the others, consistently with the SEM analysis, images of ferrite, Widmanstätten ferrite, bainite and pearlite, usually present in the same microstructures beside FCA, are shown in figures 6.23 and 6.24.

Figure 6.23a-o: *Thin foils TEM analysis, FCA structure*

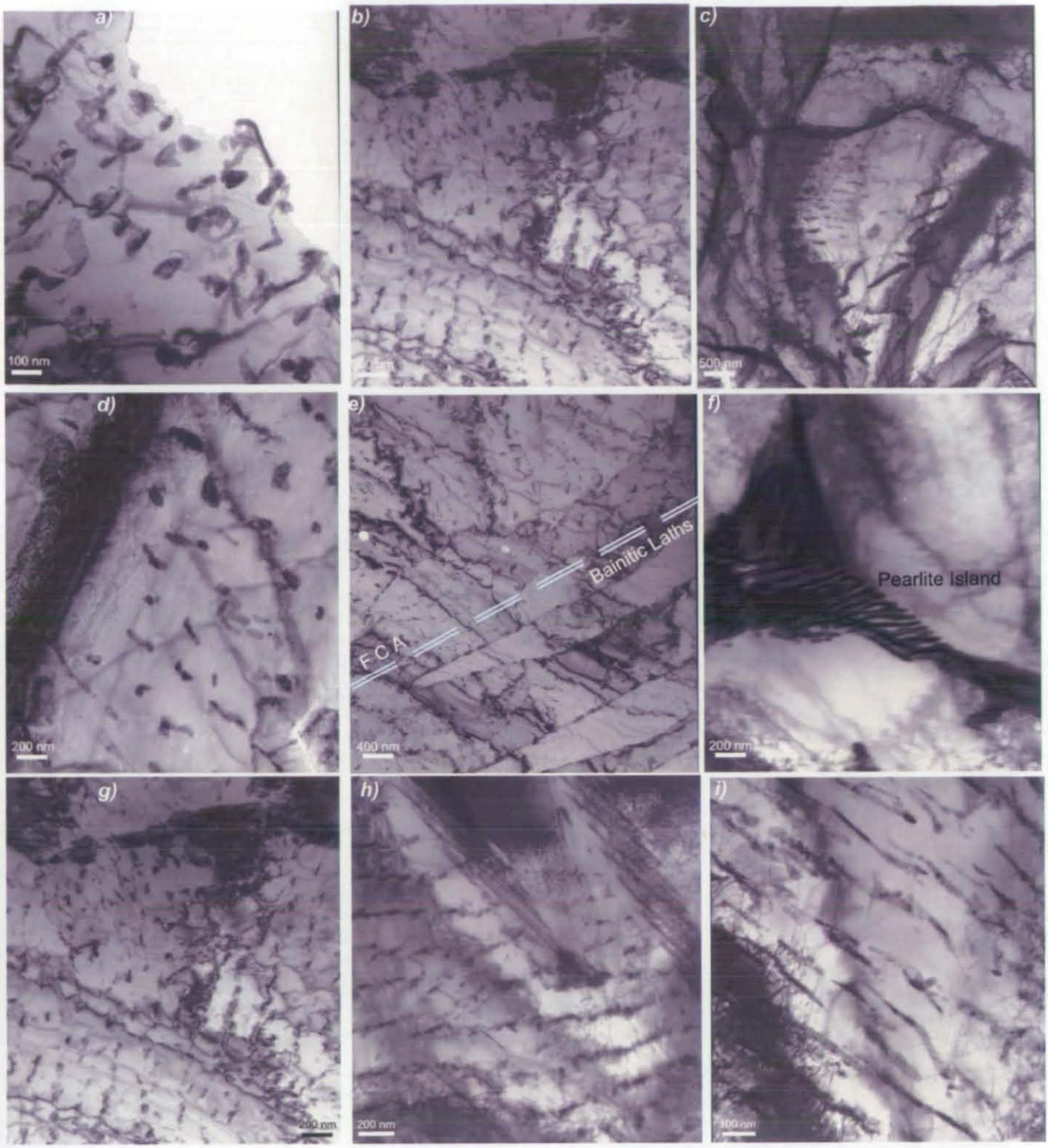

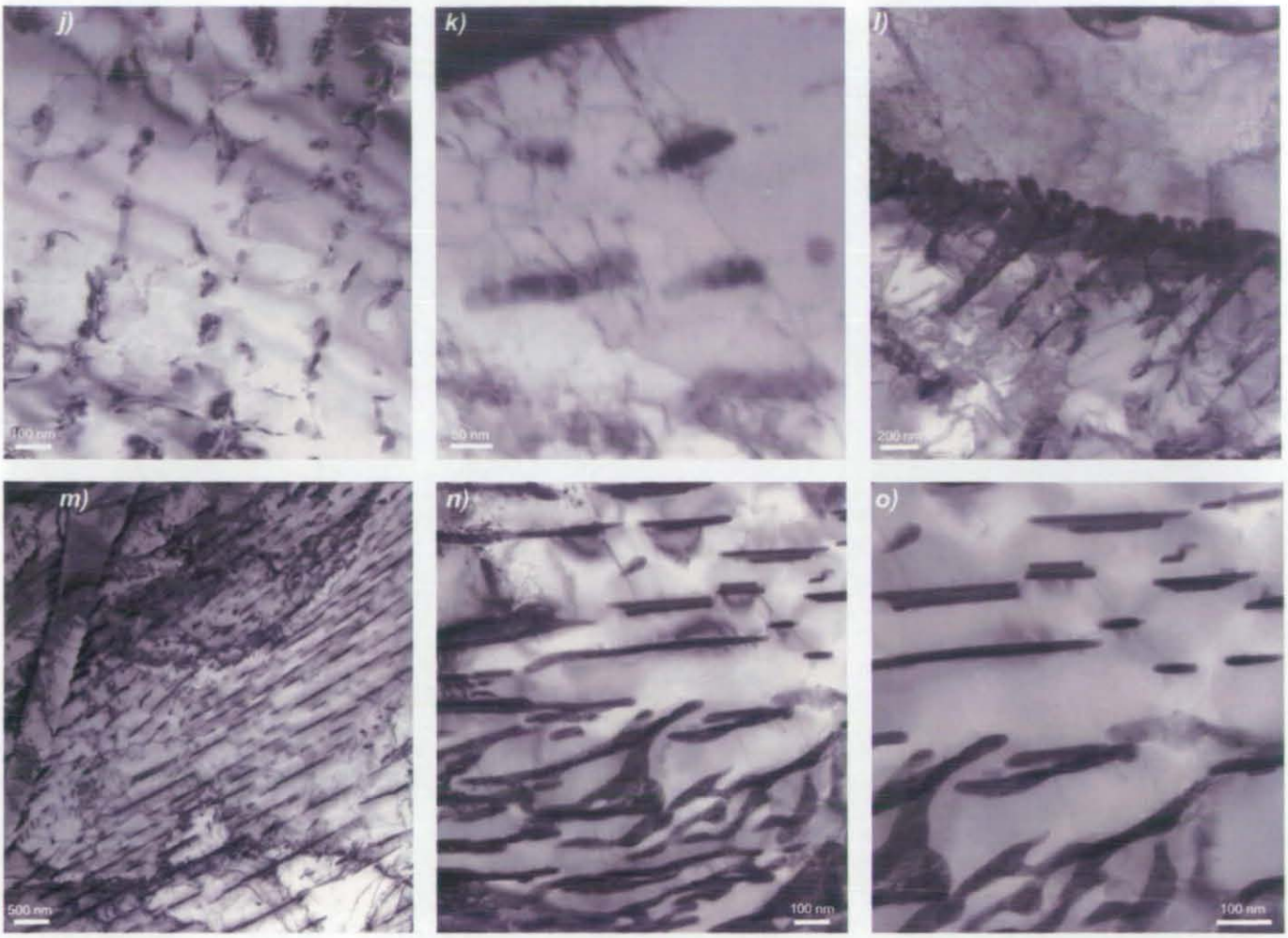

The images above (figure 6.23a-o) show in detail the morphology of the precipitates found in FCA regions, and are comparable to the previous SEM observations. The precipitates are usually distributed in arrays. The matrix appears to be ferritic and the presence of laths or sideplates is not visible. Additionally the lamellar structure of a boundary region and the subsequent break down in to particles can be seen.

Figure 6.24a-i: *Thin foil TEM analysis, pearlite, Widmanstätten ferrite and bainite structure*

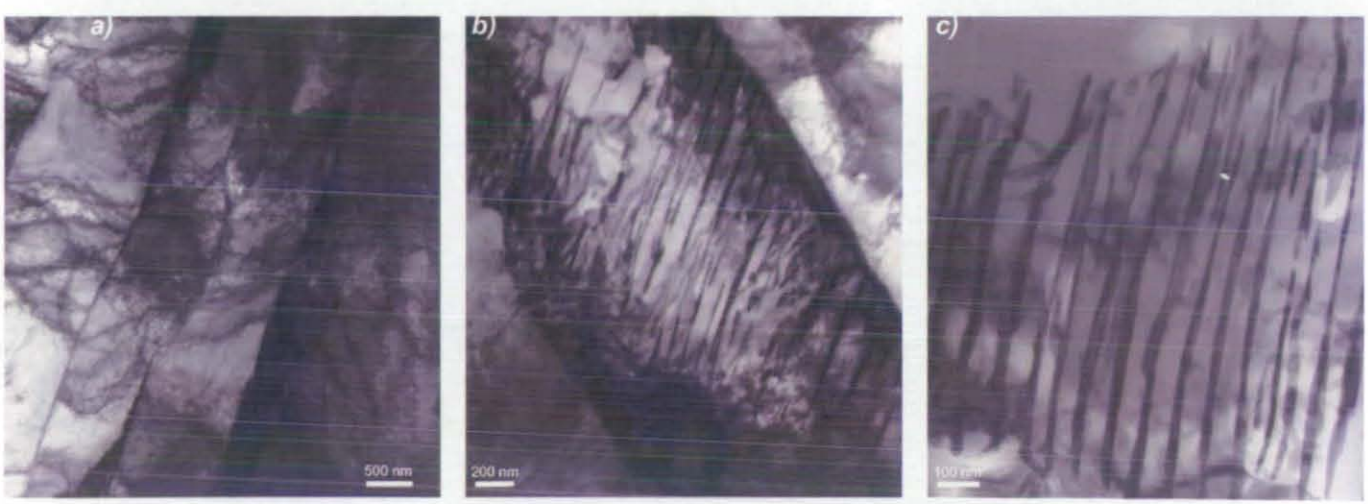

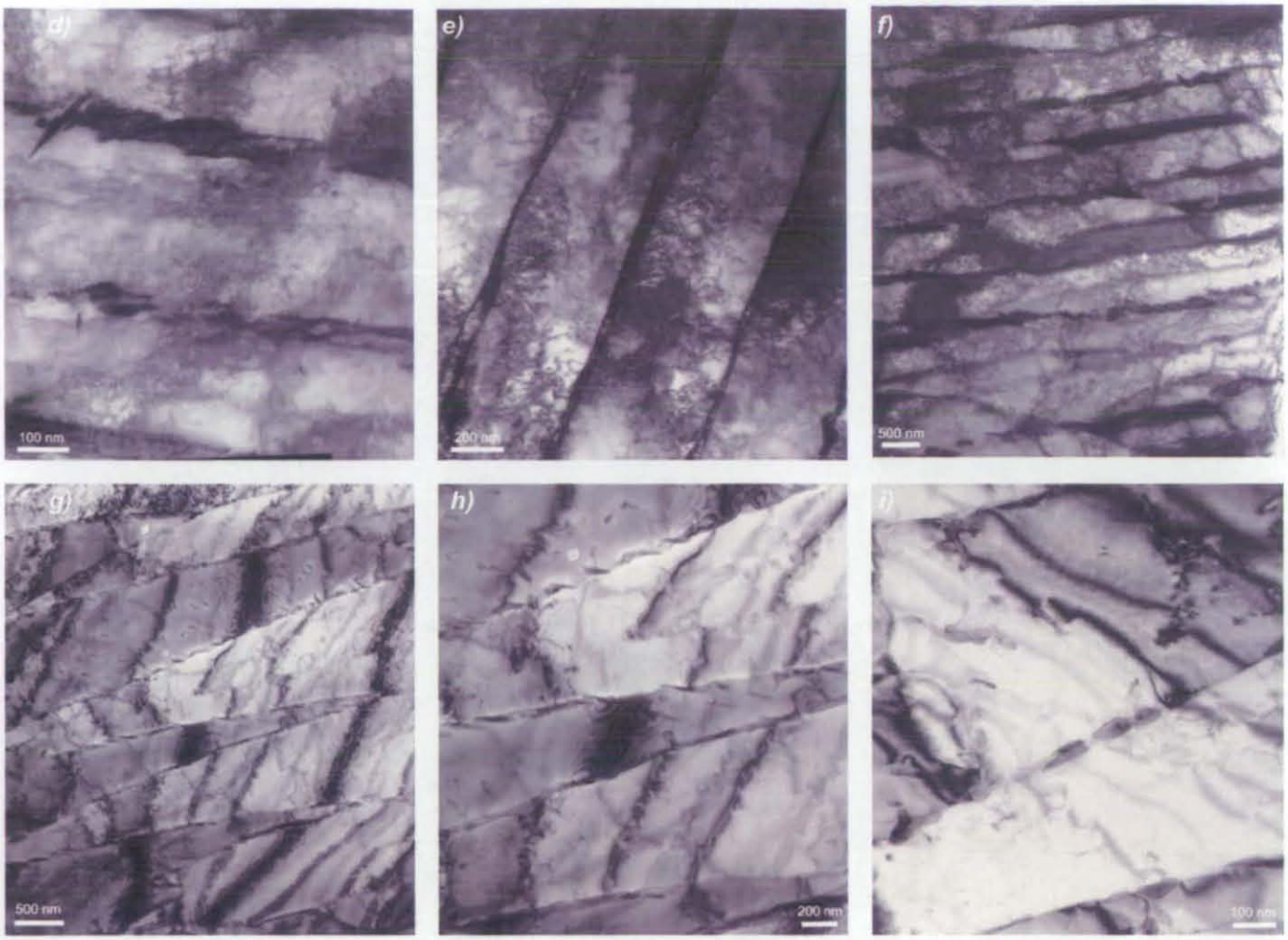

The lath structure of upper bainite can be observed in the micrographs shown above (6.24g-i). The presence of carbides between the ferritic plates, distinctive of upper bainite, has been identified. Finally, image 6.24a-f shows the larger ferrite sideplates and the microphase between them, characteristic of Widmanstätten ferrite. It is clear that the structure of these phases is completely different from FCA (alloy Y7N1 cooled at 10°C sec^{-1}).

Figure 6.25a-f: *Thin foils TEM analysis, microstructural features*

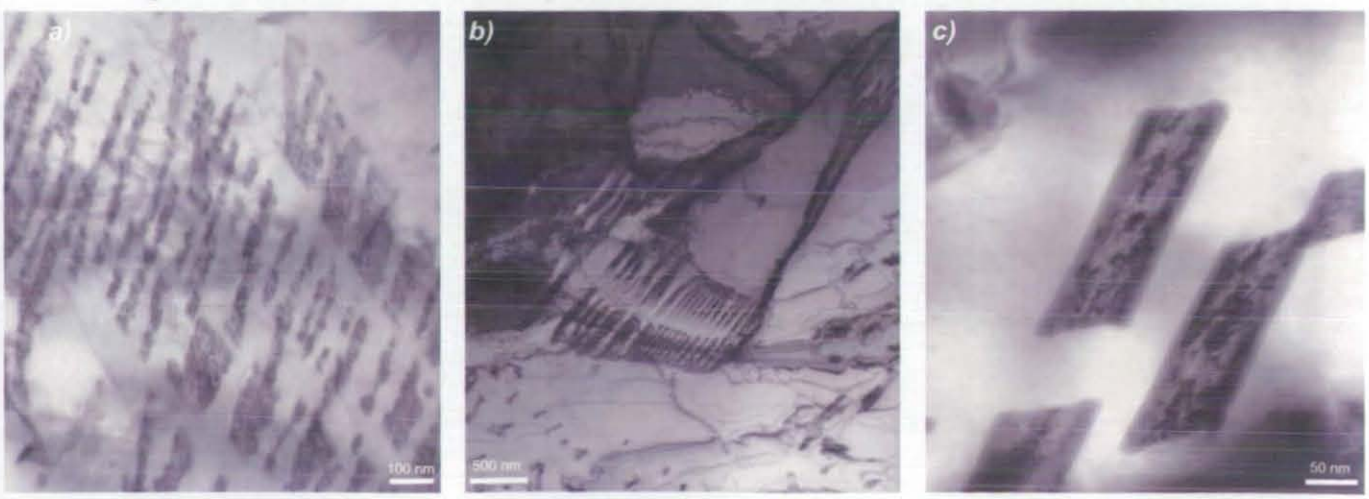

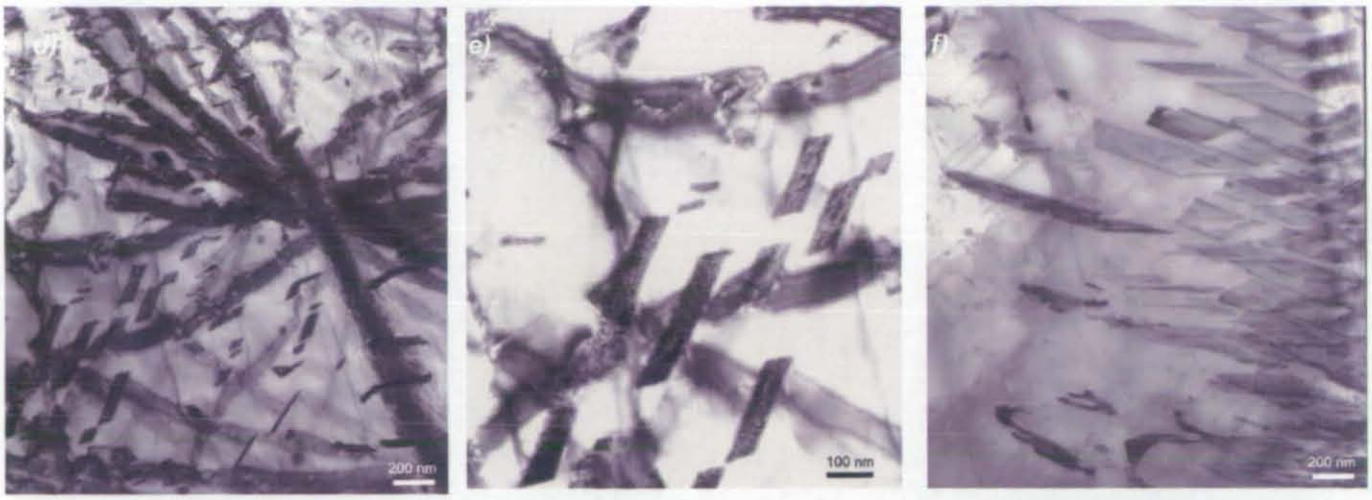

Their presence in the FCA regions is not systematic and they are usually distributed in small colonies within an FCA grain. Their shape can be irregular (figure 6.25a-b) or geometrically regular (figure 6.25c-f). The crystallographic analyses of these structures provided diffraction patterns, whose indexing was not possible in all cases apart from one, as there was no suitable symmetry which could help the identification of their nature. The only pattern that was indexed indicated that the nature was χ carbide. This appears to be very unlikely as this type of carbides has never been observed in such low carbon alloys treated under the conditions described previously. Nonetheless, they represent a fascinating aspect of phase transformation which could be further investigated. The main problem is represented by the fact that their formation appears to be a random process and the variables determining it have not been identified.

Finally, the extraction of the carbides present in an FCA region, showed that their morphology is directly comparable with that observed by means of SEM (figure 6.26).

Figure 6.26: *Comparison of FCA precipitate morphology observed by means of SEM (right) and TEM (left)*

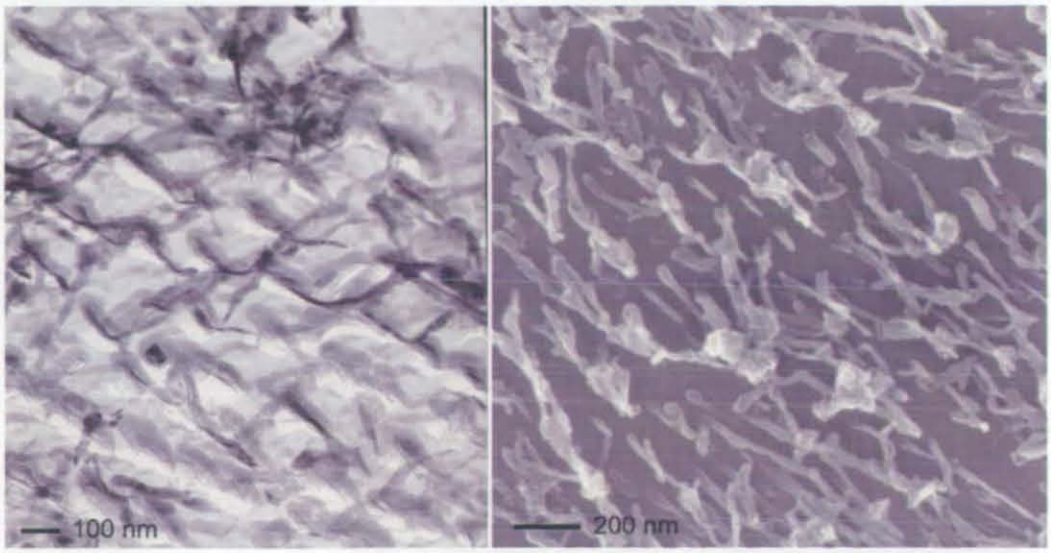

This evidence eliminates definitely the possibility of artefacts produced by etching and it confirms that the carbide structure observed by means of SEM is actual and real.

6.7.2 Matrix Analysis

Elemental analysis using EDX analysis on a thin foil TEM sample showed no significant difference between the composition of the matrix and the precipitates composition, indicating that the nature of the precipitate could be iron carbide or (Mn,Si,Fe) carbide.

Figure 6.27: *X-ray analysis of a FCA region*

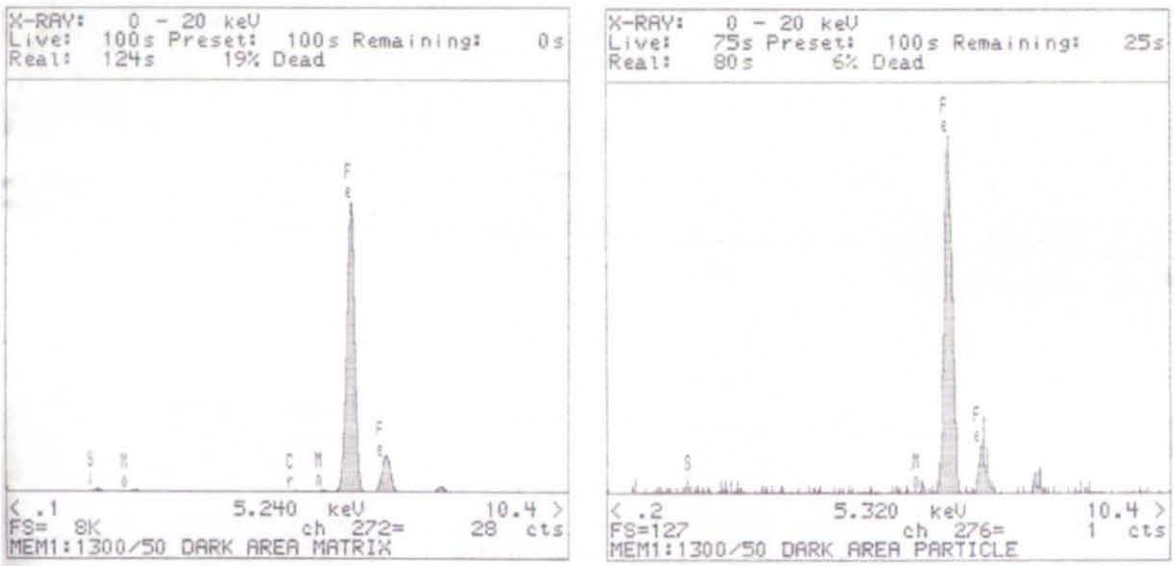

It was challenging to find an FCA region within the small area of the sample thinned by electropolishing. Additionally the fact that the thin foil samples were magnetic made tilting the very fine carbides to particular zone axes extremely difficult. However, all the patterns gathered from the matrix indicated that it was ferritic. The lattice parameter "a" was always found to be very close to that of pure BCC iron (0.02Å accuracy), which indicates that the matrix is not supersaturated with carbon. Two examples are shown in figure 6.29:

Figure 6.29: *Thin foils TEM analysis, FCA matrix patterns*

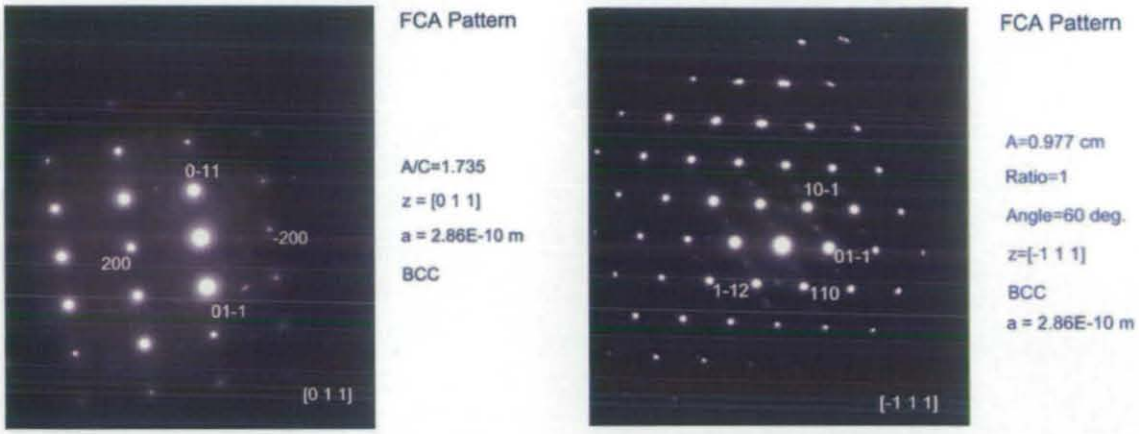

6.7.3 Carbide Morphologies Observed on Replicas

Carbon extraction replicas were used in order to eliminate the magnetic matrix in order to get good diffraction patterns from the precipitates. However, this task proved to be quite challenging as the carbides were difficult to extract and a compromise had to be found between the solution used for extraction, the etching time and the extraction time. Extraction of replica's was performed on alloys Y7N1, HOM146 and HOM148, presuming that the nature of the second phase in the three alloys should be the same. The morphology of the carbides extracted from the three alloys is shown in figure 6.30a-l and 6.31a-e. It can be seen that all the main carbide morphologies previously identified by means of SEM, have been observed: small particles, fibres, branched precipitates and finally partially interconnected tadpole-shaped particles:

Figure 6.30a-j: *TEM carbon replicas; morphologies observed in alloys HOM146 and HOM148*

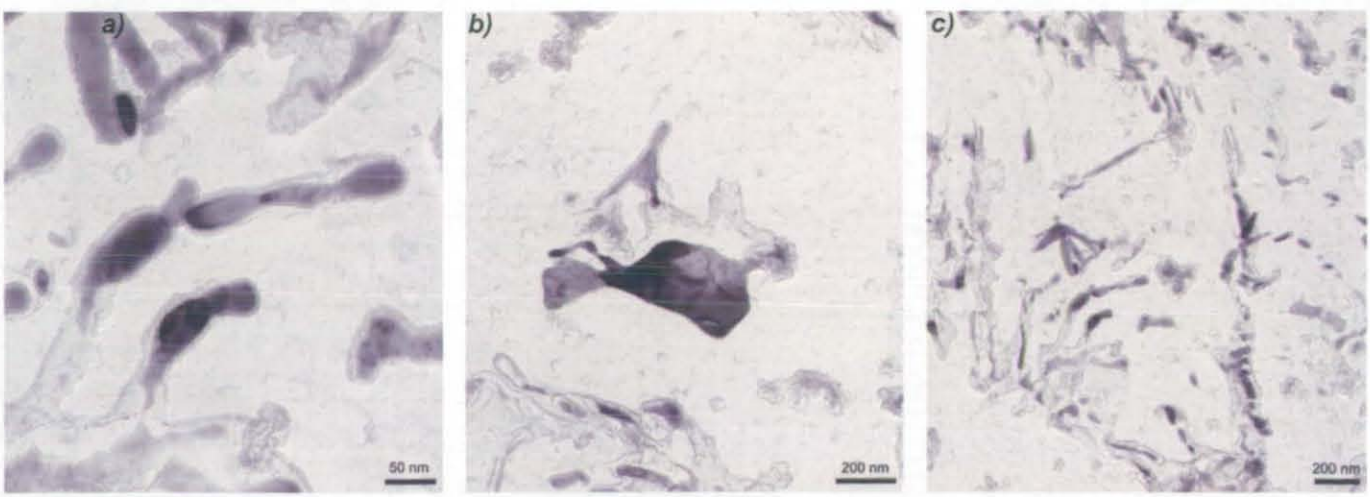


d)
200 nm

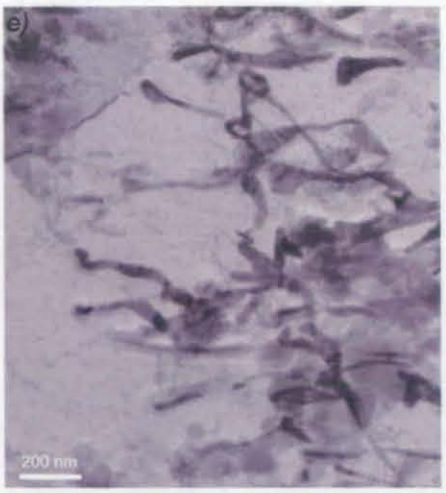
e)
200 nm


f)
50 nm

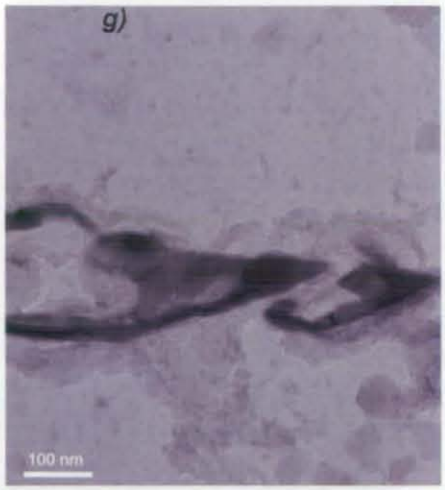
g)
100 nm

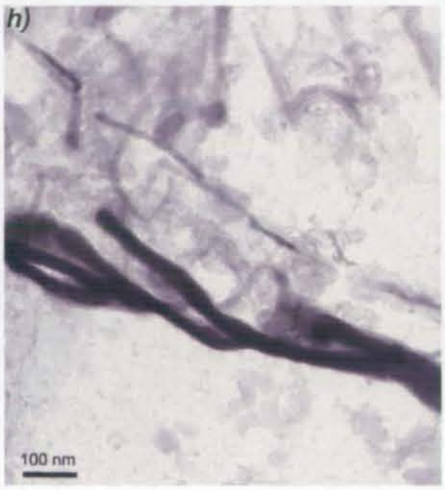
h)
100 nm

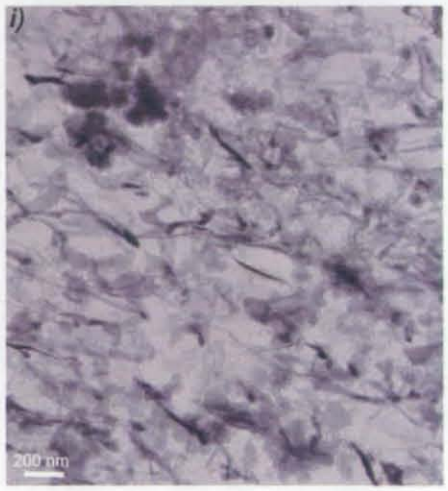
i)
200 nm

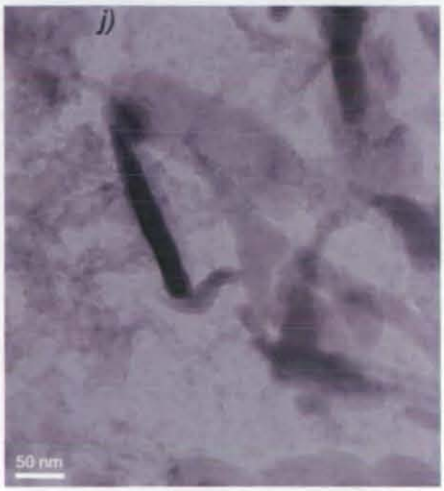
j)
50 nm

Figure 6.31a-e: *TEM carbon replicas. Morphologies observed in alloy Y7N1*

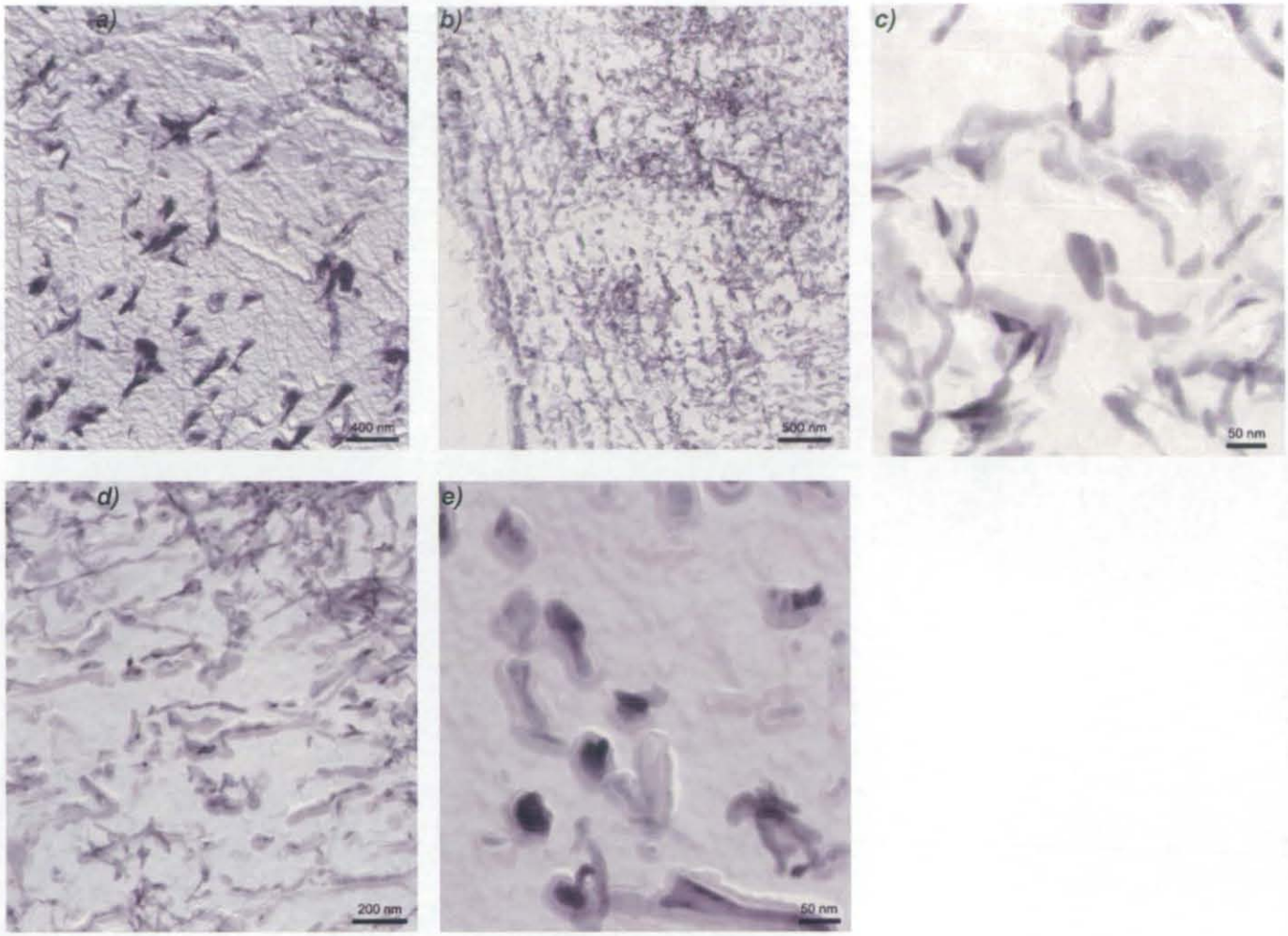

6.7.4 Electron Diffraction Patterns

Once the precipitates were extracted and analysed in most cases the patterns were indexed as being cementite. However, in some cases a positive identification could not be achieved. Furthermore, the carbides present in samples cooled at higher cooling rates (i.e. 50°C s^{-1}) did not provide good patterns when they were found in the form of interconnected particles or with "tadpole" shape as their dimensions were too small and they were too close to each other, so that the resulting patterns were too faint or contained overlapping refractions. The crystallographic analysis suggests that the precipitates are iron carbides, being cementite in most cases, although in some instance they could not be identified, most probably because the precipitates were not stoichiometric. Examples of the patterns found for the precipitates are shown in figure 6.32a-f.

Figure 6.32a-f: *FCA precipitate patterns obtained from carbon replicas*

a)

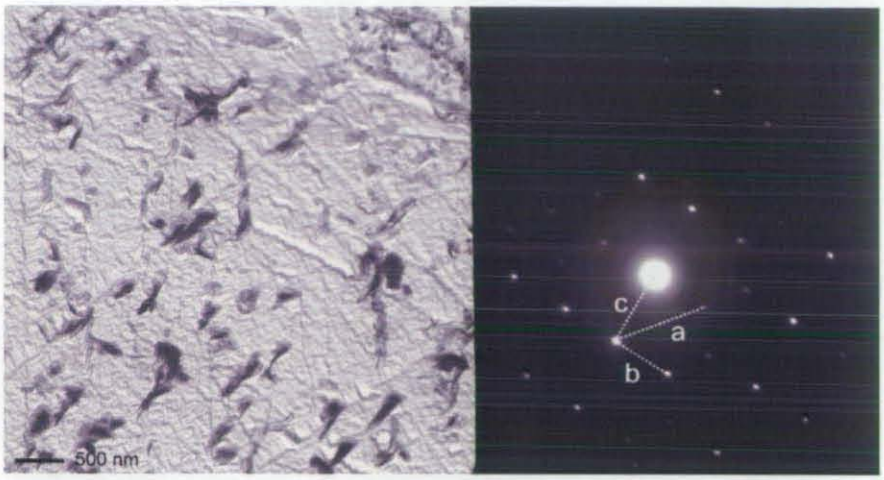

Y7N1

a = 1.65 A

b= 2.67 A

c= 2.067 A

Cementite Solution:

z = [-4 -3 2]

b)

HOM146

a = 1.81 A

b = 3.31 A

c = 2.75 A

Solutions found for cementite.

z = [-2 -2 1]

c)

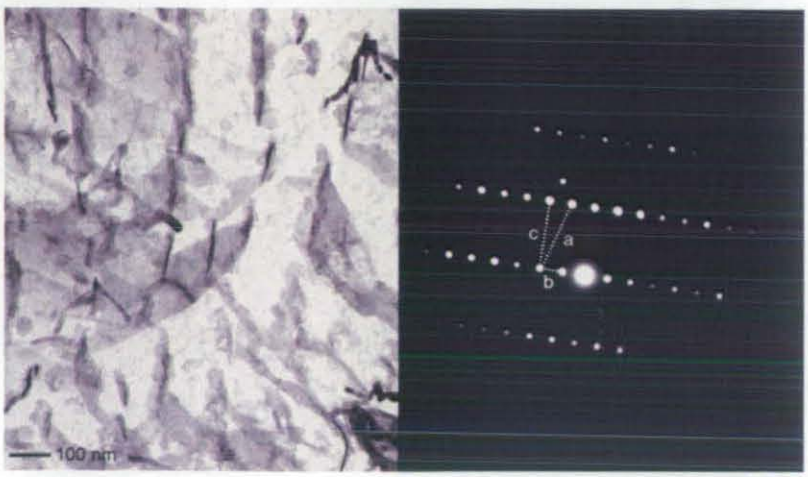

Y7N1

a = 2.07 A

b = 6.7 A

c = 2.19 A

Solutions found for cementite.

z = [2 1 0]

d)

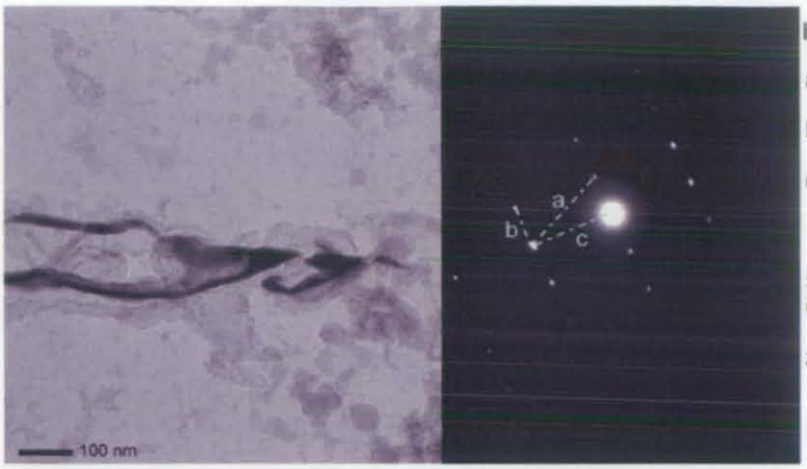

HOM146

a = 1.62 A

b = 3.67 A

c = 1.84 A

Solutions found for cementite.
Only for vector pairs a-b and b-c

z = [-2 -3 2]

e)

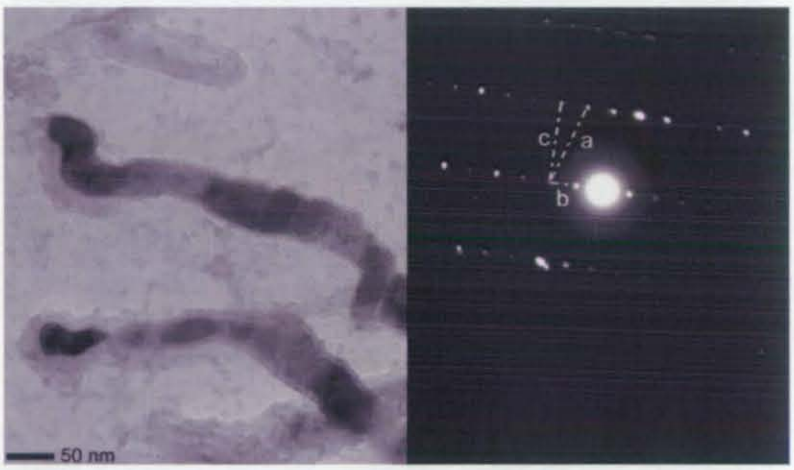

HOM148

a = 2.07 A

b = 6.61 A

c = 2.12 A

Solutions found for cementite.
Only for vector pairs a-c and a-b

z = [-2 -1 0]

f)

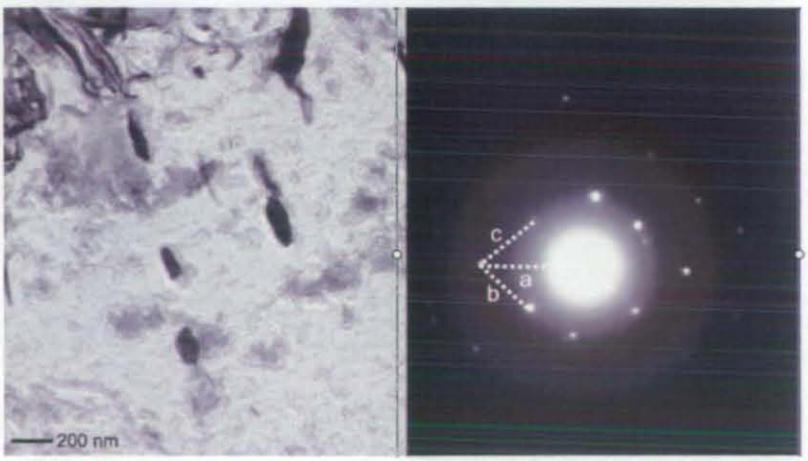

a = 1.37 A

b = 2.48 A

c = 1.98 A

No common solutions found
for the three vectors

6.8 EBSD Analysis

Electron back scattered diffraction (EBSD) was carried out to assess the orientation of the FCA regions and therefore the characteristics of the phase transformation. The TEM investigations indicated that the FCA matrix had a BCC structure; additionally, neither SEM nor TEM provided any evidence of the presence of laths within the FCA grains. Furthermore, micro-hardness data supported the hypothesis of a soft phase forming via a diffusion-based mechanism. The FCA developed across a wide range of cooling rates (between 5 and 75°C s^{-1}), and therefore the EBSD investigation was aimed at the following:

- the analysis of samples cooled at 10°C s^{-1}, containing the highest volume fraction of FCA;
- the analysis of samples cooled slowly (e.g. at 5°C s^{-1}), in order to have a means of comparison with the characteristics of pearlite;
- the analysis of samples cooled at higher cooling rates in order to compare FCA with phases whose formation mechanism involves displacive transformations, such as martensite and bainite.

Each EBSD analysis involved the determination of orientation maps for a specific region of the sample. These regions were subsequently imaged by means of SEM (InLens detection) and optical microscopy in order to assist and facilitate the identification of microstructural features of interest on the EBSD maps.

Analysis of samples cooled at 10°C s^{-1}

The areas of the sample cooled at 10°C s^{-1} consisted of primary ferrite, Widmanstätten ferrite, observed with aligned microphase in addition to end on, small pearlite islands and FCA regions. In the IPF map (local orientation distribution), the FCA regions appeared as individual grains, characterised by a uniform orientation along them. This is a common characteristic for phases formed reconstructively, such as primary ferrite, in which no evidence could be found of the presence of laths.

Figures 6.33, 6.34 and 6.35 show respectively the IPF map for alloy Y7N1 1300/10, the scanned area imaged by means of SEM and the scanned area analysed optically, superimposed to the IPF map.

Figure 6.33: *IPF map for alloy Y7N1 1300/10, the FCA regions showed a homogeneous orientation along a single grain.*

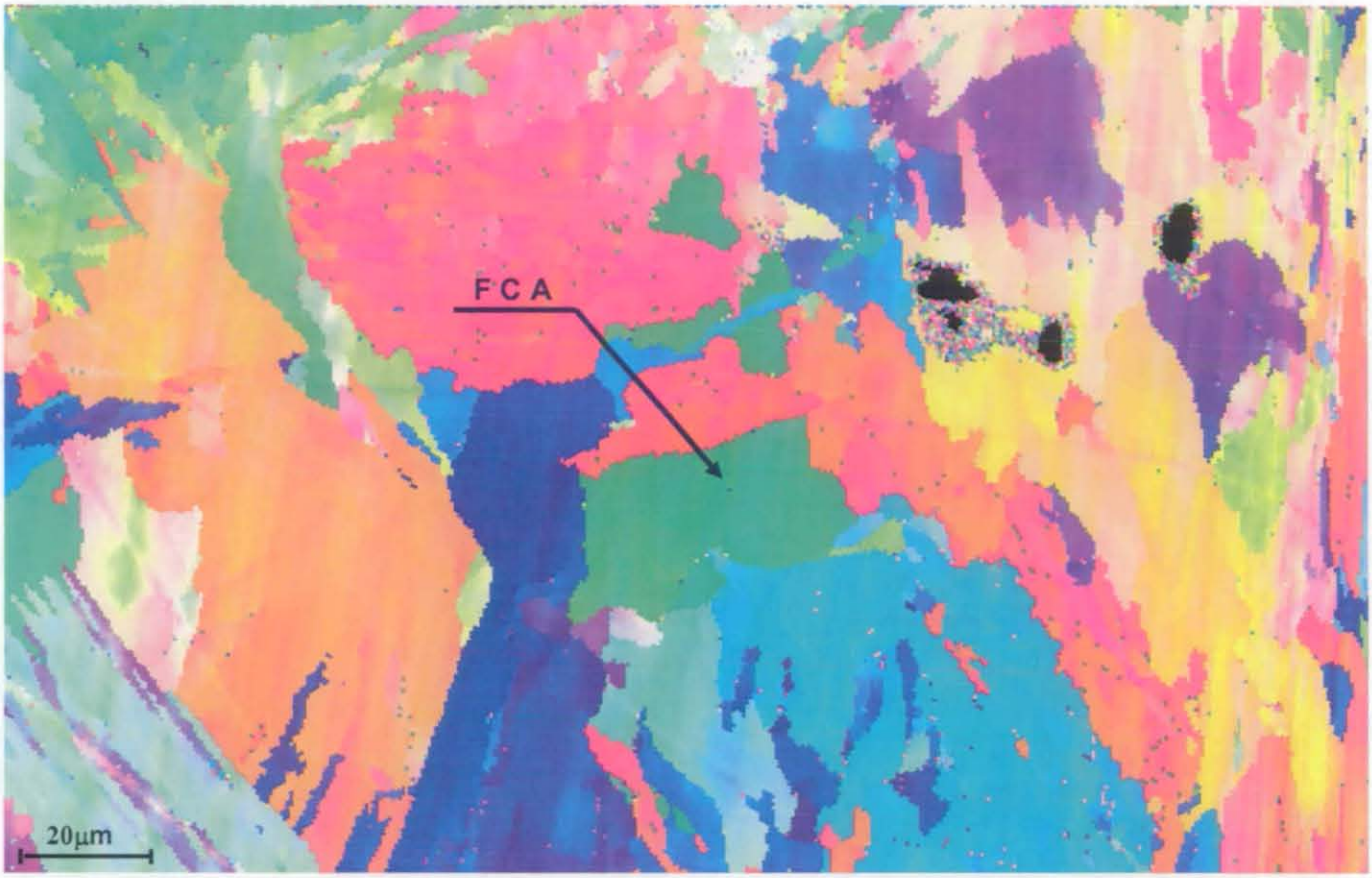

Figure 6.34: *SEM montage of the area analysed in sample Y7N1 1300/10*

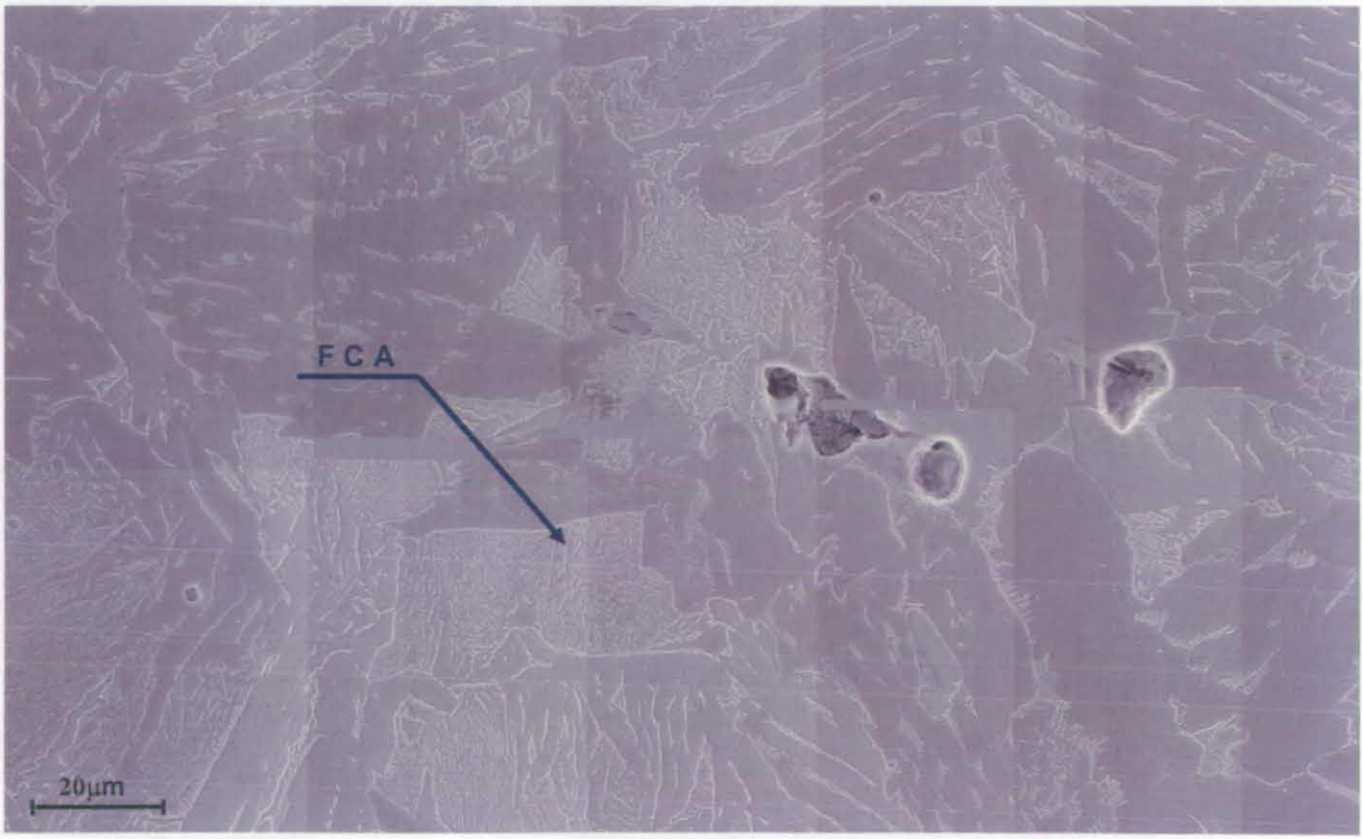

Figure 6.35: *IPF map superimposed on the area analysed in sample Y7N1 1300/10, observe optically*

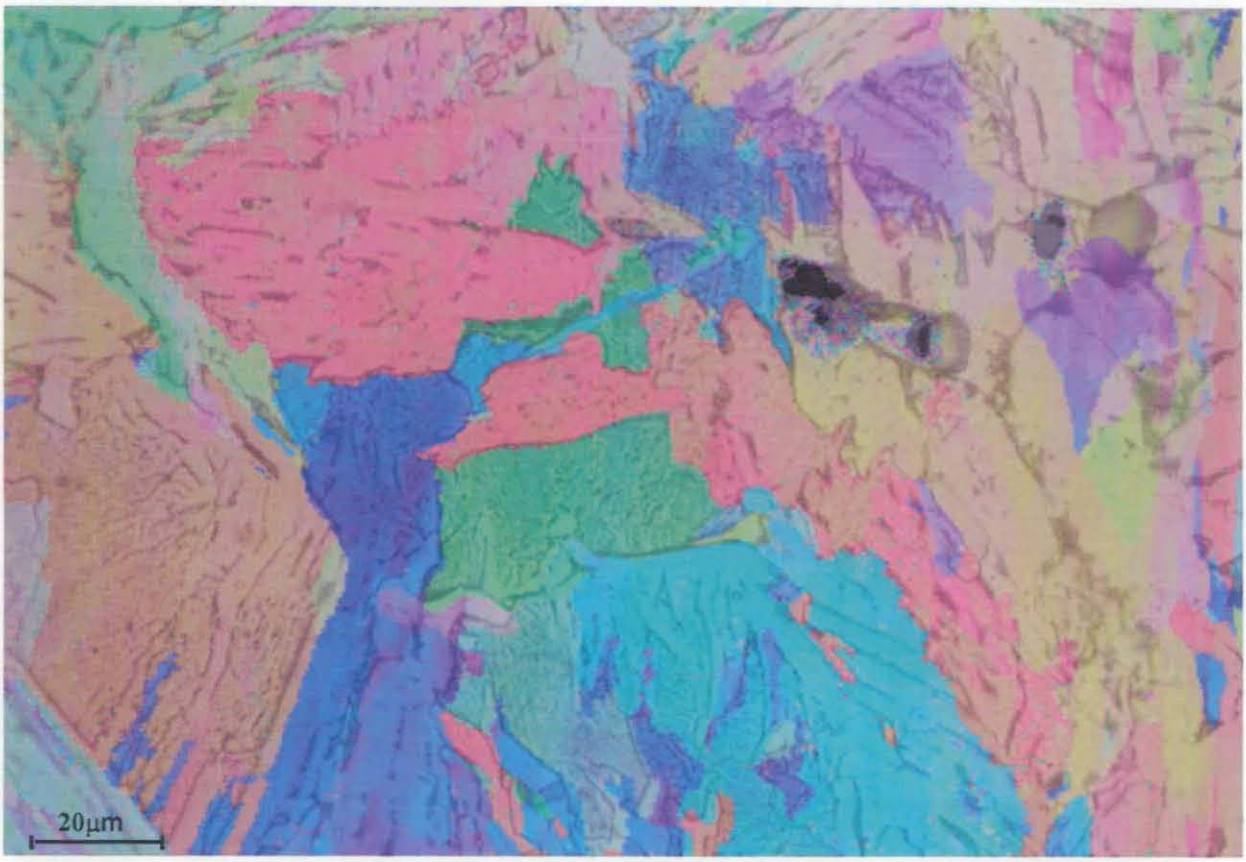

In figures 6.33 and 6.34 an FCA region is highlighted. The orientation (coloured in green) is uniform throughout the entire grain. The grain is distinct from all the adjacent ones and has an individual orientation.

Figures 6.36, 6.37 and 6.38 show the IPF map of a region of sample Y7N1 1300/10int.at587°C, the same region imaged by means of SEM and the superimposition of the area scanned with the IPF map respectively.

Figure 6.36: *IPF map for alloy Y7N1 1300/10int.587°C*

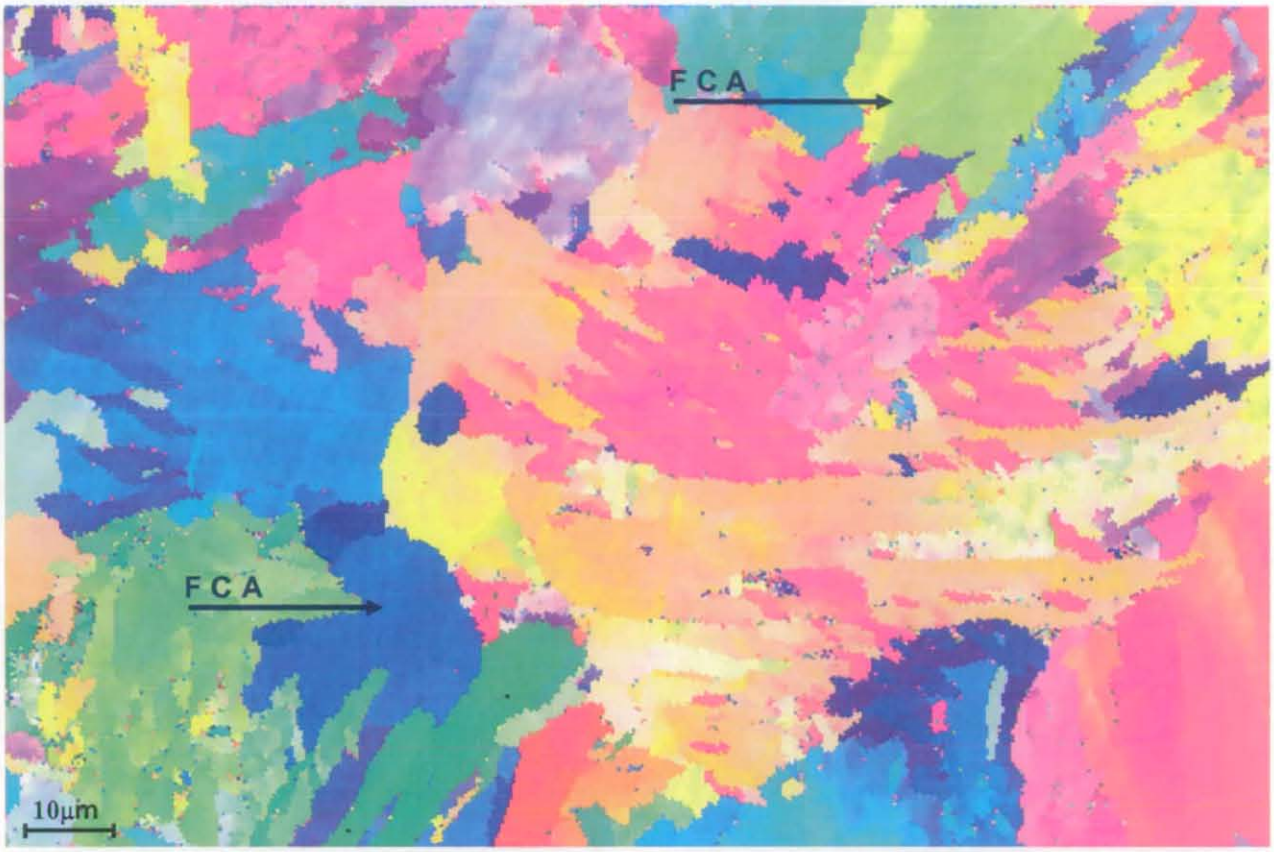

Figure 6.37: *SEM montage of the area analysed in sample Y7N1 1300/10int587°C*

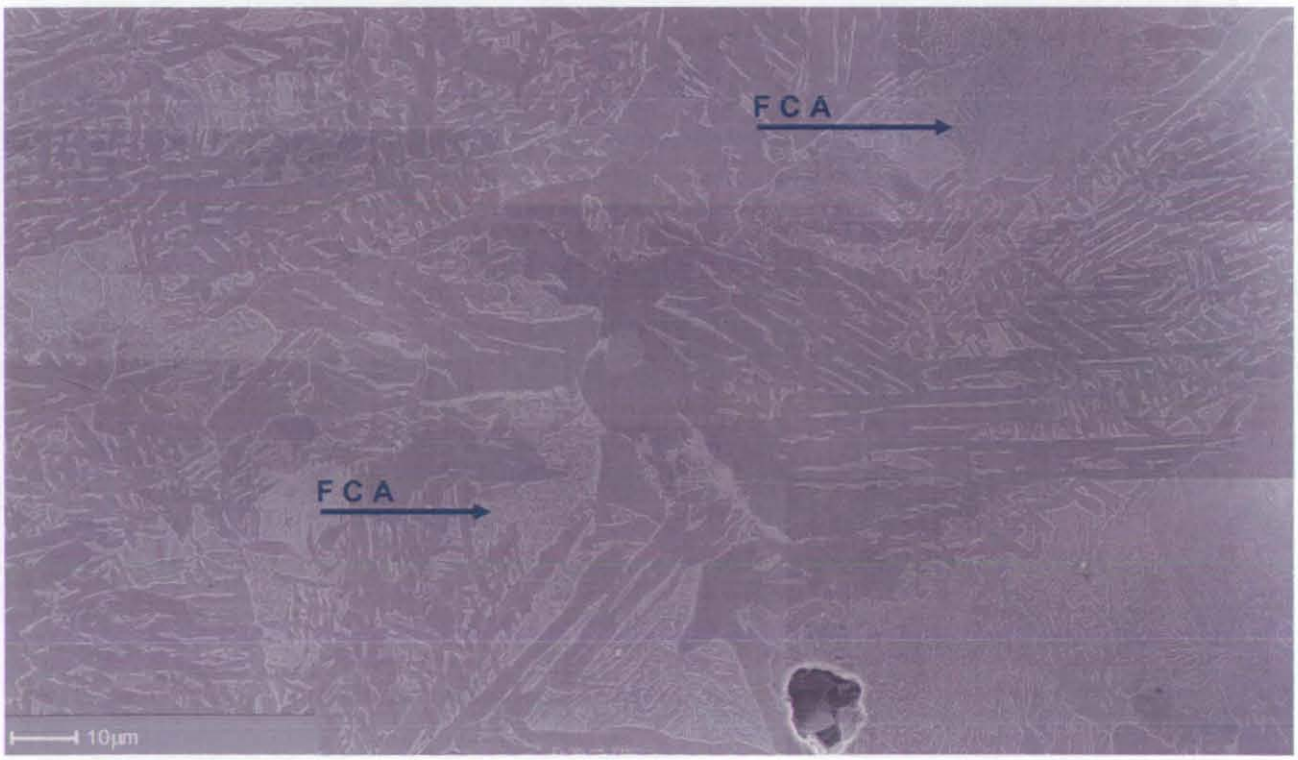

Figure 6.38: *IPF map superimposed on the SEM montage of sample Y7N1 1300/10int.587°C*

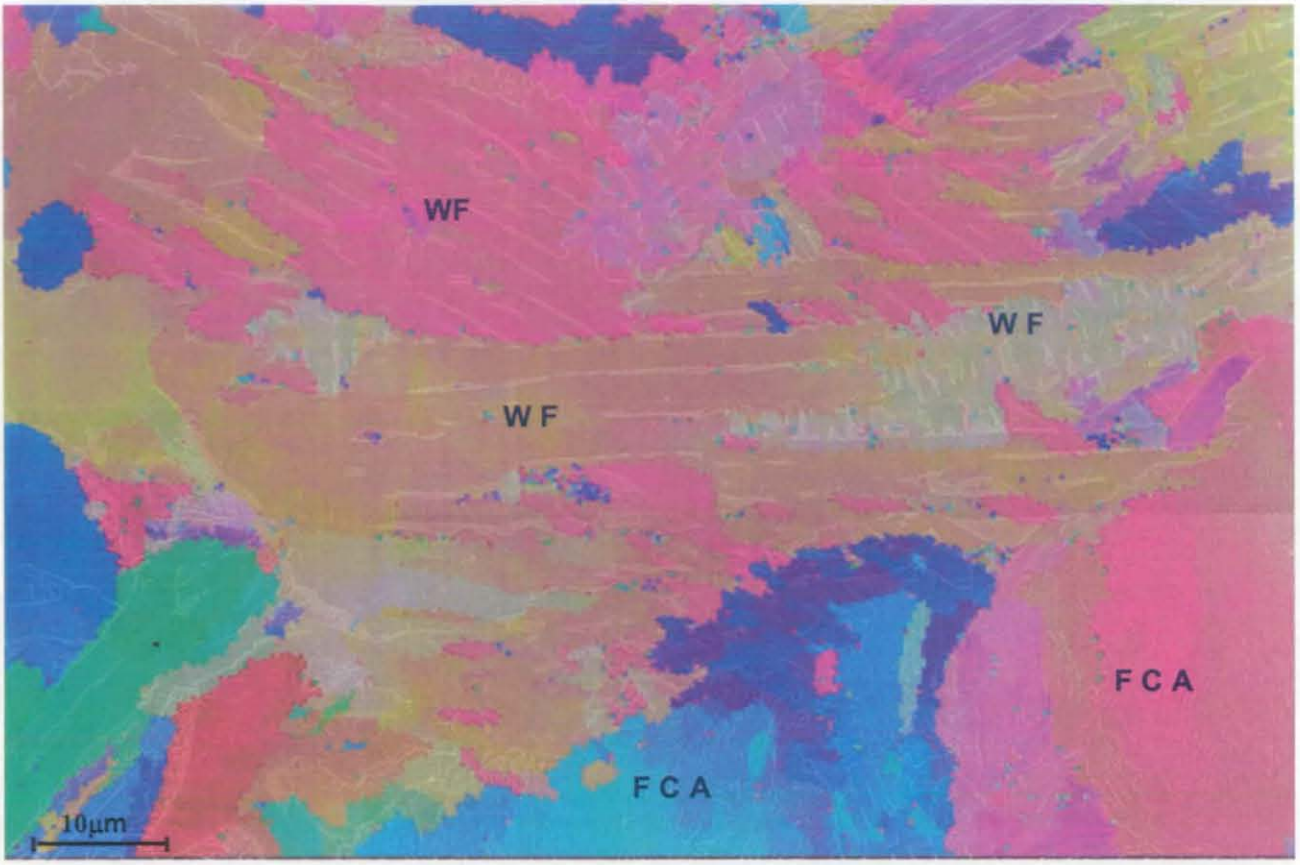

In most FCA grains, a preferred precipitation direction can be identified. As indicated by the results of high-magnification SEM investigations, the second phase nucleates at the boundaries, and then the precipitation follows a specific direction along the grain. If nucleation occurs at two different sites of a prior austenite grain, the precipitation will subsequently occur along two different directions which will eventually meet within the same grain. When this occurs, a *boundary* is created within an FCA grain, with varying dimensions and appearance. The dimensions and appearance of this type of boundary can vary. Their nature is not well understood and their morphology appears to be peculiar. An example of a boundary found within an FCA grain is shown in figures 6.39a and b. The orientation analysis of an FCA grain in which such a boundary was present, showed evidence of a slight change in orientation at the boundary, hence corresponding to the change in precipitation direction. As discussed in greater detail at the end of this section, this type of boundary has been classified as a low-angle grain boundary.

Figure 6.39a: *Orientation change in FCA phase; this depends on the precipitation direction*

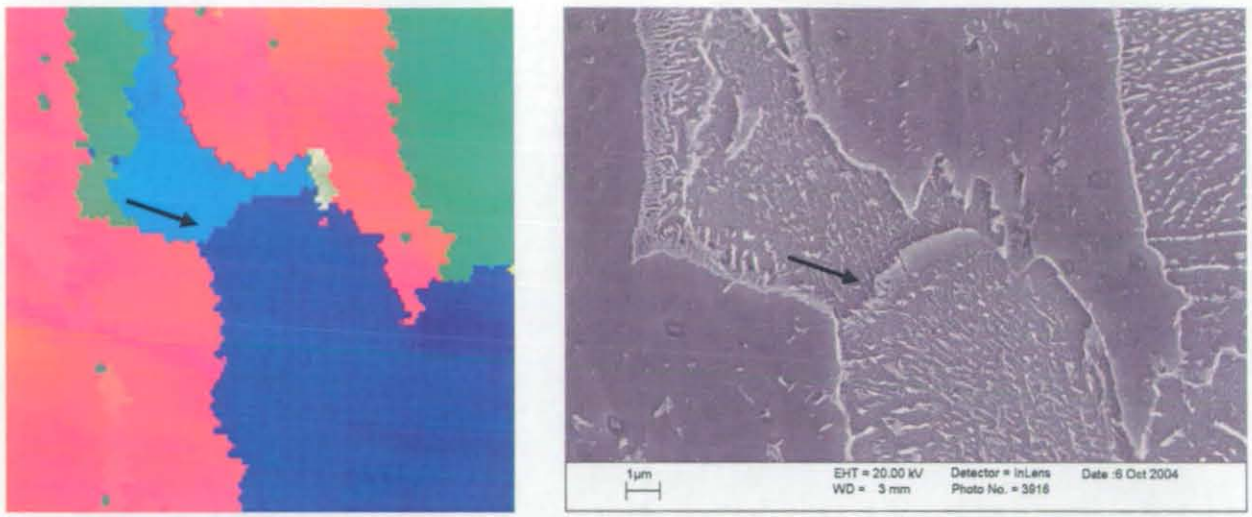

Figure 6.39b: *Morphology of a boundary within an FCA grain*

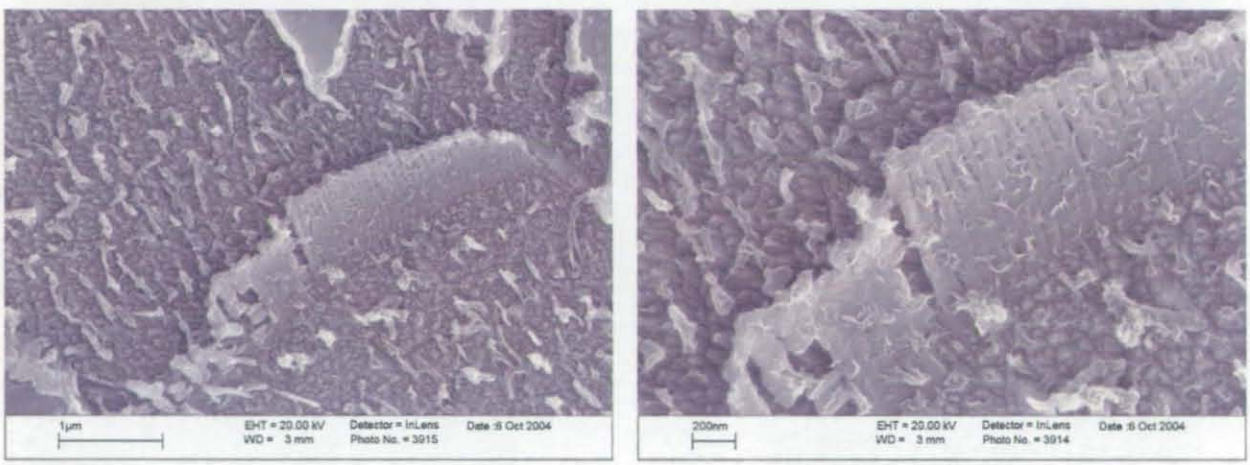

The micrographs above clearly show the unusual structure of the boundary present within the same FCA grain, corresponding to a change in precipitation direction (and therefore growth direction of the transformation front).

Figure 6.40: *Comparison between FCA and pearlite*

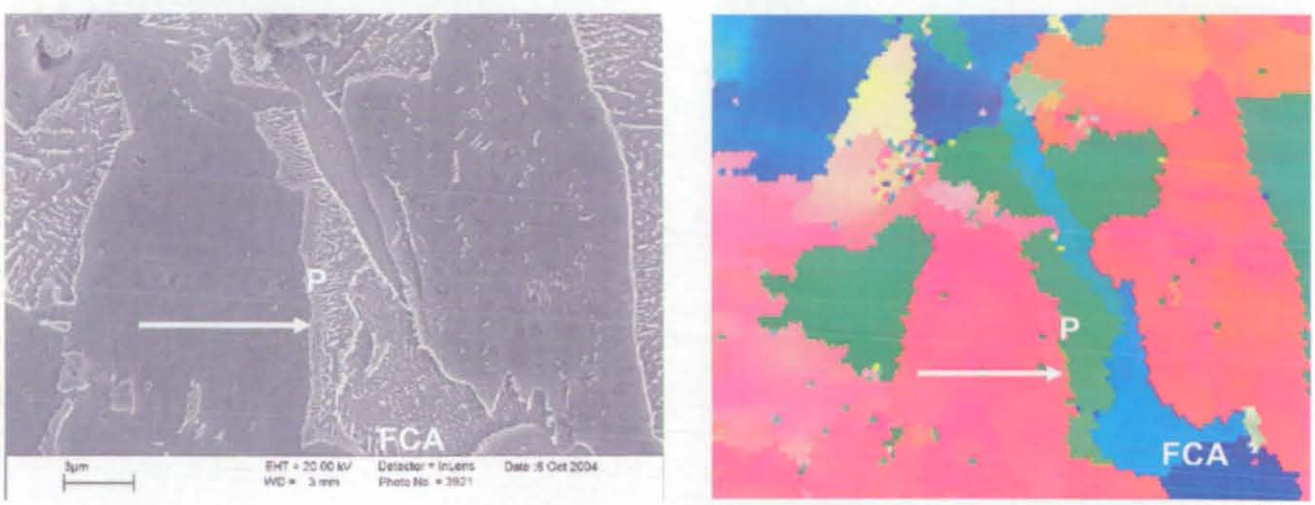

Figure 6.40 shows a region of pearlite close to an FCA region. This is the only case in which the two phases have been found adjacent and their orientations of the have been successfully analysed. Optically, the two regions appear to belong to the same grain and therefore the nature of the two phases cannot be differentiated. Furthermore, even by SEM analysis at higher magnifications, it could be argued that this could be a unique grain in which the nucleation occurs in a lamellar fashion, producing pearlite that subsequently evolves into a degenerated form of pearlite. This would be in conflict with the hypothesis of a separate nature of the FCA. The IPF map shows that the pearlitic region has a completely distinct orientation (green coloured) compared to the adjacent FCA region (light blue coloured). This indicates that the two regions have formed presumably at different times, almost certainly having nucleated at different sites. From this, it can be concluded that the two regions consist of two different phases, separated by a high angle boundary, as discussed later in this section.

Analysis of samples cooled at 5°C s^{-1}

When the cooling rate imposed on Y7N1 is 5°C s^{-1} the microstructure consists of allotriomorphic ferrite, small pearlite islands and larger FCA grains.

The region shown in figure 6.41 contains only primary ferrite and pearlite. From the orientation analysis it can be concluded that in the majority of cases, pearlite islands have the same orientation as that of the adjacent ferrite grain. In figure 6.42 particular regions have been selected for detailed analysis

Figure 6.41: *IPF map and SEM montages of the areas analysed in sample Y7N1 1100/5; the sample contained primary ferrite and pearlite (bright regions); most of the pearlitic regions visible in this two dimensional section have the same orientation of the adjacent ferrite grain*

Figure 6.42a-e: *Microstructural details of the area analysed and their orientation; the bright regions imaged by SEM represent pearlite*

a)

b)

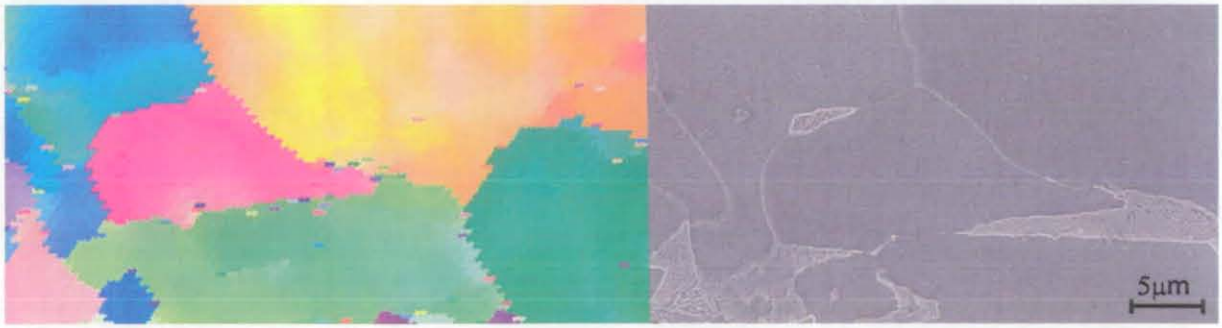

c)

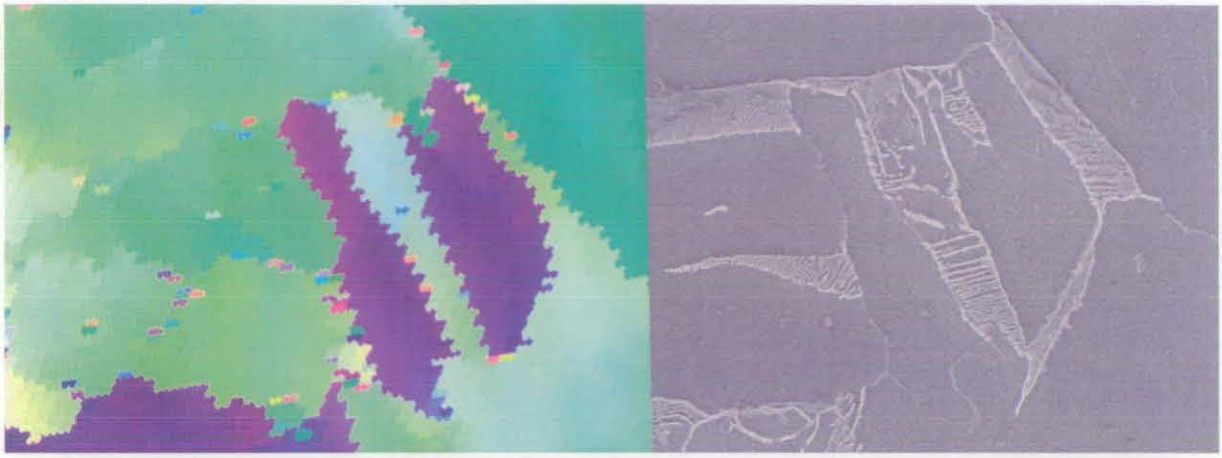

d)

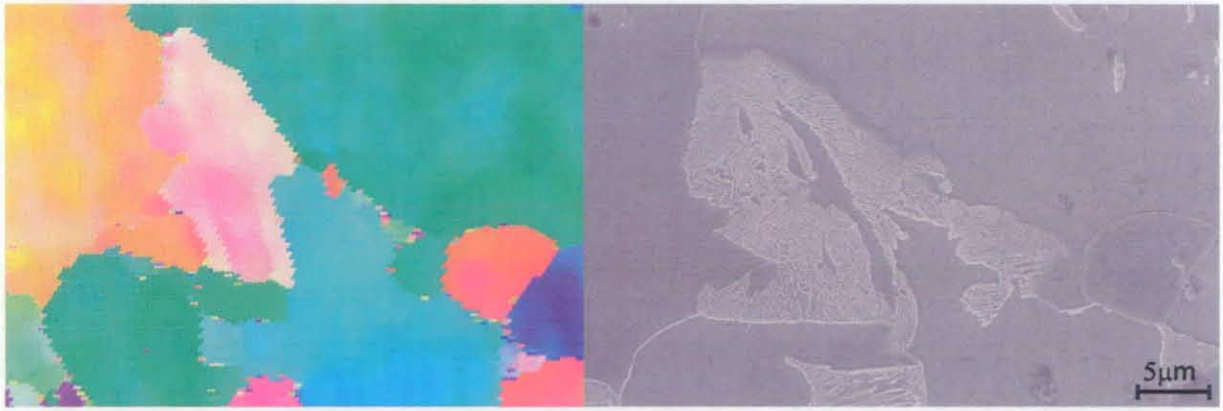

e)

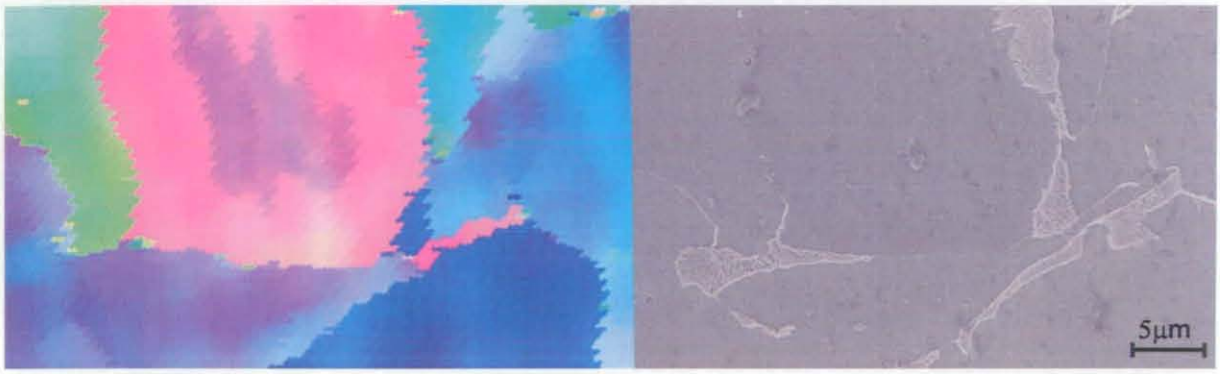

Figure 6.43: *Superimposition of the local orientation (IPF) on the SEM image reproducing a region of sample Y7N1 1100/5*

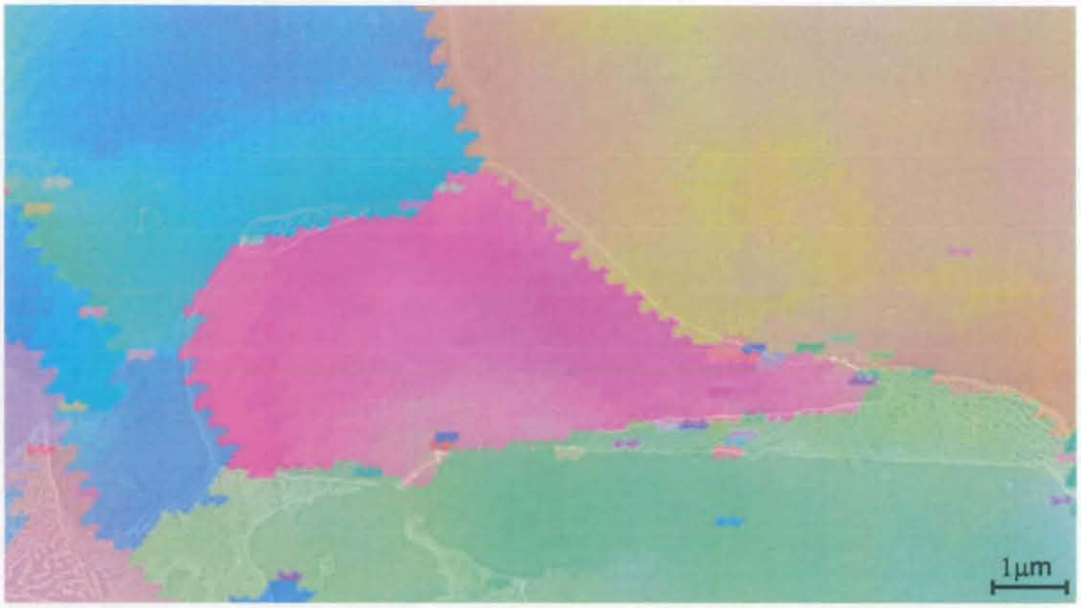

Figure 6.42a-e and 6.43 clearly show that the orientation of pearlite does not differ from the orientation of the adjacent ferrite on which the nucleation of pearlite takes place.

On the other hand, a scan performed on a region containing primary ferrite, pearlite and FCA, indicated that FCA regions, as well as being larger than the pearlite islands, are also characterised by a distinct orientation. The latter appears to be different from that of the adjacent ferrite grains (figure 6.44 and 6.45a-b, the FCA regions are indicated by an arrow).

Figure 6.44: *IPF map and SEM montages of the areas analysed in sample Y7N1 1100/5; the sample contained primary ferrite, pearlite and FCA*

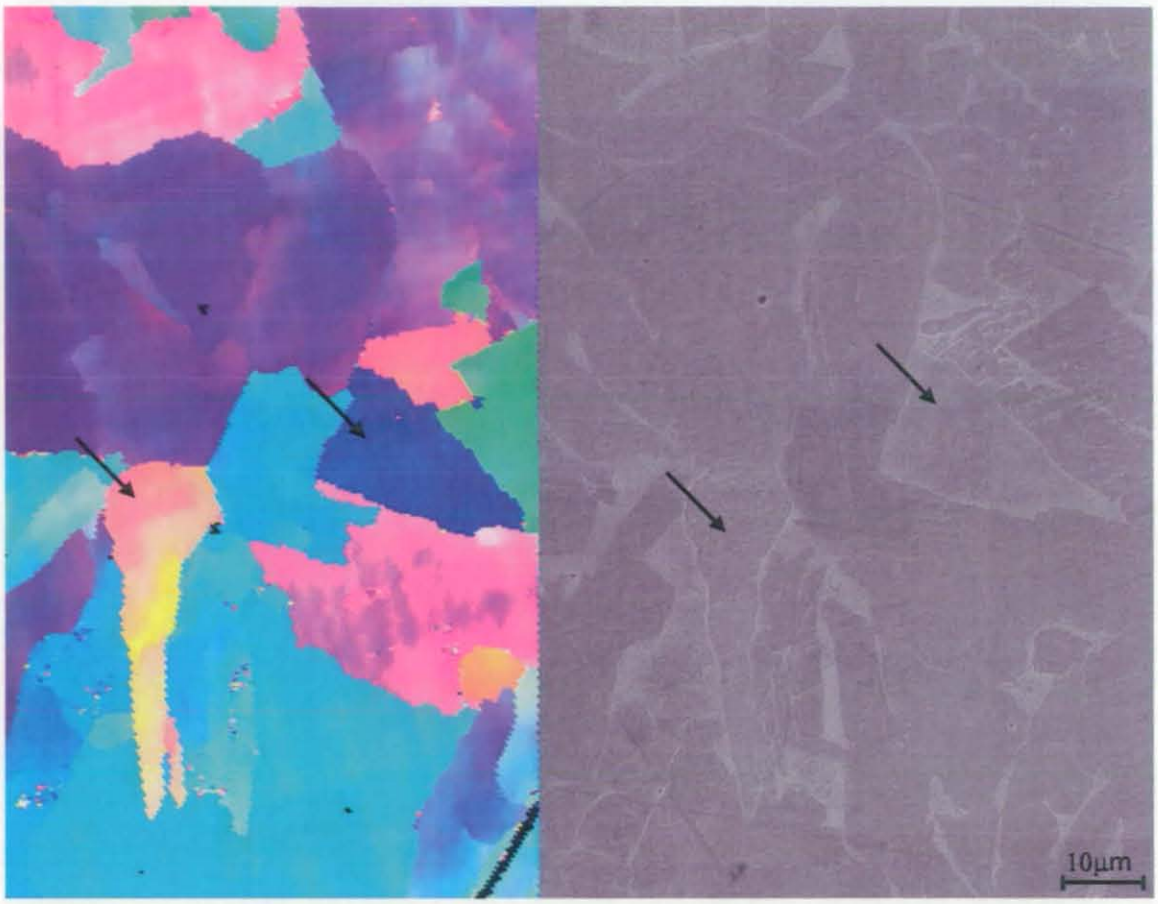

Figure 6.45a-b: *Microstructural details of the area analysed and their orientation; a) the orange grain in the IPF map represents an FCA region; b) the blue grain in the IPF map represents an FCA region*

a)

b)

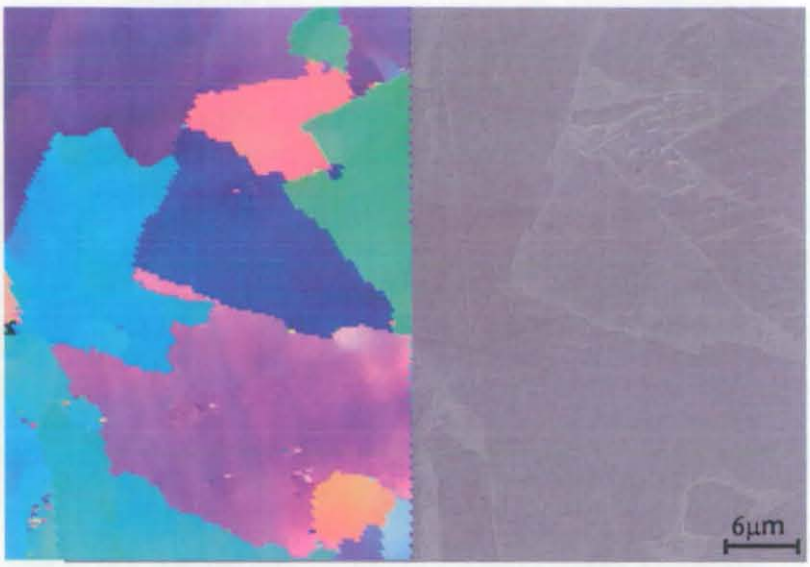

The orientation map of a pearlite region and the adjacent ferritic region indicated that they have the same orientation, with a coherent boundary between them. The very small dimensions of the pearlite regions would suggest that the two dimensional portion of microstructure analysed, contains the grain on which the pearlite lamellae nucleated. This is thought to be the adjacent ferrite grain with the same orientation. A characteristic of reconstructive transformations is that phases nucleating on prior austenite grain boundaries, which grow to form single grains, are separated by high angle boundaries. This is firstly due to the fact that they nucleate on different sites and then grow along different directions, and secondly to the absence of a coordinated movement of atoms during their growth which could justify the formation of coherent or low angle boundaries. Therefore, these factors suggest that pearlite forms after primary ferrite and it nucleates on the adjacent ferrite grain. For this reason the ferrite regions of the pearlite lamellae have the same orientation of the ferrite region on which nucleation has previously taken place. On the other hand, when analysing FCA regions it should be noted that the dimensions of a single grain are much larger compared to those of a pearlite region. It is therefore very likely that the region on which nucleation has taken place cannot be seen in the two dimensional region analysed by EBSD, and, has supported by the transformation sequence (section 6.9) nucleation can take place on prior austenite grain boundaries.

Analysis of samples cooled at 75°C s^{-1}

An important step towards the conclusive determination of the mechanism of formation of FCA was the direct comparison between martensite (diffusionless displacive mechanism) and FCA. When the carbon is "trapped" in the BCT cell of martensite, the distortion of the lattice is quite small and therefore, the EBSD pattern appears very similar to that of BCC ferritic. This happens especially in low carbon steels, where the extent of lattice distortion is not very high. As a martensitic regions are usually not always indexed as such, but as ferrite. As a result, the appearance of a martensite region in an orientation map is not uniform. The presence of two orientations is usually observed, relating to two phases (i.e. ferrite and martensite). In actual fact, the phase should be only one (i.e. martensite).

The IPF map shown in figure 6.46 represents the orientation of the region of Y7N1 sample, cooled at 75°C s^{-1}, as optically observed. Since the microstructure at this cooling rate is very fine, the SEM montage shown in figure 6.47 has been with labelled each phase. The lower bainitic regions can be more easily distinguished from the martensitic ones and the IPF map can be better understood. The inclusions present in the areas analysed should ease the identification of each region in SEM image, optical micrograph and IPF map.

Figure 6.46: *IPF map and SEM montages of the areas analysed in sample Y7N1 1100/75; the sample contained bainite and martensite; The bainitic and martensitic regions do not have uniform orientation*

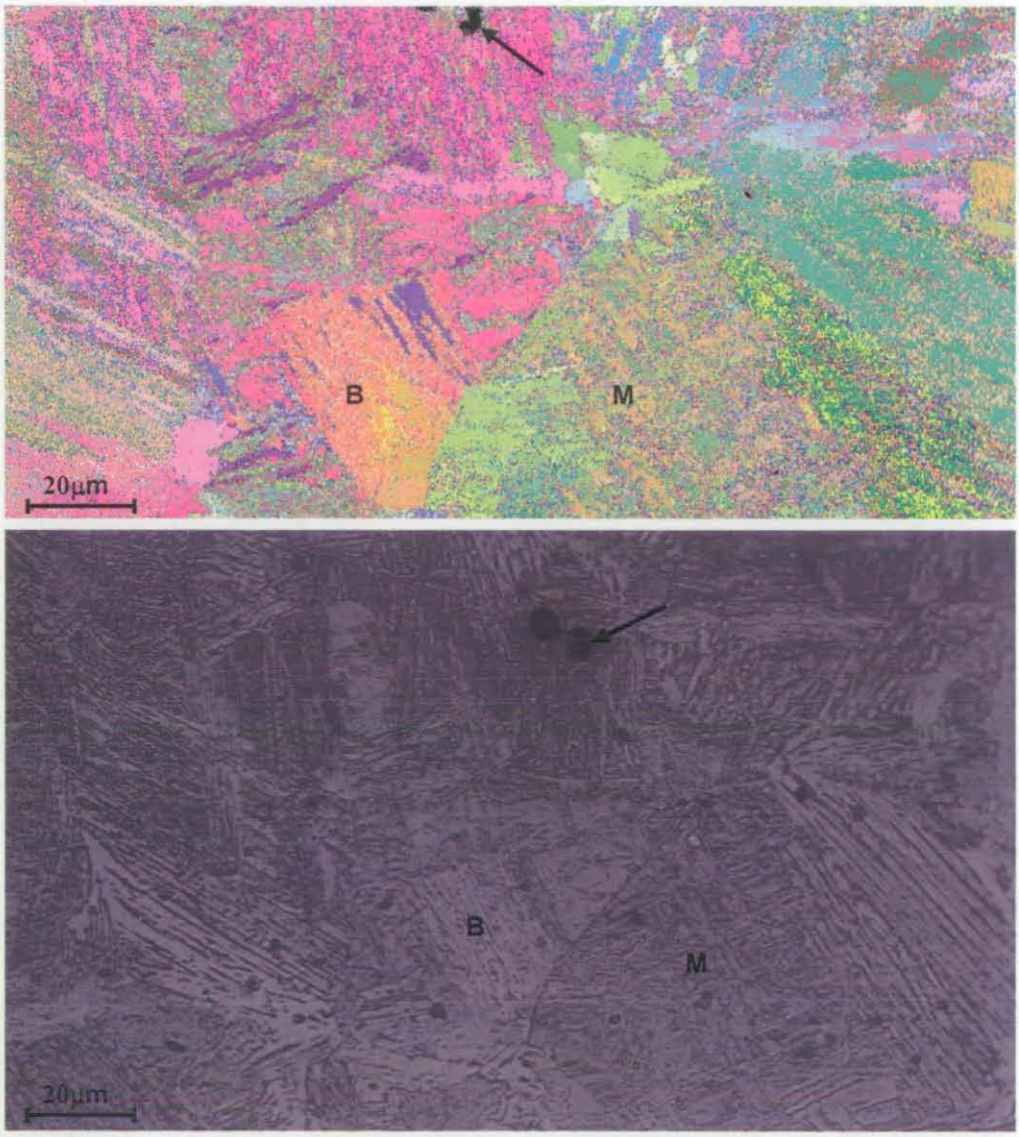

Figure 6.47: *Montage of the area analysed in sample Y7N1 1100/75. The phases have been labelled in order to ease the distinction between them and analyse better the IPF map shown in figure 6.46*

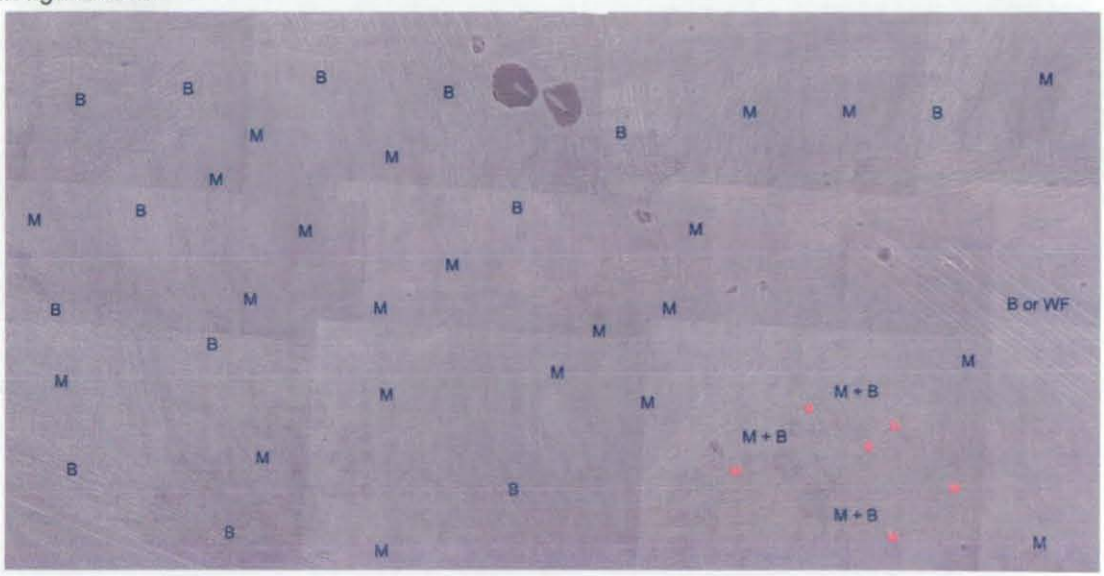

The regions of martensite and lower bainite provide patterns with not very high quality, and usually lower than that of the α-ferrite regions. This is a consequence of the displacive characteristics of the transformations. Indeed, the region of coarse upper bainite (or fine Widmanstätten ferrite) in the IPF map is characterised by a higher pattern quality, and therefore a better confidence index.

In order to improve the quality of the IPF map, three different maps have been produced: one of them excluding martensite, another one using the standard martensite patterns from the TSL database, and finally another one which uses a pattern of martensite obtained directly from the Y7N1 alloy. It should be noted that both the TSL and the Y7N1 martensite patterns are very similar to the α-ferrite one. The three maps can be compared in figure 6.48.

Figure 6.48: *Comparison between IPF maps obtained processing the data for sample Y7N1 1100/75, inputting three different settings for the identification of martensite from the EBSD patterns*

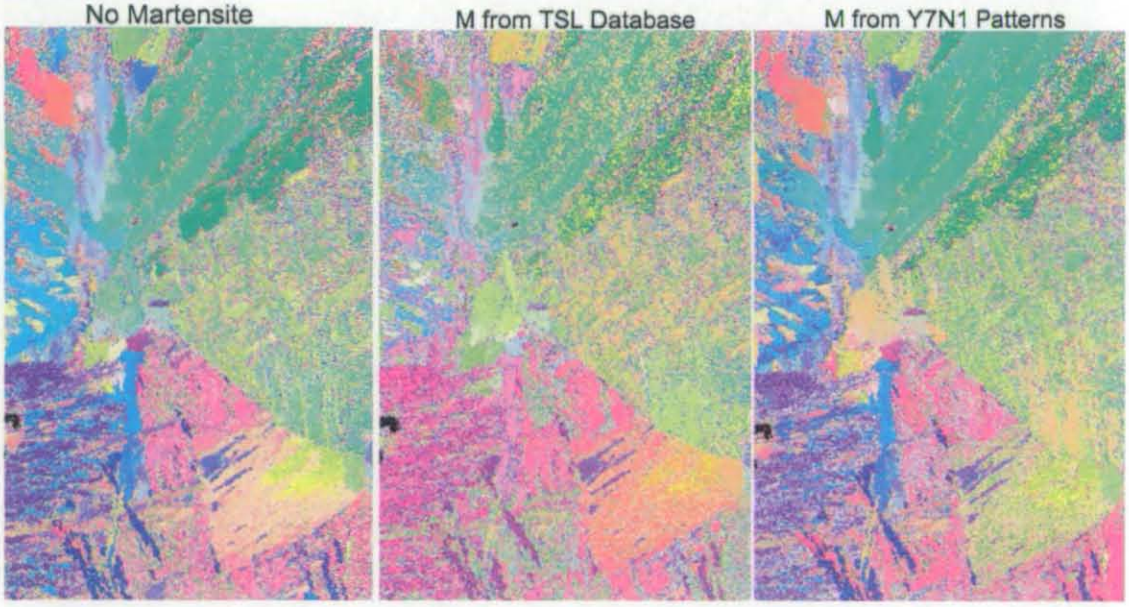

Analysis of samples whose cooling was interrupted

Finding an area in which both α and α' phases could be directly compared was not easy. The best samples were those involving an interrupted continuous cooling heat treatment in which after the high temperature transformations the remaining austenite transformed to martensite. Furthermore, such an area had to be found by scanning several times different regions of different samples. Figure 6.49 shows the

entire region of sample Y7N1 scanned; it contained primary ferrite, Widmanstätten ferrite, upper bainite and FCA.

Figure 6.49: *IPF map and SEM montages of an area of alloy Y7N1 containing both FCA and martensite*

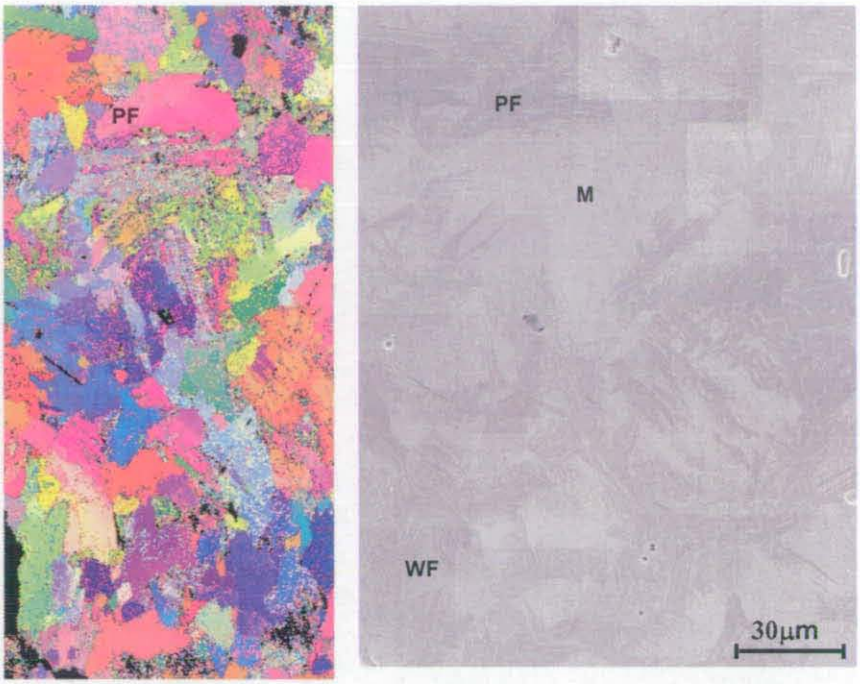

In figure 6.50 the difference between the local orientation distribution of martensite and FCA is clearly shown. The latter presents a uniform orientation and has been identified as being ferritic. It should be noted that the carbides were too small to be conclusively identified. On the other hand, the martensite region has been partially identified as martensite and partially as ferrite, producing a heterogeneous orientation distribution.

Figure 6.50: *IPF map and SEM image of the area analysed in sample Y7N1 where FCA and martensite are adjacent; FCA possesses a uniform orientation*

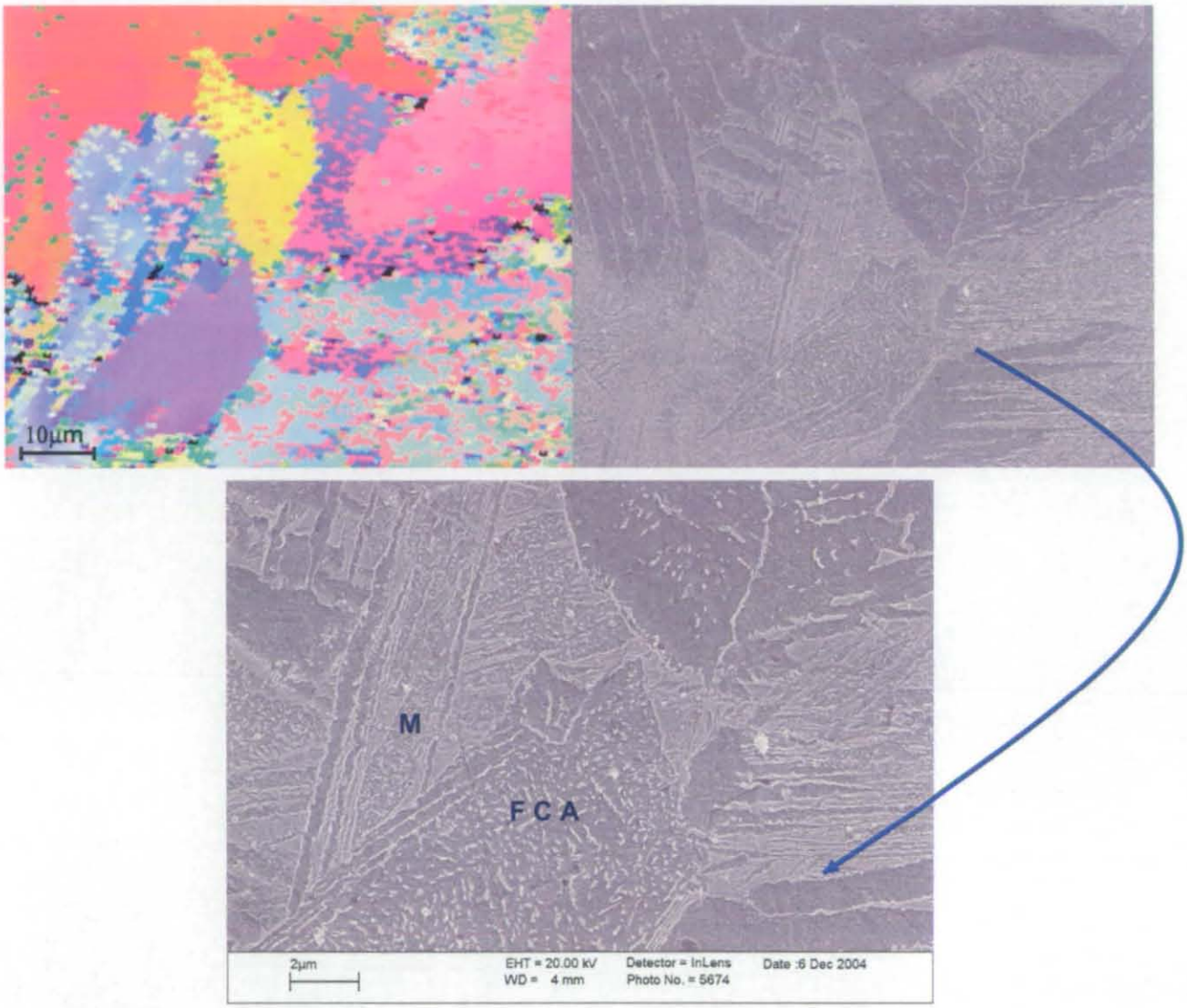

Boundary analysis

The boundary analysis performed by means of EBSD showed that FCA grains are separated from the adjacent grains by high angle boundaries. The boundaries observed within an FCA region are usually low angle boundaries. There is a great difference instead with the boundaries separating pearlite islands and the adjacent ferrite grains, which in most cases are coherent or low angle type. It is very unusual to observe a pearlite region separated by a high angle boundary from the adjacent ferrite grain. Figure 6.51, 6.52, 6.53 and 6.54 show the results obtained from the analysis of the boundaries for samples Y7N1 1100/5, 1300/10 and 1300/10int.587°C.

Figure 6.51: *Boundary analysis for alloy Y7N1 1100/5; the sample contained primary ferrite, pearlite and FCA*

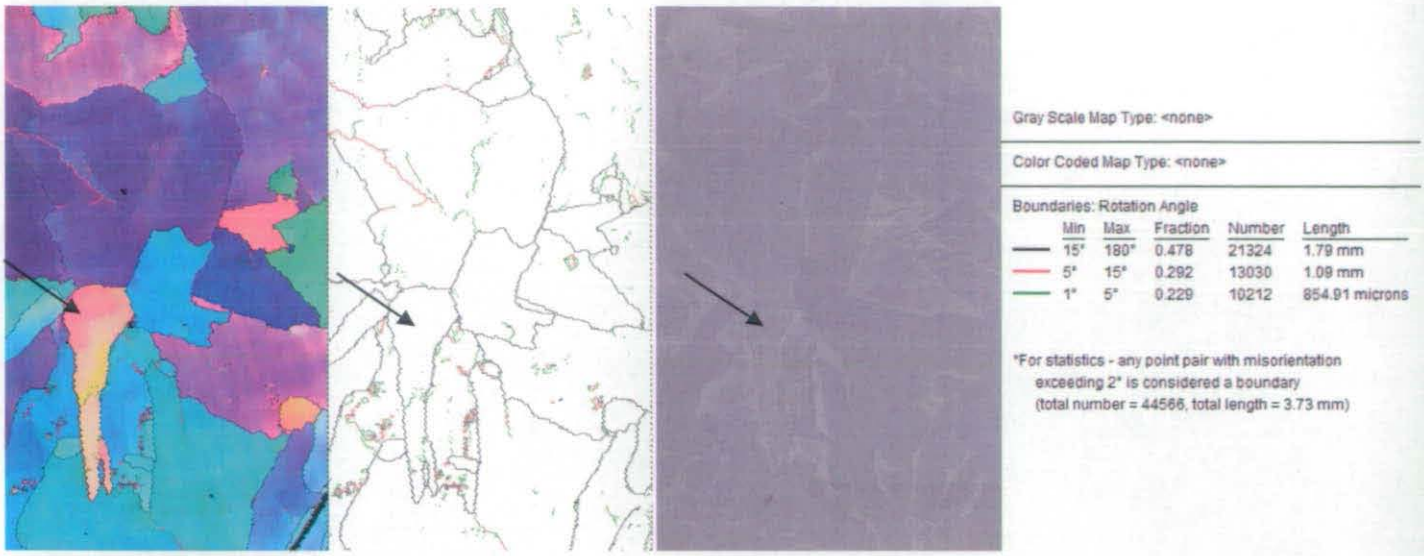

Figure 6.52: *Boundary analysis for alloy Y7N1 1100/5; the sample contained primary ferrite and pearlite*

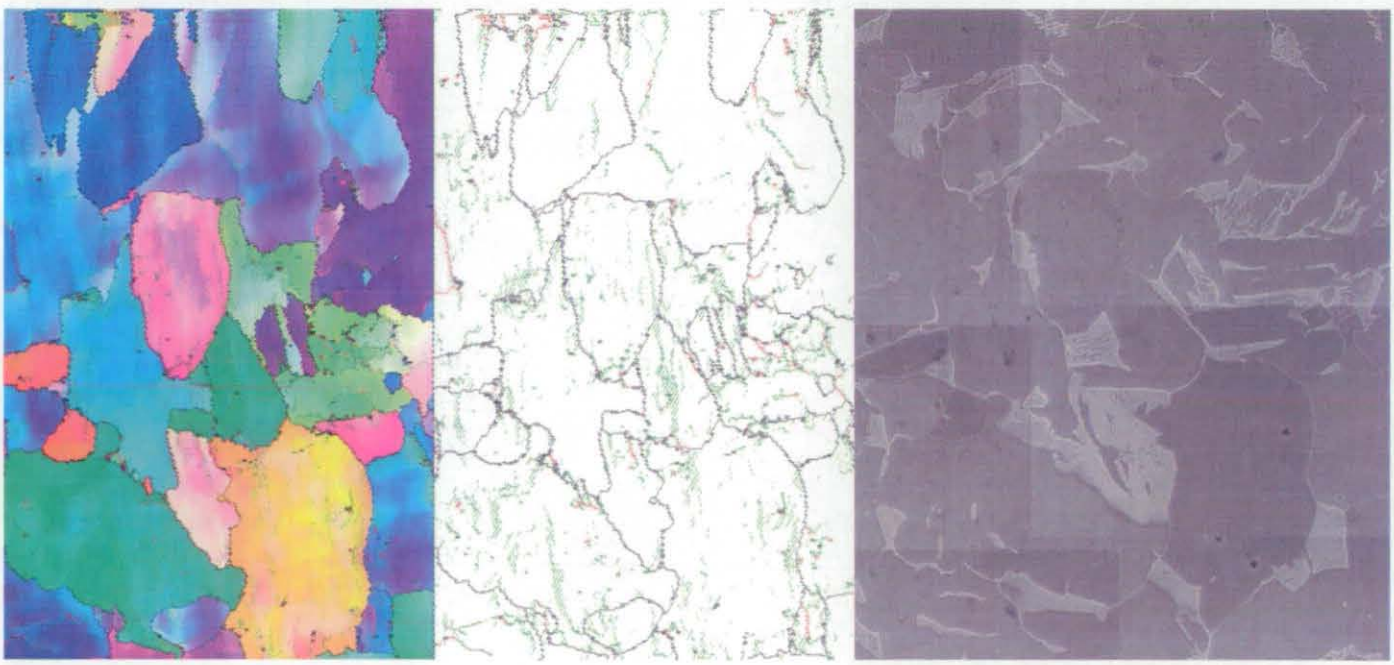

Figure 6.53: *Boundary analysis for alloy Y7N1 1300/10; the sample contained primary ferrite, Widmanstätten ferrite and FCA*

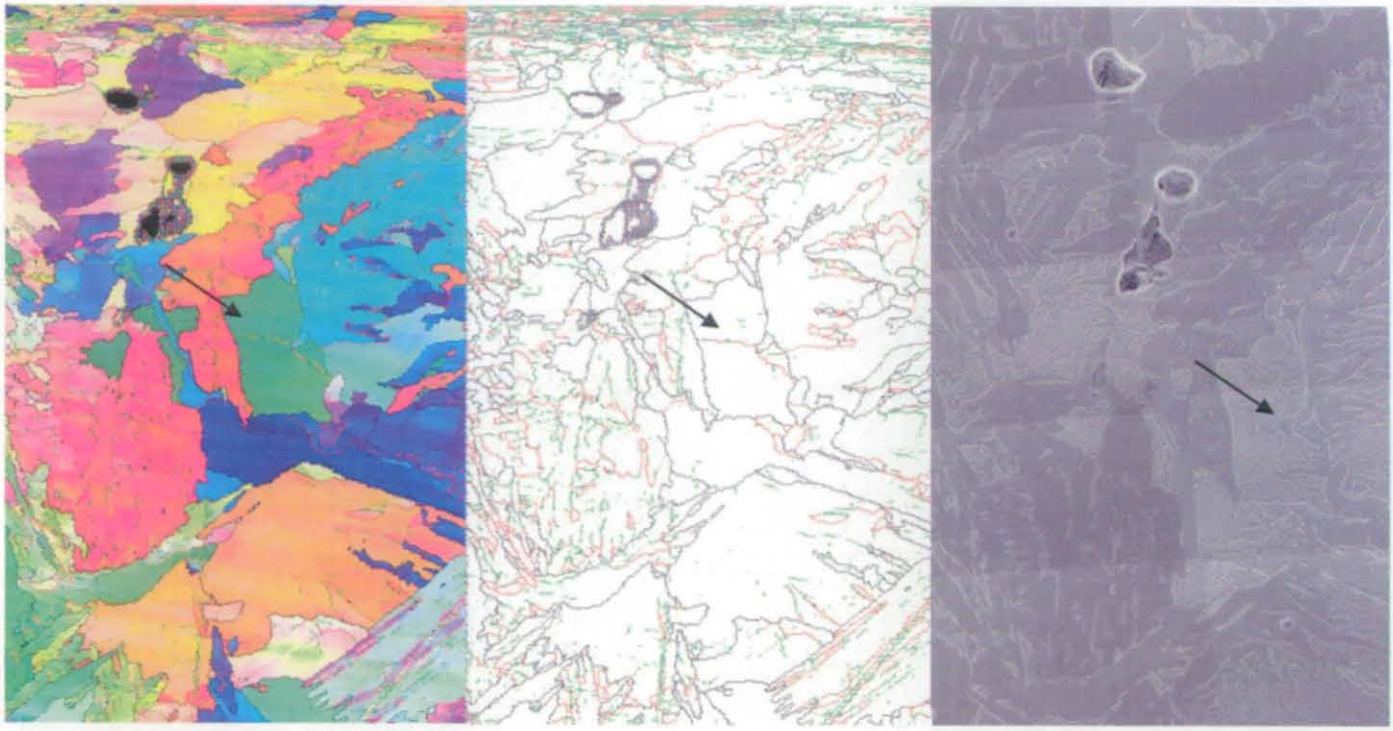

Figure 6.54: *Boundary analysis for alloy Y7N1 1100/10/int.587; the sample contained primary ferrite, Widmanstätten ferrite and FCA*

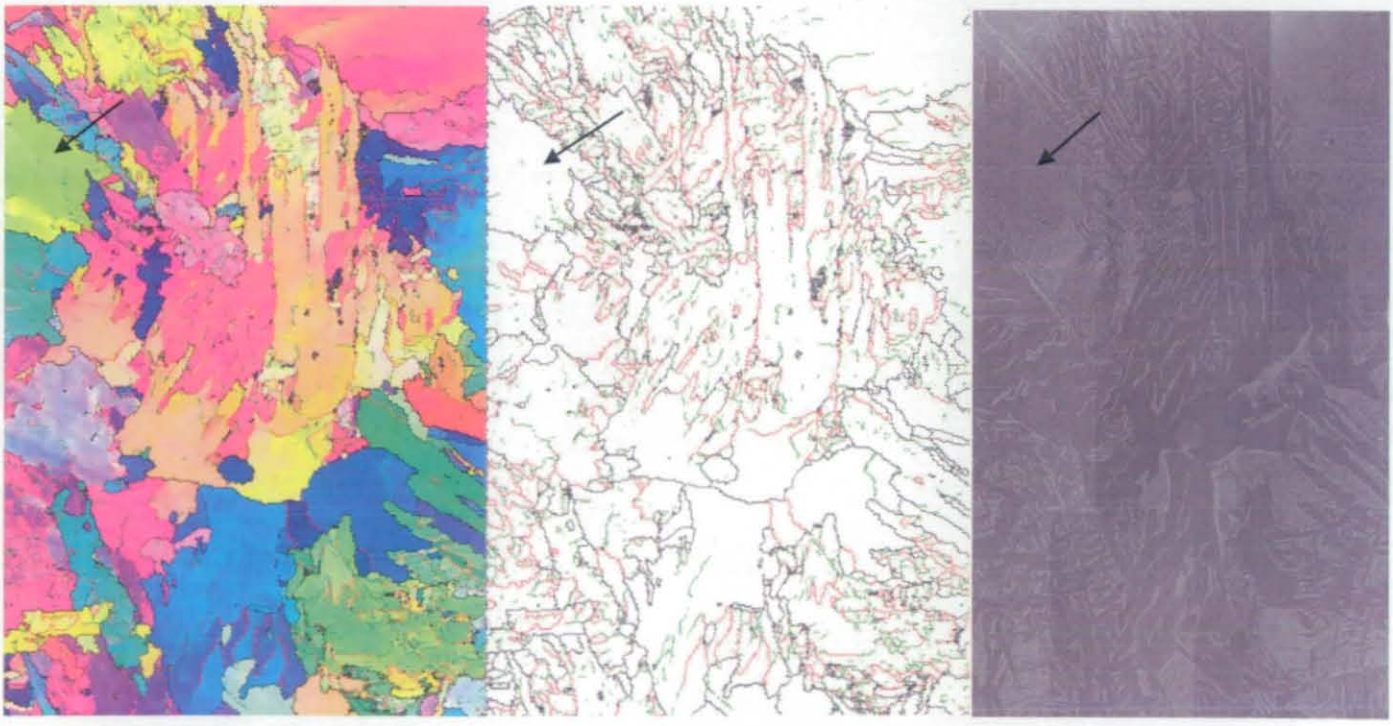

Ion the maps shown in figures 6.51 to 6.54 FCA areas are indicated by an arrow. The high angle boundaries (black) are associated to adjacent ferrite-ferrite grains, adjacent ferrite-WF grains, -FCA-ferrite and FCA-WF. Low angle boundaries are

associated to pearlite-ferrite grains. In some instance the boundaries between the microphase and the WF plate can be low angle. In the case two grains are separated by a high angle boundaries it can be concluded that the two grains have distinct orientation and that their nucleation took place on different sites at different times.

6.9 Transformation Sequence

Interrupted continuous cooling experiments were carried out on alloy Y7N1 in order to assist during the assessment of the transformation sequence taking place under continuous cooling conditions. These experiments consisted of an austenitisation stage followed by a continuous cooling stage, which was interrupted at a certain temperature at which a quenching step was performed; this was done in order to promote the formation of martensite from any residual austenite present in the microstructure.

6.9.1 Cooling rate of 10°C s^{-1}

Table 6.3a lists all the interrupted continuous cooling experiments performed with an austenitisation step at 1100°C, followed by continuous cooling at 10°C s^{-1}. The set of interrupted continuous cooling experiments, characterised by an austenitisation step performed at 1300°C, followed by continuous cooling at 10°C s^{-1}, are presented in table 6.3b.

Table 6.3a: *Interrupted continuous cooling heat treatments*

Aust. Temp (°C)	Cooling Rate (°C s^{-1})	Interrupted at (°C)	Final Cooling	Classification
1100	10	659	Quench	1100/10/i659/q
1100	10	637	Quench	1100/10/i637/q
1100	10	615	Quench	1100/10/i615/q

Table 6.3b: *Interrupted continuous cooling heat treatments*

Aust Temp (°C)	Cooling Rate (°C s^{-1})	Interrupted at (°C)	Final Cooling	Classification
1300	10	624	Quench	1300/10/i624/q
1300	10	606	Quench	1300/10/i606/q
1300	10	587	Quench	1300/10/i587/q

Table 6.3c provides details of the set of interrupted continuous cooling experiments performed with an austenitisation step at 1100°C, followed by continuous cooling at 50°C s^{-1}.

Table 6.3c: *Interrupted continuous cooling heat treatments;*

Aust Temp (°C)	Cooling Rate (°C s^{-1})	Interrupted at (°C)	Final Cooling	Classification
1100	50	606	Quench	1100/50/i606/q
1100	50	580	Quench	1100/50/i580/q
1100	50	560	Quench	1100/50/i560/q

The dilatometry curves obtained from the Y7N1 samples allowed the determination of three different temperatures, at which the cooling was interrupted and was immediately followed by quenching to room temperature. This was done in order to monitor the evolution of the microstructure at different stages of the cooling process. The three temperatures were chosen at the initial stage of transformation, at an intermediate stage and at the final stage of transformation respectively. Figure 6.55 shows the dilation curves corresponding to the three interrupted continuous cooling heat treatments performed at 10°C s^{-1}, as detailed in table 6.3a, together with the original curve of sample Y7N1, austenitised at 1100°C and cooled at 10°C s^{-1}.

Figure 6.55: *Dilation curves for interrupted continuous cooling heat treatments; austenititsation at 1100°C and cooling at 10°C s^{-1}*

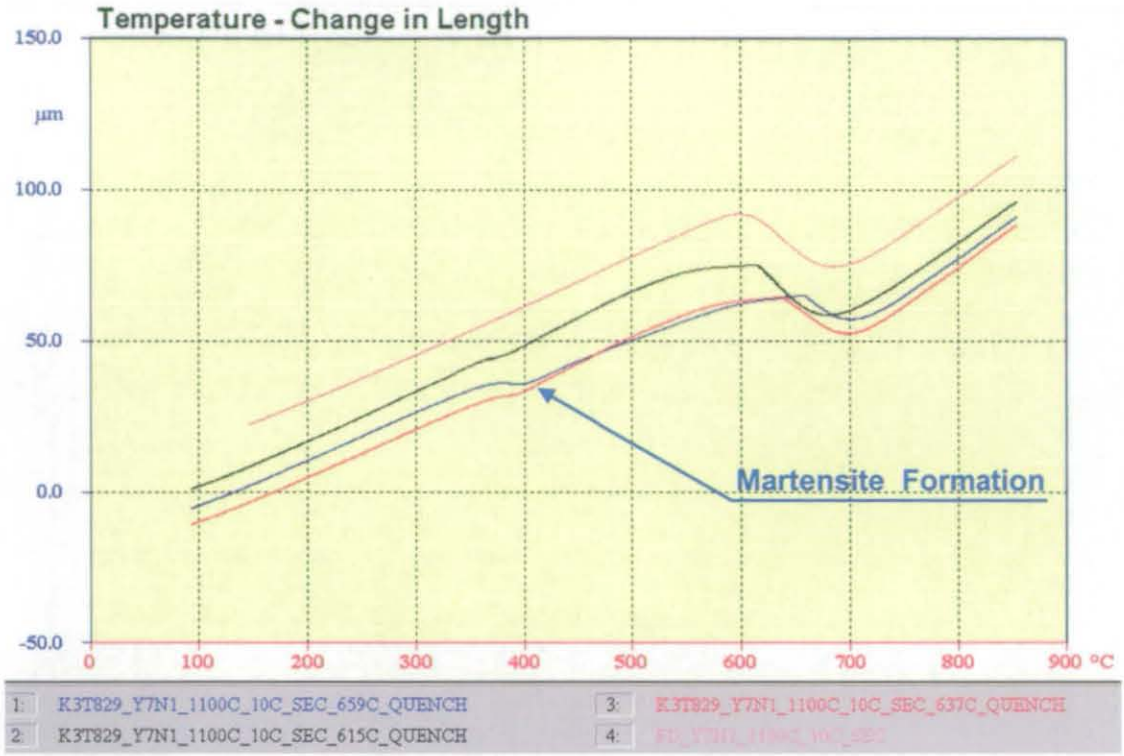

The dilation curves for the three interrupted continuous cooling heat treatments performed at 10°C s^{-1}, as detailed in table 6.3b are shown in figure 6.56, where they can also be compared to the original curve of sample Y7N1 austenitised at 1300°C and cooled 10°C s^{-1}.

Figure 6.56: *Dilation curves for interrupted continuous cooling heat treatments; austenititsation at 1300°C and cooling at 10°C s^{-1}*

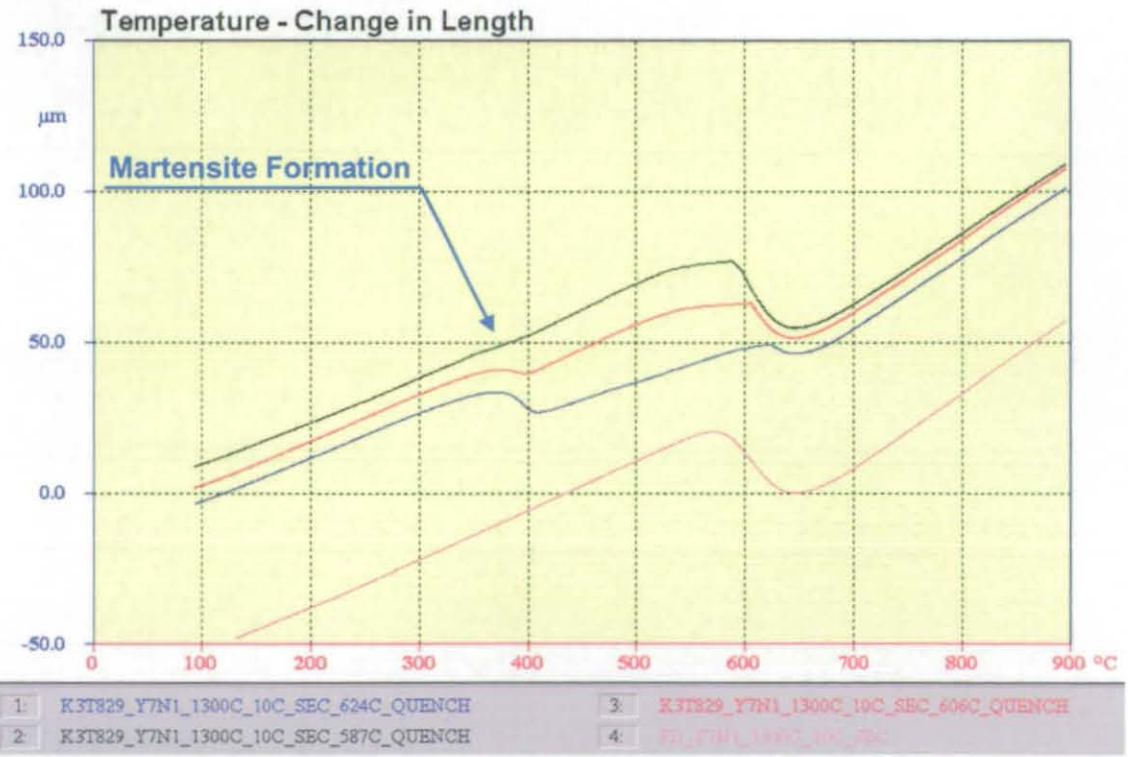

The three curves corresponding to the interrupted continuous cooling heat treatments (i.e. red, blue and black dilation curves in figures 6.55 sand 6.56), clearly show a second slope change at low temperature, i.e. in the 350-410°C temperature range for both austenitising temperatures. This is thought to be associated with a martensitic transformation. As the temperature at which the quenching step is performed decreases, the corresponding change in length gradually decreases too. This is thought to clearly result from the transformation of a smaller fraction of remaining austenite into martensite.

Microstructural analysis, performed by means of optical microscopy and SEM, showed that when the cooling is interrupted at the initial stages of transformation, only primary ferrite and some Widmanstätten ferrite plates are able to grow, whilst the rest of the austenite transforms into martensite. Similarly, at an intermediate temperature, all the primary ferrite has formed and some of the Widmanstätten ferrite, whereas the remaining austenite transforms again into martensite. The presence of FCA instead of martensite is revealed by the microstructural observations related to the later stages of transformation. The last region of austenite enriched in carbon form only after primary ferrite and Widmanstätten ferrite. The optical analysis provided supporting evidence. An example is shown in figure 6.57 for the samples austenitised at 1100°C and cooled at 10°C s^{-1}.

Figure 6.57: *Microstructures of alloy Y7N1 whose cooling was interrupted at three different stages; FCA forms at the last stages of cooling*

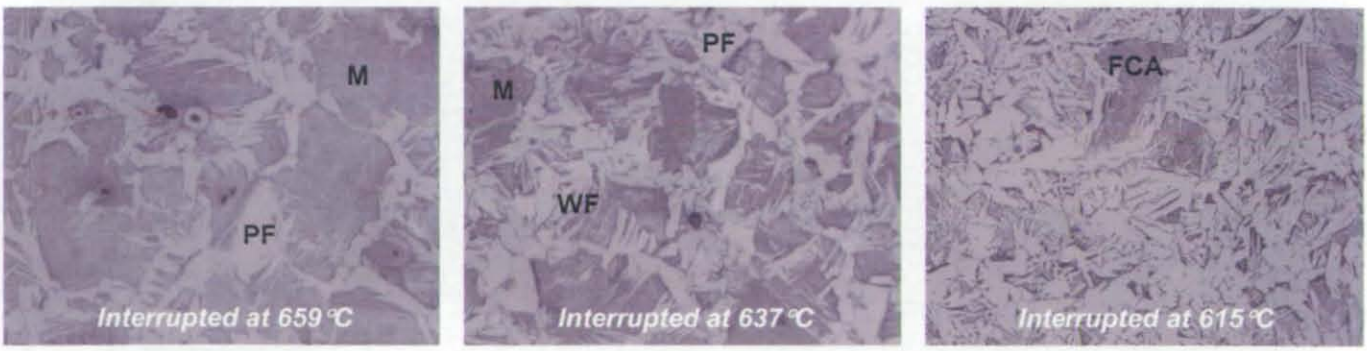

The morphology of martensite can be more easily differentiated form that of FCA by means of SEM analysis. Figure 6.58 schematically shows the temperature range and the microstructure obtained by interrupting the cooling.

Figure 6.58: *Schematic of the microstructural evolution observed by means of the interrupted continuous cooling experiments*

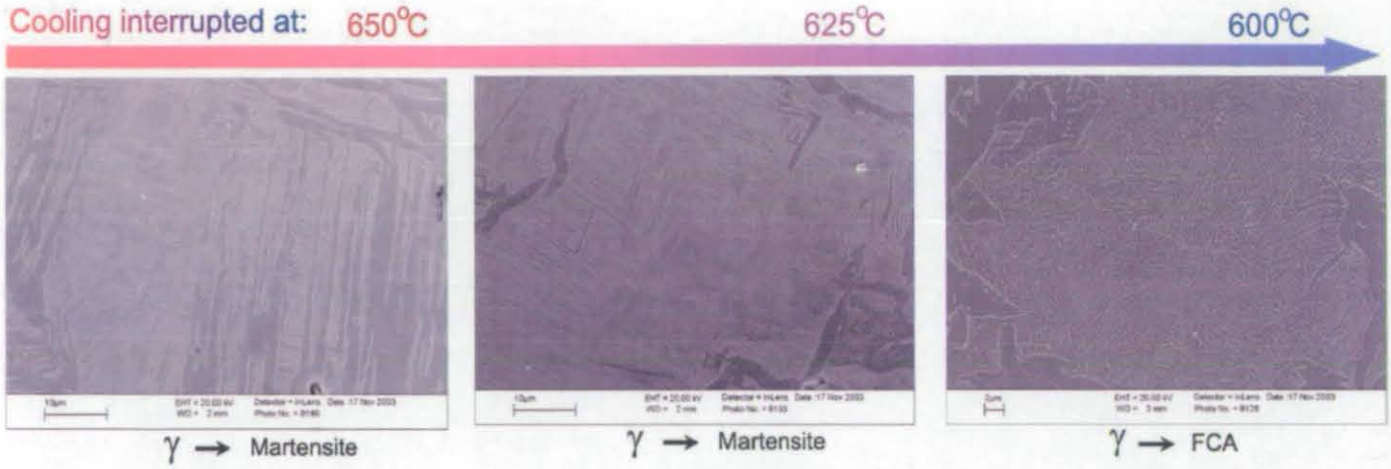

A detailed morphological analysis of the microstructures formed by interrupting the cooling at the three temperatures specified in the previous tables (6.3a-c) has been performed. The results obtained for all the samples investigated are presented hereafter in figure 6.59 to figure 6.64.

Figure 6.59: *Microstructures of alloy Y7N1 1100/10/i659/q observed by means of SEM*

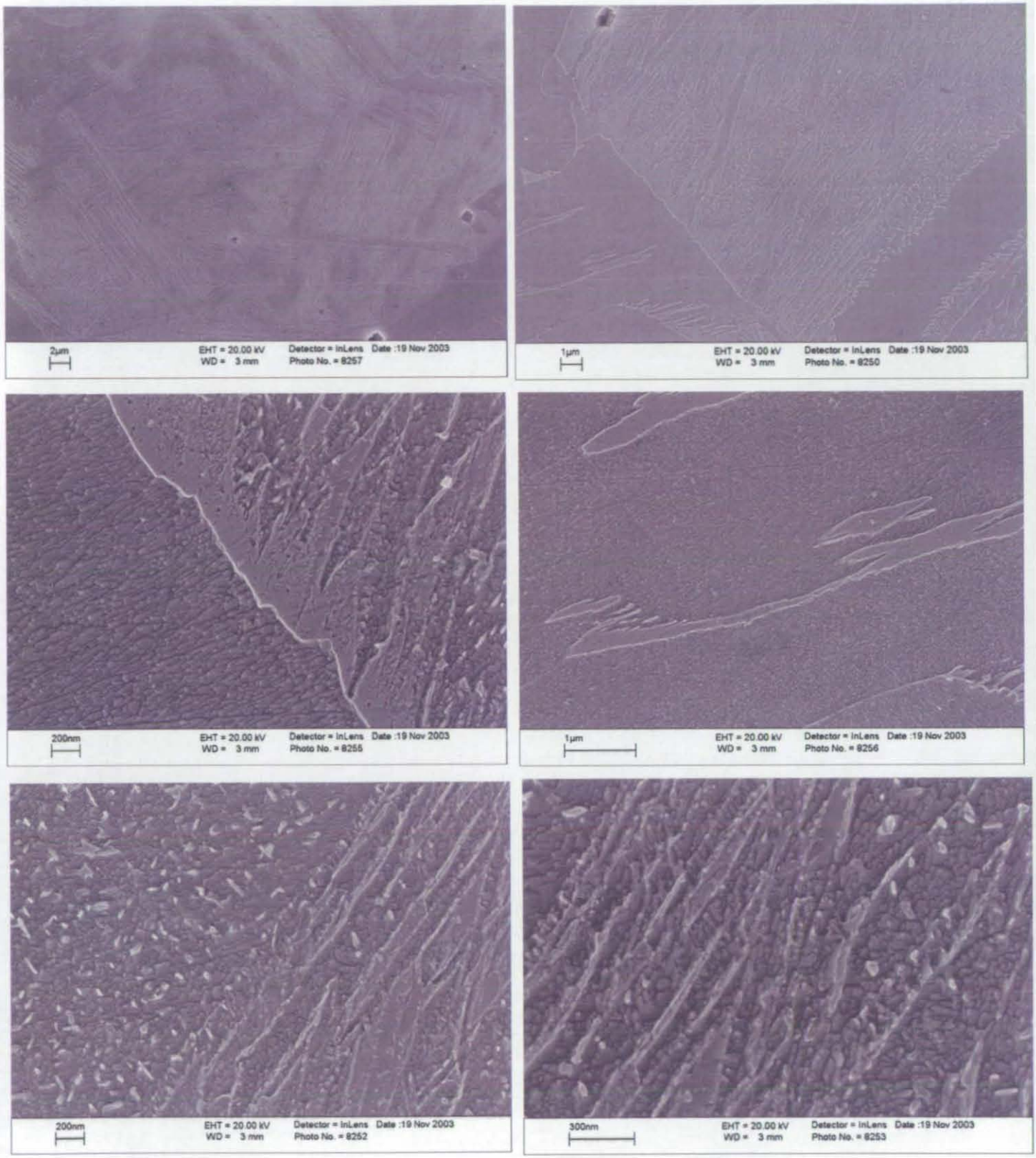

Figure 6.60: *Microstructures of alloy Y7N1 1100/10/i637/q observed by means of SEM*

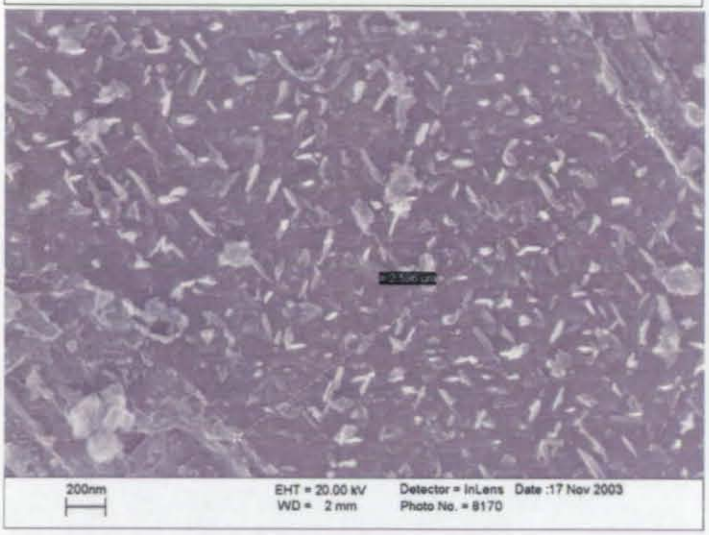

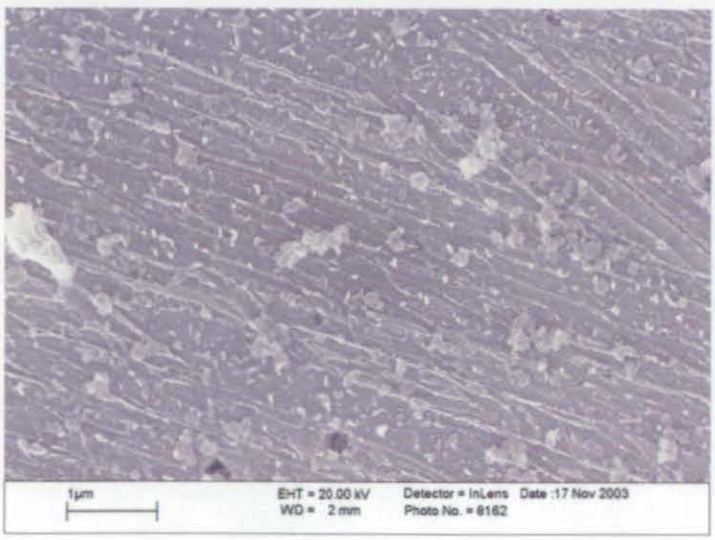

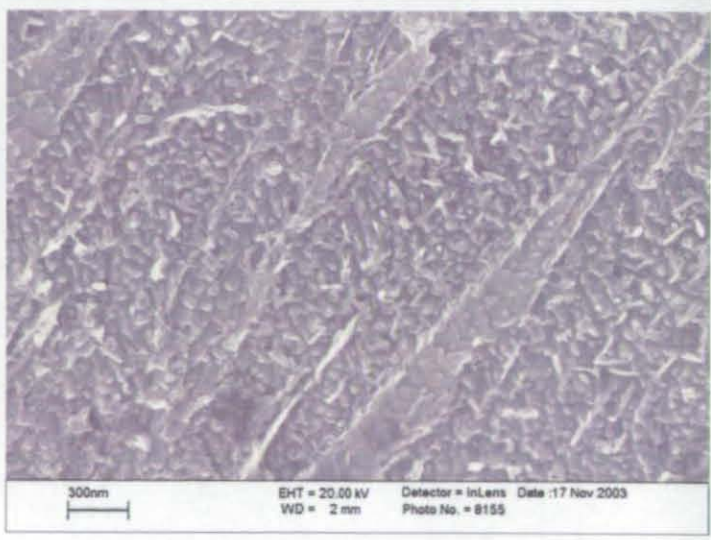

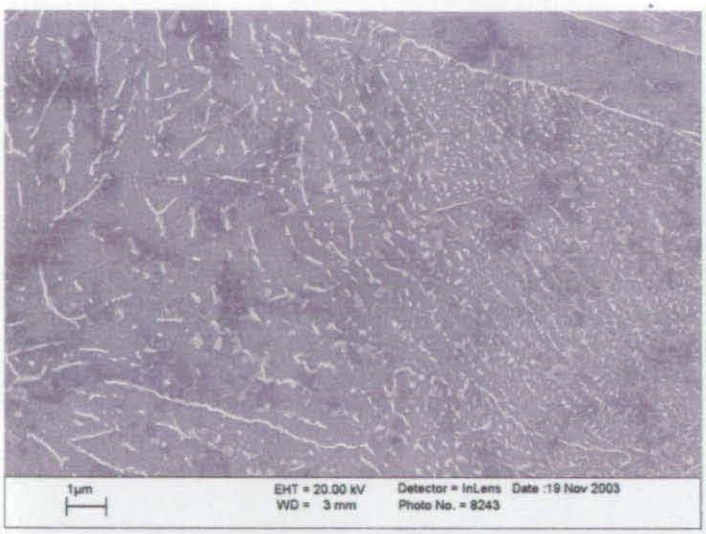
1µm
EHT = 20.00 kV
WD = 3 mm
Detector = InLens Date :19 Nov 2003
Photo No. = 8243

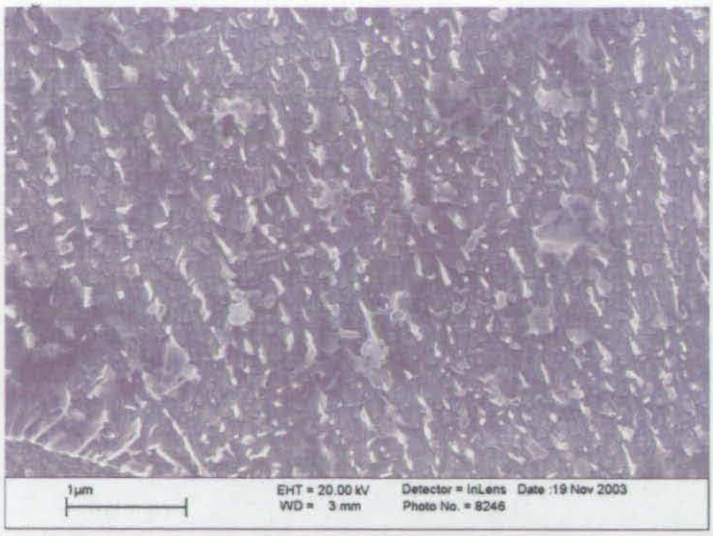
1µm
EHT = 20.00 kV
WD = 3 mm
Detector = InLens Date :19 Nov 2003
Photo No. = 8246

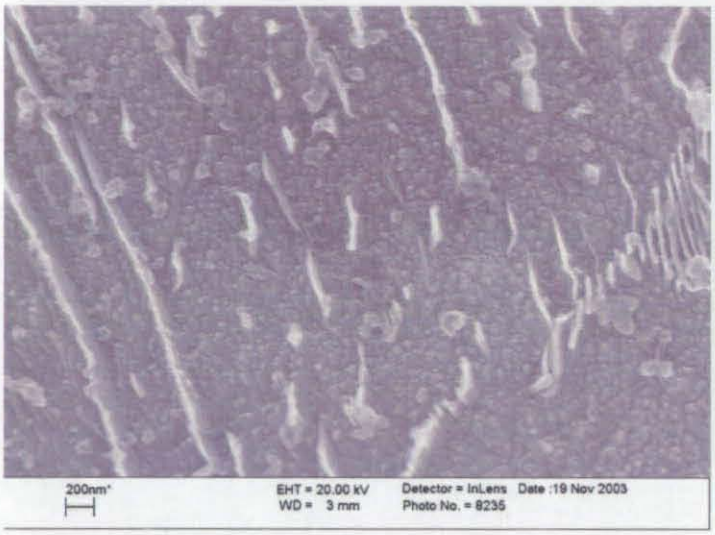
200nm*
EHT = 20.00 kV
WD = 3 mm
Detector = InLens Date :19 Nov 2003
Photo No. = 8235

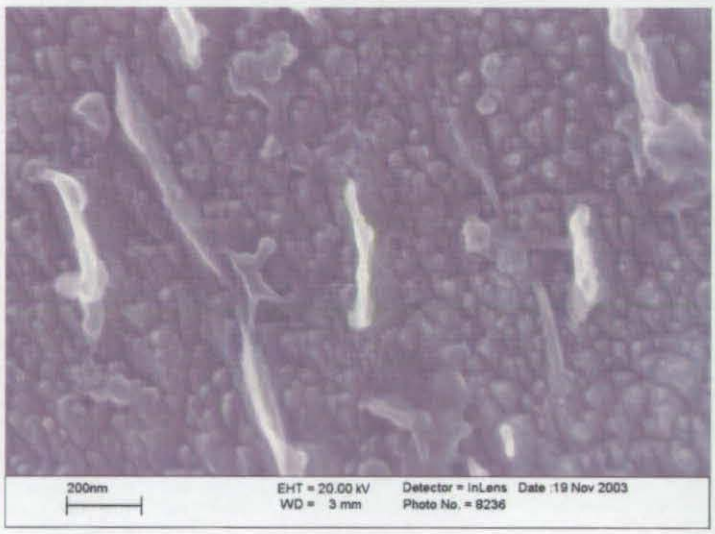
200nm
EHT = 20.00 kV
WD = 3 mm
Detector = InLens Date :19 Nov 2003
Photo No. = 8236


1µm
EHT = 20.00 kV
WD = 3 mm
Detector = InLens Date :19 Nov 2003
Photo No. = 8239

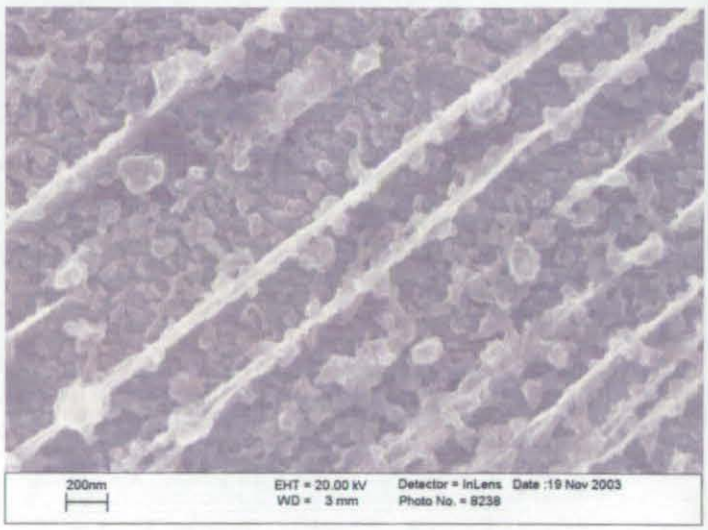
200nm
EHT = 20.00 kV
WD = 3 mm
Detector = InLens Date :19 Nov 2003
Photo No. = 8238

In figures 6.62 to 6.64, a number of micrographs are presented, showing the microstructural features of interest observed in the samples austenitised at 1300°C.

Figure 6.62: *Microstructures of alloy Y7N1 1300/10/i624/q observed by means of SEM*

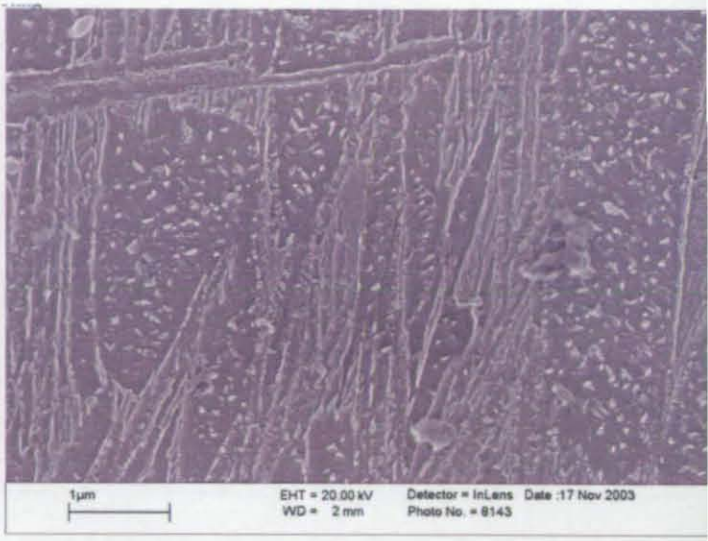

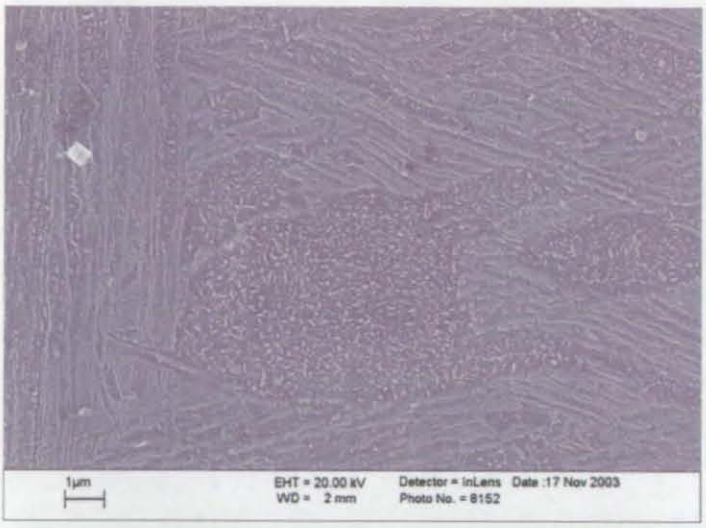

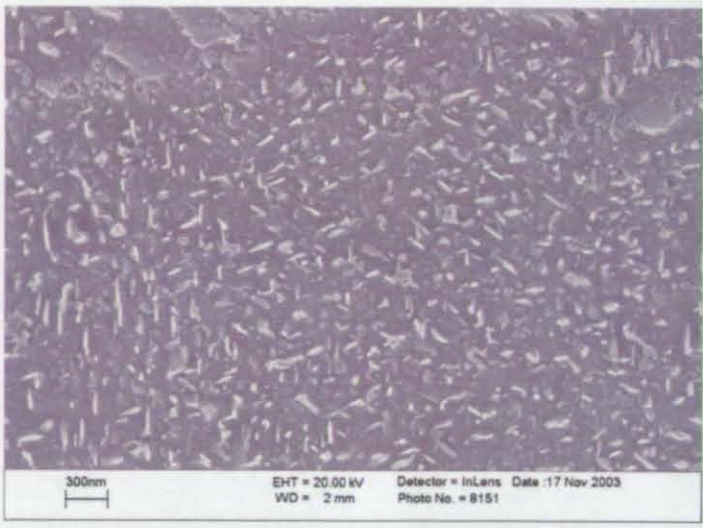

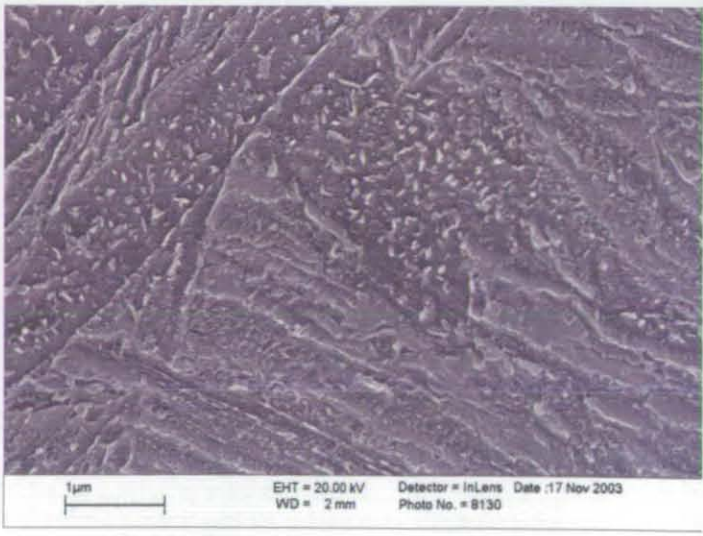

Figure 6.63: *Microstructures of alloy Y7N1 1300/10/i606/q observed by means of SEM*

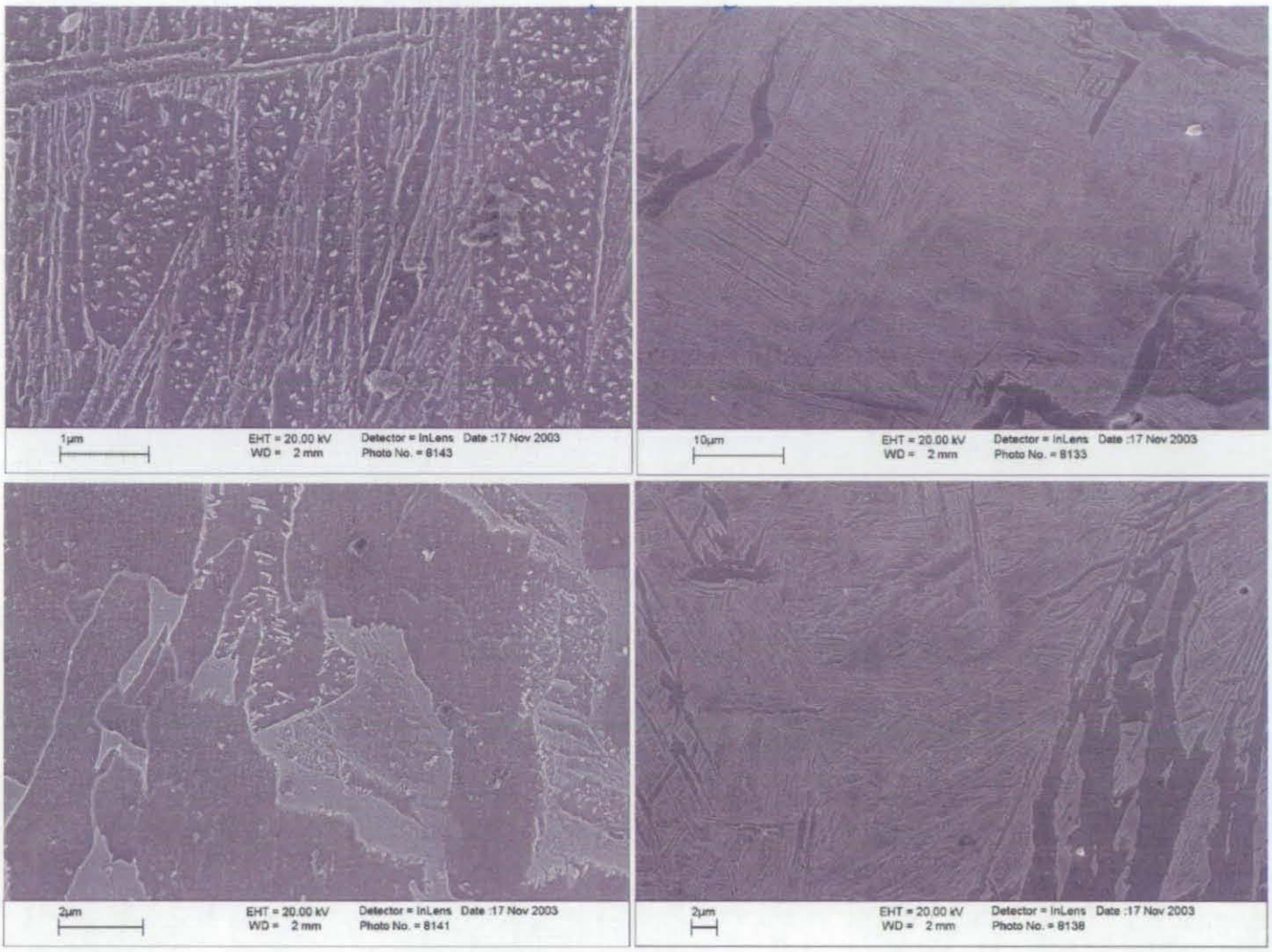


10µm
EHT = 20.00 kV
WD = 3 mm
Detector = InLens Date :17 Nov 2003
Photo No. = 8102

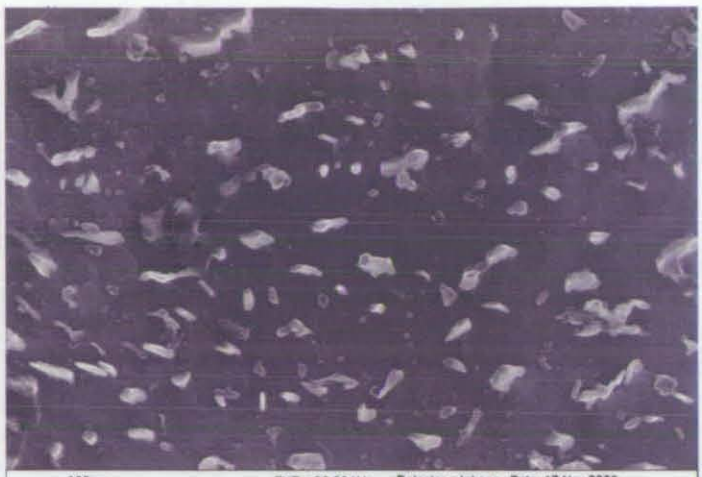
300nm
EHT = 20.00 kV
WD = 3 mm
Detector = InLens Date :17 Nov 2003
Photo No. = 8100

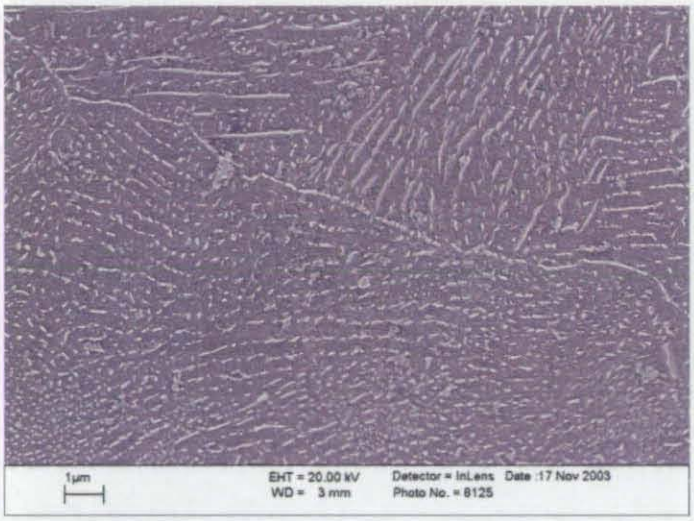
1µm
EHT = 20.00 kV
WD = 3 mm
Detector = InLens Date :17 Nov 2003
Photo No. = 8125

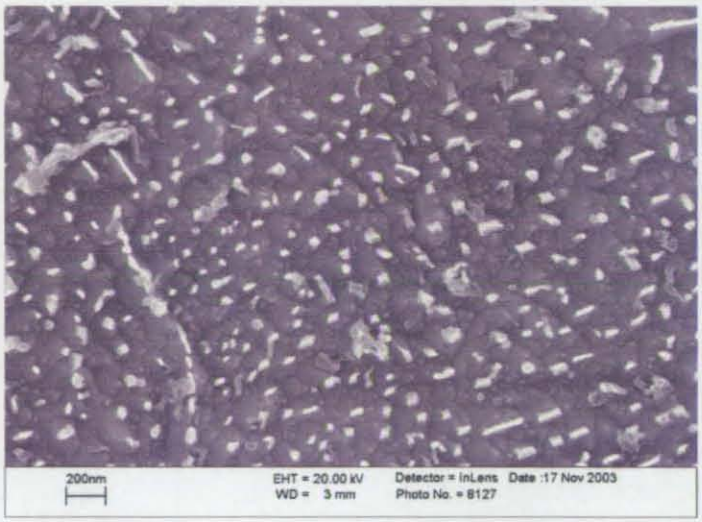
200nm
EHT = 20.00 kV
WD = 3 mm
Detector = InLens Date :17 Nov 2003
Photo No. = 8127

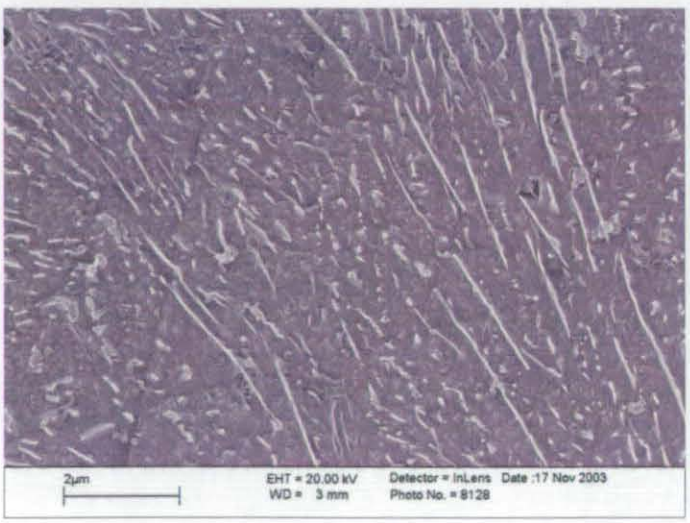
2µm
EHT = 20.00 kV
WD = 3 mm
Detector = InLens Date :17 Nov 2003
Photo No. = 8128

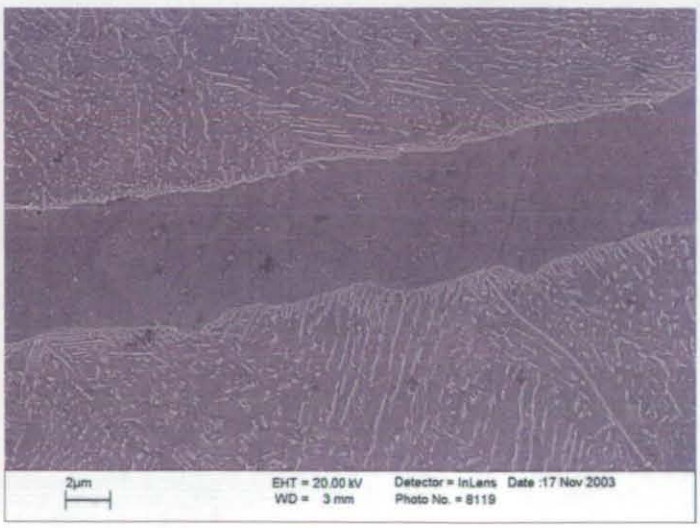
2µm
EHT = 20.00 kV
WD = 3 mm
Detector = InLens Date :17 Nov 2003
Photo No. = 8119

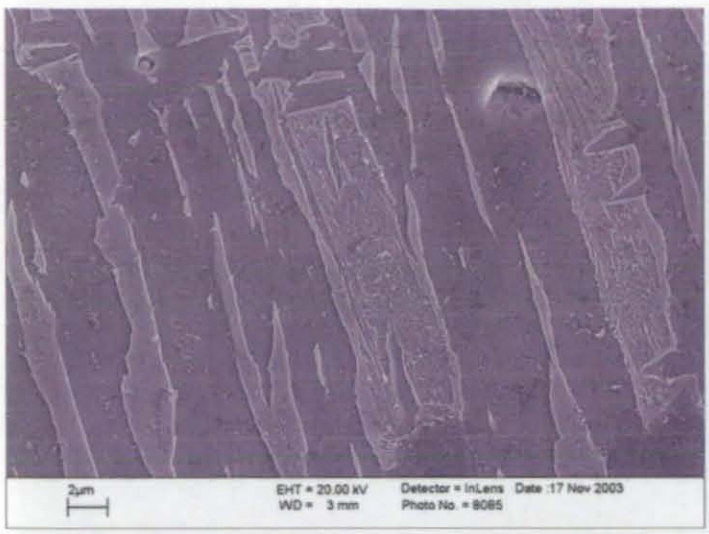
2µm
EHT = 20.00 kV
WD = 3 mm
Detector = InLens Date :17 Nov 2003
Photo No. = 8085

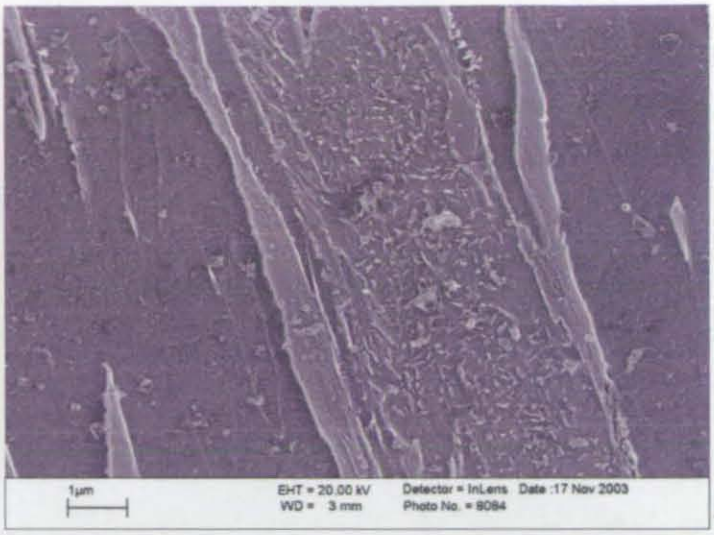
1µm
EHT = 20.00 kV
WD = 3 mm
Detector = InLens Date :17 Nov 2003
Photo No. = 8084


2µm
EHT = 20.00 kV
WD = 3 mm
Detector = InLens Date :17 Nov 2003
Photo No. = 8120

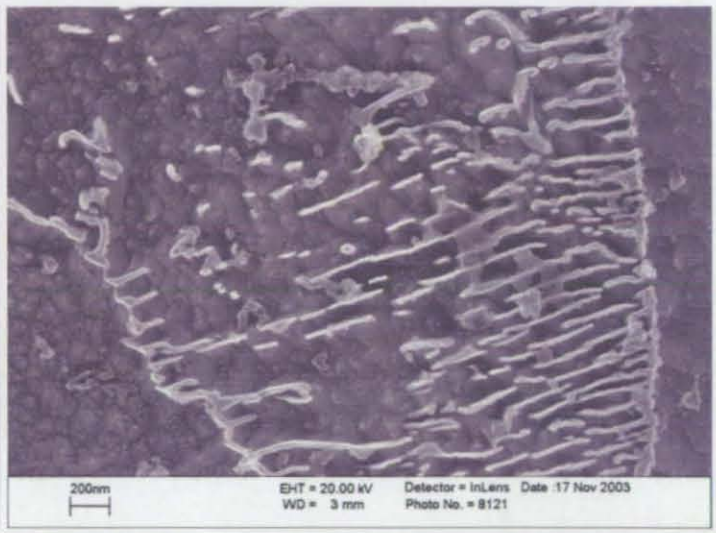
200nm
EHT = 20.00 kV
WD = 3 mm
Detector = InLens Date :17 Nov 2003
Photo No. = 8121

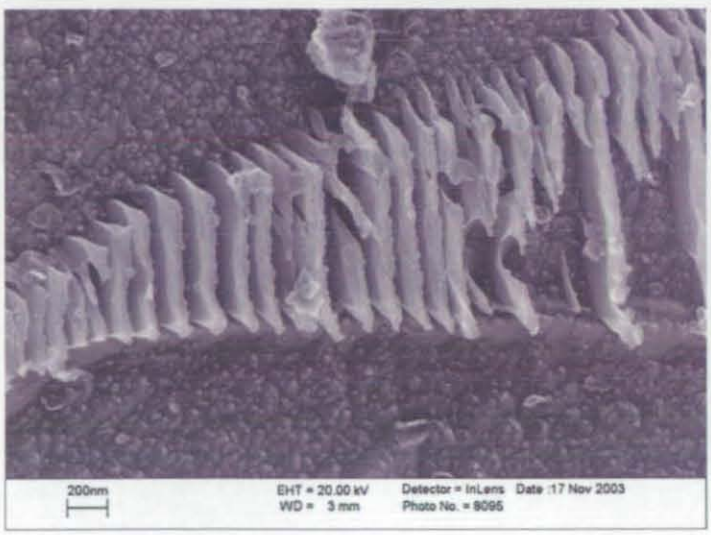
200nm
EHT = 20.00 kV
WD = 3 mm
Detector = InLens Date :17 Nov 2003
Photo No. = 8095

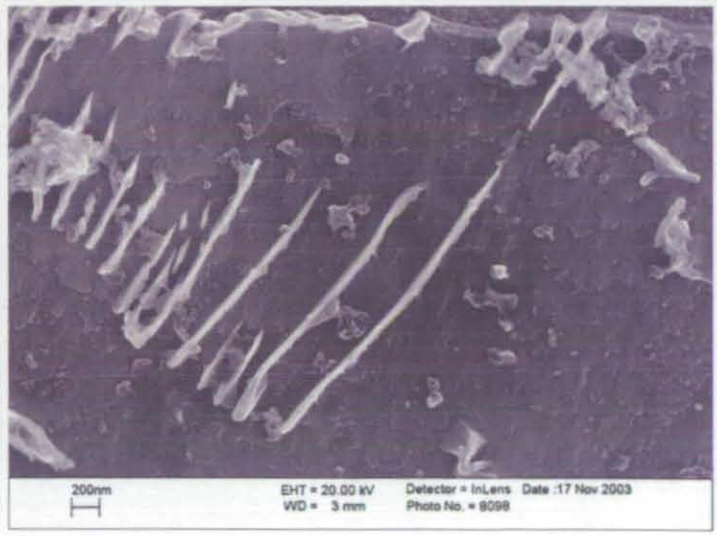
200nm
EHT = 20.00 kV
WD = 3 mm
Detector = InLens Date :17 Nov 2003
Photo No. = 8096

The accuracy of the morphological analysis has been verified by means of micro-hardness and the indentations on the supposed FCA regions have been found as shown in figure 6.65.

Figure 6.65: *Indentations observed by means of SEM*

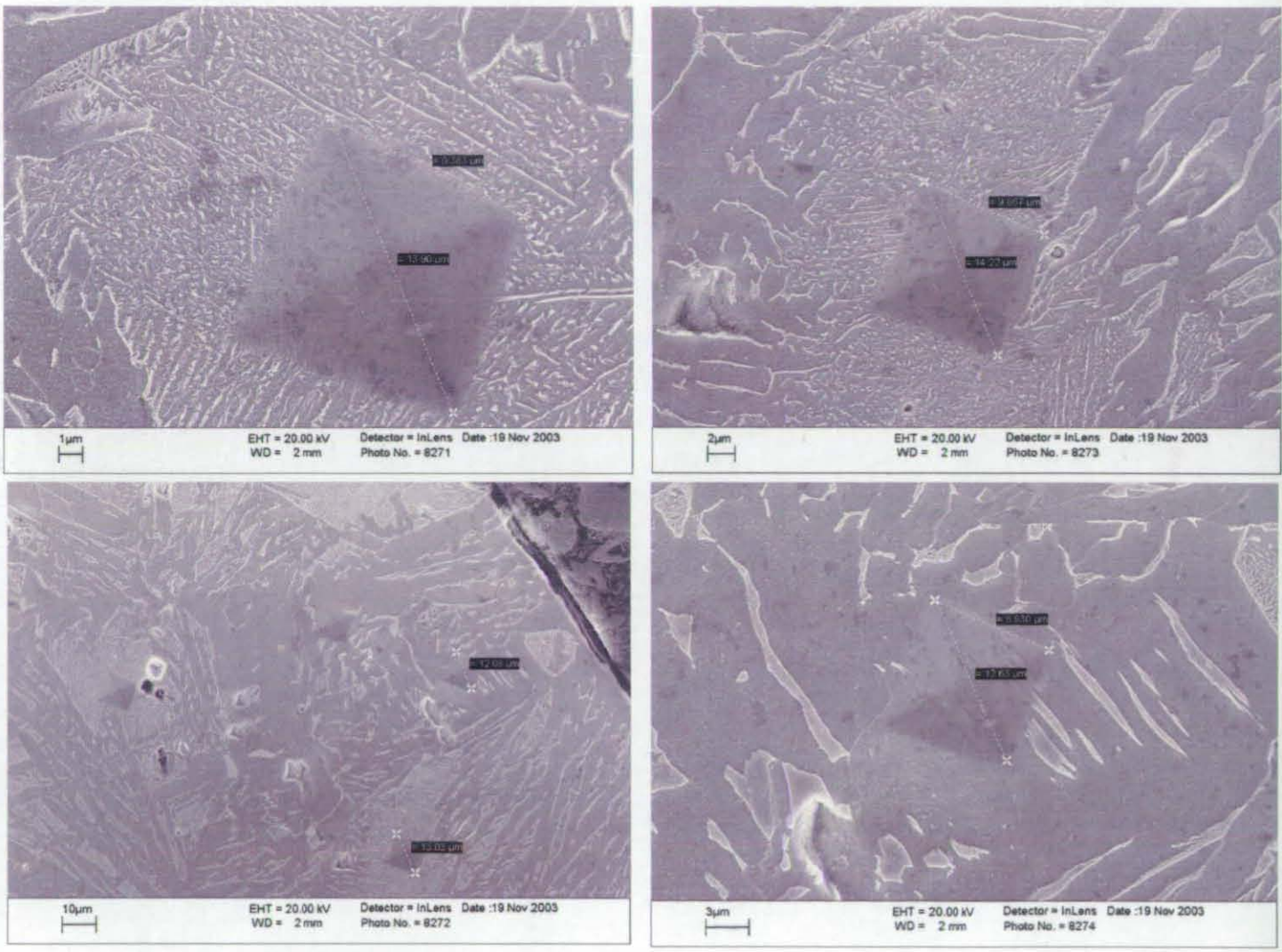

The dimensions of the indentations on the FCA regions are in agreement with those previously found in samples which were continuously cooled to room temperature without interruption.

Phase quantification data

Phase quantification performed on the three samples whose cooling was interrupted show the microstructural evolution at the different cooling stages, in terms of phase fractions, as detailed in table 6.4 and 6.5.

Table 6.4: *Phase quantification at the different stages of cooling (sample austenitised at 1100°C, cooled at 10°C s^{-1})*

PHASE	Cooling Interrupted at (°C)		
	659°C	637°C	615°C
Primary Ferrite	18 %	23 %	28 %
Widmanstätten F.	11.5 %	25 %	39 %
Microphase	0.5 %	1 %	9 %
Martensite	70 %	51 %	-
FCA	-	-	24 %

Table 6.5: *Phase quantification at the different stages of cooling (sample austenitised at 1300°C, cooled at 10°C s^{-1})*

PHASE	Cooling Interrupted at (°C)		
	624°C	606°C	587°C
Primary Ferrite	7 %	9 %	17 %
Widmanstätten F.	6 %	13 %	41 %
Microphase	0.5 %	1 %	16 %
Martensite	86.5 %	76 %	-
FCA	-	-	26 %

The phase quantification provides an indication of the microstructure evolution during continuous cooling. This, coupled with the results of the morphological analysis, allows the determination of a transformation sequence. The primary ferrite forms first, followed by Widmanstätten ferrite. The formation of FCA appears to occur at lower temperatures compared to Widmanstätten ferrite. Furthermore, the interrupted continuous cooling experiments also suggest that one of the most important parameters influencing the FCA formation is the carbon content of the austenite at a given temperature. However, it should be noted that as the local conditions vary along the sample, the transformations cannot be fully separated in a sequence. Widmanstätten ferrite formation, for instance, can occur simultaneously to the FCA formation which takes place in another region of the sample.

6.9.2 Cooling rate 50°C s^{-1}

When the cooling rate increases from 10 to 50°C s^{-1}, the formation of FCA occurs after Widmanstätten ferrite has formed, but before bainite, or simultaneously in some cases, depending on the local composition of the austenite. The SEM analysis performed on a sample for which the cooling was interrupted at a late stage of cooling, showed primary ferrite and Widmanstätten ferrite completely transformed, in addition to some regions of bainite, some of martensite which formed upon quenching, and some grains of FCA coexisting with martensite. The latter transformed from a carbon enriched austenite region, but could not reach completion before the quenching step, causing martensite to form.

Figure 6.66a-d: *Morphologies observed in sample Y7N1 1100/50/i592/q. FCA and martensite*

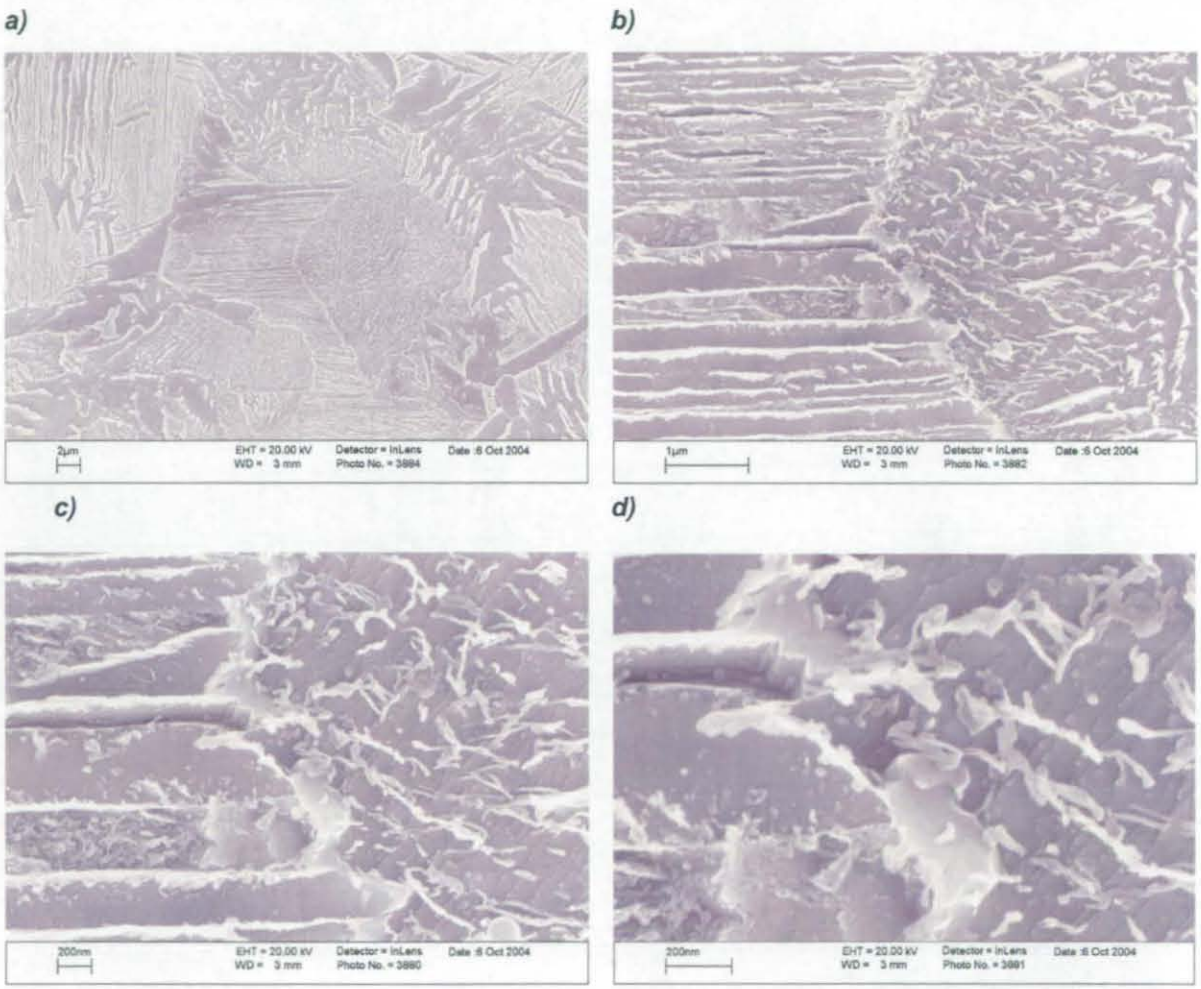

e)


1µm
EHT = 20.00 kV
WD = 3 mm
Detector = InLens
Photo No. = 3870
Date :6 Oct 2004

f)

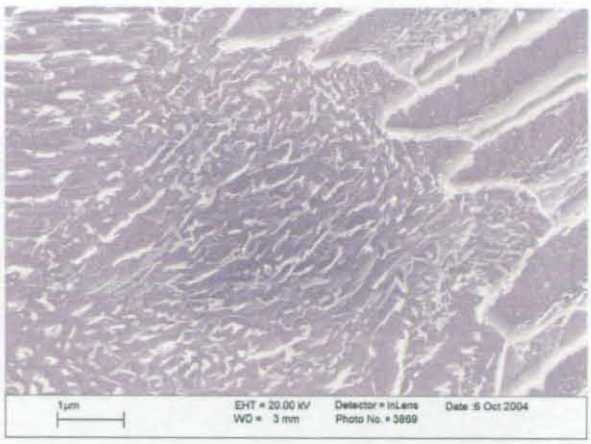
1µm
EHT = 20.00 kV
WD = 3 mm
Detector = InLens
Photo No. = 3869
Date :6 Oct 2004

g)

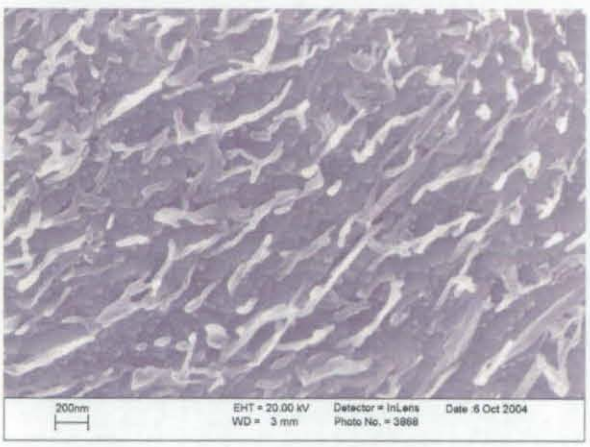
200nm
EHT = 20.00 kV
WD = 3 mm
Detector = InLens
Photo No. = 3868
Date :6 Oct 2004

h)

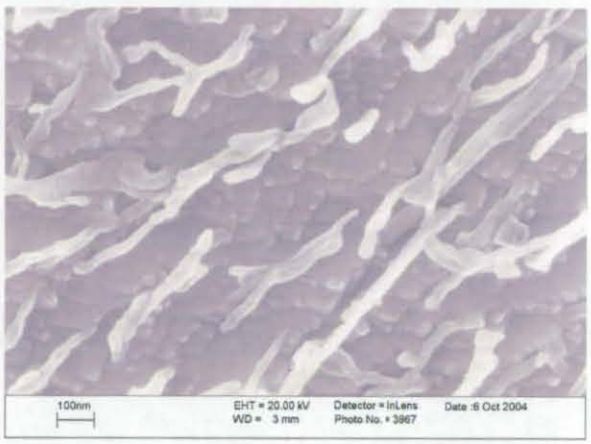
100nm
EHT = 20.00 kV
WD = 3 mm
Detector = InLens
Photo No. = 3867
Date :6 Oct 2004

i)

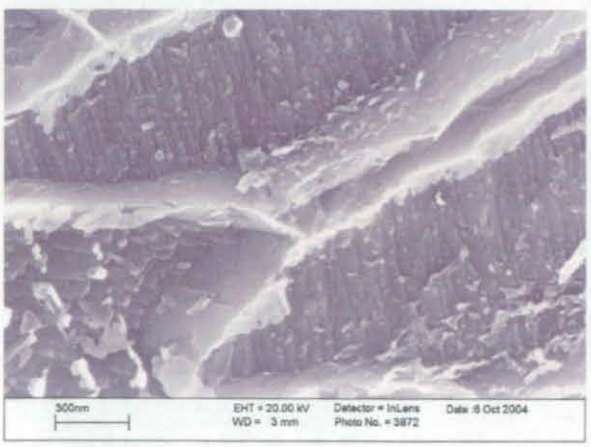
300nm
EHT = 20.00 kV
WD = 3 mm
Detector = InLens
Photo No. = 3872
Date :6 Oct 2004

k)

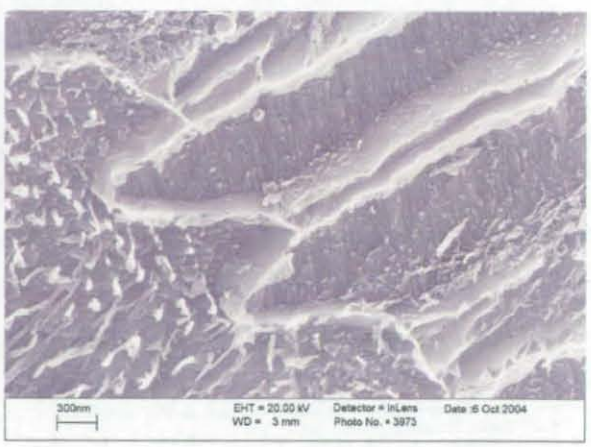
300nm
EHT = 20.00 kV
WD = 3 mm
Detector = InLens
Photo No. = 3873
Date :6 Oct 2004

l)

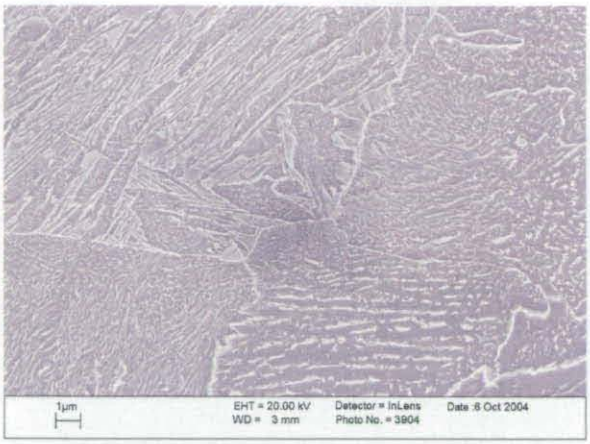
1µm
EHT = 20.00 kV
WD = 3 mm
Detector = InLens
Photo No. = 3904
Date :6 Oct 2004

m)

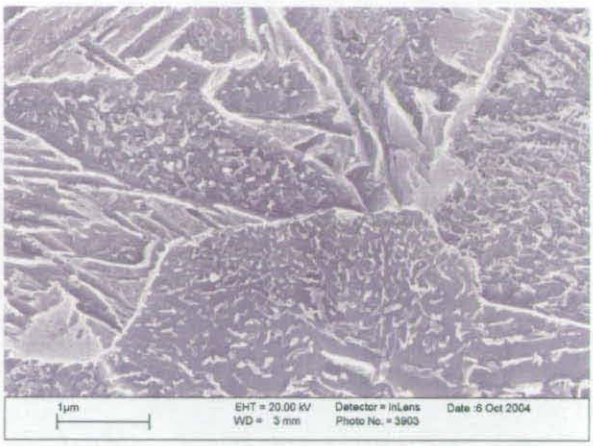
1µm
EHT = 20.00 kV
WD = 3 mm
Detector = InLens
Photo No. = 3903
Date :6 Oct 2004

n)

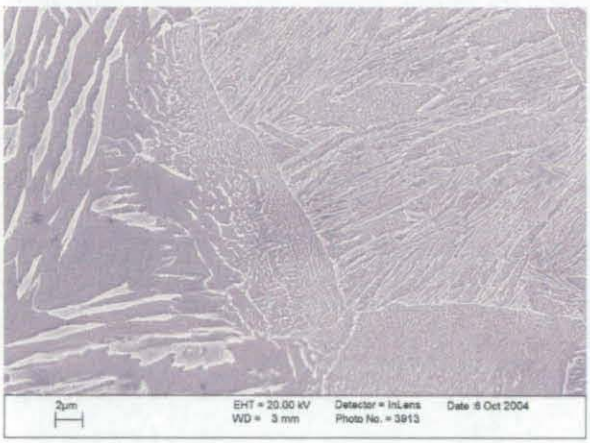
2µm
EHT = 20.00 kV
WD = 3 mm
Detector = InLens
Photo No. = 3913
Date :6 Oct 2004

o)

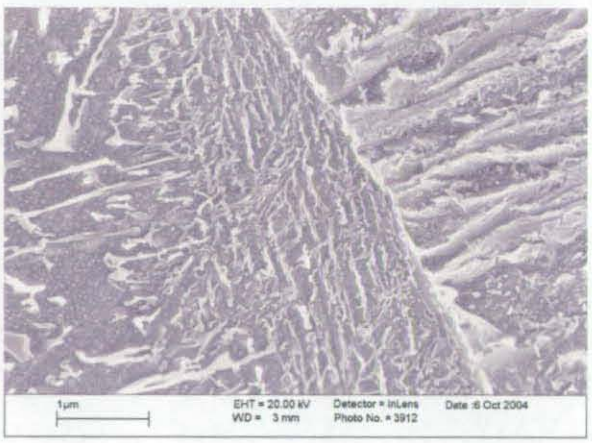
1µm
EHT = 20.00 kV
WD = 3 mm
Detector = InLens
Photo No. = 3912
Date :6 Oct 2004

p)

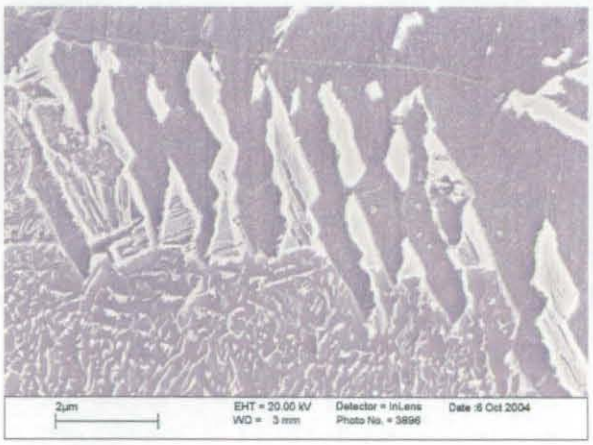
2µm
EHT = 20.00 kV
WD = 3 mm
Detector = InLens
Photo No. = 3896
Date :6 Oct 2004

q)

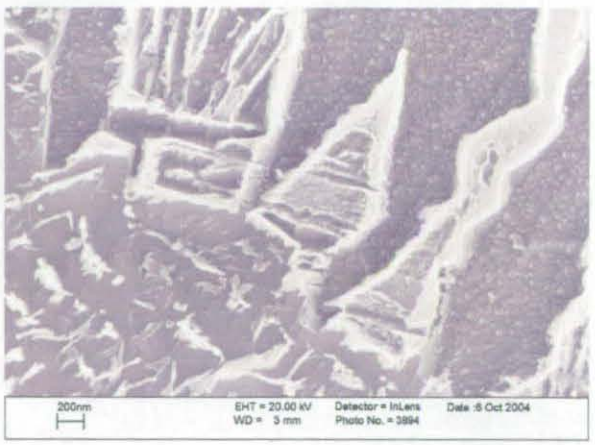
200nm
EHT = 20.00 kV
WD = 3 mm
Detector = InLens
Photo No. = 3894
Date :6 Oct 2004

r)

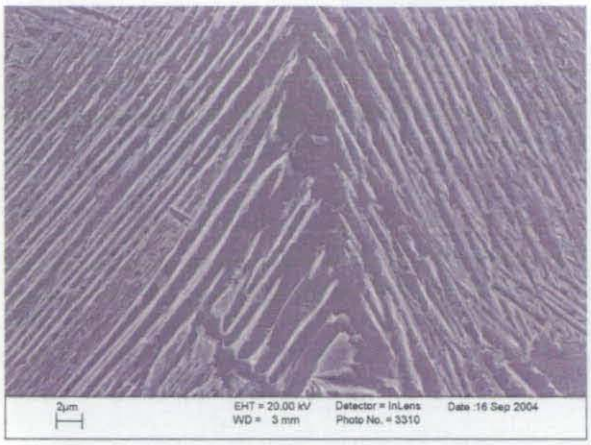
2µm
EHT = 20.00 kV
WD = 3 mm
Detector = InLens
Photo No. = 3310
Date :16 Sep 2004

s)

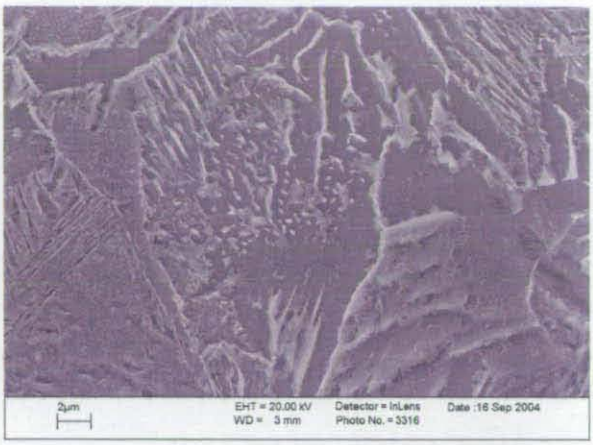
2µm
EHT = 20.00 kV
WD = 3 mm
Detector = InLens
Photo No. = 3316
Date :16 Sep 2004

t)

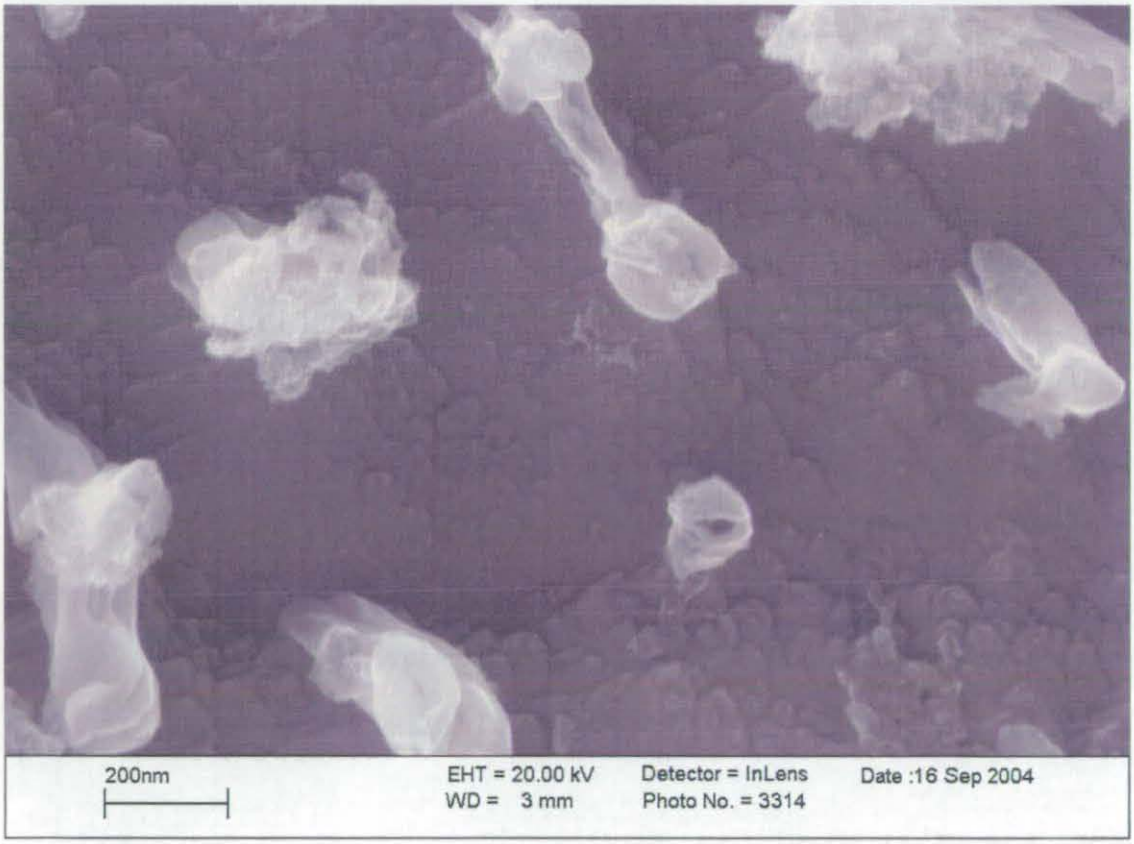
200nm
EHT = 20.00 kV
WD = 3 mm
Detector = InLens
Photo No. = 3314
Date :16 Sep 2004

u)

v)

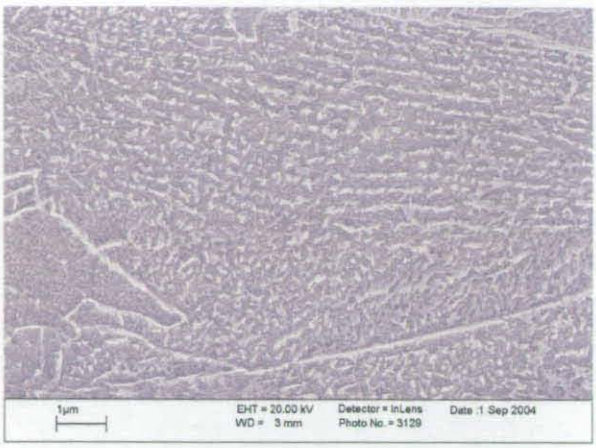

w)

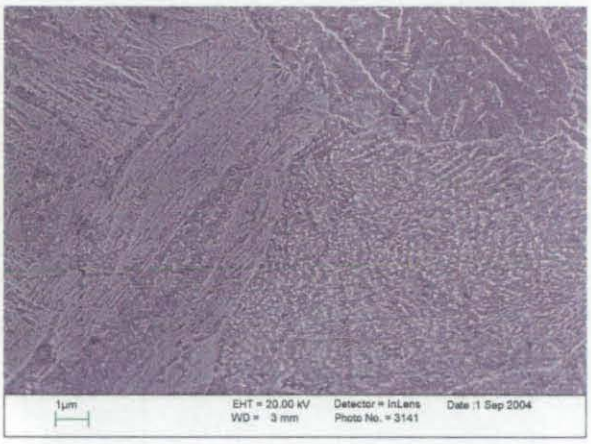

x)

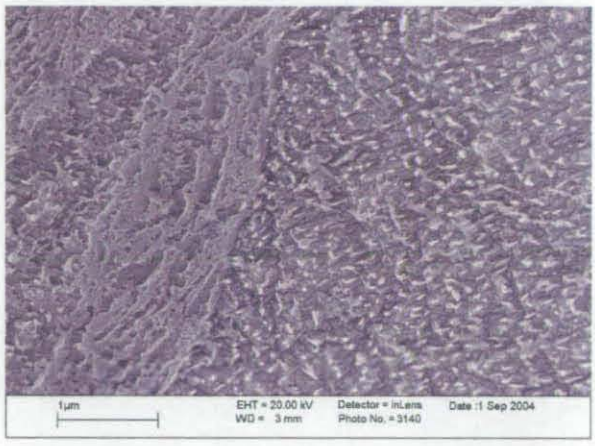

y)

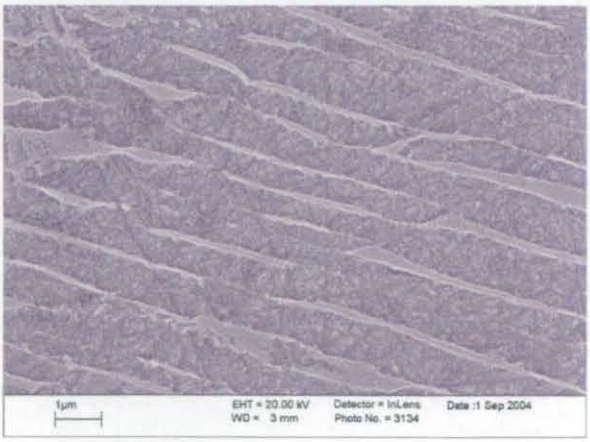

z)

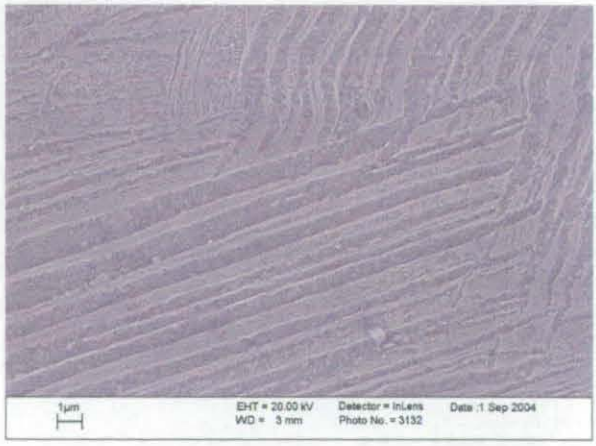

The images in figure 6.66 show an FCA region in which the carbide precipitation continues until the cooling rate is suddenly increased and the formation of martensitic laths takes place.

6.10 Summary

In this chapter, the complete characterisation of a ferrite-carbide aggregate, referred to as FCA, has been discussed. The phase identification task involved the use of several investigation techniques. The FCA phase, appearing as a dark etching phase under the optical microscope, did not fully match any of the phases listed in the contemporary phase classification schemes. The formation of this phase has been observed in alloy Y7N1 at cooling rates ranging between 5 and 75°C s^{-1}, although its fraction appeared to decrease at cooling rates higher than 50°C s^{-1}. The use of SEM (InLens detection) has allowed for the determination of the morphological characteristics of this phase, which appears to have a ferritic matrix in which fine particles (40 nm size on average) are interspersed. The particles can occur in arrays, or as interconnected particles. The TEM analysis has shown that there are no laths in the matrix of the FCA, therefore indicating that the nature of the reaction should be reconstructive. Furthermore, most particles were identified as cementite.

The reconstructive nature of the FCA phase was also confirmed by the micro-hardness data which indicated a slightly higher hardness than that of primary ferrite. The EBSD analysis confirmed the absence of laths within the FCA regions. It also allowed for a distinction to be made between the FCA phase and pearlite, providing valuable information about the nucleation and growth of the FCA in relation to the crystallographic orientation data obtained.

The determination of the stage during cooling at which the FCA would form has been possible through interrupted continuous cooling experiments. There is evidence suggesting that the formation of FCA is related to that of Widmanstätten ferrite. The FCA is thought to form after Widmanstätten ferrite, but prior to bainite. The identification of the FCA phase and the understanding of its nature is believed to be fundamental in order to assess in a more comprehensive and accurate manner all of the transformations taking place under continuous cooling conditions.

It is also thought that the conclusive identification of the FCA phase represents an essential step towards the subsequent investigation of its influence on the mechanical properties of the steel. The formation of the FCA in other low carbon steels, and the effects of varying the steel composition, are discussed in the following chapter.

7. Compositional Effects

The Effect of Chemical Composition on Phase Transformations

7.1 Introduction

The focus of this chapter is to consider the effect of variation in the steel composition of the formation of the FCA phase. Two additional steels are considered, HOM146 (0.52 wt.% Mn) and HOM148 (1.56 wt.% Mn), and are compared to the steel used throughout the rest of this work, alloy Y7N1 (0.86 wt.% Mn). The occurrence of the FCA phase in all the three alloys has been observed. This chapter considers the differences in transformations temperatures, morphology and relative volume fractions as a function of steel composition, and specifically the variation in manganese concentration.

7.2 Heat Treatments, dilatometry and optical analysis for alloy HOM146

7.2.1 Austenitisation at 1100°C; Cooling Rate of 2°C s^{-1}

Figure 7.1: *Dilation curve and optical microstructure of sample HOM146 1100/2*

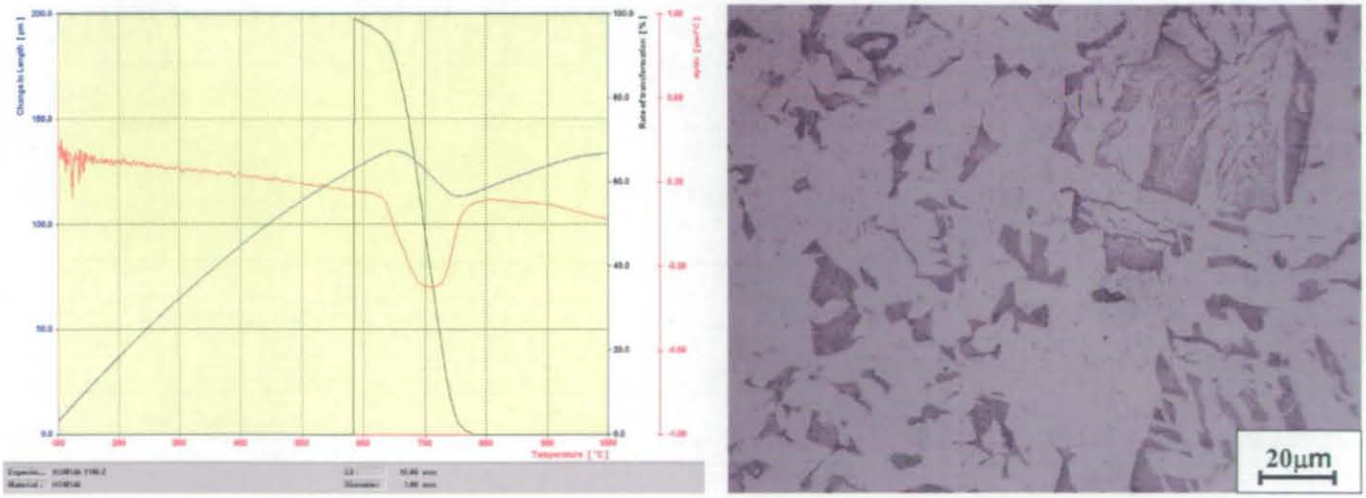

At the slowest cooling rate (i.e. 2°C s^{-1}), alloy HOM146 consists of primary ferrite and pearlite, with a microstructure coarser than that of alloy Y7N1 cooled at the same rate. The presence of FCA at this cooling rate has not been observed by means of high magnification microscopy techniques, as further discussed in the following section. It is thought that the transformations take place reconstructively over a large temperature range.

7.2.2 Austenitisation at 1100°C; Cooling Rate of 5°C s^{-1}

Figure 7.2: *Dilation curve and optical microstructure of sample HOM146 1100/5*

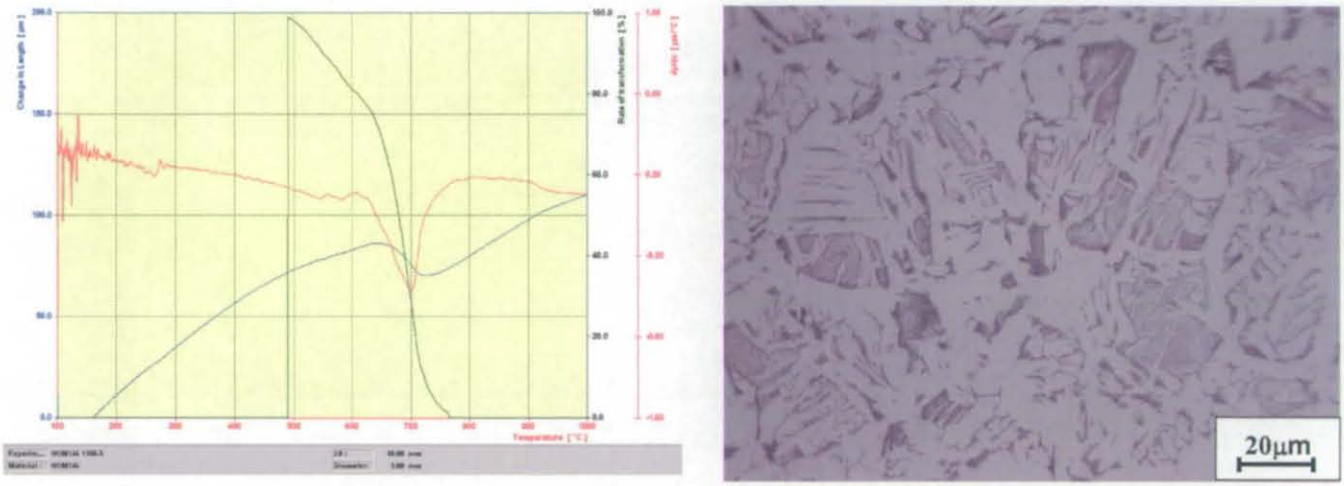

Increasing the cooling rate up to 5°C s^{-1} produces a finer microstructure, although the dominant character of the phase transformations taking place is still reconstructive. The main constituent is primary ferrite, with the pearlite still present in small regions between the grains. Some coarse Widmanstätten ferrite starts forming at this cooling rate, as does the FCA phase. The characteristics of the FCA phase formed at relatively low cooling rates, previously described for alloy Y7N1, are the same in alloy HOM146. The dimensions of the FCA phase are much larger compared to the pearlite, their shape appears irregular and the etching response is lighter than that of the pearlitic regions.

7.2.3 Austenitisation at 1100°C; Cooling Rate of 10°C s^{-1}

Figure 7.3: *Dilation curve and optical microstructure of sample HOM146 1100/10*

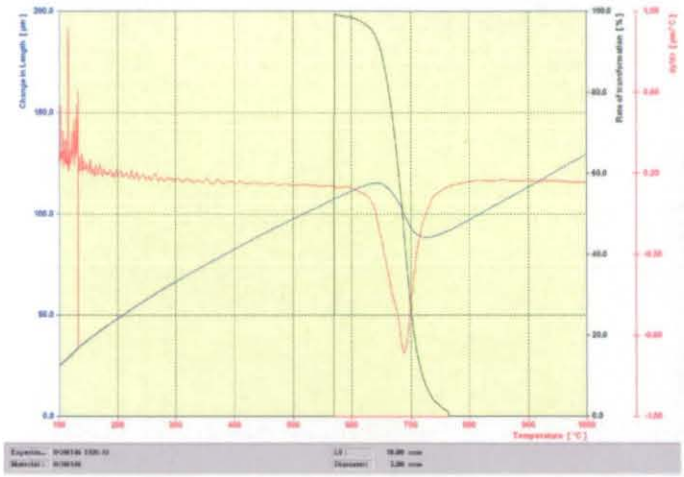

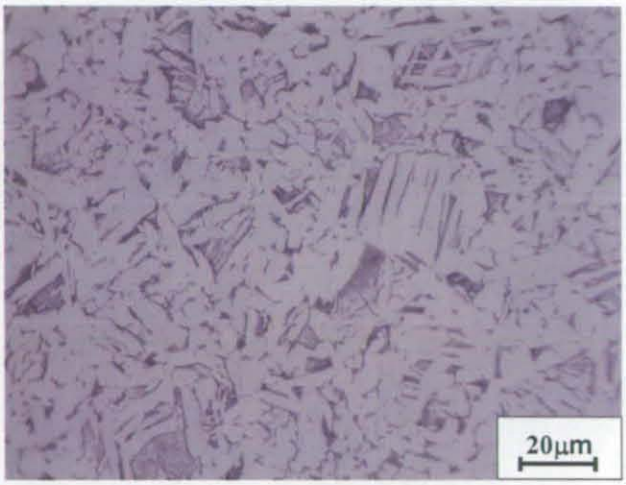

At a cooling rate of 10°C s^{-1}, the microstructure becomes finer and the proportions of Widmanstätten ferrite do not exceed those of the primary ferrite, as observed in alloy Y7N1. In this case it has been found that the amount of the FCA phase, as observed for alloy Y7N1, increases with increasing Widmanstätten ferrite. Furthermore, the ferrite sideplates are coarser compared to alloy Y7N1 cooled at the same cooling rate. Overall, the characteristics of the FCA appear consistent with the observations made for alloy Y7N1.

7.2.4 Austenitisation at 1100°C; Cooling Rate of 25°C s^{-1}

Figure 7.4: *Dilation curve and optical microstructure of sample HOM146 1100/25*

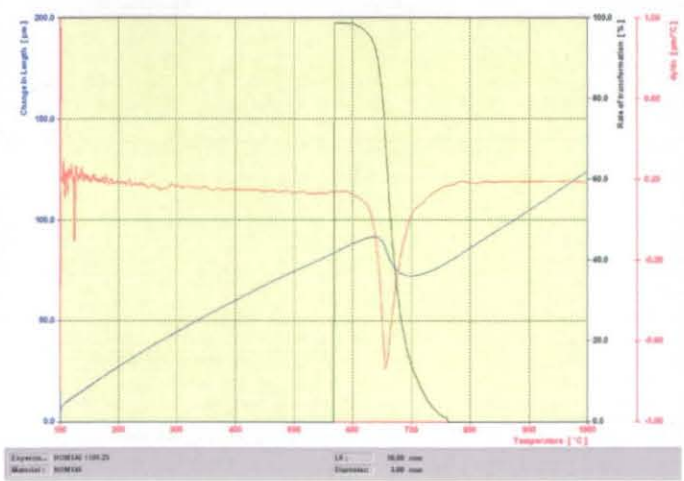

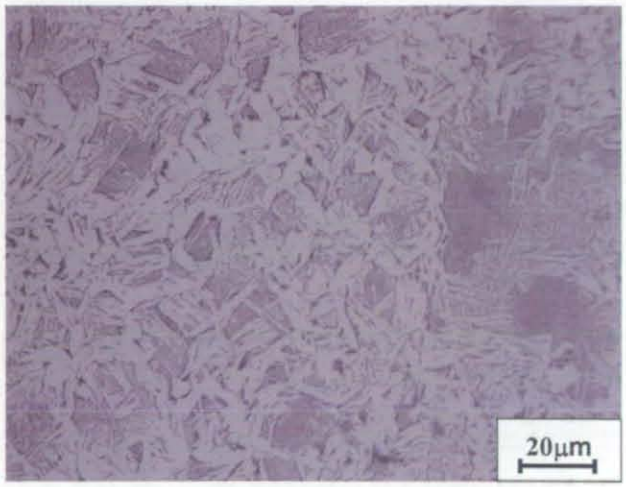

At 25°C s^{-1} the microstructure of alloy HOM146 is finer compared to that obtained at 10°Cs^{-1}. The proportion of the FCA has been found to have significantly increased at this cooling rate and together with the dimensions of the FCA grains. The growth of FCA regions occurs alongside Widmanstätten ferrite, which at this cooling rate appears to reach the same fraction as that of primary ferrite. It should be noted that at the same cooling rate, alloy Y7N1 displayed a tendency to produce Widmanstätten ferrite as its main constituent, whereas the phases forming through a purely diffusive mechanism, such as primary ferrite, were not dominant. In alloy HOM146, the opposite trend has been observed.

7.2.5 Austenitisation at 1100°C; Cooling Rate of 50°C s^{-1}

Figure 7.6: *Dilation curve and optical microstructure of sample HOM146 1100/50*

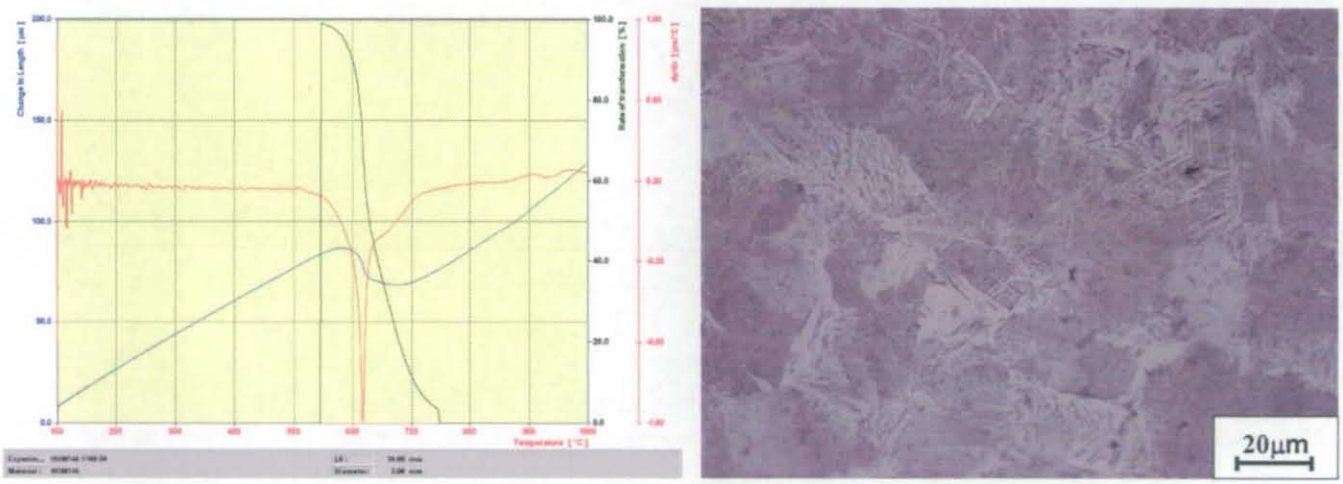

At a cooling rate of 50°C s^{-1}, the microstructure of alloy HOM146 appears to be considerably different from that observed in alloy Y7N1. The reconstructive character of the phase transformations taking place was not dominant in alloy Y7N1. In alloy HOM146 the microstructure becomes finer and the volume fraction of Widmanstätten ferrite appears to have overcome that of primary ferrite, whilst the presence of coarse upper bainite has not been observed. More importantly, the FCA phase becomes the dominant microstructural constituent of alloy HOM146. This appears to be in conflict with the behaviour of the higher-manganese alloy, as it will be discussed in section 7.3, where at a cooling rate of 50°C s^{-1} or higher, the amount of FCA would decrease and phases forming through displacive mechanisms, such as bainite, would instead become gradually dominant. Furthermore, at any of the cooling rates considered, the

FCA phase appeared to be the dominant constituent of the microstructure of alloy Y7N1.

7.2.6 Austenitisation at 1100°C; Cooling Rate of 75°C s^{-1}

Figure 7.6: *Dilation curve and optical microstructure of sample HOM146 1100/75*

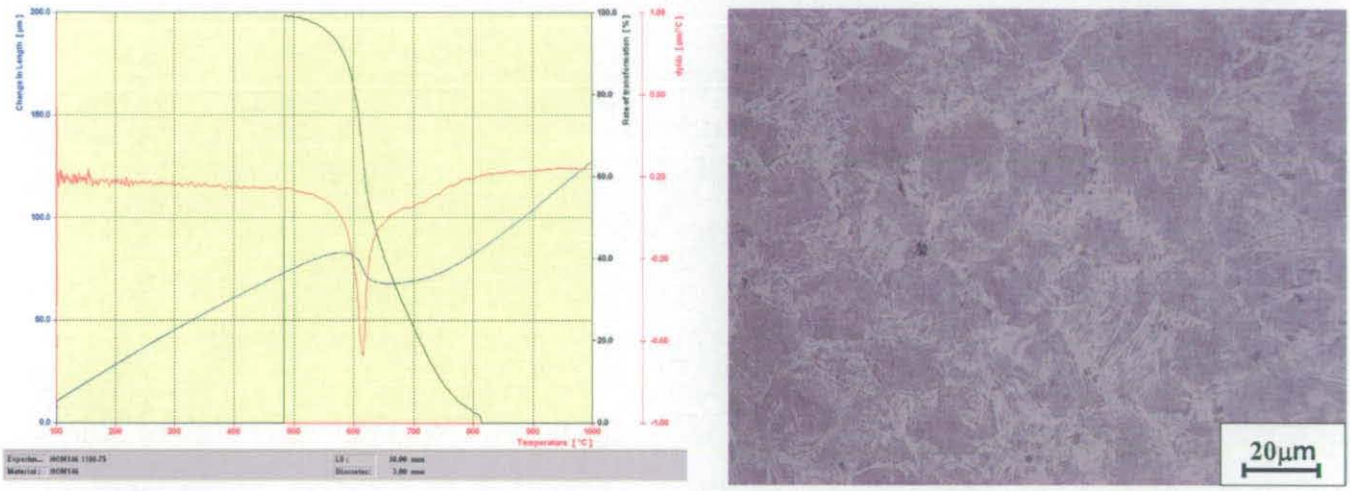

At this cooling rate, the behaviour of alloy Y7N1 was such that the phase transformations took place mainly in the displacive regime. Widmanstätten ferrite was still present in the microstrcuture as a minor constituent, whilst bainite was the dominant constituent. In the Y7N1 sample the presence of FCA was negligible. Alloy HOM146, on the other hand, behaves differently. At a cooling rate of 75°C s^{-1} bainite was not been observed, with Widmanstätten ferrite being the main ferritic component, characterised by a finer structure of the sideplates. However, as observed at a cooling rate of 50°C s^{-1}, FCA remains the main microstructural constituent. The lower manganese content appears to promote the formation of FCA and delay the formation of bainite to higher cooling rates.

7.2.7 Austenitisation at 1100°C; Cooling Rate of 100°C s^{-1}

Figure 7.7: *Dilation curve and optical microstructure of sample HOM146 1100/100*

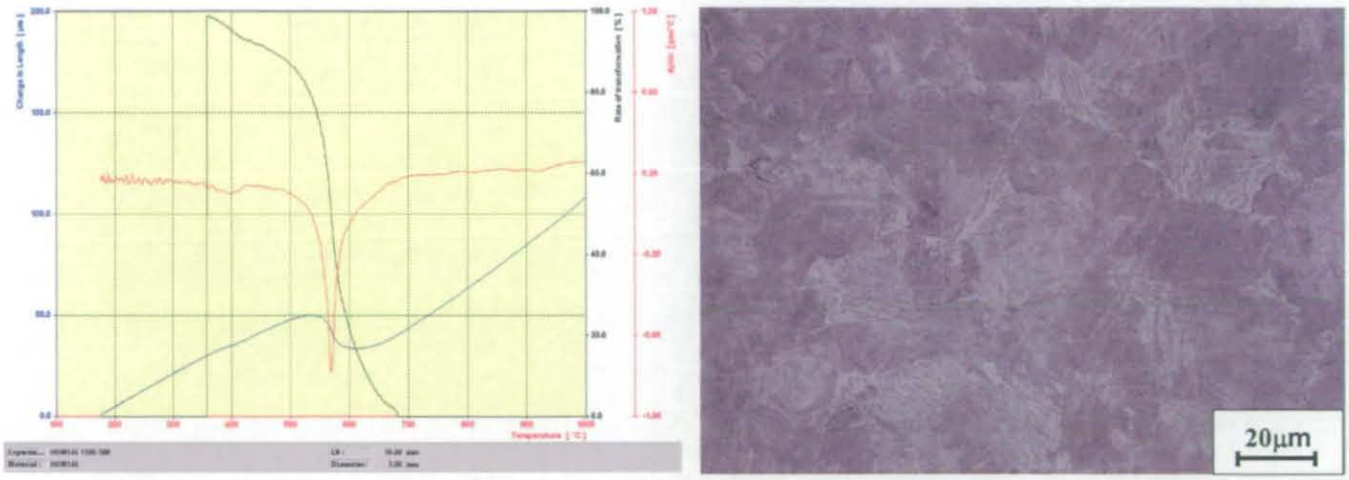

The effect of manganese is so strong that even at a cooling rate of 100°C s^{-1}, the presence of FCA was still observed, and was one of the major phases present. The microstructure overall consists of primary ferrite limited to small layers at prior austenite grain boundaries, Widmanstätten ferrite, FCA and upper bainite.

7.2.8 Austenitisation at 1100°C; Cooling Rate of 150°C s^{-1}

Figure 7.8: *Dilation curve and optical microstructure of sample HOM146 1100/150*

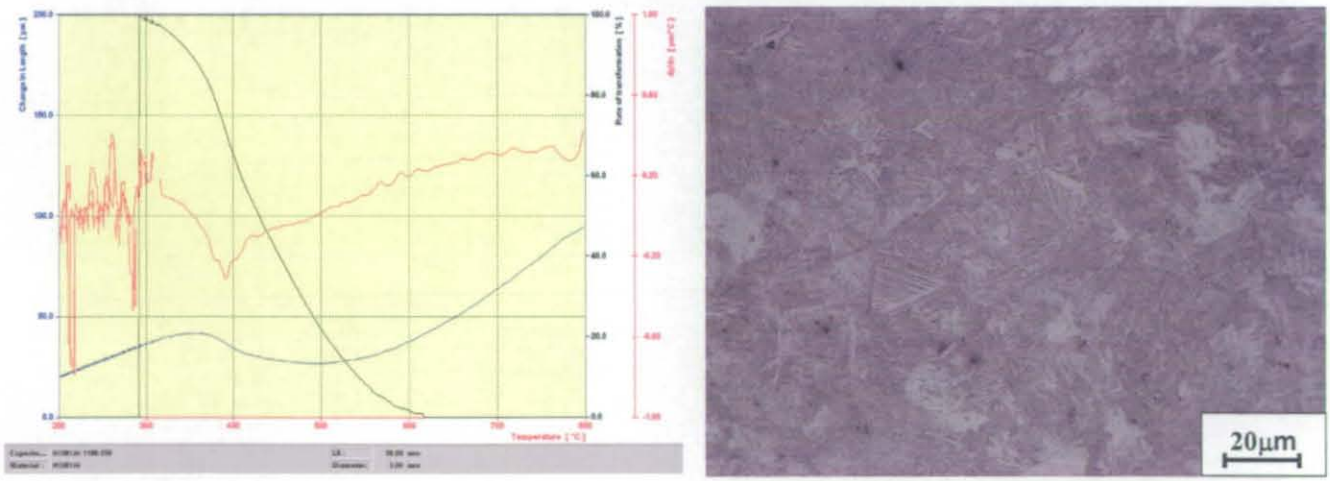

At this cooling rate the microstructure consists of Widmanstätten ferrite, FCA, upper and lower bainite, and appears very different from lower cooling rates, as on this case the main component of phase transformations being displacive. The formation of Widmanstätten ferrite and FCA, taking place at higher temperatures, is

very limited. The dimensions of the FCA grains are much smaller compared to the lower cooling rates. The dominant constituents are upper and lower bainite. Therefore, at this cooling rate it can be considered to happen the shifting from phases transformation with a strong diffusive character to the ones with a strong displacive component. This would happen at approximately 75°C s^{-1} for alloy Y7N1.

7.2.9 Austenitisation at 1100°C; Cooling Rate of 200°C s^{-1}

Figure 7.9: *Dilation curve and optical microstructure of sample HOM146 1100/200*

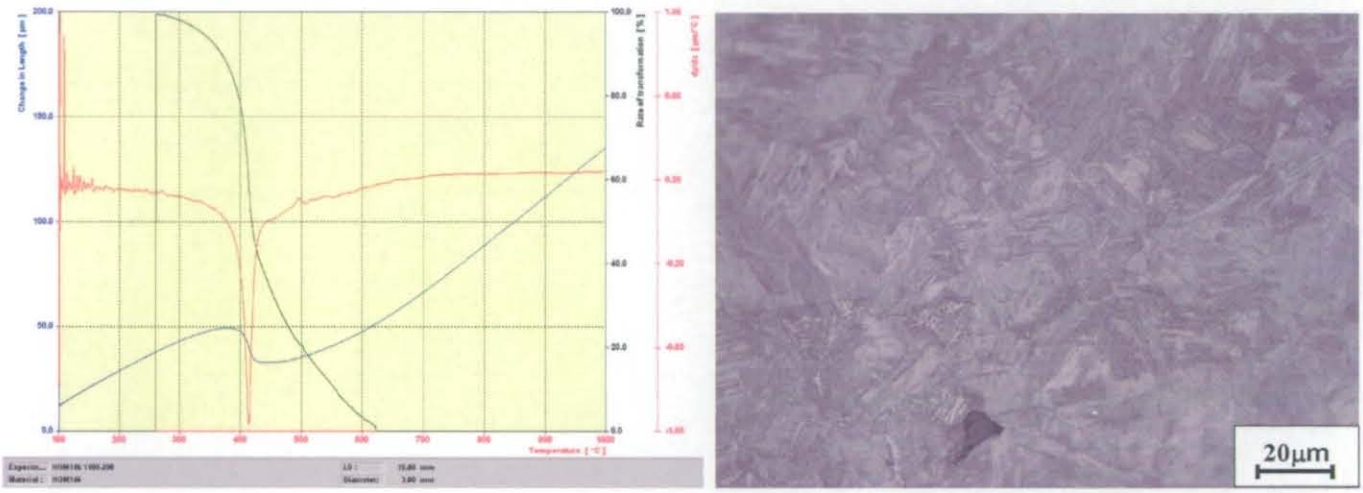

At this cooling rate, the microstructure consists solely of lower bainite and martensite.

For convenience the overall transformation start and finish temperatures are listed in table 7.1.

Table 7.1: *Transformation start and finish temperatures for alloy HOM146, continuously cooled.*

Alloy HOM146 austenitised at 1100°C		
Cooling Rate (°C s^{-1})	**T_s (°C)**	**T_f (°C)**
2	790	575
5	788	578
10	783	577
25	764	564
50	731	539
75	713	504
100	676	468
150	633	306
200	616	276

7.3 Heat Treatments, dilatometry and optical analysis for alloy HOM148

7.3.1 Austenitisation at 1100°C; Cooling Rate of 2°C s^{-1}

Figure 7.10: *Dilation curve and optical microstructure of sample HOM148 1100/2*

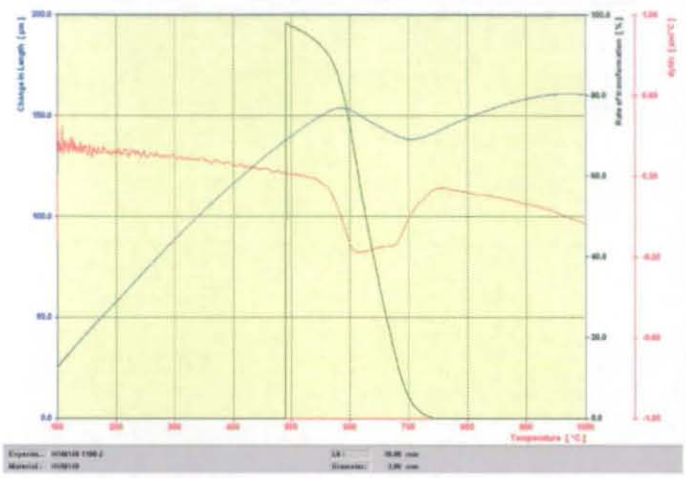

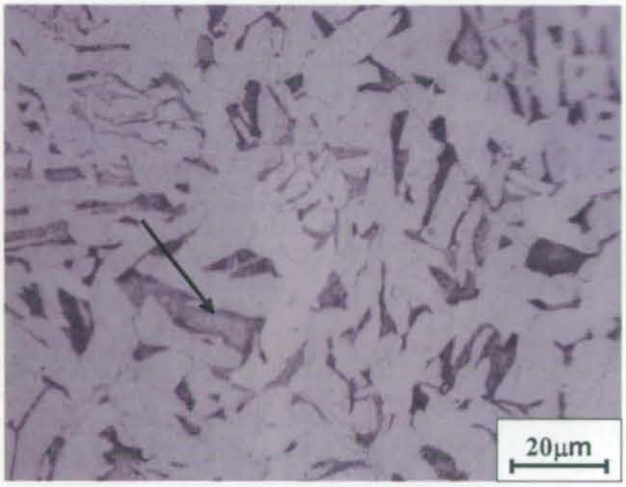

The transformations taking place in alloy HOM148 at 2°C s^{-1} produced a microstructure which is significantly different from the one observed for alloy HOM146. The effect of increasing manganese causes the formation of FCA at this low cooling rate. The microstructure consists of primary ferrite, pearlite and FCA, (indicated by an arrow in the optical image) and is finer compared to that of alloy HOM146 cooled at the same rate. The pearlitic regions appear to be smaller, but more numerous, and always forming between primary ferrite grains which nucleate on prior austenite grain boundaries. The dimensions of the ferrite grains are smaller than those in alloy HOM146 cooled at 2°C sec^{-1}. The FCA grain dimensions are in the range of 10-20 μm. The etching response of FCA, as observed in alloys HOM146 and Y7N1, is lighter than the pearlite providing the characteristic "spongy" appearance.

7.3.2 Austenitisation at 1100°C; Cooling Rate of 5°C s^{-1}

Figure 7.11: *Dilation curve and optical microstructure of sample HOM148 1100/5*

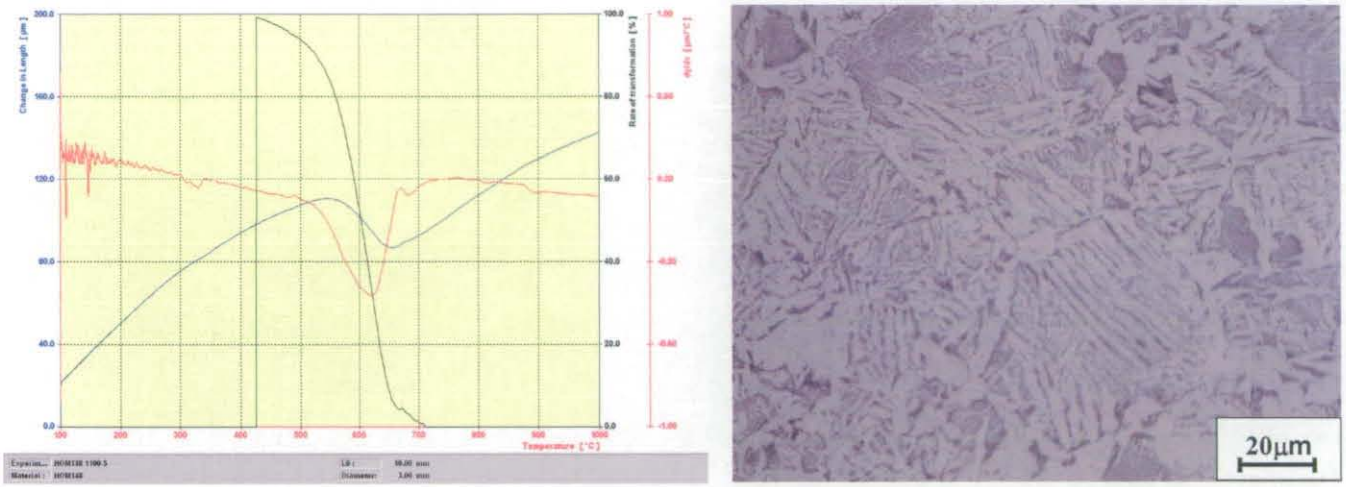

At 5°C s^{-1}, the main microstructural constituent is allotriomorphic ferrite, although the grains are more irregular and finer compared to alloy HOM146. The pearlite volume fraction decreased whilst the FCA fraction increased. Furthermore, at this cooling rate, coarse sideplates of Widmanstätten ferrite start to form, representing the second main microstructural constituent.

7.3.3 Austenitisation at 1100°C; Cooling Rate of 10°C s^{-1}

Figure 7.12: *Dilation curve and optical microstructure of sample HOM148 1100/10*

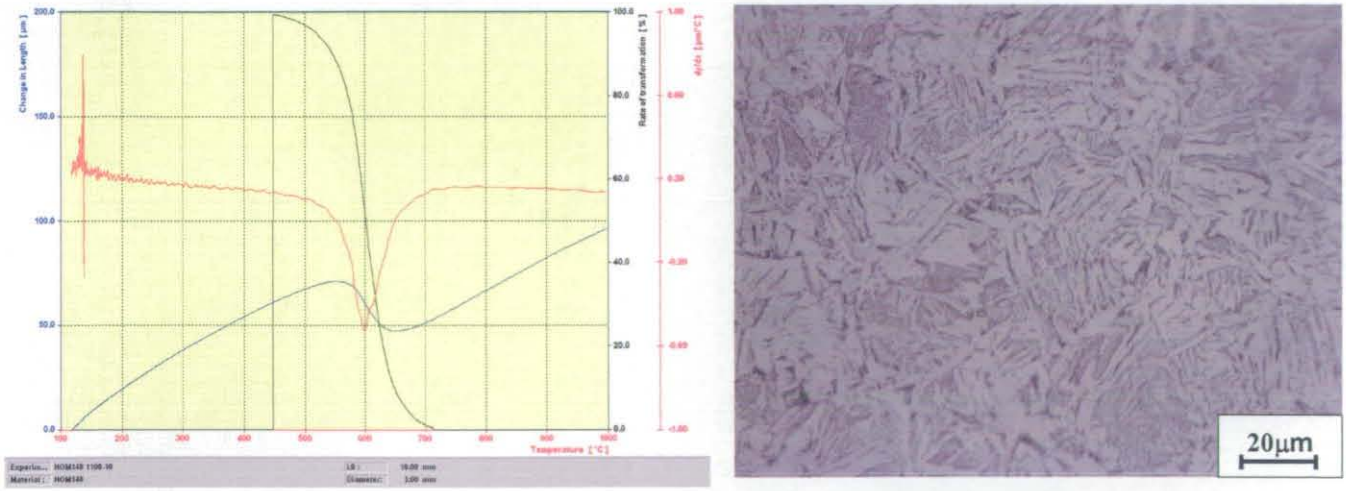

At a cooling rate of 10°C s^{-1} the effect of manganese becomes very evident. The microstructure obtained mainly consists of Widmanstätten ferrite, whose structure is

much finer, compared to alloy HOM146 and alloy Y7N1 cooled at the same rate. In most cases, the Widmanstätten ferrite is secondary, therefore nucleating on primary ferrite layers which grew at higher temperature, after nucleation on prior austenite grain boundaries. Pearlite is limited to the microphase regions within the ferrite sideplates. The FCA dimensions are very similar to those encountered in alloy Y7N1 cooled at 50°C s^{-1}. This indicates that for alloy HOM148, the range of cooling rates at which FCA form and develop is shifted to lower cooling rates. The appearance of the FCA regions is in fact very similar to that obtained at higher cooling rates in alloy Y7N1.

7.3.4 Austenitisation at 1100°C; Cooling Rate of 25°C s^{-1}

Figure 7.13: *Dilation curve and optical microstructure of sample HOM148 1100/25*

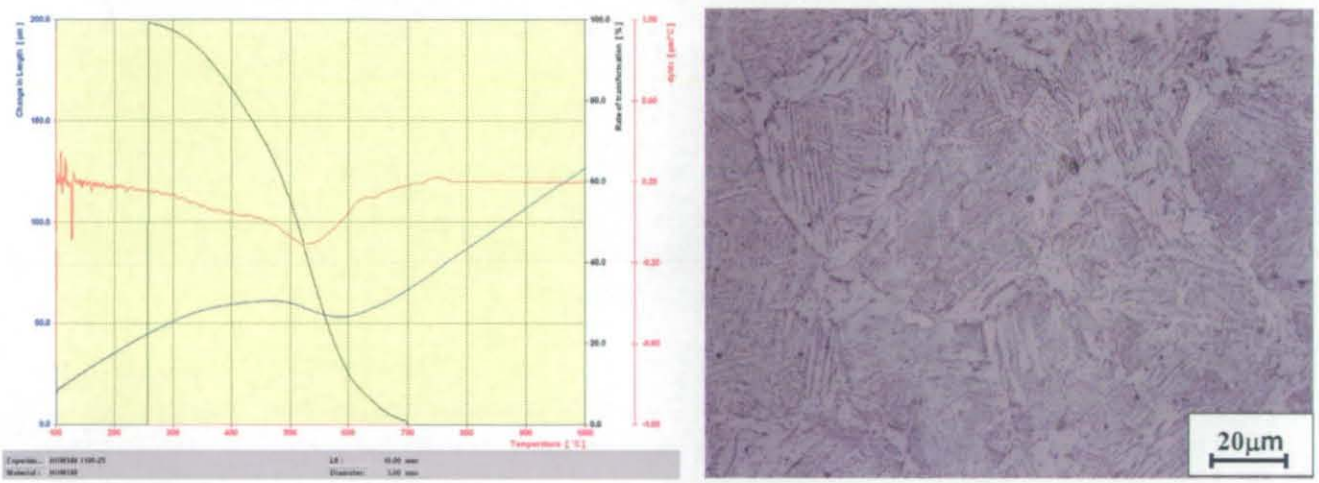

As the cooling rate is raised to 25°C s^{-1}, the optical observation of the microstructure produced suggests that the transformations taking place via diffusion based mechanisms are not favoured anymore due to the increase in the Mn concentration. The microstructure present fine layers of primary ferrite nucleating at prior austenite grain boundaries. Their growth stops at the early stages of cooling, being replaced by secondary Widmanstätten ferrite. The morphology of the sideplates is very fine. The sideplates grow into the untransformed austenite, which subsequently transforms into FCA or into upper bainite, depending on the local concentration profile and the exact transformation temperature. Therefore, the formation of upper bainite is possible at this cooling rate in alloy HOM148. This was not possible neither in alloy HOM146 nor in alloy Y7N1.

7.3.5 Austenitisation at 1100°C; Cooling Rate of 50°C s^{-1}

Figure 7.14: *Dilation curve and optical microstructure of sample HOM148 1100/50*

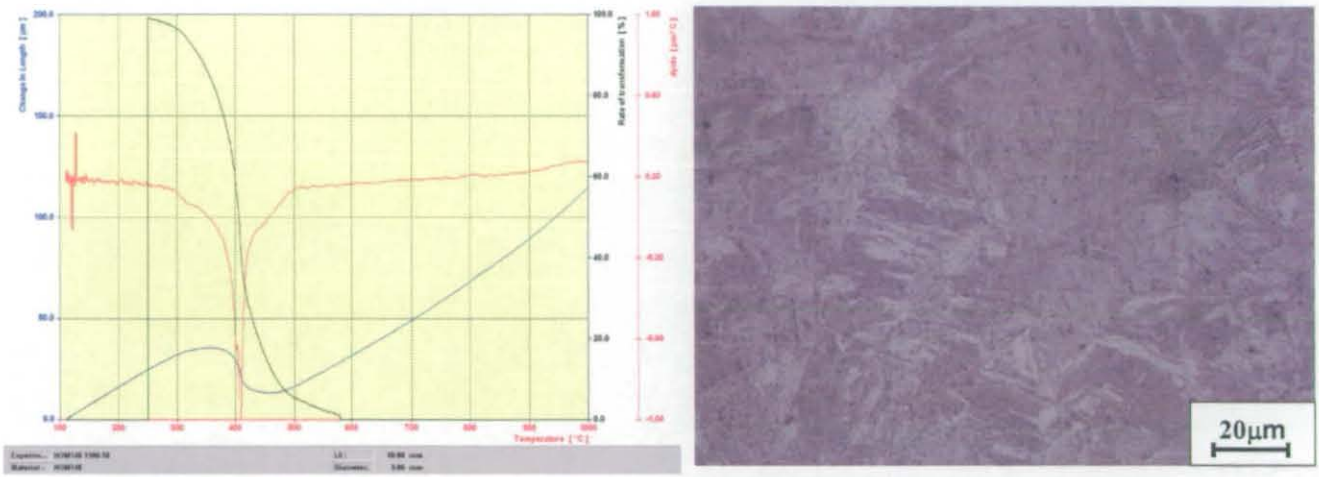

At 50°C s^{-1} the microstructure is mainly composed of upper bainite. Lower bainite starts to form although its amount is not significant. Again, this type of transformation would take place at higher cooling rates in both alloys HOM146 and Y7N1. The presence of Widmanstätten ferrite is limited to very fine plates growing from the prior austenite grain boundaries. The amount of primary ferrite is negligible and the development of FCA phase is very limited in terms of volume fraction. The grain dimensions of the FCA phase appear to be very small, whereas in alloy Y7N1 and alloy HOM146, the amount of FCA was greatest at cooling rates of 50°C s^{-1}, the tendency observed in alloy HOM148 is the opposite. In fact, at cooling rates higher than 50°C s^{-1}, the transformation leading to the formation of FCA does not take place as the conditions under which it occurs are not satisfied anymore.

7.3.6 Austenitisation at 1100°C; Cooling Rate of 75°C s^{-1}

Figure 7.15: *Dilation curve and optical microstructure of sample HOM148 1100/75*

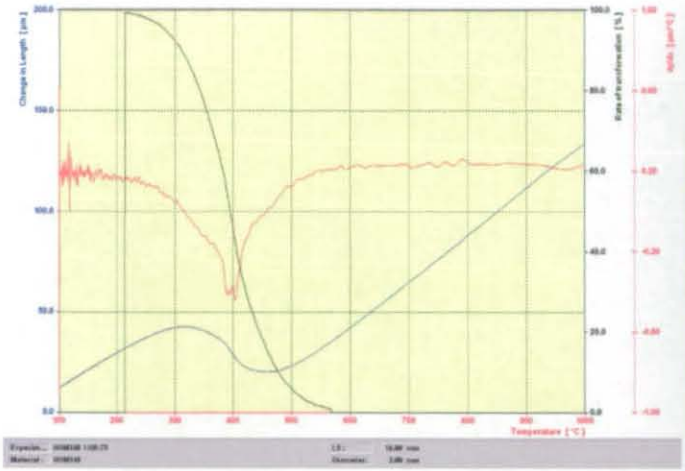

As expected by observing the transformation trend relative to the lower cooling rates, alloy HOM148 cooled at 75°C s^{-1} transforms in a displacive manner, producing upper and lower bainite. Lower bainite becomes the main microstructural constituent, in addition to fine upper bainite. Martensite starts to form, implying the fact that at this cooling rate, the temperature range where purely displacive transformations take place is reached. Some very fine regions of Widmanstätten ferrite are still able to develop at prior austenite grain boundaries. The formation of FCA does not take place.

7.3.7 Austenitisation of 1100°C; Cooling Rate of 100°C s^{-1}

Figure 7.16: *Dilation curve and optical microstructure of sample HOM148 1100/100*

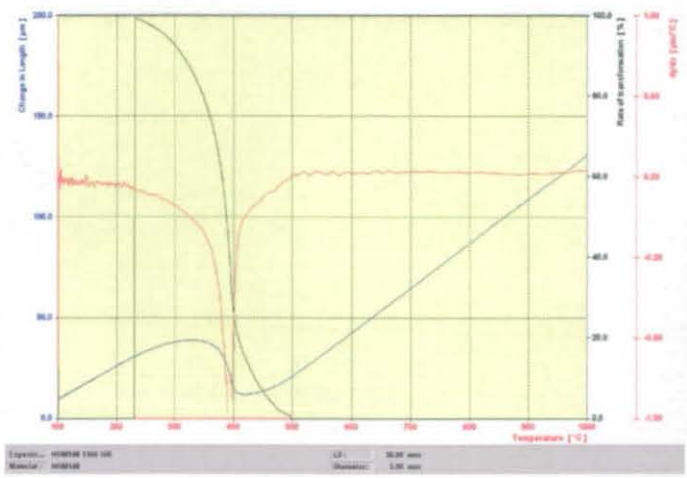

At cooling rates of 100°C s^{-1} or higher, the transformations become totally displacive. Therefore, the only microstructural constituents found are bainite in its lower morphology and martensite, the volume fractions changing as a function of the cooling rates.

7.3.8 Austenitisation at 1100°C; Cooling Rate of 150°C s^{-1}

Figure 7.17: *Dilation curve and optical microstructure of sample HOM148 1100/150*

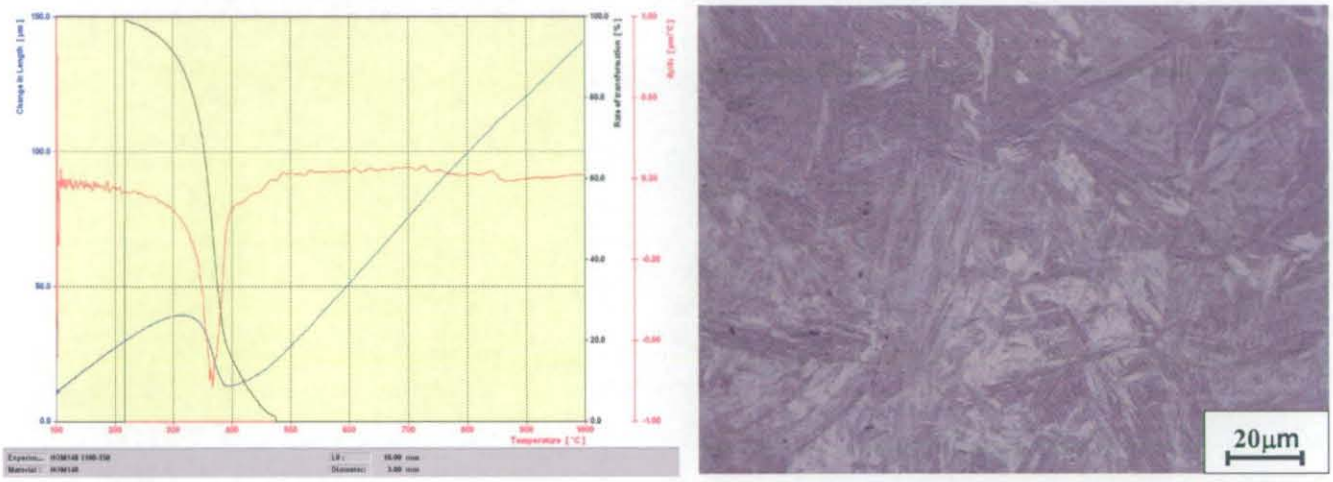

At 150°C s^{-1} martensite is the dominant constituent, whilst the amount of bainite decreases.

7.3.9 Austenitisation at 1100°C; Cooling Rate of 200°C s^{-1}

Figure 7.18: *Dilation curve and optical microstructure of sample HOM148 1100/200*

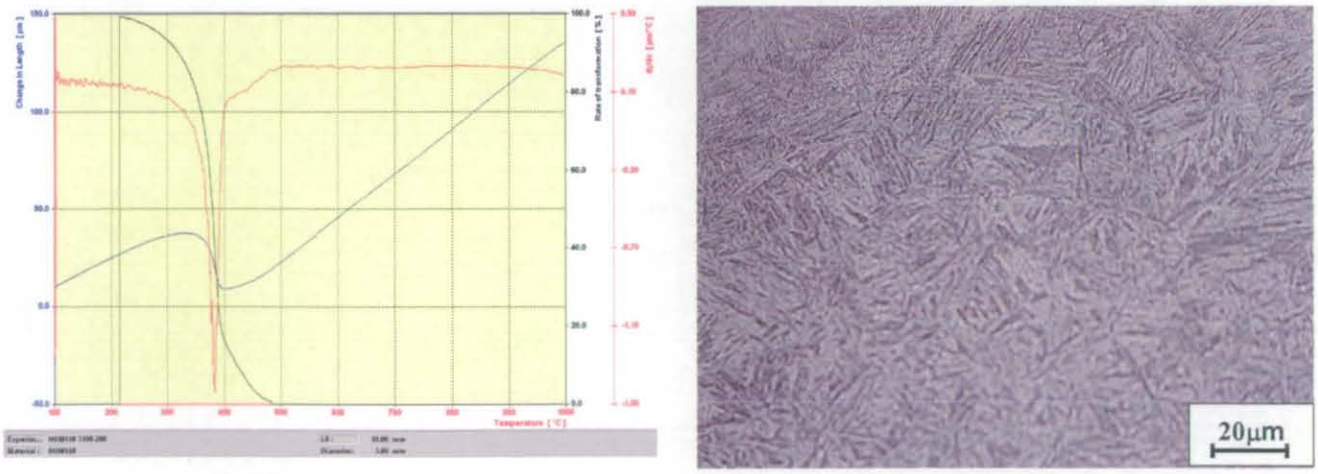

At a cooling rate of 200°C s^{-1}, and therefore at higher ones, the microstructure can be considered to be fully martensitic.

The overall transformation start and finish temperatures are listed in table 7.2.

Table 7.2: *Transformation start and finish temperatures for alloy HOM148, continuously cooled.*

Alloy HOM148 austenitised at 1100°C		
Cooling Rate (°C s^{-1})	**T_s (°C)**	**T_f (°C)**
2	747	491
5	727	471
10	*713*	*446 (FCA)*
25	*657*	*335 (B)*
50	612	284
75	575	232
100	514	222 (B + M)
150	489	215 (M)
200	484	196

7.4 High-magnification analysis of alloy HOM146

Alloy HOM146 contains a lower amount of Mn compared to alloy Y7N1 and its composition is 0.17 wt.% C, 0.29 wt.% Si, 0.52 wt.% Mn. The samples analysed were austenitised at 1100°C and cooled at rates ranging from 2 to 200°C s^{-1}. The effects of increasing cooling rate from 2°C s^{-1} to 50°C s^{-1} on the microstructure are the decrease in primary ferrite, the appearance of the FCA at the expense of pearlite and the increase in the Widmanstätten ferrite fraction. The proportion of FCA at 50°C s^{-1} from an optical observation appears to be very high, whereas the presence of bainitic ferrite was not observed.

The SEM analysis of alloy HOM146 was concentrated on three cooling rates of 2, 10 and 50°C s^{-1}, principally in order to observe the evolution of the FCA phase. The main microstructural features observed at the lowest cooling rate of 2°C s^{-1} are shown in figures 7.19a-f.

Figure 7.19a-f: *Microstructural features of sample HOM146 cooled at 2°C s^{-1}*

a) *ferritic matrix and pearlite regions*

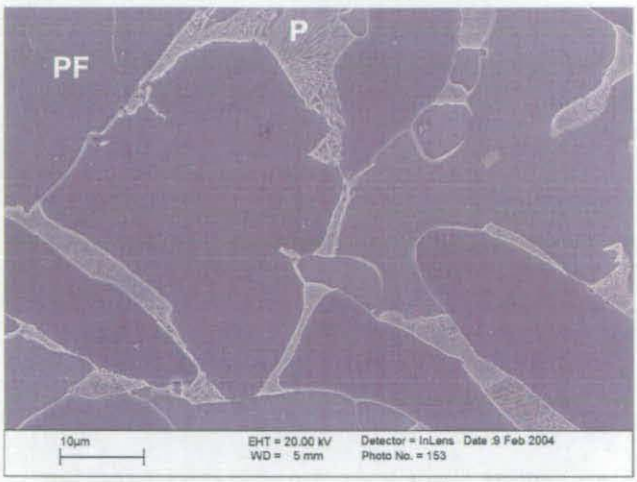

b) *ferrite and pearlite*

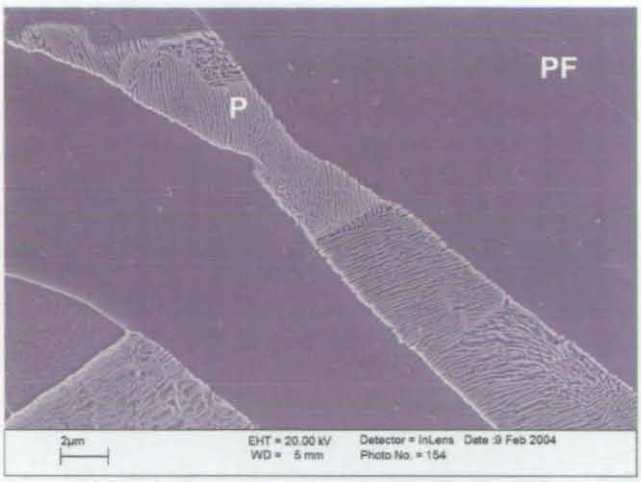

c) *pearlite island*

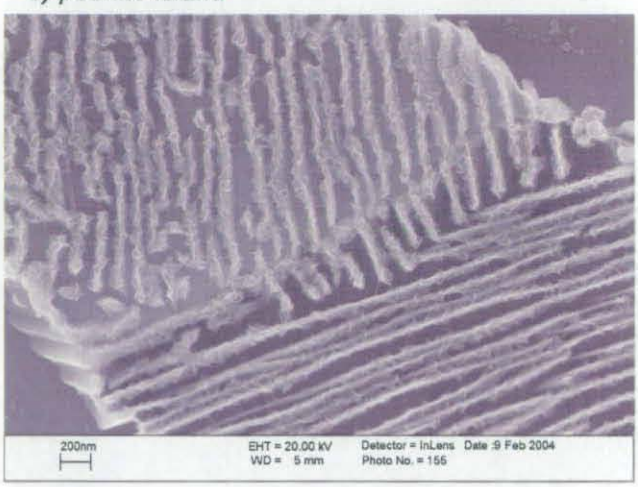

d) *pearlite and ferrite*

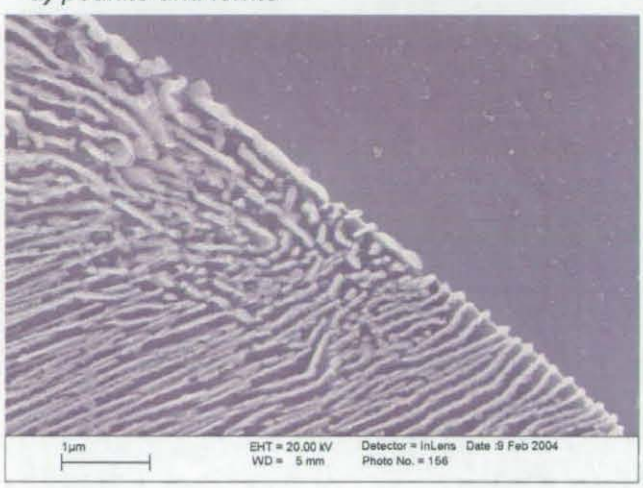

e) *ferrite-pearlite boundary*

f) *ferritic matrix*

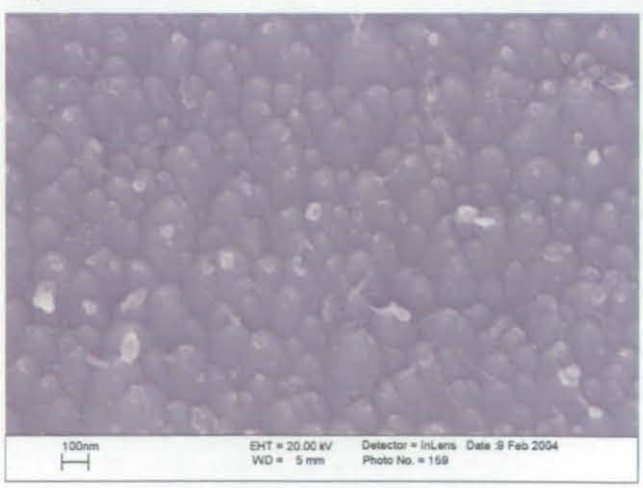

At very low cooling rates the microstructure consists of primary ferrite and pearlite. The phase transformations can take place within the high temperature regime and the diffusion of both substitutional and interstitial atoms makes these transformations fully reconstructive. The pearlite lamellae are not visible under the light microscope, as their thickness is on average between 100 and 150 nm. As shown in figure 7.20, in some cases, the pearlite islands showed different regions containing different growth directions of the lamellae. This is due to the fact that nucleation of the lamellae takes place on more than one of the surrounding ferrite grains. These primary ferrite grains grow along a specific direction, which at high magnification can be distinguished by the appearance of the ferritic matrix. Whilst the growth of the ferrite grains takes place, the surrounding austenite becomes increasingly enriched with carbon, the latter coming from different transformation fronts. Therefore, nucleation can take place on one or more primary ferrite grains. In the latter case, the lamellae present within what optically appears to be a single pearlite grain, show different growth directions.

Figure 7.20: *Pearlite lamellae orientation*

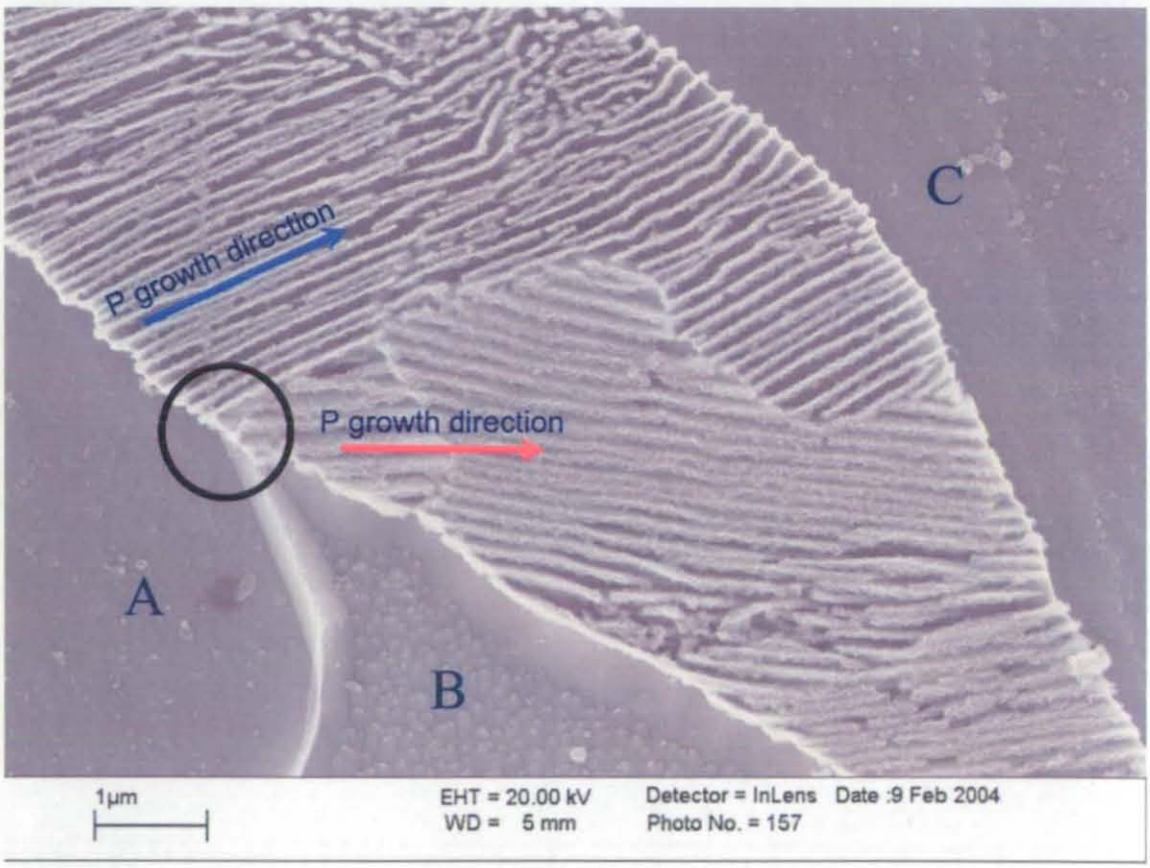

Figure 7.20 can be used to better illustrate the considerations previously made. Considering first the primary ferrite grains A and B, and the portion of the boundary

which is common to both the ferrite grains and the pearlite regions above them, the appearance of the ferrite matrix clearly indicates that the two grains have different orientation. On the other hand, two directions of growth of the pearlite lamellae can be identified. The direction changes in correspondence of the A-B boundary; it is therefore possible that nucleation of a portion of pearlite has occurred on grain B whilst another one has taken place on grain A. As a result, the pearlite region is not constituted by a single grain with a single orientation, but by tow different pearlite regions with distinct orientations. It could be argued that nucleation has taken place at two different locations of grain C, although it would be rather peculiar that the orientation of the lamellae changed in correspondence of the A-B boundary. The EBSD analysis of this region would provide crystallographic orientation information, enabling a conclusive analysis of the microstructure. The nucleation of each pearlite region would have taken place on the adjacent ferrite grain which would have had a coherent boundary with the pearlite region itself, as discussed in chapter 6, section 6.9.

With increasing cooling rate, the formation of Widmanstätten ferrite and FCA starts to occur. At a cooling rate of 10°C s^{-1} the FCA phase represents a considerable portion of the microstructure. The FCA grains have an irregular shape as in the case of alloy Y7N1, the dimensions of the grains being approximately 15 μm. The precipitates within the FCA regions are coarser compared to the higher manganese alloys and are distributed in a less regular fashion. In particular, within a single grain, more directions of precipitation can be identified. Another characteristic of the FCA is that at this cooling rate some of the grains contain discrete particles, usually coarser, whilst some others have irregularly shaped interconnected particles, usually finer (images 7.21a-t). A very interesting aspect was observed the occurrence of branching of the precipitates (image 7.21u). Precipitates with a shape similar to that shown in image 7.21u have been successfully extracted by producing carbon replicas. The analysis shown in chapter 6, section 6.5.2, indicated that the phase is cementite. Any particular orientation relationship with the matrix should be further investigated in terms of crystallography by means of TEM analysis. This task, as mentioned elsewhere (section 6.8), is very difficult, not only because of the magnetic nature of the matrix, but also because of the likelihood of being able to analyse an area containing such precipitates in a thin foil sample. Images 7.21v-x show some of the precipitates which were geometrically very regular compared to the precipitates observed in the FCA, however their formation was always associated with FCA formation. Further work is required to conclusively identify these precipitates.

Figure7.21a-x: *Microstructural features of sample HOM146 cooled at 10°C s^{-1}*

a) *microstracture at low magnification*

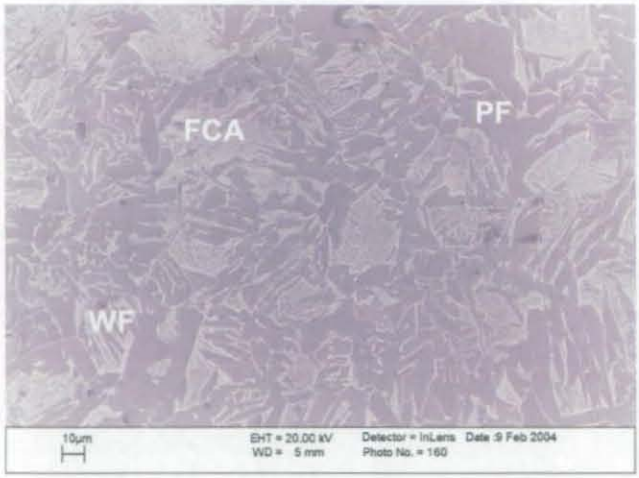

b) *FCA with large elongated precipitates*

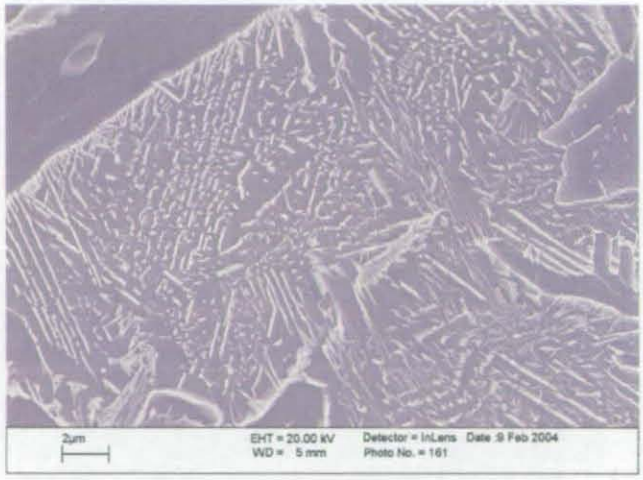

c) *ferrite and FCA*

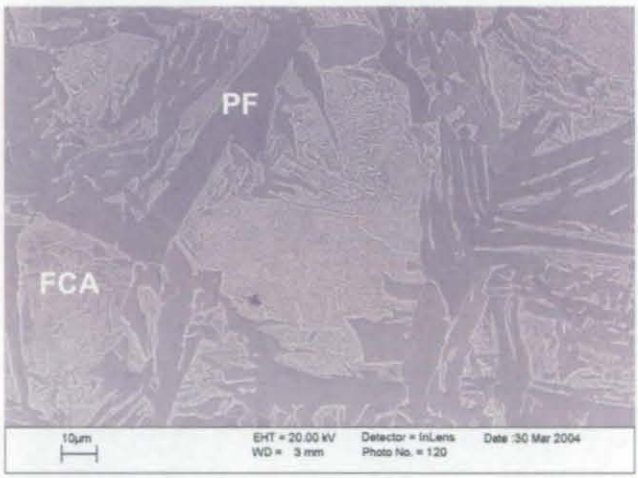

d) *WF plate within an FCA grain*

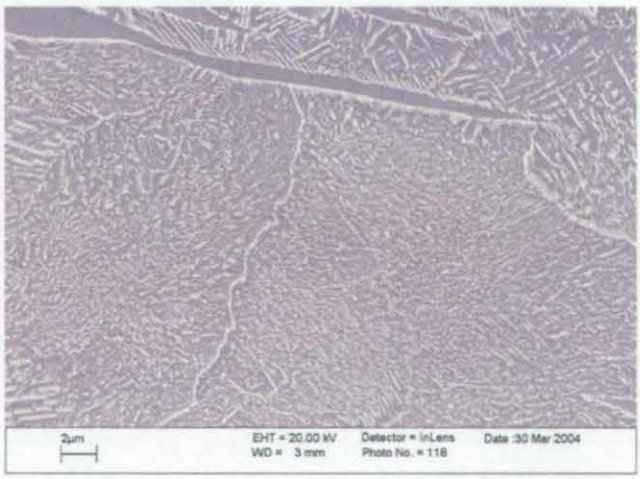

e) *large FCA grain*

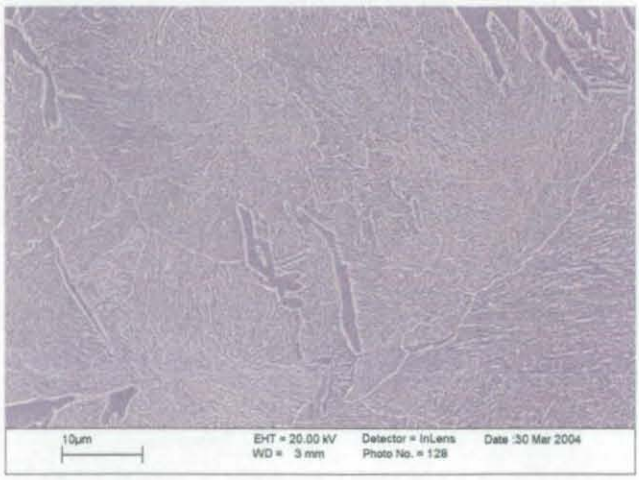

f) *FCA, pearlite ilsland and ferrite*

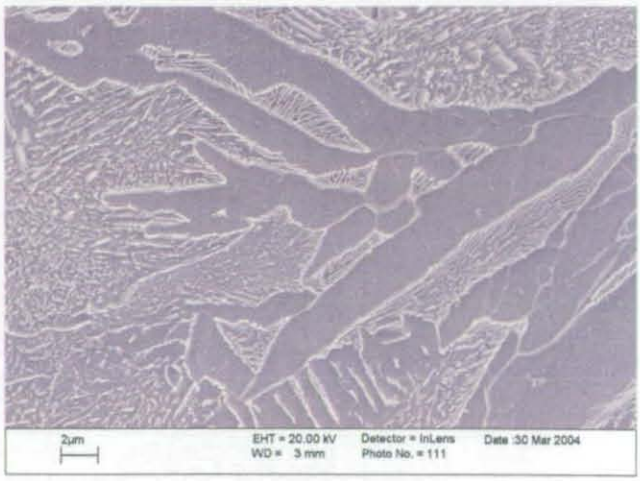

g) FCA, ferrite and pearlite islands

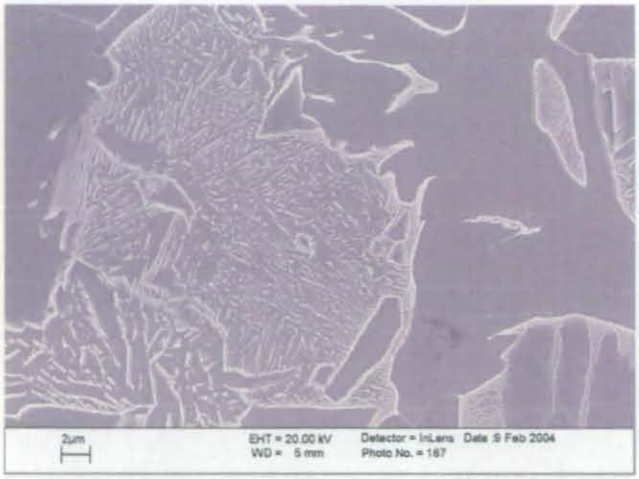

h) FCA adjacent to ferrite

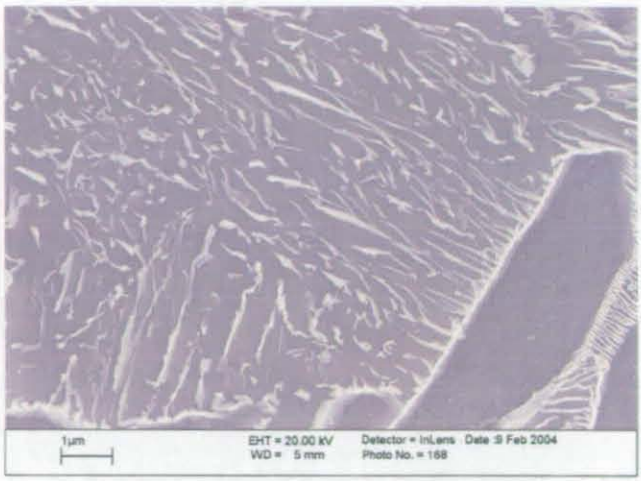

i) pearlite and ferrite

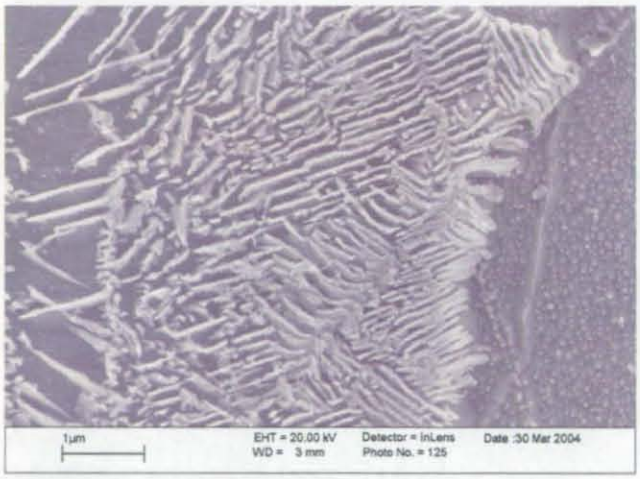

j) FCA, arrays of precipitates

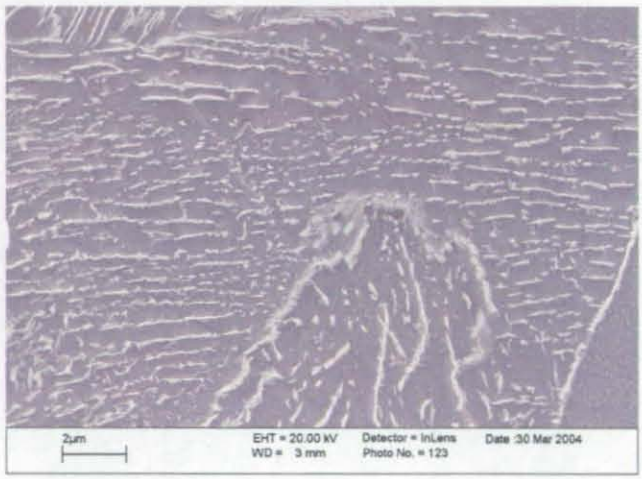

k) FCA

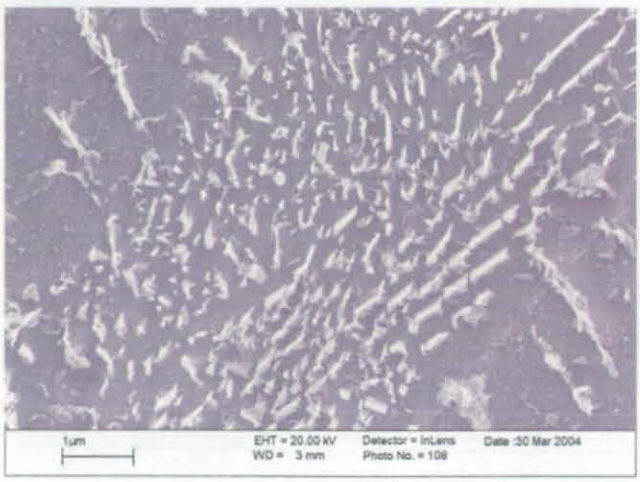

l) lamellar break-down in a P/FCA grain

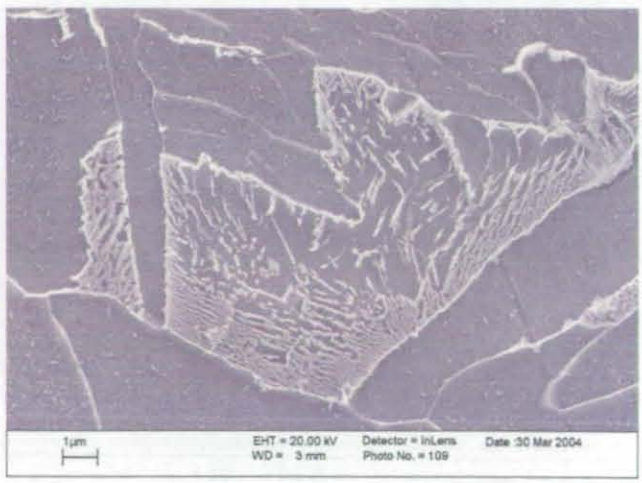

m) *FCA, 'tadpole' precipitates*

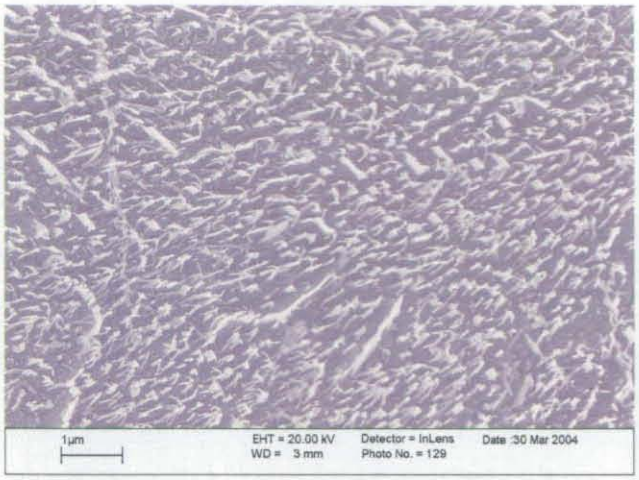

n) *FCA, elongated precipitates*

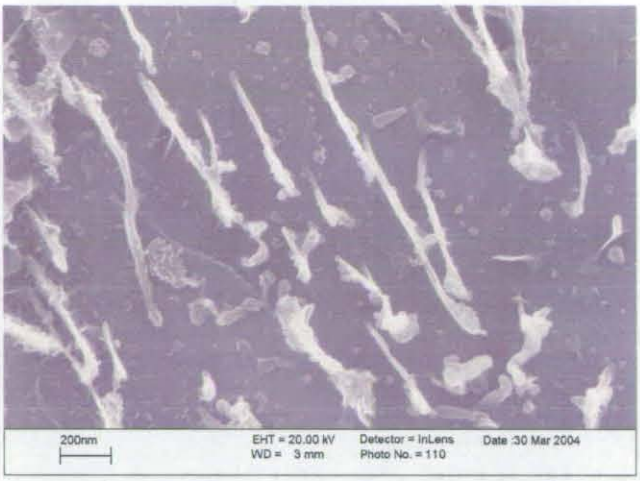

o) *FCA, 'tadpole' precipitates*

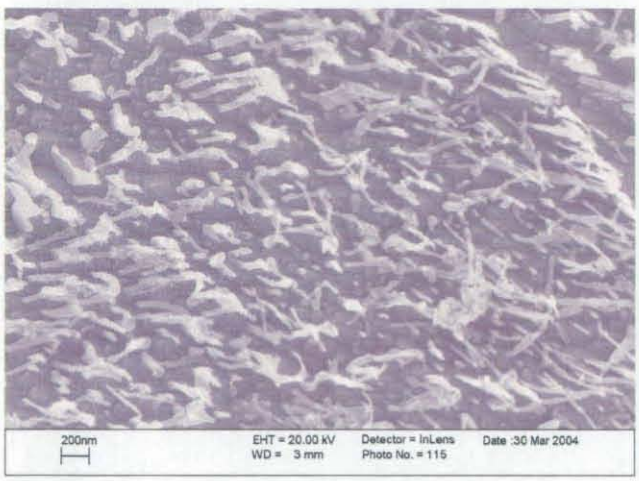

p) *FCA, precipitates*

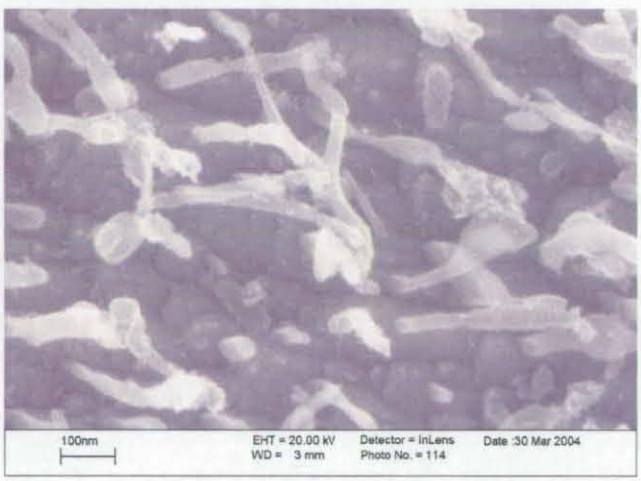

q) *FCA, branched precipitates*

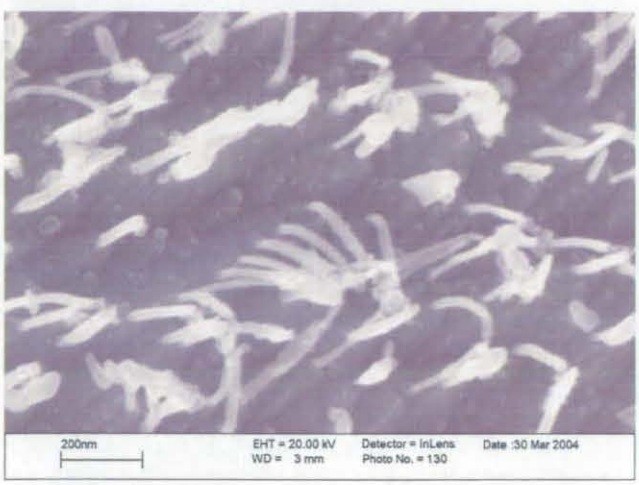

r) *FCA, precipitates and LA boundary*

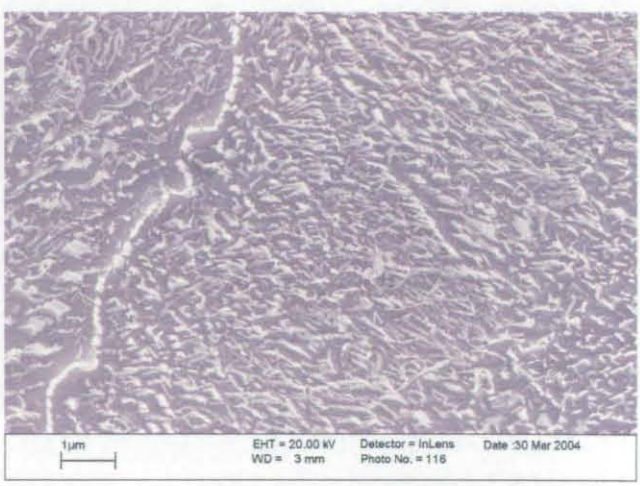

s) FCA, precipitates

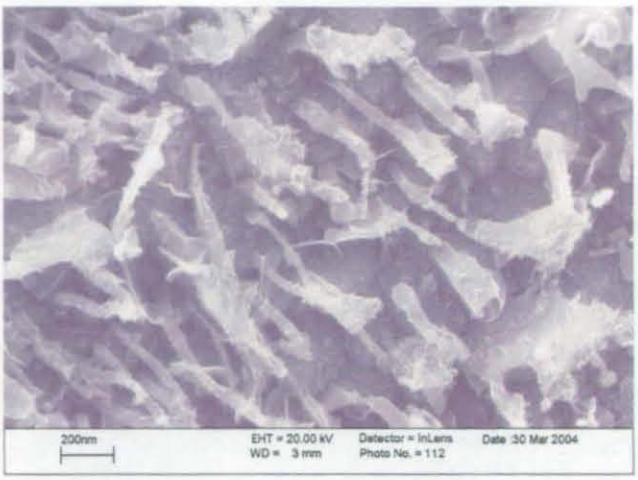

t) FCA, branched precipitates

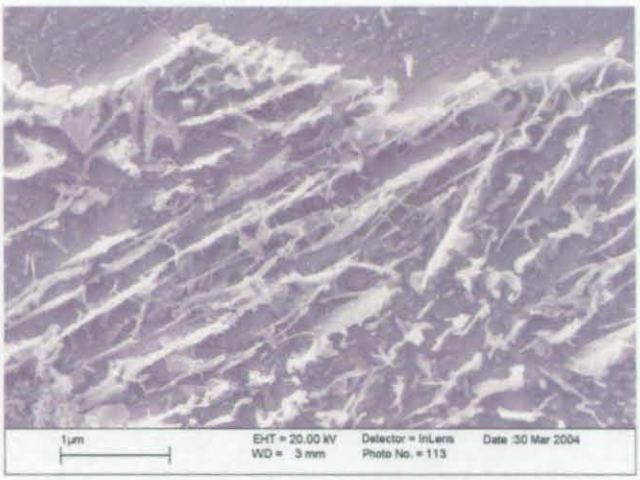

u) FCA, branched precipitated and particles

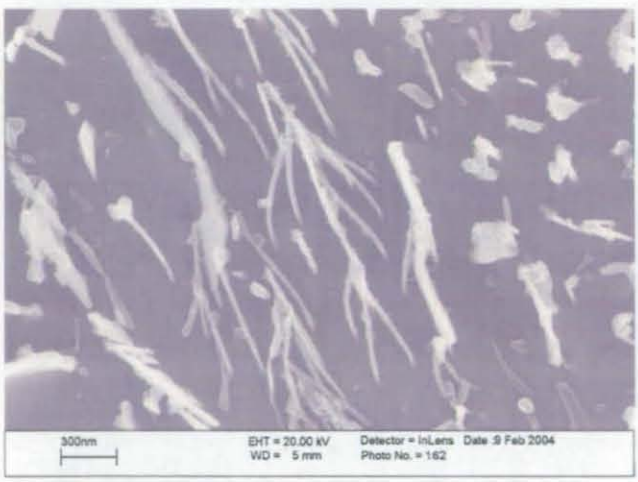

v) FCA, geometrically regular precipitates

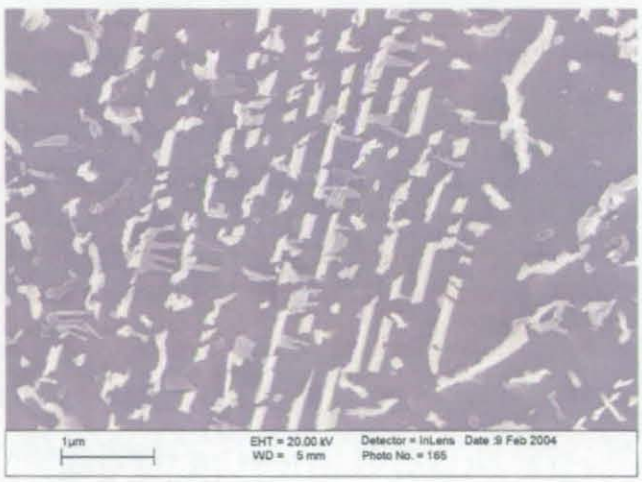

w) FCA, colony of geometrically regular precipitates

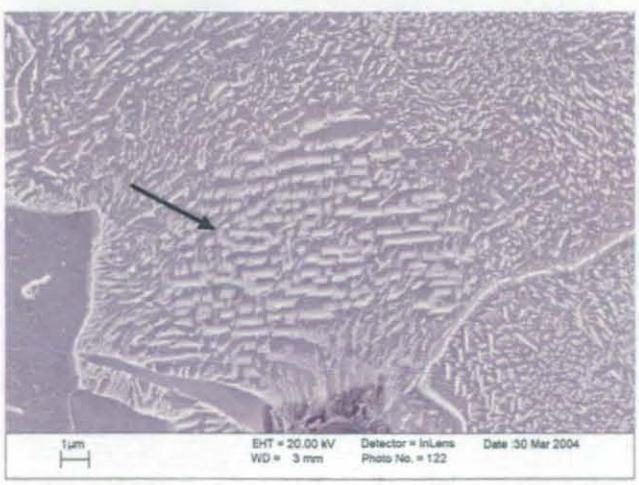

x) FCA, geometrically regular precipitates

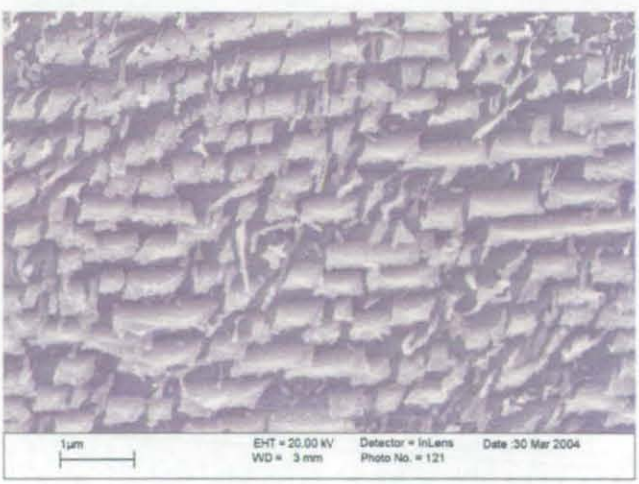

50°C s^{-1} was the highest cooling rate at which alloy HOM146 was analysed by means of SEM (InLens). At this cooling rate, unlike in the higher Mn alloys, the volume fraction of FCA instead of decreasing or remaining at the same levels produced at a cooling rate of 10°C s^{-1}, increases considerably. Qualitatively, image 7.22a shows how the FCA is the main constituent at this cooling rate. Furthermore, the remaining microstructure consists of primary ferrite and Widmanstätten ferrite (7.22a-b). The precipitates present within the FCA regions appear to be much finer compared to the lower cooling rates and partially interconnected in the majority of the cases (7.22c-d).

***Figure 7.22a-d**: Microstructural features of sample HOM146 cooled at 50°C s^{-1}*

***a)** coarse FCA, WF and primary ferrite*

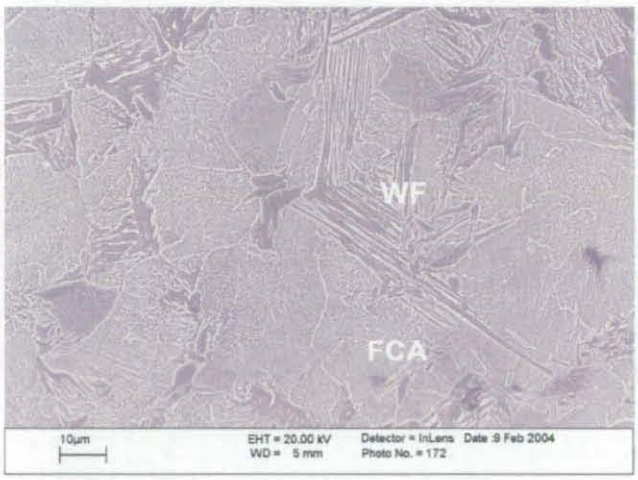

***b)** FCA, WF and ferrite*

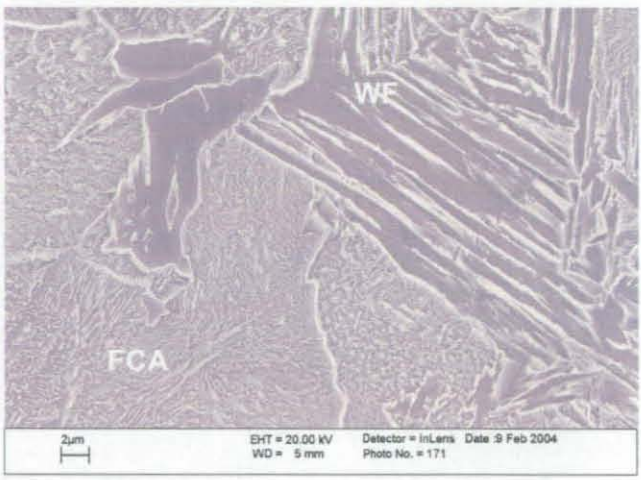

***c)** FCA, low angle boundary*

***d)** FCA adjacent to WF*

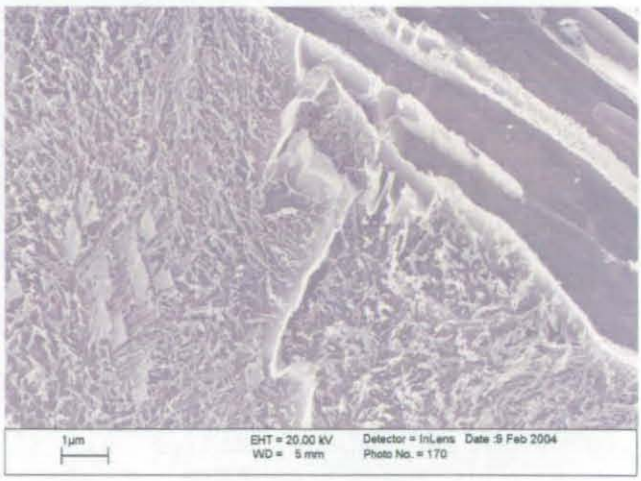

7.5 High-magnification analysis of alloy HOM148

The composition of alloy HOM148 is 0.17 wt.% C, 0.31 wt.% Si, 1.56 wt.% Mn. The manganese content is approximately three times more than that of alloy HOM146 and approximately 80% more than alloy Y7N1. The main microstructural features observed at 2, 10, 50 and 200°C s^{-1} are presented below.

At the lowest cooling rate of 2°C s^{-1} the main phases are primary ferrite and pearlite as in the case of alloy HOM146. However, there is some evidence that FCA has formed in small regions of alloy HOM148, whereas in the low Mn alloy HOM146, as well as in the intermediate Mn alloy Y7N1, this was not observed (figures 7.23a-f).

Figure 7.23a-f: *Microstructural features of sample HOM148 cooled at 2°C s^{-1}*

a)

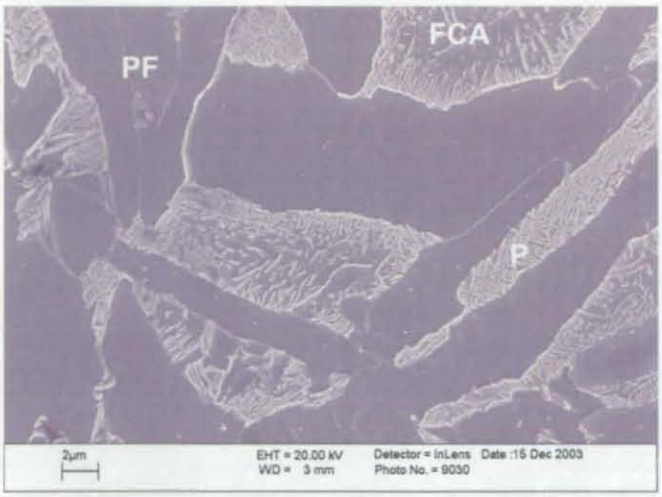

b)

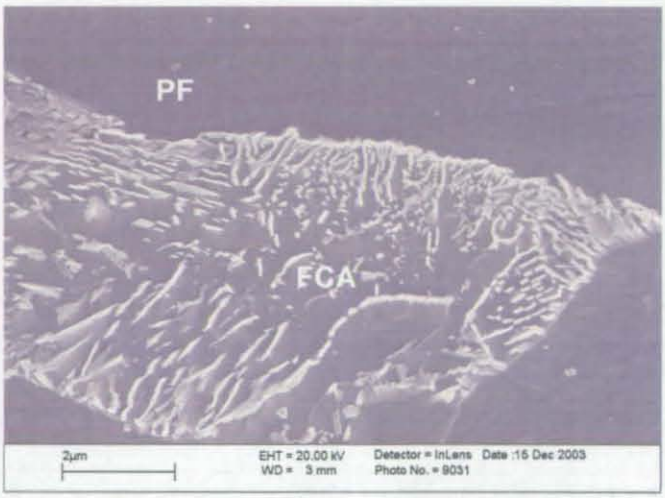

c)

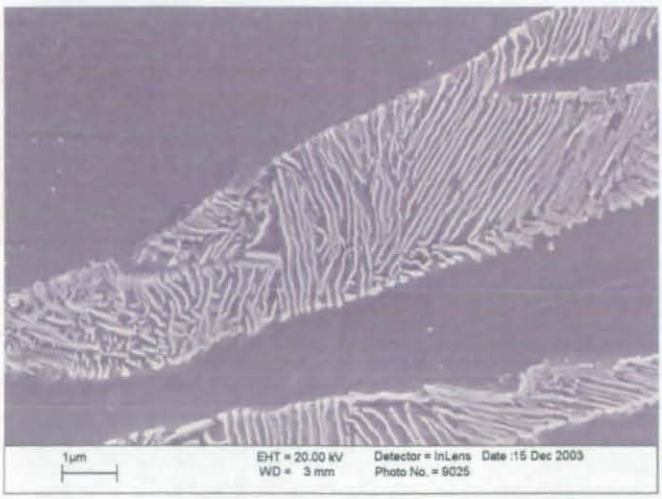

d)

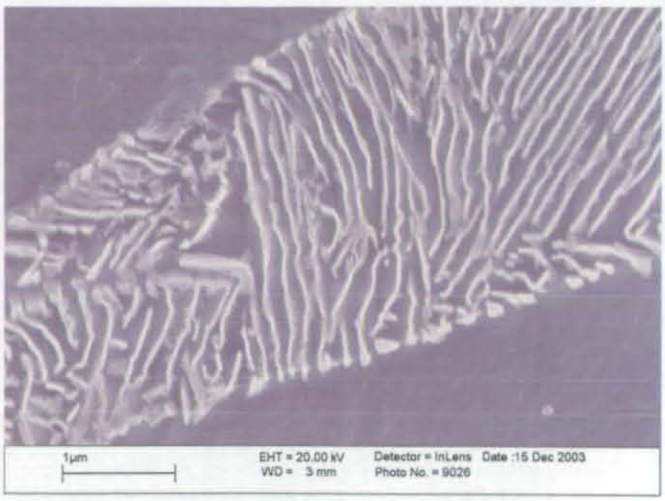

e)

f)

At a cooling rate of 10°C s^{-1} (figures 7.24a-δ) the proportion of FCA increases whilst pearlite grains disappear, although a lamellar type of growth is still observed in small pearlitic islands and at the boundaries of the FCA regions. There is a large difference between the microstructure of alloy HOM148 and alloy HOM146 cooled at 10°C s^{-1}. In fact, the microstructure in this case is much finer and it is comprised mainly of Widmanstätten ferrite at the expense of primary ferrite. The FCA grain dimension is usually less than 10 µm. This microstructure is very similar to the one produced at 50°C s^{-1} in alloy Y7N1. The morphology of the precipitates in the FCA is less regular than in alloy Y7N1, although this type of morphology has been previously observed both in the continuous cooling experiments and in the hold-quench experiments discussed in chapter 6. The precipitates usually show a common precipitation orientation within the same grain and are usually partially interconnected. Furthermore, the lamellar type of precipitation usually encountered at the FCA boundary, is more marked in this alloy, although in some cases, the direction of growth of the small lamella is not reproduced by the small particles. Images 7.24r-t show again a the peculiar and interesting morphology of very regular precipitates. However, the shape is more irregular than those observed in alloy HOM148 and they appear finer (similar to those observed in HOM146 50°C s^{-1}) although this could be due to the different plane of observation.

Figure 7.24a-δ: *Microstructural features of sample HOM148 cooled at 10°C s^{-1}*

a) *microstructure at low magnification*

b) *WF, austenitic microphase*

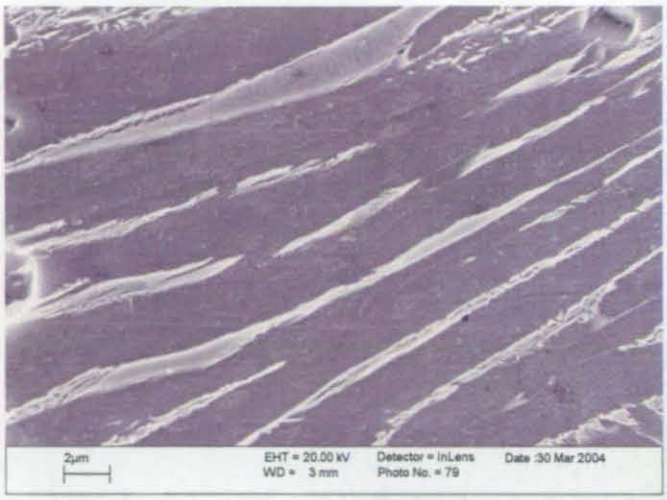

c) *WF, pearlitic microphase*

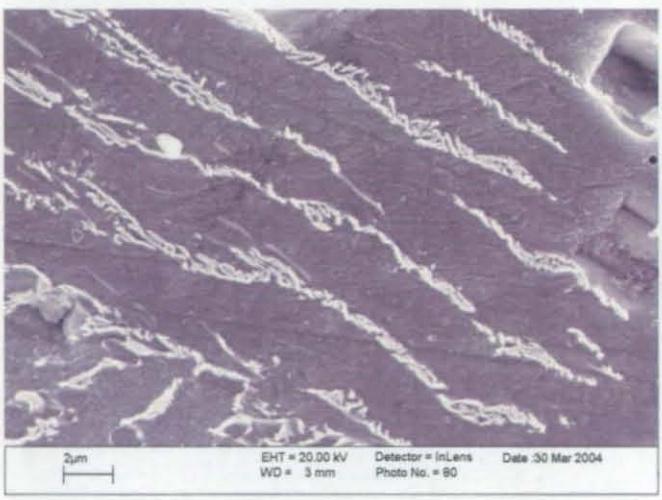

d) *WF, asutenitic and pearlitic microphase*

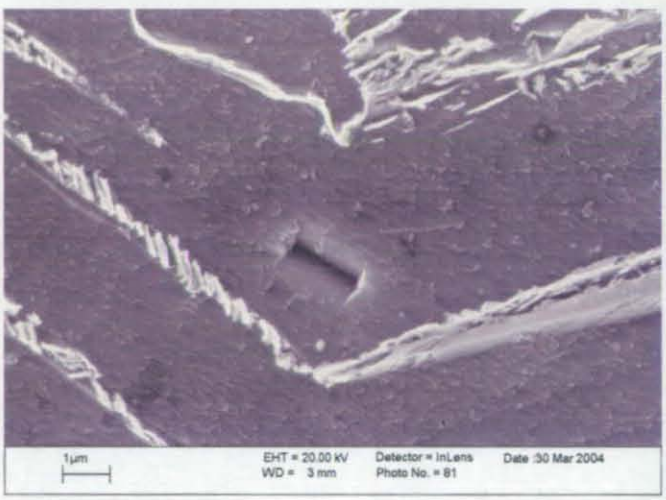

e) *ferrite, pearlite island and WF*

f) *pearlite island between ferrite*

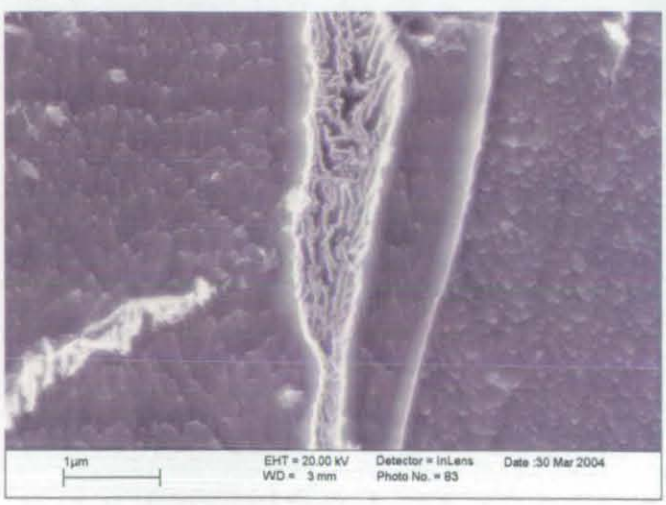

g) *primary ferrite, WF and FCA*

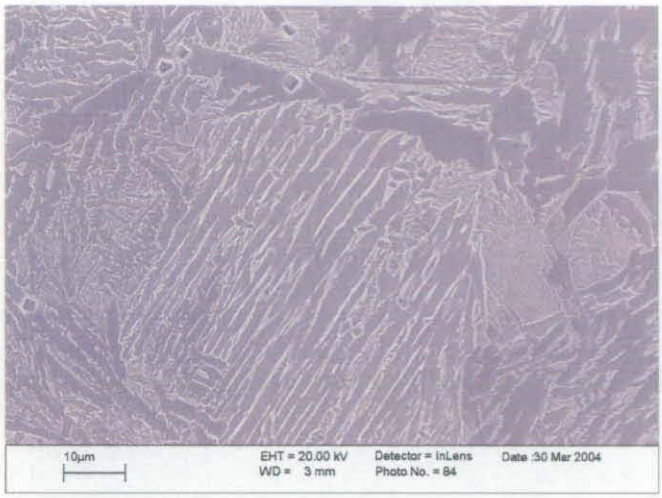

h) *martensitic microphase*

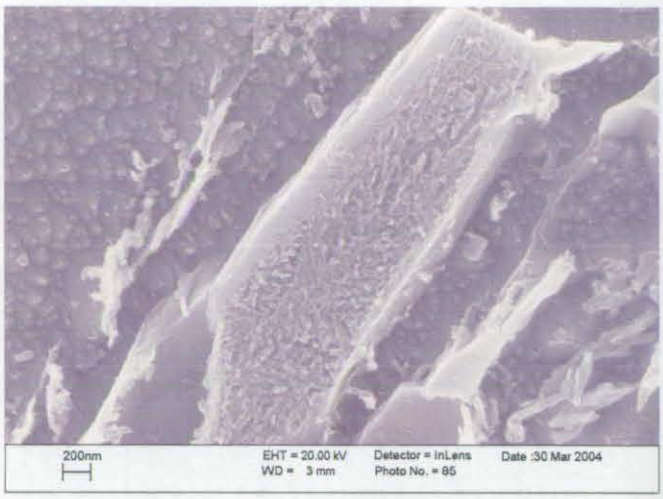

i) *FCA*

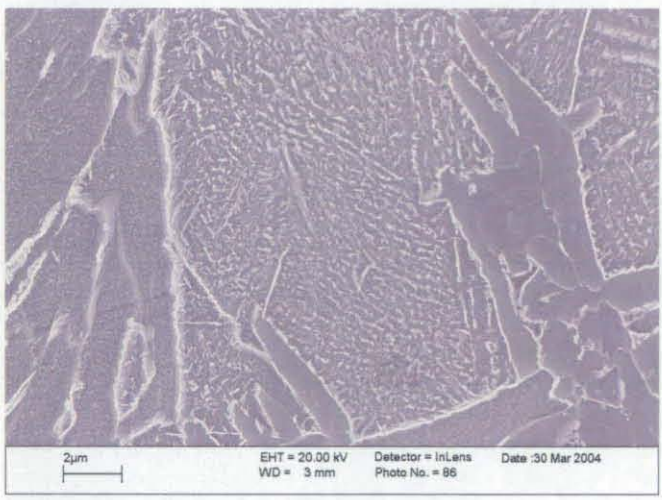

j) *FCA*

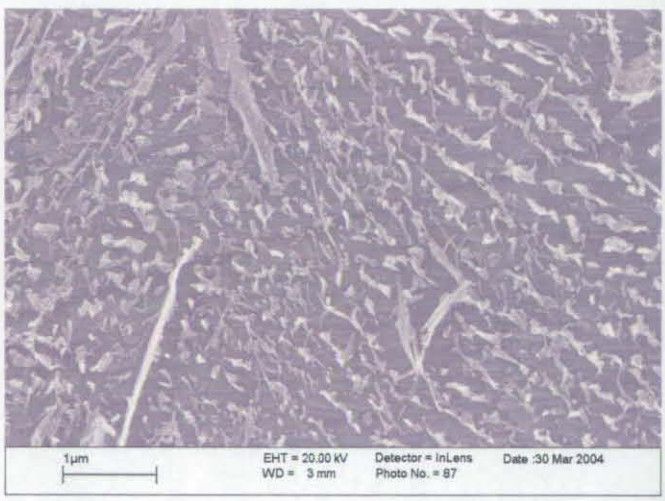

k) *FCA, precipitates*

l) *FCA, precipitates*

m) *FCA, precipitates*

n) *FCA, precipitates*

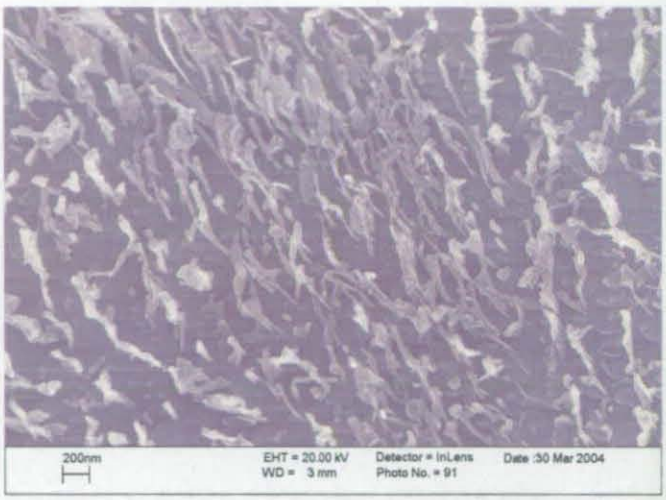

o) *ferrite (left) and FCA (right)*

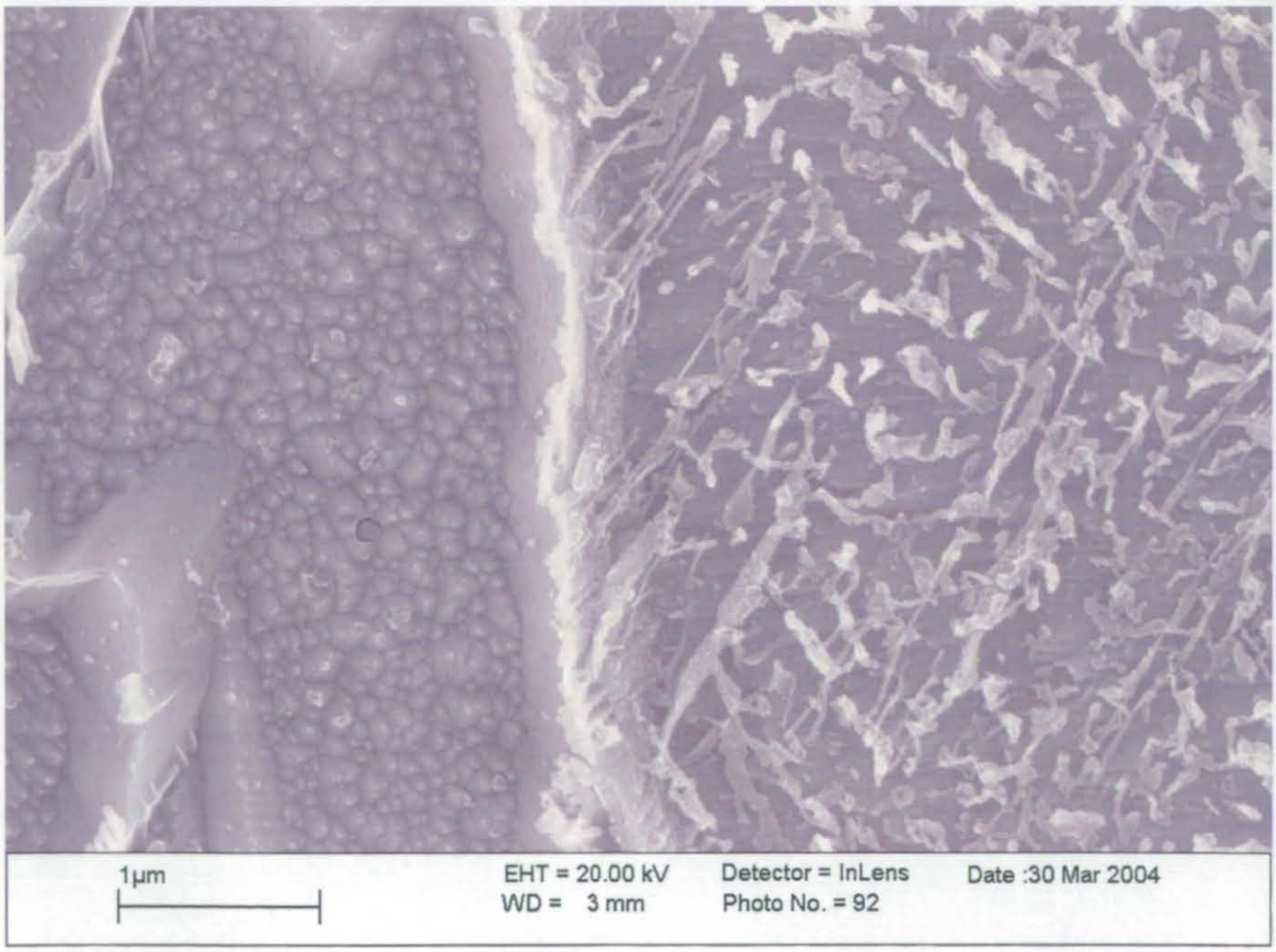

p) *FCA, boundary*

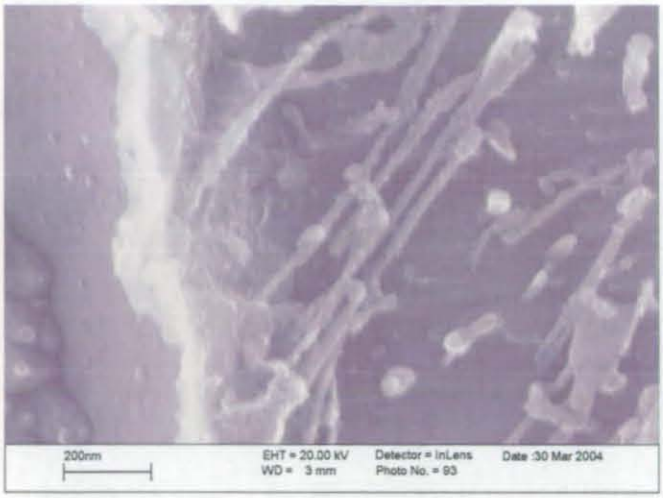

q) *FCA, precipitates*

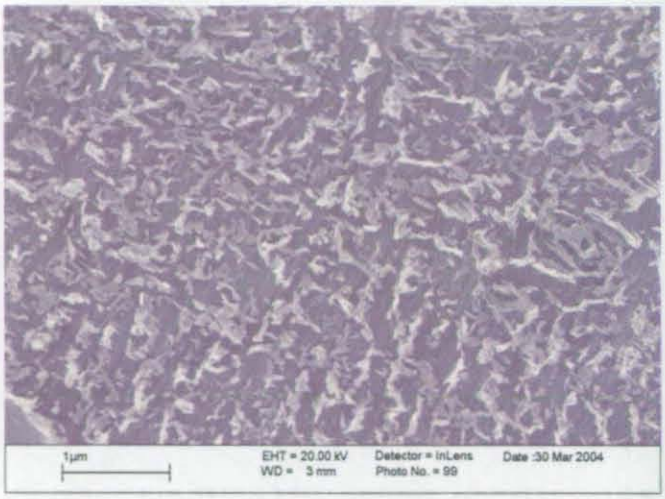

r) *FCA, precipitates (unknown nature)*

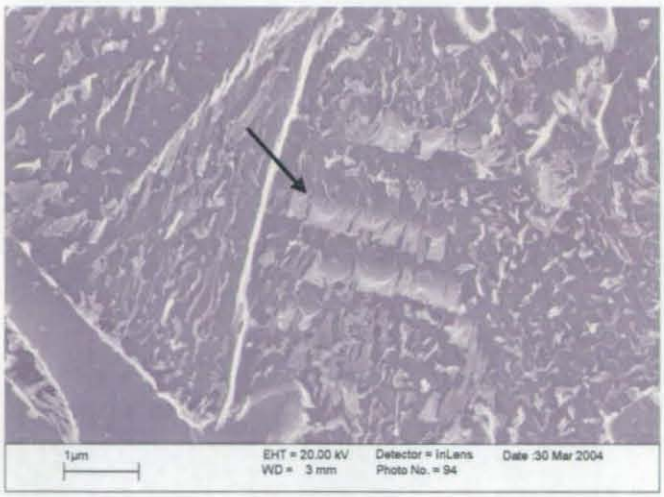

s) *FCA, precipitates (unknown nature)*

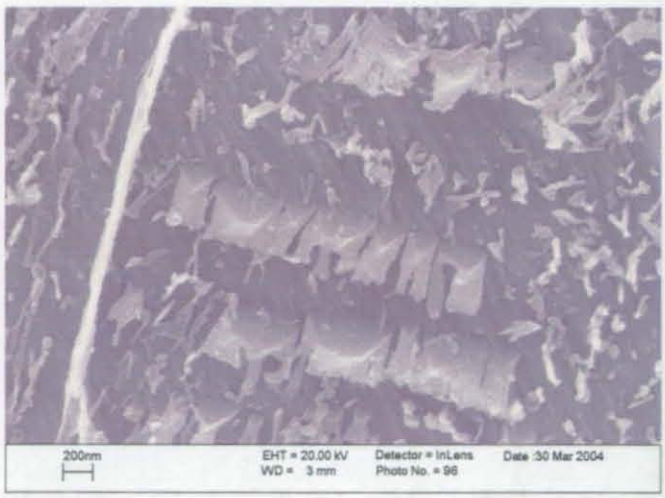

t) *FCA, precipitates (unknown nature*

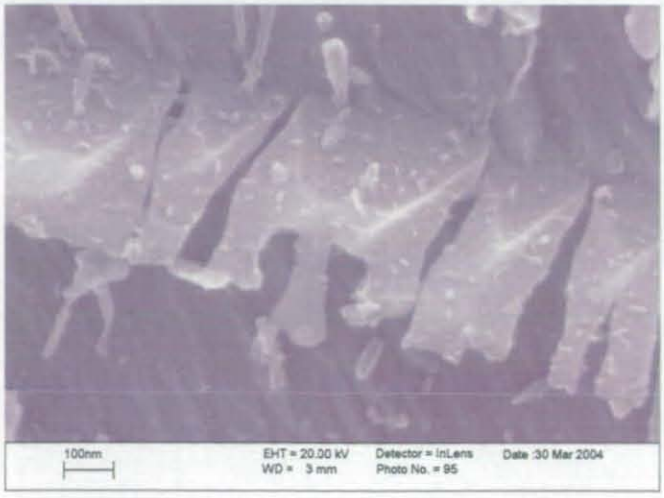

u) *ferrite and pearlite islands*

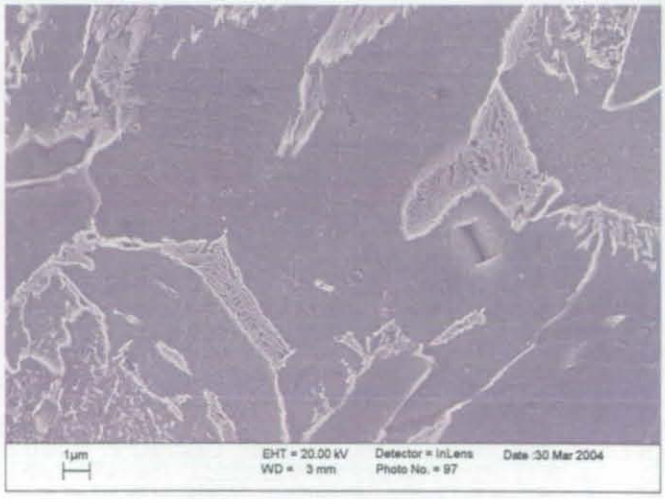

v) WF and FCA

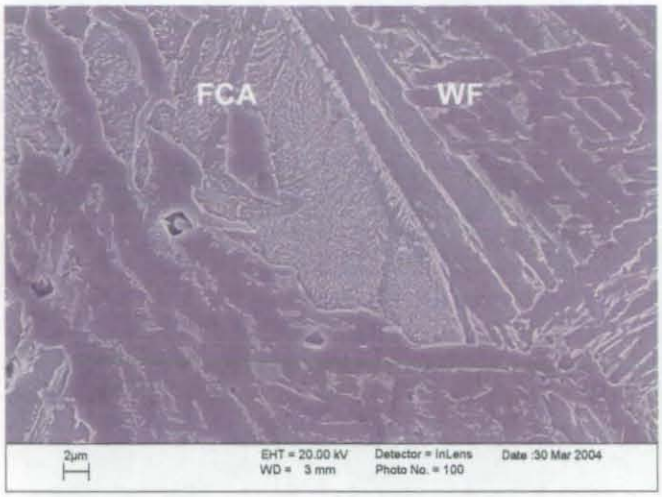

w) FCA adjacent to WF

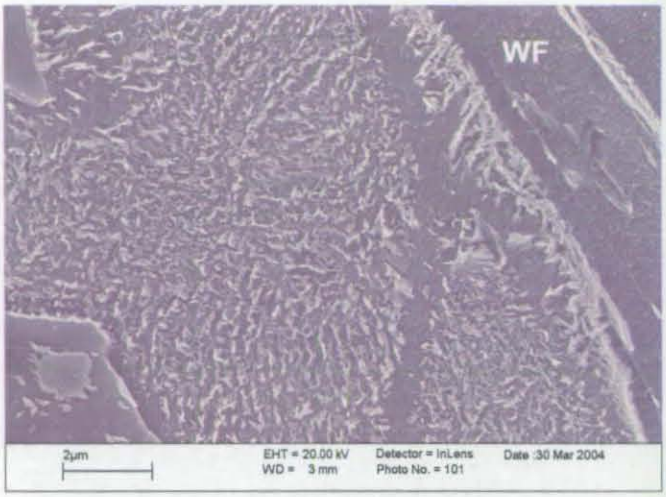

x) FCA

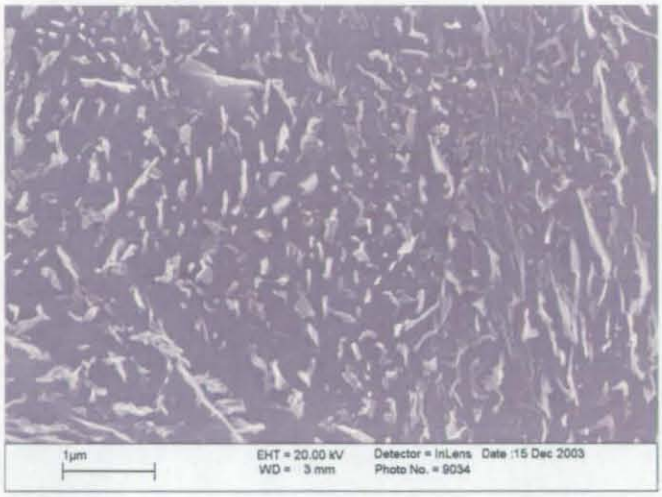

y) FCA, precipitates

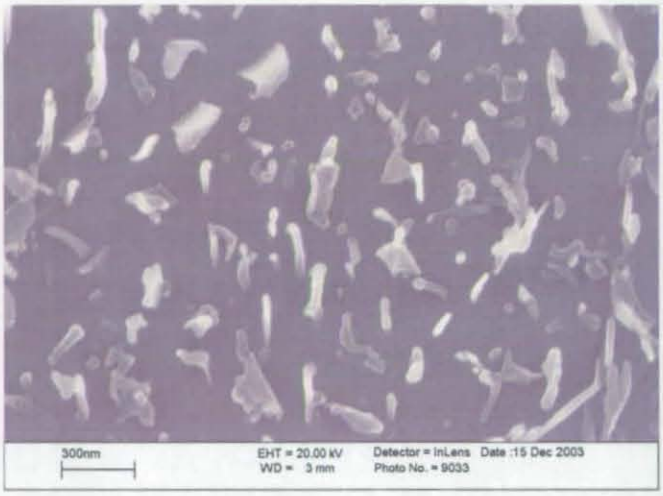

z) FCA

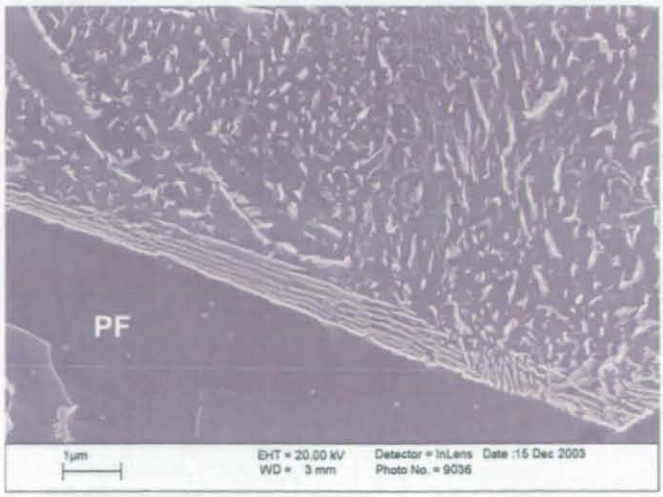

α) FCA, lamellar precipitationat the boundary

β) FCA, lamellar precipitation at the boundary

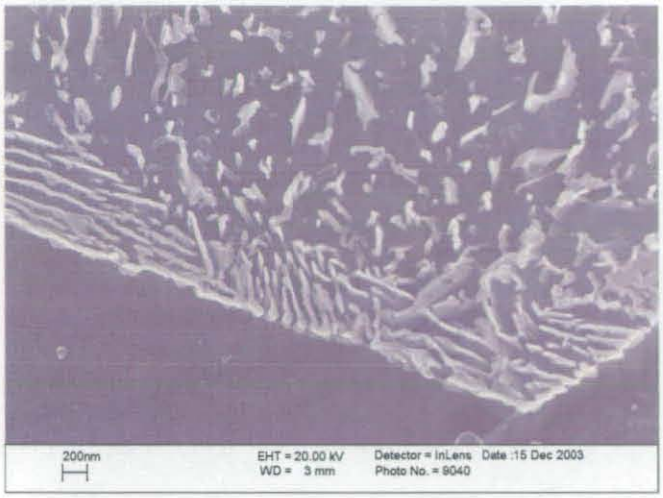

δ) FCA, lamellar precipitation at the boundary

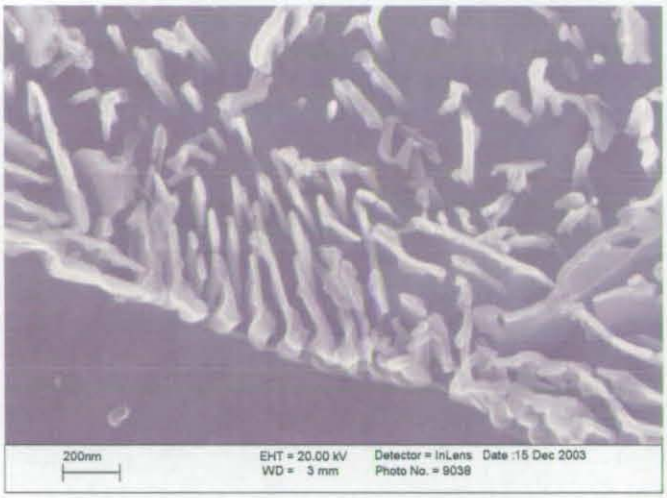

When the sample is cooled from the austenitising temperature to room temperature at a cooling rate of 50°C s^{-1} (figures 7.25a-p) the microstructure appears to be constituted of phases formed via a displacive mechanism. In figure 7.25d it can be seen that the presence of fine primary Widmanstätten ferrite sideplates is limited to small portion of the microstructure at prior austenite grain boundary sites. Most of the microstructure, on the other hand, is comprised of upper and, in smaller amount, lower bainite. SEM investigation allows easier identification of lower bainite with the characteristic precipitates between and within the laths. The appearance of both the ferritic matrix and the precipitates in the bainitic region is very different from that of the FCA regions. Portions of martensite formed upon cooling and in some instance auto-tempering took place. Increasing the Mn content causes a drastic change in the transformation kinetics which in alloy HOM148 assumes a strong displacive character at relatively low cooling rates. In fact, beside primary ferrite and pearlite, the absence of FCA is noteworthy in this alloy compared to the HOM146 and Y7N1.

Figure 7.25a-p: *Microstructural features of sample HOM148 cooled at 50°C s^{-1}*

a) *lower bainite*

b) *lower bainite*

c) lower bainite and martensite

d) lower bainite and martensite

e) lower bainite

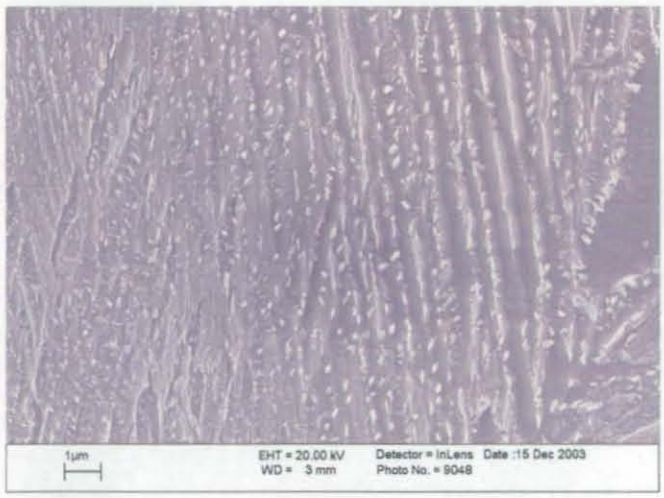

f) lower bainite

g) lower bainite, precipitates

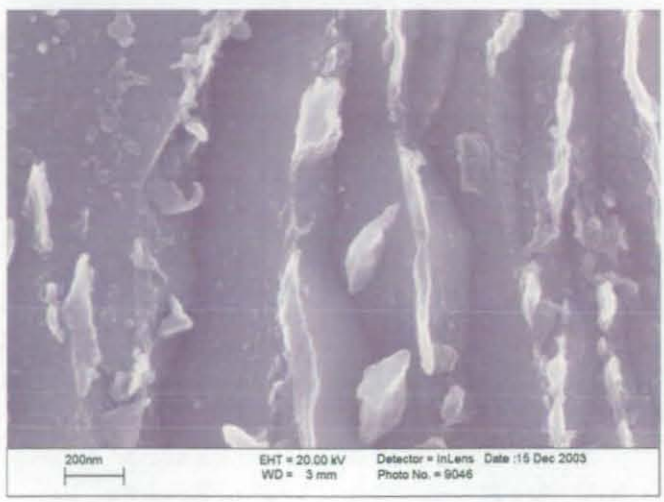

h) martensite

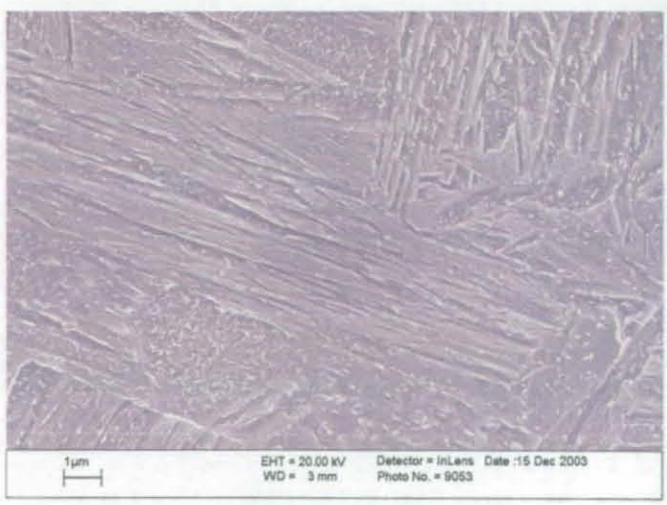

i) auto-tempered martensite

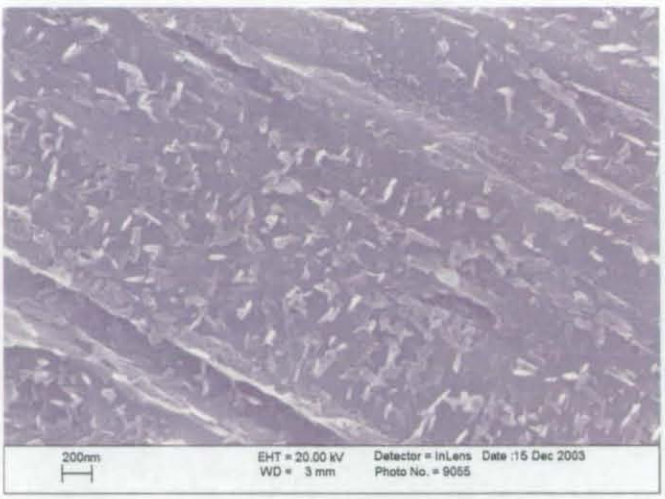

k) auto-tempered martensite

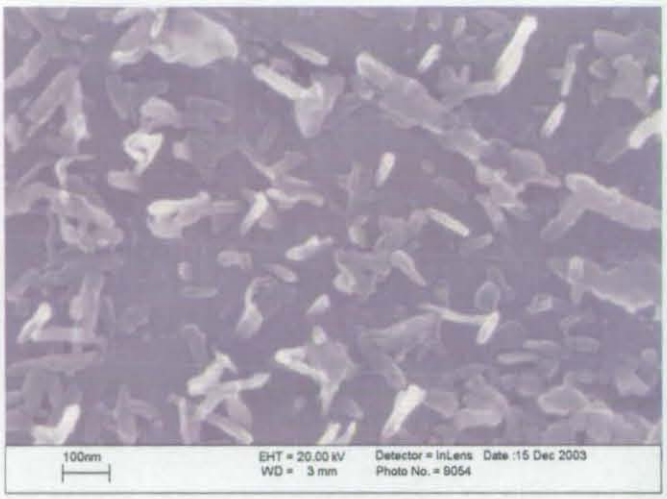

l) auto-tempered martensite, martensite and LB

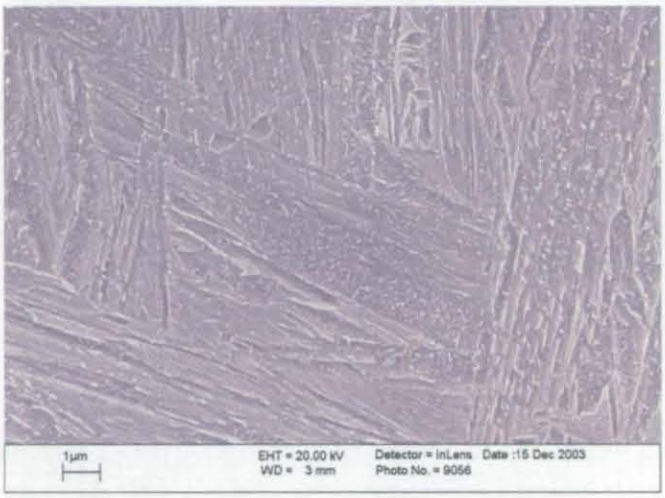

m) lower bainite

n) lower bainite

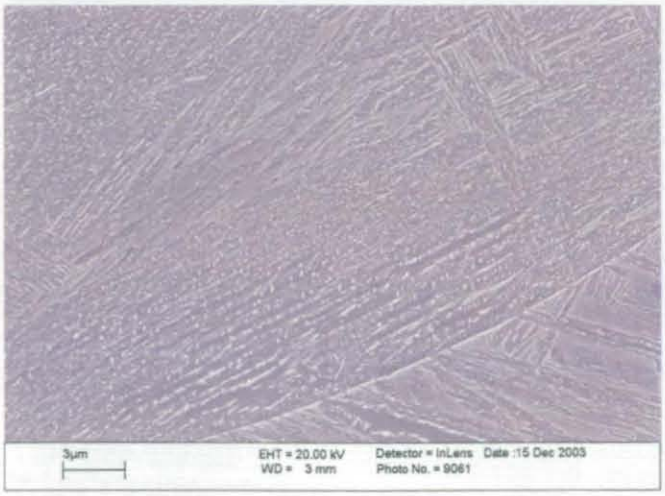

o) lower bainite, precipitates

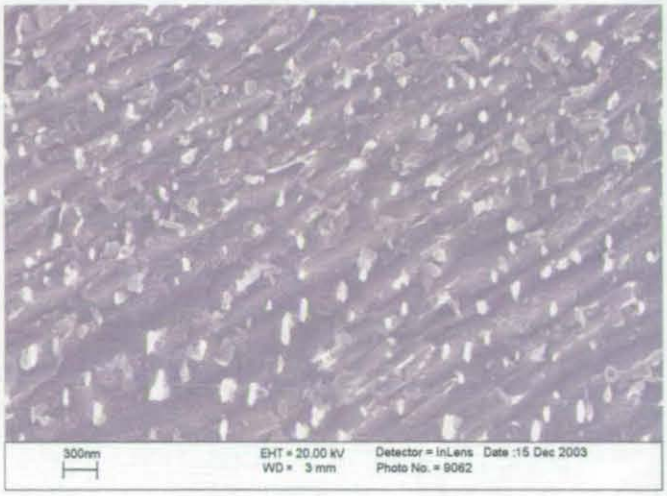

p) lower bainite, precipitates

As the cooling rate reaches 200°C s^{-1} the inevitable consequence on the alloy is a fully martensitic microstructure. This was expected, as alloy HOM148 showed that its transformation behaviour favours displacive transformations at cooling rates as low as 50°C s^{-1}. The degree of auto tempering is significant and at high magnification the carbides formed upon cooling can be observed in their typical orientations (figures 7.26a-h).

Figure 7.26a-h: *Microstructural features of sample HOM148 cooled at 200°C s^{-1}*

a) *martensite and auto-tempered martensite* ***b)*** *martensite*

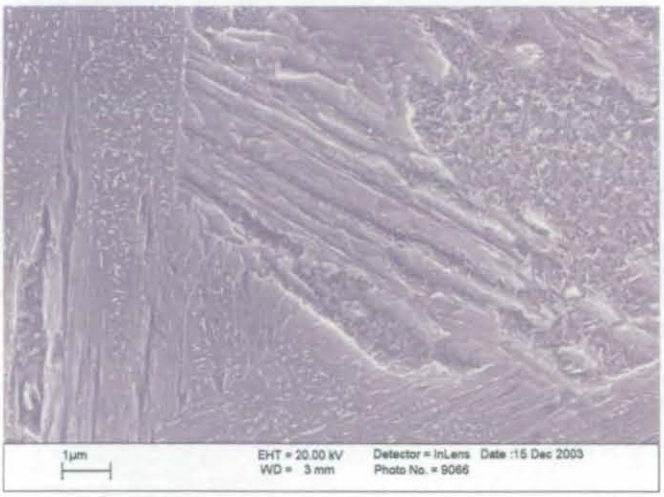

c) martensite

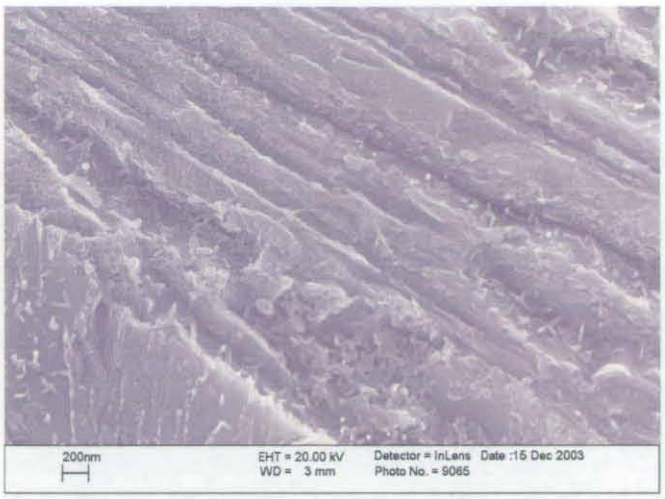

d) auto-tempered martensite

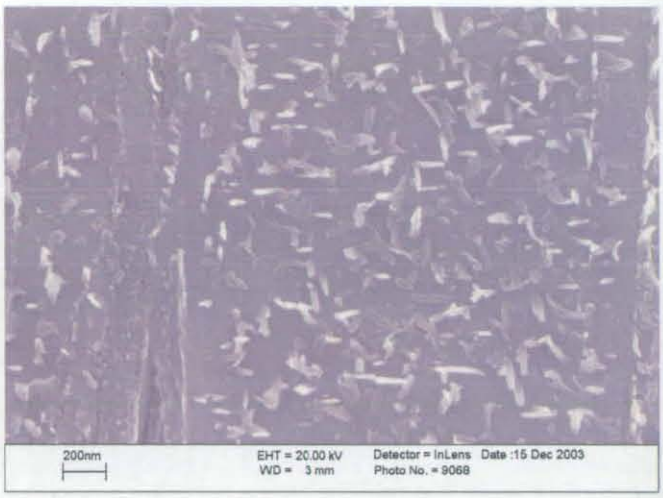

e) martensite and auto-tempered martensite

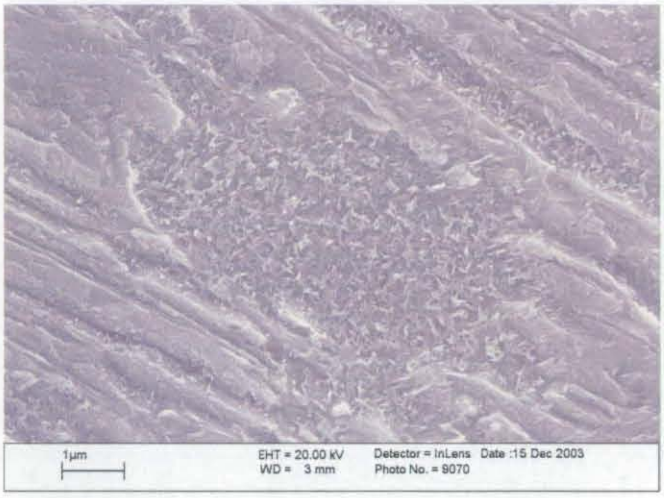

f) auto-tempered martensite

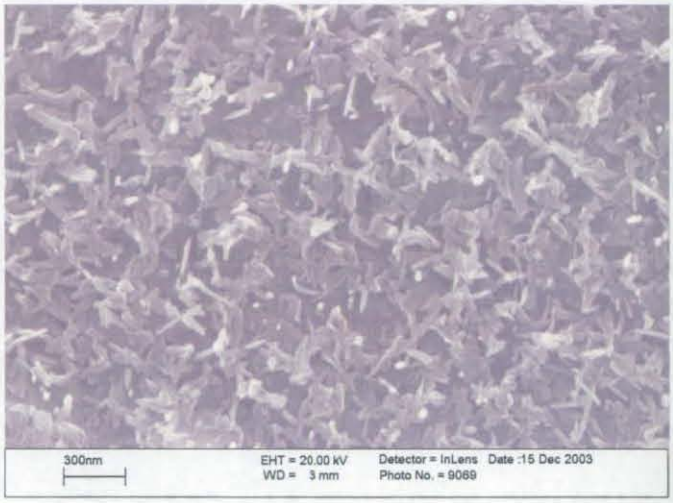

g) auto-tempered martensite

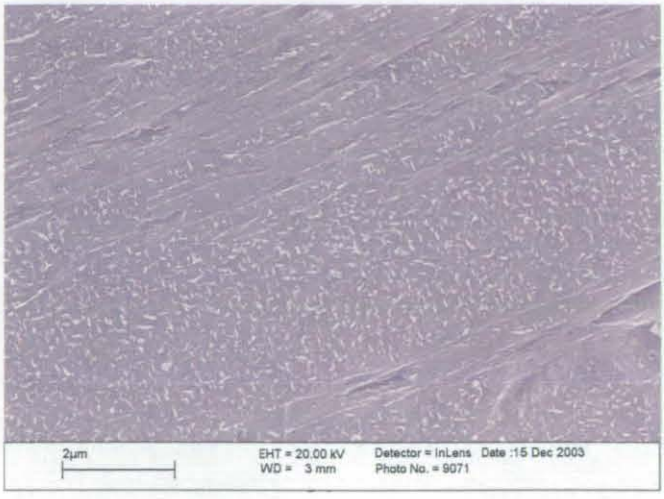

h) auto-tempered martensite

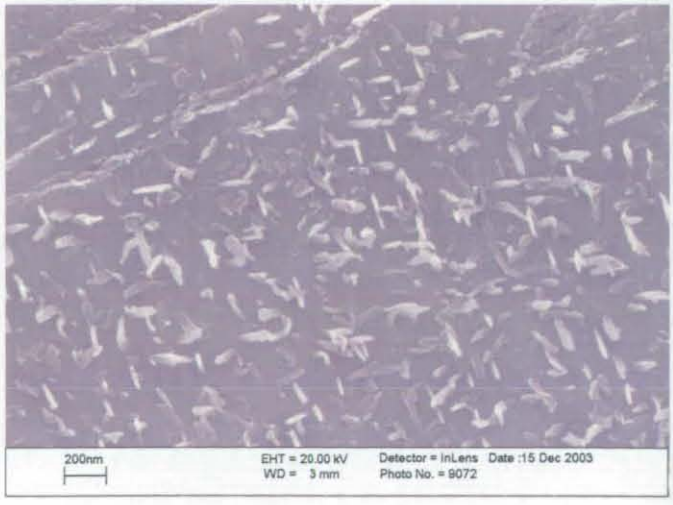

When the manganese content is increased (alloy HOM148), the formation of tadpole-shaped precipitates takes place at lower cooling rates (e.g. 10°C s^{-1}). The presence of small lamellae was not been observed. Small discrete particles are still present, although they are not the dominant morphology. In fact, when precipitation occurs in arrays the precipitates are usually irregularly shaped and the spacing between the arrays ranges usually between 100 and 200 nm. The carbide morphologies of alloy HOM148 cooled at 10°C s^{-1} are shown in figure 7.27a.

Figure 7.27a: *Precipitate morphologies in alloy HOM148 cooled at 10°C s^{-1}*

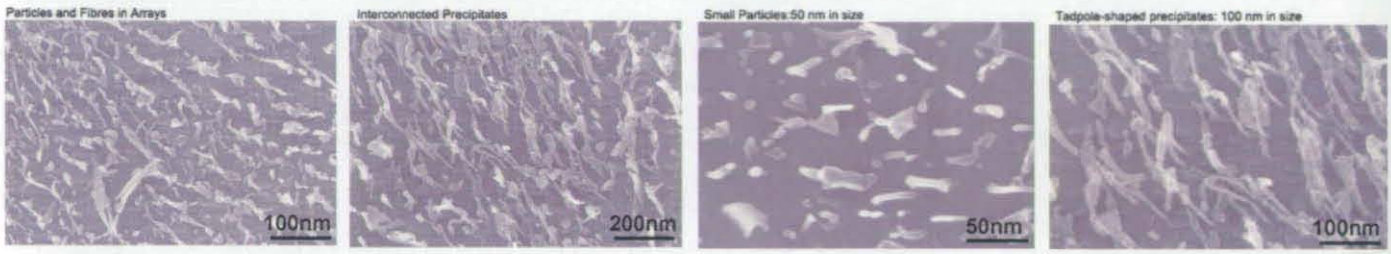

The average particle size is 50 μm. Whilst in the case of tadpole-shaped precipitates, the average size is 250 nm. The presence of particles is very limited.
When the manganese content is decreased (alloy HOM146), the formation of irregularly shaped precipitates, which are in some case discrete and in other interconnected, takes place at lower cooling rates (e.g. 10°C s^{-1}). It is very interesting that many precipitates appear as elongated branched fibres. Small lamellae were not observed. On the other hand, the presence of small fibres is significant. The spacing between the arrays, when present, ranges usually between 100 and 200 nm. The carbide morphologies of alloy HOM146 are shown in figure 7.28b:

Figure 7.28b: *Precipitate morphologies in alloy HOM146 cooled at 10°C s^{-1}*

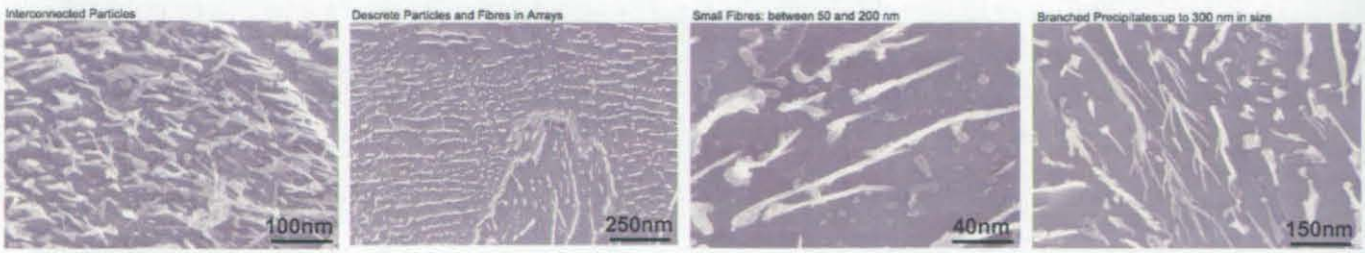

The average particle size is 50 μm. The fibres form in arrays and their dimension is bigger than in Y7N1 and HOM148, ranging between 0.2 and 1.5 μm. The average spacing between fibres arrays is 500 nm. The dimensions of the irregularly shaped particles and branched fibres ranges between 40 nm and 1 μm.

7.7 The Effects of Manganese

From sets of images showing the microstructures of alloy HOM146 and HOM148 linked to the microstructures of alloy Y7N1, the effect of manganese appears to be important for the transformation kinetics of the FCA. Generally speaking, manganese content varies as a function of the desired matrix. Typically, the effects of manganese on the $\alpha \rightarrow \gamma$ transition is to stabilise austenite at the expenses of ferrite. The effects on the growth of pearlite are the decrease in the growth rate with increasing Mn concentration. If the transformations take place in the high temperature regime, it can be added to steels whose final microstructure is aimed to contain fine pearlitic regions. On the other hand, manganese has a strong effect as well on phase transformations taking place at lower temperatures. In fact, Mn addition increases the hardenability of a steel, therefore favouring the formation of bainitic ferrite and martensite at lower cooling rates.

The transformation sequence determined by means of interrupted continuous cooling experiments showed that at low cooling rates the formation of FCA takes place at lower temperatures compared to pearlite and it is associated with Widmanstätten ferrite, whose formation precedes it, whilst pearlite formation (whose morphology is that of small grains between larger ferrite grains) takes place after primary ferrite has formed, or eventually contemporarily to Widmanstätten ferrite, when the microphase regions between the sideplates have the chance to transform into pearlite. The formation of bainite at higher cooling rates, instead, occurs at lower temperatures, after FCA formation has taken place. It is useful to highlight the transformation sequence in order to relate the effects of manganese on the FCA formation as well as trying to understand better the nature of such phase.

The SEM analysis (see figure 7.29) of alloy HOM146 showed that a low manganese content favours the formation of pearlite at very low cooling rates and delays the formation of FCA which needs higher cooling rates to form. This is in agreement with the increase in growth rate of pearlite caused by a low Mn addition. As the cooling increases, the austenite transforms mainly into products forming via a diffusion based mechanism or without a strong displacive character. In fact, at 50°C s^{-1} the microstructure is constituted of primary ferrite, coarse Widmanstätten ferrite and FCA, the latter being dominant. If this microstructure is compared with the one obtained with alloy Y7N1 under the same heat treatment conditions, it results very evident that the phases forming reconstructively are favoured and the cooling

rate regime under which they form, at the expenses of bainite and martensite, is shifted to higher cooling rates. The effects of decreasing manganese seem to be beneficial for the formation of FCA. Therefore, it seems that the low manganese addition shifts the cooling rate regime for bainite formation to higher cooling rates and favours the formation of FCA.

Increasing the manganese content (alloy HOM148) leads to the formation of FCA at low cooling rates (e.g. 2°C s^{-1}) but, on the other hand, leads to a decrease of the volume fraction of such phase at higher cooling rates (e.g. 50°C s^{-1}), favouring the formation of bainitic ferrite. The microstructure is fully constituted of bainite and martensite at cooling rates higher than 50°C s^{-1}. Therefore, increasing manganese content shifts the range of formation, under continuous cooling conditions, of the FCA to lower cooling rates, as well as the formation of bainitic ferrite.

Taking into account that Mn increases the rate of transformation of bainite, and in practice had the effect of decreasing the volume fraction of FCA, these observations suggest that the FCA's kinetics are somewhat intermediate between the pearlitic ones and the bainitic ones.

The effects of manganese on the transformation kinetics and final microstructure as a function of cooling rate are schematically represented in figure7.29.

Figure 7.29: *Effects of manganese on the formation of FCA during continuous cooling heat treatments*

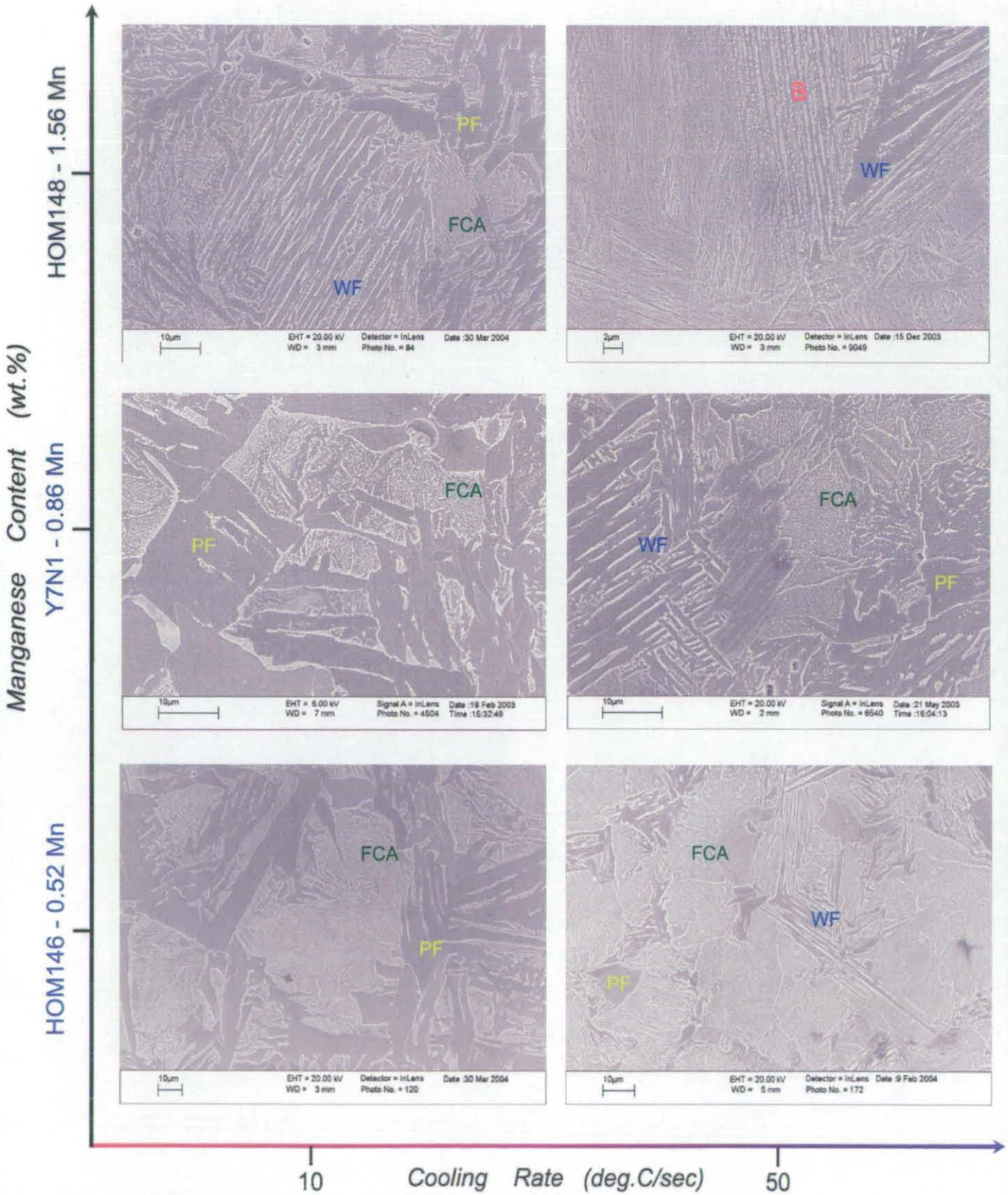

In figure 7.29 above:
PF is primary ferrite;
FCA is ferrite carbide aggregate;
WF is Widmanstätten ferrite;
B is bainite.

By comparing tables 7.1, 7.2 and 4.2 (start and finish transformation temperatures of alloys HOM146, HOM148 and Y7N1), it is evident that increasing the manganese content decreases the transformation temperature regime.

The austenite grain size measurements showed that the increase in the manganese content causes a slight increase in the austenite grain size dimension. Although the effects appears to be more marked at low cooling rates, the influences of this factor on the overall transformation kinetics caused by manganese do not seem to be the significantly important. At 50°C s^{-1} for instance, the effects on the austenite grain size and therefore on the transformation kinetics seems to be negligible.

Table 7.3: *Austenite grain sizes of alloys Y7N1, HOM146 and HOM148*

ALLOY	Cooling Rate (°C s^{-1})	Austenite (γ) Grain Size (μm)
HOM146	10	28
Y7N1	10	31
HOM148	10	38
HOM146	50	32
Y7N1	50	26
HOM148	50	31

The influence of manganese on the transformation start temperatures is better explained by referring to the dilation curves of the three alloys. Figures 7.30, 7.31 and 7.32 below compare three curves for the heat treatments involving an austenitising step performed at 1100°C followed by a cooling step to room temperature at 10°C s^{-1}, 50°C s^{-1} and 100°C s^{-1} respectively. Each curve corresponds to one of the three alloys investigated.

Figure 7.30: *1100°C-10°C s^{-1} dilation curves (black for HOM146, blue for Y7N1 and red for HOM148)*

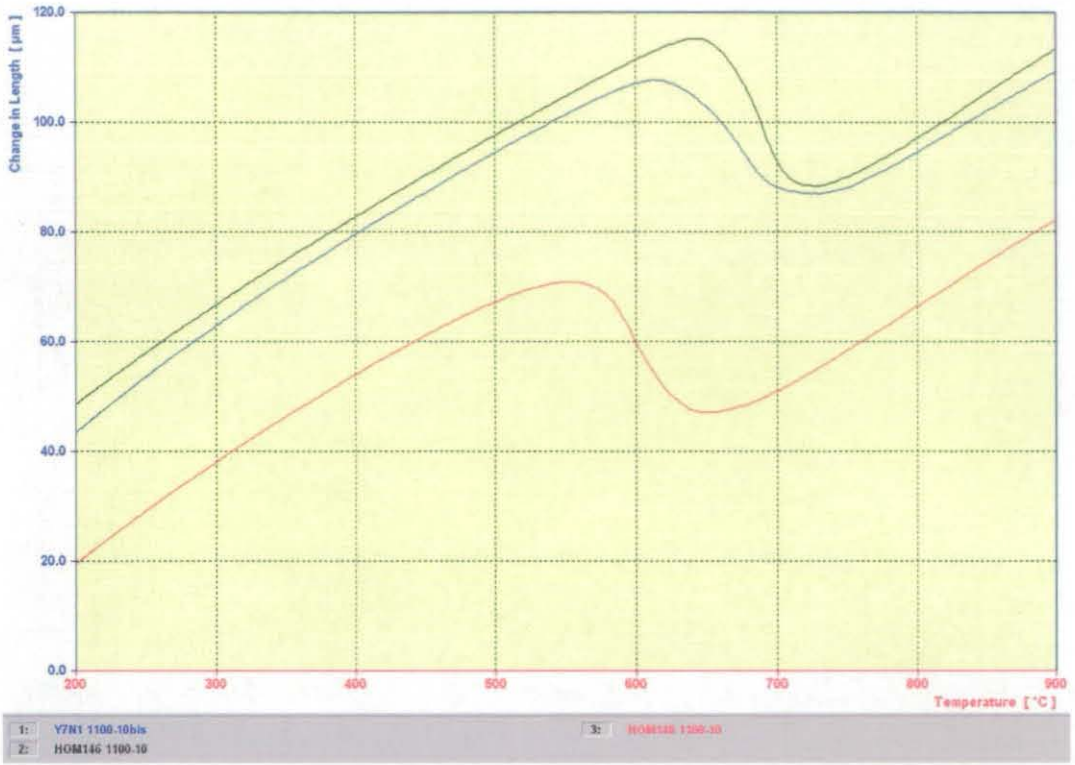

Figure 7.31: *1100°C-50°C s^{-1} dilation curves (black for HOM146, blue for Y7N1 and red for HOM148)*

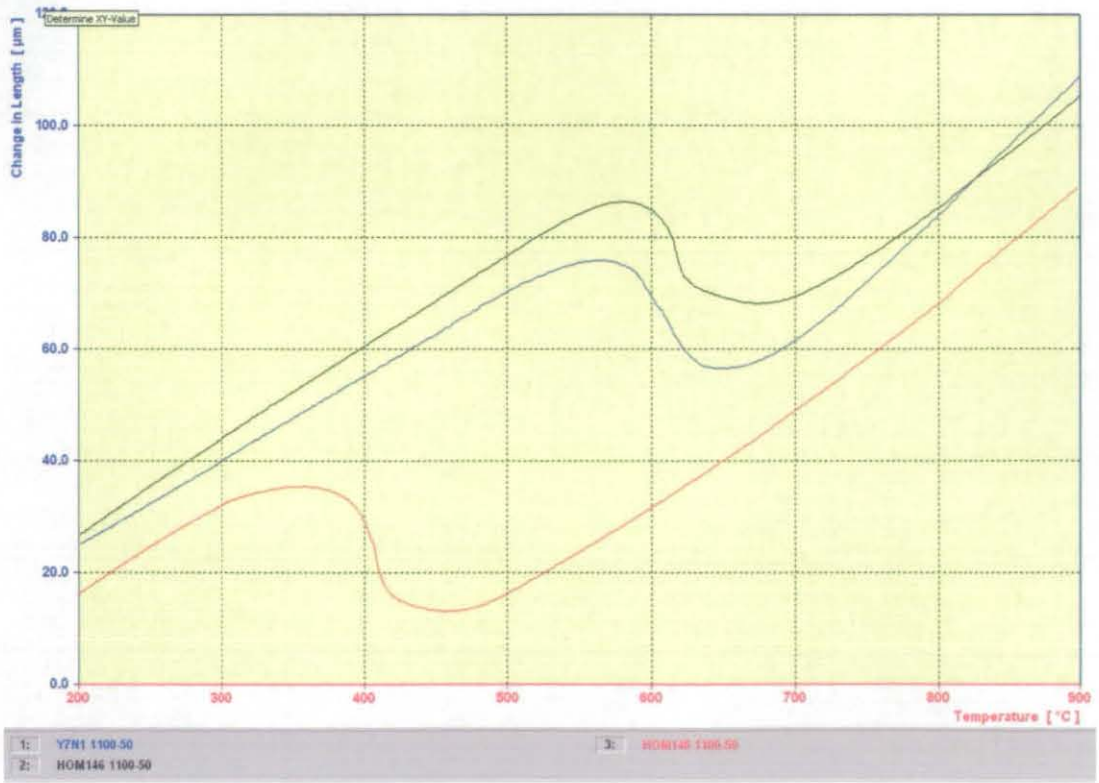

Figure7.32: *1100°C-100°C s^{-1} dilation curves (black for HOM146, blue for Y7N1, red for HOM148)*

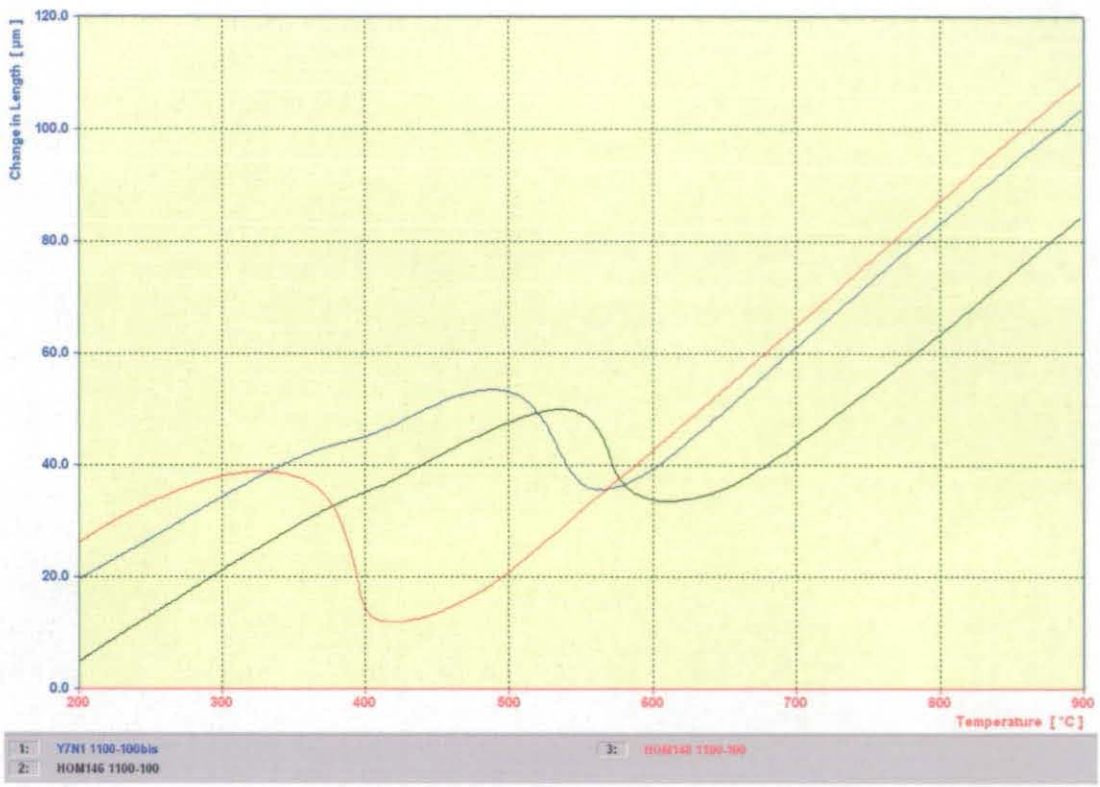

At the three cooling rates, the effect of manganese is the same and consists in depressing the transformation start temperature. As manganese belongs to the category of austenite stabilising elements the expected consequence is that of lowering the temperature at which the $\alpha \rightarrow \gamma$ transition starts. Both the A_{e1} and A_{e3} temperatures are lowered. This effect has been explained by Zener and Andrews in terms of thermodynamic factors. Naturally, a transition depends on the free energies of the initial (γ) and final (α) stages of transformations, which, in turn, depends on the enthalpies of the parent and product phase. Manganese causes the enthalpy of ferrite to be higher than that of austenite. This is translated in the fact that the overall ΔH associated to the transformation is negative, favouring the stability of austenite.

The effects is more marked as the cooling rate increases and the transformation temperature regime shifts to lower temperatures as in the case of alloy HOM148, where cooling rates of 50°C s^{-1} and above involve the formation of low temperature phases such as bainite. This is reflected as well on the larger amplitude of the change in length associated to displacive transformations.

7.8 Alloy HOM133 Analysis

In order to achieve more information primarily about the nature of the FCA, and also in order to gather useful information regarding the kinetics of simultaneous transformations and the characteristics of the complex microstructures produced, a sample from a series of electron beam welded samples has been observed by means of SEM and mechanically tested by means of micro-hardness. Comparison with the data for the continuously cooled YZN1 samples was also possible as a result of analysis.

The alloy analysed belongs to the HOM alloy series and was labelled HOM133. Its composition is 0.13 wt.% C, 0.31 wt.% Si, 1.02 wt.% Mn, 0.0044 wt.% N, balance Fe. The alloy content of phosphorous, sulphur, niobium, titanium and vanadium are below 0.005 wt.%. Therefore, the phase quantification has been previously performed on the HAZ coarse grain microstructure of the sample and the results are as follows (all the phase quantification data for alloy HOM133 have been kindly provided by Dr. Graham Thewlis from Corus):

- Primary Ferrite: 2.8%
- Pearlite: 3.1%
- Widmanstätten Ferrite: 50.8%
- Bainite: 38.9%
- Martensite: 4.2%
- Acicular Ferrite: 0.2%

The sample has been optically analysed. The microstructure is shown in figure 7.33:

Figure 7.33: *Optical micrograph of sample HOM133*

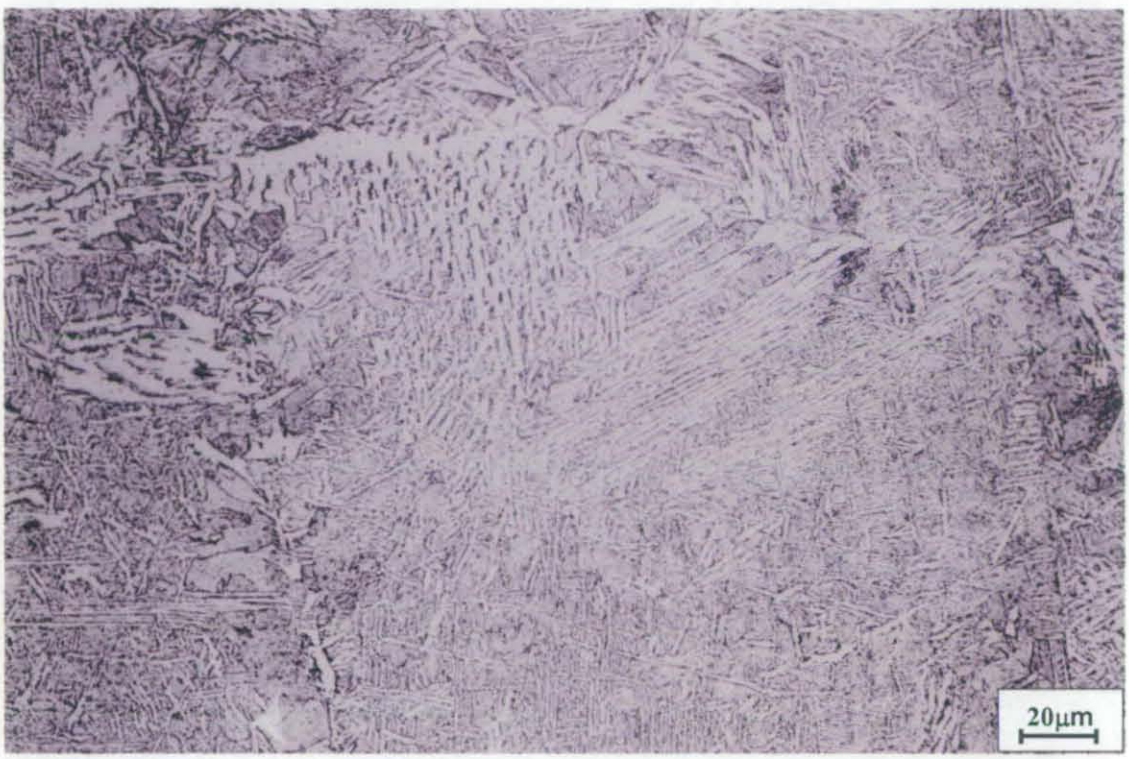

In a HAZ generally speaking, high cooling rates cause a massive transformation leading to martensite formation. The degree of auto-tempering is strictly dependent on the M_S temperature of the alloy. Decreasing the cooling rates, a range of microstructure is observed, from bainitic ferrite and/or acicular ferrite, Widmanstätten ferrite, proeutectoid ferrite and ferrite-carbide aggregate (including in this definition the FCA phase). The microstructure of the sample has additionally been observed by means of SEM at high magnifications. Attention has been focused on both the HAZ and the region away from the HAZ in order to study the coarse structure of pearlite and compare it with the structure of the FCA. It is worth note that the FCA regions have been found as well away from the HAZ. Examples of the microstructures observed are shown in figures 7.34a-n as follows.

Figure 7.34a-n: *Microstructural features of sample HOM133 (EBW)*

a) *coarse structure*

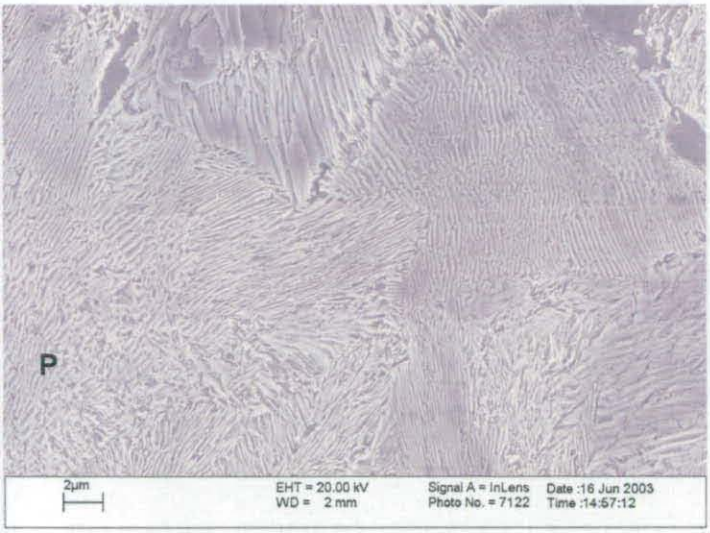

b) *pearlite lamellae*

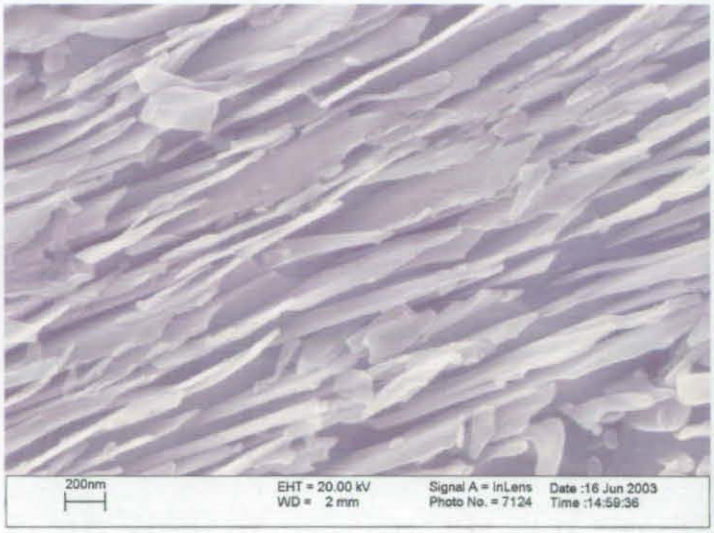

c) *coarse structure*

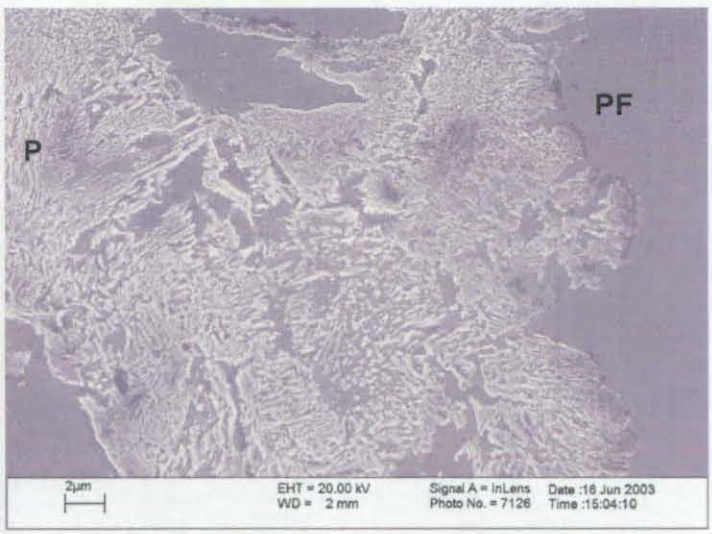

d) *degenerate pearlite*

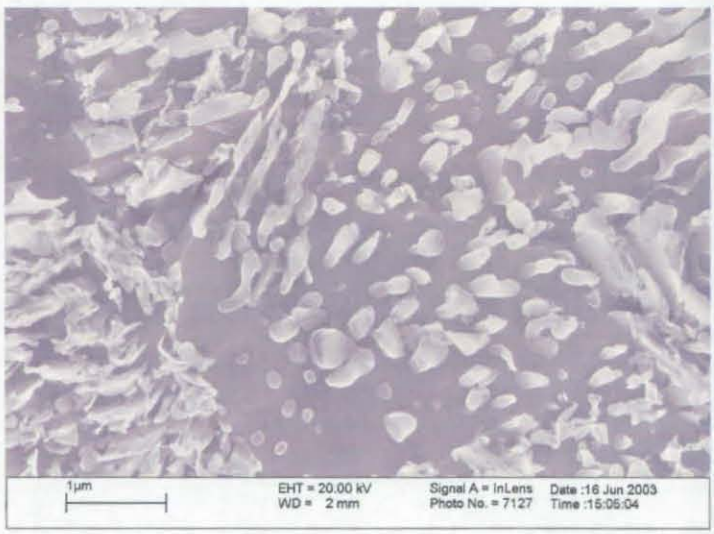

e) *fine structure (bainite – WF)*

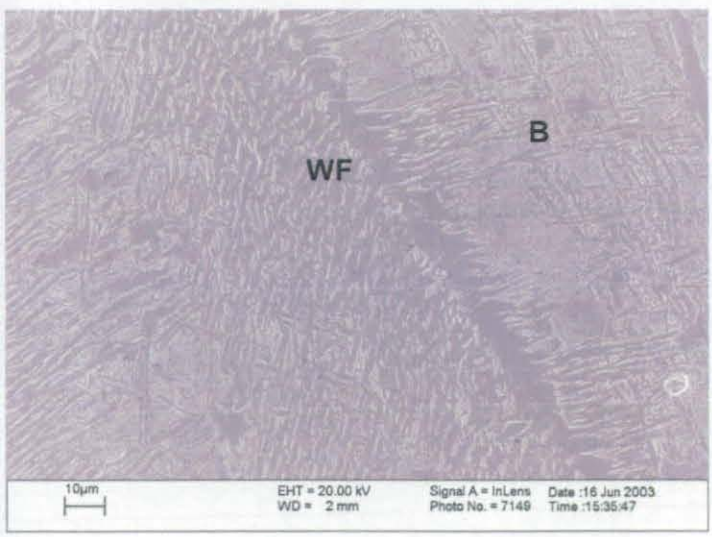

f) *microphase*

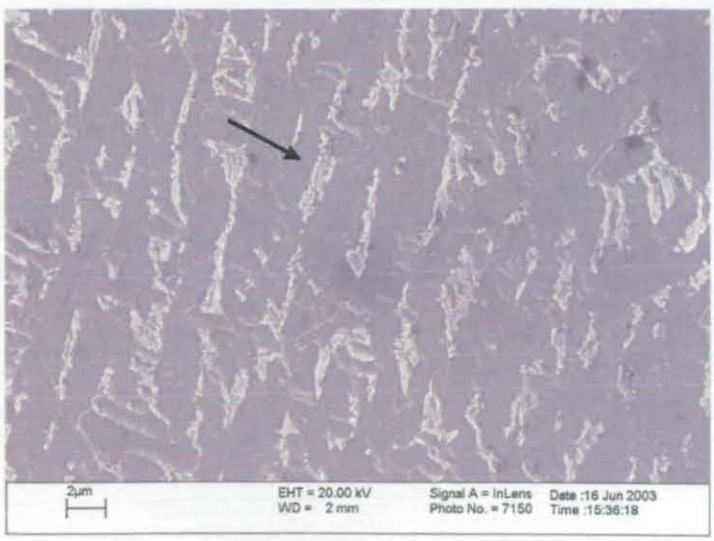

g) microphase

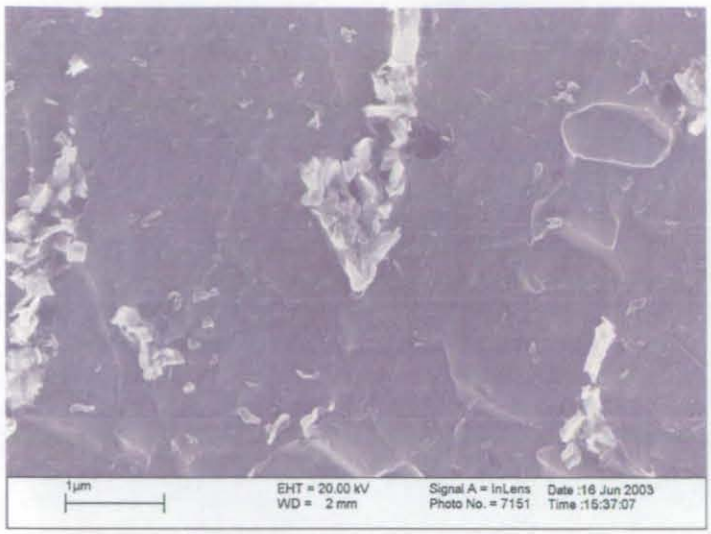

h) microphase

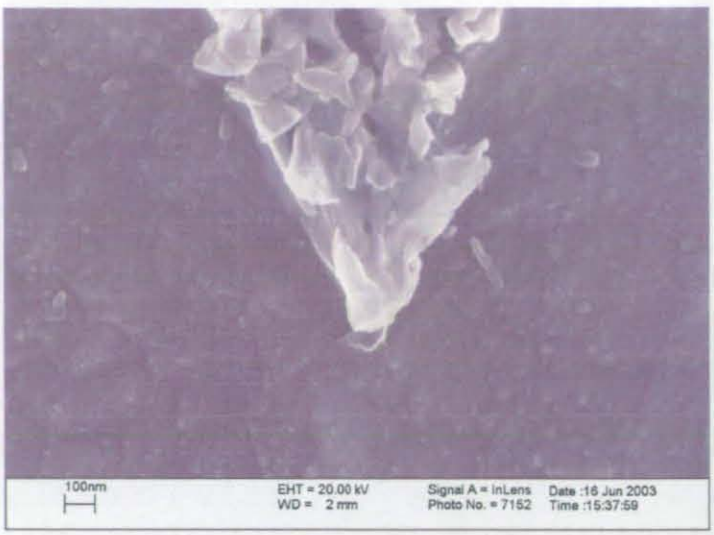

i) L bainite - martensite

j) L bainite - martensite

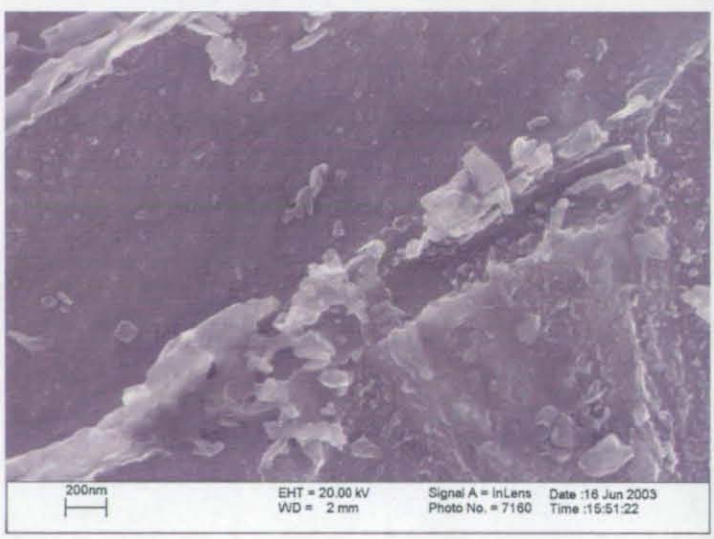

k) Widmanstätten Ferrite

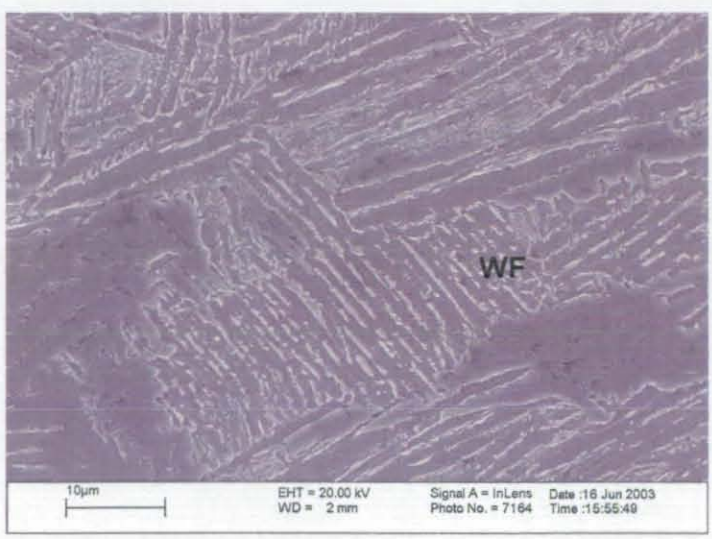

l) microphase (M/A)

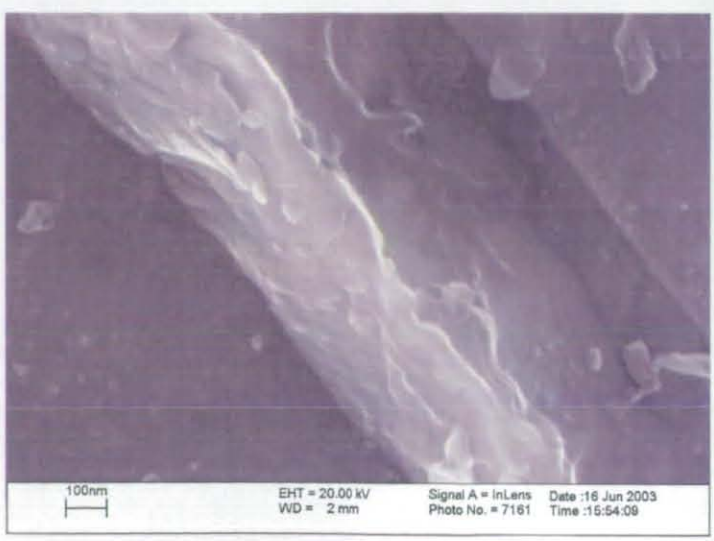

m) FCA

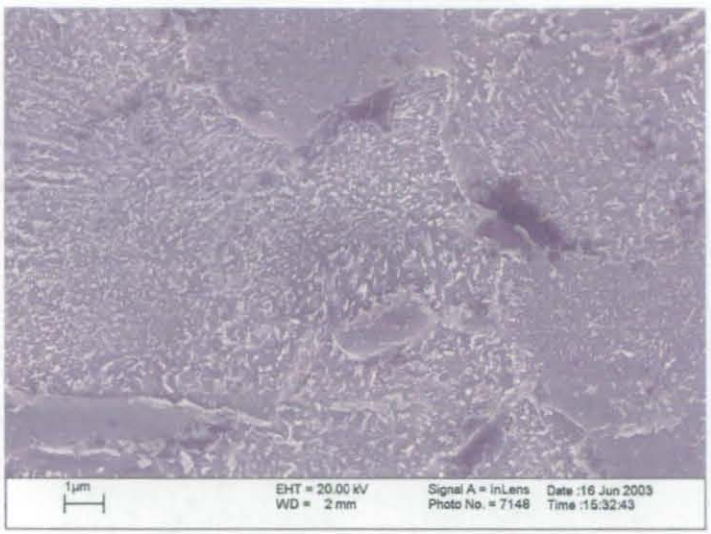

n) FCA

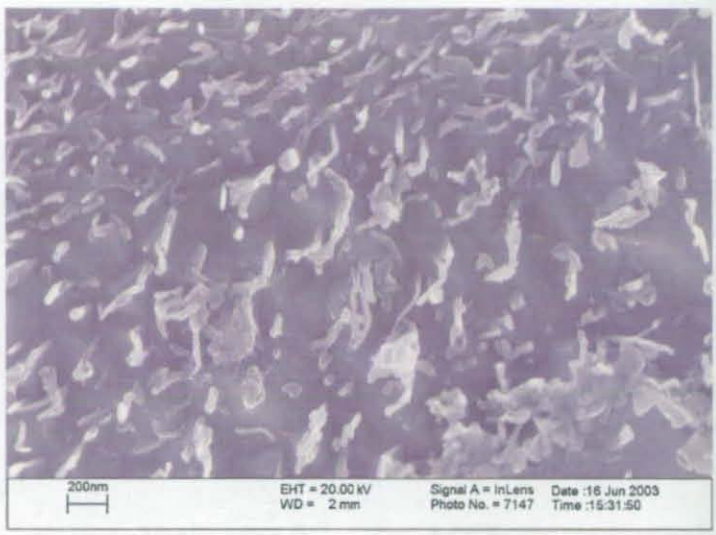

As it can be seen in the last two images, 7.34n and 7.34o, the FCA have a very similar structure to that encountered in the four continuously cooled YZN1 samples. The presence of dark etching FCA regions was revealed optically. Micro-hardness has been performed on the sample HOM133 and the data obtained (figure 7.35) are in line with the trend observed in alloys Y7N1, HOM146 and HOM148.

Figure 7.35: *Micro-hardness plot for sample HOM133 electron beam welded*

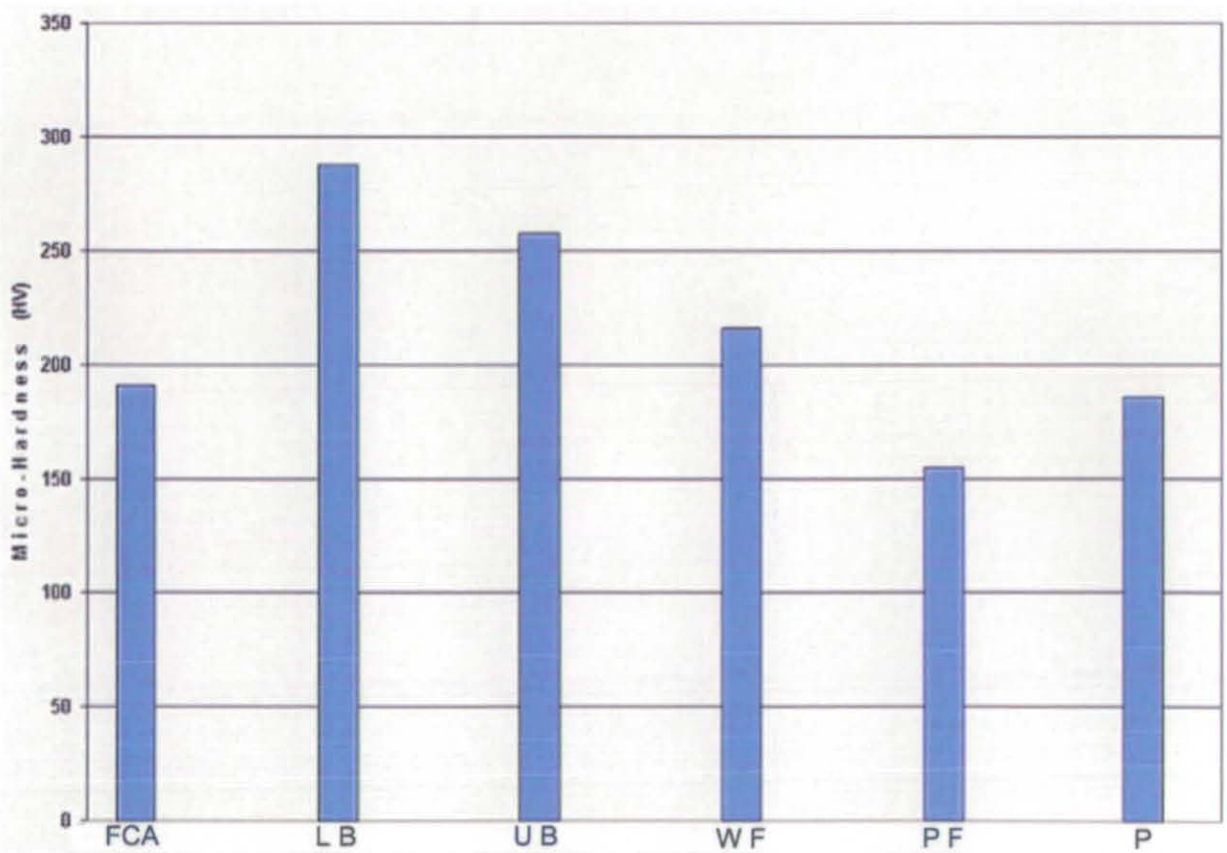

Initially, the nature of the FCA, which can be found primarily in the HAZ but also in the finer structure areas, was thought to be martensitic. However, the micro-hardness data revealed that this supposition is not very likely because the hardness is very close to that of Widmanstätten ferrite. For this reason and for the fact that the interested areas were not the ones very close to the weld, micro-hardness was not performed on the martensitic region near the welding, expected to be the hardest.

The hardness of the FCA was approximately of the same magnitude than that measured in the four continuously cooled YZN1 samples. The morphological appearance of the degenerate pearlite observed in the HOM133 sample and the fact that the micro-hardness values are very similar, suggest that there is a possibility that the FCA are constituted of a form of degenerate pearlite produced at lower temperatures. However, a strong factor which distinguishes the two phases is the fact that the degenerated pearlite lamellae have dimensions which are considerably larger compared to the particles present in the FCA regions.

7.9 Summary

The influences of varying manganese content on the transformation kinetics of the FCA phase (and therefore, the overall transformation kinetics) have been investigated. Low manganese content favours the formation of FCA and shifts the cooling rate range to higher cooling rates. Furthermore, the fraction of FCA increases as the manganese content decreases. The influence of changing composition on the carbide size and distribution has been discussed. The observed shape of the particles was more irregular when compared to alloy Y7N1, and the most common morphology encountered was that of interconnected particles

The formation of the FCA in an electron beam welded sample (alloy HOM133) has also been studied and the main characteristics of the heat affected zone investigated.

8. Thermodynamics of the FCA Formation and Kinetics of the Continuous Cooling Transformations

8.1 Introduction

This chapter draws together the results of the research discussed in previous chapters. The phase classification, phase quantification, transformation sequence and dilatometry data are linked together in order to produce CCT diagrams for all the alloys treated. This facilitates an understanding of the final microstructures in relation to the heat treatment and the kinetics of the phase transformations taking place during cooling. The role of FCA is considered, and a specific phase region in the CCT diagrams has been identified. Finally, the underpinning thermodynamics and kinetics of the FCA transformation are discussed.

8.2 Thermodynamic Considerations of FCA, Bainite and Martensite

In order to help defining the thermodynamic conditions governing the FCA formation, and in view of the fact that its formation takes place between the reconstructive and the displacive regime, in this section some of the parameters related to the formation of martensite and bainite are considered and used to help distinguishing FCA from them, in addition to providing an indication of the actual conditions under which the FCA forms.

8.2.1 Variation of the M_S Temperature

The influence of the M_S temperature on the transformation taking place during cooling in alloy Y7N1 under different heat treatment conditions has been considered especially to exclude the possibility of a martensitic (auto-tempered) nature of the FCA and to set a strong distinction between the mechanisms involved in the formation of martensite and those involved in the formation of FCA.

Figure 8.1: *M_S temperature as a function of carbon content for alloy Y7N1*

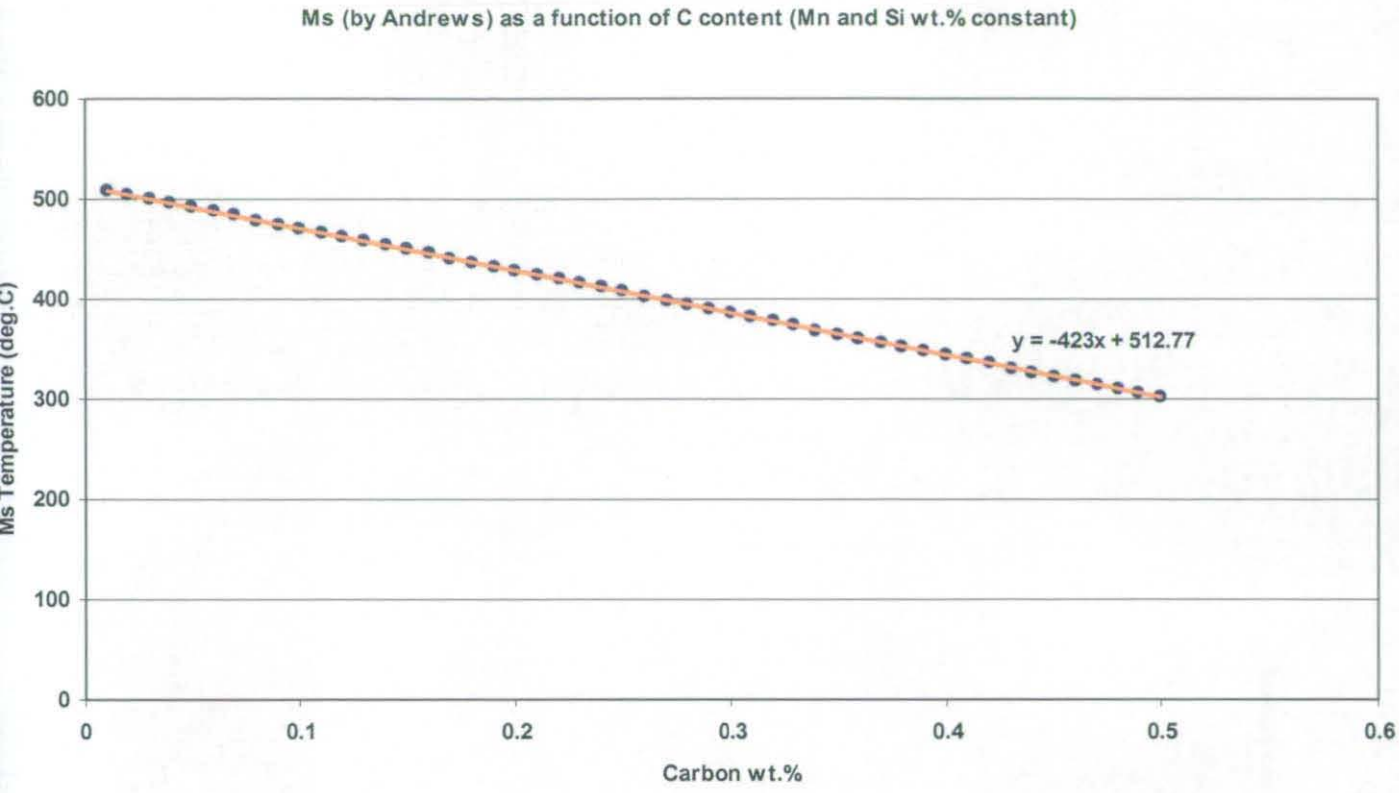

On continuous cooling, the formation of primary ferrite and Widmanstätten ferrite takes place initially accompanied by enrichment in carbon of the residual austenite, causing a decrease in the M_S temperature for the untransformed austenite. From the graph in figure 8.1, it can be seen that the M_S is below T_f for all the samples treated where the FCA formation takes place, even for low carbon enrichments of the austenite. Therefore, considering the fact that even at temperatures close to T_f for alloy Y7N1 (listed in table 4.2 in chapter 4) the microstructure is nearly fully transformed, it is virtually impossible that a martensitic transformation can be responsible for the FCA formation. Furthermore, the volume change associated with the martensitic transformation should have been recorded by the dilatometer for the samples continuously cooled to room temperature (e.g. sample 1300/10 or 1300/50). This is supported strongly by the evidence provided by the interrupted cooling experiments in addition to the micro-hardness data.

8.2.2 Variation of the T_o Temperature

Bainite can be defined as a non-lamellar mixture of ferrite and cementite. The FCA phase could be included in this broad definition if the parameters involved in the formation of bainite and the thermodynamic conditions were not very distinct.

T_0 is defined as the temperature at which γ and α of the same composition have the same free energy, as shown in figure 8.2, and is an important parameter in the context of bainitic transformations.

Figure 8.2: *Schematic diagram of the bainite reaction thermodynamic conditions*

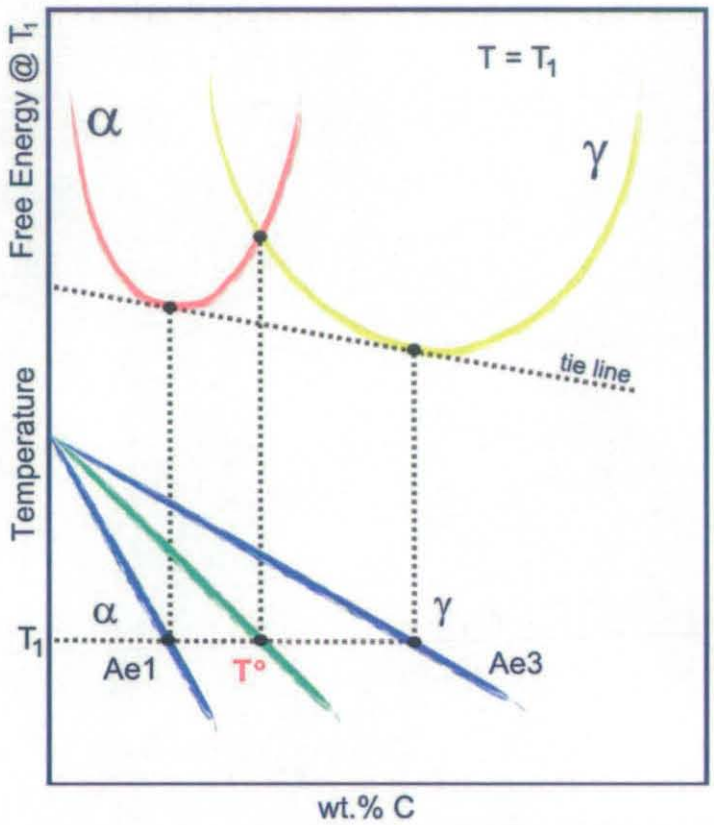

Considering the diffusionless stage of the bainite reaction, at a given temperature the transition from austenite to supersaturated bainitic ferrite is possible at carbon concentrations to the left of the T_0 curve, whilst it ceases at T_0. The T_0 line defines the incomplete reaction phenomenon which causes the formation of a volume fraction of bainitic ferrite lower than that predicted by the Ae_3 equilibrium curve.

Although the T_0 curve is defined under isothermal conditions, continuous cooling processes can be approximated by a summation of infinitesimally small isothermal steps, occurring at decreasing temperatures and the thermodynamic significance and implications of this parameter can still be preserved and applied. Therefore, assuming that the carbon content during continuous cooling transformations varies depending on the transformations that take place, a range of T_0 temperatures can be calculated as a function of carbon content.

The following table shows the calculated values of T_0 as a function of carbon content for the alloy Y7N1.

Table 8.1: *T_o as a function of carbon content, alloy Y7N1*

T_0 (K)	C wt. %
423	2.4775
528.5	2.2675
584.1	2.05
639.7	1.82
695.2	1.58
750.8	1.33
806.3	1.06
861.9	0.77
917.4	0.443
973	0.228

Figure 8.3: *T_0 variation for alloy Y7N1 as a function of carbon content*

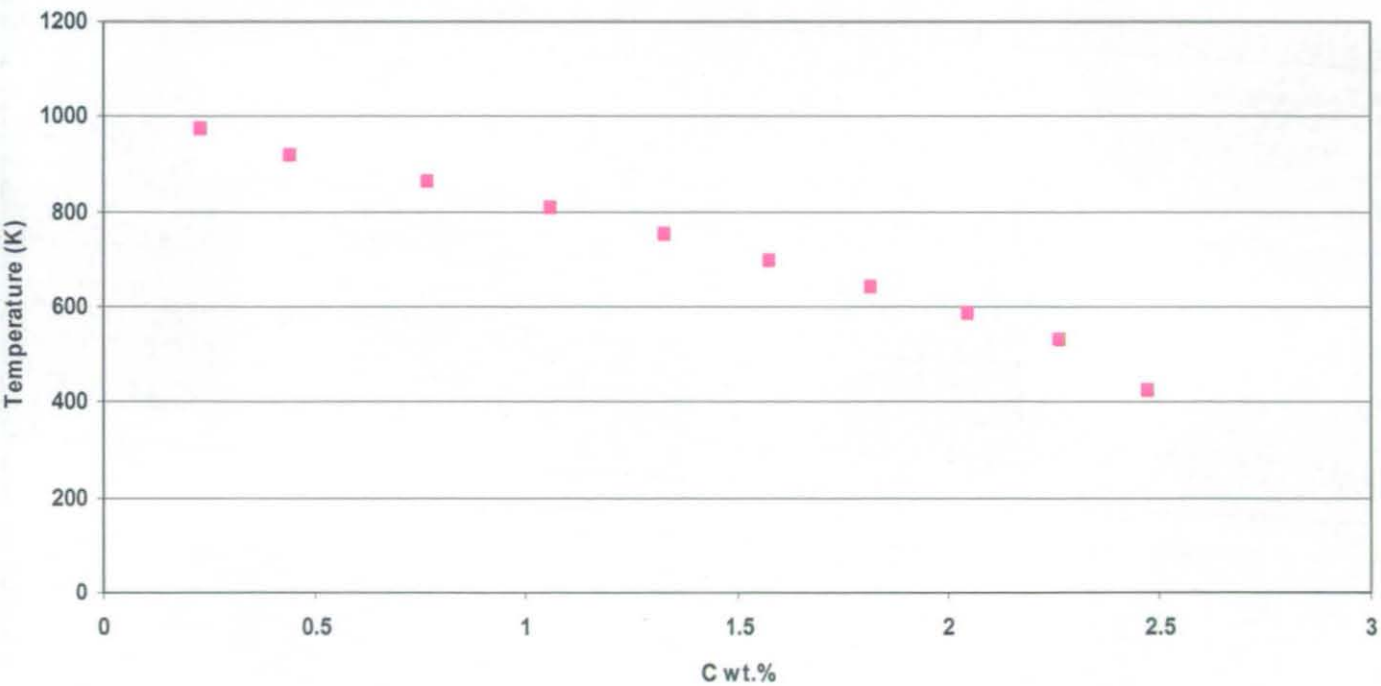

In order to consider the effect of the substitutional elements on the T_0 variation, the calculations have additionally been performed as well for a fictitious alloy whose silicon and manganese composition were respectively 0.14 wt.% Si and 1.72 wt.% Mn.

Table 8.2: *To as a function of carbon content, 0.14 wt% Si, 1.72 wt% Mn alloy*

T_0 (K)	C wt. %
473	2.4775
528.5556	2.2675
584.1111	2.05
639.6667	1.82
695.2222	1.58
750.7778	1.3275
806.3333	1.0625
861.8889	0.77
917.4444	0.4425
973	0.2275

It can be seen on both of these cases that the T_0 temperatures calculated are very similar, implying that the effect of substitutional elements such as Si and Mn is negligible.

Figure 8.4: *T_0 variation for 0.14 wt% Si 1.72 wt% Mn alloy*

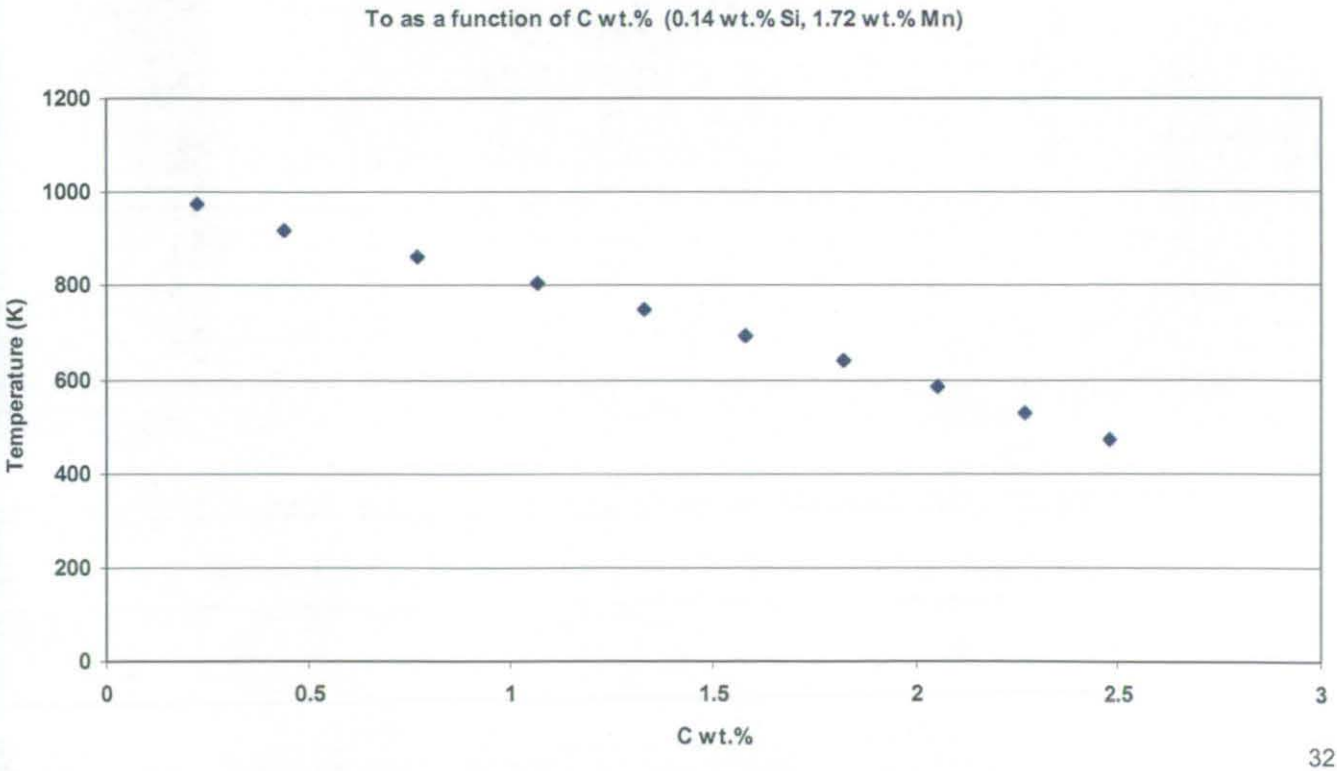

It has to be considered the fact that the accuracy of the results depends on the accuracy of the model utilised for the calculations and that the continuous cooling conditions represent a further limitation when the concepts developed for isothermal conditions are applied. The results indicate that the carbon content of the austenite before the FCA formation takes place is very close to those corresponding to the T_0 line, although, it cannot be concluded whether it is higher or lower. In the event that the carbon content is higher, the bainite formation becomes impossible. To verify quantitatively whether the FCA carbon content falls in the range where bainite formation is possible, the role of carbon specifically in the transformations taking place in alloy Y7N1 has been considered.

8.3 Role of Carbon in the FCA Formation

In chapter 6 it has been shown that the FCA formation occurs after Widmanstätten ferrite, at relatively low temperatures. If the cooling is interrupted before the FCA formation takes place, the remaining austenite transforms into martensite. This clearly involves a critical dependence on the amount of carbon present in the austenite, which, as a consequence of the cooling process, increases as the temperature decreases. The following set of tables show the phase volume fraction data obtained by quantifying the microstructures produced by carrying out interrupted continuous cooling heat treatments on alloy Y7N1. The heat treatments have been performed under different conditions, varying the austenitising temperature, the cooling rate and interrupting the continuous cooling stage at different temperatures. This allowed monitoring of the evolution of the microstructures at different cooling stages.

Table 8.3: *Phase quantification for the interrupted continuous cooling experiments performed on alloy Y7N1 1300/10*

Y7N1 1300/10	Phase Volume Fraction (%)						
Interrupted at (°C)	PF	WF	MP	FCA	UB	LB	M
624	7	5	1	-	-	-	87
606	9	11	4	-	-	-	76
587	17	41	16	26	-	-	-

Table 8.4: *Phase quantification for the interrupted continuous cooling experiments performed on alloy Y7N1 1100/10*

Y7N1 1100/10	Phase Volume Fraction (%)						
Interrupted at (°C)	PF	WF	MP	FCA	UB	LB	M
659	18	10.5	1.5	-	-	-	70
637	23	22	4	-	-	-	63
615	28	39	9	24	-	-	-

Table 8.5: *Phase quantification for the interrupted continuous cooling experiments performed on alloy Y7N1 1100/50*

Y7N1 1100/50	Phase Volume Fraction (%)					
Interrupted at (°C)	PF	WF (MP)	FCA	UB	LB	M
665	3	26.3	-	-	-	70.7
655	3	29	.	.	-	68
606	4	35	1	-	-	60
580	3	46	7.5	10	-	33.5

Table 8.6: *Phase quantification for the interrupted continuous cooling experiments performed on alloy Y7N1 1300/50*

Y7N1 1300/50	Phase Volume Fraction (%)					
Interrupted at (°C)	PF	WF (MP)	FCA	UB	LB	M
600	1	12	-	4	9 (q)	73
580	1	18	-	8	-	71
560	1	22	-	20	-	57
530	1	18	5	38	-	39
500	1	17	9.5	53. 5	-	19
470	1	21	23	55	-	-

The FCA identification at 50°C s^{-1} is sometime not very accurate. In fact, the FCA can develop in sites of the microstructure which are adjacent to martensitic regions formed during quenching. This makes the distinction between the two phases performed by optical means not very easy.

The possibility that the FCA is comprised of ferrite-carbide aggregates, forming via a diffusional mechanism which could have common features with the pearlite reaction, is strictly related to the local carbon concentration in the FCA. A high carbon concentration would prevent martensite formation and could determine a particular reconstructive mechanism allowing precipitation of carbides. In view of the low carbon content of alloy Y7N1, if this remained locally unchanged, the precipitation of such a high amount of carbides in the FCA would be unlikely. Therefore it is fair to consider local carbon enrichment.

A very useful data which has been obtained from the analysis of the interrupted continuous cooling experiments is an estimation of the carbon content in the residual austenite, monitored at different stages of the cooling. The following carbon contents represent the upper limits of available carbon in the remaining austenite after ferrite (PF and WF) formation. This carbon could be present in FCA, microphase regions (retained austenite, martensite, pearlite islands, ferrite-carbide aggregates) and/or carbides eventually present for instance in bainite. Table 8.7a show the carbon content calculations for alloy Y7N1 austenitised at 1100°C and cooled at 10°C sec^{-1} and alloy Y7N1 austenitised at 1300°C and cooled at 10°C sec^{-1}. The upper limit is obtained considering that the carbon in ferrite is zero whilst the lower limit is obtained considering that the carbon in ferrite is 0.02 wt.%. Both the two limits of .0 and 0.02 wt.% C have been considered as it is uncertain how much carbon is present in the ferritic lattice.

Table 8.7a: *Available carbon in residual austenite for alloy Y7N1*

Alloy Y7N1	**Carbon in Austenite (wt.%)**	
	Upper Limit	**Lower Limit**
1100/10	0.590	0.526
1300/10	0.497	0.431

These carbon content calculations have been made for the samples cooled at 10°C s^{-1} because at this cooling rate the bainite reaction does not take place. If bainite formation takes place (e.g. at 50°C s^{-1}) the determination of the carbon content in the remaining austenite is more difficult because carbon can be partially trapped in the bainitic sheaves.

Table 8.7b shows how the carbon content of the untransformed austenite before the FCA transformation starts to gradually increase, eventually reaching a content which is possibly higher than 0.4 wt.% C.

Table 8.7b: *Available carbon in residual austenite for alloy Y7N1*

Alloy Y7N1	Carbon in Austenite (wt.%)	
	Upper Limit	Lower Limit
1100/10	0.590	0.526
1100/10 int. at 615°C	0.542	0.486
1100/10 int. at 637°C	0.206	0.192
1100/10 int. at 659°C	0.186	0.177

In samples 1300/10, 1100/10 and 1100/10 interrupted at 615°C, where FCA is present, the carbon content is far below the eutectoid and, at the same time is higher than the carbon content corresponding to the T_0 line. In samples 1100/10 interrupted at 637°C and 1100/10 interrupted at 659°C, the carbon content in the untransformed austenite is on average lower than 0.2 wt.%, and the formation of FCA does not take place, indicating that a critical amount of carbon has to be overcome in order to trigger the FCA nucleation.

8.4 Isopleth: Section of a Phase Diagram

The phase diagram shown in figure 8.5 represents the phase fields for alloy A. The T_0 curve (red) is represented together with the extrapolated γ/Fe_3C boundary. The interception of the two lines identifies three different regions in the diagram in which different thermodynamic conditions determine the characteristics of the possible reactions.

Figure 8.5: *Predicted isopleth for alloy Y7N1, three regions are highlighted, corresponding to different possible transformations of from austenite to ferrite and cementite*

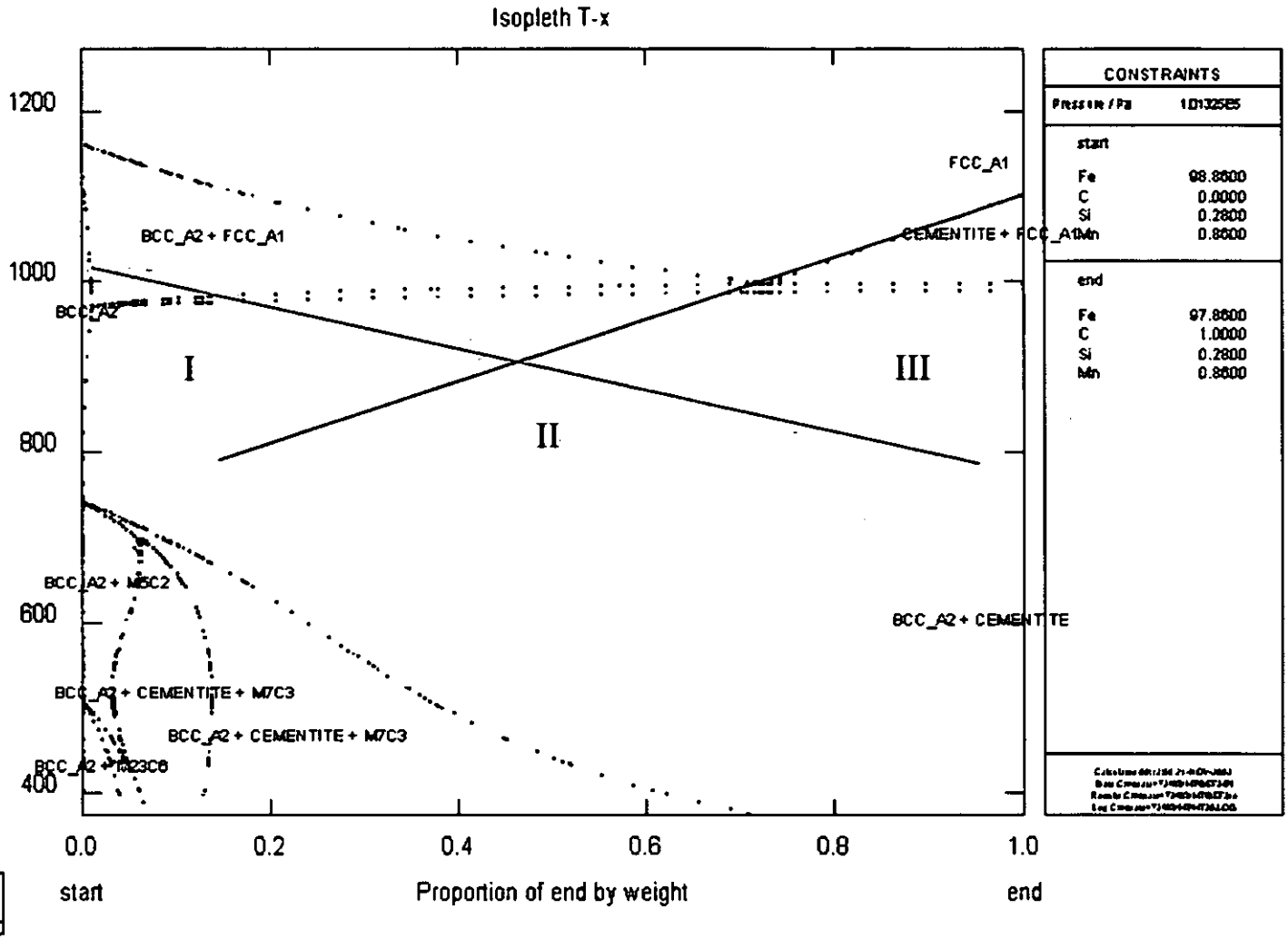

Note: if T_0' is considered (i.e. taking into account the stored energy of bainite), the red line is shifted at lower temperatures

Takahashi and Bhadeshia[49] have previously undertaken a similar approach in order to theorise the transition between upper and lower bainite.

In region I the formation of bainitic ferrite is possible whilst the precipitation of cementite is thermodynamically impossible, therefore the expected product is carbide-free ferrite. On the other hand, region II corresponds to the formation of supersaturated bainitic ferrite from the austenite accompanied by precipitation of carbides, usually cementite. In the right portion of this region, the dominating process should be the carbides precipitation, whilst in the left portion the nucleation of ferrite should be dominating. Under these thermodynamic conditions in the right portion of the region II, if the supersaturation is high enough and the partition of carbon from the supersaturated ferrite to the surrounding austenite does not entirely take place,

the precipitation of ε and η carbides (in lower bainite) is possible and it is usually more likely than the precipitation of cementite. Finally, the austenite cooled into region III is not capable of forming bainitic ferrite, but it is possible nucleation of cementite[1]. The formation of Fe_3C depletes the surrounding austenitic regions which can eventually transform to ferrite, causing an increase in carbon content of the surrounding austenite. This simplistic view suggests that is possible an alternate formation of ferrite and carbide which is strictly dependent on the local carbon concentration and the temperature at which the transformation takes place.

By linking the carbon content calculations discussed in section 8.3 and the dilatometry plots for alloys Y7N1 1100/10 the conclusion is that the thermodynamic conditions are very close to those of region III. Although this approach explains the fact that bainite formation does not take place, it does not provide an accurate description of the actual condition that determine the FCA formation. In this study the precipitation process occurring in the FCA has been classified has discontinuous. In section 2.4.1 discontinuous processes are discussed. The fact that compared to eutectoid precipitation (e.g. pearlite), they require a lower free energy for growth, which corresponds to a lower carbon concentration at the interface, would explain the fact that pearlite does not form at low temperatures (at which the FCA form) in regions which are large in dimensions (as it usually happens in the case of FCA), in which the local carbon concentration is not very high, as shown in section 8.3. The conditions under which such a type of discontinuous precipitation could take place are intermediate between those which allow pearlite formation and those allowing bainite formation. In this sense, the work carried out by Takahashi and Bhadeshia[49], explains how, depending on temperature and carbon composition, carbide precipitation from austenite without the formation of bainite is thermodynamically possible. The pattern of precipitation should be discontinuous, different from the cooperative mode found for the eutectoid reaction leading to pearlite formation[41].

As discussed in section 2.1.3 a possible mechanism of FCA could involve could be interphase cementite precipitation[15,50]. Although this type of precipitation is more common in upper bainitic structures, interphase boundary carbide precipitation (IPBC) can be applied to ferrite allotriomorphs, although the theory behind this mechanism has not been fully investigated yet. In the present case, more reliable experimental data about the carbon composition are needed.

8.5 Size Effect on Pearlite and FCA

At low cooling rates, where the simultaneous formation of pearlite and FCA is possible, there is a correlation between the dimensions of the austenite region which transforms into pearlite or FCA and the nature of the transformation product itself. The measurements performed indicated an approximate dimension limit of 5 μm above which FCA formation is favoured. It has to be borne in mind that the pearlite regions are generally smaller than 5 μm, whereas FCA regions are typically greater than 5 μm and can reach dimensions of 60 μm or more in some cases. Figures 8.6a-d illustrate this dimension effect.

Figure 8.6a: *Dimension effect of pearlite and FCA regions*

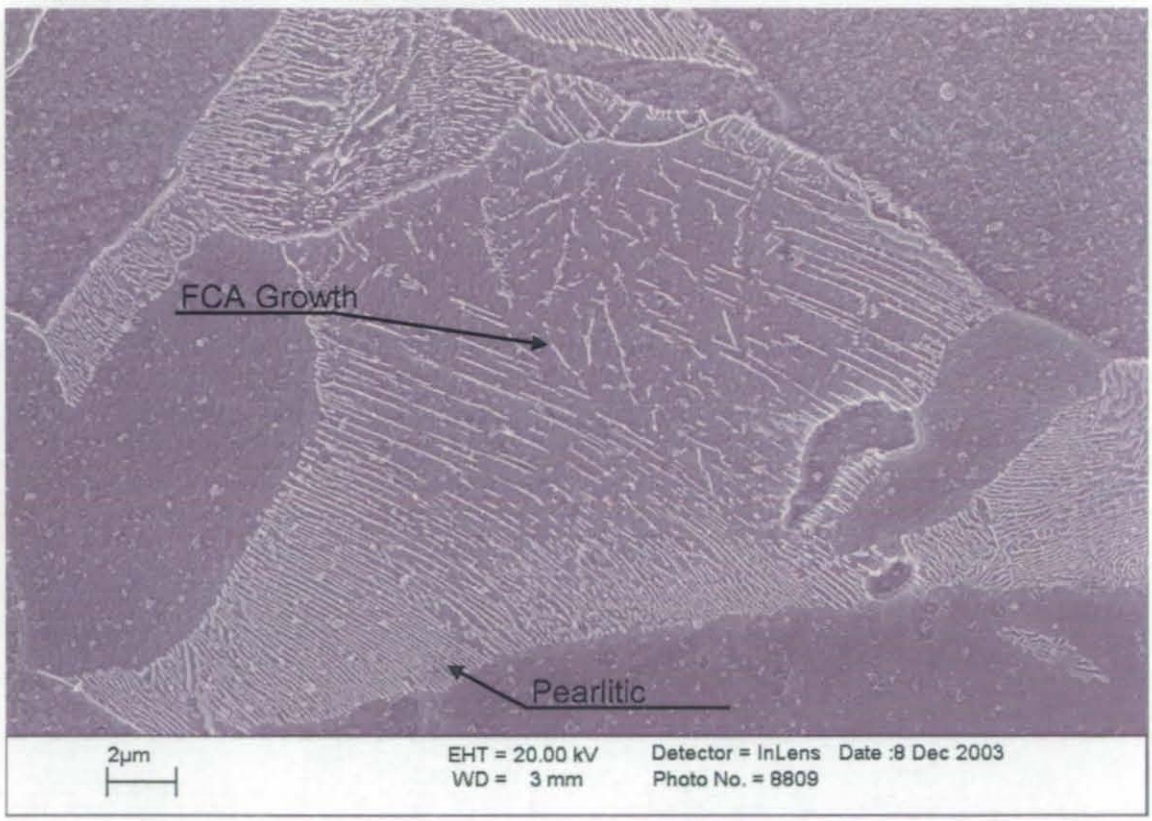

Figure 8.6b: *Dimension effect of pearlite and FCA*

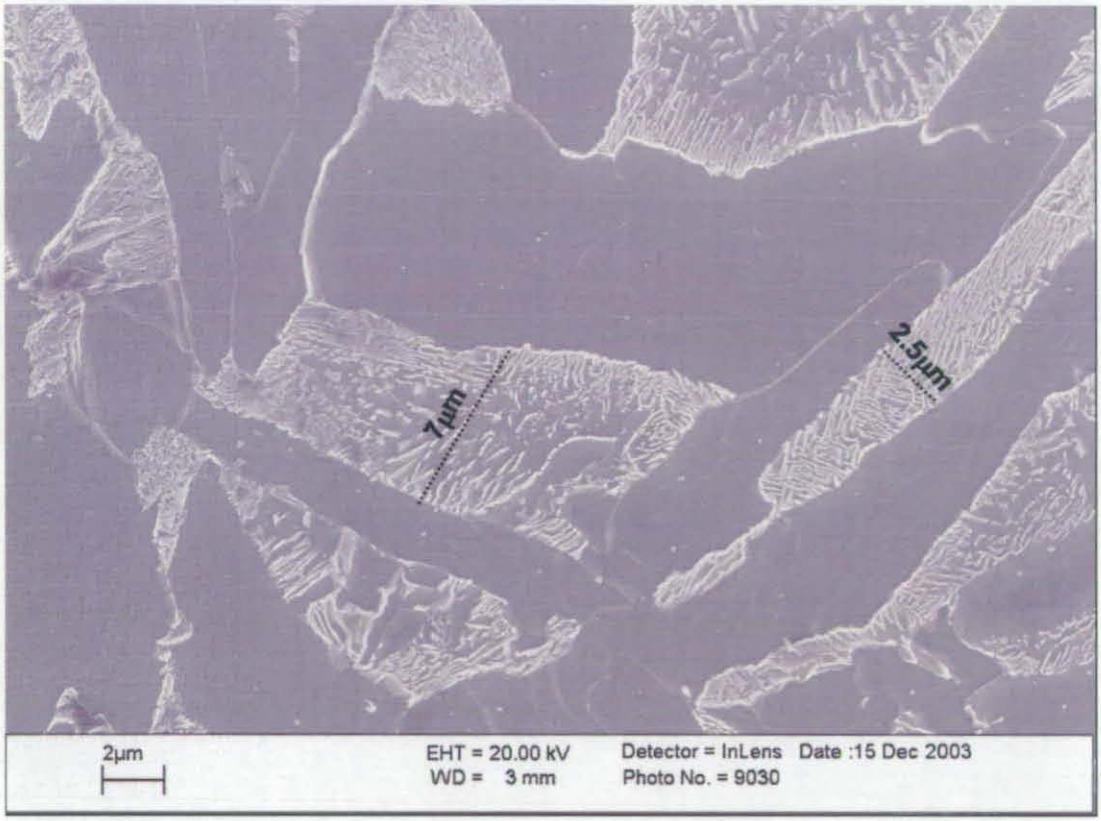

Figure 8.6c: *Dimension effect of pearlite and FCA*

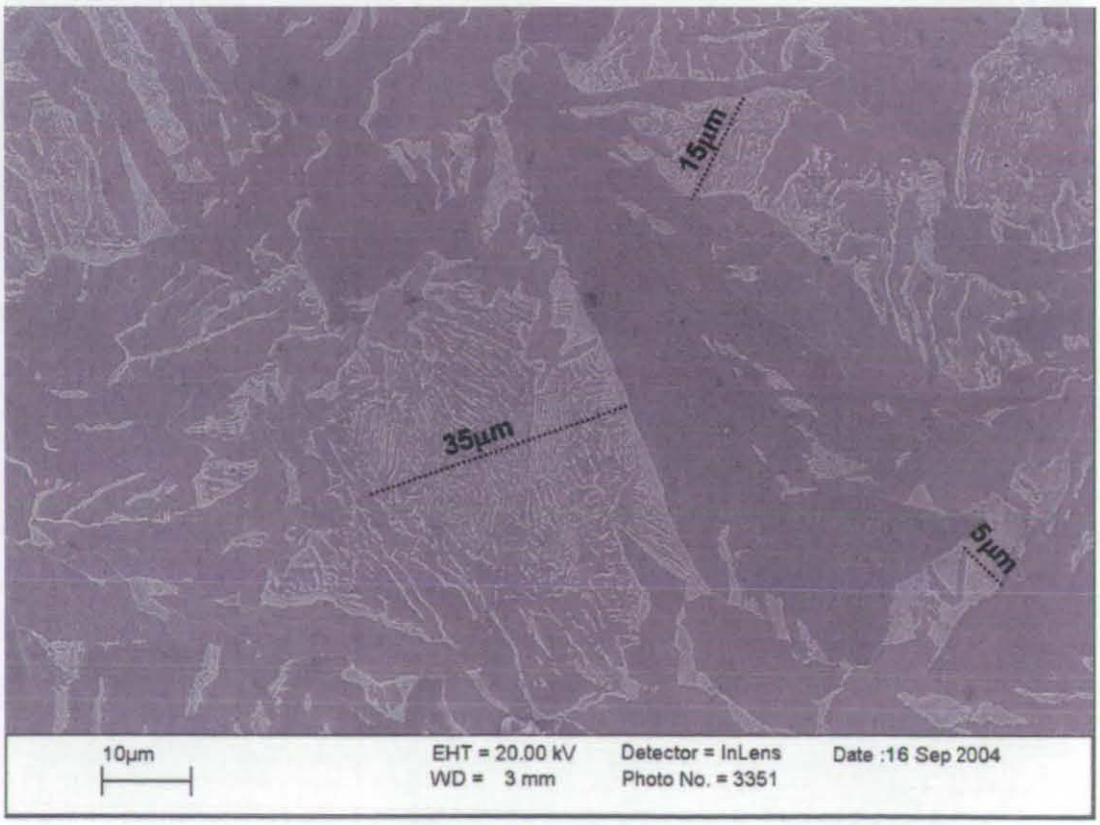

The morphological characteristics of the FCA and its dependence on the dimensions of the grain can be associated with the previous discussion in order to construct the foundation for a transformation theory. The austenite to FCA transition is the last transformation that takes place at low cooling rates (e.g. 10°C s^{-1}), while it forms prior bainite at high cooling rates (e.g. 50°C s^{-1}). Therefore, at the γ/α interface the local carbon concentration should be highest, compared to the bulk of the austenitic region which has not yet transformed to FCA. A possible concentration profile for carbon is shown in figure 8.7.

Figure 8.7: *Possible carbon concentration profile ; highest carbon concentration at the FCA-ferrite boundary*

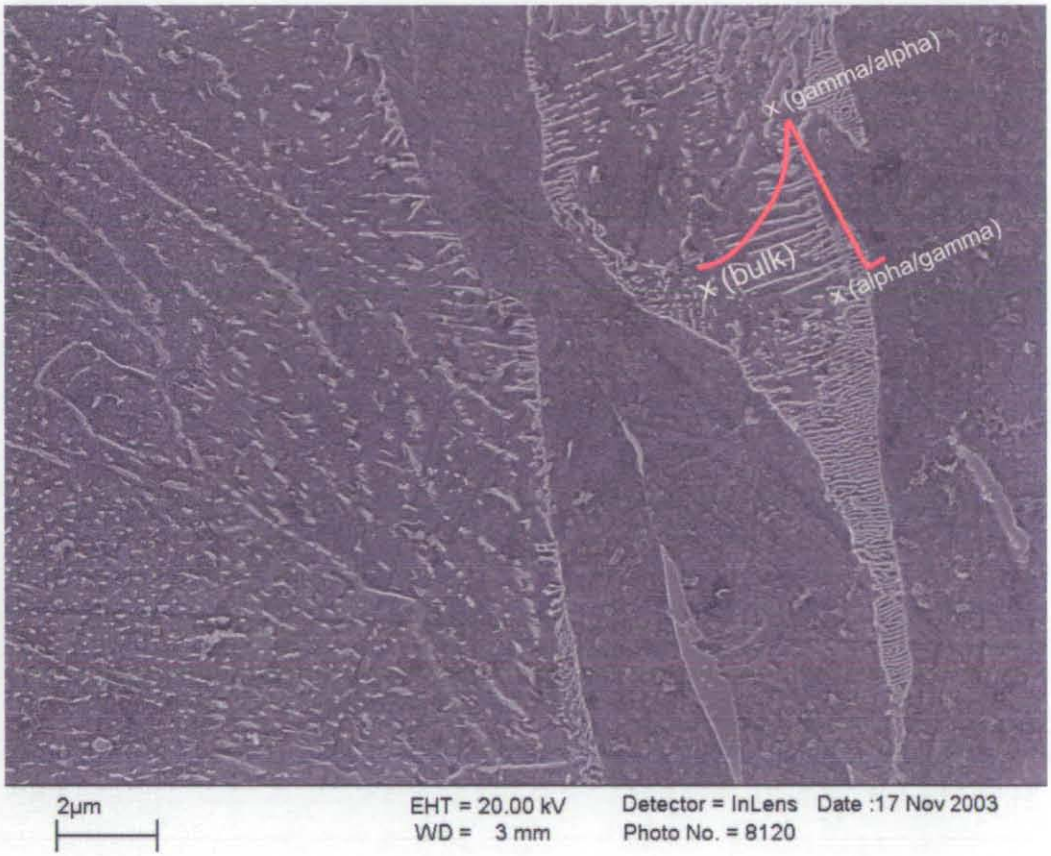

The carbon concentration decreases as the distance from the α/γ interface increases. In figure 8.7 it can be seen that the precipitation occurs in a lamellar form near the boundaries. Consequently, the lamellae break down as in the bulk the carbon content decreases, providing the typical morphology of the FCA. The effect of the grain dimensions is shown in the same image. If the dimensions are small, the carbon concentration is quite high along the distance between the two opposite boundaries, therefore the resulting structure is pearlitic. On the other hand, as the

dimensions of the austenitic region increase (and therefore the local carbon concentration is lower), the lamellar type of growth becomes impossible.

8.6 Transformation Sequence

The study of the microstructures produced under several different continuous cooling conditions, with the aid of the interrupted continuous cooling experiments and the morphological observation, has made the identification of a transformation sequence possible.

The variation in the austenitising temperature, T_γ, does not have any influence on the transformation sequence, although it naturally determines the kinetics of the each phase forming and their mutual interactions:

- the transformation start and finish temperatures of each phase change as the austenitising temperature changes
- as the $T\gamma$ changes, the kinetics become more favourable for particular phase, having as a final consequence a variation in the volume fraction of the phase itself

The order of formation of the various phases does not change with T_γ and for a given composition (in this case the alloy Y7N1) the transformation sequences, depending on the cooling rates, are the following:

$$PF \rightarrow P \ (2\ ^\circ C\ s^{-1})$$

$$PF \rightarrow P \rightarrow WF\ (coarse) \rightarrow FCA \ (5\ ^\circ C\ s^{-1})$$

$$PF \rightarrow P \rightarrow WF \rightarrow FCA \ (5\text{-}10\ ^\circ C\ s^{-1})$$

$$PF \rightarrow WF \rightarrow FCA \ (10\text{-}50\ ^\circ C\ s^{-1})$$

$$PF \rightarrow WF \rightarrow FCA \rightarrow B \ (50\ ^\circ C\ s^{-1})$$

$$PF \rightarrow WF \rightarrow FCA \rightarrow B \rightarrow M\ (50\text{-}75\ ^\circ C\ s^{-1})$$

$$WF\ (fine) \rightarrow B \rightarrow M\ (75\text{-}100\ ^\circ C\ s^{-1})$$

$$B \rightarrow M \ (100\text{-}200\ ^\circ C\ s^{-1})$$

Considering all of the cooling rates, the transformation sequence can be simplified to:

$$PF \rightarrow P \rightarrow WF \rightarrow FCA \rightarrow B \rightarrow M$$

although, depending on the cooling rate, certain phases do not have the chance to form. It is important to highlight the fact that the FCA formation takes place at intermediate cooling rates, at a temperature range intermediate between the WF and the B formation. It also has to be borne in mind that the local carbon concentration profile has a significant influence on the formation of the FCA.

The formation of the mixed microphase present between the Widmanstätten ferrite plates has been considered to occur simultaneously to the ferrite sideplate growth. This in practice is not correct, because depending on the cooling rates, the transformation of an austenitic microphase to martensite, for instance, could occur at lower temperature. It has to be considered, however, that in terms of dilatometry, the variation in volume caused by the transformation of the microphase has to be considered to be occurring at the same time of the surrounding ferrite plates, in order to identify the correct transformation start and finish temperature for the WF phase. It can be assumed that any possible transformation of the microphase, taking place after the WF has formed, does not contribute to volume changes, due to the constraint offered by the ferritic plates surrounding the microphase.

The effect of the variation in alloy composition with respect to manganese has been investigated and it can be concluded that the sequence remains unchanged. Naturally, the kinetics of the various reactions are greatly influenced by the manganese variation. This does, however, changes the respective volume fraction of each phase, the transformation temperature regimes and the cooling rates under which the phases form.

A low manganese content favours the formation of phases forming reconstructively. Therefore, the overall effect is that the sequence remains unchanged but shifted to higher cooling rates. In this case, the direct effect on the FCA formation is a broadening of the temperature range (for a given cooling rate) as well as a broadening of the cooling rates range. On the other hand, a high manganese addition shifts the formation of displacively formed phases to lower cooling rates. The FCA formation in this case, occurs at lower cooling rates, over a narrower range, as well as the temperature range (for a given cooling rate).

8.7 Phase Quantification

The series of results obtained by quantifying the phases present in each of the microstructures analysed, reflects quantitatively the qualitative considerations made in chapter 4 for alloy Y7N1 and in chapter 7 for alloys HOM146 and HOM148.

Tables 8.8, 8.9, 8.10 and 8.11 present the phase quantification data for the samples austenitised at 1100°C and 1300°C respectively. The data are presented in the form of charts in figures 8.8a-h, 8.9a-h. 8.10a-h and 8.11a-h.

Table 8.8: *Phase quantification data for alloy Y7N1 austenitised at 1100°C*

Y7N1 aust. at 1100°C	**Phase Volume Fraction (%)**							
Cooling Rate ($°Cs^{-1}$)	**PF**	**P**	**WF**	**MP**	**FCA**	**UB**	**LB**	**M**
2	81.5	18.5	-	-	-	-	-	-
5	58	9	19	5 (P)	8	-	-	-
10	25	-	41	12	22	-	-	-
25	14	-	53	15	18	-	-	-
50	3	-	42	20	21	14		-
60	1	-	27	9	17	40	6	-
75	0.5	-	9	3.5	-	36	46	5
100	0.5	-	-	-	-	11.5	20	68
150	-	-	-	-	-	-	10	90
200	-	-	-	-	-	-	-	100

Figure 8.8a: *Phase quantification data for primary ferrite as a function of cooling rate in alloy Y7N1 austenitised at 1100°C*

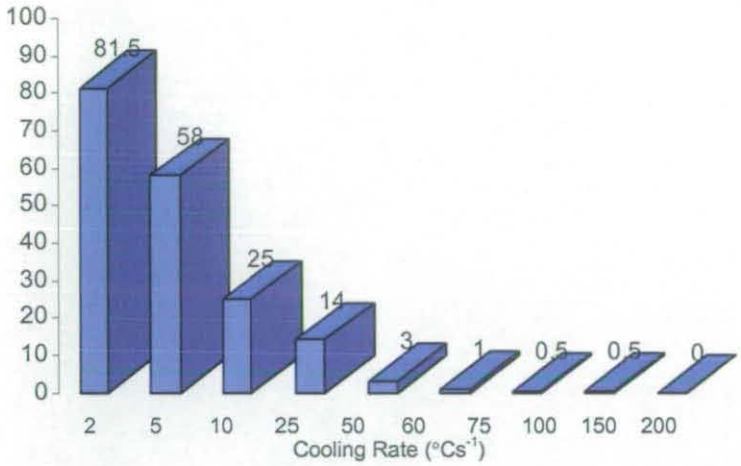

Figure 8.8b: *Phase quantification data for pearlite as a function of cooling rate in alloy Y7N1 austenitised at 1100°C*

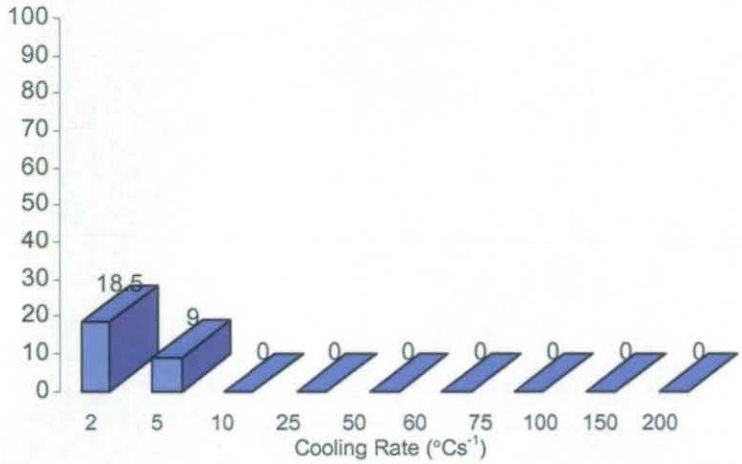

Figure 8.8c: *Phase quantification data for FCA as a function of cooling rate in alloy Y7N1 austenitised at 1100°C*

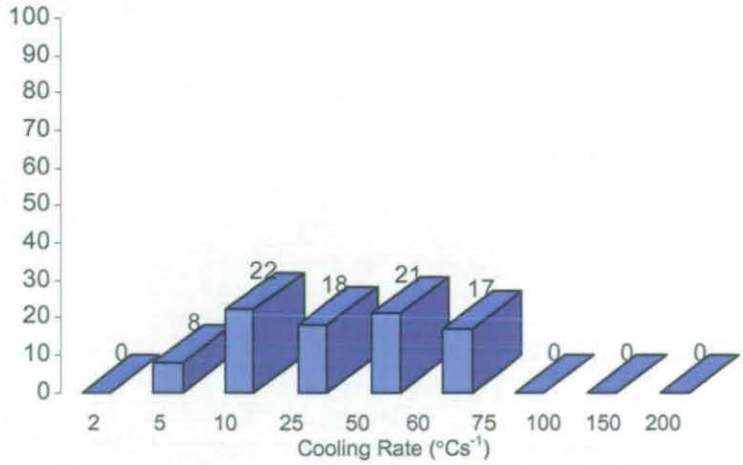

Figure 8.8d: *Phase quantification data for Widmanstätten ferrite as a function of cooling rate in alloy Y7N1 austenitised at 1100°C*

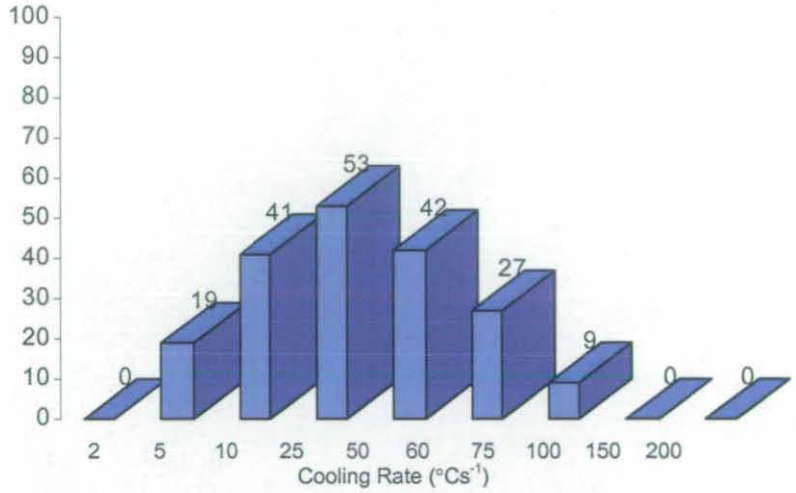

Figure 8.8e: *Phase quantification data for microphase as a function of cooling rate in alloy Y7N1 austenitised at 1100°C*

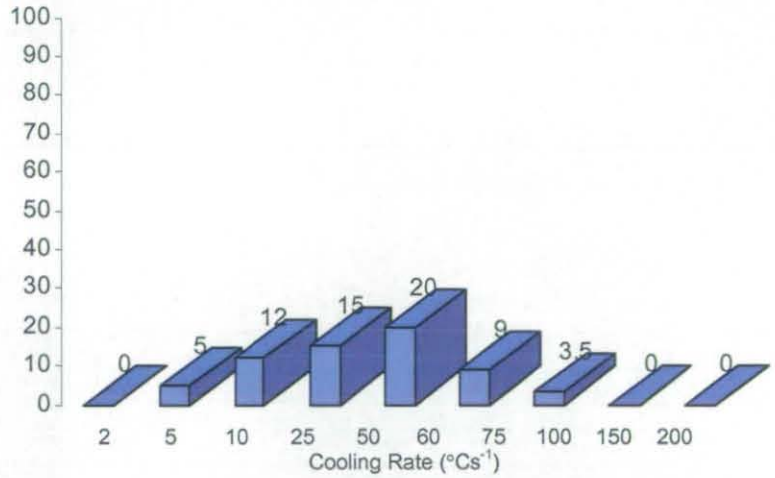

Figure 8.8f: *Phase quantification data for upper bainite as a function of cooling rate in alloy Y7N1 austenitised at 1100°C*

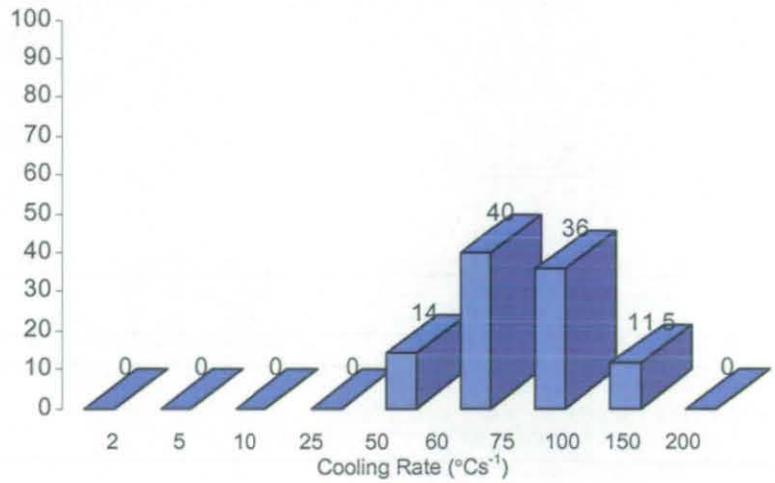

Figure 8.8g *Phase quantification data for lower bainite as a function of cooling rate in alloy Y7N1 austenitised at 1100°C*

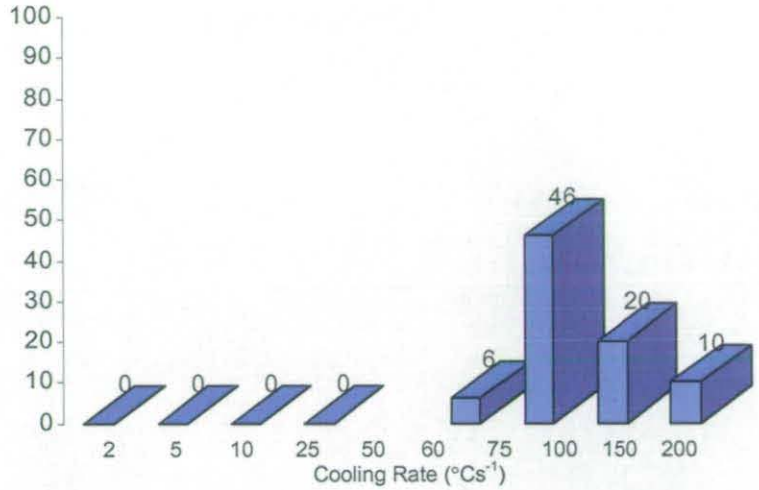

Figure 8.8h: *Phase quantification data for martensite as a function of cooling rate in alloy Y7N1 austenitised at 1100°C*

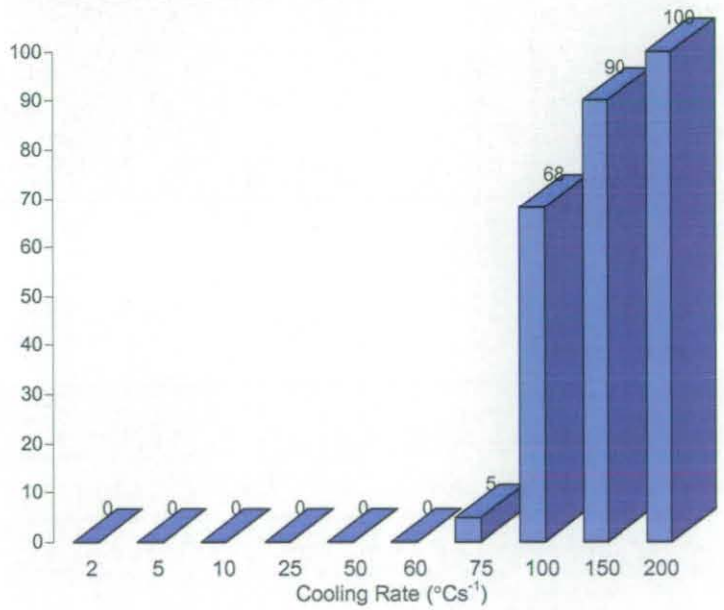

Table 8.9: *Phase quantification data for alloy Y7N1 austenitised at 1300°C*

Y7N1 aust. at 1300°C	Phase Volume Fraction (%)							
Cooling Rate ($°Cs^{-1}$)	PF	P	WF	MP	FCA	UB	LB	M
2	79.6	20.4	-	-	-	-	-	-
5	52	13	12	4.5	11.5	-	-	-
10	16	-	45	13	26	-	-	-
25	12	-	48	18	22	-	-	-
50	0.5	-	16.5	10	18	51	4	-
60	0.5	-	15.5	4.5	16	34.5	28	-
75	-	-	7	3	-	22	49	21
100	-	-	-	-	-	4	28	68
150	-	-	-	-	-	-	9	91
200	-	-	-	-	-	-	-	100

Figure 8.9a: *Phase quantification data for primary ferrite as a function of cooling rate in alloy Y7N1 austenitised at 1300°C*

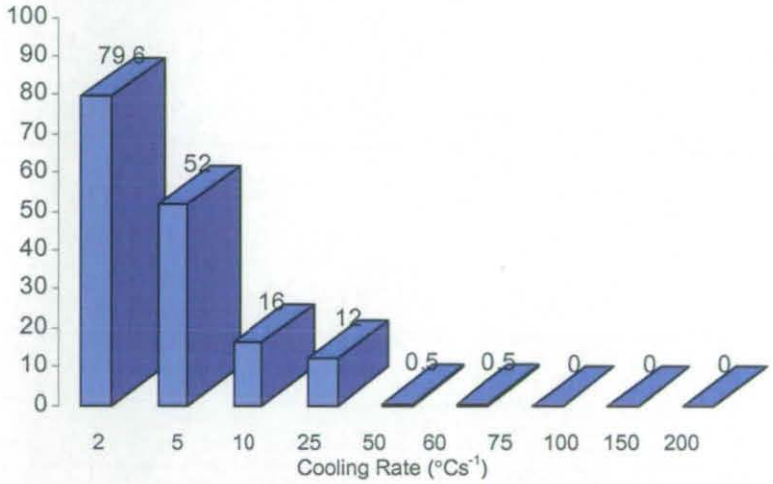

Figure 8.9b: *Phase quantification data for pearlite as a function of cooling rate in alloy Y7N1 austenitised at 1300°C*

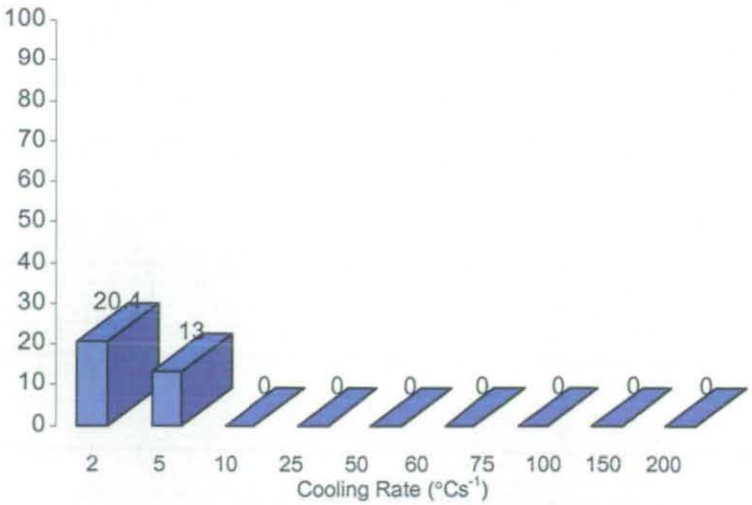

Figure 8.9c: *Phase quantification data for FCA as a function of cooling rate in alloy Y7N1 austenitised at 1300°C*

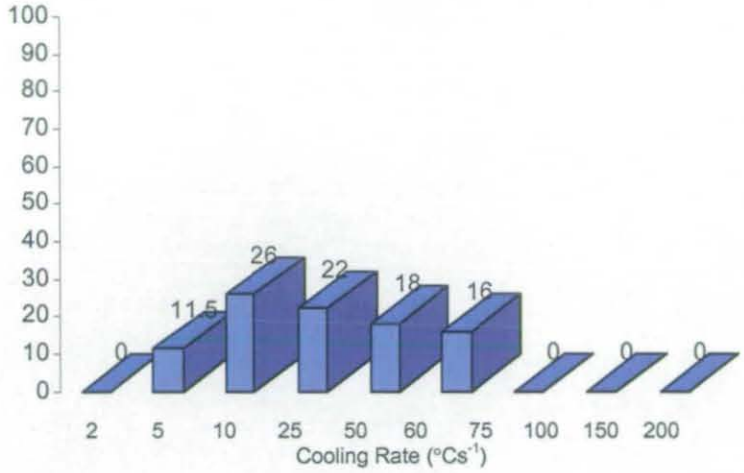

Figure 8.9d: *Phase quantification data for Widmanstatten ferrite as a function of cooling rate in alloy Y7N1 austenitised at 1300°C*

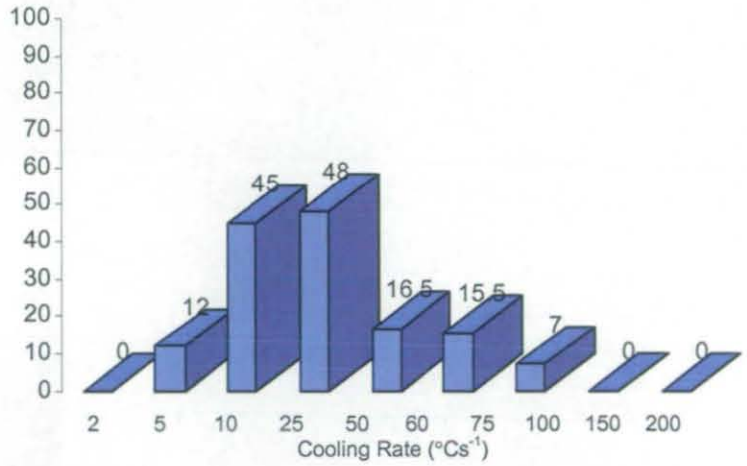

Figure 8.9e: *Phase quantification data for microphase as a function of cooling rate in alloy Y7N1 austenitised at 1300°C*

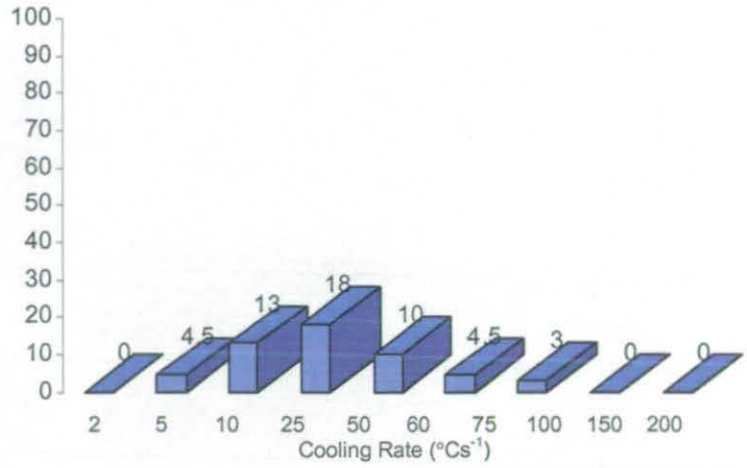

Figure 8.9f: *Phase quantification data for upper bainite as a function of cooling rate in alloy Y7N1 austenitised at 1300°C*

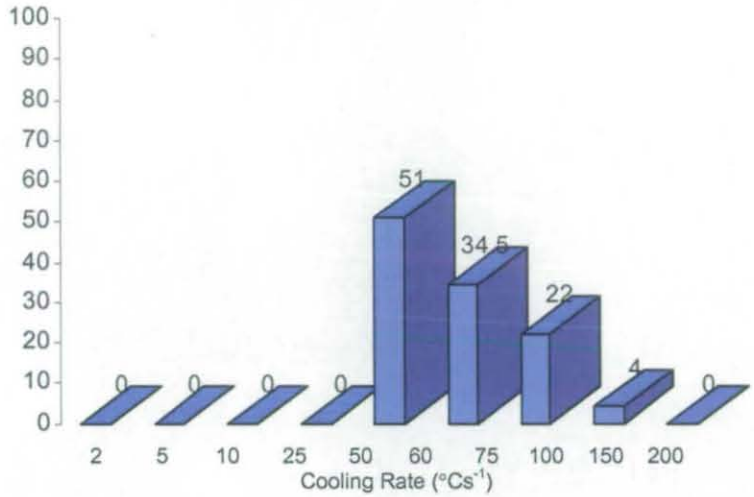

Figure 8.9g: *Phase quantification data for lower bainite as a function of cooling rate in alloy Y7N1 austenitised at 1300°C*

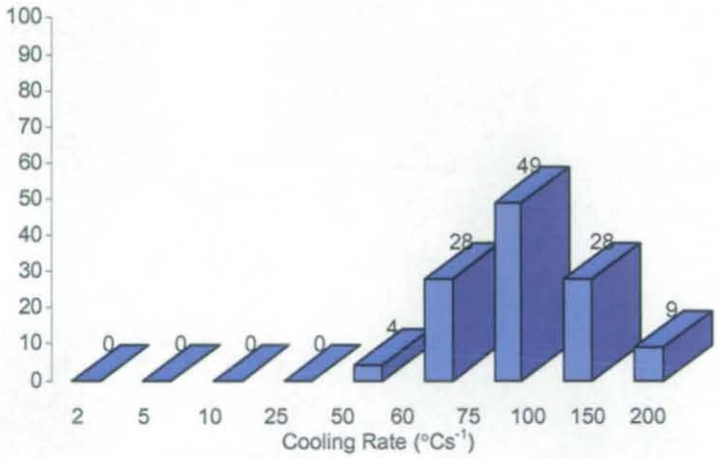

Figure 8.9h: *Phase quantification data for martensite as a function of cooling rate in alloy Y7N1 austenitised at 1300°C*

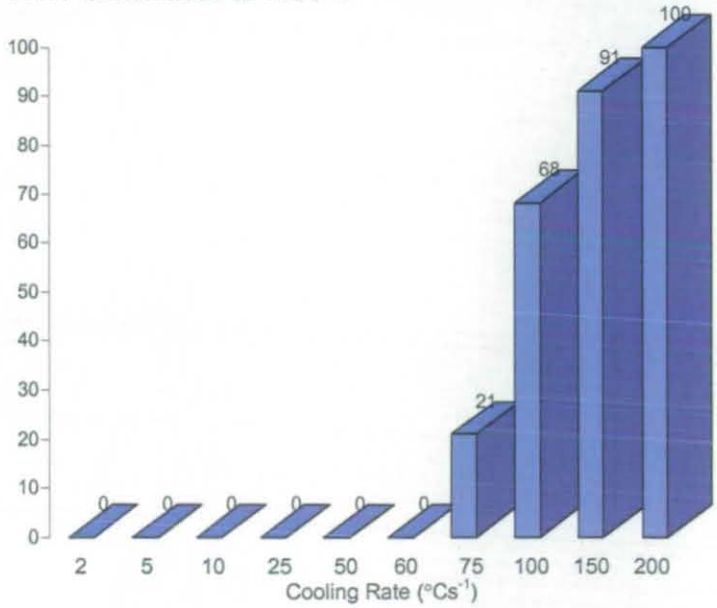

Table 8.10: *Phase quantification data for alloy HOM148 austenitised at 1100°C*

HOM148 aust. At 1100°C	Phase Volume Fraction (%)							
Cooling Rate (°Cs^{-1})	PF	P	WF	MP	FCA	UB	LB	M
2	80	12	-	-	8	-	-	-
5	40	8	29	7	16	-	-	-
10	20	-	44	16	20	-	-	-
25	7	-	34	12	23	24	-	-
50	-	-	11	4	6	52	28	-
75	-	-	2	-	-	23	66	9
100	-	-	-	-	-	-	48	52
150	-	-	-	-	-	-	14	86
200	-	-	-	-	-	-	-	100

Figure 8.10a: *Phase quantification data for primary ferrite as a function of cooling rate in alloy HOM148 austenitised at 1100°C*

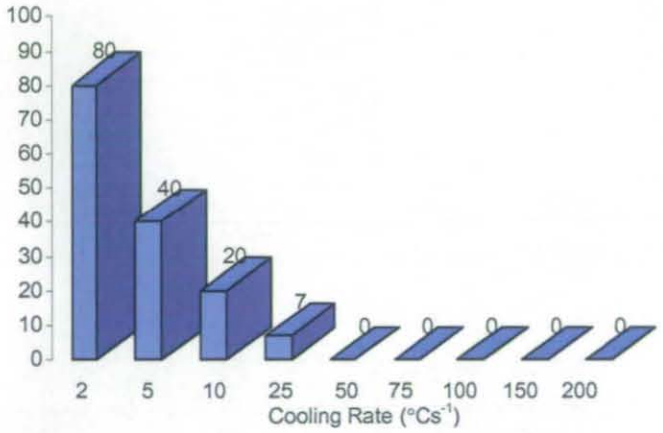

Figure 8.10b: *Phase quantification data for pearlite as a function of cooling rate in alloy HOM148 austenitised at 1100°C*

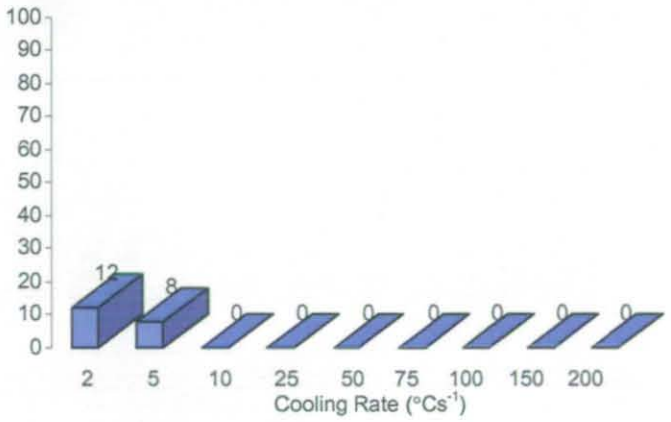

Figure 8.10c: *Phase quantification data for FCA as a function of cooling rate in alloy HOM148 austenitised at 1100°C*

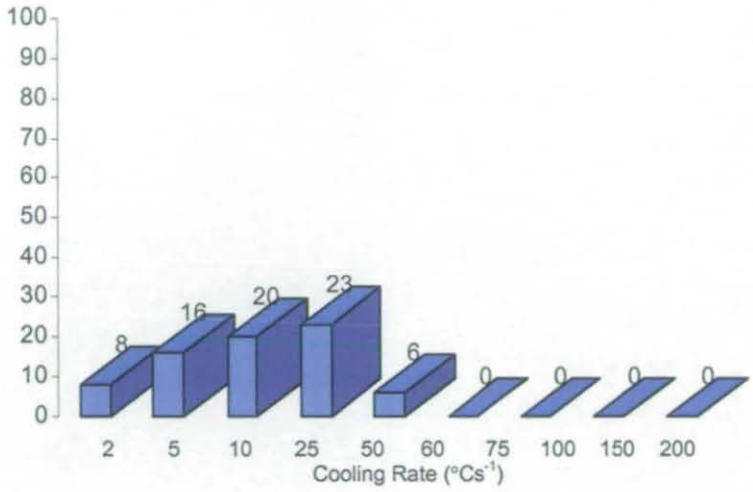

Figure 8.10d: *Phase quantification data for Widmanstätten ferrite as a function of cooling rate in alloy HOM148 austenitised at 1100°C*

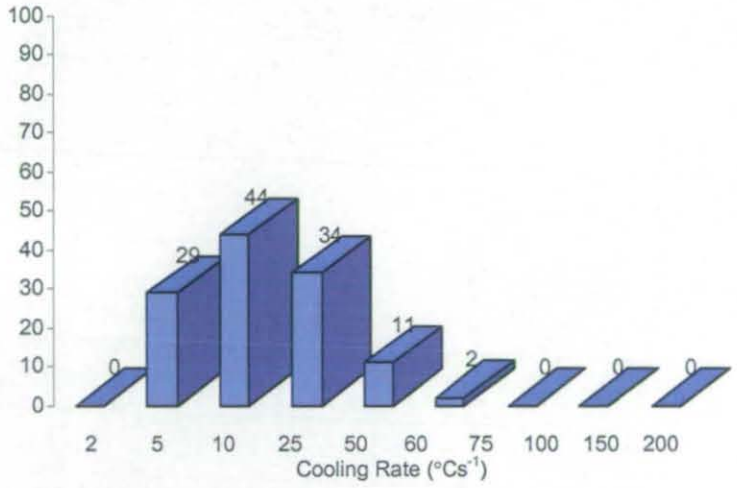

Figure 8.10e: *Phase quantification data for microphase as a function of cooling rate in alloy HOM148 austenitised at 1100°C*

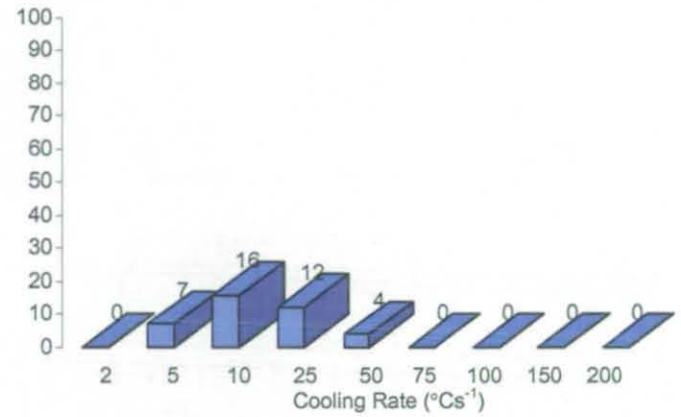

Figure 8.10f: *Phase quantification data for upper bainite as a function of cooling rate in alloy HOM148 austenitised at 1100°C*

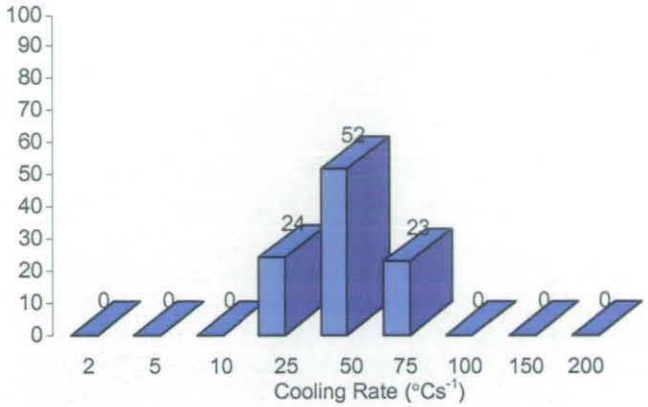

Figure 8.10g: *Phase quantification data for lower bainite as a function of cooling rate in alloy HOM148 austenitised at 1100°C*

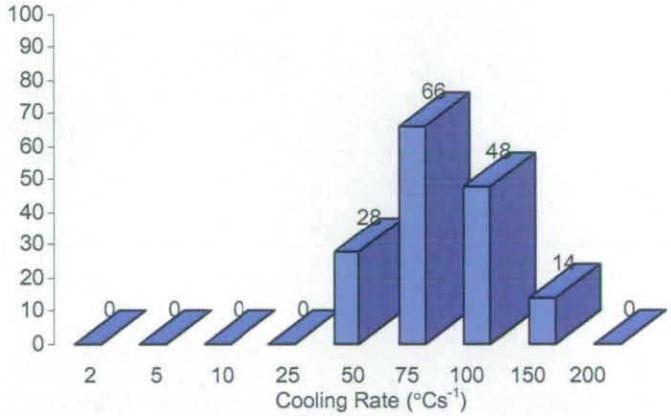

Figure 8.10h: *Phase quantification data for martensite as a function of cooling rate in alloy HOM148 austenitised at 1100°C*

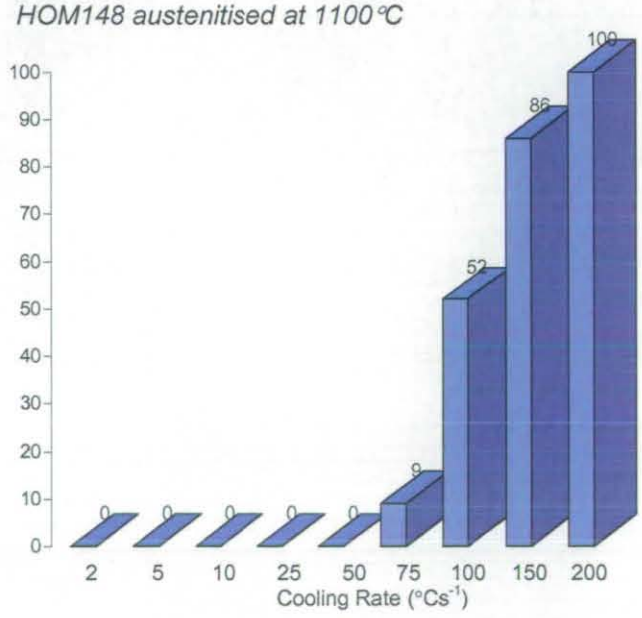

Table 8.11: *Phase quantification data for alloy HOM146 austenitised at 1100°C*

HOM146 aust. At 1100°C	Phase Volume Fraction (%)							
Cooling Rate ($°Cs^{-1}$)	PF	P	WF	MP	FCA	UB	LB	M
2	77	23	-	-	-	-	-	-
5	62	13	12	3	12	-	-	-
10	58	-	18	4	20	-	-	-
25	30	-	22	6	42	-	-	-
50	12	-	19	5	64	-	-	-
75	12	-	29	8	51	-	-	-
100	4	-	28	7	32	30	-	-
150	-	-	10	3	15	25	47	-
200	-	-	-	-	-	-	33	67

Figure 8.11a: *Phase quantification data for primary ferrite as a function of cooling rate in alloy HOM146 austenitised at 1100°C*

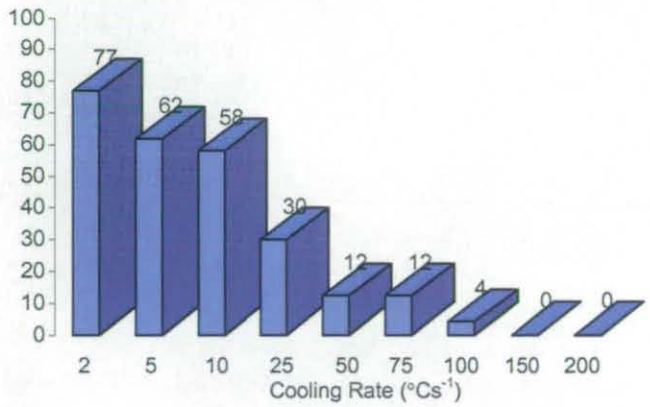

Figure 8.11b: *Phase quantification data for pearlite as a function of cooling rate in alloy HOM146 austenitised at 1100°C*

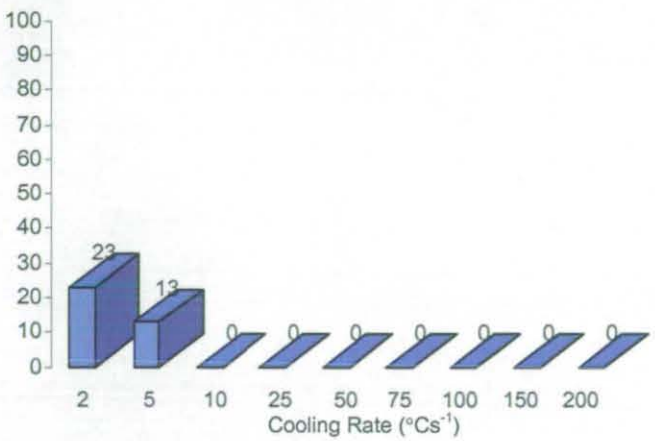

Figure 8.11c: *Phase quantification data for FCA as a function of cooling rate in alloy HOM146 austenitised at 1100°C*

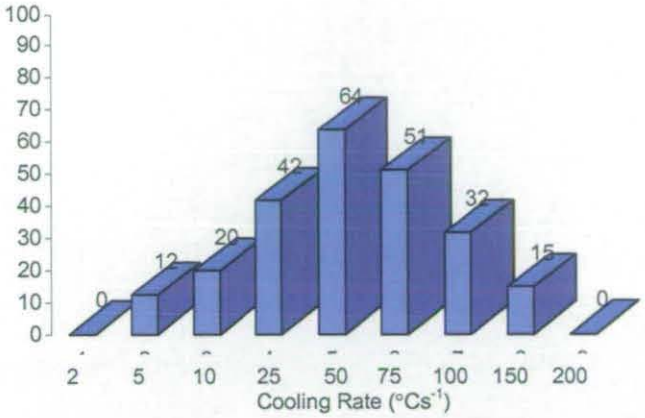

Figure 8.11d: *Phase quantification data for Widmanstätten ferrite as a function of cooling rate in alloy HOM146 austenitised at 1100°C*

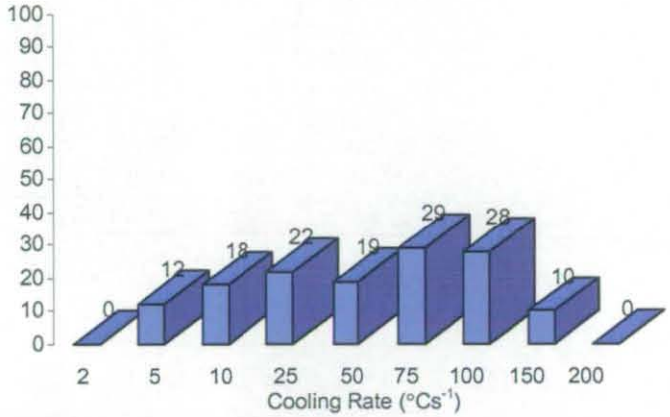

Figure 8.11e: *Phase quantification data for microphase as a function of cooling rate in alloy HOM146 austenitised at 1100°C*

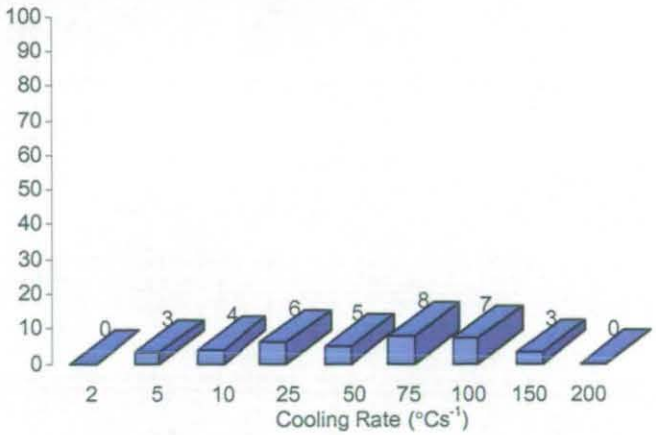

Figure 8.11f: *Phase quantification data for upper bainite as a function of cooling rate in alloy HOM146 austenitised at 1100°C*

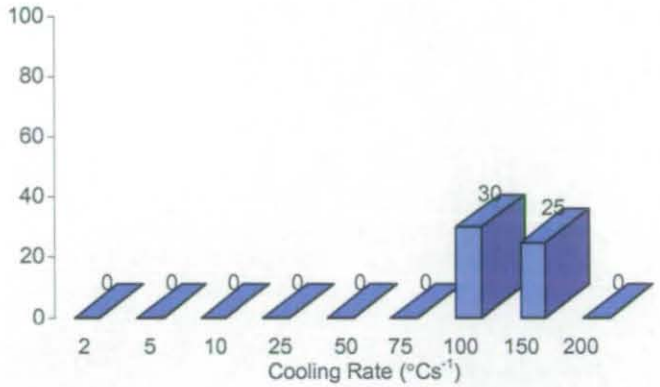

Figure 8.11g: *Phase quantification data for lower bainite as a function of cooling rate in alloy HOM146 austenitised at 1100°C*

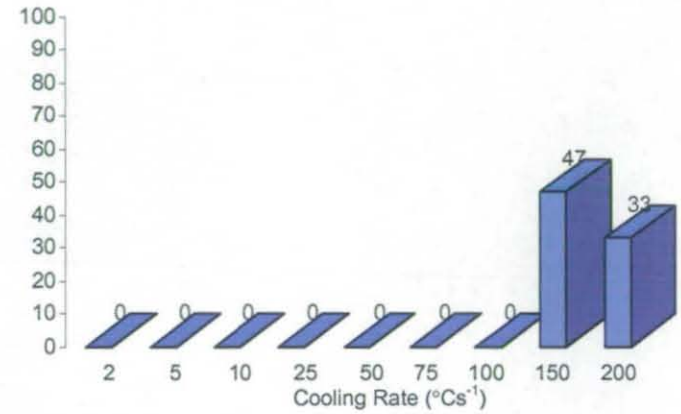

Figure 8.11h: *Phase quantification data for martensite as a function of cooling rate in alloy HOM146 austenitised at 1100°C*

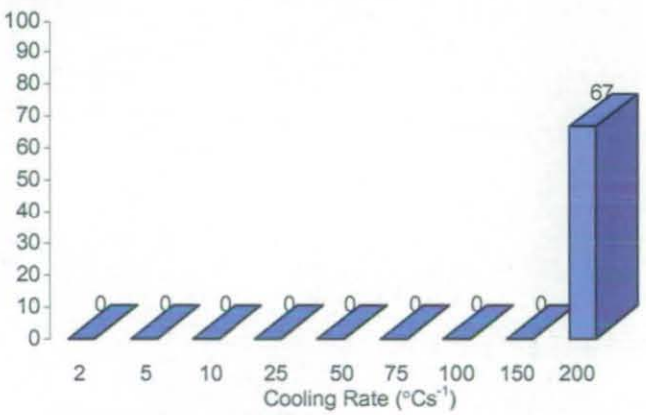

The next step of the investigation is the correlation of the microstructural data with the dilatometry data.

8.8 Discrepancies between Predictions and Measurements

Austentitisation at 1100°C for alloy Y7N1

The phase quantification data, which have been based on the detailed identification of each phase, have provided a means of evaluation of the accuracy of the CAM model. This model is capable of predicting the volume fractions of the phases produced under continuous cooling conditions, for a range of steels, which includes the low carbon category.

The following four tables (8.12 – 8.15) for alloy Y7N1 show the calculated data in addition to the predicted ones. The FCA phase is not predicted by the model and therefore this can represent a source of error. In fact, the kinetics of this particular phase are not included in the model, and therefore, depending on the particular heat treatment condition, either the kinetics of pearlite or bainite will be chosen by the model in order to satisfy better the transformation parameters.

Table 8.12: *a comparison between predicted and measured phase quantification data for alloy Y7N1 1100/10*

Alloy Y7N1 1100/10 Phase	Measured Data (%)	Predicted Data (%)
PF	25	43.4
P	-	23.4
WF + MP	53	32.2
FCA	22	x
B	-	-
M	-	-

At low austenitising temperatures and low cooling rates, the portion of primary ferrite is overestimated, whilst the model underestimates Widmanstätten ferrite. It is interesting to observe that the measured FCA volume fraction is very close to the predicted pearlite volume fraction. The model considers the formation of pearlite possible instead of FCA. However, this is not an evidence of the similarities between the two phases. Indeed, it has to be borne in mind that the model does not contain the parameters to define the FCA formation, and it cannot operate a choice between the two phases.

Table 8.13: *a comparison between predicted and measured phase quantification data for alloy Y7N1 1100/50*

Alloy Y7N1 1100/50 Phase	Measured Data (%)	Predicted Data (%)
PF	3	27.3
P	-	-
WF + MP	62	12.8
FCA	21	x
B	-	58.9
M	-	-

At low austenitising temperatures and high cooling rates, the portion of primary ferrite is overestimated whilst Widmanstätten ferrite is underestimated. In addition, the main predicted constituent is bainite, which, in the sample manually quantified, was a minor constituent. The model has not predicted the presence of pearlite and this is in accordance with the measured data. However, the presence of FCA in the microstructure could have been substituted by the presence of pearlite in the predicted data, as happened in the low cooling rate, low austenitising temperature case. This would have systematically supported the hypothesis that the kinetics of the FCA and those of pearlite could be in some way assimilated. This is not the case. The fraction of FCA which cannot be predicted has therefore been associated by the model itself to the bainite volume fraction.

Austentitisation at 1300°C for alloy Y7N1

Table 8.14: *a comparison between predicted and measured phase quantification data for alloy Y7N1 1300/10*

Alloy Y7N1 1300/10 Phase	Measured Data (%)	Predicted Data (%)
PF	16	15.6
P	-	22
WF + MP	58	61.3
FCA	26	x
B	-	-
M	-	-

At high austenitising temperatures and low cooling rates, the model predicts very well both the volume fractions of primary ferrite and Widmanstätten ferrite. Analogous to the previous low cooling rate case, the FCA phase is substituted by pearlite.

Table 8.15: *a comparison between predicted and measured phase quantification data for alloy Y7N1 1300/10*

Alloy Y7N1 1300/50 Phase	Measured Data (%)	Predicted Data (%)
PF	0.5	8.6
P	-	-
WF + MP	26.5	19.2
FCA	18	x
B	55	69.3
M	-	1.9

At high austenitising temperatures and high cooling rates, the model underestimates the amount of Widmanstätten ferrite and overpredicts the fraction of primary ferrite. Martensite was not found during manual measurements, although such a low predicted percentage could have been possibly present in areas of the sample which were not quantified. Again, the FCA fraction has been associated to the bainite volume fraction by the model (the sum of upper bainite and FCA measured, is very close to the overall fraction of bainite predicted by the model).

These data show that there is probably a gap between the kinetics of pearlite and bainite, which leads the model to predict pearlite at low cooling rates and bainite at high cooling rates instead of the FCA phase. The consequences of this prediction error are more significant at high cooling rates, because the mechanical properties of the FCA phase appear to be closer to those of pearlite (in terms of hardness at least) than to those of bainite (whose hardness is much higher). It would be interesting and useful to perform a comparison between the predicted start transformation temperatures of pearlite and bainite and the recorded start transformation temperatures of pearlite, bainite and FCA. Unfortunately the data relative to bainite and pearlite were not available.

The scenario presented in this section shows how fundamental it is to determine the nature of each phase forming during cooling, to assess the distinct kinetics of each transformation and therefore evaluate the effects on the overall microstructural evolution. A lack of knowledge of only one phase can undermine the effectiveness of a predictive model. The characterisation of the FCA phase, which has been neglected in the past reveals its importance and implications in the context of models, in which it is necessary to consider each element that comes into play in a system where each of the transformations have repercussion on the other ones. The limitations of the CAM model which in respect of the formation of ferrite carbide aggregate, can be overcome by developing a suitable transformation theory for FCA. The data collected in this study are therefore a valuable means for testing the accuracy of the model, and, the fact that the model does not provide accurate

predictions is another indication of the fact that the kinetics of FCA are different from those of pearlite and bainite.

8.9 CCT Diagrams

In order to build a CCT diagram three fundamentally important factors have to be fully considered:

- each phase present in a microstructure has to be identified
- the amount of each phase for a given cooling rate has to be quantified
- a valid transformation sequence has to be determined.

All of the above aspects have been dealt with successfully in the present research project. This allows the available dilatometry data to be used for the construction of a CCT diagram for each alloy studied. Figure 8.12 considers the dilation curve obtained for alloy HOM146 cooled at 10°C s^{-1} as an example:

Figure 8.12: *Dilation curve for alloy HOM146 1100/10 showing the determination of start temperature of a particular phase transformation occurring during cooling*

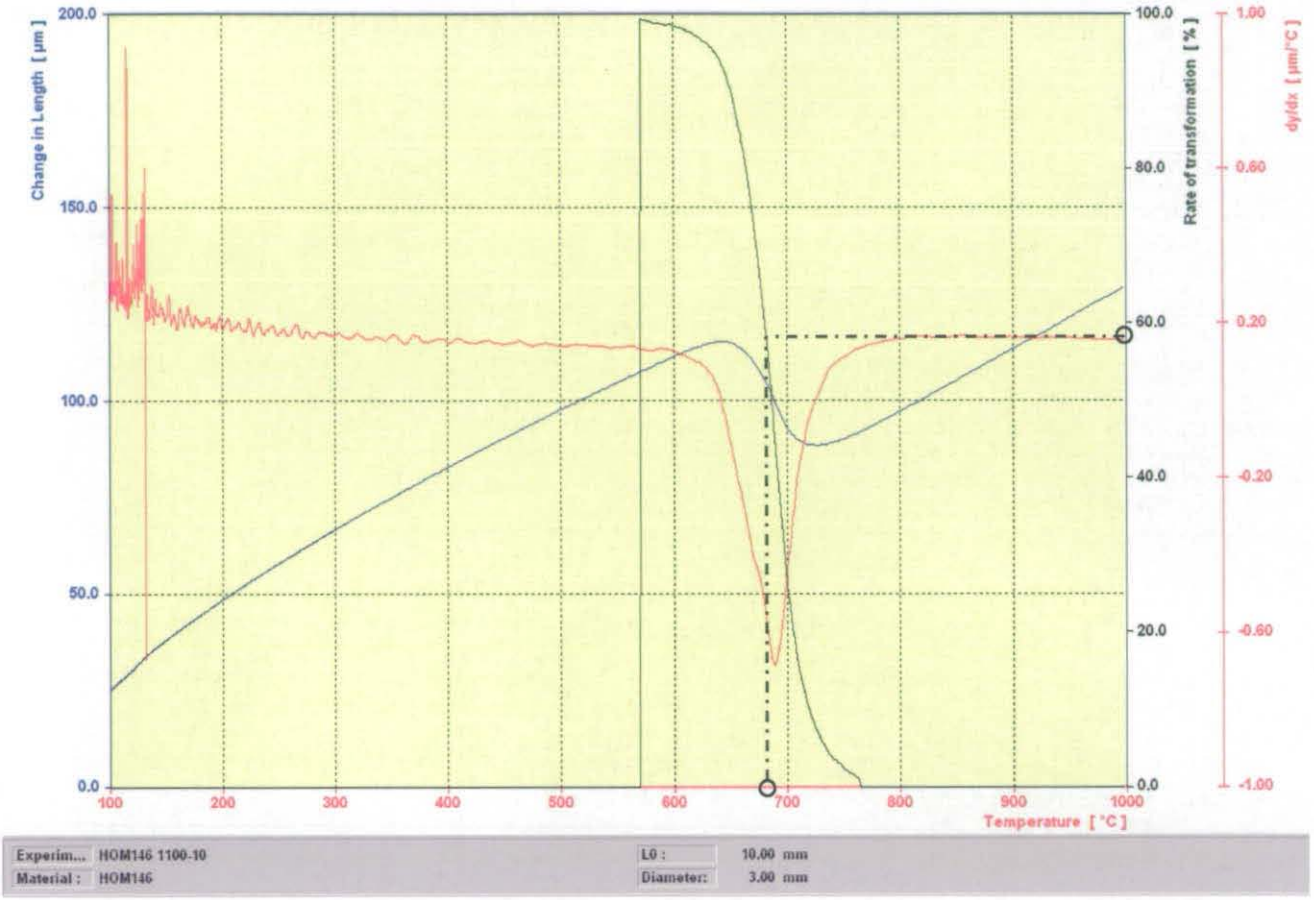

The black solid curve represents the percentage of austenite transformed as a function of temperature. From the analysis of the curve on its own, no information can be derived regarding the products of transformation as well as the phase fields relative to each phase formed during cooling. However, from the interrupted continuous cooling experiments, incontrovertible evidence is provided as to which phase forms first the subsequent phases, depending on the cooling rate, has been previously obtained. Although it is realistic to think that depending on the local thermodynamic conditions, the formation of a phase may finish in a particular part of the sample, whilst in another part the reaction is still on-going (therefore contributing to a volume change in the dilation curve), the overall influence of such heterogeneity on the dilation curve is minimal. Hence, when analysing the austenite volume fraction transformed curve, it can be assumed that each phase can be separated by the others both on a temperature and time scale. The separation reflects the transformation sequence that has been assessed. It is now known that when alloy HOM146 is cooled at 10°C s^{-1}, the first phase forming is primary ferrite, then Widmanstätten ferrite followed by FCA. It is a trivial exercise to find the temperature

relating to 58% primary ferrite and therefore determine the transformation start and finish temperatures for this phase (as shown in figure 8). The same procedure is followed in order to determine the transformation start and finish temperatures for each phase at each cooling rate. This allows the determination of the various phase fields which compose the CCT diagram and makes possible the design of a suitable heat treatment in order to obtain the desired microstructure depending on the application.

The final result of the microstructural analysis, dilatometry data analysis and phase quantification is the realisation of the following four CCT diagrams shown in figures 8.9a-d. These CCT diagrams are very important as they represent the compendium of all the information needed when procesisng the alloys studied. The phase fields, linked to the phase quantification data provide the indications needed in order to engineer a certain type of microstructure according to the desired properties. The correlation of the CCT diagrams with the phase quantificaiton is very important as the area of a single phase field on its own does not relates proportionally to the fraction of the phase in the microstructure.

A new element in these CCT diagrams is the presence of the FCA phase field. As discussed in section 8.5, a critical grain size exists below which FCA formation should not take place and, as a consequence the phase field is expected to narrow, and eventually disappear in favour of the pearlite field. In the alloys studied, however, the presence of the FCA was visible in each of the CCT diagrams. In order to determine the effects on the final properties, a more detailed investigation of the mechanical properties of this phase has to be carried out.

Alloy Y7N1 austenitised at 1300°C

Figure 8.13a: *CCT diagram for alloy Y7N1 austenitised at 1300°C*

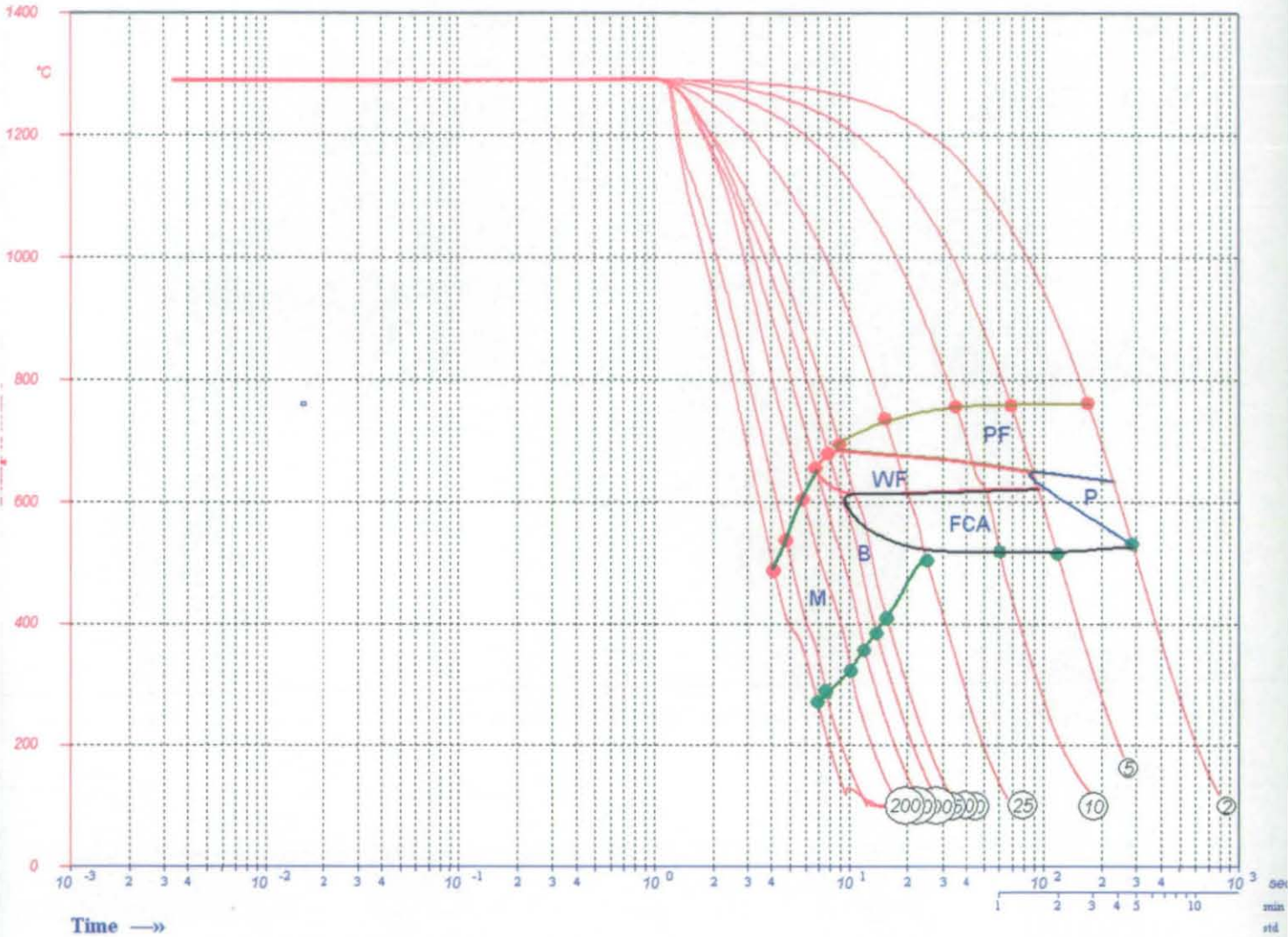

The following table 8.16 lists the transformation finish temperatures for each phase for alloy Y7N1 austenitised at 1300°C:

Table 8.16: *Transformation finish temperatures for alloy Y7N1 austenitised at 1300°C*

Phase	Cooling rate	Tf (°)
PF	2	633
PF	5	652
P	5	613
PF	10	664
WF	10	613
PF	25	664
WF	25	615
PF	50	680
WF	50	617
FCA	50	556
WF	60	621
FCA	60	585
WF	75	642

Alloy Y7N1 austenitised at 1100°C

Figure 8.13b: *CCT diagram for alloy Y7N1 austenitised at 1100°C*

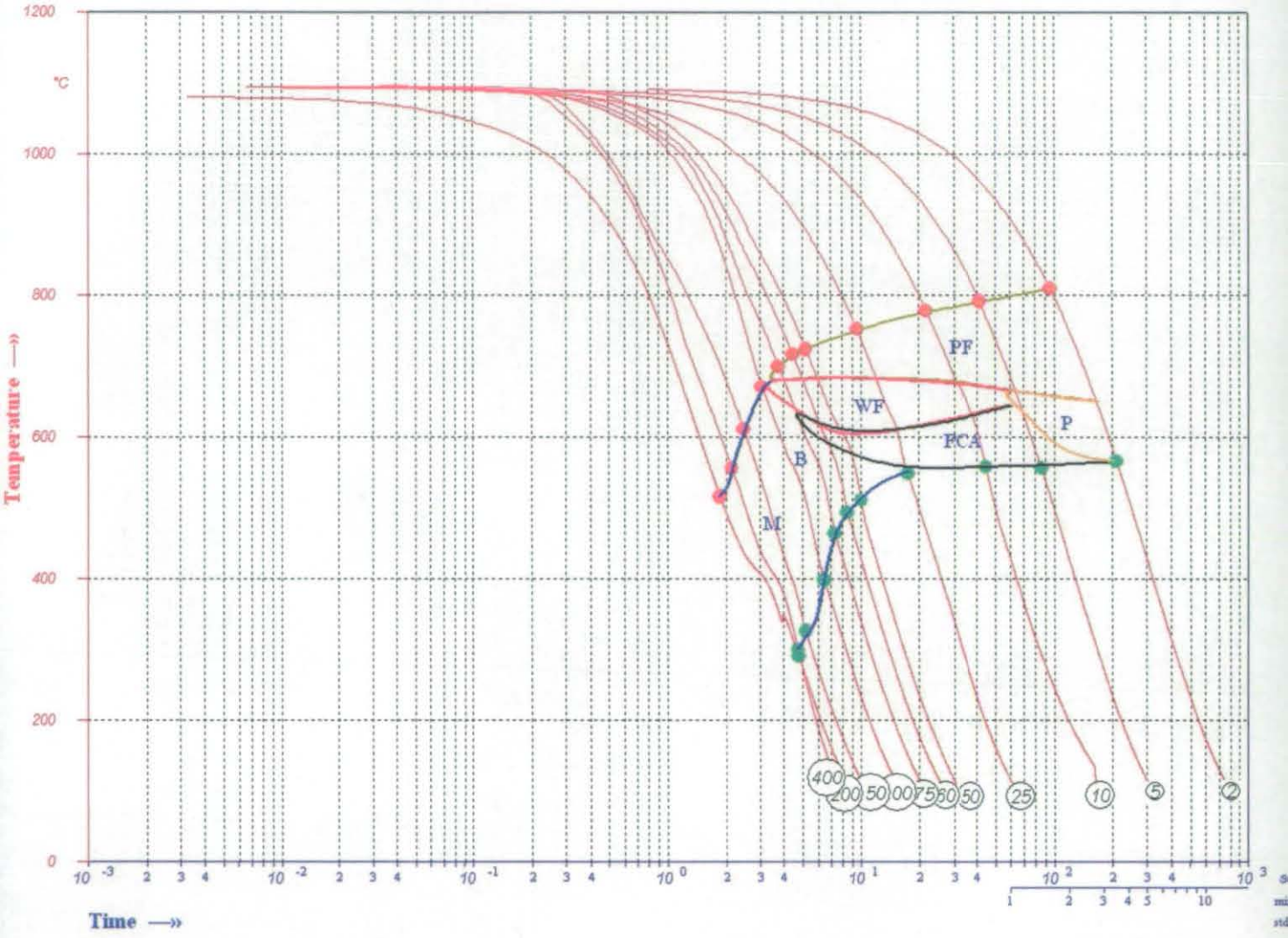

Table 8.17: *Transformation finish temperatures for alloy Y7N1 austenitised at 1100°C*

Phase	Cooling rate	Tf (°)
PF	2	651
PF	5	667
P	5	637
PF	10	678
WF	10	634
PF	25	684
WF	25	610
PF	50	681
WF	50	610
FCA	50	575
PF	60	683
WF	60	620
FCA	60	590
PF	75	679
WF	75	634
FCA	75	620

Alloy HOM148 austenitised at 1100°C

Figure 8.13c: *CCT diagram for alloy HOM148 austenitised at 1100°C*

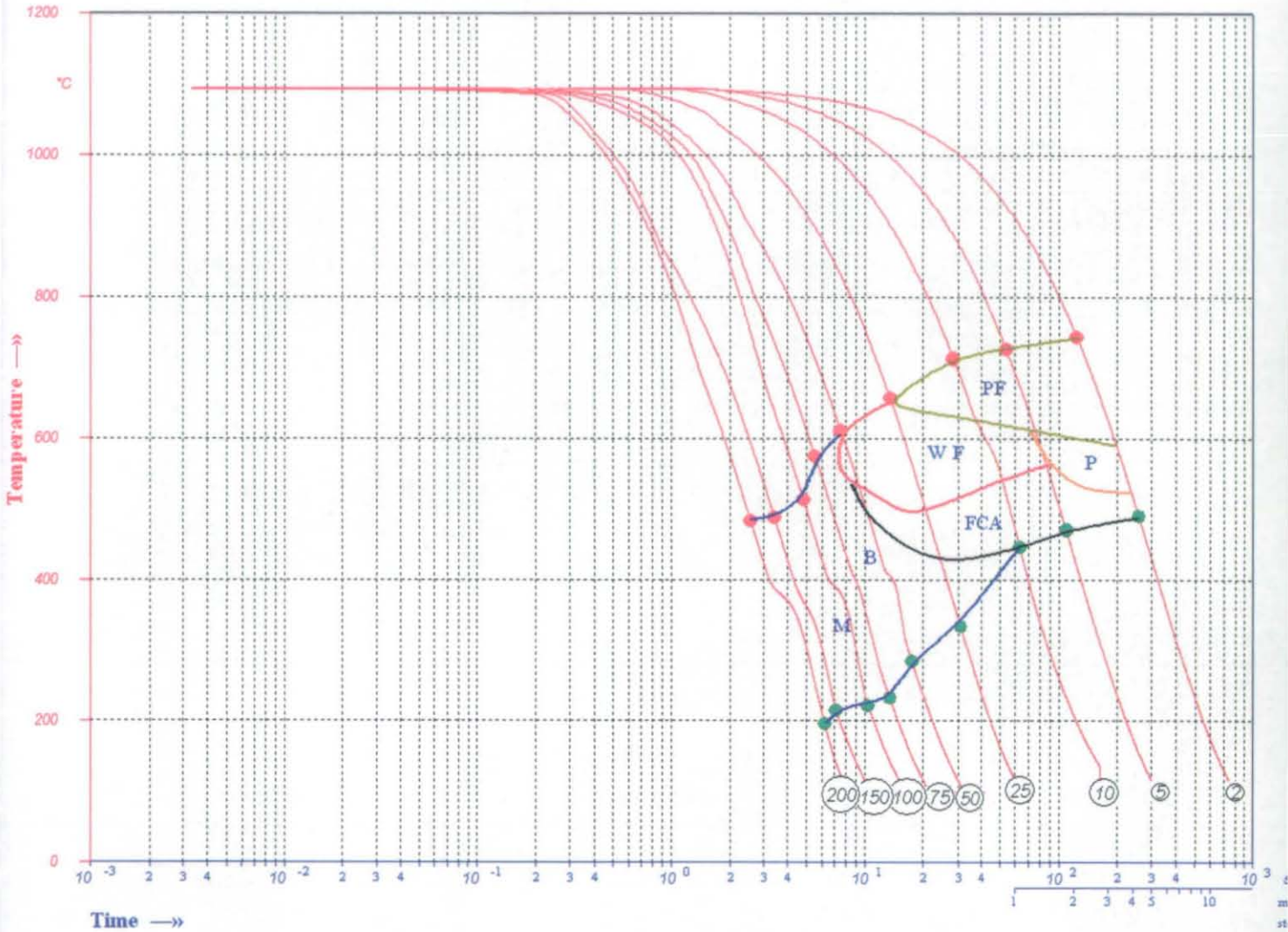

Table 8.18: *Transformation finish temperatures for alloy HOM146 austenitised at 1100 °C*

Phase	Cooling rate	Tf (°)
PF	2	584
P	2	519
PF	5	612
P	5	569
PF	10	627
WF	10	544
WF	25	500
FCA	25	431
WF	50	536
FCA	50	490

Alloy HOM146 austenitised at 1100°C

Figure 8.13d: *CCT diagram for alloy HOM146 austenitised at 1100°C*

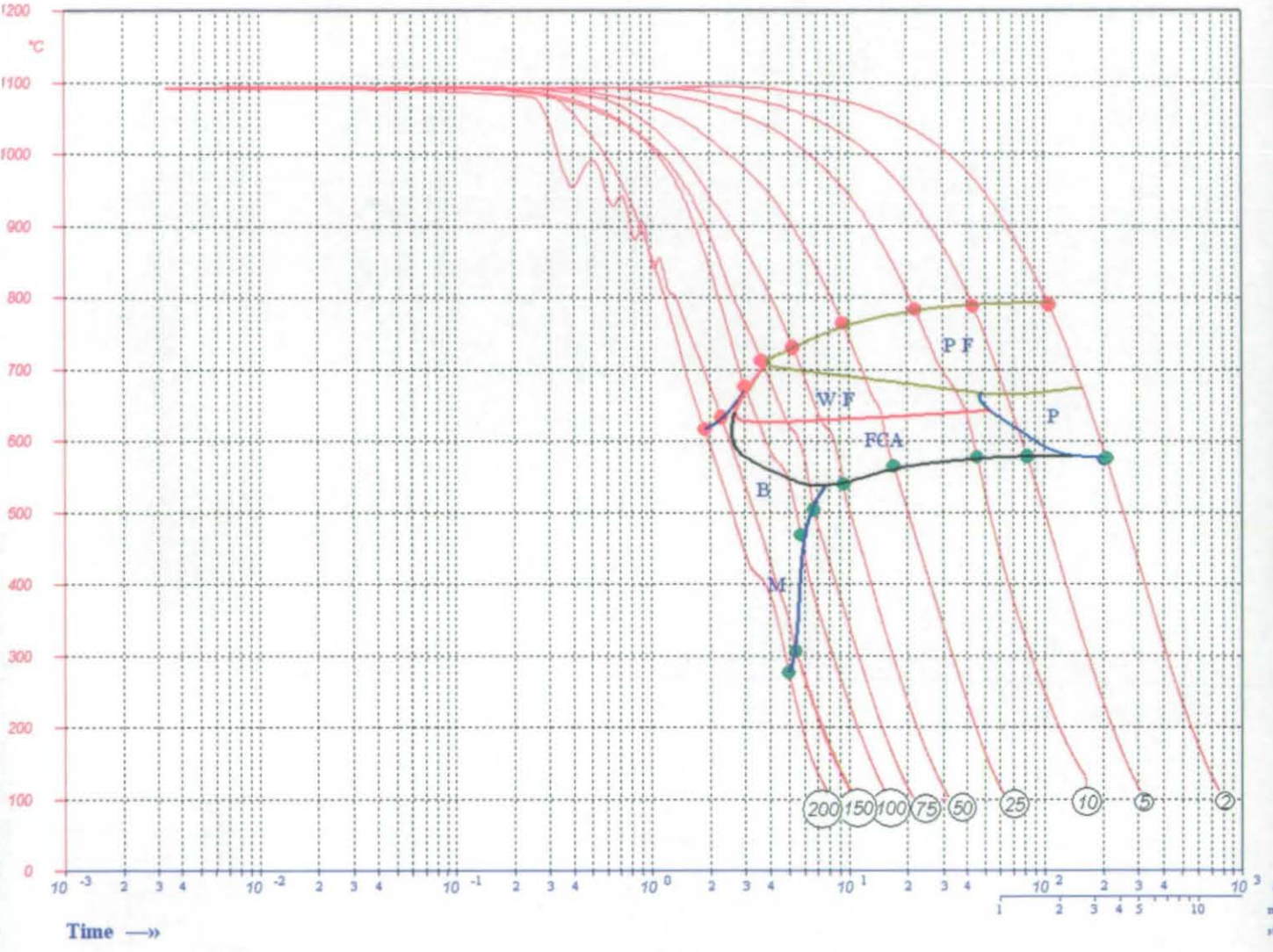

Table 8.19: *Transformation finish temperatures for alloy HOM148 austenitised at 1100°C*

Phase	Cooling rate	Tf (°)
PF	2	672
PF	5	664
P	5	613
PF	10	667
WF	10	638
PF	25	690
WF	25	634
PF	50	700
WF	50	629
WF	75	627
FCA	75	541
WF	100	626
FCA	100	547

The CCT diagrams in figure 8.9a and figure 8.9b refer to alloy Y7N1 austenitised at 1300°C and 1100°C respectively. As an effect of the higher austenitising temperature, the transformations start at lower temperatures and the bainite reaction takes place at slightly lower cooling rates at the expense of WF and FCA formation.

The effect of increasing manganese is evident in the CCT diagram shown in figure 8.9c for alloy HOM148. The phase fields of primary ferrite and Widmanstätten ferrite are wider compared to alloy Y7N1 austenitised at 1100°C, although they are shifted to much lower cooling rates due to the effects on the kinetics of the reactions discussed in chapter 7. The FCA phase forms at the lowest cooling rate although the volume fraction is quite low. In this case, the FCA phase forms close to primary ferrite regions, in the majority of the grains observed. The local carbon concentration profile has to be different from the one characterising the austenite regions transformed into pearlite. The carbon content is expected to be lower and the formation of the FCA phase is expected to take place at lower temperatures.

The CCT diagram of the alloy with the lowest manganese content reflects the discussion in chapter 7 for alloy HOM146. The transformations start at higher temperatures compared to alloy HOM148. The reconstructive transformations are favoured and as a consequence the phase fields of primary ferrite, Widmanstätten ferrite, pearlite and FCA extend to higher cooling rates compared to both alloys

HOM148 and Y7N1. The chemical composition of alloy HOM146 produces the thermodynamic conditions that favour the formation of the FCA phase causing large volume fractions of this phase even at high cooling rates (for example at 75°C s^{-1}).

8.10 Summary

The presence of the FCA phase has been included in the production of the CCT diagrams obtained for alloys Y7N1, HOM146 and HOM148. The phase field of FCA is found at temperatures between those of Widmanstätten ferrite and bainite The cooling rate range over which this phase is observed has been shown to depend on the manganese content. The identification of the separate phase fields was possible due to the detailed assessment of a transformation sequence which was successfully achieved from a combination of dilatometry data and microstructural characterisation. The phase quantification data presented in this chapter show the influence of austenitising temperatures, cooling rate and chemical composition in quantitative terms. Finally, the basis of the FCA transformation kinetics have been presented.

9. Conclusions and Further Work

9.1 Conclusions

The conclusions obtained from the various investigations carried out during this research, presented and discussed in the previous chapters, are presented below. Each section discusses the microstructural characterisation of continuously cooled steels and steel welds; the factors influencing the mutually interacting phase transformations and final microstructures; the problems related to classification schemes; the complete characterisation of ferrite-carbide aggregate previously not studied in detail; the effects of composition on the transformation kinetics; the implications of this study on the development of predictive models for microstructural evolution where phase transformations are occurring under continuous cooling conditions.

9.1.1 Microstructural Evolution during Continuous Cooling

The structural low carbon Mn-Si steel Y7N1 underwent two different austenitising heat treatments at 1100°C and 1300°C and eleven continuous cooling heat treatments with cooling rates gradually increasing from 2 to 400°C s^{-1}. The analysis of the microstructure produced showed the effects of both austenite grain size and cooling rate on microstructural evolution. The observation of the microstructures was linked to dilatometry analysis performed on each heat treatment. The optical investigations performed on alloy Y7N1 revealed the presence of primary ferrite, pearlite, Widmanstätten ferrite with the associated microphase, upper and lower bainite, martensite and a ferrite carbide aggregate which did not meet any existing classification scheme criterion and which gave a characteristic dark etching response when analysed optically. The presence of a particular phase and its fraction depended on the cooling rate, for a given austenite grain size.

After austenitising at 1100°C the austenite grain size was approximately 30 μm. Applying cooling rates ranging between 2 and 25°C s^{-1} caused the formation of phases forming in the reconstructive regime, including primary ferrite, pearlite, Widmanstätten ferrite (taking into account that this reaction is considered not to be an entirely reconstructive transformation) and the ferrite-carbide aggregate, named FCA in the present study. At cooling rates between 50 and 75°C s^{-1}, qualitatively, the dominant microstructural constituents appears to be Widmanstätten ferrite (towards

the lower cooling rate extreme) and upper bainite (toward the higher cooling rate extreme). Pearlite disappears as an isolated constituent and is sometimes present only in microphase regions. The fraction of FCA, being still large at 50°C s^{-1}, gradually decreases as the cooling rate increases. Upper bainite appears at 50°C s^{-1} and lower bainite appears at 75°C s^{-1}. At cooling rates greater than 75°C s^{-1} the character of the transformations is displacive and the microstructural constituents are upper bainite, lower bainite and martensite. Finally, as the cooling rate increases further, the phases become gradually finer, as expected.

After austenitising at 1300°C the austenite grain size was approximately 100 μm. The effect of the austenite grain coarsening is evident. The hardenability increases with increasing austenite grain size, because the grain boundary area is decreasing. The formation of upper bainite is much easier when the austenitising temperature is higher and the fraction of this phase is correspondingly higher for a given cooling rate. The reconstructive mechanisms dominate between 2 and 25°C s^{-1}, whilst the displacive mechanisms are dominant between 50 and 200°C s^{-1}. Therefore, the phases forming via displacive mechanisms constitute a larger fraction of the microstructure compared to the case where the austenitisation occurs at a lower temperature.

Therefore it can be concluded that a larger austenite grain size favours displacive transformations and promotes a finer microstructure. This is supported by the analysis of dilation curves, which were a very useful tool for understanding the phase transformations during cooling. Each dilation curve reflected the main transformation mechanisms, it indicated accurately the transformation temperature range and the transformation start and finish temperatures. For a larger austenite grain size, the transformation start temperatures decreased, the effect being more marked at higher cooling rates. On the other hand, increasing the cooling rate, for a given austenitising temperature, resulted in a decrease in the transformation start temperature.

9.1.2 Characterisation of FCA and Solution to Classification Scheme Problems

The aim of performing continuous cooling heat treatments on alloy Y7N1 was twofold: the study of the microstructure evolution as a function of cooling rate and austenite grain size and the complete characterization of the phases forming under continuous cooling conditions which are the most widely used in industrial context.

The main limits of existing classification schemes is the uncertainty concerned with phase identification of very fine phases that could not be resolved optically and the lack in some cases, of a precise guideline for the identification of phases such as ferrite-carbide aggregates. A typical case in which the classification schemes are of limited value is the identification of microphases. An example of the lack of agreement and information for the classification of a phase is the case of the FCA observed in alloy Y7N1. The consequences of incorrect phase identification are an incomplete and inaccurate understanding of the overall transformation kinetics, especially in the case of continuous cooling heat treatments, and the development of correct model which takes into account all the possible phases forming. In this context, the advantages offered by high resolution techniques have been discussed and the conclusion is an atlas of microstructures observed by means of SEM and TEM, at different magnifications, which can be directly related to the existing classification schemes, therefore aiding confident phase identification especially in the case of fine microstructures. Furthermore, a systematic examination of microstructures observed by means of high resolution SEM, has been carried out for the first time.

The FCA was observed by optical microscopy in alloy Y7N1 after cooling at rates between 5 and 75°C s^{-1}. If observed optically, it had a dark etching response, a 'spongy' appearance and irresolvable features within a single grain. The shape of the grain was irregular and the dimensions ranged from 5 to 40 μm, depending on the heat treatment conditions. The FCA phase did not meet any classification scheme criteria for its correct identification. The phase percentage of the FCA phase was 20% on average at cooling rates ranging between 10 and 60°C s^{-1}. Optically, the etching response was considerably brighter than pearlite. Furthermore, the dimensions of FCA were generally much greater than those of pearlite. On the other hand, the presence of laths was not resolvable, and the use of optical analysis alone could not rule out that its nature was bainitic. The required high magnification analysis showed that the FCA was constituted of a ferritic matrix and interspersed particles, distributed in parallel arrays at low cooling rates and partially interconnected at high cooling rates. The morphologies of the precipitates can be distinguished as small particles, small fibres, small lamellae and partially interconnected particles. At low cooling rates and low austenitising temperatures (e.g. 1100°C and 10°C s^{-1}) the average particle size was 50 nm, whilst small fibres measure on average 80 nm. Small lamellae range between 0.3 and 1μm. The particles, fibres and lamellae were usually distributed in arrays. The spacing between two precipitate arrays ranged between 100 and 400 nm approximately. At low cooling rates and high austenitising temperatures (e.g. 1300°C

and 10°C s^{-1}) the average particle size was 50 nm. The small fibre morphology was more common than particle morphology. The average size of small fibres was 150 nm. Small lamellae ranged between 0.3 and 3 μm. The precipitates were predominantly observed in the form of precipitate arrays whose spacing ranged between 100 and 400 nm approximately. When the cooling rate was increased (i.e. 50°C s^{-1}) another type of morphology was observed in addition to particles and small fibres: a 'tadpole-shaped' precipitate was observed. Furthermore, the precipitates appeared to be partially interconnected. Small lamellae formation did not take place. When precipitation occurred in arrays, the spacing between the arrays was smaller than at lower cooling rates and it usually ranged between 50 and 300 nm. These considerations apply to both austenitising temperatures.

The microhardness analysis showed that the hardness of the FCA phase was very close to that of primary ferrite and pearlite, and significantly lower than that of bainite or martensite.

Ageing experiments carried out at 200 and 400°C for 3, 6 and 9 hours showed no variation in the characteristics of the FCA phase, although in some cases a slight coarsening of the precipitates was encountered. The FCA phase appeared to be very stable.

The TEM thin foil analysis provided evidence that the matrix of the FCA phase was ferritic. The analysis of the second phase showed that the nature of the precipitates was cementite. However, the analysis of the partially interconnected precipitates forming at high cooling rates did not provide useful data due to the poor quality of the patterns.

The EBSD analysis confirmed the absence of a lath structure in the FCA grains. The orientation within a single FCA grain was uniform and was very similar to the orientation characteristics observed for primary ferrite. Slight changes in orientation have been found to correspond to peculiar boundaries within single FCA grains. These boundaries always indicate a change in the orientation of precipitation of the carbides. Usually a high angle boundary separates the FCA grain from the adjacent grains. The opposite happens in the case of pearlite, which has usually a coherent boundary (at which nucleation has taken place) with the adjacent ferrite grain. The EBSD data support the hypothesis of a reconstructive type of transformation involved with the FCA formation.

9.1.3 Transformation Sequence Assessment

Interrupted continuous cooling experiments have allowed the accumulation of enough evidence in order to assess a transformation sequence. It was shown that at low cooling rates the formation of FCA takes place at lower temperatures than pearlite, and it is associated with Widmanstätten ferrite, whose formation precedes it. This is very different from pearlite formation (whose morphology is that of small grains between larger ferrite grains) which takes place after primary ferrite has formed, or eventually contemporarily to Widmanstätten ferrite, when the microphase regions between the sideplates have the chance to transform into pearlite. The formation of bainite at higher cooling rates, instead, occurs at lower temperatures, after FCA formation has taken place. It is useful to highlight the transformation sequence in order to understand the effects of manganese on the FCA formation in addition to trying to better understand the nature of such a phase. The experiments also highlighted the importance of the local composition profile, especially the role of carbon.

9.1.4 Compositional effects

The investigation of the effects of composition and, in particular, the variation of manganese has focussed on the analysis of two alloys, HOM148 with a high manganese content, and HOM146 having a low manganese content. The various investigations carried out have led to the conclusion that low manganese content favours the formation of FCA and shifts the cooling rate range to higher cooling rates. Furthermore, the volume fraction of FCA increases as the manganese content decreases. Low manganese additions cause the opposite effects.

In both alloys the shape of the particles in the FCA regions was more irregular compared to alloy Y7N1 and the interconnected particles were the most common morphology encountered. For high manganese (alloy HOM148) the presence of small lamellae was not observed. Small discrete particles were still present, although they were not the dominant morphology. In fact, when precipitation occurred in arrays the precipitates were usually irregularly shaped and the spacing between the arrays ranged usually between 100 and 200 nm. The average particle size was 50 μm, whereas in the case of the 'tadpole-shaped' precipitates, the average size was 250 nm for both alloys. The presence of particles was very limited. When the manganese

content is decreased (alloy HOM146), the formation of irregularly shaped precipitates, which were in some case discrete and in others interconnected, took place at lower cooling rates (e.g. 10°C s^{-1}). It is very interesting that many precipitates appeared as elongated branched fibres. Small lamellae were not observed. On the other hand, the presence of small fibres was significant. The average particle size was 50 μm. The fibres form in arrays and their dimensions were larger than in Y7N1 and HOM148, ranging between 0.2 and 1.5 μm. The average spacing between fibre arrays was 500 nm. The dimensions of the irregularly shaped particles and branched fibres ranges between 40 nm and 1 μm.

The SEM analysis of alloy HOM146 showed that a low manganese content favours the formation of pearlite at very low cooling rates and delays the formation of FCA which needs higher cooling rates to form. As the cooling increases, the austenite transforms mainly into products forming via a diffusion based mechanism or without a strong displacive character. In fact, at 50°C s^{-1} the microstructure was constituted of primary ferrite, coarse Widmanstätten ferrite and FCA, the latter being dominant. This aspect was a main difference between alloy HOM146 and the other two alloys, HOM148 and Y7N1. The effects of decreasing manganese appeared to be beneficial for the formation of FCA. Increasing the manganese content (alloy HOM148) led to the formation of FCA at low cooling rates (e.g. 2°C s^{-1}) but, on the other hand, led to a decrease of the volume fraction of this phase at higher cooling rates (e.g. 50°C s^{-1}), favouring the formation of bainitic ferrite. The microstructure of alloy HOM!48 was fully constituted of bainite and martensite at cooling rates higher than 50°C s^{-1}. Therefore, increasing the manganese content shifted the range of formation, under continuous cooling conditions, of the FCA to lower cooling rates, in addition to promoting the formation of bainitic ferrite.

Taking into account that Mn increases the rate of transformation of bainite, and in practice had the effect of decreasing the volume fraction of FCA, these observations suggest that the kinetics of FCA formation are somewhat intermediate between those of pearlite and those of upper bainite.

The variation of manganese has an effect on the temperature range over which FCA formation occurs. In alloy Y7N1 the formation of FCA took place in the temperature range 620-550°C. In alloy HOM146 the transformation temperature range for FCA was 630-540°C, whilst for alloy HOM148 the range was 500-430°C.

9.1.5 Thermodynamics and Kinetics Considerations

The interrupted continuous cooling experiments proved to be an effective experimental method for the evaluation of the role of carbon in the FCA formation. These experiments showed that the formation of primary ferrite and Widmanstätten ferrite occurring before that of the FCA causes an enrichment in carbon of the untransformed austenite. Such enrichment is a crucial element determining the conditions which allow the FCA to form. Thermodynamic calculations, linked to the results obtained from the continuous cooling heat treatments, led to the construction of a phase diagram suitable for alloy Y7N1. A region in which the FCA formation takes place has been identified, corresponding to a local carbon concentration of approximately 0.4 wt.%. The austenite cooled into this region is not capable of forming bainitic ferrite, whilst the nucleation of cementite is thermodynamically possible. The formation of cementite depletes the surrounding austenitic regions which can eventually transform to ferrite, causing an increase in carbon content of the surrounding austenite.

A correlation between the grain dimensions and the possibility of FCA formation has been found. At low cooling rates, where the formation of pearlite and FCA is contemporarily possible, there is a correlation between the dimensions of the austenite region which transforms into pearlite or FCA and the nature of the transformation product itself. The measurements performed provided an approximate dimension limit of 5 μm above which the FCA formation is favoured. It has to be borne in mind that the pearlite regions are rarely larger than 5 μm and are usually smaller, whilst the FCA regions are on average greater than 5 μm and can reach dimensions of 60 μm in some cases.

The basis for the construction of a reaction theory are quite important especially for the optimization of existing predictive models which do not take into account the formation of FCA. This is the case for a number of models which are capable of predicting the volume fractions of the phases produced under continuous cooling conditions, for a range of steels, which includes the low carbon category.

The phase quantification data showed the influence of austenitising temperatures, cooling rate and chemical composition in quantitative terms. They were fundamental for the determination of the start and finish transformation temperatures for each phase forming during cooling and the production of the CCT diagrams for alloys Y7N1, HOM146 and HOM148. Furthermore, the measured phase quantification results have been used as a means for optimization of existing predictive models.

The CCT diagrams produced are the final result of the microstructural analysis, dilatometry data analysis and phase quantification. The new element in these CCT diagrams is the presence of the FCA phase which provides a more accurate indication needed in order to engineer a certain product with the confidence to achieve the desired properties.

The results in this thesis provide a firm foundation for the detailed analysis and prediction of complex microstructures formed under continuous cooling conditions and are applicable to both steels and steel welds. A thorough microstructural characterisation, fundamental for a further development in this field of research has been achieved and the results obtained represent an aid for a better understanding of the unresolved issues related to simultaneous transformations.

9.2 Further Work

A number of areas of future work have been identified as a result of this research work, and they are discussed below.

Mechanical properties should be investigated for the FCA phase. Specifically, the intrinsic properties of the phase as well as the overall effect on the final properties of the alloy should be better understood. In view of the low hardness of the FCA phase, the influence of its presence on the toughness of the part produced is an aspect that should be considered, together with the behaviour of FCA during crack formation and propagation. This would provide a way to assess the influence of the microstructural differences observed on the final mechanical performance.

The influence of austenite grain size on the formation of FCA, and therefore, on the overall transformations occurring during continuous cooling in the three alloys studied should be further investigated. A critical austenite grain size should be identified in order to suppress the FCA formation.

Focussed ion beam (FIB)/FEGSEM analysis could be a useful technique for a thorough study of the nucleation and growth behaviour of the FCA phase. In particular a sequential analysis of 2D sections of the same sample should be performed in order to obtain a 3D picture of the microstructure where the FCA develops. The experimental information derived from this type of analysis would help assessing the

sites at which the FCA nucleate, the way the phase grows in three dimension and would provide a more systematic understanding of the morphology of the precipitates. On the same way, 3D EBSD maps could then be produced, providing a valuable validation of the results obtained during the present study.

Significant differences were detected in the microstructures of alloys HOM146 and HOM148 in relation to compositional changes. It is therefore necessary to widen the range of alloy compositions so that a detailed and systematic set of data regarding the microstructural evolution of low carbon, low alloy steels, including the compositional limits within which the FCA can form, can be achieved. Furthermore, the production of more CCT diagrams would be possible.

A crystallographic orientation relation between the precipitates in the FCA and the ferritic matrix should be achieved. This can be successfully done by obtaining patterns of high quality from the second phase, which could be suitable for such an analysis. Still, this task represents a very challenging task due to the magnetic nature of the phase.

The carbon content in the FCA should be quantitatively determined in order to understand accurately the conditions under which FCA can form. In this context, the use of dual beam FIB to produce a sharp tip suitable for atom analysis could be the solution[51]. The use of FIB can effectively substitute the limitations connected to electropolishing, therefore allowing the identification of FCA prior the production of the tip. In fact, the advantage of atom probe is the complete determination of the composition. If accurate data related to the composition could be gathered, the possibility of interphase precipitation could therefore be better investigated.

Improved modelling approaches should be developed. These are essential to allow for carbon diffusion and spatial position prediction. For this purpose numerical modelling scheme using two dimensional finite difference methods might be appropriate. In order to develop a suitable model, the bases for the transformation mechanism for FCA formation have been discussed.